UNIVERSITY OF LIVERPOOL

# Super-resolution imaging to investigate the nanoscale localisation of proteins

Thesis submitted in accordance with the requirements of the University of Liverpool for the degree of Doctor in Philosophy by

**Jennifer Elizabeth Francis**

November 2018

## Acknowledgments

Firstly, I would like to thank my primary supervisor Raphaël Lévy, who shaped me into the independent scientist I am today. Special thanks also goes to collaborators Violaine Sée, Helen Wright, and Kevin Hamill who generously shared their knowledge, resources, and time in proofreading parts of this thesis. I also extend my gratitude to colleagues of laboratory B and the Liverpool Centre for Cell Imaging (CCI) team, including Jen Adcott, Marco Marcello, and David Mason, whose expertise and assistance was invaluable to this project. Working within the field of super-resolution microscopy, it was a privilege to undertake an internship at Carl Zeiss Microscopy GmbH in Jena under the supervision of Thomas Kalkbrenner, who kindly introduced me to the world of research and development outside of academia. I am also particularly grateful to Peter Dedecker who made me feel welcome during a visit to his laboratory at KU Leuven in Belgium. I dedicate this thesis to my loving parents who have always been there to offer kind words of encouragement and motivation to spur me on. This PhD journey has been a life-changing experience and now that it has come to an end I look forward to the exciting opportunities that this new chapter in life holds.

## Abstract

Any optical microscopy technique that overcomes the diffraction limit of light (250 nm) is considered to be super-resolution. Super-resolution optical fluctuation imaging (SOFI) can resolve structures below 250 nm by correlating fluctuations from probes that repeatedly switch between a fluorescent and non-fluorescent state. SOFI exists as an open-source algorithm that can be applied to fluorescent images from any optical system without additional hardware. Previous publications demonstrated the resolving capability of SOFI on filamentous structures without addressing any specific biological question. Therefore, through interdisciplinary collaboration, this work aimed to use SOFI as a tool to investigate complex biological systems. Several different proteins including hypoxia inducible factor two alpha (HIF-2α), components of neutrophil extracellular traps (NETs), and extracellular matrix (ECM) proteins such as laminins were resolved with SOFI by labelling their structures with a suitable fluctuating probe. Quantum dots (Qdots) have advantageous photophysical properties for SOFI, but they cannot specifically label nuclear proteins, so alternative approaches were employed, including the use of reversibly switching fluorescent proteins (RSFPs). The localisation of HIF-2α into speckles and its interaction with other HIF-related proteins was investigated using SOFI. Potential co-localisation of laminin N-terminus alpha 31 (LaNt α31) and laminin alpha 3 (LM α3), a subunit of laminin-332 (LM-332), was also more accurately probed using two-colour SOFI. Moreover, other super-resolution techniques were explored, including super-resolution radial fluctuations (SRRF), which enabled the fast-moving protein HIF-2α to be super-resolved in live cells. To achieve optimal super-resolution images, acquisition and post-processing parameters were stringently tested, with the image quality and resolution determined using quantitative software, such as the ImageJ plugin NanoJ-Super-resolution quantitative image rating and reporting of error locations (SQUIRREL). As well as two-dimensional (2D) SOFI, the reconstruction of three-dimensional (3D) SOFI images was also explored, to obtain additional z information about the protein of interest. Overall, using total internal reflection fluorescence (TIRF), light-sheet, and epifluorescence microscopy, a resolution enhancement for different proteins was achieved with SOFI by exploiting the random blinking of Qdots and using the RSFP Skylan-S. Through out-of-focus light removal and enhanced signal-to-noise ratio (SNR), additional structural information was obtained about several proteins, which could help to better understand their involvement in biological mechanisms related to pathological disease, which subsequently could lead to the development of new therapeutic targets in the future.

Table of contents

## Abbreviations and acronyms

σ: Standard deviation

2D: Two-dimensional

3D: Three-dimensional

ACTN4: Actinin four

AFM: Atomic force microscopy

ARNT: Aryl hydrocarbon receptor

BCA: Bicinchoninic acid

BSA: Bovine serum albumin

bSOFI: Balanced SOFI

CARE: Content-aware image restoration

CBP: CREB binding protein

CCD: Charged-coupled device

CCI: Centre for cell imaging

Cdots: Carbon nanodots

CdSe: Cadmium selenide

CdTe: Cadmium telluride

CitH3: Citruillinated histone H3

CLEM: Correlative light and electron microscopy

CLSM: Confocal laser scanning microscope

CMOS: Complementary metal oxide semiconductor

CPU: Central processing unit

Cy5: Cyanine 5

DANA: DNA area and NETosis analysis

DIBO: Dibenzocyclooctyne

DIC: Differential interference contrast

DMEM: Dulbecco's modified Eagle's medium

DMOG: Dimethyloxalylglycine

DMSO: Dimethyl sulfoxide

DNA: Deoxyribonucleic acid

dSTORM: Direct STORM

ECM: Extracellular matrix

EDC: 1-ethyl-3-(3-dimethylaminopropyl) carbodiimide

EGFP: Enhanced green fluorescent protein

ELISA: Enzyme-linked immunosorbent assay

EM: Electron microscopy

EMCCD: Electron-multiplying charge-coupled device

EPAS1: Endothelial PAS domain protein one

EPO: Erythropoietin

FACS: Fluorescence activated cell sorting

FAPs: Fluorogen-activating-proteins

FBS: Foetal bovine serum

FCS: Fluorescence correlation spectroscopy

FFT: Fast Fourier transform

FIH: Factor inhibiting HIF

FIRE: Fourier Image REsolution

FITC: Fluorescein isothiocyanate

FOV: Field-of-view

FRAP: Fluorescence recovery after photobleaching

FRC: Fourier ring correlation

FRET: Förster resonance energy transfer

FSC: Fourier shell correlation

FWHM: Full-width at half-maximum

GaAsP: Gallium Arsenide Phosphide

GAG: Glycosaminoglycan

GFP: Green fluorescent protein

GPU: Graphics processing unit

GUI: Graphical user interface

HA: Hyaluronan

HAF: Hypoxia associated factor

HIF: Hypoxia inducible factor

HILO: Highly inclined and laminated optical sheet

HLF: HIF-1α-like protein

HPLC: High-performance liquid chromatography

HRE: Hypoxia response element

HRF: HIF-related factor

iSIM: Instant structured illumination microscopy

JACoP: Just another co-localisation plugin

JEB: Junctional epidermolysis bullosa

KF: Keloid fibroblasts

LaNt α31: Laminin N-terminus alpha 31

LED: Light-emitting diode

LM α3: Laminin alpha 3

LM-332: Laminin-332

LN: Laminin N-terminal

LSFM: Light-sheet fluorescence microscopy

LUT: Look-up-table

MAP4: Microtubule-associated protein four

MOP2: Members of the PAS super-family two

MPO: Myeloperoxidase

MEA: mercaptoethylamine

MEM: Minimum essential medium

NA: Numerical aperture

NADPH: NOX-dependent NETosis

NaOH: Sodium hydroxide

NE: Neutrophil elastase

NEAA: Non-essential amino acids

NET: Neutrophil extracellular traps

NF: Normal dermal fibroblasts

ODDD: Oxygen dependent degradation domain

PAD4: Peptidylarginine deiminase 4

PAFP: Photoactivatable fluorescent proteins

PALM: Photoactivated localization microscopy

PBS: Phosphate buffered saline

PCFP: Photoconvertible fluorescent protein

PCR: Polymerase chain reaction

PcSOFI: Photochromic SOFI

Pdots: Polymer dots

PEG: polyethylene glycol

PFA: Paraformaldehyde

PHDs: Prolyl-hydroxylase domains

Phospho Ser5 RNA Pol II: Phosphorylated serine 5 ribonucleic acid polymerase two

PL: Photoluminescence

PLA: Proximity ligation assay

PMA: Phorbol-12-myristate-13-acetate

PRILM: Phase ramp imaging localization microscopy

PRISM: Phase retrieval instrument with super-resolution microscopy

PSF: Point spread function

pVHL: Von Hippel-Lindau protein

Qdot: Quantum dot

Qdot-Ab: Qdot-conjugated antibodies

RFP: Red fluorescent protein

ROI: Region of interest

ROS: Reactive oxygen species

RSF: Resolution scaling function

RSFP: Reversibly switching fluorescent protein

RSE: Resolution-scaled error

RSP: Resolution scaled Pearson

RT: Room temperature

SEC: Size-exclusion chromatography

sCMOS: Scientific CMOS

SEM: Scanning electron microscopy

SIM: Structured illumination microscopy

SLE: Systemic lupus erythematosus

SMLM: Single-molecule localization microscopy

SNR: Signal-to-noise ratio

SOFI: Super-resolution optical fluctuation imaging

SPIM: Selective plane illumination microscopy

SQUIRREL: Super-resolution quantitative image rating and reporting of error locations

SRRF: Super-resolution radial fluctuations

STED: Stimulated emission depletion

STORM: Stochastic optical reconstruction microscopy

Sulfo-NHS: Sulfo-N-hydroxysuccinimide

TAE: Tris-acetate-EDTA

TEM: Transmission electron microscopy

TIRF: Total internal reflection fluorescence

UV: Ultra violet

VANIMA: Versatile antibody-based imaging approach

VEGF: Vascular endothelial growth factor

VISION: Variance imaging for super-resolution

ZnS: Zinc sulfide

# Chapter 1: Introduction

## 1.1 Basics of microscopy

### 1.1.1 Brief history of microscopy

Fluorescence microscopy is crucial for visualising structural information of cells, which aids understanding of underlying biological processes. Although brightfield microscopy and differential interference contrast (DIC) are able to obtain limited structural information of unstained cells, most commonly individual structures are probed in fixed cells with fluorescent dyes conjugated to antibodies or in living cells with genetically-encoded fluorescent proteins. These probes emit different wavelengths of light, which enable structures to be differentiated through pseudo-colour. A microscope magnifies objects that are undetectable by the naked eye. Using a magnifying lens a convolved image is formed, which appears as a blurred reconstruction of the original object due to the diffraction of light. This lens-based approach is referred to as far-field microscopy. The use of glass lenses to bend light, which ultimately led to the invention of the microscope, dates back to 1595 when Zacharias Janssen and his father Hans Janssen altered the distance between two lenses inside a tube. However, the first visualisation of organisms with a light microscope was by Dutch draper Antony van Leeuwenhoek and English physicist Robert Hooke in 1665 (1, 2). It was through detailed illustrations in Robert Hooke's published book, Micrographia, that other scientists became aware of microscopy. In the 1850s a German instrument manufacturer, Carl Zeiss, employed Otto Schott to make high quality glass optical lenses, which improved the performance of the microscope and formed the basis of modern microscopes as they are known today. Later in 1911, the first fluorescence microscope was developed.

### 1.1.2 Principle of fluorescence

When a fluorescent molecule is illuminated with a light source, electrons absorb energy of a specific wavelength, become excited, and move to a higher energy level. Fluorescence occurs when electrons later lose energy, fall to a lower energy level or ground state, and emit a photon (Figure 1). Some vibrational energy is also dissipated as heat in a process known as internal conversion. Electrons may also transition from the lowest energy level to a triplet state via intersystem crossing, where phosphorescence occurs if electrons later return to the

ground state. The time taken for electrons to return to the ground state is referred to as fluorescence lifetime, whilst the difference between absorption and emission wavelength of a fluorescent molecule is known as Stokes shift (3).

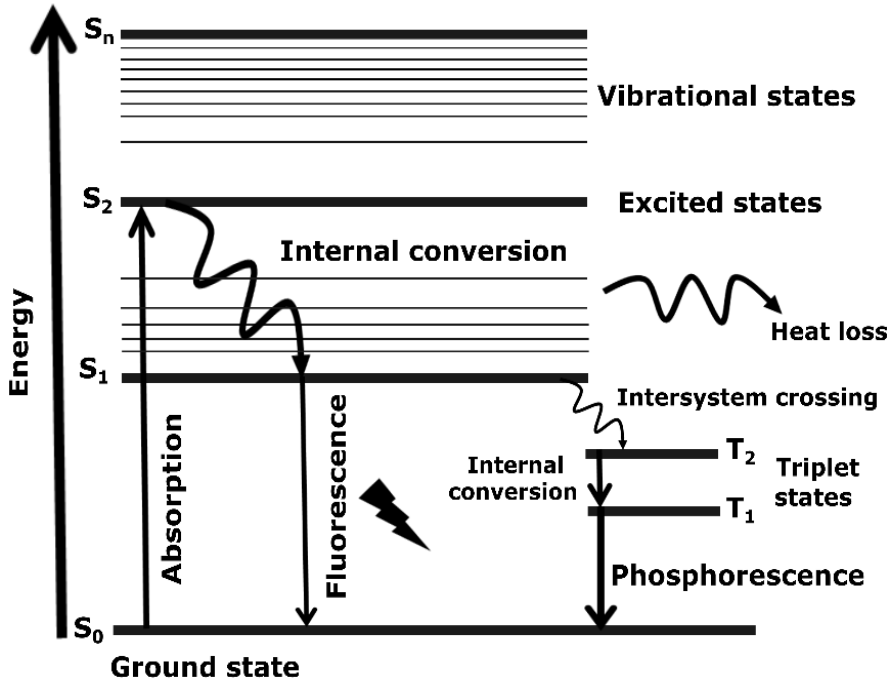


**Figure 1. Jablonski diagram depicting the process of fluorescence.** Electrons absorb light energy of a specific wavelength and become excited, moving to higher energy levels ($S_1$-$S_3$). When electrons lose energy, they fall to a lower energy level or ground state ($S_0$) and emit a photon (fluorescence). Electrons can also transition from the triplet state ($T_1$) to $S_0$, resulting in phosphorescence.

### 1.1.3 Definition of resolution

Resolution is defined as the ability to distinguish two objects that are in close proximity. The attainable resolution of a wide-field microscope is restricted by the diffraction of light to 250 nm laterally (half the λ of light) and 500 nm axially (4). Ernst Abbe derived a formula in 1873 to describe resolution (5), $d = \lambda/2nSin\theta$ (Figure 2), which states that resolution (d) is dependent on the emission wavelength of the dye (λ) and the numerical aperture (NA) of the objective lens, since $d = \lambda/2NA$. NA is equal to $nSin\theta$, where n is the sample medium refractive index and θ is the maximum angle of light the objective can collect.


**Figure 2. Ernst Abbe memorial containing the formula of resolution.** Friedrich Schiller University of Jena in Germany placed a stone to commemorate Ernst Abbe who determined that resolution (d) is equal to the wavelength of light (λ) divided by 2nSinθ, where n is the refractive index of the medium between the objective lens and the object of interest.

Ernst Abbe was the first to propose the resolution limit of an optical system using the wavelength of light and the NA of the objective lens (λ/2NA), to define the smallest object that can be resolved by the system. Rayleigh later published a resolution criterion that not only takes into consideration the wavelength of light and the NA of the objective lens (0.61λ/NA), but also the Airy disk (diffraction of light into concentric rings of decreasing fluorescence intensity from the centre). According to Rayleigh, two objects are considered to be resolved if the centre of their Airy disks do not overlap and is defined as being the minimum angular distance between the centre of one diffraction pattern and the centre of an adjacent diffraction pattern. In this way, two point emitters can only be identified as individual objects if they are at a minimum distance of 250 nm apart; this concept is known as the Rayleigh criterion (6) (Figure 3). When there is an improvement in resolution, features in an image can be more distinguished. According to the Rayleigh criterion, the spatial resolution of a microscope is 0.61λ/NA, which is the Airy disk diameter. The shape of the point spread function (PSF) is defined as an Airy disk, whereby any point emitter will appear as a blurred spot, with a bright centre surrounded by lower intensity rings when imaged on a microscope. The PSF can be fitted with a Gaussian function to determine the resolving

capability of an optical setup. Typically, the full-width at half-maximum (FWHM) of the PSF can be calculated as a measure of spatial resolution (FWHM ≈ 0.353λ/NA or $2\sqrt{2ln2} * \sigma$ or 2.35482*σ, where σ is the standard deviation) (7). The narrower the FWHM, the better the resolution of a microscope.

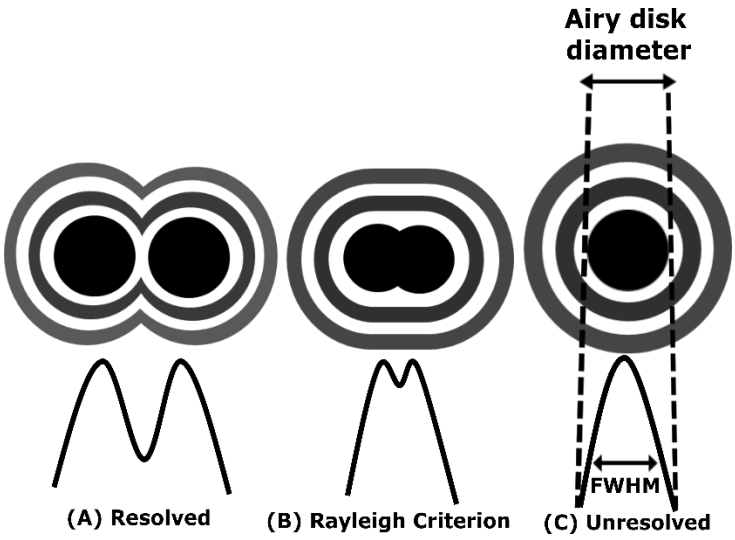


**Figure 3. Schematic of the Rayleigh criterion.** Intensity curves for the radial distribution of diffracted light for different separations with circles depicting fluorescent molecules. When two fluorescent molecules are separated by a distance greater than 250 nm apart, they are fully resolved with two intensity peaks (A). Exactly 250 nm apart, the fluorescent molecules can still be distinguished as separate molecules, known as the Rayleigh criterion (B); whilst the fluorescent molecules will be unresolved if they are less than 250 nm apart and will display as only one peak (C).

### 1.1.4 Sampling

An object is convolved with the PSF of the optical system and its analog signal is converted into a digital signal, which is represented as a reconstructed digital image consisting of pixels with intensity values. Spatial resolution of a digital image is affected by the sampling interval, which is the number of pixels per unit distance in the image (pixel size). To achieve optimum spatial resolution and accurately reconstruct a digital image of an object, Nyquist sampling must be adhered to. Increasing the magnification of the objective lens does not affect the attainable resolution, but it does make the pixel size smaller. Similarly, increasing the number of pixels of an image does not necessarily improve the resolution of a microscope, but satisfying the Shannon-Nyquist sampling theorem during acquisition ensures that the optimal image resolution (axial resolution in the z-direction and lateral resolution in the xy direction) is obtained (8, 9). Over-sampling (small pixel size) occurs when the sampling interval is smaller than required, so more information is recorded than necessary, which does

not give any additional information, and therefore does not further improve image resolution. Since the signal in an over-sampled image may be reduced, longer exposure times are needed to compensate for this loss in signal, which in turn may photobleach the sample (10). In contrast, under-sampling is when the sampling interval is too large to capture all of the information correctly, causing spatial aliasing artefacts, and, therefore, does not represent the object, because structures cannot be discerned. If the pixel size is too large, the PSF will be concentrated within too few pixels (under-sampled) and there will be insufficient spatial resolution, as information will be lost. Nyquist sampling is the maximum sampling interval in which the main information is captured to accurately represent the structure being imaged; it is dependent on the resolving power of the optical setup and the pixel size of the detector.

Nyquist sampling for an objective is calculated based on the resolving power of the optical system (NA) and not the magnification used (λ/NA), whereas for an object the sampling interval (pixel size of the image) is dependent on the magnification (physical size of one pixel on the detector divided by the total magnification of the optical system). To determine the correct sampling interval to use, the ratio of resolution of the optical system and pixel size of the image is calculated. According to Ernst Abbe, to satisfy Nyquist, the sampling interval (pixel size in the image) must be at least two-times smaller than the smallest object in the image that can be resolved by the detector (λ/2NA) (11, 12). Therefore, when using a camera based microscope, the resolution (λ/2NA) using a 100x objective with an NA of 1.4 and a red dye with an emission wavelength of 625 nm would be approximately 223 nm (size of the smallest resolvable object). The pixel size of the image should be two-times smaller than 223 nm, so the image should be sampled every 111.5 nm. If the physical size of one pixel on the charged-coupled device (CCD) camera is 16 µm, then the pixel size of the image would be 160 nm (<111.5 nm). With these parameters, the image would be under-sampled and Nyquist sampling not satisfied, because a ratio of $\frac{\text{Calculated resolution (nm)}}{\text{Calculated pixel size (nm)}}$ would not be at least half the size of the smallest resolvable structure in the image (>2) (Table 1).

| Magnification | Magnifying lens | λ (nm) | NA | Physical pixel size (μm) | Calculated resolution (nm) | Calculated pixel size (nm) | Satisfy Nyquist Sampling? |
|---|---|---|---|---|---|---|---|
| 63x | 1 | 625 | 1.4 | 16 | 223 | 254 | Under-sampled (0.9 < 2) |
| 100x | 1 | 625 | 1.4 | 16 | 223 | 160 | Under-sampled (1.4 < 2) |
| 63x | 1.6 | 625 | 1.4 | 16 | 223 | 159 | Under-sampled (1.4 < 2) |
| 100x | 1.6 | 625 | 1.4 | 16 | 223 | 100 | Nyquist-sampled (2.2 > 2) |
| 63x | 2.5 | 625 | 1.4 | 16 | 223 | 102 | Nyquist-sampled (2.2 > 2) |
| 100x | 2.5 | 625 | 1.4 | 16 | 223 | 64 | Over-sampled (3.5 > 2) |

**Table 1: Conditions to meet Nyquist sampling with a camera based microscope.** Theoretical calculations to determine whether the Nyquist sampling criterion will be met are dependent on the resolution of the microscope and the pixel size. For Nyquist sampling to be satisfied, the sampling interval should be less than two-times smaller than the smallest resolvable structure. A ratio of calculated resolution/calculated pixel size gives the factor by which the sampling would be smaller than the smallest resolvable structure.

### 1.1.5 Imaging in three-dimensions

Although satisfying Nyquist sampling ensures that the best attainable image resolution is achieved for 2D images, the axial resolution is still poor in comparison to lateral resolution. Whilst 2D imaging is commonly used amongst biologists, with traditional *in vitro* methods involving cell monolayers grown on glass coverslips, this only partially represents the true structure of 3D samples, which can make any interpretation of dynamic information misleading (13). For this reason, the use of 3D imaging has increased over the last decade, through the use of optical sectioning, to better understand biological processes. To improve z-resolution and provide additional depth information, optical sectioning can be done using a confocal laser scanning microscope (CLSM), which was first commercially developed in 1982 by Colin Sheppard (14). With wide-field microscopy the entire sample is illuminated, whilst with CLSM the sample is scanned with a laser line-by-line. Light is focused through a

pinhole and photons are wasted, which at first seems illogical, but it is this removal of out-of-focus light that improves the SNR of images compared to wide-field microscopy. Despite this, CLSM is not suited to imaging deep tissues, so instead multiphoton can be used (15). Although challenging, imaging in 3D (x, y, and z), giving voxels (volume pixels), has also been achieved with astigmatism (16) and with the use of phase ramp imaging localization microscopy (PRILM) (17). Astigmatism employs a cylindrical-shaped lens in the optical path, which causes there to be two focal planes for x and y. As the fluorophore changes its z-position, the image orientation is also changed (16). Instead, PRILM splits the PSF of the fluorophore into two equal lobes; where the angle of the lobes depends on their z-position (17). Although similar to the double-helix PSF approach, with PRILM these two lobes do not move circularly, but instead have a linear motion (17). The use of PRILM, however, does cause the signal to be dimmer, since it splits the fluorescent emitter equally into two lobes. PSF engineering has more recently been used to spectrally separate multiple emitters and simultaneously acquire a dual-colour super-resolution image. To obtain a complex multicolour super-resolution image, the channels must either be acquired sequentially or a set up with more than one camera must be used and filters employed to image different spectral colour emissions. However, colour has been encoded into the PSF through the use of optical phase masks with different PSFs for specific wavelengths of light. To achieve a dual-colour super-resolution image simultaneously, the PSF can be vertically elongated for the red emitter and horizontally elongated for the green emitter. In this way, colour can be assigned according to the direction of elongation. Although a complex design is required, up to 5 different colours have been encoded thus far (18).

### 1.1.6 Deconvolution

To further improve the quality of images in all three directions, deconvolution was introduced to the microscopy community in 1983 (19). Deconvolution is a post-processing imaging technique based on the PSF, which can re-assign out-of-focus light to restore the degraded signal so that the image better resembles the original object with greater contrast and SNR (20). There are many such algorithms available, including the most widely used Lucy-Richardson deconvolution (21, 22), which is iterative so may be repeated until an improved version of the image is estimated. Commercial deconvolution such as Huygens and open-

source deconvolution, such as the ImageJ plugin DeconvolutionLab2 has also been developed by the Biomedical Imaging Group at École Polytechnique Fédérale de Lausanne.

### 1.1.7 Super-resolution imaging

Despite the addition of deconvolution to sharpen conventional images, the attainable resolution is still not much better than the diffraction limit of light, however, most of the interesting biology occurs below the diffraction limit of light. Many advanced microscopy techniques have, therefore, been developed to overcome this diffraction limiting barrier and resolve beyond 250 nm; this field is referred to as super-resolution microscopy. The 2014 Nobel Prize in Chemistry was jointly awarded to three scientists: Eric Betzig, William E. Moerner, and Stefan Hell, for their contributions to the development of super-resolution microscopy. A hallmark of a super-resolution technique is when structural details are discerned that would otherwise not be possible with conventional diffraction-limited microscopy; e.g., the ability to study the organisation of focal adhesion proteins at the nanoscale (23). Each super-resolution microscopy technique has pros and cons associated with its use, with either the spatial or temporal resolution being compromised. The most expensive aspect of super-resolution microscopy is the equipment required to acquire the images, which varies from technique to technique. One such expense is the use of a camera, such as an electron-multiplying charged-coupled device (EMCCD). However, super-resolution imaging has successfully been performed on a mobile phone (24) and an industry-grade complementary metal oxide semiconductor (CMOS) camera, which are much more affordable options (25), compared to scientific-grade CMOS (sCMOS). As well as having a larger number of pixels, the pixel size on sCMOS camera chips are also smaller than that of EMCCD cameras, which enables higher spatial resolution. In addition, sCMOS cameras have a readout speed that is much faster than EMCCD cameras, so are ideal for imaging live cells (26). Although, sCMOS cameras are susceptible to pattern artefacts and perform poorly with dim fluorophores, they have a large field-of-view (FOV) allowing organisms to be imaged.

## 1.2 Microscopy techniques

Over the past 25 years, several microscopy techniques have been developed to further understand biological structures, including those that overcome the diffraction limit of light, to provide information that would otherwise be lost with standard wide-field microscopy. Numerous acronyms exist for the many super-resolution techniques currently available, but most require sophisticated hardware, except for SOFI, SRRF, and single-molecule localization microscopy (SMLM) methods. The resolution attainment of some of the most prominent super-resolution techniques, including stimulated emission depletion (STED), structured illumination microscopy (SIM), stochastic optical reconstruction microscopy (STORM)/photoactivated localization microscopy (PALM), is highlighted below (Figure 4).

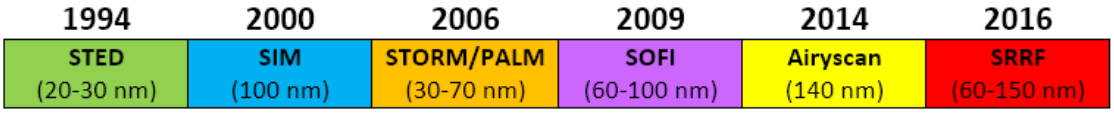


**Figure 4. Super-resolution microscopy timeline.** Development of select super-resolution microscopy techniques over the past 25 years from inception to the present day.

### 1.2.1 Light-sheet fluorescence microscopy

Most super-resolution techniques have high spatial resolution, but require high laser power for acquisition. However, light-sheet fluorescence microscopy (LSFM), otherwise known as selective plane illumination microscopy (SPIM), can image large specimens at a relatively high-resolution, comparable to CLSM, but with low excitation power (27). Unlike wide-field and CLSM, LSFM excites a sample in the focal plane from one side, with a thin sheet of illumination perpendicular to the detection objective (Figure 5). To remove out-of-focus light and improve the SNR of an image, Gaussian Bessel beams can be shaped into sheets of light using cylindrical lenses (28). LSFM also minimises photobleaching, because only a thin (1-10 µm) sheet of light illuminates the sample at any one time, so LSFM offers a gentler approach to optical sectioning than CLSM. LSFM is most suited to imaging whole living organisms such as developing embryos or drosophila, which would otherwise be imaged on a CLSM as fixed physical sections that are stitched together to reconstruct the whole organism. Instead, LSFM can offer deep penetration and thin optical sectioning of live cleared samples, which can capture dynamic processes at a fast acquisition. Images can also be taken at different

angles, to create a 3D multi-view reconstruction. Conventional LSFM has been improved through the use of digital scanned laser LSFM (DSLM) (29), multiple non-diffracting Bessel beams (30), and a lattice light-sheet (31), by creating a narrower sheet of light. The optical sectioning capability of LSFM has also been complemented with super-resolution techniques to further improve the SNR and spatio-temporal resolution (32).

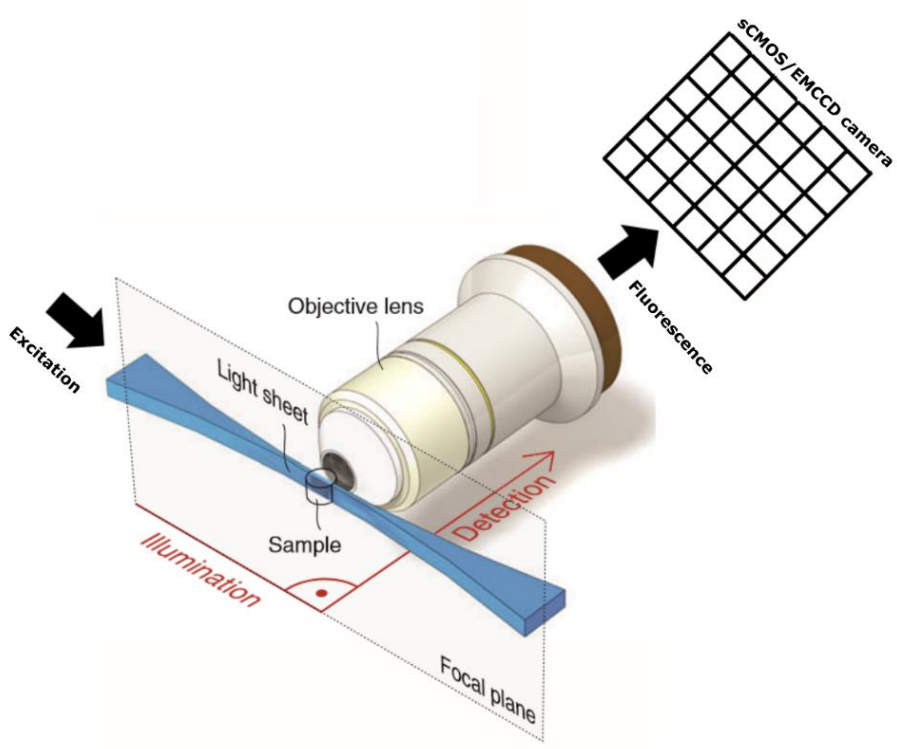


**Figure 5. Concept of conventional LSFM.** A thin sheet of light is used to excite a sample in the focal plane that is perpendicular to the detection objective and an image obtained on a camera. Schematic diagram was adapted from (28).

### 1.2.2. Total internal reflection fluorescence

Another way to remove out-of-focus light, to improve image contrast, is to use TIRF microscopy (33), but this technique only illuminates the surface of cells near the plasma membrane adjacent to the coverslip, and is thus suitable for imaging membrane-bound organelles, the ECM, and focal adhesion proteins. Only adherent cells can be imaged with TIRF and it is not suitable for thick samples. However, since only a thin section of a cell is excited, TIRF yields less phototoxic effects than epifluorescence illumination. If the incidence angle ($\theta_i$) of the excited light is greater than the critical angle ($\theta_c$), when the angle of refraction ($\theta_r$) is 90 °, then the excited light undergoes TIRF. According to Snell's law: $n_1 \sin\theta_i$

= $n_2 \sin\theta_r$ ($n_1$ and $n_2$ is the refractive index of the coverslip and sample, respectively), TIRF only takes place if $n_1$ is greater than $n_2$. Most of the incident light is reflected, but in the case of TIRF some energy from the incident light reaches the sample, not as a propagating wave, but an evanescent wave (opposite of epifluorescence) (Figure 6). In contrast to epifluorescence, where all of the fluorescent molecules are excited with light, only those that are within the evanescent wave, approximately 100 nm away from the coverslip, will be excited (34). Akin to TIRF, another microscopy technique called highly inclined and laminated optical sheet (HILO) has been developed to achieve higher SNR images, by using an inclined illumination beam (35). The incident beam of light is highly inclined and refracted by a large angle to form a thin sheet of light, which excites fluorescent molecules at the coverslip-sample surface (35). TIRF only allows single-molecule imaging, at the cell surface, whereas HILO can perform single-molecule imaging inside of cells.

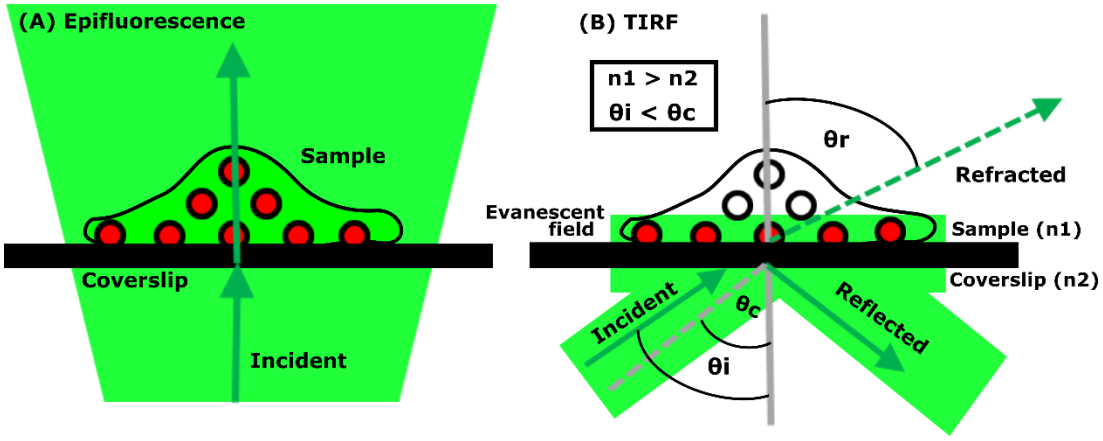


**Figure 6. Principle of epifluorescence versus TIRF illumination.** In epifluorescence microscopy, the excited light propagates to the entire sample, because it passes directly through the coverslip (A). TIRF only excites fluorescent molecules that are approximately 100 nm away from the coverslip, because the incident angle ($\theta_i$) is greater than the critical angle ($\theta_c$). Whilst most of the excited light is reflected off the coverslip, some is refracted and goes to the sample, creating an evanescent wave (B).

### 1.2.3 Electron microscopy

Much higher resolution can be achieved with electron microscopy (EM) than any other microscopy technique, including TIRF and those that are considered to be super-resolution (36). However, dynamics of biological structures cannot be studied with EM, as samples need to be fixed, dehydrated, and imaged in a vacuum; which can often lead to unwanted artefacts. Unlike super-resolution microscopy, EM cannot distinguish specific proteins, since

two-colour EM does not exist. Instead, EM relies on contrast, using metallic nanoparticles, to highlight structures. However, EM has been combined with fluorescence microscopy, to image specific proteins and surrounding structures, in a process called correlative light and electron microscopy (CLEM) (4). EM is fundamentally different from conventional light microscopy, which illuminates a sample with a light source, whereas EM uses magnets to focus a beam of electrons at thin sections (37). This short wavelength of electrons yields high-resolution images compared to conventional wide-field microscopy. There are two types of EM, scanning electron microscopy (SEM) (38) and transmission electron microscopy (TEM) (39). TEM uses a concentrated beam of electrons (transmitted), whereas in SEM an electron beam is scanned across the sample (scattered). Of the two types, TEM gives a higher resolution than SEM and is routinely used to characterise probes, such as high contrast nanoparticles, for use in biological imaging.

### 1.2.4 Atomic force microscopy

Another high-resolution imaging technique, atomic force microscopy (AFM) (40), has been used to investigate biological structures of the nanoscale. There are three AFM imaging modes: contact, non-contact, and tapping. In contact mode, a sharp silicon-coated tip, attached to a cantilever, is raster-scanned across the surface of a sample using a piezo-scanner. During cantilever movement, small nanonewton forces between the micron-sized tip and cell surface, according to Hooke's law, are detected and a laser is reflected off the top of the cantilever. The relative intensity of the deflected laser is subsequently measured using a photodetector (Figure 7). From this measurement, a topographical map of the cell surface can be formed (41). Contact mode is not suited to live biological samples, because the tip can damage cells, so a non-contact mode has been developed, where the tip is not touching the sample, but the cantilever oscillates above the surface near its resonant frequency (42). The third mode, tapping is a combination of contact and non-contact mode, where the cantilever oscillates, but only occasionally touches the surface (43). An advantage of AFM compared to EM, is that the sample preparation is simple as it does not require the use of a vacuum, labelling with dye, or freezing of the specimen (44). Since AFM can only obtain structural information about the surface of cells, it can be combined with super-resolution techniques, to enable the multiplex labelling capability of fluorescence microscopy to more specifically determine the precise localisation of different proteins (45-

47). Apart from red diode lasers, long wavelength infrared (IR) lasers are preferred for AFM, because they prevent photodestruction of fluorescently labelled biological samples (48).

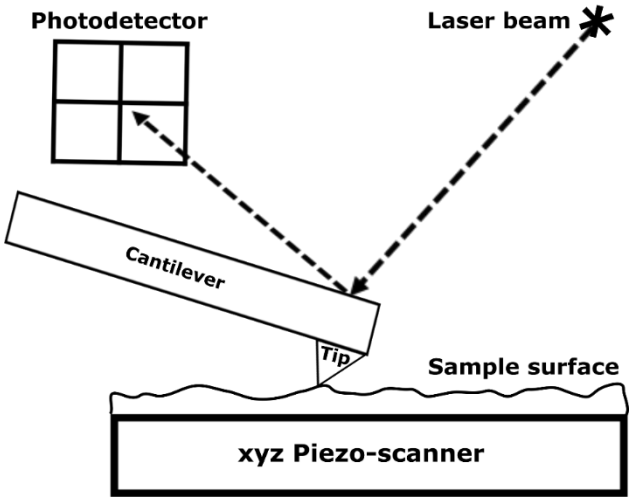


**Figure 7. Principle of contact mode AFM.** A micron-sized silicon tip is attached to a cantilever and moved across a sample surface using a piezo-scanner. During cantilever movement, the laser beam is deflected onto a photodetector and relative intensity of the reflected laser beam is detected.

### 1.2.5 Structured illumination microscopy

Although AFM provides high-resolution images of cell surfaces, it cannot image proteins inside cells, which is why fluorescent super-resolution techniques, such as SIM (49) are used instead. Linear SIM can surpass the resolution limit of light by a factor of two when using conventional fluorophores (50). SIM exploits pattern illumination, through the use of a diffraction grating with a known grid pattern, which is overlaid on an unknown biological structure to form low frequency interference patterns, otherwise referred to as a Moiré fringes (Figure 8). Multiple images are taken by rotating the diffraction grating at different angles, to create new interference patterns that can be post-processed with a Fourier transform (spatial domain is converted to the frequency domain as a set of sine and cosine waves) to produce a high-resolution SIM image (51). Instead of illuminating the sample with uniform light, a pattern of sinusoidal light in the form of a grating of grid lines is used in linear SIM. Interference patterns created are of lower frequency than the pattern of the biological structure, so post-processing is done to extract high resolution information and reconstruct a SIM image. With linear SIM, the spatial frequency obtained is restricted by the diffraction limit of the objective lens and the resolution is improved by a factor of two (100 nm in xy and 250-350 nm in z) (50). However, an interference pattern can be created with higher

frequencies by exploiting non-linear processes of fluorescent dyes, to get much higher resolution (theoretically unlimited), through saturation of fluorescent dyes to produce pattern harmonics in a method called non-linear SIM (52). Most of the fluorescence in non-linear SIM is saturated due to intense illumination and resolution is only limited by photobleaching of dye molecules. An alternative approach to saturated non-linear SIM is to use photoswitchable proteins, which requires less illumination (53).

Despite the improved resolution of non-linear SIM, the rotation of a physical grating and acquisition of multiple images means that it is not ideal for live cell imaging. Spot-scanning SIM or instant SIM (iSIM) allows faster imaging by removing the need to acquire many images at different angles and subsequently combining these images so that a SIM image can be produced in real-time (54). Using iSIM, motion blur, which typically occurs when acquiring living samples, is minimised. Using optical hardware such as a microlens array, processing is done optically rather than computationally with iSIM. After deconvolution, a two-fold improvement in resolution is attainable in x, y, and z with iSIM, which is comparable to linear SIM. As well as combining SIM with other microscopy techniques, including LSFM (55) and TIRF (56), to offer better optical sectioning, a SIM image has also been achieved in 3D and in multi-colour (57). Although, SIM can be performed with any fluorescent probe, including photoswitchable proteins (53), it is not immune to motion artefacts with fast-moving proteins, so exposure times must be reduced (58). The quality of SIM images can be assessed using the open-source ImageJ plugin SIMcheck (59).

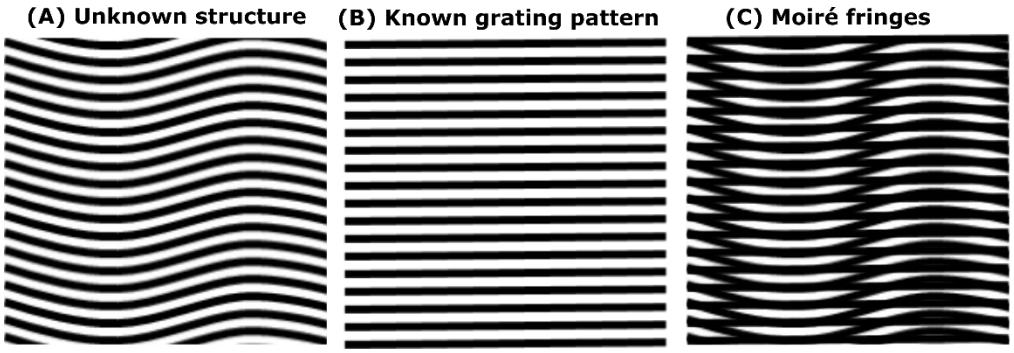


**Figure 8. Principle of SIM.** Unknown pattern of a biological structure (A) is imaged through a diffraction grating that creates illumination of a known pattern (B). The diffraction grating rotates multiple times, to produce images of high spatial frequency that contain Moiré fringes at different orientations (C). These interference patterns are Fourier transformed to yield a SIM image with a factor 2 improvement in spatial resolution compared to conventional wide-field microscopy.

### 1.2.6 Single molecule localization microscopy

Despite SIM surpassing the diffraction limit of light by a factor of two, SMLM techniques such as STORM (60) and PALM (61) are capable of much higher resolution. Compared to conventional wide-field microscopy (250 nm resolution laterally and 500 nm axially), SMLM can achieve 20 nm in xy and 50 nm in z (16). The type of microscope and the choice of fluorescent probe differentiates STORM from PALM. STORM typically uses conventional photoswitchable dyes such as Alexa Fluor 647 with the addition of an oxygen scavenger system containing glucose oxidase and a thiol such as mercaptoethylamine, whereas PALM uses photoswitchable proteins such as Dronpa. STORM was first demonstrated by Rust in 2006 using Cy3-Cy5 pairs as the optical switch to activate a subset of fluorophores (60). Heilemann later introduced a variant of STORM in 2008 called direct STORM (dSTORM), which uses conventional photoswitchable fluorescent probes that are able to be reversibly switched between a fluorescent and a non-fluorescent state using different wavelengths of light, without requiring an activator fluorophore (62).

SMLM uses particle detection to achieve high resolution. Although a fluorophore is only nanometres in size, its image appears larger with an approximate Gaussian intensity profile. The position of the fluorophore can be determined with nanometre precision by fitting its PSF. When multiple fluorophores are positioned close together such that they are separated by a distance less than the PSF width of the optical system, they overlap, and this prevents their accurate localisation. A solution is to use optically switchable fluorophores: molecules that can be switched from a non-fluorescent to fluorescent state by exposure to high intensity illumination. The fluorescence emission can be controlled so that only a sparse subset of fluorophores are activated to ensure that individual fluorescent molecules are not overlapping, allowing each to be localised with high precision. When fluorophores are deactivated, a new subset of fluorophores can then be activated and imaged. The process is repeated over thousands of frames until nearly all of the fluorescent molecules have been imaged. The positons of all of the imaged fluorescent molecules are detected, their centres located, and fitted with a Gaussian function using a measured PSF to reconstruct a super-resolution image (Figure 9). A disadvantage of using SMLM is that is requires a large number of frames (for example 30,000) and stationary fluorophores, which is not applicable for live cell imaging, to capture dynamics. However, two-colour SMLM has been used to capture slow moving proteins, such as focal adhesions (23, 63).

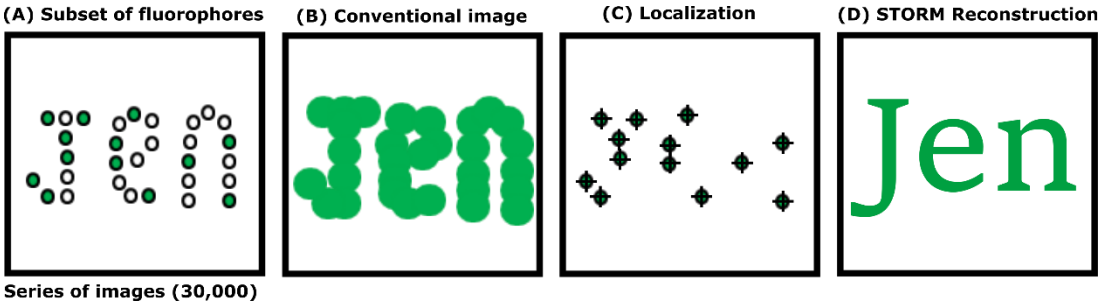


**Figure 9. Principle of SMLM.** A structure of interest is labelled with a fluorescent probe and single molecules are switched on in subsets, at different time points (A). A conventional image is formed (B). Individual molecules are localised (C), and a super-resolution image reconstructed (D).

### 1.2.7 Stimulated emission depletion

Analogous to SMLM, STED microscopy can also achieve high-resolution, but without the need for photoswitching fluorophores. STED was first introduced by Stefan Hell in 1994 and improves the resolution of CLSM to less than 50 nm in xy (64). STED involves the use of two overlapping laser beams. One laser beam excites the fluorescent molecules and a second doughnut-shaped laser beam is used to deplete the fluorescence, by returning electrons back to the ground state, except the centre of the doughnut-shape (Figure 10). In this way, the PSF is engineered to be reduced. The doughnut-shaped laser beam can be created by passing the laser through a phase mask (glass of varying thickness). The excitation and co-aligned doughnut-shaped laser beam are scanned across the sample, so that only a subset of fluorescent molecules are capable of emitting a signal (65). After a STED image is obtained, no post-processing is required, but Huygens deconvolution can be applied. Theoretically, any synthetic organic dye (66) or fluorescent protein (67) can be used for STED, but in practice, those that are bright and less susceptible to photobleaching, such as ATTO647N, are preferred. A commercially available STED system is provided by Leica and Abberior Instruments GmbH, which makes STED more accessible to biologists than SMLM methods that require knowledge of photoswitchable fluorophores. However, STED is expensive compared to freely available super-resolution algorithms such as SOFI and SRRF. Conventional fluorescent beads or commercially available deoxyribonucleic acid (DNA) nanorulers from GATTAquant can be used to calibrate a STED instrument (68). STED has been combined with other techniques including fluorescence correlation spectroscopy (FCS) (69) and dual-colour 3D STED has been successfully achieved (70). However, due to the high intensity lasers used, live cell imaging with STED is difficult, due to the phototoxic effects.

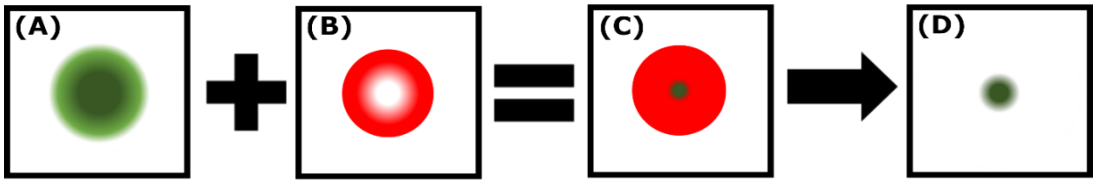


**Figure 10. Concept of STED.** A molecule is excited with a short laser (A) and a longer STED doughnut-shaped beam (B) depletes fluorescence, except the centre of the doughnut-shape (C). This depleted fluorescence, yields a smaller effective PSF (D).

### 1.2.8 Airyscan

An additional high-resolution CLSM technique Airyscan is commercially available from Carl Zeiss Microscopy GmbH. In CLSM the sample is illuminated with a scanned focused laser beam. The emitted fluorescence is sent to a detector through a pinhole, which rejects out-of-focus light. Making the pinhole smaller increases resolution, but decreases SNR. Airyscan improves both the SNR and resolution of images by re-distributing light that would otherwise be rejected by the confocal pinhole, through the previously documented pixel re-assignment method (71). In CLSM there is one pinhole, whereas an Airyscan detector consists of 32 Gallium Arsenide Phosphide (GaAsP) detector elements arranged in a hexagonal array. With Airyscan (1.25AU) a bigger area is scanned than confocal (1AU), because each hexagonal detector element is considered as an individual pinhole (0.2 AU). All of the emission light is collected with Airyscan, because the confocal pinhole remains open, so additional spatial information is obtained. The central detector element has the highest fluorescence intensity and smallest PSF, so signals from offset detector elements are re-assigned to this position and summed to a yield a final Airyscan image with a smaller PSF and higher SNR (Figure 11). In this way, lateral resolution of 140 nm and axial resolution of 400 nm is possible (72). Unlike SMLM, Airyscan can image structures in live cells, without the need for photoswitchable fluorophores and with less illumination than STED (73).

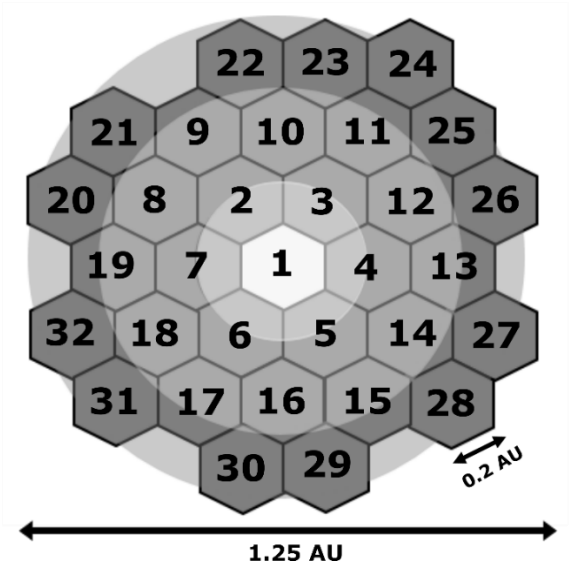


**Figure 11. Airyscan honeycomb-shaped detector.** The 32 GaAsP elements that make up the honeycomb-shaped detector. For a high-resolution Airyscan image, the pinhole can be set to 1.25 Airy units (AU), where each detector is 0.2 AU.

### 1.2.9 Post-processing super-resolution techniques

#### 1.2.9.1 Super-resolution radial fluctuations

##### 1.2.9.1.1 Principle of SRRF

Aside from super-resolution implementations that require sophisticated hardware, Ricardo Henriques' group at University College London, UK, recently developed SRRF, pronounced surf, which is an open-source ImageJ plugin called NanoJ-SRRF (74). SRRF is based on the already theoretically documented radial fluctuations concept (75) and involves analysing the degree of local intensity gradient convergence in a series of wide-field images to generate a super-resolution reconstruction. Resolution in the order of 60-150 nm is possible with SRRF, with as little as 100 frames, and multi-colour achieved through sequential acquisition of different channels. Although SMLM has achieved resolutions beyond 60 nm, it is limited to fixed cells. SRRF has been demonstrated in live cells and can be used with a wide-range of microscopes, including confocal (76) and TIRF (77). SRRF can also be performed with conventional dyes, without the need for blinking. The minimal illumination required for SRRF also means that it is less phototoxic to cells than SMLM and STED. As well as low power illumination, SRRF has a fast acquisition time (1 s) and reduces non-linear response to brightness. To compensate for SRRF being computationally demanding, a graphics

processing unit (GPU) with 240 cores can be used in replace of a central processing unit (CPU) with 4 core processors, for example. SRRF-Stream is commercially available by the company Andor Technology, which allows a real-time SRRF image to be formed. Although, SRRF improves resolution in xy (60-150 nm), it is limited in z to 600 nm, so 3D SRRF is not possible.

During SRRF-processing, pixels (picture elements) are magnified into sub-pixels. For every sub-pixel, a non-binary value (a value that is neither 0 nor 1), termed radiality, is assigned based on the probability of a fluorescent molecule being present within that sub-pixel. For every sub-pixel in the image, radiality is measured according to how the intensity of a sub-pixel containing a fluorescent molecule converges towards a central sub-pixel within a symmetrical circular radius of known size (Figure 12). Those sub-pixels closest to the centre of a fluorescent molecule will be assigned a high radiality value, because the convergence of fluorescent intensity will be high, whereas those sub-pixels further away from a fluorescent molecule will be given a low radiality value (78). In this way, a new stack of radiality images are formed, containing sub-pixels with non-binary values. Temporal correlation analysis of fluctuations in the radiality stack can then be performed, to yield a SRRF image.

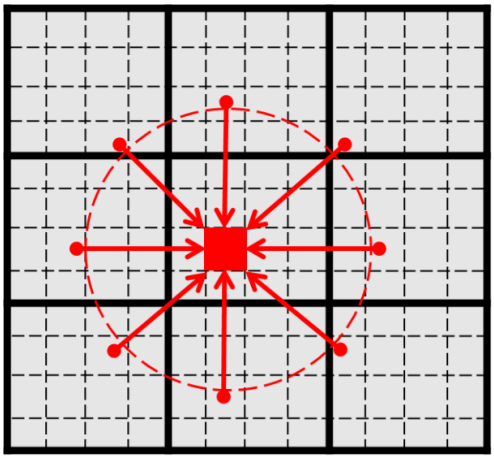

**Figure 12. Principle of SRRF.** Pixels (solid lines) are divided into sub-pixels (dashed lines). Radiality is calculated for each sub-pixel to determine if a fluorescent molecule is present. Sub-pixels closest to a fluorescent molecule (red square) will be assigned a high radiality value, whilst sub-pixels further away from a sub-pixel, containing a fluorescent molecule, will be assigned a low radiality value.

#### 1.2.9.1.2 Assessing the resolution and quality of SRRF images

As with all post-processing super-resolution techniques, SRRF is prone to artefacts. As a SRRF image is a super-resolution map and not a diffraction-limited image, the reconstructed

information may not be accurate. Therefore, Ricardo Henriques' research group implemented an open-source NanoJ- SQUIRREL ImageJ plugin to quantitatively assess the quality and resolution of super-resolution images (79). Using the NanoJ-SQUIRREL algorithm, a SRRF image is convolved with the PSF of the microscope to generate a new diffraction-limited image, which can be compared against the original diffraction-limited image. If the convolved SRRF image has a high similarity to the original diffraction-limited image, this indicates that the SRRF image contains few artefacts and is of high quality. The NanoJ-SQUIRREL algorithm produces a resolution-scaled error (RSE) map as a way to quantitatively compare the convolved SRRF against the original diffraction-limited image and shows areas where the two differ (Figure 13). Using a look-up-table (LUT), regions on the map where there are low errors are highlighted purple, whilst high errors are blue-yellow. Although useful for identifying artefacts in images, RSE values are not normalised, so RSE maps cannot be compared across different super-resolution images. Resolution-scaled Pearson (RSP) and RSE values are also obtained, where RSP is the Pearson's correlation coefficient (RSP>0.95 = good SRRF image) and RSE is the root-mean-square error between the diffraction-limited image and the convolved SRRF image. It is worth mentioning that small-scale artefacts, less than 150 nm, cannot be detected with NanoJ-SQUIRREL (78). Prior to acquisition, a parameter sweep can be run to find optimal settings to achieve a high quality SRRF image.

As well as determining the quality of a SRRF-processed image, through calculating RSP and RSE values, the resolution can also be determined using a built-in block-wise Fourier ring correlation (FRC) functionality in NanoJ-SQUIRREL. FRC was first used to determine the resolution of EM images (80), but has since been applied to fluorescent images, and is a metric that calculates the amount of similarity between spatial frequencies in two independently reconstructed images (81). Images are Fourier transformed (spatial domain converted to the frequency domain as a set of sine and cosine waves) and different spatial frequencies (frequency in space) for each image correlated. Resolution is calculated as the inverse of spatial frequency (1/spatial frequency) when the FRC value is set at a threshold of 1/7 (≈0.143), so any value below this threshold is considered noise (82). NanoJ-SQUIRREL uses this threshold value to determine resolution and create a FRC map by splitting the raw dataset into even and odd number of frames before being separately SRRF-processed and input into the NanoJ-SQUIRREL FRC implementation. Prior to FRC analysis, the two SRRF images are split into blocks (each block contains a number of pixels) and a FRC value determined for each block, however, nearby blocks are combined to yield sufficient correlations. If there are insufficient correlations, nearest neighbour interpolation can be

applied, where nearby pixel values are used instead, which is why some shapes in the FRC map are not square. At least two pixels are required for a FRC calculation, because the spatial frequency of one pixel cannot be measured; this is why there are less pixels in the FRC map than the super-resolution image. Using a LUT, red regions in the map represent low-resolution (high FRC value), whereas blue regions in the map represent high-resolution (low FRC value) (83). Colour keys for the RSE and FRC map show the minimum and maximum pixel values. The resolution of an image is often used as an indicator of whether a super-resolution image is of high quality, but high-resolution does not always yield a super-resolution free of artefacts and resolution is heterogeneous across an image. NanoJ-SRRF and NanoJ-SQUIRREL are both a part of a NanoJ toolbox, which includes other ImageJ plugins, such as NanoJ-VirusMapper, NanoJ-Core, and NanoJ-Fluidics (84).

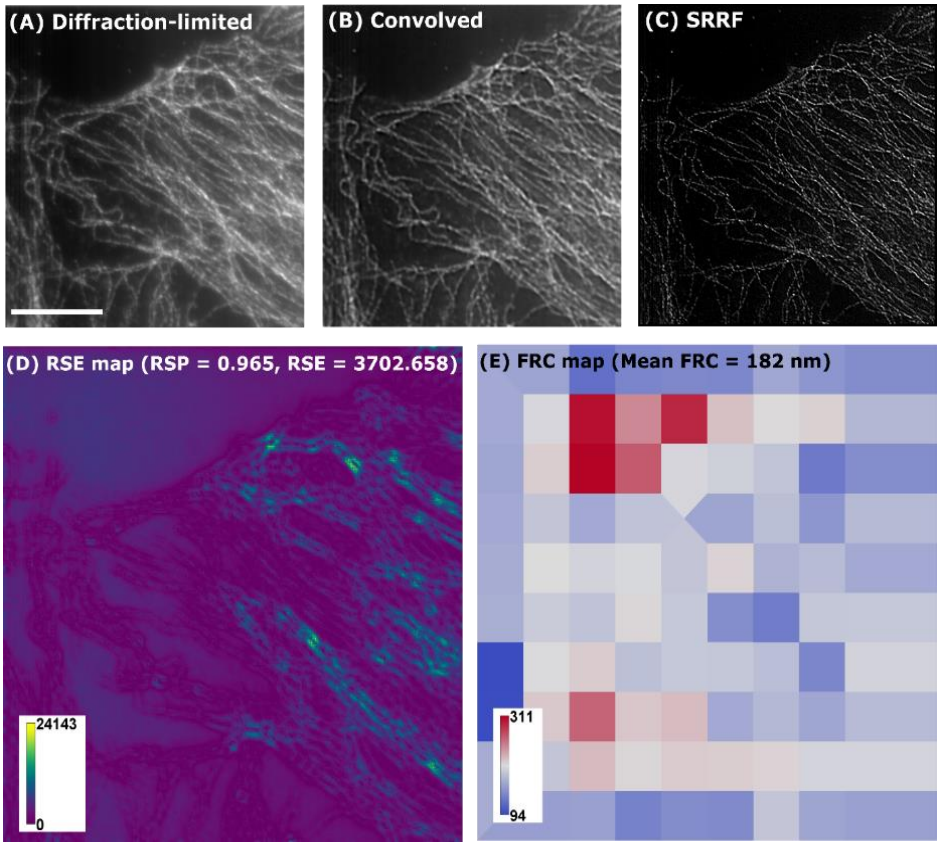


**Figure 13. NanoJ-SQUIRREL processs.** A diffraction-limited image (A) was compared against a SRRF-convolved image (B) to determine the quality of the SRRF image (C). A resolution scaled error (RSE) map (D) is produced, with low errors in purple and high errors in blue-yellow. RSP and RSE values are also obtained (RSP>0.95 = good SRRF image). Resolution was determined with the FRC implementation of NanoJ-SQUIRREL. A FRC-map (E) has red regions for low-resolution (high FRC value) and blue regions for high-resolution (low FRC value). The colour keys shows minimum and maximum values. Scale bar = 10 µm.

#### 1.2.9.2 Super-resolution optical fluctuation imaging

##### 1.2.9.2.1 Theory of SOFI

Another technique with low requirements in terms of hardware is SOFI (85) since it can be implemented on any microscopy platform, including wide-field and TIRF, with a fast camera (26). As well as EMCCD cameras, SOFI has also been performed on sCMOS and industry-grade CMOS cameras (25). SOFI can resolve structures spatially in x, y, and z, and has a relatively high temporal resolution, compared to other super-resolution techniques. SOFI is also capable of reconstructing 3D super-resolution images, through the acquisition of different z-positions (86). The principle of SOFI (Figure 14) was first described in 2009 by Thomas Dertinger (University of California, USA) (85). To generate a SOFI image, the structure of interest must first be labelled with a probe that fluctuates spontaneously between a fluorescent and non-fluorescent state (86). Signals produced from these fluctuations are recorded in a series of frames on a sensitive EMCCD camera (512-by-512 pixel), connected to a wide-field microscope. Each pixel in the wide-field image contains a signal that can be correlated (similarity compared) against a signal in a different pixel (cross-correlation) or against itself (autocorrelation) over time (87). For autocorrelation, zero time lags (shift in increment of time) are used, but for higher-orders time lags need to be introduced, for example, $4^{th}$ order requires 4 time lags (85). At zero time lag, the SOFI signal is at its highest, since fluctuations within the signal are correlated, but as the lag time increases, fluctuations are de-correlated and the SOFI signal becomes negligible. Cross-correlation uses neighbouring pixels to calculate cross-cumulants from different pixel combinations, which generates additional virtual pixels that contain more sub-pixel information. Therefore, for cross-correlation a SOFI-processed image (1016-by-1016 pixels) will have twice the number of pixels compared to the average image. When generating virtual pixels, cross-correlated pixel combinations are given a weight, which is determined by the distance between pixels, known as the distance factor, to compensate for differences in intensity by applying the inverse of the distance factor to smooth the pixelated appearance of SOFI images (88). Using a SOFI processing algorithm in software such as Localizer (89), implemented in MATLAB or Igor Pro software, higher-order statistical analysis is performed to correlate fluctuations from signals generated by emitters (85). Signals that are correlated are assigned a positive cumulant value, whereas those that are not correlated are given zero and will not contribute to the SOFI image (90). Noise is dampened during SOFI-processing, because it is uncorrelated

in time, so this creates contrast and high SNR images. By drawing a line scan across a single point emitter or small structure in the SOFI image, a normalised intensity versus pixel distance graph can be plotted and a one-component Gaussian curve fitted (91). The FWHM of this curve can be used as a measure of resolution enhancement. A resolution improvement (PSF width decrease) proportional to $\sqrt{n}$ or n by implementing interpolation and Fourier re-weighting (85, 88), have been determined (where n is the order of processing).

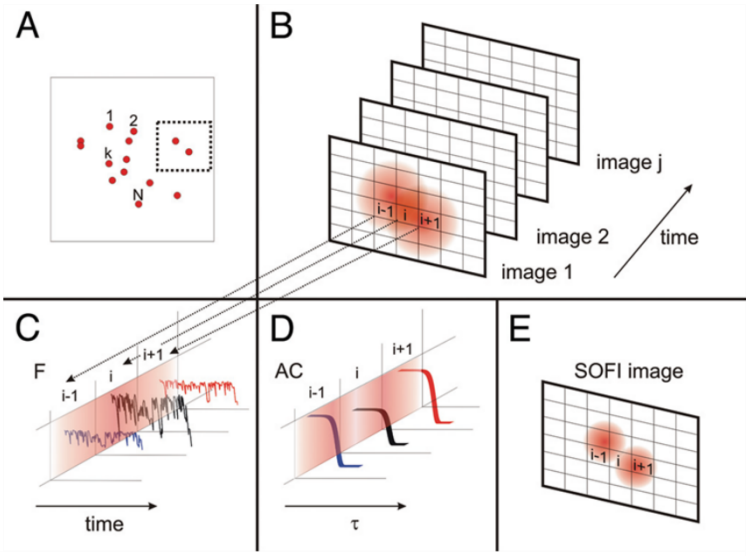


$$I(r,t) = \sum_{k=1}^{N} \varepsilon_k U(r - r_k)$$

| Symbol | Explanation |
|---|---|
| I | fluorescence intensity signal |
| r | pixel position of the fluorescence intensity signal |
| t | time |
| N | number |
| k=1 | fluctuating emitter |
| $U(r - r_k)$ | point spread function |
| Σ | sum |
| $\varepsilon_k$ | molecular brightness |

**Figure 14. Principle of SOFI.** SOFI assumes that emitters are in a fixed position, but can fluctuate between a fluorescent and non-fluorescent state when illuminated with light (A). A series of images are acquired on a camera of two emitters fluctuating, but because of the diffraction limit of light cannot be resolved as separate entities (B). The signal from each pixel is recorded over time (C) and can be correlated by autocorrelation (D) to create a SOFI image in which the structures are better resolved (E). When a molecule is illuminated, a fluorescence intensity signal I is produced at a fixed position r. If fluorescence is intermittent, a number of molecules N fluctuate k=1 over time t. The distribution of fluorescence can be determined for any image by the sum Σ of each molecule's PSF $U(r-r_k)$ and molecular brightness $\varepsilon_k$. SOFI reduces the PSF of a molecule. Schematic diagram was adapted from (85).

#### 1.2.9.2.2 Different SOFI implementations

Although, SOFI resolution is further improved by calculating higher-order cumulants, this increases the dynamic range of the resulting image, so there will be some fluorescent molecules that are extremely bright and others that are dim (92). The large dynamic range of SOFI means that low emitting fluorescent molecules will be masked when close to neighbouring fluorescent molecules that have higher fluorescence intensities, whilst those fluorescent molecules that are always switched "ON" will not fluctuate, and will therefore be removed from the SOFI-processed image. Since SOFI was first implemented by Dertinger and co-workers in 2009, an extended version, balanced SOFI (bSOFI) has been developed, which takes into consideration non-linear variation in molecular brightness by generating molecular density (number of molecules per pixel area) maps through combining SOFI images of different cumulant orders to produce a final balanced contrast SOFI image (93). However, bSOFI can produce artefacts in images, which has been rectified with local dynamic range compression SOFI by calibrating higher-order SOFI images against the brightness of the $2^{nd}$ order image (92). Another caveat of earlier versions of SOFI, involving the calculation of cross-cumulants, was the checker board pattern present when additional pixels were created (89, 93), however this pixilation issue was corrected for by using Fourier transform interpolation (94). During cross-correlation, neighbouring pixels are combined, but those at the edge cannot be cross-correlated, so often there is a black border around the edges of the SOFI image. In addition, calculating higher-order cumulants is complex and computationally demanding. To improve the use of higher-order SOFI, a low-pass denoising operator can be applied to reject shot-noise and increase in lateral resolution up to $16^{th}$ order (95).

To record a sufficient amount of fluctuations for correlation, a minimum number of images need to be acquired. Since SOFI requires fewer frames than SMLM to reconstruct an image, it yields a better temporal resolution. Previously, SOFI's temporal resolution was limited to 60 s, which was not capable of capturing dynamics of fast-moving proteins (96). Temporal resolution of SOFI has since been improved by modifying the SOFI algorithm (97). Instead of calculating higher-order cumulants, variance analysis has been used to achieve an 80 ms temporal resolution with 10 frames, and this adapted SOFI method was termed variance imaging for super-resolution (VISION) (98).

Like all super-resolution microscopy techniques, SOFI is not artefact free, as movement of the sample during acquisition in the x, y, or z positions, can affect the resolution and cause

motion blur artefacts in the resulting SOFI-processed image. Movement is, therefore, a real limitation for live cell SOFI of very motile proteins (99). A workaround to studying the dynamics of a fast moving protein, is to capture the movement with the shortest possible acquisition rate or fix at time-points, as a compromise. Although, SOFI does not require as many images as SMLM, it still needs at least 10 frames, so motion blur is still evident. As well as cell movement, artefacts can occur due to sample drift, loss of focus, or microscope vibration. Although, drift correction algorithms exist, which can correct movement that occurs systematically, motion blur as a result of live cell movement is challenging to predict, because this is random (100). To an extent photobleaching can be accounted for by splitting the stack into sub-stacks and SOFI-processing these stacks to give an average SOFI image.

Both SOFI and SRRF do not rely on sparse activation of fluorophores, unlike SMLM. However, SRRF has the advantage of using conventional fluorophores, whereas SOFI requires probes that fluctuate on a suitable timescale. Many fluorophores have short blinking or stochastic blinking, such as Qdots, which is sometimes not on a suitable timescale for SOFI. Therefore, it is preferential that better fluorescent probes are developed that have controlled blinking (101). However, SOFI has been performed with non-fluctuating probes, through the use of speckle patterns illumination (102), which has also been employed in SIM (103). To date, SOFI has been used with a variety of fluorescent probes including, Qdots (85), a Tag-red fluorescent protein (RFP) (104), RSFP (Dronpa and Skylan-S) (105, 106), carbon nanodots (cdots) (107), polymer dots (pdots) (108), and synthetic organic dyes (109). High blinking Qdots have also been developed for SOFI, by synthesising Qdots with a thinner shell (98). Other creative ways to use SOFI without fluorescent labelling with a fluctuating probe, include exploiting the local concentration of zeolite aggregates (110). Labelling structures with Qdots often appears discontinuous, which makes it difficult to establish the degree of resolution enhancement of SOFI via a line scan. This has been largely corrected for using joint-tagging SOFI (JT-SOFI), which labels the same structure with multiple Qdots and combines the resulting SOFI images (111).

#### 1.2.9.2.3 Advantages of SOFI

Regardless of the implementation used, SOFI has the capability to provide better co-localisation information between proteins than wide-field microscopy. By using multiple

probes, to differentially label structures within a cell, different coloured channels can be sequentially SOFI-processed and then composited for analysis (111, 107, 112). Unique microscopy combinations have also been tried, including the use of SOFI with FCS (113), LSFM (32), STORM (114), dSTORM (115), PALM (116), SIM (117), AFM (45), and ultrasound imaging (118). Despite SMLM giving better spatial resolution, SOFI enhances temporal resolution using fewer frames. In addition, SOFI does not require densely labelled samples or high SNR images, and is suitable for live cell imaging of slow moving proteins (85, 119, 120). Although, EM also yields high-resolution images, special sample preparation and high contrast probes are required, which means that all samples are fixed unlike the non-invasive SOFI method (85, 55). Another high-resolution technique, AFM, does not require the sample to be fluorescently labelled, but this means that it cannot specifically resolve multiple proteins within the same sample, unlike SOFI. AFM also has a slow scan speed, whereas SOFI has a fast acquisition of the order of seconds. In contrast to AFM, which is a surface technique, SOFI can reveal intracellular structural and dynamic information inside of cells, which may provide a better understanding about how a protein functions (121). Since SOFI removes out-of-focus light, essentially uncorrelated noise, it can be applied prior to deconvolution to give a better performance of these algorithms (85). Although, some implementations of SOFI are available free as open-source code, an even easier approach would be to implement SOFI into an ImageJ plugin, which has previously been described in the literature using the QuickSOFI approach (122).

#### 1.2.9.2.4 Assessing the resolution and quality of SOFI images

Despite the benefits of SOFI-processing, quantifying the resolution and quality of SOFI images has been addressed by few researchers in the imaging community (123, 116, 81). Resolution and image quality is dependent on factors such as sample preparation and image acquisition (81), and the two do not always correlate. The quality of a SOFI image has previously been judged by benchmarking against reference images typically of filamentous structures, such as microtubules, taken with other super-resolution techniques. A SOFI simulation tool has been developed that can aid the acquisition of high quality SOFI images by testing optimal parameters, such as the labelling density, before any experimental work begins (124). Any visible change in resolution, such as narrowing of structures, can be subjectively checked by eye or quantitatively by drawing a line through the structure of

interest and plotting its intensity. A smaller FWHM or dip in the line profile indicates resolution enhancement. To determine resolution, line profiles must be taken for a number of structures within an image to reduce human bias, because resolution is not homogenous and choosing the narrowest structure for the measurement is not representative of image resolution. A less biased approach would be to use FRC, because it takes into consideration all of the pixels in an image. Deschout *et al.,* (116), were the first to use FRC specifically for resolution evaluation of SOFI images. As discussed earlier, FRC re-writes a super-resolution image as a sum of oscillations and compares the similarity of spatial frequencies (measure of how often sinusoidal waves repeat per unit distance) formed from two independent reconstructions (81). To calculate FRC, an image stack is randomly split into two independent sub-stacks, pixels binned (combine pixels to yield fewer pixels), and Fourier transformed (spatial domain is converted to the frequency domain as a set of sine and cosine waves). SOFI images should have a higher spatial frequency (low FRC value) than wide-field images, because they contain more information (more waves). Due to live cell movement, FWHM analysis can give a lower resolution value than that of FRC (74). Another caveat of FRC is that it incorrectly assumes that samples are homogenous, which can skew the estimation of resolution, so sectorial FRC has been introduced to combat this (116). FRC has been developed into a BIOP ImageJ plugin referred to as Fourier Image REsolution (FIRE). Analysis on the SNR of SOFI images has also been described, as a way to estimate quality. Similar to FRC, the image stack is divided into sub-stacks to minimise the effect of photobleaching, but one frame is deleted from each sub-stack to generate several SOFI images with pixel-wise variations in SNR (delete-1 jackknife re-sampling). As described previously, NanoJ-SQUIRREL, a freely available ImageJ plugin (79) can also be used to quantitatively assess the quality of SOFI images without any *a priori* information about the fluorophores.

## 1.3 Fluorescence correlation spectroscopy

SOFI uses temporal correlation analysis similar to FCS, which is a single molecule detection technique first developed in 1972. FCS analyses spontaneous fluctuations of fluorescent intensity within a femtolitre ($10^{-15}$ L) detection volume, produced from fluorescent molecules (in the nM range) freely diffusing in and out of this volume (125). An autocorrelation function G(τ), inversely proportional to the number of fluorescent molecules ($\frac{1}{N}$), compares the similarity of a fluorescent signal to itself over time by copying the fluorescent intensity signal

and shifting it using time lags (126). A laser beam is focused on a low concentration of fluorescent molecules in solution (1-10 molecules in the confocal volume) for detection. Using the Stokes-Einstein equation: $D = \frac{kT}{6\pi\eta R}$ , where D is the diffusion coefficient ($\mu m^2/s$), k is the Boltzmann constant (1.3806504 x $10^{-23}$ J/K), T is the absolute temperature (K), and η is viscosity, the hydrodynamic radius R of fluorescent molecules can be calculated. FCS has been used previously to determine the hydrodynamic size of Qdots (127-130). Since Qdots that have been conjugated to proteins are larger in size than unconjugated Qdots, they will move more slowly through a confocal volume and will thus have different diffusion times (128). However, there are some limitations of using FCS for Qdot size determination. Qdot blinking can cause the correlation function to be altered (131, 132). Variations have also been observed between Qdot hydrodynamic radii measurements taken using FCS and TEM due to differences in sample preparation (133). In addition, Qdot aggregation can also cause a change in the autocorrelation curves, due to their increased diffusion times, and so FCS can be used as a measure of their colloidal stability (128, 134).

## 1.4 Fluorescent probe size and labelling

To study single molecules and biological structures inside cells, they must be labelled with a fluorescent probe, so that they can be visualised under the microscope. A prerequisite of fluorescent probes is that they must be bright, water-soluble, and functionalised to target the specific protein of interest. It is common practice to fix cells first and then label with a fluorescent dye conjugated to an IgG antibody. However, by fixing cells, the dynamic processes that proteins are involved in cannot be studied in real-time, unless fixed at specific time points. Antibodies are invaluable to fluorescence microscopy, because when fluorescently labelled, they can locate specific proteins within a cell (135). Since IgG antibodies are approximately 150 kDa (14.5 nm x 8.5 nm x 4 nm), there is a linkage error between the structure of interest and the fluorescent dye attached to the antibody (136, 137). It is beneficial for super-resolution microscopy to have a small probe, which will reduce the binding distance to the protein of interest. Nanobodies, single variable domains of heavy chain antibodies, are much smaller at approximately 13 kDa (1.5 nm x 2.5 nm) (138). Being small, nanobodies penetrate better through tissue and recognise epitopes that cannot be accessed by antibodies (139). Originally derived from Camelidae, nanobodies are robust: they maintain stability at high temperatures, have a long shelf-life, and are resistant to

extreme pH (140, 141). Secondary antibodies are considerably larger than nanobodies, being 150 kDa (10-15 nm), and when used with primary antibodies are 20-30 nm. A toolbox of secondary anti-IgG nanobodies against mouse and rabbit IgG have been deposited on the repository Addgene for general use in super-resolution microscopy (142). In addition to nanobodies, commercial custom-made affirmers, 10 kDa domain proteins, have also been used as an alternative to antibodies in super-resolution imaging, because these binding proteins have greater stability than antibodies at high temperatures (143). Super-resolution relies on the optical properties of fluorophores. Although, random fluctuations are considered a nuisance in single-particle tracking, it is advantageous for SOFI to use probes that oscillate continuously between a non-fluorescent and fluorescent state, on a suitable time scale, of the order of milliseconds. It is assumed that during acquisition, the point emitters are stationary, so they should retain their position in each frame, and that the fluctuations produced from each point emitter are independent of fluctuations from neighbouring point emitters (90, 91). Neighbouring emitters fluctuate simultaneously, so when one emitter is switched “ON” and the other is “OFF”, they can be distinguished along a structure as separate entities. Qdots are therefore a good probe choice for SOFI, because they fluctuate stochastically under UV light (85).

### 1.4.1 Quantum dots

Qdots are semiconductor nanocrystals (2-10 nm), which are typically composed of an inorganic core of cadmium selenide (CdSe) or cadmium telluride (CdTe), a zinc sulfide (ZnS) shell, and a layer consisting of hydrophilic ligands such as polyethylene glycol (PEG) to make them water-soluble for biological application (98). The blinking phenomenon of Qdots is spontaneous, occurs on all timescales (144), and can be described using a power law (145). Qdots blink when subjected to a continuous light source, as their fluorescence can become quenched due to non-radiative Auger recombination, which intermittently puts the Qdots in the dark state (146). The size of a Qdot determines the colour it emits. Large Qdots emit red light, whereas small Qdots emit blue light (Figure 15). Typically, Qdots have a broad excitation spectra, but narrow emission spectra. Therefore, Qdots facilitate multiplex imaging, because they can be excited with a wide range of wavelengths, having a broad excitation peak, yet have a narrow emission peak.

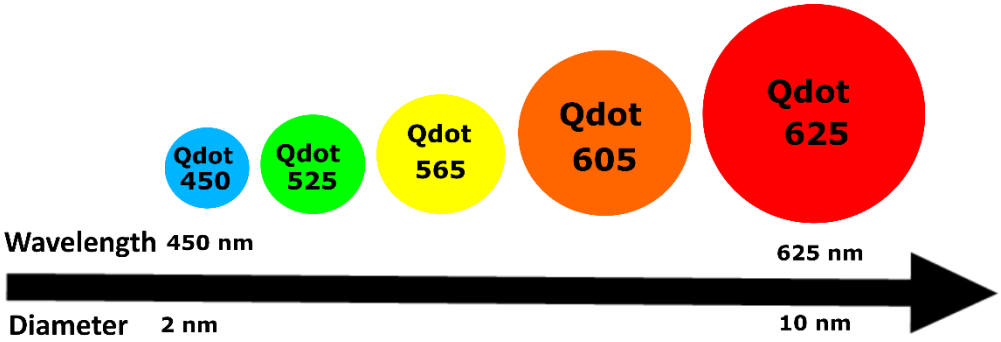


**Figure 15. Size determines the colour emitted by Qdots.** Large CdSe/ZnS core-shell Qdots excited with UV light emit long wavelengths of light in the red region of the spectra, whilst smaller Qdots emit shorter wavelengths of light in the blue region of the spectra. Wavelengths and diameter sizes shown in this schematic diagram depict several commercially available Qdots.

Through conjugating Qdots to antibodies, several groups have successfully labelled structures with Qdot-conjugated antibodies (Qdots-Abs) (147, 148) and have achieved multiplex imaging (112). However, Qdot labelling of nuclear proteins still presents challenges and protocols need further optimisation, such as shorter fixation times and longer permeabilisation with detergents such as Triton X-100, to access the nucleus (149). Although, Qdots are considerably brighter than synthetic organic dyes (150), they are larger than synthetic organic dyes (1 nm), because one Qdot (2-10 nm) attaches many antibodies (10 nm). Qdots are, therefore, limited to *in vitro* imaging, because their large size can lead to steric hindrance. The size of Qdots can be measured with TEM, FCS, and dynamic light scattering. For live cell imaging, Qdot-Abs must be microinjected into cells, which is tedious, invasive, and often leads to aggregation, so cannot specifically target the protein of interest. Cells readily take up Qdots by endocytosis, so there is often high non-specific labelling.

### 1.4.2 Reversibly switching fluorescent proteins

Apart from using Qdot-Abs, proteins can be labelled genetically through transient transfection with cDNAs encoding fusions with fluorescent proteins. Although, the green fluorescent protein (GFP) is the most widely used fluorescent protein all over the world, this was not the case 30 years after to its initial discovery from the jellyfish *Aequorea Victoria* in 1961, by Osamu Shimomura (151). It was not until after the chromophore structure of GFP was later identified in 1979 that it became routinely used in live cell imaging (152). After the development of GFP, several other different coloured fluorescent proteins were synthesised

by Roger Tsein, which were named after fruits, including mCherry (153). More recently, the development of GFP-like proteins have revolutionised biological imaging for their ability to repeatedly switch from a non-fluorescent to a fluorescent state under controlled illumination with a wavelength of light that switches the protein "ON" and another wavelength of light that switches the protein "OFF" (154). This photoswitching is not photobleaching, because the loss of fluorescence due to excitation is not permanent. RSFPs are distinct from the photoconvertible fluorescent protein (PCFP) Dendra, where the photoswitching of green to red, through UV illumination is irreversible (155). However, different photoactivatable fluorescent proteins (PAFP) can undergo irreversible or reversible (in the case of Dronpa) switching from a non-fluorescent to a fluorescent state using specific wavelengths of light (Figure 16) (156). Many RSFP variants, including Dronpa (157, 158), Dreiklang (159), and Skylan-S (106), accessible from Addgene, are utilised in super-resolution microscopy.

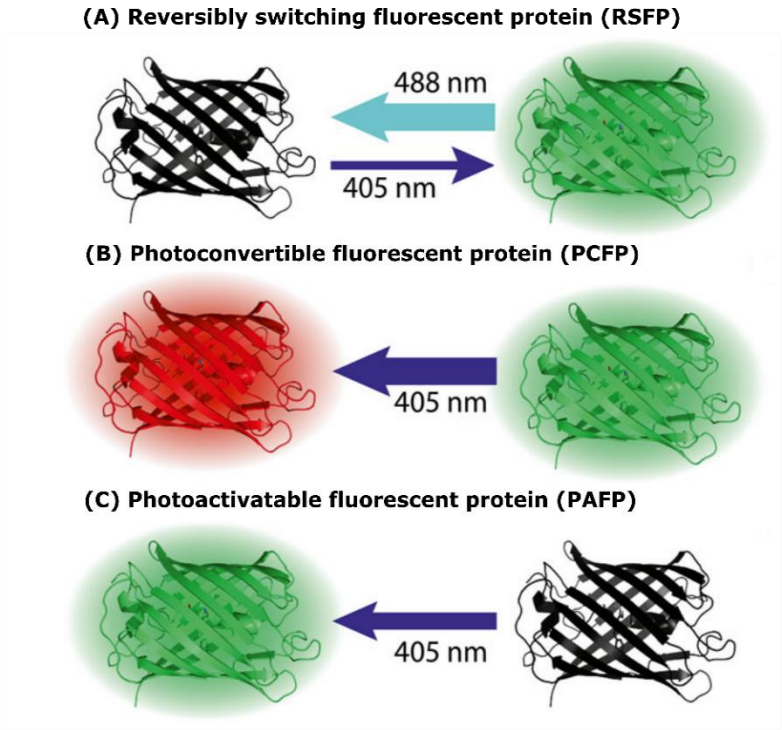


**Figure 16. RSFPs are distinct from PCFPs and PAFPs.** Green RSFPs can be switched "OFF" with high intensity 488 nm illumination, whilst low intensity 405 nm illumination switches them "ON", in a reversible manner (A). In contrast, green PCFPs can be irreversibly converted to a red fluorescent protein using 405 nm illumination (B) and different PAFPs can be converted from a non-fluorescent state to a fluorescent state, with 405 nm light, either irreversibly or reversibly (C). Figure was adapted from (155).

The first GFP mutant cited in the literature took several minutes of illumination to switch from a fluorescent to a non-fluorescent state (160). However, the most widely used RSFP in super-resolution imaging, Dronpa, a green monomeric RSFP that was originally cloned from coral Pectiniidae in 2004 (157), can repeatedly switch within milliseconds (158). When irradiated with high intensity 488 nm light, Dronpa is switched "OFF", but when it is irradiated with low intensity 405 nm light it is switched "ON". A yellow RSFP, Dreiklang (159), has been successfully used in super-resolution, including SOFI (161). The most recent RSFP, Skylan-S, developed specifically for SOFI, is brighter and more photostable than Dronpa, so it yields higher resolution images (106). The advantage of using RSFPs for super-resolution is that their genetic encoding allows the direct imaging of proteins, without the need for labelling with antibodies. The use of SOFI with RSFPs is termed photochromic SOFI (pcSOFI) (162). Overexpressed RSFPs can cause artefactual aggregation. An ideal RSFP is one that is monomeric, so that it is less likely to oligmerise, preserving the localisation and function of the fused protein of interest, and also bright, to minimise photodamage to the biological structure by using lower intensity illumination (163). As well as using RSFPs for high-resolution live cell imaging, fluorogen-activating-proteins (FAPs) (164), non-fluorescent single chain antibody fragments (140 amino acids long) have also been utilised in super-resolution microscopy, through binding a small non-fluorescent far-red synthetic organic dye (flurogen), such as malachite green, to form a FAP-fluorogen complex (165).

### 1.4.3 Synthetic organic dyes

Small molecule fluorescent dyes, readily referred to as synthetic organic dyes, have been widely used to study biological processes, but unlike RSFPs they can only be used in fixed cells and are not suitable for live cell imaging of intracellular protein dynamics (119). However, RSFPs are less photostable than synthetic organic dyes and have a lower quantum yield. Synthetic organic dyes are subject to photobleaching and are less bright than Qdots. Despite this, synthetic organic dyes (1 nm) are smaller than Qdots (2-10 nm), so they can more specifically label the structure of interest when conjugated to antibodies (10 nm) (166). Although, fluctuations of synthetic organic dyes are insufficient for SOFI, using specific wavelengths of light and an oxygen scavenger cocktail of enzymes (glucose oxidase or catalase) and thiols (MEA), strong blinking of single molecules can be induced.

The most commonly used synthetic organic dyes for super-resolution microscopy are the far-red carbocyanine dyes, cyanine 5 (Cy5) and Alexa Fluor 647, which can reversibly switch from a fluorescent to a non-fluorescent state, through irradiation with specific wavelengths of light (167). Similar to the RSFP Dronpa, Cy5 can also be switched within milliseconds and up to 100 times without photobleaching (62). A long wavelength of light switches Cy5 from the fluorescent state to the non-fluorescent state, whilst a short wavelength of light returns Cy5 molecules back to the fluorescent state (168). Photoswitching of Cy5 can be modulated by coupling to a Cy3 dye, creating a Cy5-Cy3 pair (60). One mechanism that proposes to cause this photoswitching behaviour is the cis-trans isomerisation of carbocyanine dyes. In the cis state, the dye is non-fluorescent, whilst in the trans state, the dye is fluorescent (169). Since carbocyanine dyes have short triplet state lifetimes, oxygen can be removed using glucose oxidase, to lengthen the time the synthetic organic dye spends in the dark state. Alternatively, a low amount of the reducing agent β-MEA and laser light can also prolong the triplet state of the dye, which is more compatible with live cell imaging, since a low concentration of thiols such as glutathione are already present in cells (170). Oxygen scavengers can also help to prevent photobleaching of synthetic organic dyes, by capturing reactive oxygen species (ROS), and are added to Vectashield mounting medium, to preserve fluorescent samples (169). Controlling the blinking of multiple coloured synthetic organic dyes, for multiplex super-resolution imaging, using the oxygen scavenger approach is challenging (118). Alexa Fluor 647 fluorescence has also been shown to be quenched in the presence of Vectashield, but this does not affect dSTORM (171).

## 1.5 Application of super-resolution to biological systems

Back in 2014, when this PhD project started, all of the papers published on SOFI demonstrated its resolving ability on filamentous structures such as microtubules, but none addressed specific biological questions, especially involving nuclear proteins. Through interdisciplinary collaboration, this research aimed to use SOFI as a tool to investigate protein localisation in several complex biological systems, including the nuclear protein HIF-2α. HIF-1α and HIF-2α are differential regulators of oxygen homeostasis, so when this goes awry in tumours they develop hypoxic regions, which are resistant to chemotherapy. SOFI was used to probe the localisation of HIF-2α into speckles, which may help to establish its potential use as targeted cancer therapeutics. SOFI was needed to resolve these speckles, so that their

size and abundance could be more accurately determined, through the removal of out-of-focus light. However, when higher resolution techniques were used, the HIF-2α speckles were no smaller than 100 nm, so SOFI was apt for the imaging of HIF-2α speckles.

Although, the resolving capability of SOFI (60-100 nm) was sufficient for HIF-2α speckles, other structures might benefit from higher resolution techniques, such as STED or dSTORM. NETs are extracellular fibres that are below the diffraction limit of light and resolving ability of SOFI. However, SOFI can remove out-of-focus light to better visualise the granular proteins dotted along the NET fibres, which help to identify them. Understanding the protein composition of NETs, using SOFI, may uncover their role in immunity and lead to the development of therapeutics against autoimmune diseases. Unlike NET fibres, fibronectin fibres are of a size that is resolvable with SOFI, so the orientation of fibronectin fibres in scarred skin cells, within a complex ECM environment, can be investigated in greater detail. The current treatment of scarred skin is invasive, so by researching the organisation of ECM proteins using SOFI, the mechanism of ECM remodelling impairing scar formation may be better understood. Other ECM proteins such as laminins could also benefit from the resolution attainable with SOFI, as it may help to depict whether the deposition pattern of overexpressed LaNt alters LM-332. In doing so, SOFI may shed light on the organisation of LM-332, revealing its role in genetic skin fragility disorders.

### 1.5.1 Hypoxia inducible factor two alpha

Many of the fluorescent probes and microscopy techniques discussed here, have been used to investigate the localisation of several proteins, including a nuclear transcription factor involved in the oxygen-sensing pathway. Oxygen is fundamental to maintaining physiological processes, such as embryonic development and wound healing. Hypoxia occurs when tissues experience deficiency in oxygen, as a result of trauma or pathological conditions, such as cancer, pre-eclampsia, anaemia, and myocardial ischaemia. Hypoxia inducible factor (HIF) is a heterodimeric protein, consisting of HIFα and HIF-1β subunits, that controls oxygen homeostasis, through the regulation of gene transcription in response to changing oxygen levels (172). HIF exists as three isoforms: HIF-1α (173), HIF-2α (174), and HIF-3α (175). HIF-1α was the first subunit of HIF to be identified and is a basic helix-loop-helix-PER/ARNT/SIM (PAS) protein (176). Since HIF is involved in a number of pathological conditions, it is a potential therapeutic target, therefore its role in the HIF pathway (Figure 17) is of interest.

Under normoxia (atmospheric oxygen levels of 21% or physiological oxygen levels of 1.5%), prolyl-hydroxylase domains (PHDs) use oxygen to hydroxylate two proline residues (p402 and P564) in the oxygen dependent degradation domain (ODDD) of the HIF-α subunit. This hydroxylation allows the von Hippel-Lindau protein (pVHL) to target HIF-α for degradation. Also, in the presence of oxygen, factor inhibiting HIF (FIH) hydroxylates an asparagine residue (Asn803) of HIF-α, which prevents interaction with transcription co-factors P300 and CREB binding protein (CBP) (177). Under hypoxia (low oxygen conditions of 1% or less), PHDs (isoforms 1-3) and FIH can no longer hydroxylate HIF-α, so it avoids degradation, accumulates, and is translocated from the cytosol to the nucleus, through HIF-1α/HIF-2α binding to the HIF-1β subunit to form a HIF heterodimer. In the nucleus, HIF then binds to the promoter region of genes, the hypoxia response element (HRE), where it interacts with co-factors P300 and CBP, leading to transcription (178). Vascular endothelial growth factor (VEGF), which stimulates the production of blood vessels, in a process called angiogenesis, (179) and the glycoprotein hormone erythropoietin (EPO), which regulates red blood cell production (173), are both upregulated during hypoxia.

Here, the focus is on HIF-2α, also known as HIF-1α-like protein (HLF) (180), endothelial PAS domain protein one (EPAS1) (174), HIF-related factor (HRF) (181), and members of the PAS super-family two (MOP2) (182), which is a transcription factor that localises in the nucleus under hypoxia and normoxia (183), as nuclear dots (184) or speckles (185). The localisation of HIF-2α in speckles has been proposed to be in active transcription sites (185) and a potential binding partner of phosphorylated Serine 5 ribonucleic acid polymerase two (Phospho Ser5 RNA Pol II) (186). The movement of HIF-2α molecules within speckles has been shown to be slower than that of HIF-1α (185). Although, HIF-1α and HIF-2α share 48% amino acid sequence similarity, unlike HIF-2α, the localisation of HIF-1α is homogenous and it is only present in the nucleus under hypoxia (174). Both HIF-1α and HIF-2α are helix-loop-helix-PAS proteins (187), with the PAS domains being highly conserved, but there are differences in the C-terminal region of HIF-1α and HIF-2α (181). Protein stabilities of HIF-1α and HIF-2α also differ. Despite all three PHD isoforms being involved in regulating HIF-1α and HIF-2α, PHD2 has been shown to be the main regulator of HIF-1α levels (188), whilst PHD3 is the principal controller of HIF-2α levels (177). HIF-1α and HIF-2α are transcribed by different genes, HIF1A and EPAS1, respectively (189). Furthermore, HIF-1α is expressed in many different cell types (190), whereas HIF-2α is mostly present in endothelial cells (arterial) (181) and lung epithelial cells (191), which are exposed to higher oxygen than most cells in the body. The differential expression of HIF-1α and HIF-2α may account for different functions,

as HIF-1α and HIF-2α are responsible for regulating different genes: HIF-2α targets EPO in the liver, but HIF-1α does not (192). Since HIF-1α and HIF-2α can both dimerise with HIF-1β, formerly known as aryl hydrocarbon receptor nuclear translocator (ARNT) (193), HIF-1β is a known binding partner of HIF-2α. Similarly, hypoxia associated factor (HAF), previously known as $SART1_{800}$, also binds to HIF-2α. HAF promotes transactivation of HIF-2α, but degrades HIF-1α (194). Spatial and temporal dynamics of HIF-2α with potential binding partners has been studied previously using conventional microscopy techniques (185). However, conventional images contained out-of-focus light in between the HIF-2α speckles, so these would benefit from being imaged with SOFI to enhance SNR and resolution.

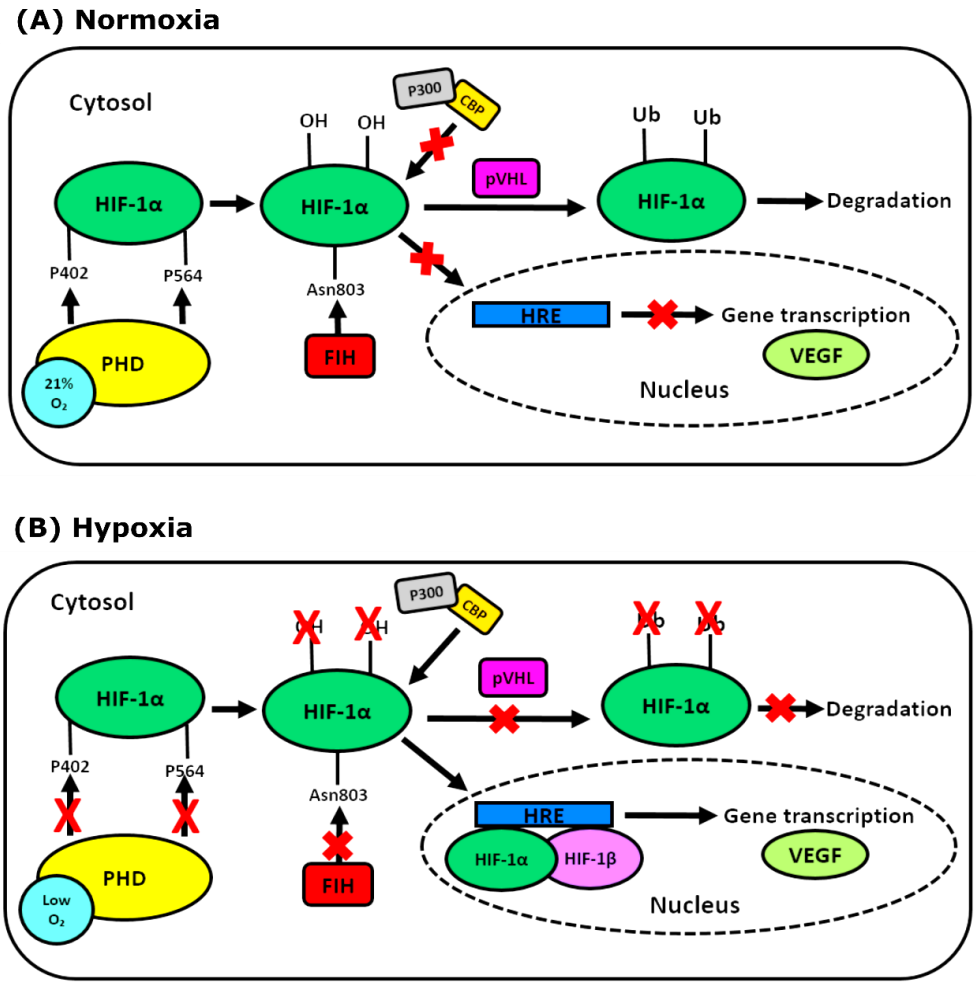


**Figure 17. HIF pathway in response to normoxia and hypoxia.** Under normoxia (atmospheric oxygen levels of 21% or physiological oxygen levels of 1.5%), PHDs use oxygen to hydroxylate 2 proline residues in the ODDD of HIF-α, whilst FIH hydroxylates an asparagine residue on HIF-α, allowing pVHL to degrade HIF-α and prevents interaction with co-factors P300/CBP, so transcription cannot take place (A). Under hypoxia (low oxygen levels, below 1%), PHDs and FIH can no longer degrade HIF-α, so it accumulates and is translocated to the nucleus, through the binding of HIF-1β, to form a HIF heterodimer, that can interact with co-factors P300/CBP and bind to HRE to transcribe genes (B).

### 1.5.2 Extracellular matrix proteins

As well as intracellular targets, such as nuclear proteins, extracellular structures would also benefit from super-resolution microscopy, because these proteins are located in complex environments, so an improvement in SNR would help to better understand the assembly and organisation of the ECM. The ECM is heterogeneous and is composed of structural proteins, such as collagen, elastin, fibronectin, and laminins, which are primarily synthesised by fibroblasts (Figure 18). ECM acts as a scaffold for cells and is involved in a number of physiological processes, including embryonic development, wound healing, and angiogenesis, leading to tumour progression (195). The ECM is the medium through which intracellular communication occurs. Integrins, heterodimeric transmembrane receptors of αβ subunits, are also involved in cell adhesion and cell migration by anchoring the ECM to cells via the actin cytoskeleton, allowing cells to communicate with their environment through cell signalling (196). A short cytoplasmic tail on the β subunit of integrin connects it to actin cytoskeleton. Specific αβ subunit combinations of integrins recognise different ligands, including collagen (α1β1), fibronectin (α5β1), and laminin (α3β1) (197). The most abundant protein in the ECM is collagen, making up approximately 30% of protein in the human body, and is comprised of three right-handed polypeptide α-chains, forming a super-coiled triple helical structure. In vertebrates, 28 different types of collagen exist, including type I, III, and V, which provide tensile strength (198).

Collagen is closely associated with elastin, another major fibrous ECM component that allows tissues to stretch and extend, in a flexible manner, without causing deformation. Elastin is a predominately insoluble polymer, synthesised from its monomer tropoelastin, and has a low turnover (199). The globular protein fibronectin is a ubiquitous dimer comprised of 220-250 kDa subunits (200). Plasma fibronectin resides in the blood, where it is ready to restore haemostasis by forming a fibrin clot, whereas cellular fibronectin is produced by cells to create a fibrous network (201). Basement membrane laminins are large heterodimeric proteins (400-900 kDa), made up of α, β, and γ subunits, that regulate cell migration (202). Another component of the ECM, proteoglycans such as syndecans, are macromolecules that also help to regulate physiological processes, through their interacting glycosaminoglycan (GAG) chains. Additionally, Hyaluronan (HA), a linear polymer that primarily exists in the ECM as large molecules ($2 \times 10^4$ kDa), inhibits cell proliferation and migration, but can also promote these processes if they are cleaved to smaller molecules (3-300 kDa) (203).

The mechanical stiffness of the ECM is often an indicator of disease and it has been found that tumours are stiffer than healthy tissue (198). AFM can be used to measure the stiffness of the ECM. The ECM is highly dynamic, it is altered during the aging process and wound healing. There is also a re-organisation of the ECM in response to inflammation, after tissue injury. Abnormal wound healing can result in an overproduction of ECM proteins collagen and fibronectin, in a process called fibrosis, which forms a hypertrophic scar or keloid (204). During fibrosis, the organisation of collagen fibres is changed, and instead of being in a basket weave formation, where the fibres are orientated perpendicular to one another, they are distributed in a parallel fashion (205).There is also twenty times more collagen and four times more fibronectin produced in keloids compared to healthy skin (196). Collagen fibres have also been shown to be much thicker in keloids than in healthy skin, whilst they are thinner in hypertrophic scars (206, 207). Only adult humans are susceptible to developing a keloid-like scar, with developing foetuses unable to form a scar (196). Keloid scars extend beyond where the initial injury took place, whereas hypertrophic scars are confined to this original site (208). ECM can be isolated from cells, using ammonium hydroxide, and its components imaged with fluorescence microscopy (209). Most investigations of the ECM have been done with 2D imaging, on cell monolayers, but to better represent the microenvironment, 3D imaging has now been employed (200). The organisation of collagen fibres in keloids has been investigated by combining multiphoton microscopy with fast Fourier transform (FFT) analysis (210), whilst fibronectin fibres have been imaged with dSTORM (211).

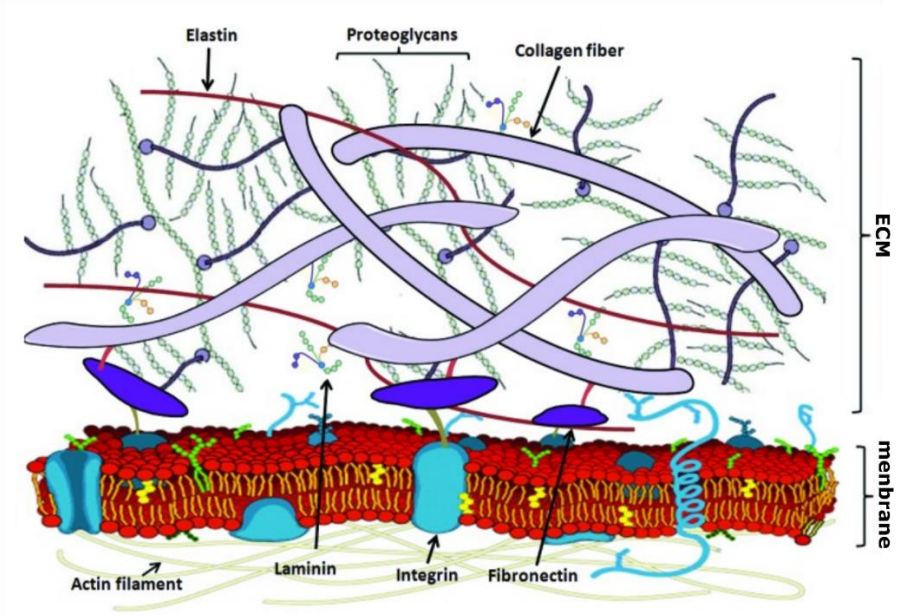


**Figure 18. Key components of the ECM.** The ECM consists of structural proteins elastin, proteoglycans, collagens, fibronectin, and laminin, which are anchored to cells using glycoproteins, such as integrins, and act as a scaffold for actin filaments. Figure was adapted from (196).

### 1.5.3 Neutrophil extracellular traps

Although high-resolution TEM has previously been used to image extracellular fibres, including NETs, the composition of these fragile structures would be best suited to super-resolution microscopy, due to the less invasive sample preparation. Neutrophils, a type of white blood cell, defend the body against pathogens, by creating an innate immune response, to engulf (phagocytose) and kill bacteria. As well as inflammatory stimuli, such as bacterial peptides and cytokines, when artificially stimulated with chemicals such as phorbol-12-myristate-13-acetate (PMA), neutrophils become activated and release nuclear DNA and associated molecules (histones, proteases) to form NETs (Figure 19) (212). Before, their discovery in 2004 (213), these peculiar string-like structures were originally mistaken as imaging artefacts (214). During NETosis (215), a type of cell death that differs from apoptosis (216) and necrosis (217), neutrophils die and release NET filaments ~17 nm in diameter, which are below the diffraction limit of a light (250 nm) (218). Using super-resolution microscopy, the protein composition of NETs, which is dependent on the stimulus type, can be visualised in more detail. As well as TEM, NETs have also been imaged at high-resolution with SEM (219), but these DNA structures are often difficult to distinguish from fibrin, which is also string-like (220). However, unlike fibrin, NETs have additional 50 nm granular proteins dotted along their structures (218). As well as NETs being string-like, they can also present as cloud-like structures, as a result of hydration, when they are not fixed (218).

Production of ROS by NADPH oxidase (NOX2, termed NOX-dependent NETosis) or release of mitochondrial ROS (NOX-independent NETosis) is vital for NETs to form (221). Many strains of bacteria and fungi are stimulators of NETosis, as well as ROS, such as hydrogen peroxide (218). There is evidence of NET release after just 10 minutes of incubation with an activator, making NETosis a quicker process than apoptosis, but this response is dose and agonist dependent (213). PMA stimulation results in NOX-dependent NETosis, whereas the calcium ionophore A23187 causes NETosis, which is NOX-independent (217). Neutrophils have a relatively short life span, as they die once granule proteins are released (221). Under PMA stimulation there is an abundant release of granule proteins such as neutrophil elastase (NE) and myeloperoxidase (MPO), whereas with A23187 stimulation, proteins such as peptidylarginine deiminase 4 (PAD4) and citrullinated histone H3 (citH3) are released from the NETs. Some of these NET-associated proteins have been identified using proteomics (219). Prior to NETosis, unstimulated neutrophils, otherwise known as polymorphonuclear leukocytes (222), have multi-lobed nuclei, but once stimulated, the nuclei lose their lobes

and become decondensed (221). During NETosis, proteins such as PAD4, an enzyme that catalyses the conversion of arginine residues to citrulline, in a process called citrullination, a form of post-translational protein modification, are abundant (223). PADs exist in four different types: I, II, III, and IV, where IV is nuclear whilst all the others are cytoplasmic, although IV (PAD4) is the most studied PAD in human NETs (224).

NETs have a vital role within the immune system and neutrophils from species other than humans also make NETs, such as fish, birds (218), and dogs (225). The importance of NETs has been echoed by the fact that they are associated with a number of human diseases (220), including rheumatoid arthritis (226), pre-eclampsia (227), periodontitis (228), appendicitis (213), cystic fibrosis (229), and systemic lupus erythematosus (SLE) (230). To date, NET formation has been analysed using enzyme-linked immunosorbent assay (ELISA) (231), fluorescence activated cell sorting (FACS) (232), and mass spectrometry (233). The morphology of NETs has also been visualised with fluorescence microscopy, TEM, and SEM. Preparing NET samples for visualisation requires great care, because these structures are extremely fragile (234). Previously, the number of NET-associated proteins have been counted by eye, as an evaluation of NET formation, but this is laborious and subject to human bias (235). NET quantification in fluorescent images has been achieved with ImageJ software, which relies on unstimulated neutrophils having higher intensity lobulated nuclei when stained with a DNA intercalating dye than stimulated neutrophils that have decondensed nuclei, expelling their DNA into the extracellular space (236). Quantification has also been automated using NETQUANT, a free app for MATLAB (237) and made high-throughput using DNA Area and NETosis Analysis (DANA), an open-source ImageJ program (238).

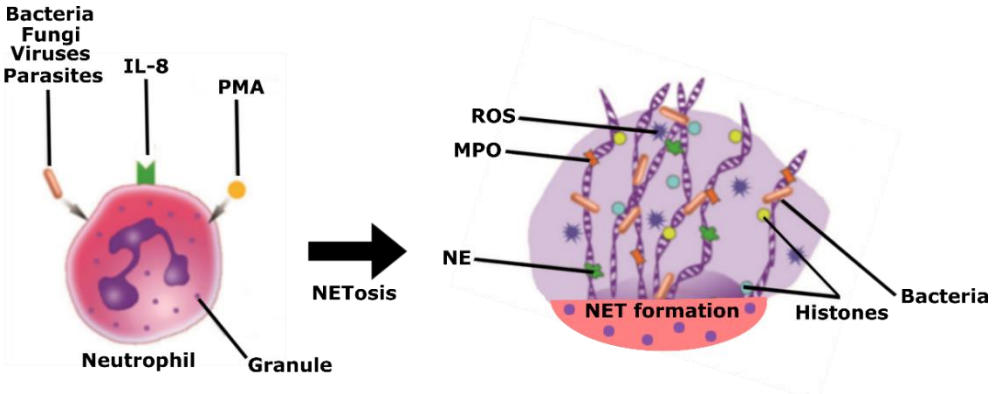


**Figure 19. Process of NETosis.** Receptors on the surface of neutrophils are stimulated by external stimuli, such as bacteria or PMA, which causes nuclei to decondense and granule enzymes to attach to DNA. As a response, NETs containing NE and MPO are released, trapping bacteria. Figure was adapted from (217).

### 1.5.4 Laminins

Co-localisation of other extracellular components, such as laminin-laminin interactions will also benefit from super-resolution microscopy, because higher spatial resolution will better determine if two proteins interact. Laminins are a family of large (400-900 KDa) ECM glycoproteins. These heterotrimeric proteins are cross-shaped molecules, with one long arm and 2-3 shorter arms. Each laminin is composed of α, β, and γ polypeptide chains and are named based on their subunit composition (239). Currently sixteen laminins have been identified, which display context and temporal differences in their expression profiles; all tissues contain laminins, with expression beginning during embryonic development.

LM-332, previously laminin-5 or α3β3γ2, is a heterotrimer made up of α3, β3, and γ2 subunits (240). LM-332 is important for most epithelium homeostasis and mutations in LM-332 subunits can cause the blistering disease junctional epidermolysis bullosa (JEB) (241). Laminins are deposited onto the basement membrane region of the ECM in patterns. LM-332 interacts with the α6β4 integrin receptor associated with the hemidesmosome and α3β1 integrin receptor associated with focal adhesions. These LM-332-α6β4 and LM-332-α3β1 interactions leads to regulation of LM-332 organisation within the ECM, which determines migration patterns in cells (242). In stationary keratinocytes (skin cells), LM-332 is in a rose-like pattern, whereas in non-stationary keratinocytes, LM-332 is assembled into trail-like patterns. Beyond a requirement for integrin binding, the precise mechanisms regulating laminin deposition and assembly into matrices is unknown (202). Highly regulated laminin matrix formation has been visualised in live cells using adenoviral vectors, to better understand laminin deposition (243).

A new family of alternative splice isoforms, derived from the 5'-end of genes (LAMA3 and LAMA5), which encode α3 and α5 products, were identified in 2009 (244). These alternative splice isoforms do not contain the domains required for laminin heterotrimerisation, but do contain a laminin N-terminal (LN) domain and hence, were named laminin N-terminal (LaNt) proteins. Little is known about these relatively small proteins, but studies have suggested that the 64 kDa LaNt α31 protein, may share the role of laminin-related netrins by regulating laminin-laminin interactions that form the laminin-network, as they both have an LN domain (Figure 20). Competition in the joining of LN domains between LaNt and netrins (netrin-4, netrin-1, 3), may compromise the stability of this laminin-network (244).

LaNt α31 has been found to be expressed in skin (244) and eyes (245). Localisation of LaNt α31 is distinct from LM-332, as LaNt α31 is clustered towards the edge of cells in puncta and only partially co-localises with LM-332 (244). The basement membrane of corneal epithelial cells is rich in LM-332 and the LAMA3 gene is expressed at high levels in these cells. As well as being highly abundant in the basement membrane, LaNt α31 has also been found in epithelial regions above the basement membrane (245). The distribution of LaNt α31 is also conserved amongst different species, including human, pig, and mouse (245). A dynamic re-distribution of LaNt α31 occurs in the form of increased expression when a scratch is introduced into 2D (244) and 3D (245) models of wound repair. An increase in the expression of LaNt α31 also reduces the migration of corneal cells, which may adversely affect wound healing (245). Being extracellular, laminins are a target for wound healing therapeutics, and peptides have been identified that can mimic the function of laminins (246).

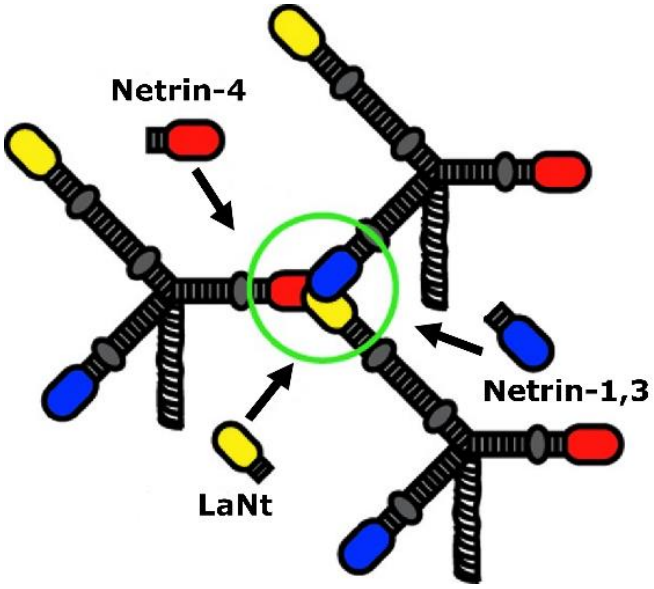


**Figure 20. Structural similarity of LaNts and netrins.** Both LaNt and netrins are cross-shaped molecules, with one long arm and 2-3 shorter arms. LaNt and netrins also share α, β, and γ LN domains, which join to form laminin-networks. However, LaNt and netrin LN domains can compete to de-stabilise this laminin-network. Figure was adapted from (246).

## 1.6 Project aims

The overall aim was to explore SOFI's potential use in cell biology by using it to provide nanoscale information about a variety of biological systems. At the start of this project there was no super-resolution microscope available at the CCI. SOFI was chosen, because it is open-source and can be applied to any optical system. It was anticipated that SOFI would be developed into a commercial add-on software that could be applied to more affordable microscopes, but SRRF-Stream became a better version of this. By rigorously investigating the use of SOFI in different biological applications, it was hoped that the advantages and limitations would be identified to help other researchers decide whether SOFI is the right technique for their own application. A prerequisite of SOFI is that structures must be labelled with a fluctuating probe, so a number of different labelling strategies were explored for specific proteins, including the use of Qdot-Abs, RSFPs, and synthetic organic dyes. A robust immunocytochemistry protocol for Qdot-Abs was optimised, however, they could not specifically label intracellular targets, such as HIF-2α (Chapter 3). Further collaborations were, therefore, set up resolving extracellular proteins associated with NETs and the ECM. As an alternative to Qdots, HIF-2α was tagged to the RSFP Skylan-S.

In the research laboratory of Violaine Sée (University of Liverpool, UK), HIF-2α was shown to localise within the nucleus in speckles, whilst HIF-1α was more homogenously distributed (185). It was hypothesised that HIF-2α speckles may be in active transcription sites and co-localise with Phospho Ser5 RNA Pol II. The distribution and co-localisation of HIF-2α with potential binding partners, such as Phospho Ser5 RNA Pol II, was investigated using different super-resolution techniques in fixed cells (Chapter 5). Towards the end of this project, the CCI purchased a spinning disk confocal microscope with SRRF-Stream capability, so HIF-2α speckles were also imaged at high resolution in live cells.

To obtain an optimal super-resolution image, acquisition settings for different open-source SOFI implementations were tested, as well as higher-order SOFI. The performance of SOFI in terms of accurately reconstructing structures in an image was also compared against other super-resolution techniques (Chapter 4). The quality and spatial resolution of super-resolution images was determined with different quantitative tools, including FRC. As well as 2D two-colour SOFI, 3D SOFI has also been accomplished. In addition, SOFI has been applied not only to epifluorescence and TIRF data, but also to light-sheet data.

# Chapter 2: Materials and methods

## 2.1 Materials

All chemicals used were purchased from Sigma-Aldrich (UK), unless stated otherwise in the methods. Cell culture medium was purchased from Gibo (USA), tissue culture treated plasticware from Corning (USA), transfection reagent from Roche (UK), and Qdot-conjugated antibodies from Thermo Fisher Scientific (UK).

## 2.2 Methods

### 2.2.1 Cell culture (chapters 3-5)

Human cervix epithelial carcinoma (HeLa) cells were cultured in 75 $cm^2$ flasks at 37 °C with 5 % (v/v) $CO_2$, minimum essential medium (MEM, Life Technologies, UK) supplemented with 10% (v/v) foetal bovine serum (FBS), and 1 % (v/v) non-essential amino acids (NEAA). HeLa cells (kind gift from Violaine Sée, University of Liverpool, UK) were split 1,000,000 cells/mL when $\geq$80% confluent with trypsin-EDTA. Rat mammary (Rama) 27 fibroblasts (kind gift from Phillip Rudland, University of Liverpool, UK) and HaCaT cells were cultured in a 75 $cm^2$ flask at 37 °C with 5% (v/v) $CO_2$, Dulbecco's modified Eagle's medium (DMEM, Life Technologies, UK) supplemented with 10% (v/v) FBS (Life Technologies, UK), 0.75% (w/v) sodium biocarbonate, 4 mM L-glutamine, 50 ng/mL insulin, and 50 ng/mL hydrocortisone (Sigma-Aldrich, UK). Rama27 and HaCaT were split 1:8 when $\geq$60% confluent with trypsin-EDTA. A stable cell line TC7 3xGFP (expressing tubulin-GFP) (kind gift from Chöle Bulinkski, Colombia University, USA) was cultured in 75 $cm^2$ flasks at 37 °C with 5% (v/v) $CO_2$, MEM (Life Technologies, UK) supplemented with 10% (v/v) FCS, 1% (v/v) NEAA, and fluorescence selected for using genetitin (Sigma-Aldrich, UK). TC7 3xGFP cells were split 1:15 when $\geq$80% confluent with trypsin-EDTA. Normal dermal fibroblasts (NF) and keloid fibroblasts (KF) (purchased from Tebu-Bio Ltd, USA) were cultured in 75 $cm^2$ flasks at 37 $^oC$ with 5% (v/v) $CO_2$, MEM supplemented with 10% (v/v) FBS, and split when 80% confluent with trypsin-EDTA. NF and KF were used between passages 4 and 6. NF, consisting of fibroblasts isolated from normal skin adjacent to keloid 110 (nskF110, Tebu-Bio Ltd), were purchased at passage 3, after tissue from the left cheek of a 9 year old Malay was surgically removed. KF (KF111) were also purchased after being surgically removed from the right back of a 21 year old Chinese female. As recommended by the manufacturer (Cell Research Corporation, Singapore), NF and KF were used between passage 4 and 6 for the following experiments.

All cells tested negative for mycoplasma contamination using a detection kit (Lonza, UK). Fixed neutrophil and immortalised corneal epithelial cells (hTCEpi) were kindly provided by Helen Wright (Institute of Ageing and Chronic Disease at University of Liverpool, UK) and Kevin Hamill (Department of Eye and Vision Science, at the Institute of Ageing and Chronic Disease at University of Liverpool, UK), respectively.

### 2.2.2 Quantum dot characterisation and conjugation

#### 2.2.2.1 UV-visible absorption and photoluminescence spectra (section 3.2.1: Figure 22)

Absorbance measurements of CdTe red and green Qdots (kindly provided by Vittorio Saggiomo, Netherlands) were taken at room temperature (RT) on a SpectraMax 34 Plus spectrophotometer (Molecular Devices, UK). Photoluminescence (PL) emission and excitation spectra of CdTe water-soluble Qdots were measured in a quartz cuvette (Starna Scientific, UK) with a path length of 10 nm using a Varian Cary Eclipse fluorescence spectrophotometer (Varian, Australia) at RT between 350-850 nm (λ excitation= 450 nm).

#### 2.2.2.2 Capturing blinking quantum dots (section 3.2.1: Figures 23 and 24)

Commercially available Qdot 625-Abs fluctuating “ON” and “OFF” was analysed by fixing Qdot 625-Abs to the surface of a glass coverslip. A movie of a ‘single’ immobilised Qdot 625-Ab blinking was captured at 10 fps on an epifluorescence microscope (63x 1.4NA plus a 2.5x magnifying lens) and an intensity time trace extracted using ImageJ. By applying a threshold and using the Analyze Particles feature in ImageJ, the number of Qdots was quantified.

#### 2.2.2.3 Conjugating anti-GFP nanobodies to CdTe quantum dots (section 3.2.2.1: Figure 26)

Anti-GFP nanobody-Qdot conjugation was applied via a direct covalent approach using cross-linking reagents 1-ethyl-3-(3-dimethylaminopropyl) carbodiimide (EDC) and sulfo-N-hydroxysuccinimide (sulfo-NHS). The carboxylate group on water-soluble CdTe Qdots was coupled to the amine group on anti-GFP nanobodies, forming an amide bond. Approximately 150 µL CdTe Qdots (3-10 µM) was added to 25 µL 20 mM sodium borate buffer pH 7.4 and 5 µL 50 mM sulfo-NHS/EDC activator, before being left to rotate for 30 min at 4 °C. After unreacted sulfo-NHS/EDC was removed with a 10 kDa centrifugal filter (Merck Millipore, Germany) and buffer-exchanged 3x with PBS (10,000 rpm, 5 min, RT), an excess of 13 kDa (2.5 nm x 4.5 nm) 15 µL 80 µM anti-GFP nanobodies (Allele Biotechnology, USA) was added and left to react for 2 h at 4 °C. After 2 h, the anti-GFP nanobody-Qdot conjugate was run for

30 min on a 1% (w/v) agarose gel at a constant voltage of 100 V with a running buffer of 1x Tris-acetate-EDTA (TAE), pH 8. The gel was imaged on a UV transilluminator.

#### 2.2.2.4 Site Click Qdot 625 antibody conjugation – antibody modification (section 3.2.3)

For conjugation of Qdots to anti-GFP, a site click Qdot 625 antibody labelling kit was used (S10452: Thermo Fisher Scientific, UK). Briefly, a concentrator filter was initially washed with 450 µL of $ddH_2O$ by centrifuging at 5,000 g for 6 min and the flow through discarded. Anti-GFP antibody (Roche Limited, UK), 2mg/mL, was buffer-exchanged in the concentrator by adding 62.5 µL to 437.5 µL preparation buffer (provided by the manufacturer) and centrifuged at 5,000 g for 6 min, with the flow through discarded. Preparation buffer (450 µL) was added to the concentrator and centrifuged for a further 6 min at 5,000 g. The concentrator was inverted into a collection tube and centrifuged at 1,000 g for 3 min to collect 50 µL of the concentrated antibody. The carbohydrate domain of the antibody was then modified by adding 10 µL of β-galactosidase and incubated for 4 h at 37 °C. For attachment of an azide, 75 µL $ddH_2O$, 10 µL of 20x Tris buffer (pH 7), 25 µL of buffer additive, 80 µL of GalT enzyme, and 220 µg UDP-GalNAz were added. The tube was sealed with Parafilm, centrifuged for 3 min at 1,000 g, and incubated overnight at 30 °C.

#### 2.2.2.5 Site Click Qdot 625 antibody conjugation – quantum dot attachment (section 3.2.3)

A large concentrator was washed with 1 mL 1x Tris buffer pH 7 by centrifuging at 1,200 g for 10 min. Flow through was discarded from the concentrator and 1.75 mL of 1x Tris buffer pH 7 was added with 250 µL of the modified antibody. The concentrator was centrifuged at 1,200 g for 6 min. Once the flow through was disposed of, 1.8 mL of 1x Tris buffer pH 7 was added and centrifuged for 10 min at 1,200 g (x2). The flow through was discarded and 1.8 mL of 1x Tris buffer pH 7 was added and centrifuged at 1,400 g for 10 min. The final volume in the concentrator was 100 µL. The filter was inverted into a collection tube and the concentrated antibody was collected through centrifugation at 1,000 g for 3 min. The 100 µL concentrated antibody was transferred to a 1.5 mL centrifuge tube and 50 µL of dibenzocyclooctyne (DIBO)-modified Qdot 625 nanocrystal was added, centrifuged at 5,000 g for 3 min, and incubated overnight at 25 °C. The conjugate was stored in the dark at 4 °C until use.

#### 2.2.2.6 Site Click Qdot 625 Antibody Conjugation – Determining Qdot 625 concentration (section 3.2.3)

The concentration of the Qdots in the conjugate was calculated to be 3 µM using the equation $c = \frac{A}{\varepsilon}$, where c is the concentration of DIBO-modified Qdot 625 attached to the primary antibody, A is the absorbance of Qdot 625, and Ɛ is the extinction coefficient of Qdot 625 (500,000 $M^{-1}cm^{-1}$). The absorbance between 605 nm-612 nm (step 10 nm) was measured to be 1.5 a.u. using a quartz cuvette with a 1 cm path length, on a SpectraMax 34 Plus spectrophotometer (Molecular Devices, UK).

### 2.2.3 Transmission electron microscopy (section 3.2.3)

Qdot 625-Ab was centrifuged at 1,000 g for 5 min to remove any aggregates. A 5 µL sample (0.5 µL Qdot 625-Ab 1 µM, diluted in 100 µL dd$H_2O$) was added to a formyar/carbon electron microscopy grid and left to air dry before imaging. TEM image of Qdot 625 core/shell was taken on a TEM. The core/shell size of Qdot 625 was measured for all particles in the calibrated TEM image using the Analyze particles tool in ImageJ and a bar chart plotted in MATLAB to show the distribution of core/shell sizes. A threshold was set and joint particles were separated by applying a watershed filter.

### 2.2.4 Size-exclusion high-performance liquid chromatography (section 3.2.3)

A BIO-Gel TSK 40 XL (300 x 7.8 mm) size-exclusion chromatography (SEC) column (Bio-Rad) was set up on a Dionex ICS-3000 high-performance liquid chromatography (HPLC) system and pre-equilibrated with 0.2 um filtered phosphate buffered saline (PBS). The separation range was up to 669 kDa. A 50 µL Qdot 625-Ab (0.1 µM) sample was injected into the column and run with PBS at a flow rate of 0.5 mL/min. Elution was monitored at 214, 280, 400, 500 and 600 nm. The column was calibrated by running standard proteins under the same conditions. The SEC-HPLC result for Qdot 625-Ab, using the 214 nm detection wavelength was plotted. Standard proteins of a known molecular weight were used as markers to calculate the molecular weight of Qdot 625-Ab.

### 2.2.5 Fluorescence correlation spectroscopy (section 3.2.3)

A Zeiss Axio Observer Z.1 780 CLSM (Zeiss, Germany) attached to a PicoQuant system (PicoQuant GmbH, Germany) was used. Point measurements were acquired for 60 s at 37 °C

using a 40x 1.2 NA water-immersion objective and a 485 nm pulsed diode laser (POL 828 Sepia II Multichannel Picosecond Diode Laser, PicoQuant GmbH, Germany). Samples were loaded into a custom-built chamber made out of a glass coverslip and Parafilm welded onto a glass microscope slide using a heating block to prevent evaporation. The sample was drawn up into the channel by capillary action and inverted with the glass coverslip facing the objective. For calibration of the confocal volume ($r_o$), 10 nM ATTO 488 (ATTO-Tec, Germany) was used. Since the diffusion coefficient (D) of 400 µm²/s for ATTO 488 was known at a temperature (T) of 25 °C (PicoQuant, Germany), the diffusion coefficient (D) of ATTO 488 was determined to be 536 µm²/s at 37 °C using $D(T) = D(25\ °C) \times \frac{T\ (K)}{298.15\ K} \times \frac{(8.9x\ 10^{-4}\ PaS)}{n(T)}$, where n is the viscosity of water. During calibration, the correction collar of the 40x water-immersion objective was adjusted to 0.17 mm to match the thickness of the coverslip used. ATTO 488 was fitted with a pure diffusion model and $r_0$ was determined to be 0.6.fL after fixing the concentration to 10 mM and D to 536 µm²/s. A standard reference sample of 30 nm fluorescent latex beads (Sigma-Aldrich, UK), diluted 1:500 in water, was used as a comparison to the Qdot-Abs. Each FCS measurement was repeated 5 times at different positions in the channel and the 5 repeats for 1 position plotted. A 615 nm long pass filter was placed in front of the detector for Qdots to block excitation light and a 520/35 short band pass filter was used for the ATTO 488 and fluorescent beads. SymPhoTime software (PicoQuant, Germany) was used to fit the autocorrelation function of ATTO488/beads to a pure diffusion model and the Qdot-Abs to a triplet model. The hydrodynamic diameter of the Qdot625-Ab and Qdot525-Ab was determined using: $d_{Qot} = d_{ST} \times \frac{\tau_{Qdot}}{\tau_{ST}}$, where d is the hydrodynamic diameter, Qdot refers to quantum dot, ST is the standard, and τ is the diffusion time (128).

### 2.2.6 Immunocytochemistry (chapters 3-5)

Cells were seeded onto 16 mm circular glass coverslips (5 mm coverslips for light-sheet imaging) and grown until confluent (24 h), washed once in PBS (37 °C), and fixed in 4% (w/v) paraformaldehyde (PFA) for 10 min or 100% ice cold methanol (5 min). Cells were washed 3x in PBS (5 min), permeabilised with 0.25% Triton X-100 in PBS for 60 min (except methanol fixation), washed again 3x in PBS (5 min), and incubated with 6% bovine serum albumin (BSA, Sigma-Aldrich, UK) in PBS (60 min). Primary antibodies produced in mouse or rabbit were diluted (Table 2) in 6% (w/v) BSA and incubated overnight at 4 °C. Cells were washed 3x in PBS (5 min) and incubated with secondary antibodies diluted (Table 2) in 6% BSA at RT (60

min). Before preparation of the Qdot 625 conjugated secondary antibodies, the vial was centrifuged at 5,000 g for 3 min to remove any aggregates. After 3 washes in PBS (10 min), coverslips were mounted onto slides with ProLong Gold mounting medium (Thermo Fisher Scientific, UK), and stored at 4 °C overnight. A negative control of secondary antibody only was also prepared to show any non-specific background staining. For dual labelled samples, cells were sequentially incubated with different species of primary and secondary antibodies.

| | Antibody | Supplier | Dilution |
|---|---|---|---|
| Primary antibodies | Anti-Neutrophil Elastase rabbit polyclonal antibody | Abcam (ab68672) | 1:100 |
| | Anti-MPO mouse monoclonal antibody | Abcam (ab25989) | 1:100 |
| | Anti-Histone H3 (citrulline R2 + R8 + R17) rabbit polyclonal antibody | Abcam (ab5103) | 1:100 |
| | Anti-Histone H3 mouse monoclonal antibody | Abcam (ab195277) | 1:100 |
| | Anti-PAD4 mouse monoclonal antibody | Abcam (ab128086) | 1:00 |
| | Anti-HIF-2-alpha recombinant Rabbit monoclonal antibody | Bethyl Laboratories (BL-95-1A2) | 1:100 |
| | Anti-HIF-1β mouse monoclonal antibody | Abcam (ab2771) | 1:100 |
| | Anti-HIF-1α mouse monoclonal antibody | BD Biosciences (610959) | 1:100 |
| | Anti-SART1 (HAF) mouse polyclonal antibody | Abcam (ab88583) | 1:100 |
| | Anti-RNA Polymerase II (Phospho Ser5) mouse monoclonal antibody | Novus-Biologicals (NBP2-59219) | 1:50 |
| | Anti-Nucleolin mouse monoclonal antibody | Thermo Fisher Scientific (39-6400) | 1:100 |
| | Anti-GFP from mouse (clones 7.1 and 13.1) antibody | Roche (11814460001) | 1:100 |
| | Anti-GFP rabbit polyclonal antibody | Abcam (ab290) | 1:100 |
| | Anti-GFP (biotin) rabbit polyclonal antibody | Abcam (ab69313) | 1:100 |
| | Anti-β-tubulin TUB 2.1 mouse monoclonal antibody | Sigma-Aldrich (T5201) | 1:100 |
| | Anti-alpha Actinin 4 rabbit monoclonal antibody | Abcam (ab108198) | 1:100 |
| | Anti-SC35 nuclear speckle marker mouse monoclonal antibody | Abcam (ab11826) | 1:100 |
| | Anti-fibronectin rabbit polyclonal antibody | Abcam (ab2413) | 1:100 |

| | | | |
|---|---|---|---|
| | 3E11 mouse monoclonal antibody against LaNt α31 | Kindly provided by Kevin Hamill (University of Liverpool, UK) | 1:100 |
| | RG13 mouse monoclonal antibody against the LM α3 subunit of LM-332 | Kindly provided by Kevin Hamill (University of Liverpool, UK) | 1:100 |
| | Anti-mCherry monoclonal primary antibody | Sigma-Aldrich (SAB2702291) | 1:100 |
| | Anti-Talin-1 monoclonal antibody produced in mouse (clone 8d4) | Sigma-Aldrich (T3287) | 1:100 |
| | Phallodin-Alexa Fluor 488 | Thermo Fisher Scientific (A12379) | 1:40 |
| **Secondary antibodies** | F(ab')2-Donkey anti-Mouse IgG (H+L) Secondary Antibody, Qdot 625 conjugate | Thermo Fisher Scientific (Q22085) | 1:50 |
| | Donkey anti-Mouse IgG (H+L) Secondary antibody, Qdot ® 525 conjugate | Thermo Fisher Scientific (Q22073) | 1:50 |
| | Donkey anti-Mouse, IgG (H+L) Secondary Antibody, Alexa Fluor 647 conjugate | Thermo Fisher Scientific (A-31571) | 1:500 |
| | F(ab')2-Goat anti-Rabbit IgG (H+L) Secondary Antibody, Qdot 625 conjugate | Thermo Fisher Scientific (A10194) | 1:50 |
| | Donkey anti-Rabbit IgG (H+L) Secondary antibody, Qdot ® 525 conjugate | Thermo Fisher Scientific (Q22074) | 1:50 |
| | Goat anti-Rabbit IgG (H+L) Cross-Adsorbed Secondary Antibody, Alexa Fluor 488 | Thermo Fisher Scientific (A-11008) | 1:500 |
| | Goat anti-Mouse IgG (H+L) Cross-Adsorbed Secondary Antibody, Alexa Fluor 488 | Thermo Fisher Scientific (A11001) | 1:500 |
| | Goat anti-rabbit IgG (H+L) Cross-Adsorbed Secondary Antibody, Alexa 647 | Thermo Fisher Scientific (A-21244) | 1:500 |
| | Qdot 625 streptavidin conjugate | Thermo Fisher Scientific (Q22063) | 1:50 |
| | Anti-mouse IgG (whole molecule) F(ab')2 fragment-Cy3 antibody produced in sheep | Sigma-Aldrich (C2181-1ML) | 1:500 |

**Table 2. Primary and secondary antibodies for immunocytochemistry.** Working primary and secondary antibody dilutions for use in immunocytochemistry.

### 2.2.7 Western blot (section 5.2.1: Figure 86)

Approximately 50,000 cells/mL of NF or KF were seeded onto 10 cm cell culture treated dishes (Corning, USA) and left to grow for 48 h. For cell treatment, cells were incubated for a further 24 h either in normal medium (DMEM + 10% FBS), no serum (DMEM only), or DMEM medium supplemented with 10 ng/mL BSA. Confluent cells were washed in 1x PBS and lysed on ice in lysis buffer (50 mM Tris-HCl pH 7.5, 1 mM EDTA, 1 mM EGTA, 0.5 mM $Na_3VO_4$, 1% (v/v) Triton X-100, 50 mM NaF, 5 mM sodium pyrophosphate, 10 mM sodium B-glycerophosphate) containing 10 µg/mL phosphatase inhibitor cocktail for 1 min. After cell scrapping, the samples were centrifuged at 13,000 g for 5 min at 4 °C. A bicinchoninic acid (BCA) assay (Thermo Fisher Scientific, UK) was performed to determine the protein concentration of the supernatant (A562 nm), with BSA used as the protein standard. Lysate was diluted in lysis buffer and boiled at 95 °C in 9 uL Laemmli (2×) buffer (25% v/v 0.5 M Tris base pH 6.8, 20% v/v glycerol, 10% w/v SDS, 5% v/v β-mercaptoethanol, 0.1% w/v bromophenol blue) for 10 min. Between 10 ug – 30 ug of protein (45 µL) and 20 µL color-coded pre-stained protein marker 43 – 315 kDa high range (New England Biolabs, UK) was loaded into a SDS polyacrylamide gel consisting of 4% stacking gel (4% v/v acrylamide, 0.4 M Tris pH 6.8, 0.65 ng/µL APS, 0.325% v/v TEMED) and 7.5% resolving gel (7.5% v/v acrylamide, 0.4 M Tris pH 8.8, 0.1% w/v SDS, 0.25 ng/µL APS, 0.125% v/v TEMED), which was run at 100 V for 90 min (RT) in 1x running buffer (192 mM glycine, 25 mM Tris, 3.4 mM SDS). Empty wells were loaded with 45 µL Laemmli (2x) buffer. Proteins were transferred onto 0.2 µm nitrocellulose membrane (Bio-Rad, UK) overnight at 30 mA (4 °C) with transfer buffer (192 mM glycine, 25 mM Tris, 20% v/v methanol). Membrane was stained with Ponceau S stain (Sigma Aldrich, UK) and washed in 1x TBST pH 7.6 (0.2 M Tris, 0.1% v/v Tween-20, 0.14 M NaCl) for 2 min, before being incubated in 5% (w/v) non-fat milk (Marvel) in 1x TBST. After blocking, the membrane was incubated in primary antibodies overnight (4 °C). Primary antibodies (β-actin 1:3000, fibronectin 1:2000, and collagen I 1:1000) were all diluted in 5% BSA (w/v) in 1x TBST. Once washed 3x with 1x TBST (10 min), the membrane was incubated for 60 min in secondary antibodies (Table 3) (mouse 1:5000 and rabbit 1:3000, both diluted with 5% (w/v) BSA in 1x TBST). Before imaging, the membrane was washed 3x with 1xTBST and signal detected with ECL developer on a Syngene G-Box (Geneflow, UK). Protein abundance was quantified using ImageJ.

| | Antibody | Supplier | Dilution |
|---|---|---|---|
| Primary antibodies | Anti-beta-actin mouse monoclonal antibody | Abcam (ab8226) | 1:3000 |
| | Anti-collagen I rabbit polyclonal antibody | Abcam (ab34710) | 1:1000 |
| | Anti-fibronectin rabbit polyclonal antibody | Abcam (ab2413) | 1:2000 |
| Secondary antibodies | Anti-rabbit IgG HRP secondary antibody | Cell Signalling (7074S) | 1:3000 |
| | Sheep anti-mouse IgG H&L (HRP) | Abcam (Ab6808) | 1:5000 |

**Table 3. Primary and secondary antibodies used in western blotting.** List of supplied primary and secondary antibodies and their working dilutions for use in western blot.

### 2.2.8 Molecular biology

#### 2.2.8.1 DNA recovery before transformation into cells (sections 3.3, 5.1.1, and 5.1.5)

Skylan-S constructs (Kind gifts from Pingyong Xu, Institute of Biophysics, Chinese Academy of Sciences, Beijing, China) (106), spotted on paper, were cut out and placed into a 1.5 mL Eppendorf tube. The DNA was dissolved in 100 µL of TE buffer and incubated at RT for 5 min. The DNA was centrifuged and 10 µL of supernatant was used to transfect E.coli.

#### 2.2.8.2 Transformation (sections 3.3, 5.1.1, and 5.1.5)

E.coli DH5α (100 µL) competent cells was thawed on ice and added 10 µL of plasmid DNA was added. The cells were kept on ice for 30 min, heat shocked at 42 °C for 90 s, and then returned to ice for 2 min. 500 µL SOC microbial growth medium was added and incubated for 30 min at 37 °C. 100 µL of bacterial culture was spread onto agar plates containing 50 µg/mL kanamycin and incubated overnight at 37 °C. A control plate containing no plasmid DNA was also prepared. One colony of bacteria was selected, transferred to 5 mL of LB broth with 5 µL of 50 ug/mL kanamycin using an inoculation loop and left on an orbital shaker at 37 °C until cloudy. The all-day culture (1 mL) was added to 100 mL of LB broth containing 100 uL 50 ug/mL kanamycin and left on an orbital shaker at 37 °C overnight. The cells were harvested by centrifuging at 4,000 g for 10 min at 4 °C. Glycerol stocks consisting of 500 µL 80% glycerol and 500 µL day culture were prepared in cryovials.

#### 2.2.8.3 Plasmid DNA purification (sections 3.3, 5.1.1, and 5.1.5)

*Small scale (Mini-prep)*: 2 mL of overnight culture was centrifuged (8,000 rpm) for 2 min and the DNA was purified using a GeneJET plasmid kit (Thermo Fisher Scientific, UK). In short, the pellet was re-suspended in 250 µL resuspension solution and 250 µL lysis solution was added.

The tube was inverted 4-6 times, until the solution was slightly clear, 350 µL neutralisation solution was added and the tube again inverted 4-6 times. Solution was centrifuged 1,200 g for 5 min to get a white pellet. Supernatant was transferred to a spin column and centrifuged at 12000 g for 1 min, flow through was discarded, and 500 µl wash solution added (x3). Empty spin column was centrifuged at 12000 g for 1 min and top half of spin column transferred to a 1.5 mL Eppendorf tube with 50 µL elution buffer added, left for 2 min at RT, and then centrifuged at 12000 g for 2 min. Elute was transferred to a fresh Eppendorf tube and the amount of DNA determined using a NanoDrop ™ spectrophotometer (Thermo Fisher Scientific, UK).

*Large scale (Maxi-prep)*: The plasmid DNA was purified using a Purelink TM HiPure Plasmid Filter Purification Kit (Thermo Fisher Scientific, UK). Briefly, the supernatant from the harvested cells was removed and the pellet was re-suspended in 10 mL of buffer containing RNase A. Lysis buffer (10 mL) was added and when homogenous, 10 mL of precipitation buffer was added. Elution buffer (15 mL) was used to collect the plasmid DNA and the inner tube of the column discarded. Isopropanol (10.5 mL) was added to the eluted plasmid DNA and left to incubate for 2 min at RT. The plasmid DNA was centrifuged at 12,000 g for 30 min at 4 °C. The supernatant was removed and the pellet was re-suspended in 5 mL of 70% ethanol. Precipitation buffer (10 mL) was added to the lysate, mixed gently, and the pellet allowed to air-dry for 10 min. The pellet was re-suspended in 200 mL of TE buffer and the DNA was diluted to a final concentration of 1 µg/mL.

#### 2.2.8.4 Restriction digest (sections 3.3, 5.1.1, and 5.1.5)

Restriction enzyme XhoI (NEB) 1.5 µL was added to 3 µL 1µg/µL Skylan-S, 2 µL smart buffer (NEB), and 13.5 µL dd$H_2O$ to give a total volume of 20 µL (Table 4). Skylan-S-N1 was singularly digested with restriction enzyme XhoI, by checking its plasmid map using SnapGene software (Figure 21A), to open up the backbone vector for the insertion of amplified HIF-2α.

| **Component** | **Volume (µL)** |
|---|---|
| XhoI (NEB) | 1.5 |
| 1 µg/µL Skylan-S | 3 |
| Smart buffer (NEB) | 2 |
| dd$H_2O$ | 13.5 |

**Table 4. Restriction digest preparation.** Regents required to linearise the vector of Skylan-S for In Fusion ® cloning of Skylan-S-HIF-2α.

### 2.2.8.5 Polymerase chain reaction (sections 3.3, 5.1.1, and 5.1.5)

Forward and reverse primers were designed (Table 5), from the nucleotide sequence of pG-enhanced green fluorescent protein (EGFP)-HIF-2α (Kind gift from James Bagnall, University of Manchester, UK), and reagents prepared (Table 6). Plasmid DNA, pG-EGFP-HIF-2α, was amplified via the polymerase chain reaction (PCR) using a Px2 thermal cycler (Thermo Fisher Scientific, UK) and a temperature gradient was used to find the optimum temperature (55.1 °C). Thirty cycles were used, including an initial denaturation step at 95 °C for 20 s, annealing temperature of 60.5 °C for 15 s, and elongation at 70 °C for 60 s (700 bp of DNA).

| Plasmid | Primer | Sequence 5'to 3' |
|---|---|---|
| pG-EGFP-HIF-2α | Forward | CTACCGGACTCAGATCATGACAGCTGACAAGGAGAAGAAAAGG |
| | Reverse | GAAGCTTGAGCTCGAGGGTGGCCTGGTCCAGGC |

**Table 5. Skylan-S primer design.** Forward and reverse PCR primers to amplify HIF-2α for In Fusion ® cloning of Skylan-S-HIF-2α.

| Component | Volume (µL) |
|---|---|
| 10x hot start KOD polymerase buffer (EMD Millipore) | 5 |
| $MgSO_4$ | 3 |
| DNTP | 5 |
| 1 µg/µL pG-EGFP-HIF-2α | 1 |
| 10 µM Forward HIF-2α primer | 1.5 |
| 10 µM Reverse HIF-2α primer | 1.5 |
| $ddH_2O$ | 32 |
| KOD polymerase | 1 |

**Table 6. Polymerase chain reaction preparation.** Regents required for the amplification of HIF-2α by PCR for In Fusion ® cloning.

### 2.2.8.6 Agarose gel electrophoresis (sections 3.3, 5.1.1, and 5.1.5)

DNA fragments were ran at 100 V for 45 min on a 1% (w/v) agarose gel (1 g agarose + 100 mL TAE), to separate the bands by size. The gel contained 5 µL midori green DNA dye, to enable the bands to be visualised under UV (Figure 21B). Gel bands were excised from the gel and an E.Z.N.A ® gel extraction kit (Omega Biotek, USA) was used to purify the DNA fragments, following the manufacturer's instructions. The purified DNA was quantified by its

absorbance on a Nanodrop UV-visible spectrophotometer and the amount of DNA, required for In-Fusion ® HD cloning, was calculated using a Clontech calculator.

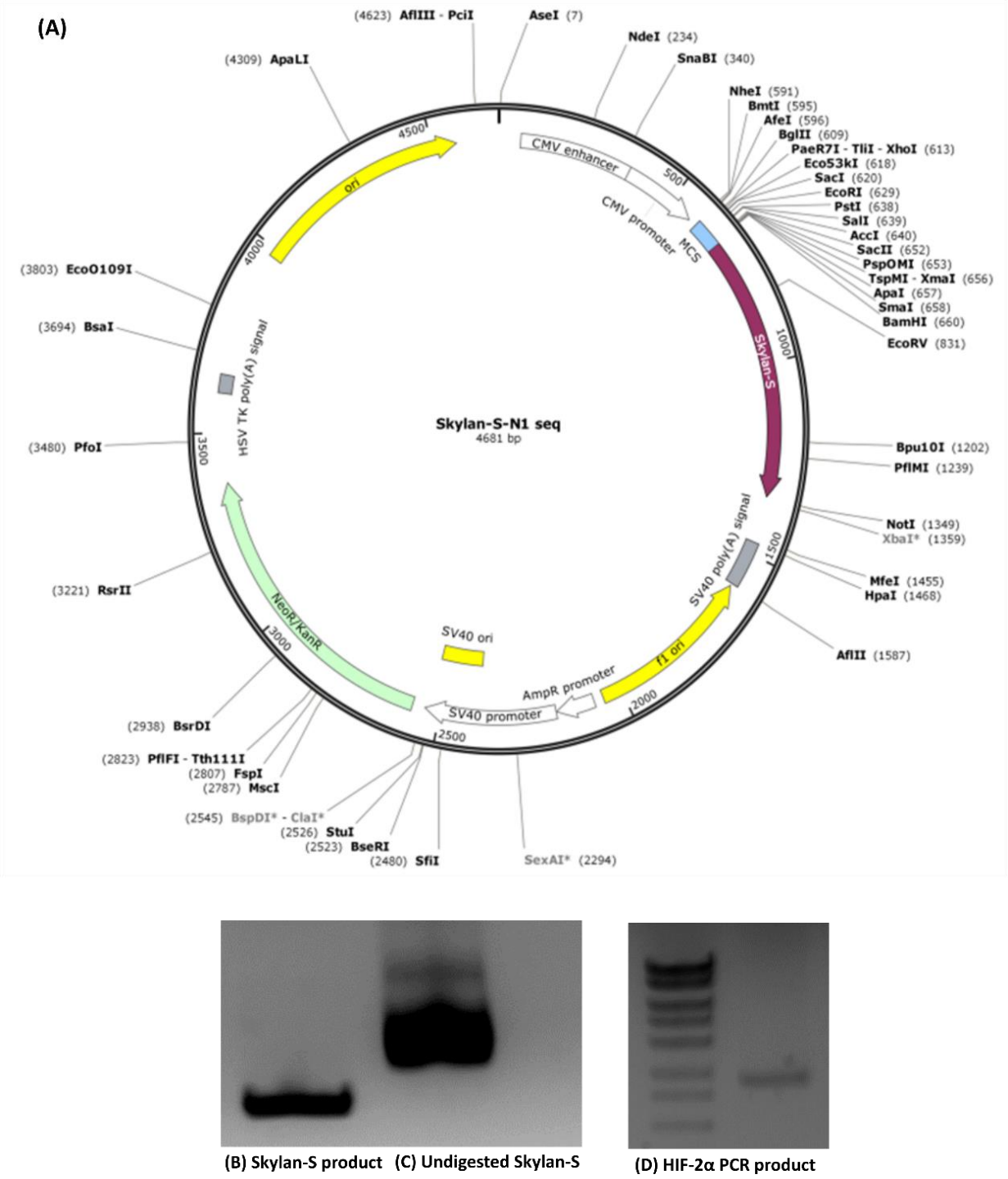


**Figure 21. Infusion cloning of HIF-2α-Skylan-S.** Skylan-S-N1 (kindly provided by Pingyong Xu, Chinese Academy of Sciences in Beijing, China) was mapped using SnapGene software (A), to locate the restriction site to cut with XhoI (NEB) enzyme and digest Skylan-S-N1 (B). An undigested control of uncut Skylan-S-N1 (4681 bp) was also loaded onto the agarose gel (C). PCR was used to amplify the HIF-2α (D) from pG-EGFP-HIF-2α (Kind gift from Violaine Sée, University of Liverpool, UK). As Skylan-S-N1 (4681 bp) was unconjugated, soluble, and diffuse, it was ideal for cloning purposes.

### 2.2.8.7 In Fusion ® HD cloning (sections 3.3, 5.1.1, and 5.1.5)

A HIF-2α encoding insert was fused to the vector encoding the fluorescent tag Skylan-S using the In-Fusion ® HD Cloning method (Clontech Laboratories Inc., USA). In Fusion ® Reaction was prepared according to Table 7 and incubated for 15 min at 50 °C. Proteinase k (1µL) was added and incubated for 10 min at 37 °C. DNA (5 ng) was added to 50 µL Stellar cells and placed on ice for 30 min. Cells were heat shocked for 45 s at 42 °C. SOC medium was added to give a total volume of 500 µL, incubated at 37 °C for 1 h (225 rpm). After 1 h, the transformed cells were plated onto warm agar plates and left to incubate at 37 °C overnight. A single colony was picked off the agar plate, transferred to 5 mL LB broth containing 5 µL kanamycin, and incubated at 37 °C for 8 h. The 8 h culture (1 mL) was added to 100 mL of LB broth containing 100 uL 50 ug/mL kanamycin and left on an orbital shaker at 37 °C overnight in preparation for plasmid DNA purification (see mini-prep). After purification, the cloned DNA was transfected into HeLa cells to check the correct localisation of the resulting HIF-2α-Skylan-S construct and it was also validated by sending it for sequencing (GATC, Germany).

| **Component** | **Volume (µL)** |
|---|---|
| Purified HIF-2α PCR product (insert) | 5.6 |
| Skylan-S restriction digest product (linearised vector) | 1.3 |
| 5x infusion enzyme | 2 |
| dd$H_2O$ | 1.1 |

**Table 7. In-Fusion ® cloning.** Vector and insert amounts required for In-Fusion ® cloning of HIF-2α-Skylan-S.

### 2.2.8.8 Transient transfection (sections 3.2.3, 3.3, and 5.1)

HeLa cells (100,000 cells/mL) were seeded onto 35 mm glass bottom dishes (Greiner Bio-One International) and transfected with HIF-2α-Skylan-S, LifeAct-Skylan-S, Microtubule-associated protein four (MAP4)-Skylan-S, talin-EGFP, soluble-EGFP, HIF-2α-EGFP, HIF-1β-DsRed, or HAF-EGFP using FuGENE6 transfection reagent (Roche Limited, UK), following the manufacturer's protocol (3:1 transfection reagent:DNA plasmid). For co-transfection 3:0.5:0.5 transfection reagent:DNA plasmid 1: DNA plasmid2 was used. Skylan-S constructs were kindly provided by Pingyong Xu, Institute of Biophysics, Chinese Academy of Sciences,

Beijing and EGFP constructs were kindly provided by Violaine Sée, University of Liverpool, UK.

### 2.2.9 Image acquisition and processing

#### 2.2.9.1 Diffraction-limited imaging

##### 2.2.9.1.1 Epifluorescence Imaging (chapters 3-5)

Unless otherwise stated in the figure legends, 1,000 images were acquired on a wide-field epifluorescence microscope (Zeiss Axio Observer Z.1, Germany), equipped with a 16 µm 512 x 512 pixel sensitive EMCCD camera (Andor iXon 897 Ultra) and UV polychromatic mercury arc lamp (HBO120). A 100x 1.4 NA oil-immersion objective plus a 2.5x magnifying lens was used to achieve an effective pixel size of 64 nm and to satisfy Nyquist sampling. Acquisition of images was controlled using Micro-Manager software (247). Qdot 625 and Qdot 525 were imaged with Chroma filter sets 39106 and 39101(Chroma Technology Corporation, USA), respectively. The exposure time was varied according to the sample from 5-100 ms (see figure legends for appropriate exposure time). Two colour images were obtained by sequentially acquiring 1,000 frames in one channel and then 1,000 frames in the other channel. Grayscale images are displayed for single channel data and false colour for composite images using the Channels Tool in ImageJ. Nucleolin-Alexa Fluor 488 (fixed in 4% w/v PFA) was imaged in wide-field mode (100x 1.46 NA plus 1.6x magnifying lens) with 50% (1.2 mW) of a 30 mW 488 nm laser, at different exposure times (5 ms, 10 ms, 50 ms, and 100 ms), on a LSM 880 BioAFM system (Zeiss Axio Observer Z1, Zeiss Microscopy, Germany). HIF-2α-Skylan-S was imaged (1,000 frames) in laser wide-field mode on a LSM 880 BioAFM system (Zeiss Axio Observer Z1, Zeiss Microscopy, Germany) with a 100x oil immersion 1.46 NA objective with 50% (1.2 mW) of a 30 mW 488 nm laser at 10 ms.

##### 2.2.9.1.2 Microinjection (section 3.2.2.2: Figure 27)

HeLa cells were cultured as described previously, seeded onto 35 mm glass bottom gridded dishes (ibidi GmbH) at a density of 10,000 cells per 2 mL MEM, and injected with 5 mg/mL fluorescein isothiocyanate dextran (FITC-dextran, molecular weight: 150,000, Sigma Aldrich, UK) using a 0.1 µm glass microcapillary needle tip (Eppendorf, UK). The micropipette tip is found at 10x magnification with the aid of coarse controls on the micromanipulator. Before microinjection, the camera mode was switched from electron-multiplying to conventional. Images of injected cells were obtained immediately after microinjection using a wide-field

epifluorescence microscope at 20x magnification. The following microinjector system (Eppendorf FemtoJet, Germany) settings were used: compensation pressure (Pc) 50 hPa to prevent back flow of the medium into the needle, injection pressure (Pi) 300 hPa, and injection time (ti) 0.3s. The cells were incubated throughout at 37°C and 5% $CO_2$.

#### 2.2.9.1.3 Total internal reflection fluorescence (section 3.3: Figures 28 and 29)

MAP4-Skylan-S (kindly provided by Pingyong Xu, Institute of Biophysics, Chinese Academy of Sciences, Beijing) was imaged using continuous illumination (100x 1.46 NA) on a LSM 880 BioAFM system (Zeiss Axio Observer Z1, Zeiss Microscopy, Germany) with 10% (0.14 mW) of a 30 mW 488 nm laser (68 ° TIRF) and 20% 365 nm light-emitting diode (LED) at 10 fps (100 ms exposure time). LifeAct-Skylan-S (kindly provided by Pingyong Xu, Institute of Biophysics, Chinese Academy of Sciences, Beijing) was illuminated via spontaneous recovery by initially switching "ON" with 365 nm colibri LED (20%) for up to 60 s, before being turned "OFF" completely with continuous illumination using 1% of a 30 mW 488 nm laser (100x 1.46 oil immersion objective). For Lifect-Skylan-S, 1,000 frames were acquired on a LSM 880 BioAFM system (Zeiss Axio Observer Z1, Zeiss Microscopy, Germany), at 30 ms, in TIRF mode (68˚).

#### 2.2.9.1.4 Light-sheet fluorescence microscopy (section 4.6.1: Figures 66 and 67)

HeLa cells were grown on 5 mm-by-5 mm glass circular coverslips (Agar Scientific, UK), fixed with methanol, and β-tubulin labelled with Qdot 625 by indirect immunofluorescence with antibodies. A specialised sample holder, on loan from Carl Zeiss Microscopy GmbH (Jena, Germany), comprising tweezers to suspend a 5 mm-by-5 mm coverslip, was used to image cell monolayers of β-tubulin-Qdot 625 on the light-sheet Z.1. One hour before acquisition, the light-sheet was set to RT. The coverslip was positioned at a 45 ° angle to the detection objective (40x 1.4 NA, plus maximum zoom) and 1,000 frames acquired at 4 different z-positions with 100% of a 20 mW 561 nm laser in ZEN software, on a sCMOS camera. After SOFI-processing each z-stack, a maximum intensity projection of the SOFI-processed z-stack was taken in ImageJ, to display a complete cell in focus.

#### 2.2.9.2 Diffraction-unlimited imaging

##### 2.2.9.2.1 Direct stochastic optical reconstruction microscopy (sections 3.4, 4.5, and 5.1.5)

HeLa cells were fixed with 4% (w/v) PFA in a 6-well compartment dish (Nunc ® Lab-Tek II chambered coverglass, Sigma-Aldrich, UK) with β-tubulin (sample kindly provided by Carl Zeiss Microscopy GmbH, Jena, Germany) and HIF-2α labelled with Alexa Fluor 647. HIF-2α-Alexa Fluor 647 and β-tubulin-Alexa Fluor 647 samples were incubated with a freshly prepared oxygen scavenger buffer, consisting of 800 µL $ddH_2O$, 100 µL 10x PBS, 100 µL 1M MEA (pH 9) (Sigma-Aldrich, UK), and 10 µL 10 nM sodium hydroxide (NaOH) (Sigma-Aldrich, UK). For dSTORM imaging, 30,000 frames were sequentially acquired on an EMCCD camera attached to a Zeiss Elyra P.S.1 system (63x 1.4 NA). A region of interest (ROI) was cropped and illuminated with 100% of a 150 mW 642 nm laser (Long pass filter: 655 nm) and 0.5% of a 50 mW 405 nm laser in laser wide-field mode, with an additional FOV lens with TIRF-ultra high power (TIRF-UHP), at 20 ms. Raw image stack of HIF-2α-Alexa Fluor 647 and β-tubulin-Alexa Fluor 647 was post-processed with dSTORM using ZEN software with a measured PSF.

##### 2.2.9.2.2 Super-resolution optical fluctuation imaging

###### 2.2.9.2.2.1 Two-dimensional SOFI (chapters 3-5)

Unless stated elsewhere in the figure legends, 1,000 wide-field images were used for SOFI-processing. Localizer and bSOFI were both implemented in MATLAB R2016a (MathWorks Inc., USA), using open-source codes available from bitbucket (https://bitbucket.org/pdedecker/localizer) and MATLAB Toolbox (https://documents.epfl.ch/users/l/le/leuteneg/www/BalancedSOFI), respectively. The script to run the Localizer code in MATLAB (MathWorks Inc., USA) code was compiled by David Mason (University of Liverpool, UK). MATLAB scripts can be found in the appendix. SOFI images were computed with time lag zero. Higher-order SOFI images for Localizer were re-scaled by taking roots of the pixel values, so for 3$^{rd}$ order SOFI, the cube root was taken. For two-colour SOFI, single channel data was SOFI-processed and then a composite image formed in ImageJ.

#### 2.2.9.2.2.2 Three-dimensional SOFI with PRILM (section 4.6.3: Figure 70)

To test the combination of PRILM and SOFI in obtaining additional information in z, an angular cylindrical-shaped glass lens (phase ramp) was inserted into the light path to split the PSF of the fluorophores into two equal lobes that were later reformed with SOFI-processing. β-tubulin was labelled with Qdot 625 by indirect immunofluorescence and 1,000 frames acquired on an Elyra PS.1 system (63x 1.4NA plus 1.6x magnifying lens) at 30 fps (33 ms exposure time), in the presence of a 1.5' wedge angle phase ramp (Zeiss 3D PALM slider). A 3D cross-cumulants algorithm was applied to the dataset in ZEN software (kindly provided by Yauheni Novikau at Carl Zeiss Microscopy GmbH, Jena, Germany).

#### 2.2.9.2.2.3 SOFI simulation tool (section 4.2.5: Figure 61)

A SOFI simulation tool (124), implemented in MATLAB R2016a (MathWorks Inc., USA) was used to generate simulated bSOFI Siemens star pattern data up to $4^{th}$ order, based on the following acquisition settings: Density in sample: 6.3968 $\mu m^{-2}$ (Number on camera: 10,000 $\mu m^2$), Signal per frame: 400 photons, Background: 4 photons, On-state lifetime: 10 ms, Off-state lifetime: 50 ms, Average bleaching time: 1 s, Readout noise: 1.6 ms, Dark: 0.06 electrons/pixel/s, Quantum efficiency: 0.7, Gain: 4, Pixel size: 16 x 16 $\mu m^2$, Pixel number: 512 x 512, NA: 1.4, Wavelength: 625 nm, Magnification: 100, acquisition time: 100 s, number of frames: 1,000, and acquisition rate (number of frames/acquisition time): 10 frames/s. Experimental data was also acquired by labelling β-tubulin with Qdot 625-Abs and imaging on an epifluorescence microscope (100x 1.4NA), using the same parameters as set in the SOFI simulation tool. ROIs were taking using open-source ImageJ software.

#### 2.2.9.2.2.4 Applying Lucy-Richardson deconvolution to SOFI (section 4.4: Figure 64)

A Lucy-Richardson deconvolution algorithm was used on SOFI images processed with the Localizer algorithm, not to remove noise, as SOFI images should be noise-free, but to linearise the differences in molecular brightness from the SOFI processing. Lucy-Richardson deconvolution has already been incorporated into the bSOFI algorithm (93), but not the SOFI Localizer algorithm (89). To test the performance of the Lucy-Richardson algorithm on correcting the large variation in intensity of images processed with SOFI Localizer, for display purposes, a Lucy-Richardson algorithm, within the open-source DeconvolutionLab2 ImageJ

plugin (20), was applied to SOFI images processed with Localizer and the number of iterations varied from 5-20 (standard iteration is 10).

#### 2.2.9.2.3 Super-resolution radial fluctuations

##### 2.2.9.2.3.1 NanoJ-SRRF (sections 4.2.4.1, 4.5, 5.1.2, 5.1.4, and 5.1.5)

Unless otherwise stated in figure legends, 100 frames of wide-field images, acquired at 5 ms on an epifluorescence microscope (100x 1.4 NA plus 2.5 magnifying lens) equipped with an arc mercury lamp source and an Andor iXon Ultra 897 EMCCD camera were post-processed with an ImageJ plugin NanoJ-SRRF. Default settings were used: ring radius 0.5, radiality magnification 5, axes in ring 6, and temporal radiality analysis (TRA). All default acquisition settings were kept constant unless one was varied for testing purposes, including the number of frames (50, 100, 500, and 1,000) and exposure time (5 ms, 10 ms, 50 ms, and 100 ms). Default post-processing parameters were also kept constant, unless varied for testing purposes, including ring radius (0.1, 0.25, 0.5, 1, 2, and 3), radiality magnification (1x, 5x, and 10x), and axes in ring (2, 6, and 8).

##### 2.2.9.2.3.2 SRRF-Stream (sections 4.2.4.2 and 5.1.6)

SRRF-Stream images were acquired on a Leica DMi8 spinning disk confocal (100x 1.4 NA plus 2x magnifying lens), equipped with an Andor iXon 888 EMCCD camera. Alexa Fluor 647 and Alexa Fluor 488 was acquired with a 140 mW 637 nm laser and a 50 mW 488 nm laser, respectively. Large FOV (1024-by-1024) was captured with an effective pixel size of 65 nm (13 µm camera pixel size and 100x 1.4 NA plus 2x magnifying lens). Unless otherwise stated, default NanoJ-SRRF settings were used: ring radius of 0.5 and radiality magnification of 5x, as well as 100 frames and a 5 ms exposure time.

#### 2.2.9.2.4 Stimulated emission depletion (sections 4.5 and 5.1.5)

All STED images were acquired by Peter Hemmerich at the imaging facility in the Leibniz Institute on Ageing (Fritz Lipmann Institute, Jena, Germany). The fluorescent protein HIF-2α-EGFP was transfected into HeLa cells grown under normoxia, before being fixed with 4% PFA (w/v), and labelled with anti-GFP-NANObooster-ATTO647N, whilst β-tubulin was labelled with a primary anti-tubulin antibody and a secondary antibody conjugated to Abberior STAR

580. For STED imaging of proteins, a Leica TCS SP8 STED 3x microscope (100x 1.4NA) was used to acquire a z-stack of images with a 1.5 mW pulsed (80 MHz) excitation laser tunable from 470 to 670 nm (647 nm used at 100% for ATTO647N and 580 nm used at 100% for Abberior STAR 580) and a 100% of a 1.85 W pulsed (80 MHz) 775 nm STED depleted doughnut laser. The resulting STED z-stack post-processed with Huygens deconvolution software. The deconvolved STED image was displayed as a maximum intensity z projection.

#### 2.2.9.2.5 Structured illumination microscopy (sections 4.5 and 5.1.5)

A z-stack of β-tubulin-Alexa Fluor 647 (10 positions) and transfected HIF-2α-EGFP (7 positions) was acquired with a 1% of a 150 mW 642 nm laser and 2% of a 100 mW 488 nm laser, respectively, at 100 ms. All images were acquired on a sCMOS camera (no gain) with the Zeiss Elyra P.S.1 system using 5 rotations (34 µm grid). SIM-processing was done in ZEN software and a maximum intensity z projection was performed on the raw data in ImageJ.

#### 2.2.9.2.6 Airyscan imaging (sections 5.1.3, 5.1.4, and 5.1.5)

Airyscan images were acquired on an LSM 880 confocal laser scanning Zeiss Axio Examiner Z1 upright microscope (Carl Zeiss Microscopy GmbH, Germany), with a 30 mW 488 nm laser and a 20 mW 561 nm laser, in ZEN software. A pinhole of 1.25 AU was selected and a 63x 1.4 NA water immersion dipping objective used.

### 2.2.9.3 Quantitative analyis

#### 2.2.9.3.1 Co-localisation analysis (sections 4.1.5 and 5.1.4)

A freely available ImageJ plugin Just Another Co-localisation Plugin (JACoP) (248) was used to perform quantitative co-localisation analysis. By setting a threshold, Manders and Pearson's correlation coefficients were calculated. Pearson correlation coefficient scatter plots of Qdot 625 and Alexa Fluor 488/GFP were produced in MATLAB (MathWorks Inc., USA) (249). Manders' Correlation Coefficients (250) were determined using JACoP (248) in ImageJ (251, 252). To determine the range of Pearson's correlation coefficient and Manders coefficient values that result in two proteins being considered to definitely co-localise, benchmark computer stimulated red and green channel ground-truth images of a known % co-localisation, were ran through JACoP (248). Image set CBS001RGM-CBS010RGM from the

Colocalization Benchmark Source (available from www.colocalization-benchmark.com) was used to validate co-localisation between HIF-2α and Phospho Ser5 RNA Pol II, HIF-1β, HAF, or HIF-1α.

#### 2.2.9.3.2 Measuring the experimental point spread function

##### 2.2.9.3.2.1 Preparation of 100 nm red fluorescent beads (section 4.3: Figure 63)

To measure the PSF of an epifluorescence microscope, a 100 nm red fluorescent bead sample was prepared as described previously (10). In brief, 100 nm red fluorescent beads (Thermo Fisher Scientific, UK) were vortexed and serially diluted from 1:100 ($10^2$ dilution) to reach a final dilution of 1:1,000,000 ($10^6$ dilution), with $ddH_2O$. Before the final dilution, the previously diluted bead solution ($10^4$ dilution) was sonicated in a water bath, at RT, for 20 min to ensure that the beads were well dispersed. For the final dilution ($10^6$ dilution), the $10^4$ diluted bead solution was diluted 1:100 with 70% (v/v) ethanol and $ddH_2O$: 1 µL $10^4$ diluted beads, 900 µL 70% (v/v) ethanol, and 9 mL $ddH_2O$. The $10^6$ diluted bead solution was vortexed, before 4 µL was added to a 16 mm round coverslip (VWR International Ltd.) and immobilised by drying on a heating block. ProLong Gold Antifade mounting medium (7 µL) was added to a microscope slide and the coverslip containing the diluted beads was inverted onto it. Edges of the coverslip were sealed with nail varnish and left to dry overnight at RT.

##### 2.2.9.3.2.2 Determining the PSF from imaging beads (section 4.3: Figure 63)

A z-stack of well-contrasted, uniform, 100 nm red fluorescent beads (Thermo Fisher Scientific, UK), with an emission maxima of 605 nm, was acquired with a 100x 1.4NA oil immersion objective, on an epifluorescence microscope (Zeiss Axio Observer Z.1, Germany). The focal plane was moved through the bead, starting at 5 µm above the bead and ending at 5 µm below the bead, using a step size of 0.2 µm. Using orthogonal view in ImageJ, an in focus xy front view (lateral PSF), xz side view (axial PSF), and yz side view (axial PSF), of the bead was obtained. A 36 pixels-by-36 pixels ROI was selected at the z-position where the bead was most in-focus. A line was drawn through a single bead and the plotted intensity profile of its PSF fitted with a one component Gaussian, to calculate its FWHM, as a measure of the optical system's resolution capability. A theoretical PSF and automatically calculated PSF was also determined for the same optical system and 100 nm red fluorescent bead z-stack dataset using PSF Generator, a MetroloJ Image J plugin (253), by inputting the type of microscope (wide-field), emission wavelength of the beads (605 nm), and NA of the 100x oil

immersion objective (1.4 NA). From the plugin, a report is generated, including xy, xz, and yz maximum intensity projections, fitted and theoretical resolutions, and Gaussian profiles. Refer to MetroloJ ImageJ manual for detailed instructions on how to use it (254).

#### 2.2.9.3.3 Calculating FWHM as a measure of resolution (section 4.2.1: Figures 38, 39, and 40)

Images were calibrated to pixels per micron in ImageJ using $\frac{Pixel\ size}{total\ magnification}$. Due to cross-correlation, the SOFI image will have double the number of pixels compared to the average image, so the average image (512-by-512 pixels) must be up-scaled to 1016-by-1016 pixels, to match the size of the SOFI-processed image. In ImageJ, a line of interest was drawn through a structure of interest in the average wide-field and SOFI images, to plot an intensity profile (a Gaussian PSF is assumed for SOFI). The intensity values for the average wide-field and SOFI-processed images were normalised from 0 to 1. A one-component Gaussian was fitted to the normalised intensity profiles in MATLAB R2016a (MathWorks Inc., USA) and the standard deviation (σ) of the data was used to calculate the FWHM ($2\sqrt{2ln2}$ σ ≈ 2.355*σ) (7). In MATLAB R2016a (MathWorks Inc., USA) the general model Gauss1 was used: fit(x) = a1*exp (-((x-b1)/c1) ^2) [equation 1] with coefficients (95% confidence bounds) a1 (amplitude), b1 (average), and c1 (standard deviation, width of the curve) generated. For equation 1, FWHM ≈ $2\sqrt{ln2} * c1$ and not $2\sqrt{2ln2} * c1$ so to account for the factor of $\sqrt{2}$ difference, the final FWHM value was divided by $\sqrt{2}$. A decrease in the width of the Gaussian profile (smaller FWHM), denotes narrowing of structures, which can be interpreted as an increase in resolution. The improvement in resolution was calculated as a percentage of FWHM decrease: $\left(\frac{(Average\ FWHM\ -FWHM\ SOFI)}{Average\ FWHM}\right) * 100.$

#### 2.2.9.3.4 Computing spatial resolution using Fourier ring correlation (section 4.2.2: Figure 41)

The spatial resolution of SOFI images was computed using FIRE, an open-source BIOP ImageJ plugin, by splitting a raw wide-field dataset (1,000 frames) into two independent even and odd number sub-stacks (500 frames), which were individually SOFI-processed to 2$^{nd}$ order with bSOFI and Localizer. At a given spatial frequency, the degree of correlation was computed for the two SOFI-processed images. Within the FIRE ImageJ plugin, images of the same FOV were Fourier transformed to the frequency domain. Spatial frequency (μm$^{-1}$) versus normalised FRC plots were plotted for the wide-field, bSOFI, and SOFI Localizer

images. Noisy FRC curves were smoothed by fitting with a LOESS (local polynomial regression) curve. Spatial resolution was determined by computing the inverse of the spatial frequency value (1/spatial frequency), and was the point where the smoothed FRC curve first crossed the set threshold cut-off value of 1/7 ≈ 0.143 (frequency of the signal before it became noise) (81).

#### 2.2.9.3.5 SNR estimation of SOFI images using jackknife re-sampling (section 4.2.3: Figures 42 and 43)

A prototype evaluate SOFI tool, developed by Wim Vandenberg of the Dedecker laboratory (KU Leuven, Belgium), was implemented in Igor Pro 7.08.1 64-Bit (WaveMetrics) to assess the SNR of sparsely labelled β-tubulin-Qdot 625 (100x 1.4 NA plus a 2.5x magnifying lens). Through input of a stack of images (N), containing blinking fluorophores, delete-1 jackknife re-sampling systematically deleted one frame from the dataset, to create a number of datasets, which varied by just one frame (N-1). These newly formed datasets were SOFI-processed, yielding several different SOFI-processed images. The similarity of these SOFI images was compared by estimating the degree of variance in SNR between pixels in each SOFI image: $\frac{S}{\sqrt{Var(S)}}$ , where S is signal of a SOFI pixel and Var(S) is the variance associated with that SOFI signal. A spatial de-correlation plot, and SNR histogram were output from the evaluate SOFI program.

#### 2.2.9.3.6 Image quality and resolution with NanoJ-SQUIRREL (section 4.2.4: Figures 44-60)

A super-resolution image and a reference image (diffraction-limited average wide-field image up-scaled to the same size as the super-resolution image), were input into the open-source ImageJ plugin NanoJ-SQUIRREL for resolution and quality analysis. For quality assessment, a RSE map, colour-coded with purple for low error and yellow-blue for high error was generated. RSP value of 0-1 was calculated, where RSP > 0.95 was considered a good quality image. Resolution was estimated with the built-in FRC option in NanoJ-SQUIRREL by splitting a dataset into even and odd frames, post-processing each dataset with a super-resolution algorithm, such as SRRF or SOFI, and inputting two super-resolution images, to generate a FRC map and metric. The FRC map is colour-coded blue for regions in the image that are of high-resolution (low FRC values) and red for regions in the image that are of low-resolution (high FRC values).

#### 2.2.9.3.7 Measuring FWHM of HIF-2α speckles (section 5.1.5: Figure 82)

An open-source ImageJ code (https://bitbucket.org/davemason/fwhm_spotanalysis/src) was kindly written by CCI image analyst, David Mason (University of Liverpool, UK), to automatically measure the FWHM and abundance of HIF-2α speckles in microscopy images, based on a set threshold tolerance. The script works by drawing a horizontal or vertical line, of a set length, through each spot-like object in the calibrated image and a one component Gaussian fitted to the line profile. Only FWHM values, where the Gaussian fit yields an R-squared value greater than 0.85, are used in the analysis. FWHM values greater than 10 times the expected size were excluded. A statistics table was generated.

#### 2.2.9.3.8 Directionality analysis of fibronectin fibres (section 5.2.2: Figures 88 and 89)

Differences in fibronectin fibre orientation (direction) and angular distribution of the fibres aligned in a given direction (dispersion), in wide-field and SOFI-processed images was assessed using a Directionality plugin (255), developed by Jean-Yves Tinevez (Institut Pasteur, Paris), in ImageJ (251, 252). Amount of fibronectin fibres in a given direction was plotted as a histogram and the highest peak fitted with a Gaussian. Dispersion was measured from σ of the Gaussian. A Broad σ of the histogram indicated a high dispersion in the fibres (disorganised fibronectin), whereas a narrow σ, indicated aligned fibres. To eliminate bias, a ROI was always taken, so that there was at least one nucleus (Hoechst 33342) in the FOV. One-way ANOVA was performed on the data in MATLAB (MathWorks Inc., USA).

#### 2.2.9.3.9 Determining neutrophil extracellular trap formation (section 5.3.1: Figure 90-92)

Mean fluorescence intensities of DNA release (Hoechst 33342 channel) and NET proteins (Qdot 625 channel) was compared (same lamp power and gain used) using ImageJ by drawing a line profile through a single granule protein in a neutrophil and its corresponding nuclei in a composite image. Lower Hoechst 33342 (Thermo Fisher Scientific, UK) fluorescence intensity compared to NET fluorescence intensity, confirms NET release (236).

# Chapter 3: Labelling structures with fluctuating probes

## 3.1 Introduction to the use of fluctuating probes in SOFI

SOFI relies on independent and continuous fluorescence intermittency of fluorophores that can switch between a fluorescent and non-fluorescent state, over time, when constantly illuminated with light (86). It is assumed that the fluorophores are immobile when the consecutive images are being acquired. In this way, any changes in the photon count is due to fluctuations, which can be correlated in time, during SOFI-processing. However, in the presence of photobleaching, the fluorescent signal emitted is no longer constant and cannot be considered as independent (256). Although, labelling density is not an issue for SOFI, one limitation is that it requires structures to be labelled with a fluctuating probe. To date, several fluctuating probes have been utilised in SOFI. The first paper demonstrating SOFI was using Qdots (85), but since then there have been other attempts to label structures of interest with suitable probes for SOFI, including the use of synthetic organic dyes (109), pdots (108), cdots (107), and RSFPs (158, 106). Despite the array of fluorescent probes available for SOFI, there are some advantages and disadvantages associated with each type, in terms of photostability and specificity in labelling proteins of interest. Here, the suitability of Qdots, RSFPs, and synthetic organic dyes for SOFI was investigated.

## 3.2 Quantum dot labelling

### 3.2.1 Quantum dot characterisation

Since Qdots fluctuate stochastically in response to light irradiation (144) and are resistant to photobleaching, they are a good probe choice for SOFI (98). As discussed in section 1.4.1, Qdots are semiconductor nanocrystals, 2-10 nm in diameter, that typically consist of a metallic core of CdSe or CdTe and an inorganic ZnS shell (147, 257). For biological applications, it is desirable for Qdots to be rendered water-soluble by coating their surfaces with hydrophilic ligands, such as PEG (258), or encapsulating Qdots with amphiphilic polymers (259). Qdots are an attractive alternative to traditional synthetic organic dyes, because they are much brighter and more photostable (148). In contrast to synthetic organic dyes, Qdots can also be excited with a wide range of wavelengths and have narrow emission

spectra; which is advantageous for multiplex imaging (260, 261). The emission spectra of Qdots are dependent on their size, with the emission peak for large Qdots being in the red end of the spectra and smaller Qdots in the green-blue region (147). Here, the optical properties of large red CdTe Qdots and smaller green CdTe Qots (kindly provided by Vittorio Saggiomo, Netherlands) were characterised by plotting their UV-visible absorption and excitation-emission spectra. UV-visible absorption spectra were measured from 350 nm-850 nm for two differently sized water-soluble CdTe Qdots (Figure 22A). There was a change in the UV-visible spectra, as the absorption peaks are shifted to a shorter wavelength for small green Qdots and a longer wavelength for larger red Qdots. The photoluminescence (PL) excitation and emission spectra of red and green CdTe Qdots were also plotted (Figure 22B). The emission peaks shifted to a longer wavelength with increasing size (Figure 22B).

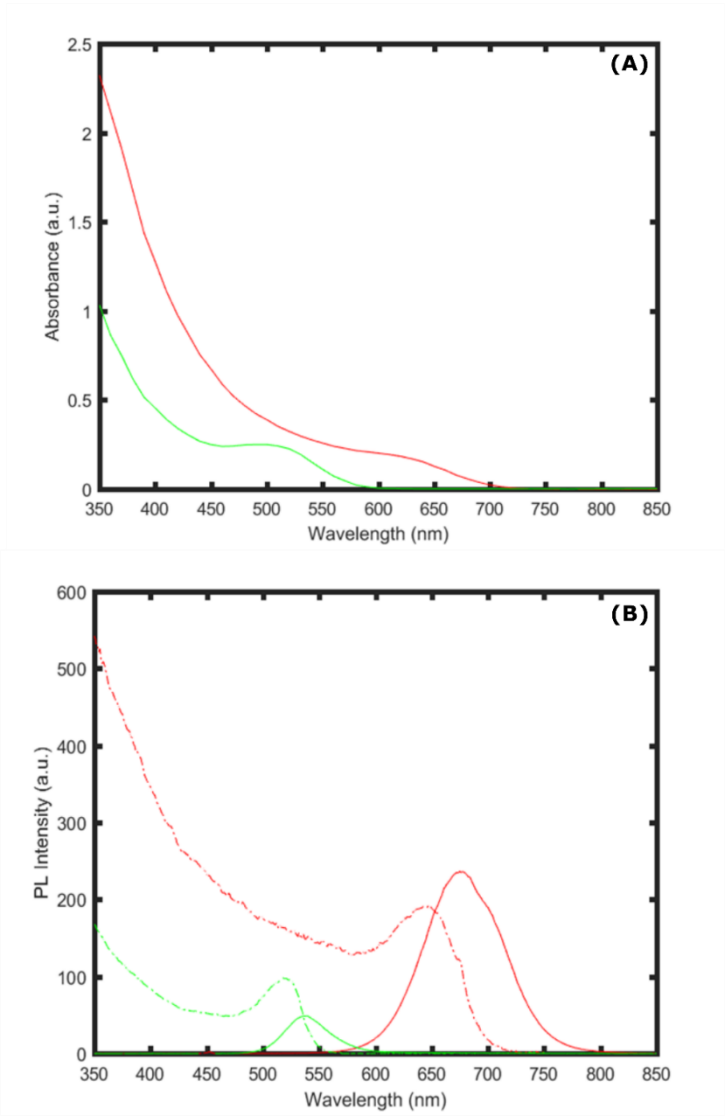


**Figure 22. UV-visible spectra and excitation-emission spectra of CdTe Qdots.** The absorbance of two differently sized CdTe Qdots was measured from 350-850 nm (A). The absorption peak of small green Qdots was shifted further left to a shorter wavelength compared to larger red Qdots, which shifted

towards a longer wavelength. Emission and excitation spectra of two differently sized CdTe Qdots (red and green) was also obtained (B). Photoluminescence (PL) intensity of red and green CdTe Qdots were measured. The dotted and solid lines in (B) represent the excitation and emission, respectively.

Despite the blinking nature of Qdots being suitable for achieving SOFI images of immobile structures, they are not ideal for real-time measurements, because some Qdots may spend long periods of time in the non-fluorescent state, so to capture enough fluctuations for reconstructing a satisfactory SOFI image, a large number of images or longer exposure times are needed (98). The temporal resolution of SOFI has been improved previously by engineering Qdots with a thinner outer ZnS shell, which resulted in faster transitions between a fluorescent and non-fluorescent state, so fewer images were required (10 frames) (98). The concept of shell thickness affecting Qdot photostability has been described earlier in 1997 (262). Once coated with ZnS shells and subsequently conjugated to antibodies, the overall hydrodynamic radii of Qdots (15-20 nm) are much larger than that of synthetic organic dyes conjugated to antibodies (263). One large Qdot may attach many antibodies, as opposed to many synthetic organic dye molecules being coupled to one specific antibody (264). In-house Qdot-Abs are generally smaller than commercial Qdot-Abs, so have better control over the stoichiometry and blinking. However, blinking enhanced Qdots are not currently commercially available, which unfortunately hinders their use by others. Here, the performance of commercially available Qdot 625-Abs fluctuating “ON” and “OFF” was analysed, by fixing Qdot 625-Abs to the surface of a glass coverslip. The blinking of a ‘single’ immobilised Qdot 625-Ab was captured at 10 fps on an epifluorescence microscope (63x 1.4NA plus a 2.5x magnifying lens) and an intensity time trace extracted using ImageJ (Figure 23). Peaks indicated that the Qdot was in the “ON” state, whereas troughs showed that the Qdot was in the “OFF” state for a period of time. Since the blinking nature of Qdots is uncontrolled and exists on all timescales, there were some Qdots that blinked fast, whilst others remained in the “ON” state indefinitely during image acquisition, which will lead to unwanted heterogeneities of brightness in the SOFI-processed image (85).

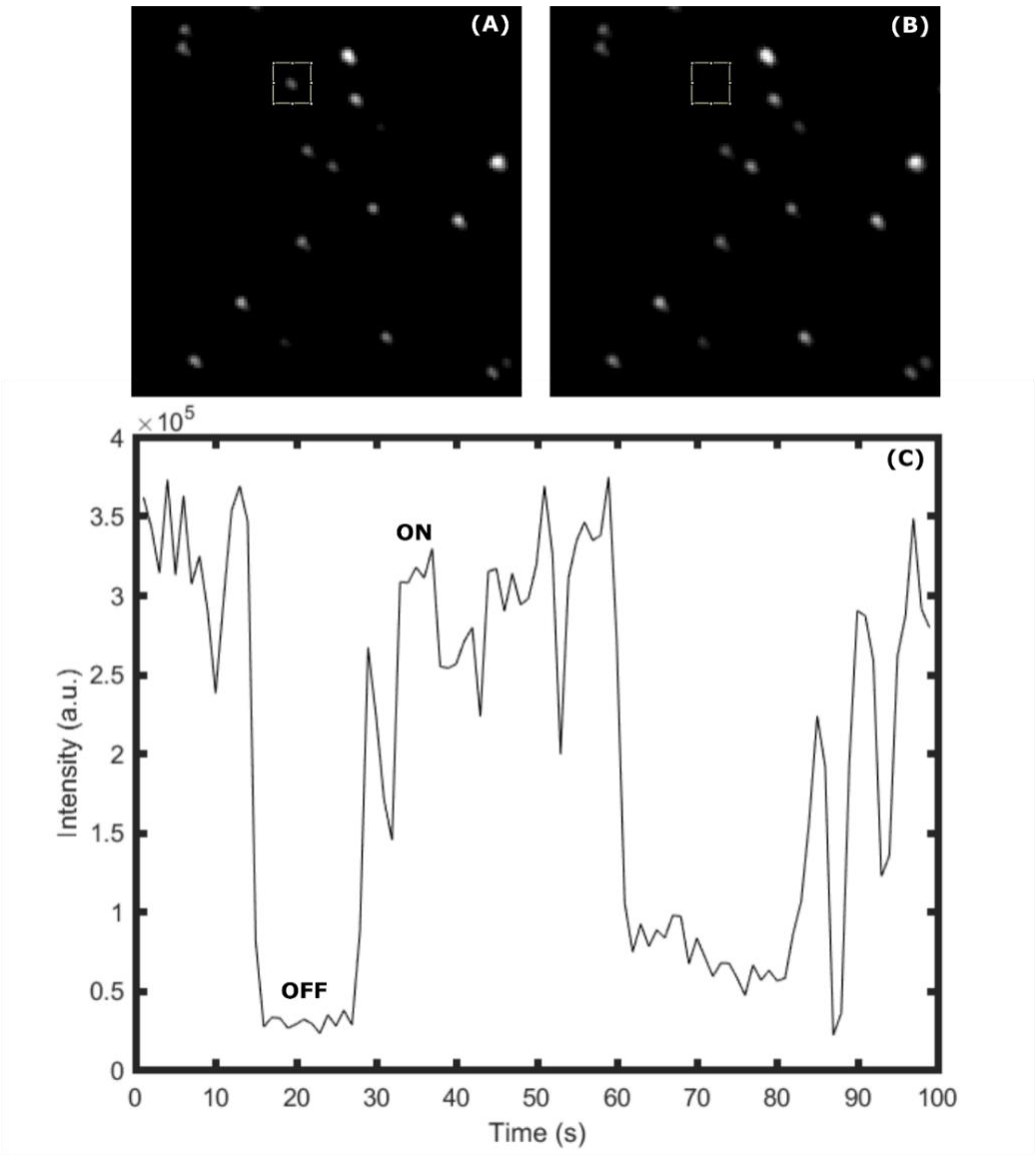


**Figure 23. Qdots blinking stochastically**. Screenshot of a single frame from a movie of a ROI Qdot 625 fluctuating "ON" (A) and "OFF" (B). Intensity time trace of a single Qdot 625 with peaks when the Qdot is "ON" and troughs when the Qdot is "OFF" (C).

To determine how these fluctuating Qdot 625-Abs perform in SOFI-processing, the same blinking dataset was SOFI-processed up to 2$^{nd}$ order SOFI with Localizer, implemented in MATLAB R2016a (Mathworks Inc., USA) (Figure 24). Second order was chosen to minimise the negative effect the SOFI algorithm has on the loss of dim Qdots from being masked by brighter Qdots, because at higher orders variations in brightness increase substaintially with the Localizer implementation of SOFI. A line was drawn through a 'single' Qdot in both the average wide-field image and SOFI-processed image. Qdots blinking in close proximity in the average wide-field image are displayed as one Qdot (265), but in the SOFI-processed image, they are discerned as two separate Qdots. Line profiles showed one large peak for the

average wide-field Qdot and two narrower peaks for the SOFI-processed Qdots. Inconsistent blinking of Qdots meant that multiple Qdots, in close proximity, which were constantly switched “ON” during the image acquisition were considered as one large saturated Qdot, and as a result were removed in the SOFI-processed image. By applying a threshold and using the Analyze Particles feature in ImageJ, the number of Qdots was quantified, with 240 Qdots being detected in the average wide-field image, but only 229 Qdots detected in the SOFI-processed image. The loss of Qdots in the SOFI image may be as a result of the SOFI processing, where those Qdots that do not fluctuate on a suitable timescale for SOFI, by remaining in the fluorescent or non-fluorescent state for too long, are removed from the image, or due to dim Qdots being masked by brighter Qdots. Likewise, saturated Qdots may also be removed from the SOFI image, creating an artefact. Missing Qdots may have severe consequences for the interpretation of biological structures labelled with Qdot-Abs. For example, if too many Qdots are absent from the centre of a spherical structure, it may be incorrectly suggested to be a doughnut shape, which will affect its function. To confirm whether it is the SOFI algorithm responsible for the loss of fluorophores, or the stochastic blinking of Qdots themselves, a control experiment could be performed by analysing different dyes, such as Alexa Fluor 647 or Alexa Fluor 488, pre and post SOFI processing. Alternatively, this analysis could have been run on simulated data.

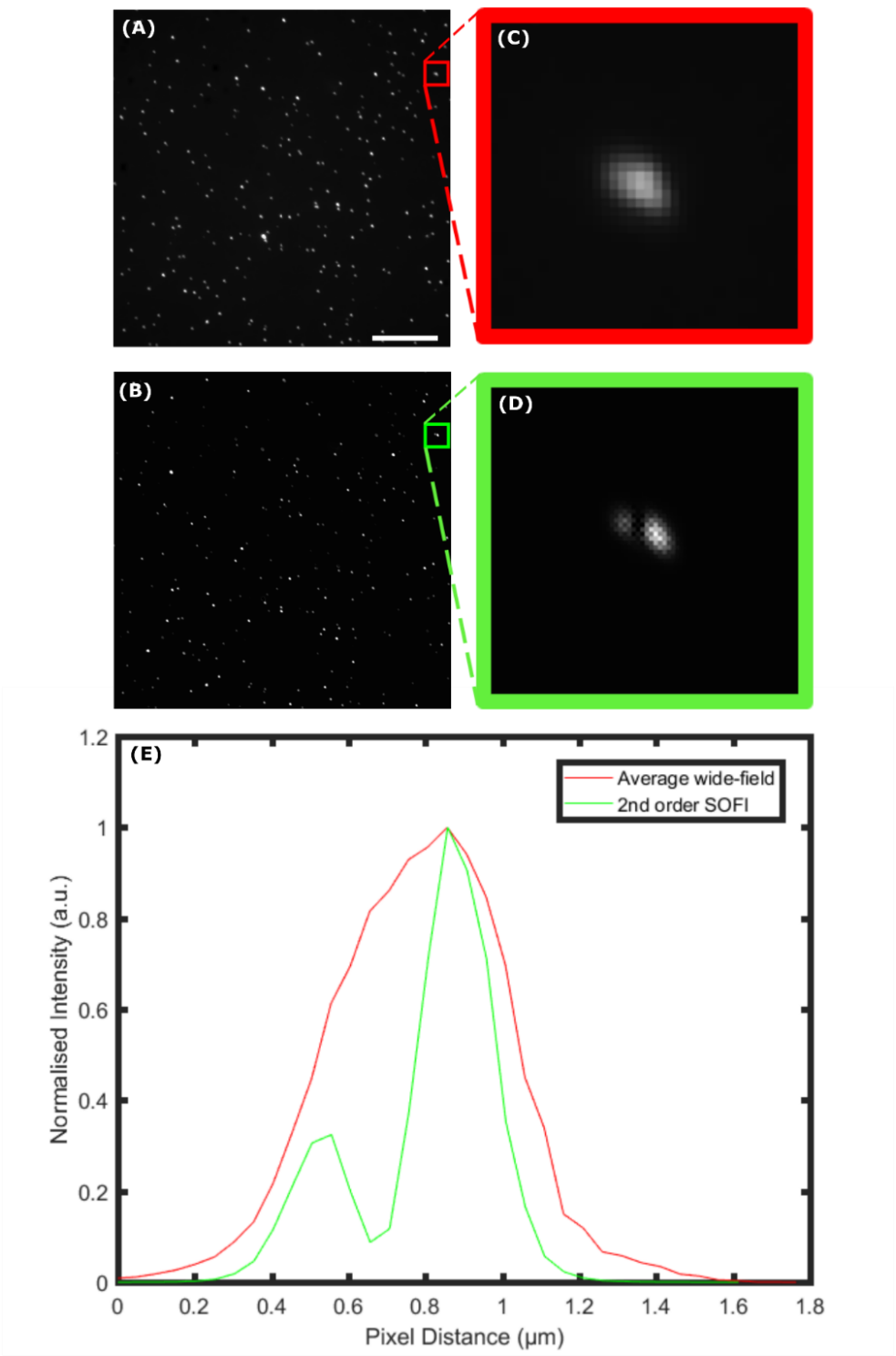


**Figure 24. SOFI-processed Qdots.** Qdot 625-Abs were immobilised on a glass coverslip and imaged on an epifluorescence microscope (63x 1.4NA plus 2.5x magnifying lens) at 10 fps. A stack of 99 wide-field images were SOFI-processed up to 2$^{nd}$ order SOFI using Localizer, implemented in MATLAB. A line was drawn through a 'single' Qdot in an average wide-field image (A) and SOFI-processed image (B), to determine the resolving power of SOFI. One Qdot in the average wide-field ROI (C) is resolved into two Qdots in the SOFI-processed ROI (D). The line profiles were plotted (E), to show one large peak for the average wide-field Qdot and two narrower peaks for the SOFI-processed Qdot. A total of 240 Qdots are present in the average wide-field image and 229 Qdots in the SOFI-processed image. Scale bar = 10 µm.

### 3.2.2 Development of Qdot nanoprobes to specifically label proteins

#### 3.2.2.1 Anti-GFP nanobody-Qdot conjugation

Although, it has been established that the blinking of commercial Qdot 625-Abs is sufficient for SOFI-processing, the price per unit volume is considerably higher than that of synthetic organic dyes, such as Alexa Fluor 488 (266). To date, Qdot 625-Ab (100 µL) supplied at 1 µM cost £193.00, whilst Alexa Fluor 488 (500 µL) supplied at 2 mg/mL (based on the molecular weight of Alexa Fluor 488 being 145 g/mol according to Thermo Fisher Scientific UK datasheet), cost £183.00. The initial stock concentration of Alexa Fluor 488 is 13.8 µM, but for use in immunocytochemistry needs to be diluted 1:500 to give a final working concentration of 4 µg/mL (equivalent to 30 nM). For specific labelling with Qdots, an initial 1 µM stock concentration of Qdot 625-Ab is diluted to 1:50, to give a final working concentration of 20 nM for immunocytochemistry. Therefore, Alexa Fluor 488 (30 nM) and Qdot 625-Ab (20 nM) are used at a similar concentration, however, Qdot 625-Ab is sold at a much lower stock concentration (1 µM) than Alexa Fluor 488 (13.8 µM), for an equivalent price. If there is an issue in that some Qdots are lost after SOFI-processing (3.2.1 Quantum dot characterisation), it might not be worth the extra cost of using Qdot-Abs in SOFI compared to lower priced Alexa Fluor 488. In addition, the size of these commercially available Qdot 625-Ab is considerably larger than synthetic organic dyes, which is an issue when labelling small proteins. One way to reduce their size, is to replace antibodies (150 kDa) conjugated to Qdots (2-10 nm) with nanobodies (13 kDa), also known as nano-traps or chromobodies, which are single domain binding fragments derived from heavy-chain antibodies of Camelidae (267, 268). The attachment of anti-GFP nanobodies to Qdots has been achieved recently (269). Here, the development of smaller nanoprobes was attempted by conjugating anti-GFP nanobodies (ChromoTek, Germany) to water-soluble CdTe Qdots (kindly supplied by Vittorio Saggiomo, Netherlands). Compared to using a commercial Qdot-conjugated secondary antibody with a primary antibody, the probe size of an anti-GFP nanobody-Qdot conjugate will be minimal, as this nanoprobe will more specifically bind to the protein of interest. A direct covalent approach was used with cross-linking reagents EDC and sulfo-NHS. The carboxylate group (COOH) on water-soluble CdTe Qdots, capped with 3-mercaptopropionic acid, was coupled to the amine group ($NH_2$) on anti-GFP nanobodies, forming an amide bond (Figure 25).

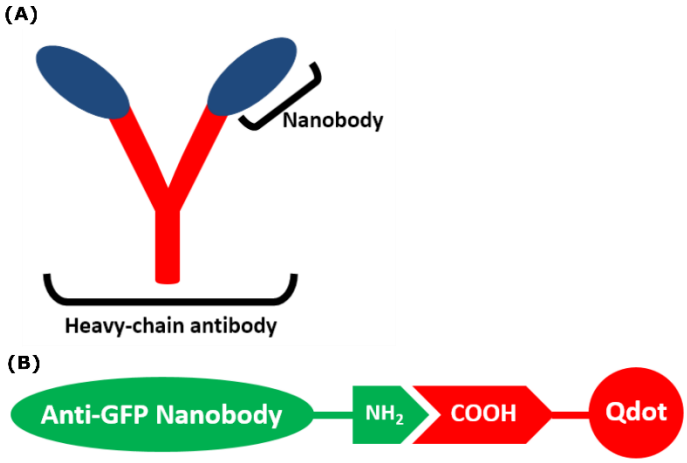


**Figure 25. Anti-GFP nanobody-Qdot conjugation.** A nanobody is a 13 kDa single domain binding fragment, derived from heavy-chain antibodies of Camelidae (A). The amine group ($NH_2$) on an anti-GFP nanobody can be linked to a carboxylate group (COOH) on a Qdot (B).

Agarose gel electrophoresis was used to verify the success of the anti-GFP nanobody-Qdot conjugation (Figure 26). The unconjugated Qdots ran towards the anode (positively charged electrode) at a faster rate due to their small size and negative charge, whereas the anti-GFP nanobody-Qdot conjugate ran slightly slower due to an increased size. However, the shift between unconjugated Qdots and anti-GFP nanobody-Qdot conjugate was much smaller than anticipated and the anti-GFP nanobody-Qdot conjugate band was faint, so it was difficult to confirm the anti-GFP nanobody Qdot conjugation and this conjugate was therefore not used for immunocytochemistry.

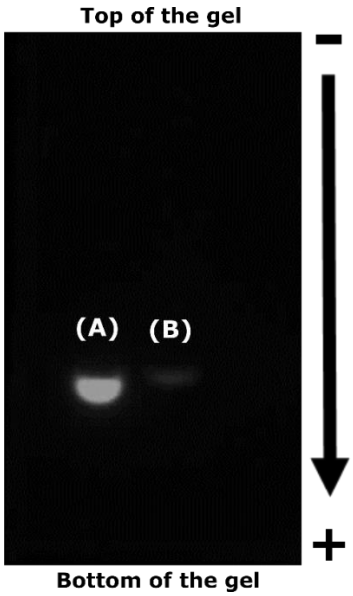


**Figure 26. Anti-GFP nanobody-Qdot conjugation confirmation via agarose gel electrophoresis.** Unconjugated red CdTe Qdots (A) migrated at a faster rate towards the anode than the anti-GFP nanobody-QD conjugate (B). Gel result is representative of 3 repeats (N=3).

Many challenges have been faced over the Qdots aggregating and their fluorescence becoming quenched during the conjugation process, which led to difficulty over visualising the Qdots in a gel. Too much activator (sulfo-NHS and EDC) caused aggregation and subsequently a loss in Qdot fluorescence, which was overcome by using lower controlled activator amounts. There was also a possibility that the loss in fluorescence when running a gel was due to the running buffer used (1xTAE), as running the gel for a longer length of time made the conjugate band less visible. The conjugation of an anti-GFP nanobody to Qdots, using this EDC-coupling approach was abandoned, and instead a commercial conjugation kit (S10452: Thermo Fisher scientific, UK), involving click chemistry was used. In this way, an anti-GFP primary antibody and an anti-β-tubulin antibody was successfully conjugated to Qdot 625 (3.2.3 Evaluation of Qdot-conjugated antibodies for immunofluorescent labelling).

#### 3.2.2.2 Microinjecting a fluorescent dye into cells

Qdot-Abs are not membrane permeable and, therefore, are not suitable for live cell imaging, unless they can be microinjected into cells, so are unlikely to replace synthetic organic dyes conjugated to antibodies (119). Anti-GFP nanobody-Qdot conjugates were intended to be microinjected into live HeLa cells, so that the nucleus, where the proteins of interest are located, will be directly targeted. To validate the microinjection system, wild-type HeLa cells were manually microinjected with an inexpensive fluorescent glucose based dye FITC-dextran (5 mg/mL), using a epifluorescence microscope at 20x magnification (Figure 27). Cells were imaged immediately after microinjection and FITC-dextran was homogeneously distributed throughout the cells. However, this was not easily reproducible, as often cells swelled and became damaged, as the cell membrane was harshly penetrated, resulting in leakage of FITC-dextran. When tried with Qdots, these aggregated at the tip of the microinjection needle. As result of these experiments, it was decided not to pursue the microinjection of anti-GFP nanobodies conjugated to Qdot 625.

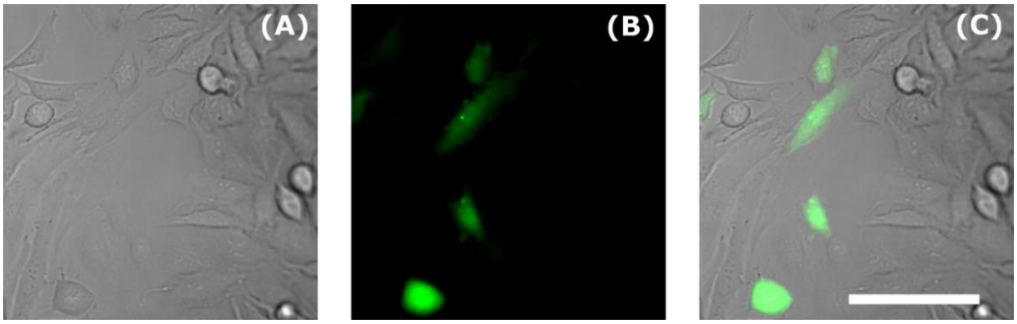


**Figure 27. HeLa cells microinjected with FITC-dextran.** Wild-type HeLa cells (A) were injected at 45° with 5 mg/mL FITC-dextran (B). A composite of (A) and (B) is shown (C). Microinjection system was set at a hPc of 50 hPa, Pi of 300 hPa, and ti of 0.3 s. Scale = 100 µm.

### 3.2.3 Evaluation of Qdot-conjugated antibodies for immunofluorescent labelling

Preface:

The majority of the work involving the labelling of proteins with Qdot-Abs, was part of a peer-reviewed publication: J.E. Francis, D. Mason, and R. Lévy. Evaluation of quantum dot conjugated antibodies for immunofluorescent labelling of cellular targets. *Beilstein Journal of Nanotechnology*. **8**: 1238-1249. (2017). Briefly, the use of Qdot-Abs, for the labelling of different protein targets, was investigated and it was found that whilst ECM proteins could be specifically targeted with Qdot-Abs, other intracellular targets could not be labelled. Steric constraints prevented access of Qdots to intricate intracellular complexes, as well as nuclear locations, even after extensive permeabilisation of cells.

Specific contributions to this publication include:

Text and figure 2 in “Labelling of extracellular antigens” section

Text and figure 3 in “Labelling of cytosolic structures” section

Text and figures 4&5 in “Labelling intracellular complexes” section

Text of “Optimising sample preparation” section

Text of “Size limiting access to the nucleus” section

Text and figure 6 in “Labelling with alternative Qdot-Abs” section

Text and figure 7 in “Assessing nuclear accessibility of Qdots” section

Text and figures in “Supporting Information” section

Author contributions:

Jennifer Elizabeth Francis

- Designed the experiments (except Figure 7)
- Did all of the laboratory work for the sections above
- Performed all of the imaging experiments
- Data analysis
- Produced figures and graphs
- Wrote the paper
- Reviewed drafts of the paper

David Mason

- Came up with the initial experimental idea in Figure 7
- Advised on data analysis (Manders coefficient)
- Prepared schematic diagram (Figure 1)
- Reviewed drafts of the paper

Raphaël Lévy:

- Advised on experiments
- Reviewed drafts of the paper

Manuscript:

BEILSTEIN JOURNAL OF NANOTECHNOLOGY

# Evaluation of quantum dot conjugated antibodies for immunofluorescent labelling of cellular targets

Jennifer E. Francis[1], David Mason[2] and Raphaël Lévy[*1]

Full Research Paper

Open Access

Address:
[1]Department of Biochemistry, Institute of Integrative Biology, Biosciences Building, Crown Street, Liverpool, L69 7ZB, United Kingdom and [2]Centre for Cell Imaging, Institute of Integrative Biology, Biosciences Building, Crown Street, Liverpool, L69 7ZB, United Kingdom

Email:
Raphaël Lévy* - rapha@liverpool.ac.uk

* Corresponding author

Keywords:
imaging; immunofluorescence; microscopy; nanoparticles; quantum dots

*Beilstein J. Nanotechnol.* **2017,** *8,* 1238–1249.
doi:10.3762/bjnano.8.125

Received: 29 November 2016
Accepted: 09 May 2017
Published: 09 June 2017

Associate Editor: M. Stenzel



## Abstract

Semiconductor quantum dots (Qdots) have been utilised as probes in fluorescence microscopy and provide an alternative to fluorescent dyes and fluorescent proteins due to their brightness, photostability, and the possibility to excite different Qdots with a single wavelength. In spite of these attractive properties, their implemenation by biologists has been somewhat limited and only a few Qdot conjugates are commercially available for the labelling of cellular targets. Although many protocols have been reported for the specific labelling of proteins with Qdots, the majority of these relied on Qdot-conjugated antibodies synthesised specifically by the authors (and therefore not widely available), which limits the scope of applications and complicates replication. Here, the specificity of a commercially available, Qdot-conjugated secondary antibody (Qdot-Ab) was tested against several primary IgG antibodies. The antigens were labelled simultaneously with a fluorescent dye coupled to a secondary antibody (Dye-Ab) and the Qdot-Ab. Although, the Dye-Ab labelled all of the intended target proteins, the Qdot-Ab was found bound to only some of the protein targets in the cytosol and could not reach the nucleus, even after extensive cell permeabilisation.

## Introduction

Quantum dots (Qdots) are nanometre-sized semiconductor nanocrystals that typically consist of a metallic core of cadmium selenium (CdSe) and an inorganic zinc sulfide (ZnS) shell and have been applied as fluorescent probes for the labelling of biological structures [1,2]. To make Qdots water soluble, and thus suitable for biological applications, their surface is modified either by coating with hydrophilic ligands (such as poly(ethylene glycol) (PEG) [3,4]) or they are encapsulated in amphiphilic polymers [5]. Antibodies that recognise specific biological targets can then be conjugated to these Qdots for use in immunofluorescence. Conventional immunocytochemistry (ICC) protocols involve the chemical fixation of

cells, followed by permeabilisation with a detergent. This creates pores in the cell membrane, allowing primary and secondary antibodies to gain access to the protein of interest.

Qdots are an attractive alternative to traditional fluorescent dyes for ICC because they are much brighter and more photostable [6,7]. In contrast to fluorescent dyes, Qdots can be excited with a wide range of wavelengths and have narrow emission spectra, which is advantageous for multiplex imaging [8,9]. The emission maxima of Qdots are dependent on their size; the emission peak for large Qdots is in the red end of the spectra and smaller Qdots in the blue region [1]. Qdots are also an ideal probe choice for super-resolution imaging techniques that require stochastic optical fluctuation, as they exhibit well-characterised blinking between fluorescent and non-fluorescent states [10,11].

Despite these favourable characteristics, the overall hydrodynamic radius of a Qdot (15–20 nm) is much larger than that of a fluorescent dye molecule [12-14]. As a result, one large Qdot may host many antibodies, whereas many fluorescent dye molecules can be coupled to a single antibody [9,15]. Furthermore, the overall size of commercially available Qdots is further enlarged by the addition of protective layers to maintain stability and shelf life [13,16]. Qdot-conjugated antibodies (Qdot-Abs) are therefore unlikely to replace fluorescent dyes in ICC due to their inferior penetration capability [17,18]. Despite the assumption that manufactured Qdots are quality controlled, the considerable batch-to-batch variability means that each time a new lot is purchased, the labelling conditions need to be optimised [19]. The use of commercial Qdot-Abs is also expensive, as they are used in quantities on the order of 20 nM, yet are supplied at a higher price per unit volume compared to fluorescent dyes [16,20,21]. Despite having been around for several decades, Qdots are rarely used in routine ICC [1].

There are some notable examples of Qdot-Abs in the published literature where they have been used to label glycine receptors [22], glial fibrillary acidic proteins (GFAPs) [12], mortalin [23], erythrocytes [24], GRP78 protein [25], caveolin-1 [26], golgi [20], and nuclear HER2 targets [6]. The majority of this labelling, however, was done with in-house synthesised Qdots rather than commercially available Qdots [27]. The use of commercially available Qdots allows for the controlled synthesis and thus the size of the Qdot-Abs can be kept to a minimum. However, it has been noted that specific labelling of nuclear and some cytoplasmic structures with Qdot-Abs is not always reproducible [1,6,13,20,28]. Another concern amongst users of commercial Qdot-Abs is non-specific labelling and the formation of aggregates, which may introduce artifacts and lead to misinterpretation of false positive results [12,13].

Here, we focus on the specificity of commercially available Qdot 625 conjugated antibodies (Thermo Fisher Scientific, UK), with an emission maxima of 625 nm (excitation and emission spectra available in Figure S1 in Supporting Information File 1), in fixed cells (Figure 1). Different protein targets were labelled simultaneously with both a secondary antibody conjugated to a fluorescent dye (Dye-Ab) and a Qdot 625 conjugated secondary antibody (Qdot 625-Ab). A Qdot 525 conjugated secondary antibody (Qdot 525-Ab) was also evaluated, with an emission maxima of 525 nm (excitation and emission spectra available in Supporting Information File 1, Figure S2); along with an anti-GFP Qdot 625 conjugate (Qdot 625-GFP), anti-tubulin Qdot 625 conjugate (Qdot 625-Tubulin), and Qdot 625

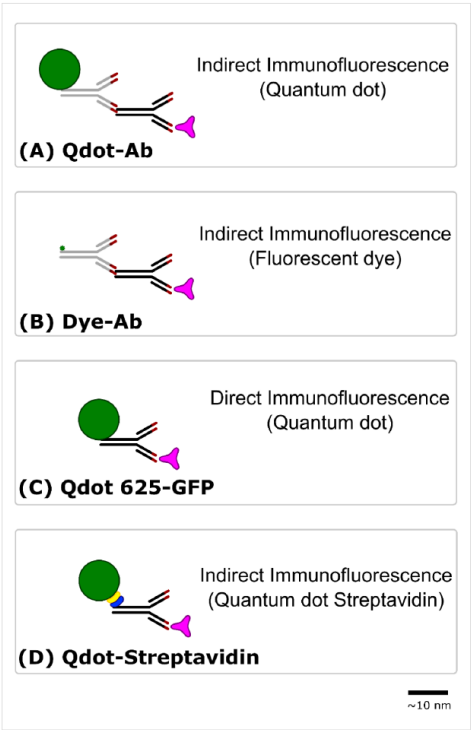


**Figure 1:** Strategies for immunofluorescence labelling. A fluorescent label (green) is conjugated to a secondary antibody (grey) or directly to a primary antibody (black), containing antigen-binding sites (red), which recognises and binds to a specific antigen (pink). Immunofluorescence labelling was either indirect with a primary antibody and a Qdot 625/Qdot 525 (Qdot-Ab) (A) or fluorescent dye such as Alexa Fluor 488/Cyanine 3 (Dye-Ab) (B) conjugated to a secondary antibody, or direct with an anti-GFP primary antibody conjugated to Qdot 625 (Qdot 625-GFP) (C). An alternative Qdot 625 was tried for indirect immunofluorescence labelling using a Qdot 625 streptavidin (yellow) conjugate (Qdot-Streptavidin) and biotinylated (blue) primary antibody (D). Scale bar is 10 nm.

conjugated to streptavidin (Qdot-Streptavidin). We found that while the prototypical target of Qdot-Abs: tubulin, could be easily labelled, several other protein targets including nuclear proteins and components of large cytosolic protein complexes could not be labelled with Qdot-Abs. We posit that this may be due to steric hindrance associated with the size of the Qdot-Abs.

## Results and Discussion

**Labelling of extracellular antigens:** To investigate the specificity of commercial Qdot-Abs for intracellular targets, different types of proteins were stained simultaneously with conventional Dye-Abs and Qdot-Abs and imaged using an epifluorescence microscope. To eliminate the possibility of competition between the Dye-Abs and Qdot-Abs, for the antigen binding sites, which could affect the labelling, samples were also prepared separately with either a Dye-Ab or Qdot-Ab. A Qdot 625-Ab concentration of 20 nM was used, as it has been shown that a high concentration of Qdot-Abs improves specific labelling and signal-to-noise ratio [21]. Initially, to assess the labelling efficiency of Qdot-Abs, the extracellular matrix (ECM) protein fibronectin was dual labelled with Qdot 625-Ab and Dye-Ab (Alexa Fluor 488). Fibronectin is abundant at the cell surface and therefore, would not be expected to display any artifacts associated with accessibility. Indeed, in this case similar labelling was achieved with Qdot 625 and Alexa Fluor 488 (Figure 2).

**Labelling of cytosolic structures:** The vast majority of studies using Qdots show tubulin staining [6,12,16,18,20], therefore we sought to label this abundant cytosolic protein in order to have a positive control for our labelling protocol. After incubation with an anti-tubulin primary antibody and a Qdot 625-Ab, we once again found labelling which was comparable to samples (simultaneously or separately) labelled with Alexa Fluor 488 (Figure 3).

To investigate whether the same structure (microtubules) could be labelled with a different fluorophore-antibody conjugate, direct ICC was performed using a Qdot 625 conjugated directly to an anti-GFP primary antibody (see Methods for details). Cells expressing tubulin-GFP were labelled with the anti-GFP Qdot 625 conjugate (Qdot 625-GFP) and gave similar results to those imaged with indirect ICC (Figure 3). By inspection it was clear, that β-tubulin had been labelled with Qdot 625 (Figure 3C), however, to compare the two labelling techniques, an intensity correlation plot was produced (Figure 3D). A Pearson's correlation coefficient ($r^2$) value of 0.93 suggested that there was an almost perfect correlation between Qdot 625 and Alexa Fluor 488 labelled microtubules. In addition, the degree of co-localisation was measured using the Manders coefficient [29]. The average Manders coefficient of Alexa Fluor 488 overlapping with Qdot 625 (M1) was 0.99 (SD = 0.007, $N$ = 3) and Qdot 625 overlapping with Alexa Fluor 488 (M2) was 0.99 (SD = 0.005, $N$ = 3), confirming that the correlation between Qdot 625 and Alexa Fluor 488 was very good. In addition, an anti-tubulin primary antibody was also conjugated to Qdot 625 (Qdot 625-Tubulin) (Figure S3 in Supporting Information File 1). A negative control containing Alexa Fluor 488-Ab and Qdot 625-Ab only, with no anti-tubulin primary antibody was also prepared, showing negligible unspecific binding of Alexa Fluor 488 and Qdot 625 to HeLa cells (Figure S4 in Supporting Information File 1).

**Labelling intracellular complexes:** Both fibronectin and β-tubulin are highly abundant proteins. Furthermore, their antigens are relatively accessible. We therefore, looked to antigens present in more complex intracellular structures, including the focal adhesion protein talin and nuclear splicer marker SC35. Talin exists in a dynamic equilibrium with both a bound pool (forming focal adhesions) and a cytosolic pool. Using the same primary antibody, Alexa Fluor 488 labelled both the cytosolic

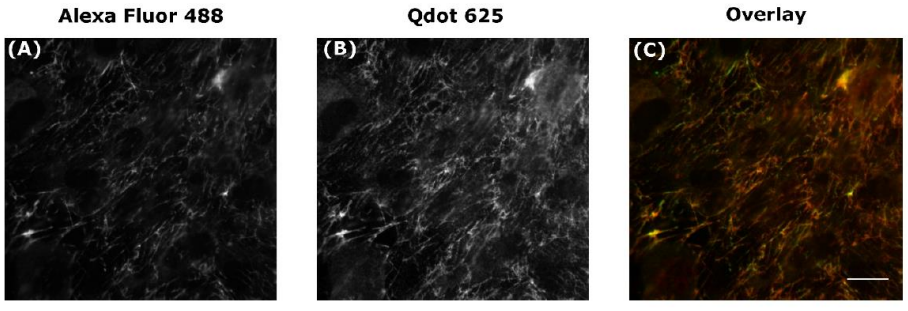


**Figure 2:** Specific labelling of fibronectin with Qdots. Fixed rat mammary (Rama) 27 fibroblasts were dual labelled with green Alexa Fluor 488 (A) and a red Qdot 625 (B) to produce an overlaid wide-field image (C). Scale bar is 20 μm.

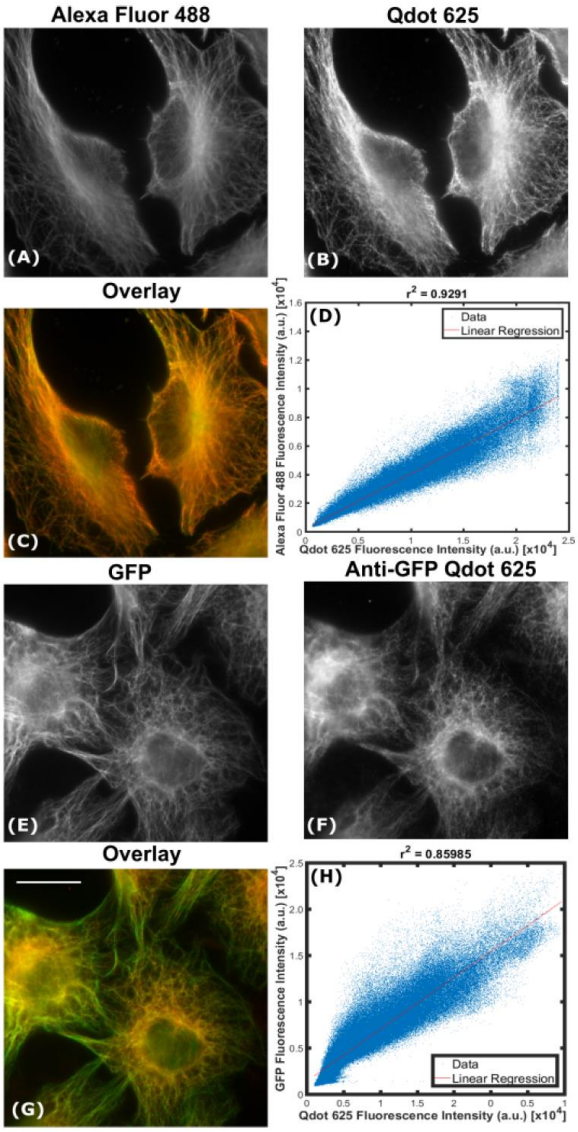


**Figure 3:** Specific labelling of tubulin with Qdots. Methanol-fixed HeLa cells were labelled indirectly with a primary anti-tubulin antibody, green Alexa Fluor 488 (A), and red Qdot 625 (B), to produce an overlaid wide-field image (C). As a measure of co-localisation between Alexa Fluor 488 and Qdot 625, fluorescence intensities of the overlaid wide-field image (C) were analysed using a custom-written Matlab code to produce a correlation scatter plot (D). Pearson's correlation coefficient ($r^2$) of 0.93 indicates very high correlation. The average Manders coefficient of Alexa Fluor 488 overlapping with Qdot 625 (M1) was 0.99 (SD = 0.007, $N$ = 3) and the average Manders coefficient of Qdot 625 overlapping with Alexa Fluor 488 (M2) was 0.99 (SD = 0.005, $N$ = 3, as determined using JACoP. Paraformaldehyde fixed TC7 cells, expressing tubulin-GFP (E), were also labelled directly with an anti-GFP Qdot 625 conjugate (F) to produce an overlaid wide-field image (G,) and a corresponding correlation scatter plot (H); with a Pearson's correlation coefficient ($r^2$) of 0.86. Scale bar is 20 µm.

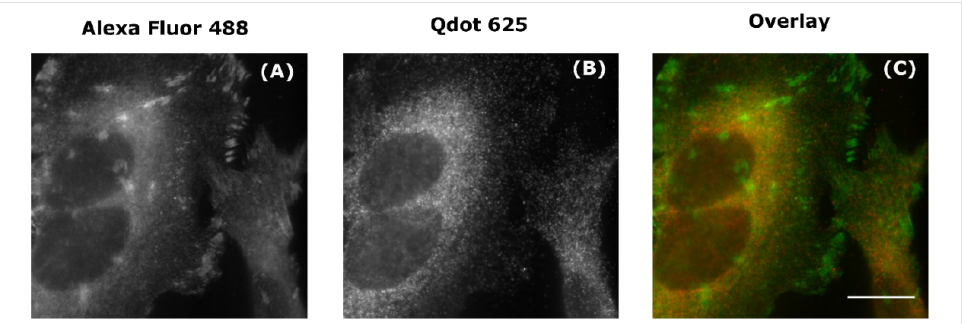


**Figure 4:** Non-specific labelling of talin with Qdots. Fixed HeLa cells were dual labelled with green Alexa Fluor 488 (A) and red Qdot 625 (B) to produce an overlaid wide-field image (C). Scale bar is 20 µm.

pool of talin and the bound pool forming focal adhesions, whereas Qdot 625 appeared to only label the cytosolic regions (Figure 4). At the same time, a control sample was prepared, consisting of HeLa cells incubated simultaneously with an Alexa Fluor 488-Ab and Qdot 625-Ab, without prior addition of an anti-talin primary antibody (Figure S5 in Supporting Information File 1). Here, it appears that the low signal of Qdot 625, is an indication that that the Qdot 625-Ab actually binds non-specifically to cells.

Unlike β-tubulin and talin, SC35 is not only intracellular, but contained within the nucleus, which is crowded with deoxyribonucleic acid (DNA) and proteins. Under conditions identical to the previous experiments, the labelling of SC35 with the Qdot 625-Ab was non-specific, diffuse, and predominately cytosolic (Figure 5). The intensity correlation of Qdot 625 and Alexa Fluor 488 labelling of SC35 was assessed by plotting fluorescence intensities (Figure 5D) within the overlaid image (Figure 5C). A Pearson's correlation coefficient ($r^2$) value of 0.006 suggested that there was practically no correlation between Qdot 625 and Alexa Fluor 488 signals. Once more, the degree of co-localisation was quantified using the Manders' coefficient. The average Manders' coefficient of Alexa Fluor 488 overlapping with Qdot 625 (M1) was 0.19 (SD = 0.035, $N = 3$) and the average Manders' coefficient of Qdot 625 overlapping with Alexa Fluor 488 (M2) was 0.08 (SD = 0.031, $N = 3$), which confirms that the labelling of SC35 with Qdot 625 showed no co-localisation with Alexa Fluor 488. To control for non-specific binding of the Qdot 625-Ab to cells, a negative control was introduced, whereby the cells were incubated with the Qdot 625-Ab only (Figure S6 in Supporting Information File 1). In the absence of a primary antibody, there was negligible labelling detected with the Qdot 625-Ab, which suggests that the SC35 cytosolic signal is due to the presence of minority pool of SC35 in the cytosol.

**Optimising sample preparation:** Since Qdot-Abs may be sensitive to certain fixation protocols [13,19,30], as well as using paraformaldehyde, ice cold methanol was also tried. Methanol fixation and harsher permeabilisation with up to 1% Triton X-100 was used in an attempt to increase accessibility of the Qdots to complex intracellular antigens. Although methanol fixation gave better signal-to-noise ratio and specific Qdot 625 labelling of β-tubulin (Figure 3B), without the need for further permeabilisation, there was non-specific labelling observed for talin and SC35.

**Size limiting access to the nucleus:** We suspected that the size of the commercial Qdot 625-Ab and the associated accessibility to targets was the reason behind the inability to label complex cytosolic and nuclear structures. Although, the manufacturer (Thermo Fisher Scientific, UK) has approximated that Qdot 625 (17 nm) has an overall hydrodynamic size of 30 nm with a couple of antibodies per Qdot, we have provided our own measurements of Qdot 625 in the Supporting Information File 1. We attempted to measure the size of Qdot 625 using different methods: transmission electron microscopy (TEM), size-exclusion high-performance liquid chromatography (SEC-HPLC), and fluorescence correlation spectroscopy (FCS). The TEM and SEC-HPLC results are in agreement with the provider's data, giving a core size of ≈8 nm (Figure S7 in Supporting Information File 1) and a hydrodynamic diameter of ≈15 nm (Figure S8 in Supporting Information File 1), respectively. However, the FCS results indicate a much larger size of ≈76.84 nm for the Qdot 625-Ab (Figure S9 in Supporting Information File 1), suggesting some degree of Qdot aggregation (although this is not seen in the SEC-HPLC nor in the TEM data). Due to the discrepancy observed for Qdot 625-Ab, using different methods, we decided to take FCS measurements for a presumably smaller green Qdot 525-Ab. The size obtained for the Qdot 525-Ab was more compatible with the provider's data

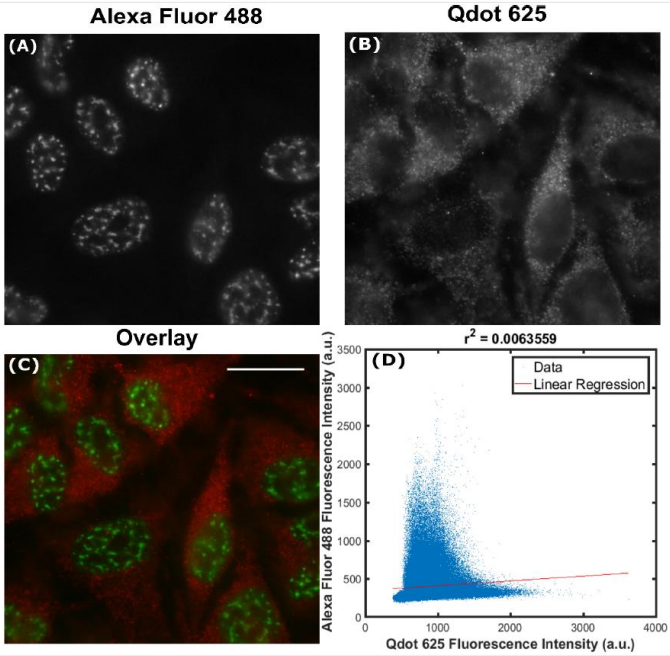


**Figure 5:** Non-specific labelling of SC35 with Qdots. Fixed HeLa cells were dual labelled with green Alexa Fluor 488 (A) and red Qdot 625 (B) to produce an overlaid wide-field image (C). Scale bar is 20 µm. As a measure of co-localisation between Alexa Fluor 488 and Qdot 625, fluorescence intensities of the overlaid wide-field image (C) were analysed using a custom-written Matlab code to produce a correlation scatter plot (D). Pearson's correlation coefficient ($r^2$) of 0.006 indicates no co-localisation. The average Manders' coefficient of Alexa Fluor 488 overlapping with Qdot 625 (M1) was 0.19 (SD = 0.035, *N* = 3) and the average Manders' coefficient of Qdot 625 overlapping with Alexa Fluor 488 (M2) was 0.08 (SD = 0.031, *N* = 3), as determined using JACoP.

at 41.72 nm (Figure S10 in Supporting Information File 1). ATTO488 (Figure S11 in Supporting Information File 1) was used to calibrate the confocal volume and fluorescent latex beads (Figure S12 in Supporting Information File 1), of a known size, were used as a standard to compare against Qdot-Abs (For methods see Supporting Information File 1). These results are robust and reproducible (including two different batches of Qdot 625-Ab).

**Labelling with alternative Qdot-Abs:** A Qdot 525 conjugated secondary antibody (Qdot 525-Ab), with presumably smaller dimensions, was further tried against the same anti-tubulin primary antibody (Figure S13 in Supporting Information File 1), anti-talin primary antibody (Figure S14 in Supporting Information File 1), and anti-SC35 primary antibody (Figure S15 in Supporting Information File 1), with the similar results obtained as for Qdot 625-Ab. An alternative Qdot 625 conjugated to the biotin-binding protein streptavidin (Qdot-Streptavidin) (Thermo Fisher Scientific, UK) was also evaluated. To test the specificity of Qdot-Streptavidin for nuclear targets, a transcription factor, which localises in the nucleus as speckles (sub-nuclear foci), known as hypoxia inducible factor two alpha (HIF2α) was labelled. Fixed HeLa cells were transfected with HIF2α tagged with the fusion protein EGFP (EGFP-HIF2α), incubated with anti-GFP biotin primary antibody, and Qdot-Streptavidin. All of the endogenous biotin sites in the cell were blocked before addition of the biotinylated anti-GFP primary antibody with an endogenous biotin-blocking kit (Thermo Fisher Scientific, UK). Similar results were obtained as previously for Qdot 625-Ab, with Qdot-streptavidin binding to any cytosolic pool of HIF2α without labelling the distinct speckles in the nucleus (Figure 6). Since the transfected cells have a cytosolic pool of EGFP-HIF2α, this was labelled by Qdot-streptavidin more than in the untransfected cells, where there was no GFP present; hence the very bright fluorescent Qdot signal in the cytosol.

**Assessing nuclear accessibility of Qdots:** Fluorescent in situ hybridisation (FISH) is another application where specific intracellular targeting is required. Like many applications, FISH

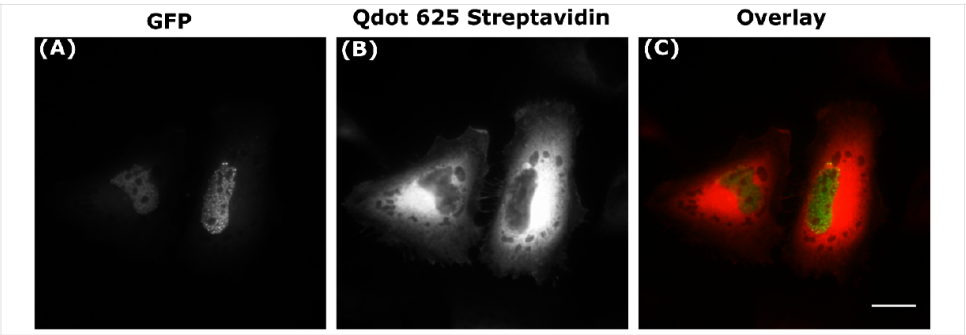


**Figure 6:** Partial labelling of HIF2α with Qdot-Streptavidin. Fixed HeLa cells were transfected with EGFP-HIF2α (A), incubated with a primary anti-GFP biotinylated antibody and Qdot 625 streptavidin conjugate (Qdot-Streptavidin) (B), to produce an overlaid image (C). Scale bar is 20 μm.

benefits from bright photostable probes, and indeed several studies have been published using Qdots for FISH [31]. Much of the FISH data however, describe metaphase chromosomes (where breakdown of the nuclear envelope has occurred) or chromosomal spreads devoid of cell membranes altogether [32-34]. Furthermore a 2009 appraisal of the use of Qdots for FISH considers them unsuitable in their current form "… because of the lack of reproducibility of the experiments" when using these materials [35]. Interestingly, in all of our Qdot 625 images, even when the staining was non-specific, there was no labelling within the nucleus (Figure 2–6). This suggested that, specificity issues aside, the Qdot-Abs could not access the nucleus at all. This hypothesis was tested by transfecting cells with an unconjugated soluble GFP, which diffuses throughout the cytoplasm and nucleus. We then labelled with either a direct anti-GFP Qdot 625 conjugate (Qdot-GFP) or indirectly with a primary anti-GFP antibody and Qdot 625-Ab. Both approaches yielded homogenous labelling in the cytosol, with the Qdot signal being excluded from the nucleus (Figure 7). There was also little non-specific Qdot 625 staining in the non-transfected cells (Figures S16 and S17 in Supporting Information File 1). Unlike Qdot 625, when the unconjugated soluble GFP was immunolabelled with a secondary antibody coupled to the fluorescent dye cyanine 3 (Cy3), there was labelling in both the cytosol and nucleus (Figure 7E). To assess the extent at which Qdot 625 did not label soluble GFP within the nucleus, fluorescence intensities of Qdot 625 and GFP were plotted from line scans taken across a section of the cell, including the cytosolic region and nucleus (Figure 7K). There was an obvious decline in the fluorescence intensity of Qdot 625 in the nucleus. Under continuous illumination, the fluorescence intensity of Qdot 625 in the cytosol was greater than that of GFP, due to the superior brightness of Qdots. Multichannel images were taken without adjustment to the focus to rule out different focal planes explaining the absence of Qdots from the nucleus.

## Conclusion

Fluorescent Qdots are bright and photostable and hence have been promoted as having significant potential for imaging in biology, including for the immunolabelling of cellular structures. However, even after several years of promising articles and reviews, Qdots have not found routine use in biological research. Here, we examine the performance of some of the few Qdot conjugates commercially available for immunofluorescence (Table S1 in Supporting Information File 1). While all tested antigens could be labelled using antibodies conjugated to fluorescent dyes (Dye-Abs) (e.g. Alexa Fluor 488), only tubulin and extracellular fibronectin could be labelled specifically with Qdot-Abs. Neither a nuclear protein (SC35) nor an antigen within a large complex (talin) could be labelled with the Qdot-Abs. Our hypothesis is that the specificity of Qdot-Abs is dependent upon the type of protein, its abundance, and location within the cell. This is most likely due to the size of the Qdot-Abs, leading to steric hindrance and limited access to certain epitopes. Additionally, if cross-linking of the target protein has occurred, Qdot 625 aggregates may restrict access to the epitope and thus affect the specific labelling of these proteins [36].

Therefore, we conclude that these Qdot-Abs are not suitable to detect complex intracellular structures unless the proteins are abundant and have multiple, accessible antigens along the structure. Although Montón et al. suggest that Qdot-Abs were more specific for proteins that are scarce in the cell [20], here we find that the specific labelling of proteins such as SC35 and talin could not be achieved with the with commercial Qdot-Abs.

The parameters that may affect the ability of Qdots to penetrate intracellular targets (such as foci adhesion complexes or nuclear proteins) include the labelling ratio between Qdots and func-

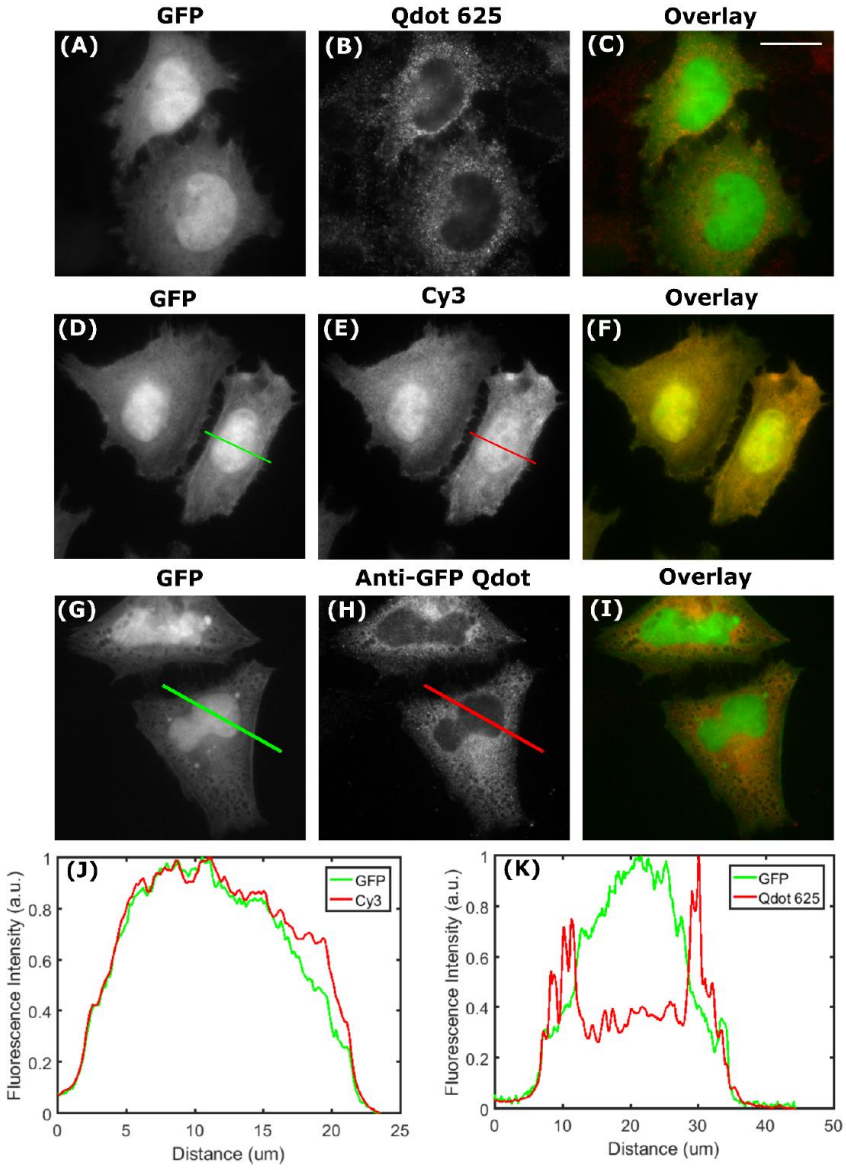


**Figure 7:** Qdot-Abs are unable to access the cell nucleus. Fixed HeLa cells were transfected with unconjugated soluble GFP (A), incubated with a primary anti-GFP antibody, and red Qdot-Ab (B) to produce an overlaid image (C). Fixed HeLa cells were also transfected with unconjugated soluble GFP (D), incubated with a primary anti-GFP antibody, and red cyanine 3 conjugated to a secondary antibody (E) to produce an overlaid image (F). Direct ICC was done by incubating fixed HeLa cells, transfected with unconjugated soluble GFP (G), with an anti-GFP Qdot 625 conjugate (H) to produce an overlaid image (I). Normalised fluorescence intensities of unconjugated soluble GFP labelled with Cy3 (J) and Qdot 625 (K) were plotted from corresponding lines scans to show no labelling within the nucleus with Qdot 625. Scale bar is 20 µm.

tional antibodies, the overall surface charge of Qdot-Ab conjugates, and whether there is a presence of a protein corona. The labelling ratio of Qdots to antibodies present within commercially available Qdot-Ab conjugates has been previously evaluated, where the non-specific labelling of proteins was attributed to the lack of IgG molecules per Qdot [37]. Depending on the chosen Qdot-Ab conjugation method, the binding affinity of the antibody for the Qdots can be increased. However, regardless of the variability in the Qdot synthesis and antibody conjugation protocols, the orientation in which the IgG molecules bind to Qdots cannot be controlled [37]. The binding affinity of Qdot-Abs can also be affected by the surface charge they possess. For instance, positively charged Qdots are taken up by cells more readily than negatively charged or zwitterionic Qdots, which suppress protein adsorption and thus the formation of a protein corona [38]. Qdots with a zwitterionic surface have a zeta potential of near zero, are resistant to non-specific binding onto cells, and have a high colloidal stability [39]. Commercially available Qdot-Abs evaluated in this report were used in fixed, permeabilised cells that were blocked with BSA (negatively charged). One way to assess the non-specific binding of these Qdot-Abs to cells would be to use flow cytometry.

Beyond those commercially available Qdots, there have been a number of ICC protocols published for the labelling of different proteins with Qdot-Abs [6,20,24]. These reports, however, were mostly focused on the unproblematic labelling of tubulin for their proof-of-principle experiments. We suggest that future developments of Qdot-Abs include other more challenging targets as benchmarks, for example, those evaluated in this article. The ideal scenario would be a toolbox of commercially available Qdot-Abs that can be consistently used to label any biological structure of interest and not just tubulin and extracellular targets.

# Methods

## Cell culture

Human cervix epithelioid carcinoma (HeLa, ECACC number 930210a3) cells were cultured in a 75 $cm^2$ flask at 37 °C with 5% $CO_2$, minimum essential media (MEM, Life Technologies, UK) supplemented with 10% (v/v) foetal calf serum (FCS), and 1% non-essential amino acids (NEAA). Cells were split 1,000,000 cells/mL when ≥80% confluent with trypsin-EDTA. Rat mammary (Rama) 27 fibroblasts were cultured in a 75 $cm^2$ flask at 37 °C with 5% $CO_2$, Dulbecco's modified Eagle's medium (DMEM, Life Technologies, UK) supplemented with 10% (v/v) FCS (Life Technologies, UK), 0.75% (w/v) sodium bicarbonate, 4 mM L-glutamine, 50 ng/mL insulin, and 50 ng/mL hydrocortisone (Sigma-Aldrich, UK), as described previously [40]. Cells were split 1:8 when ≥60% confluent with trypsin-EDTA. A stable cell line TC7 3xGFP (expressing tubulin-GFP) was cultured in a 75 $cm^2$ flask at 37 °C with 5% $CO_2$, MEM (Life Technologies, UK) supplemented with 10% (v/v) FCS, 1% NEAA, and genetitin (Sigma-Aldrich, UK), as described previously [41]. Cells were split 1:15 when ≥80% confluent with trypsin-EDTA.

## Transfection

HeLa cells were seeded onto 16 mm glass coverslips (100,000 cells/mL) in a 12-well plate and transfected with pG-EGFP-A (soluble GFP) or pG-EGFP-HIF2α (EGFP-HIF2α) using FuGENE6 transfection reagent (Roche Limited, UK), following the manufacturer's protocol (3:1 transfection reagent/DNA plasmid).

## Site click conjugation of Qdot625 to anti-GFP

Following the manufacturer's protocol, a commercial site-click Qdot 625 antibody conjugation kit (Thermo Fisher Scientific, UK) was used to conjugate a primary mouse (clones 7.1 and 13.1) anti-GFP antibody (Roche Limited, UK) to dibenzocyclooctyne (DIBO) modified Qdot 625. The concentration of the Qdots in the conjugate was calculated to be 3 μM using the equation $c = A/\varepsilon$, where $c$ is the concentration of DIBO-modified Qdot 625 attached to the primary antibody, $A$ is the absorbance of Qdot 625, and ε is the extinction coefficient of Qdot 625 (500,000 $M^{-1}{\cdot}cm^{-1}$). The absorbance between 605–612 nm (step 10 nm) was measured to be 1.5 a.u. using a quartz cuvette with a 1 cm path length, on a SpectraMax 34 Plus spectrophotometer (Molecular Devices, UK).

## Immunofluorescence

An overview of the immunofluorescence procedure is shown in Figure 8. Briefly, cells were seeded onto glass coverslips and grown until confluent, washed once in phosphate buffered saline (PBS) (37 °C), and fixed in 4% (w/v) paraformaldehyde (PFA) for 10 min or 100% ice cold methanol (5 min). Cells were washed 3× in PBS (5 min), permeabilised with 0.25% Triton X-100 in PBS for 60 min (except methanol fixation), washed again 3× in PBS (5 min), and incubated with 6% bovine serum albumin (BSA, Sigma-Aldrich, UK) in PBS (60 min). Primary antibodies produced in mouse (anti-β-tubulin TUB 2.1, Sigma-Aldrich, UK; anti-GFP Roche Limited, UK; anti-SC35, Abcam, UK; and anti-talin, Sigma-Aldrich, UK), those produced in rabbit (anti-fibronectin, Sigma-Aldrich, UK), and biotinylated anti-GFP (Abcam, UK) were diluted 1:100 in 6% BSA and incubated overnight at 4 °C. Cells were washed 3× in PBS (5 min) and incubated simultaneously with either a mixture of Donkey anti-mouse IgG H+L secondary antibody Qdot 625 conjugate, Qdot 625 anti-GFP conjugate, F(ab')2-Goat anti-rabbit IgG H+L secondary antibody Qdot 625 conjugate, or Qdot 625 streptavidin conjugate (Thermo Fisher Scientific, UK), diluted 1:50 to 20 nM in 6% BSA, and goat anti-

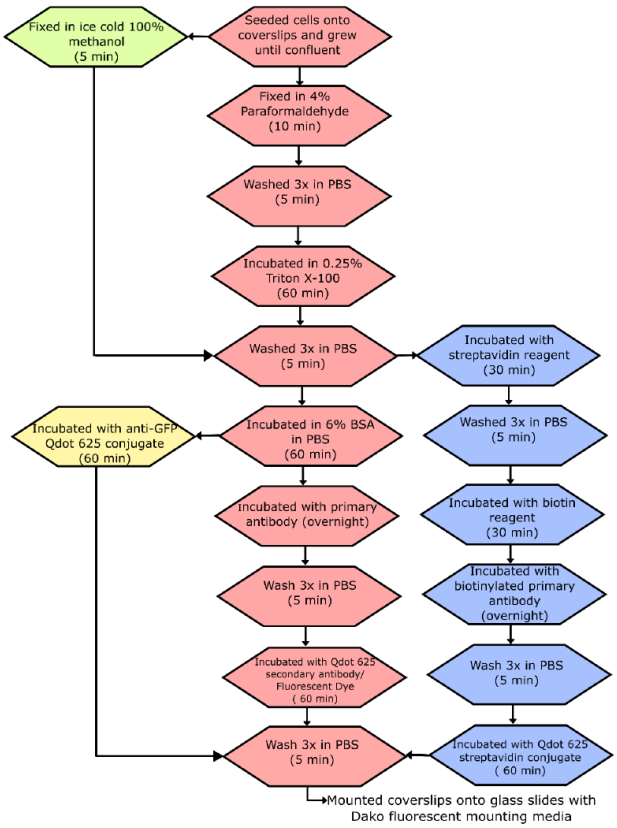


**Figure 8:** Immunofluorescence protocol. The pink boxes show the method for use with a primary antibody and Qdot 625/Fluorescent dye conjugated to a secondary antibody, green box is for methanol fixation, yellow boxes for the anti-GFP Qdot 625 conjugate, and blue boxes are for biotinylated primary antibody with Qdot 625 streptavidin conjugate.

rabbit Alexa Fluor 488 or goat anti-mouse Alexa Fluor 488 (Thermo Fisher Scientific, UK), diluted 1:500 to 4 µg/mL in 6% BSA; or anti-mouse cyanine 3 (Sigma-Aldrich, UK) diluted 1:500 to 4 µg/mL in 6% BSA, at room temperature (60 min). Before preparation of the Qdot 625 conjugated secondary antibody, the vial was centrifuged at 5,000 g for 3 min to remove any aggregates. After 3 washes in PBS (10 min), coverslips were mounted onto slides with Dako fluorescent mounting media (Dako, UK), and stored at 4 °C. A negative control of Qdot 625 conjugated antibody only was also prepared to show any background staining.

## Wide-field imaging

Images were taken on a wide-field epifluorescence microscope (Carl Zeiss Axio Observer Z.1, Germany) with a 16 µm 512 × 512 pixel sensitive electron-multiplying charge-coupled device (EMCCD) camera (Andor iXon 897 Ultra), polychromatic mercury arc lamp, 39106-AT-QDot 625 filter set (Chroma Technology Corporation, USA), and a 100× 1.45 NA oil-immersion objective. Fluorescent and corresponding bright-field images were acquired using Micro-Manager software [42]. The same acquisition settings were used for each set of images, including lamp power, exposure time, and gain.

## Co-localisation analysis

Pearson correlation coefficient scatter plots of Qdot 625 and Alexa Fluor 488/GFP were produced using a custom-made Matlab code [43]. Manders' correlation coefficients were determined using a Just Another Co-localization Plugin (JACoP) [29] in FIJI [44].

## Supporting Information

### Supporting Information File 1

Additional data.
[http://www.beilstein-journals.org/bjnano/content/supplementary/2190-4286-8-125-S1.pdf]

## Acknowledgements

We express gratitude to Professor Chöle Bulinkski from Colombia University for the TC7 3xGFP cells and also appreciation to Professor Philip Rudland from University of Liverpool for supplying the rat mammary (Rama) 27 fibroblasts. We would like to acknowledge and thank the Liverpool Centre for Cell Imaging (CCI) for training and access to equipment. We would also like to thank Dr Sumaira Ashraf for acquiring the TEM images of core/shell Qdot 625, Dr Mark Wilkinson for performing SEC-HPLC of Qdot 625-Ab, and Dr James Boyd for advice on FCS measurements of Qdot 625-Ab; all from University of Liverpool. The epifluorescence microscope used in this study was funded in part and DM was fully funded by the Medical Research Council (Grant number: MR/K015931/1). All of the experiments were carried out using funding from an iCASE BBSRC studentship.

## References

1. Bruchez, M., Jr.; Moronne, M.; Gin, P.; Weiss, S.; Alivisatos, A. P. *Science* **1998,** *281,* 2013–2016. doi:10.1126/science.281.5385.2013
2. Chan, W. C. W.; Nie, S. *Science* **1998,** *281,* 2016–2018. doi:10.1126/science.281.5385.2016
3. Li, Y.; Shen, B.; Liu, L.; Xu, H.; Zhong, X. *Colloids Surf., A* **2012,** *410,* 144–152. doi:10.1016/j.colsurfa.2012.06.034
4. Mei, B. C.; Susumu, K.; Medintz, I. L.; Delehanty, J. B.; Mountziaris, T. J.; Mattoussi, H. *J. Mater. Chem.* **2008,** *18,* 4949–4958. doi:10.1039/b810488c
5. Pellegrino, T.; Manna, L.; Kudera, S.; Liedl, T.; Koktysh, D.; Rogach, A. L.; Keller, S.; Rädler, J.; Natile, G.; Parak, W. J. *Nano Lett.* **2004,** *4,* 703–707. doi:10.1021/nl035172j
6. Wu, X.; Liu, H.; Liu, J.; Haley, K. N.; Treadway, J. A.; Larson, J. P.; Ge, N.; Peale, F.; Bruchez, M. P. *Nat. Biotechnol.* **2003,** *21,* 41–46. doi:10.1038/nbt764
7. Zhao, J.-J.; Chen, J.; Wang, Z.-P.; Pan, J.; Huang, Y.-H. *Mol. Med. Rep.* **2011,** *4,* 425–429. doi:10.3892/mmr.2011.457
8. Jaiswal, J. K.; Mattoussi, H.; Mauro, J. M.; Simon, S. M. *Nat. Biotechnol.* **2002,** *21,* 47–51. doi:10.1038/nbt767
9. Resch-Genger, U.; Grabolle, M.; Cavaliere-Jaricot, S.; Nitschke, R.; Nann, T. *Nat. Methods* **2008,** *5,* 763–775. doi:10.1038/nmeth.1248
10. Dertinger, T.; Colyer, R.; Iyer, G.; Weiss, S.; Enderlein, J. *Proc. Natl. Acad. Sci. U. S. A.* **2009,** *106,* 22287–22292. doi:10.1073/pnas.0907866106
11. Nirmal, M.; Dabbousi, B. O.; Bawendi, M. G.; Macklin, J. J.; Trautman, J. K.; Harris, T. D.; Brus, L. E. *Nature* **1996,** *383,* 802–804. doi:10.1038/383802a0
12. Pathak, S.; Cao, E.; Davidson, M. C.; Jin, S.; Silba, G. A. *J. Neurosci.* **2006,** *26,* 1893–1895. doi:10.1523/JNEUROSCI.3847-05.2006
13. Barteneva, N.; Vorobjev, I. Quantum dots in microscopy and cytometry: immunostaining applications. 2010; pp 710–721.
14. Silva, G. A. *Prog. Brain Res.* **2009,** *180,* 19–34. doi:10.1016/S0079-6123(08)80002-7
15. Jaiswal, J. K.; Simon, S. M. *Trends Cell Biol.* **2004,** *14,* 497–504. doi:10.1016/j.tcb.2004.07.012
16. Kingeter, L. M.; Schaefer, B. C. *BMC Biotechnol.* **2009,** *9,* 49. doi:10.1186/1472-6750-9-49
17. Parak, W. J.; Pellegrino, T.; Plank, C. *Nanotechnology* **2005,** *16,* R9. doi:10.1088/0957-4484/16/2/R01
18. Deerinckm, T. J. *Toxicol. Pathol.* **2008,** *36,* 112–116. doi:10.1177/0192623307310950
19. Chattopadhyay, P. K.; Perfetto, S. P.; Yu, J.; Roederer, M. *Wiley Interdiscip. Rev.: Nanomed. Nanobiotechnol.* **2010,** *2,* 334–348. doi:10.1002/wnan.75
20. Montón, H.; Nogués, C.; Rossinyol, E.; Castell, O.; Roldán, M. *J. Nanobiotechnol.* **2009,** *7,* 4. doi:10.1186/1477-3155-7-4
21. Ness, J. M.; Akhtar, R. S.; Latham, C. B.; Roth, K. A. *J. Histochem. Cytochem.* **2003,** *51,* 981–987. doi:10.1177/002215540305100801
22. Dahan, M.; Lévi, S.; Luccardini, C.; Rostaing, P.; Riveau, B.; Triller, A. *Science* **2003,** *302,* 442–445. doi:10.1126/science.1088525
23. Kaul, Z.; Yaguchi, T.; Kaul, S. C.; Hirano, T.; Wadhwa, R.; Taira, K. *Cell Res.* **2003,** *13,* 503–507. doi:10.1038/sj.cr.7290194
24. Tokumasu, F.; Dvorak, I. *J. Microsc.* **2003,** *211,* 256–261. doi:10.1046/j.1365-2818.2003.01219.x
25. Xu, W.; Liu, L.; Brown, N. J.; Christian, S.; Hornby, D. *Molecules* **2012,** *17,* 796–808. doi:10.3390/molecules17010796
26. Chen, H.; Xue, J.; Zhang, Y.; Zhu, X.; Gao, J.; Yu, B. *J. Mol. Histol.* **2009,** *40,* 261–268. doi:10.1007/s10735-009-9237-y
27. Sukhanova, A.; Devy, J.; Venteo, L.; Kaplan, H.; Artemyev, M.; Oleinikov, V.; Klinov, D.; Pluot, M.; Cohen, J. H. M.; Nabiev, I. *Anal. Biochem.* **2004,** *324,* 60–67. doi:10.1016/j.ab.2003.09.031
28. Ling, J. *Proc. SPIE* **2008,** *6866,* 68660T. doi:10.1117/12.763359
29. Bolte, S.; Cordelières, F. P. *J. Microsc.* **2006,** *224,* 213–232. doi:10.1111/j.1365-2818.2006.01706.x
30. Williams, Y.; Byrne, S.; Bashir, M.; Davies, A.; Whelan, Á.; Gun'ko, Y.; Kelleher, D.; Volkov, Y. *J. Microsc.* **2008,** *232,* 91–98. doi:10.1111/j.1365-2818.2008.02083.x
31. Bentolila, L. A.; Weiss, S. *Cell Biochem. Biophys.* **2006,** *45,* 59–70. doi:10.1385/CBB:45:1:59
32. Pathak, S.; Choi, S.-K.; Arnheim, N.; Thompson, M. E. *J. Am. Chem. Soc.* **2001,** *123,* 4103–4104. doi:10.1021/ja0058334
33. Xiao, Y.; Barker, P. E. *Nucleic Acids Res.* **2004,** *32,* e28. doi:10.1093/nar/gnh024
34. Ma, L.; Wu, S.-M.; Huang, J.; Ding, Y.; Pang, D.-W.; Li, L. *Chromosoma* **2008,** *117,* 181–187. doi:10.1007/s00412-007-0136-2
35. Ioannou, D.; Tempest, H. G.; Skinner, B. M.; Thornhill, A. R.; Ellis, M.; Griffin, D. K. *Chromosome Res.* **2009,** *17,* 519–530. doi:10.1007/s10577-009-9051-0
36. Chang, Y.-P.; Pinaud, F.; Antelman, J.; Weiss, S. *J. Biophotonics* **2008,** *1,* 287–298. doi:10.1002/jbio.200810029
37. Pathak, S.; Davidson, M. C.; Silva, G. A. *Nano Lett.* **2007,** *7,* 1839–1845. doi:10.1021/nl062706i
38. Ashraf, S.; Park, J.; Bichelberger, M. A.; Kantner, K.; Hartmann, R.; Maffre, P.; Said, A. H.; Feliu, N.; Lee, J.; Lee, D. *Nanoscale* **2016,** *8,* 17794–17800. doi:10.1039/C6NR05805A
39. Park, J.; Nam, J.; Won, N.; Jin, H.; Jung, S.; Jung, S.; Cho, S.-H.; Kim, S. *Adv. Funct. Mater.* **2011,** *21,* 1558–1566. doi:10.1002/adfm.201001924

40. Rudland, P. S.; Twiston Davies, A. C.; Tsao, S.-W. *J. Cell. Physiol.* **1984,** *120,* 364–376. doi:10.1002/jcp.1041200315
41. Faire, K.; Waterman-Storer, C. M.; Gruber, D.; Masson, D.; Salmon, E. D.; Bulinski, J. C. *J. Cell Sci.* **1999,** *112,* 4243–4255.
42. Edelstein, A.; Amodaj, N.; Hoover, K.; Vale, R.; Stuurman, N. *Computer Control of Microscopes Using μManager;* John Wiley & Sons, Inc.: New York, NY, U.S.A., 2010.
43. *MATLAB*, Version R2014a; Mathworks, Inc.: Natick, MA, United States, 2014.
44. Schindelin, J.; Arganda-Carreras, I.; Frise, E.; Kaynig, V.; Longair, M.; Pietzsch, T.; Preibisch, S.; Rueden, C.; Saalfeld, S.; Schmid, B.; Tinevez, J.-Y.; White, D. J.; Hartenstein, V.; Eliceiri, K.; Tomancak, P.; Cardona, A. *Nat. Methods* **2012,** *9,* 676–682. doi:10.1038/nmeth.2019

# Supporting Information
# for
# Evaluation of quantum dot conjugated antibodies for immunofluorescent labelling of cellular targets

Jennifer E. Francis[1], David Mason[2], and Raphaël Lévy[*1]

Address: [1]Department of Biochemistry, Institute of Integrative Biology, Biosciences Building, Crown Street, Liverpool, L69 7ZB, United Kingdom and [2]Centre for Cell Imaging, Institute of Integrative Biology, Biosciences Building, Crown Street, Liverpool, L69 7ZB, United Kingdom

Email: Raphaël Lévy - rapha@liverpool.ac.uk

*Corresponding author

## Additional Data

### Introduction

In this Supporting Information, we provide:

1.1 Emission and excitation spectra

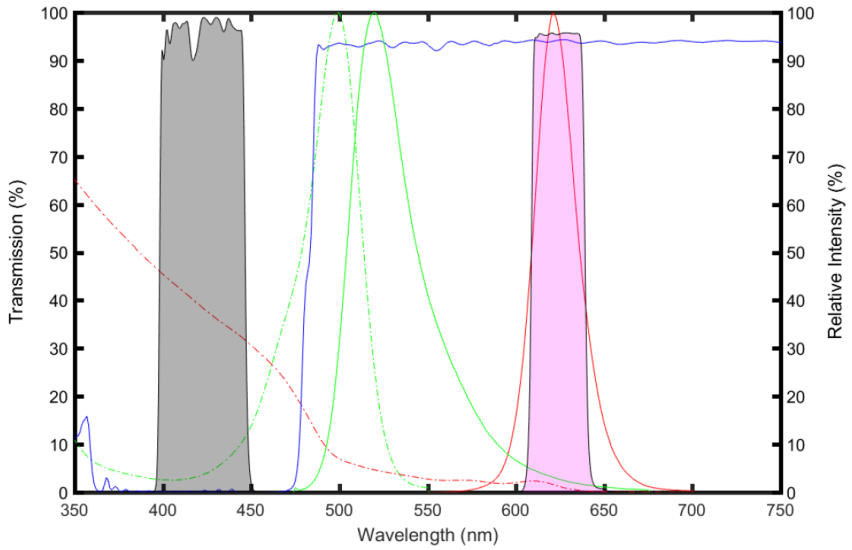


**Figure S1: Excitation and emission spectra of Qdot 625-Ab and Alexa Fluor 488-Ab.** Excitation of Qdot 625-Ab (red dotted line) and Alexa Fluor 488-Ab (green dotted line) were plotted along with the emission of Qdot 625-Ab (red solid line) and Alexa 488-Ab (green solid line). Data for the excitation and emission spectra was exported from Fluorescence SpectraViewer on the Thermo Fisher Scientific, UK website. A Qdot 625 filter set (39106, Chroma, UK) has also been added to the spectra, with excitation (grey shaded region), beam splitter (solid blue line), and emission (red shaded region), which were obtained from the Chroma website.

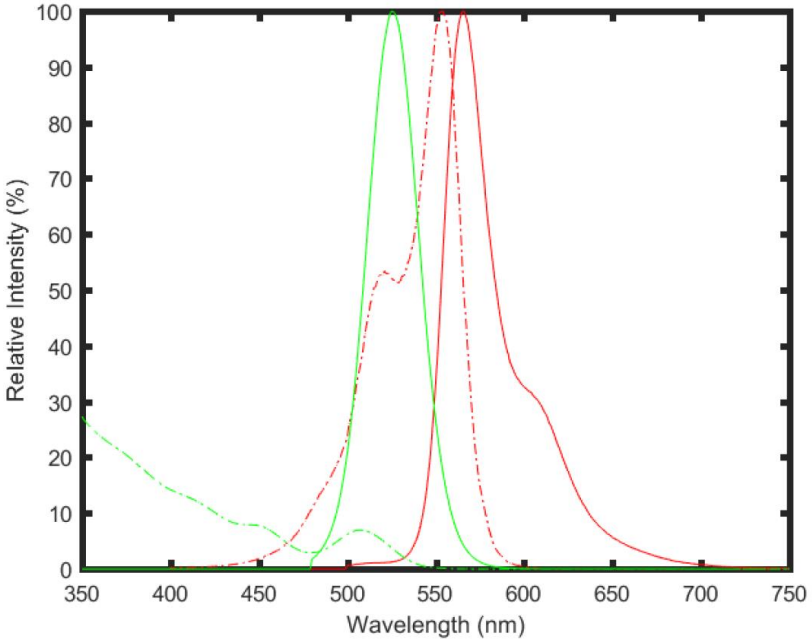


**Figure S2: Excitation and emission spectra of Qdot 525-Ab and Cy3-Ab.** Excitation of Qdot 525-Ab (green dotted line) and Cy3-Ab (red dotted line) were plotted along with the emission of Qdot 525-Ab (green solid line) and Cy3-Ab (red solid line). Data was exported from Fluorescence SpectraViewer on the Thermo Fisher Scientific, UK website.

## 2.1 Anti-tubulin Qdot 625 conjugate

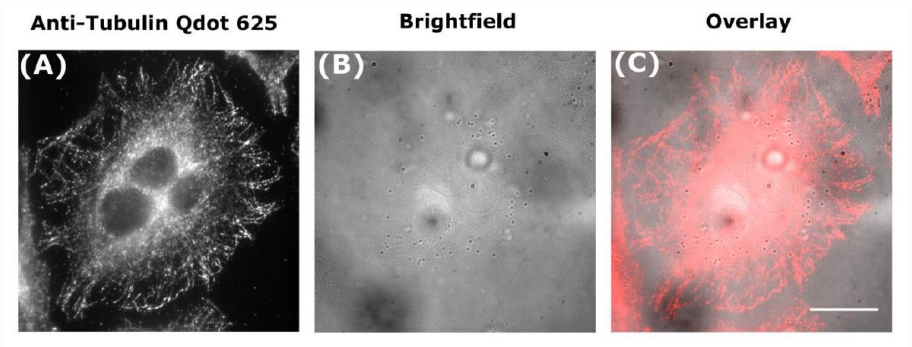


**Figure S3: Specific labelling of tubulin with anti-tubulin Qdot 625 conjugate.** An anti-tubulin primary antibody was conjugated to Qdot 625 via click chemistry (as described in the

Methods section of the paper for anti-GFP). HeLa cells were fixed and incubated with an anti-tubulin Qdot 625 conjugate (A). A corresponding brightfield image was taken (B) and overlaid image produced (C). Scale bar is 20 µm.

### 3.1 Negative controls with Qdot 625-Ab

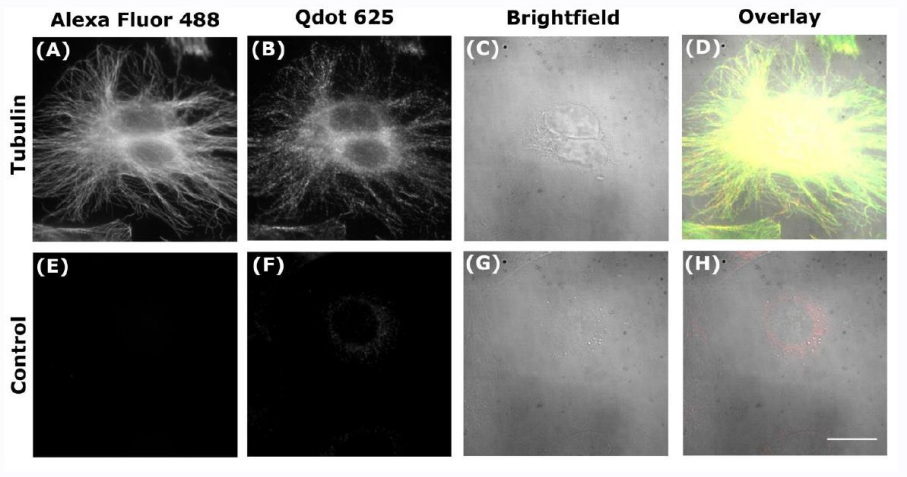


**Figure S4: Labelling of Tubulin with Qdot 625.** Fixed HeLa cells were dual labelled with green Alexa Fluor 488 (A) and red Qdot 625 (B). A corresponding brightfield image of HeLa cells (C) was also taken to produce an overlaid wide-field image (D). A negative control of HeLa cells incubated simultaneously with green Alexa Fluor 488 (E) and red Qdot 625 (F), without the addition of a primary antibody, was done. The corresponding brightfield (G) and overlay image (H) is shown. Scale bar is 20 µm.

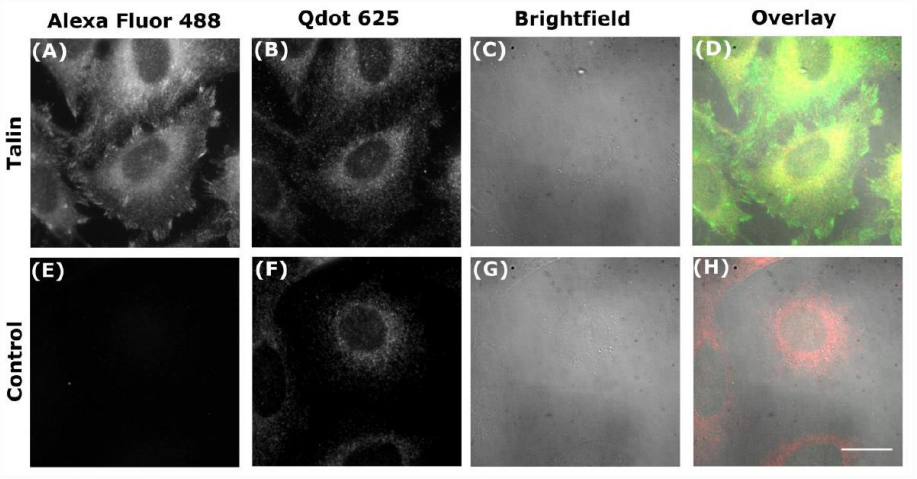


**Figure S5: Labelling of Talin with Qdot 625.** Fixed HeLa cells were dual labelled with green Alexa Fluor 488 (A) and red Qdot 625 (B). A corresponding brightfield image of HeLa cells (C) was also taken to produce an overlaid wide-field image (D). A negative control of HeLa cells incubated simultaneously with green Alexa Fluor 488 (E) and red Qdot 625 (F), without the addition of a primary antibody, was done. The corresponding brightfield (G) and overlay image (H) is shown. Scale bar is 20 µm.

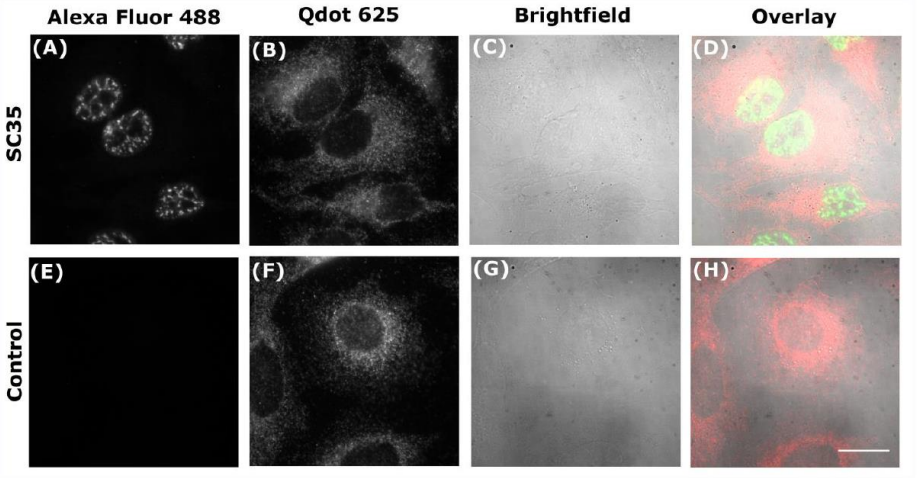


**Figure S6: Labelling of SC35 with Qdot 625.** Fixed HeLa cells were dual labelled with green Alexa Fluor 488 (A) and red Qdot 625 (B). A corresponding brightfield image of HeLa cells (C) was also taken to produce an overlaid wide-field image (D). A negative control of HeLa cells incubated simultaneously with green Alexa Fluor 488 (E) and red Qdot 625 (F), without the addition of a

primary antibody, was done. The corresponding brightfield (G) and overlay image (H) is shown. Scale bar is 20 µm.

## 4.1 Size measurements: TEM, SEC-HPLC, and FCS

### Transmission electron microscopy method:

Qdot 625-Ab was centrifuged at 1,000 g for 5 min to remove any aggregates. A 5 µL sample (0.5 µL Qdot 625-Ab 1 µM, diluted in 100 µL water) was added to a formyar/carbon electron microscopy grid and left to air dry before imaging. Transmission electron micrograph image of Qdot 625 core/shell was taken on a Tecnai G3 spirit transmission electron microscope (TEM). The core/shell size of Qdot 625 was measured for all particles in the calibrated TEM image using the Analyze particles tool in Fiji and a bar chart plotted in Matlab to show the distribution of core/shell sizes. A threshold was set and joint particles were separated by applying a watershed filter.

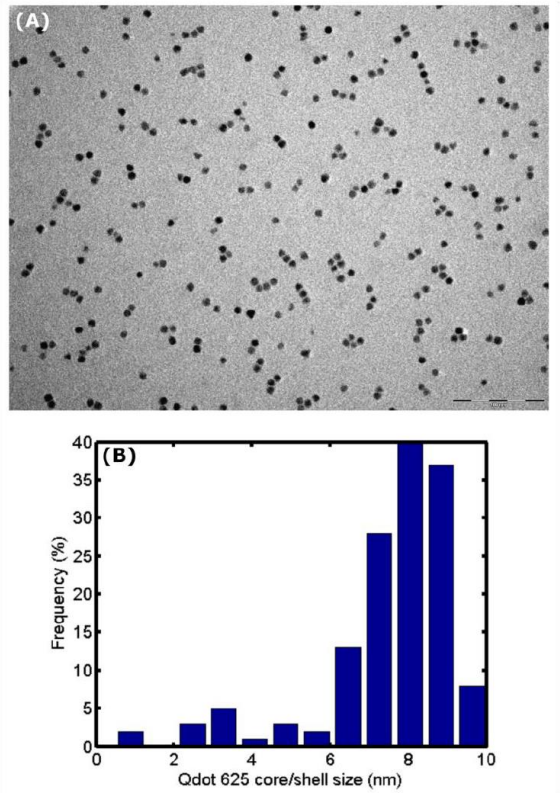


**Figure S7. TEM of Qdot 625-Ab.** Core/shell of Qdot 625 was imaged using TEM (A) and corresponding diameters plotted as a bar chart to determine the average core/shell size of Qdot 625 to be 8 nm (B). Scale bar is 100 nm.

## Size-exclusion-high performance liquid chromatography (SEC-HPLC) method:

A BIO-Gel TSK 40 XL [300 x 7.8 mm] size-exclusion chromatography (SEC) column [Bio-Rad] was set up on a Dionex ICS-3000 high-performance liquid chromatography (HPLC) system and pre-equilibrated with 0.2 um filtered PBS. A 50 µL Qdot 625-Ab (0.1 µM) sample was injected into the column and run with PBS at a flow rate of 0.5 mL/min. Elution was monitored at 214, 280, 400, 500 and 600 nm. The column was calibrated by running standard proteins under the same conditions.
The SEC-HPLC result for Qdot 625-Ab, using the 214 nm detection wavelength, was plotted. Standard proteins of a known molecular weight were used as markers to calculate the molecular weight of Qdot 625-Ab.

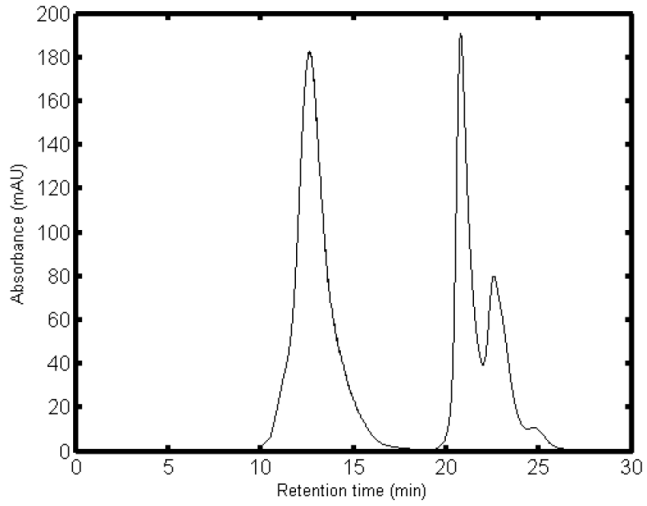


**Figure S8. SEC-HPLC chromatograph for Qdot625-Ab.** Molecular weight of Qdot625-Ab was determined to be 1,100 kDa (~15 nm) by comparing against known standard proteins. Using PBS as a buffer, Qdot625-Ab was eluted at 13 min using a 214 nm detection wavelength.

## Fluorescence correlation spectroscopy (FCS) method:

A Zeiss Axio Observer Z.1 780 confocal microscope (Zeiss, Germany) attached to a PicoQuant system (PicoQuant GmbH, Germany) was used. Point measurements were acquired for 60 s at 37 °C using a 40x 1.2 NA water-immersion objective and a 485 nm pulsed diode laser (POL 828 Sepia II Multichannel Picosecond Diode Laser, PicoQuant GmbH, Germany). Samples were loaded into a custom-built chamber made out of a glass coverslip and Parafilm welded onto a glass microscope slide using a heating block to prevent evaporation. The sample was drawn up into the channel by capillary action and inverted with the glass coverslip facing the objective. For calibration of the

confocal volume ($r_o$), 10 nM ATTO 488 (ATTO-Tec, Germany) was used. Since the diffusion coefficient (D) of 400 µm²/s for ATTO 488 was known at a temperature (T) of 25 °C (PicoQuant, Germany), the diffusion coefficient (D) of ATTO 488 was determined to be 536 µm²/s at 37 °C using D (T) = D (25 °C) x $\frac{T\ (K)}{298.15\ K}$ x $\frac{(8.9x\ 10^{-4}\ PaS)}{n(T)}$, where n is the viscosity of water. During calibration, the correction collar of the 40x water-immersion objective was adjusted to 0.17 mm to match the thickness of the coverslip used. ATTO 488 was fitted with a pure diffusion model and $r_0$ was determined to be 0.6.fL after fixing the concentration to 10 mM and D to 536 µm²/s. A standard reference sample of 30 nm fluorescent latex beads (Sigma-Aldrich, UK), diluted 1:500 in water, was used as a comparison to the Qdot-Abs. Each FCS measurement was repeated 5 times at different positions in the channel and the 5 repeats for 1 position plotted. A 615 nm long pass filter was placed in front of the detector for Qdots to block excitation light and a 520/35 short band pass filter was used for the ATTO 488 and fluorescent beads. SymPhotime software (PicoQuant, Germany) was used to fit the autocorrelation function of ATTO488/beads to a pure diffusion model and the Qdot-Abs to a triplet model. The hydrodynamic diameter of the Qdot625-Ab and Qdot525-Ab was determined using: $d_{Qot} = d_{ST}$ x $\frac{\tau_{Qdot}}{\tau_{ST}}$, where d is the hydrodynamic diameter, Qdot refers to quantum dot, ST is the standard, and τ is the diffusion time [1].

## Fluorescence correlation spectroscopy (FCS) results:

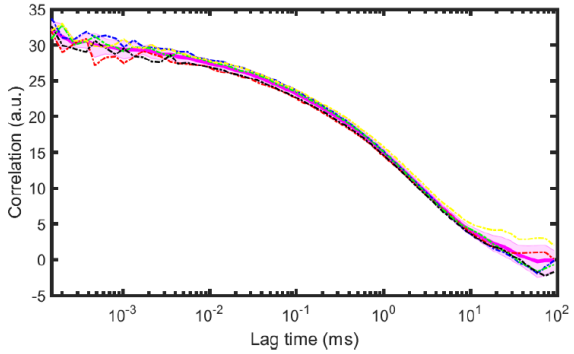


**Figure S9. Fluorescence autocorrelation curves of Qdot 625-Ab.** FCS measurements were taken *of Qdot 625-Ab (2 nM) diffusing in a confocal volume. The blue dotted line is repeat 1, red dotted line is repeat 2, green dotted line is repeat 3, black dotted line is repeat 4, and yellow dotted line is repeat 5. The solid pink line is the mean, with the shaded pink region showing the standard error. The hydrodynamic size of Qdot625-Ab, with an average diffusion time of 2.3 ms (N=5), was calculated to be 76.84 nm.*

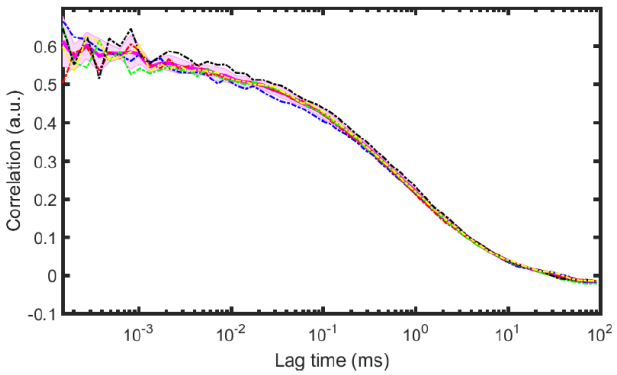


**Figure S10. Fluorescence autocorrelation curves of Qdot 525-Ab.** FCS measurements were taken *of Qdot 525-Ab (2 nM) diffusing in a confocal volume. The blue dotted line is repeat 1, red dotted line is repeat 2, green dotted line is repeat 3, black dotted line is repeat 4, and yellow dotted line is repeat 5. The solid pink line is the mean, with the shaded pink region showing the standard error. The hydrodynamic size of Qdot525-Ab, with an average diffusion time of 1.25 ms (N=5), was calculated to be 41.72 nm.*

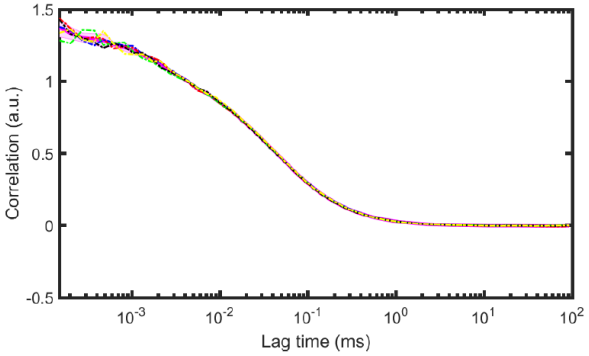


**Figure S11. Fluorescence autocorrelation curves of ATTO488.** FCS measurements were taken *of ATTO 488 (10 nM) diffusing in a confocal volume. The blue dotted line is repeat 1, red dotted line is repeat 2, green dotted line is repeat 3, black dotted line is repeat 4, and yellow dotted line is repeat 5. The solid pink line is the mean, with the shaded pink region showing the standard error. ATTO488, with an average diffusion time of 0.04 ms (N=5) was used to calibrate the confocal volume (0.6 fL).*

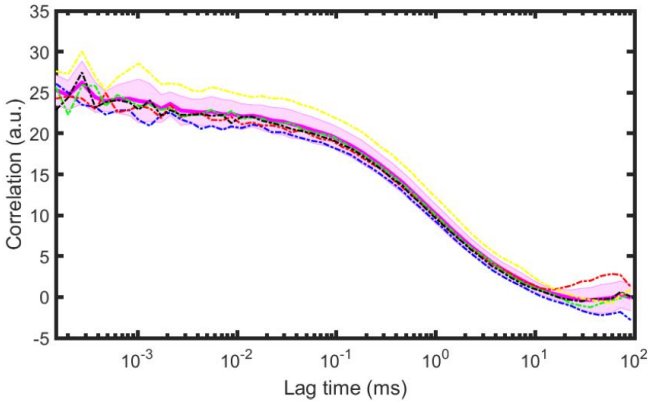


**Figure S12. Fluorescence autocorrelation curves of 30 nm beads.** FCS measurements were taken *of 30 nm beads diffusing in a confocal volume. The blue dotted line is repeat 1, red dotted line is repeat 2, green dotted line is repeat 3, black dotted line is repeat 4, and yellow dotted line is repeat 5. The solid pink line is the mean, with the shaded pink region showing the standard error. Beads of a known hydrodynamic size of 30 nm (quoted by the supplier) and an average diffusion time of 0.9 ms (N=3) were used to calculate the hydrodynamic size of the Qdot-Abs.*

## 5.1 Labelling with Qdot 525-Ab

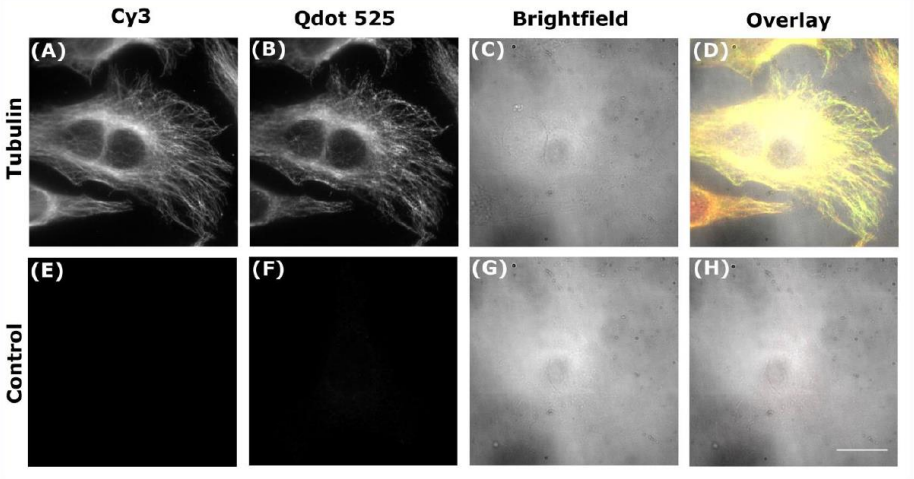


**Figure S13: Labelling of tubulin with Qdot 525.** Fixed HeLa cells were dual labelled with red Cy3 (A) and green Qdot 525 (B). A corresponding brightfield image of HeLa cells (C) was also taken to produce an overlaid wide-field image (D). A negative control of HeLa cells incubated simultaneously with red Cy3 (E) and green Qdot 525 (F), without the addition of a primary antibody, was done. The corresponding brightfield (G) and overlay image (H) is shown. Scale bar is 20 µm.

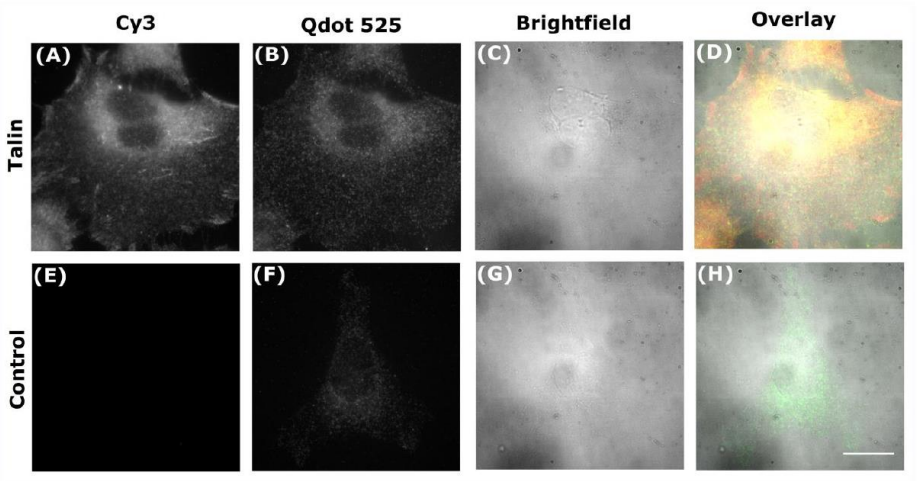


**Figure S14: Labelling of talin with Qdot 525.** Fixed HeLa cells were dual labelled with red Cy3-Ab (A) and green Qdot 525 (B). A corresponding brightfield image of HeLa cells (C) was also taken to produce an overlaid wide-field image (D). A negative control of HeLa cells incubated simultaneously with red Cy3 (E) and green Qdot 525 (F), without the addition of a primary antibody, was done. The corresponding brightfield (G) and overlay image (H) is shown. Scale bar is 20 µm.

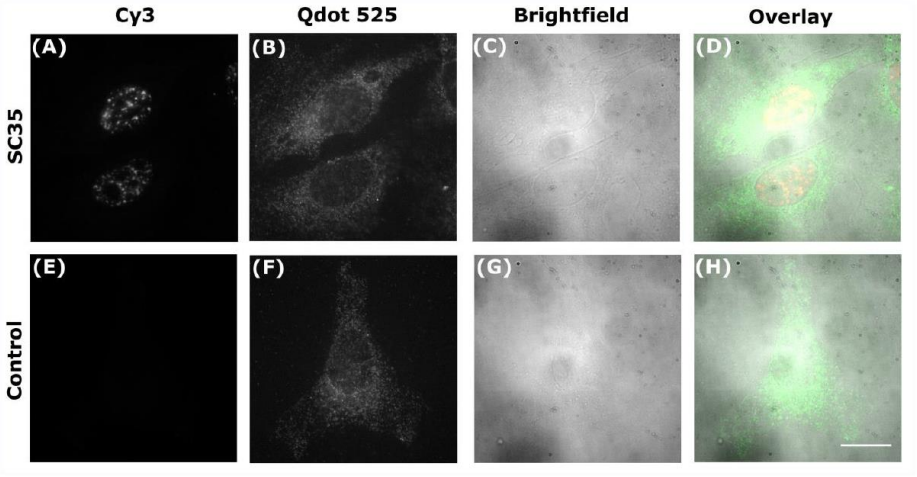


**Figure S15: Labelling of SC35 with Qdot 525.** Fixed HeLa cells were dual labelled with red Cy3-Ab (A) and green Qdot 525 (B). A corresponding brightfield image of HeLa cells (C) was also taken to produce an overlaid wide-field image (D). A negative control of HeLa cells incubated simultaneously with red Cy3 (E) and green Qdot 525 (F), without the addition of a primary antibody, was done. The corresponding brightfield (G) and overlay image (H) is shown. Scale bar is 20 µm.

6.1 Non-transfected controls

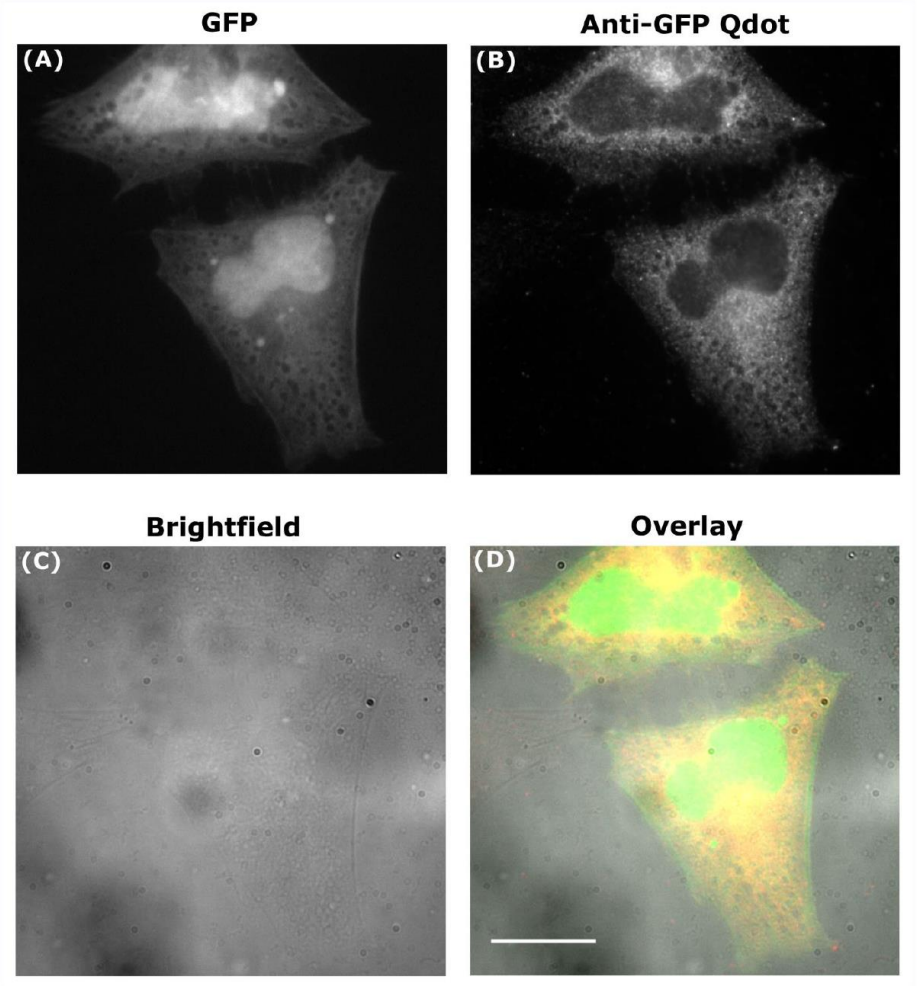


**Figure S16. Qdot-Abs are unable to access the cell nucleus.** Fixed HeLa cells were transfected with green unconjugated soluble GFP (A), incubated with a red anti-GFP Qdot 625 conjugate (B). A brightfield image was taken (C) and an overlay (D) to show both transfected and non-transfected cells. Scale bar is 20 μm.

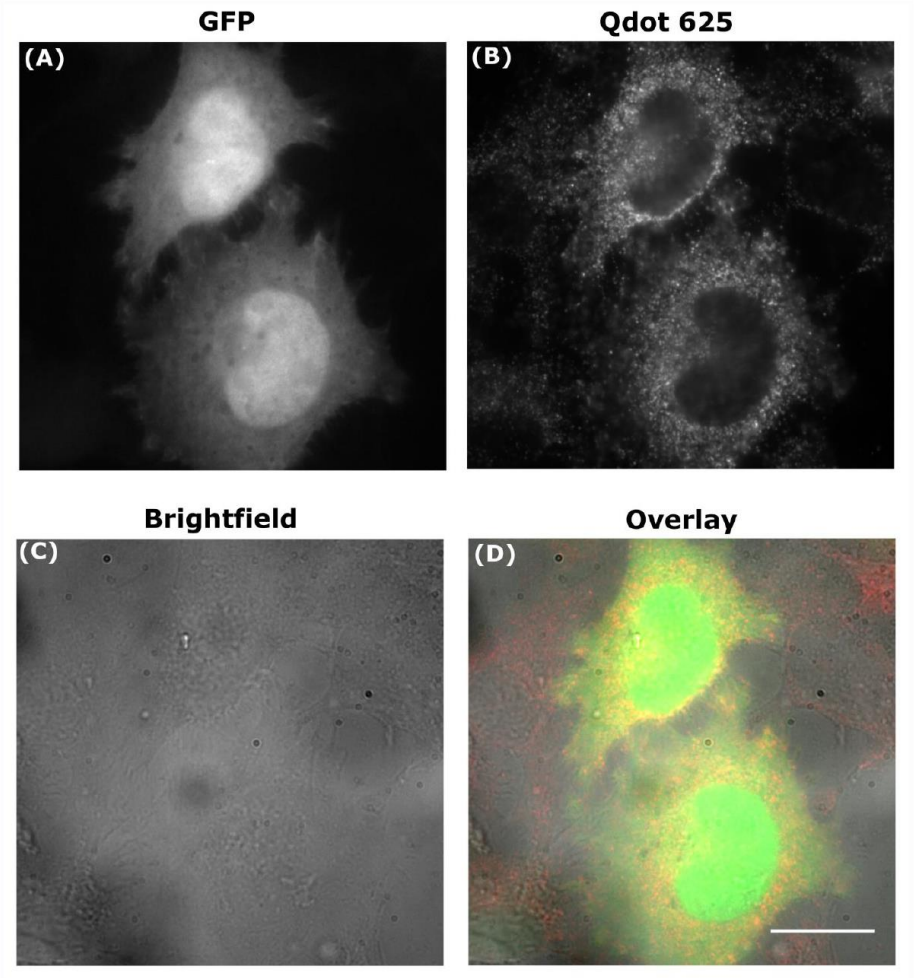


**Figure S17. Qdot-Abs are unable to access the cell nucleus.** Fixed HeLa cells were transfected with green unconjugated soluble GFP (A), incubated with a primary anti-GFP antibody, and red Qdot 625 conjugated secondary antibody (B). A brightfield image was taken (C) and an overlay (D) to show both transfected and non-transfected cells. Scale bar is 20 μm.

## 7.1 Qdot labelling summary table

| Fluorescent probe | Specific binding to protein of interest | | Corresponding figure(s) |
|---|---|---|---|
| Alexa Fluor 488 | Fibronectin | ✓ | Figure 2A |
| | Tubulin | ✓ | Figure 3A and Figure S4A |
| | Talin | ✓ | Figure 4A and Figure S5A |
| | SC35 | ✓ | Figure 5A and Figure S6A |
| Cy3 | Tubulin | ✓ | Figure S7A |
| | Talin | ✓ | Figure S8A |
| | SC35 | ✓ | Figure S9A |
| | Soluble GFP | ✓ | Figure 7E and Figure S10 |
| Qdot 625-Ab | Soluble GFP | ✓ | Figure 7B and Figure S11 |
| | Fibronectin | ✓ | Figure 2B |
| | Tubulin | ✓ | Figure 3B and Figure S4B |
| | Talin | X | Figure 4B and Figure S5B |
| | SC35 | X | Figure 5B and Figure S6B |
| Qdot 525-Ab | Tubulin | ✓ | Figure S7B |
| | Talin | X | Figure S8B |
| | SC35 | X | Figure S9B |
| Qdot 625-Tubulin | Tubulin | ✓ | Figure S3A |
| Qdot 625-GFP | Soluble GFP | ✓ | Figure 7H |
| | Cells expressing Tubulin-GFP | ✓ | Figure 3F |
| Qdot-Streptavidin | Tubulin | ✓ | Figure S3C |
| | EGFP-HIF2α | X | Figure 6B |

**Table S1. Summary of protein specific binding using different commercial antibody conjugates.** Each antibody conjugate was checked as to whether it specifically bound to the protein of interest (✓) or instead non-specifically bound to cells (X). Corresponding figures where the result can be found is supplied.

## References:


1. Tiwari, D,K.; Tanaka, S.; Inouye, Y.; Yoshizawa, K.; Watanabe, T,M. Sensors **2009**, 9, 9332-9354.

## 3.3 Reversibly switching fluorescent proteins

As discussed earlier, only extracellular structures can be specifically labelled with Qdots, which restricts their use in SOFI applications where intracellular proteins are the focus of the study. Although fluctuations of conventional fluorescent proteins, such as GFP, are not sufficient for SOFI-processing, an RFP (104), as well as several RSFPs have been used successfully in SOFI, such as Dronpa (105), Skylan-S (106), and Dreiklang (161). Skylan-S, a monomeric green mutant of mEos3.1, yields higher spatial resolution than Dronpa, because it is much more photostable and has a higher average fluorescence intensity (106). Compared to Qdots RSFPs are not so bright, but SOFI can still work on images of low SNR and where the signal emitted from fluorophores is weak (123). RSFPs are fluorescent proteins that can be continuously switched between a non-fluorescent and fluorescent state, multiple times, in response to specific wavelengths of light. Photoswitching is reversible, unlike photobleaching, where the fluorescence is switched "OFF" permanently (270). Since most RSFPs are spectrally similar, it is optically difficult to distinguish between two different coloured RSFPs, so they have to be imaged sequentially with appropriate lasers to get suitable photoswitching for SOFI (271). Although, simultaneous two-colour SOFI has been achieved with RSFPs without a two-camera setup in live cells, through spectral unmixing using information about their distinct blinking behaviour (272). A slow and fast blinking RSFPs can easily be spectrally distinguished, when imaged simultaneously (272).

The main advantage of using RSFPs, as opposed to Qdots, is that they are genetically-encoded in cells, so they can be imaged in real-time. Despite RSFPs being suitable for live cell imaging and widely available from Addgene, cloning a protein of interest into a fusion protein is time-consuming and overexpression or dimerisation may change the localisation or cause aggregation of the protein, respectively, which can introduce unwanted artefacts. In addition, SOFI assumes that the fluorophores are immobile, so any fast movement would result in motion blur artefacts in the SOFI image. Although, fixing at time points can recover lost dynamic information, this can cause a change in a RSFP's characteristics (273).

RSFP Skylan-S was tested for bSOFI-procesing. MAP4-Skylan-S was continuously illuminated with 20% 365 nm LED (switches Skylan-S on) and 10% of a 30 mW 488 nm laser (switches Skylan-S off). Images were bSOFI-processed up to 4$^{th}$ order in MATLAB (Figure 28). Skylan-S gave sufficient fluctuations for SOFI-processing with improved SNR in all SOFI images. The FWHM of the average wide-field image (1453 nm) decreased by 49% with 2$^{nd}$ order bSOFI (746 nm), 60% with 3$^{rd}$ order bSOFI (576 nm), and 73% with 4$^{th}$ order bSOFI (389 nm). However, there were

structures missing from the higher-order bSOFI images. When assessed with the NanoJ-SQUIRREL ImageJ plugin, image resolution and quality decreased (Figure 28), indicating that the processing narrowed structures (shrunk the FWHM), rather than improve resolution.

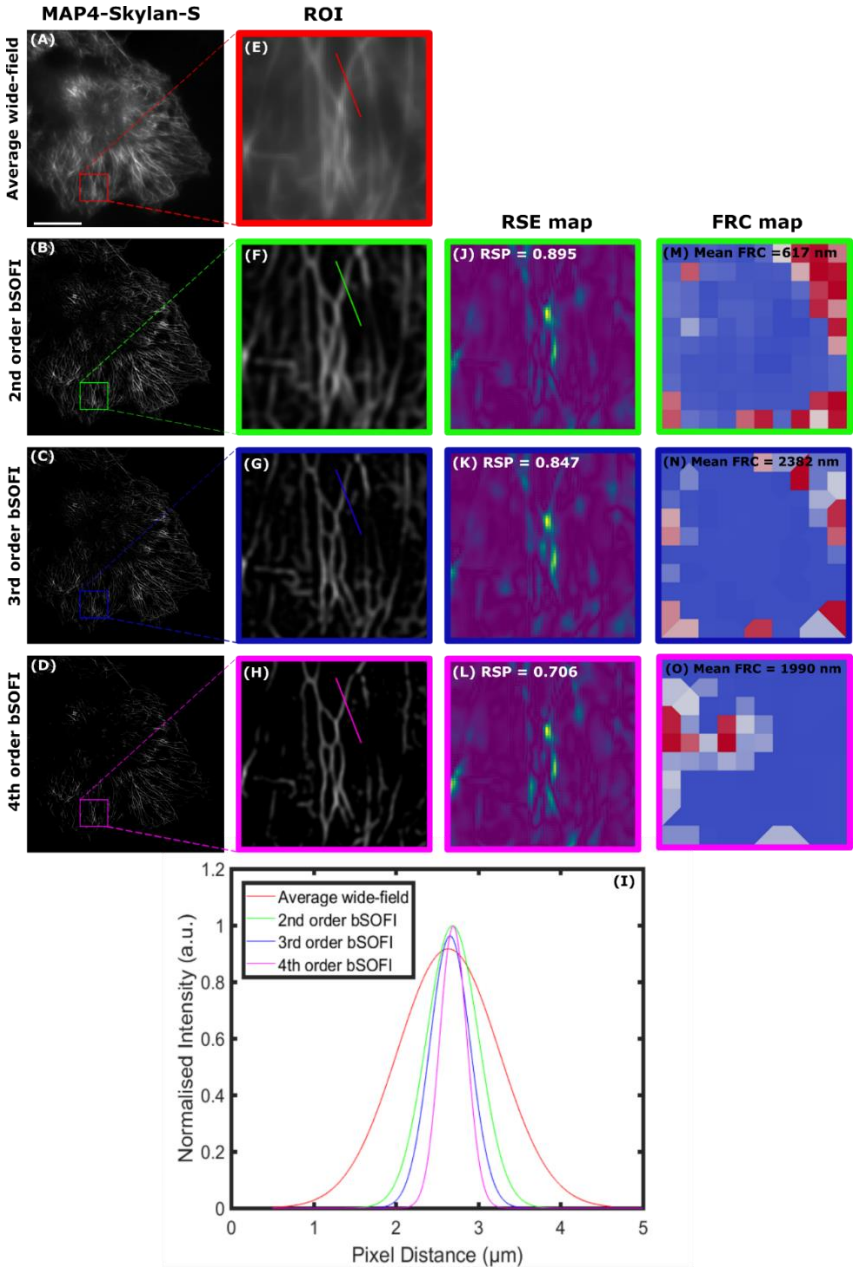


**Figure 28. bSOFI processed MAP4-Skylan-S using continuous illumination.** MAP4-Skylan-S was continuously illuminated with 488 nm and 365 nm light. Images were bSOFI-processed up to 4th order in MATLAB to give average (A) and bSOFI (B-D) images. ROIs (E-H) were taken from images A-D and a line drawn through a structure of interest to determine the FWHM by fitting a line profile with a one-component Gaussian curve (I). The FWHM of the average image (1453 nm) decreased by 49 % with 2nd order bSOFI (746 nm), 60 % with 3rd order bSOFI (576 nm), and 73 % with 4th order bSOFI (389 nm). Resolution-scaled error (RSE) maps (J-L) of F-H and Fourier ring correlation (FRC) maps of B-D were created using NanoJ-SQUIRREL ImageJ plugin. Red regions in the FRC maps are low-resolution (high FRC value), whereas those in blue are of high-resolution (low FRC value). High error regions (likely artefacts) are in blue-yellow (RSP<0.95) and low error regions (unlikely artefacts) in purple (RSP>0.95). Scale bar = 20 µm.

A different approach involved LifeAct-Skylan-S initially being switched "ON" by shining 365 nm LED (20%) on the sample for a few seconds (up to 60 s), before being turned "OFF" completely using continuous illumination with a 30 mW 488 nm laser (1%). In this way, there was a spontaneous recovery of fluorescence, with fluctuations present without the 365 nm excitation source. However, there was a gradual decline in fluorescence intensity, partly due to the switching "OFF" of the protein or photobleaching, which resulted in structures missing from the SOFI-processed image. Photobleaching can be accounted for, to some extent, by SOFI-processing sub-stacks. Here, the SOFI image may have formed as a result of photobleaching, which has been observed by other researchers (256, 274, 275). Visually, the resolution attainment of the SOFI-processed image, in comparison to the average image, was poor, perhaps due to insufficient switching of the RSFP. Rather than measuring the FWHM, resolution and quality of the SOFI-processed image was assessed using the NanoJ-SQUIRREL ImageJ plugin (Figure 29). Resolution was not as low as expected (FRC >250 nm) and the quality of the SOFI image was low (RSP < 0.95) as there were high-error regions highlighted (blue-yellow) in the RSE map, which were likely to be processing artefacts.

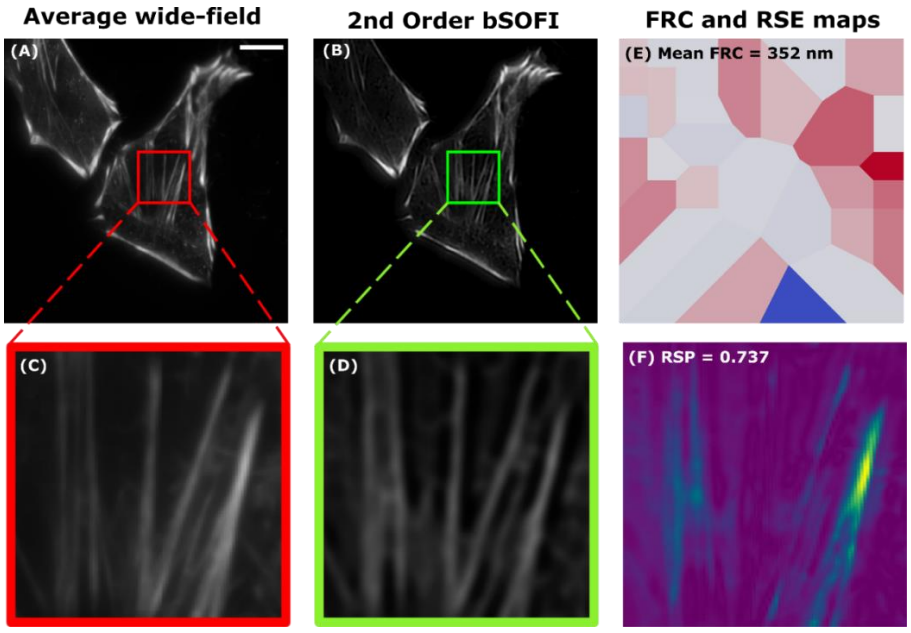


**Figure 29. Testing spontaneous recovery of LifeAct-Skylan-S for SOFI-processing.** LifeAct-Skylan-S was initially illuminated with 365 nm LED (20%) to switch the protein "ON" for 60 s and then the protein was switched "OFF" with continuous illumination with a 30 mW 488 nm laser (1%) for 1,000 frames. The wide-field images (A) were SOFI-processed up to 2nd order with bSOFI (B), implemented in MATLAB. ROIs from the average wide-field image (C) and bSOFI image (D) are shown, as well as a Fourier ring correlation (FRC) map (E) and resolution-scaled error (RSE) map (F). Red regions in the FRC maps are low-resolution (high FRC value), whereas those in blue are of high-resolution (low FRC value). High error regions (likely artefacts) are in blue-yellow (RSP<0.95) and low error regions (unlikely artefacts) in purple (RSP>0.95). Scale bar = 20 µm.

### 3.4 Synthetic organic dyes

Despite Qdots and RSFPs being widely available to biologists, synthetic organic dyes and fluorescent proteins are still the most commonly used fluorescent probes in biological applications. One advantage of using synthetic organic dyes is that they are much smaller than Qdots, so they can label any structure of interest, unlike Qdots that are restricted to extracellular proteins. Synthetic organic dyes are also much brighter and more photostable than RSFPs (273). However, the use of synthetic organic dyes for SOFI still remains a challenge, because they do not fluctuate on a suitable timescale (276). However, fluctuations of synthetic organic dyes can be controlled by altering their photophysics with the introduction of an oxygen scavenger and reducing agent, such as the thiol cysteamine, to the imaging system (93, 109, 167, 275). The exact mechanism by which the photoswitching of synthetic organic dye molecules from a fluorescent state to the triplet state is greatly facilitated by the oxygen scavenger approach is unclear (277). However, it is known that the absence of oxygen prolongs the triplet state (276). Enzymes such as glucose oxidase and catalase can be used to reduce the local oxygen concentration by converting it into gluconic acids (270). In addition to using a freshly prepared oxygen scavenger, it has been reported that conventional synthetic organic dyes such as Alexa Fluor 647 and Cy5 can be switched reversibly between a fluorescent and non-fluorescent state using simultaneous laser irradiation with 647 nm red light and 514 nm green light (62,276).

The duration of the switching is dependent on the intensity of the excitation wavelength, oxygen levels, and thiol concentration (62). If the rate of fluctuations from the fluorescent dye is too high, the thiol concentration and pH can be increased. Alternatively, if the fluctuations are too weak, the thiol concentration and pH can be decreased (278). Although, a combination of oxygen scavenger, thiol, and high irradiation works with fixed samples, it is toxic to live cells and the synthetic organic dyes are susceptible to photobleaching. To minimise the effect of photobleaching, a large stack of images can be recorded and then divided into smaller frame sub-stacks. Each sub-stack can be processed individually to give many noisy SOFI images and finally recombined to produce an averaged SOFI image, which is less noisy. In this way photobleaching within a set of images is minimised and will have a negligible effect on the SOFI-processing (90). An adaptation to the SOFI algorithm can be made to compensate for the lower SNR and photobleaching effect of synthetic organic dyes.

To test the use of synthetic organic dyes for SOFI, β-tubulin in fixed HeLa cells was labelled with the photoswitchable cyanine dye Alexa Fluor 647 (sample kindly provided by Carl Zeiss Microscopy GmbH, Jena, Germany) and incubated with a freshly prepared oxygen scavenger buffer, consisting of 1M MEA (pH 9) and 10 nM NaOH, before imaging. The SMLM technique dSTORM was used on the Zeiss Elyra P.S.1 system (63x 1.4 NA), equipped with a high power 642 nm laser. To achieve an optimal dSTORM image, 30,000 frames were acquired on an EMCCD camera sequentially, in laser wide-field mode, with an additional FOV lens (TIRF-UHP), at 20 ms. To get single molecule blinking, sufficient for dSTORM-processing, the cropped image was illuminated with 100% of a 150 mW 642 nm laser (Long pass filter: 655 nm) and 0.5% of a 50 mW 405 nm laser. The same raw image stack of β-tubulin-Alexa Fluor 647 was post-processed separately with both dSTORM using ZEN software with a measured PSF and SOFI Localizer implemented in MATLAB (Figure 30), similar to reported in the literature (115). The sparse blinking of Alexa Fluor 647 dye molecules could be reconstructed to give SOFI and dSTORM images, however, there was missing structures in the SOFI image that were present in the dSTORM image. Despite this, SOFI works with any labelling density and less frames than dSTORM, so it can be used on datasets that do not meet the optimal conditions for dSTORM-processing. SOFI has been successfully combined with dSTORM to obtain additional information from high density labelled structures (115).

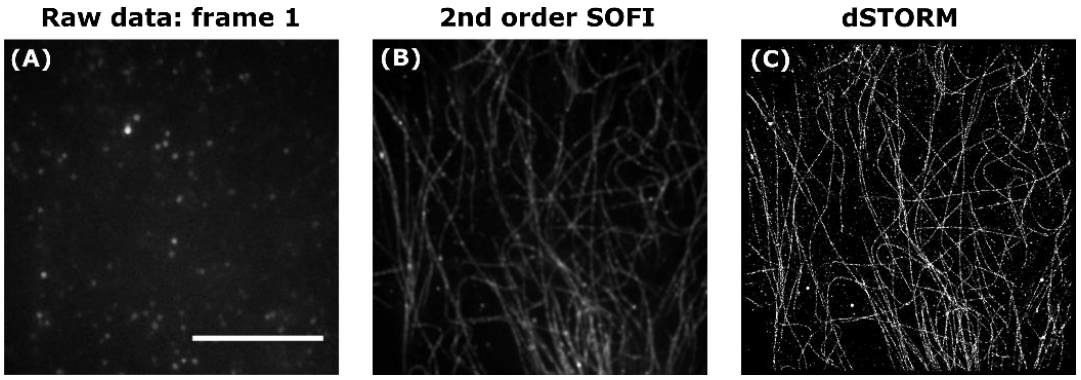


**Figure 30. SOFI-processed and dSTORM-processed β-tubulin-Alexa Fluor 647.** β-tubulin-Alexa Fluor 647 (fixed sample kindly supplied by Carl Zeiss Microscopy GmbH, Jena), was imaged (30,000 frames) using high 642 nm laser intensity and imaging buffer. The same image stack was post-processed with SOFI Localizer implemented in MATLAB as dSTORM in ZEN software. First frame from the stack (A), 2$^{nd}$ order SOFI-processed image (B), and dSTORM-processed image(C) are shown. Scale bar = 10 µm.

## 3.5 Assessing available fluctuating probes for use in SOFI

Conventional fluorescent probes are suitable for super-resolution techniques such as STED, SRRF, and SIM, but SOFI requires modified probes that can provide sufficient fluctuations during image acquisition. Attainable spatial resolution of SOFI varies depending on the type of fluorescent probe used and the current emphasis is on using smaller fluorescent probes attached to nanobodies, rather than large antibodies (279). Recently, anti-GFP nanobody-Qdot conjugates have been developed that have the ability to specifically label any structure of interest, genetically-encoded into cells (269). Since the hydrodynamic radii of Qdots themselves are large, it would advantageous to synthesise small Qdots, whilst still maintaining high blinking (280, 98). Choosing a suitable fluctuating probe is dependent on the biological application, for instance if live cell imaging is needed, for studying a protein's dynamics, RSFPs are best, however, due to their increased fluorescence intensity, Qdots are preferred for fixed cell surface proteins and synthetic organic dyes for intracellular targets. Although, SOFI works at any labelling density, a sparse labelling can lead to discontinuous structures, whilst dynamic fluctuations are decreased when a high number of fluorophores label the structure of interest, producing artefacts (163). Since brightness affects image resolution, it is crucial that brighter probes are developed for SOFI, because a higher fluorescence intensity equates to a higher photon count reaching the detector, which results in a higher SNR image and an optimal SOFI image (163). Skylan-S has a higher average fluorescence intensity compared to both Dronpa and Tag-RFP, which means that, to date, it is the best RSFP for SOFI. However, to do dual-colour SOFI with RSFPs, a far-red version is highly sought after (163). In addition, since the spontaneous blinking of Qdots, in response to light irradiation, creates heterogeneities in brightness in SOFI images, fluorescent probes that have uniform or controlled blinking would be preferable for SOFI. Fluctuations required for SOFI is not restricted to changes in fluorescence intensity, using Qdots or RSFPs, as oscillations can also be achieved through other means, including rotation of plasmon metal nanoparticles (85, 90, 281). Despite several caveats with Qdot labelling, with regards to Qdot-Abs accessing only extracellular targets, Qdots are still the simplest approach to SOFI, and were therefore used throughout this thesis for testing different SOFI implementations and in the application of SOFI to different biological questions, involving ECM proteins. For nuclear targets, RSFPs (Skylan-S) and synthetic organic dyes (Alexa Fluor 647) were utilised in replacement of Qdot-Abs.

# Chapter 4: Testing different SOFI implementations

## 4.1 Comparing available SOFI implementations

Over the last decade, several super-resolution microscopy techniques have been developed, that have provided new insights into live biological systems, which would otherwise be unresolved with standard fluorescence microscopy. William E. Moerner, Eric Betzig, and Stefan Hell were awarded the Nobel Prize in Chemistry in 2014 for introducing the scientific community to super-resolution microscopy. Commercial super-resolution microscopes are expensive, and are therefore inaccessible to many biological researchers. In addition, although home-built super-resolution systems are more affordable and offer flexibility, they are not user friendly for biologists with limited expertise in optics, whose research would benefit the most from advanced imaging techniques. Additionally, super-resolution systems typically require specific fluorophores and high light exposures, which are incompatible for live cell imaging. As the demand for user friendly yet cheaper super-resolution techniques increased, alternative open-source post-processing options were developed; including SOFI. Although SOFI is a well-tested software, it is not yet widely used by biologists, perhaps because it does not have a graphical user interface (GUI) and requires some knowledge of a programming language. The performance of available implementations need to be explored and rigorously tested. In particular, two different SOFI implementations, Localizer and bSOFI, were compared on the same dataset. As well as investigating the effect acquisition settings has on the SOFI output, the accuracy of different implementations to reconstruct a SOFI image at higher-orders was also evaluated. Here, current SOFI implementations were compared against other super-resolution methods, such as SRRF and SIM, in terms of attainable resolution enhancement and image quality, using accessible quantitative approaches. Although a line profile was used as standard, to assess the resolution attainment of SOFI, other quantitative methods were tried, including FRC, jackknife re-sampling, and NanoJ-SQUIRREL.

### 4.1.1 SOFI Localizer and bSOFI

Since its introduction to the microscopy community in 2009 (85), there have been several SOFI implementations described in the literature, including the open-source tools SOFI Localizer (89) and bSOFI toolbox (93). These implementations, freely available to biologists, were compared in terms of performance and ease of use. Localizer can simultaneously provide SOFI and STORM analysis, from the same dataset, whilst bSOFI can extract additional information about the emitter's molecular brightness and blinking properties. Localizer can be run in both Igor-Pro and MATLAB, with the same SOFI-processed images attained, but for direct comparison with bSOFI, Localizer and bSOFI were both implemented in MATLAB for the following experiments. To compare SOFI Localizer and bSOFI, β-tubulin was labelled with Qdot 625 via indirect immunofluorescence with antibodies, and the same stack of 512-by-512 pixel images was SOFI-processed with each implementation. Pixel saturation is problematic for SOFI-processing, as very bright non-fluctuating Qdots in the image can mask dimmer Qdots, so are either removed completely or saturated Qdots are turned into artefacts, which can be misinterpreted as real structures (282). All data was therefore acquired within an intensity range of 0-1 gray levels, where the Qdots would not be saturated. The two SOFI implementations result in distinctly different looking SOFI-processed images. Both implementations performed well in reducing out-of-focus light and improving the SNR of the wide-field image, through the removal of uncorrelated signal, to enhance the contrast of β-tubulin (Figure 31).

However, the output from SOFI Localizer at 1016-by-1016 pixels (an increase in the number of pixels), left a checkerboard effect when zooming in on the processed image. Averaging when downsizing the SOFI-processed image to 512-by-512 pixels, and then upscaling the image back to 1016-by-1016 pixels, removed this checkboard effect, through interpolating the pixels. However, downsizing the SOFI image would also remove the resolution enhancement from smoothing the virtual pixels, so this is not a correct way to resolve the issue. The checkerboard effect is documented elsewhere and has instead been corrected for using Fourier interpolation (94). Although, an EMCCD camera has a finite pixel size, a SOFI image can achieve a resolution smaller than this by creating virtual pixels in between the physical pixels, in a process known as cross correlation (XC-SOFI) (88). However, these virtual pixels differ in brightness from the original pixels, which causes a checkerboard effect in the up-scaled SOFI image, also referred to as being pixelated or having artefacts described as being grid-like (94). The virtual pixel weights differ from the original pixels in the SOFI images,

so a distance factor can be applied to correct for this via a process referred to as flatten cumulants (88). In addition, Fourier interpolation reduces the pixel size of the raw images in a stack, before they are SOFI-processed, by re-calculating the pixel values through Fourier transform to form a finer grid (interpolates the existing pixels), which enables SOFI images to be generated that contain the same number of pixels, of the same size, as the average wide-field image (94). In this way, the information, contained within the image, is unchanged. The checkerboard effect with SOFI Localizer, is therefore, due to the pixel size in the original dataset being larger than the pixel sizes of the SOFI-processed image.

For resolution enhancement comparisons, the average wide-field image was always up-scaled, without averaging, to match the number of pixels in the SOFI image. SOFI Localizer yields a raw SOFI image, whereas the bSOFI result represents the raw SOFI image, with extra linearisation and Lucy-Richardson deconvolution steps built into the algorithm. Although bSOFI appeared to give thinner structures than the SOFI Localizer implementation, there was an element of over processing, which made the images look artificial, due to the deconvolution. The quality of bSOFI-processed and SOFI Localizer-processed images were therefore assessed using the NanoJ-SQUIRREL ImageJ plugin (Figure 31). Although the RSP value for the SOFI Localizer image was higher than the bSOFI image, there were more high error regions (potential artefacts) in the RSE map for the SOFI Localizer image compared to the bSOFI image. As a result, the mean resolution of the bSOFI image was estimated, using FRC, to be 241 nm, which is below the diffraction limit of light. The acquisition settings required to optimise the SOFI-processing, such as the number of frames, were explored using the SOFI Localizer and bSOFI implementations in MATLAB.

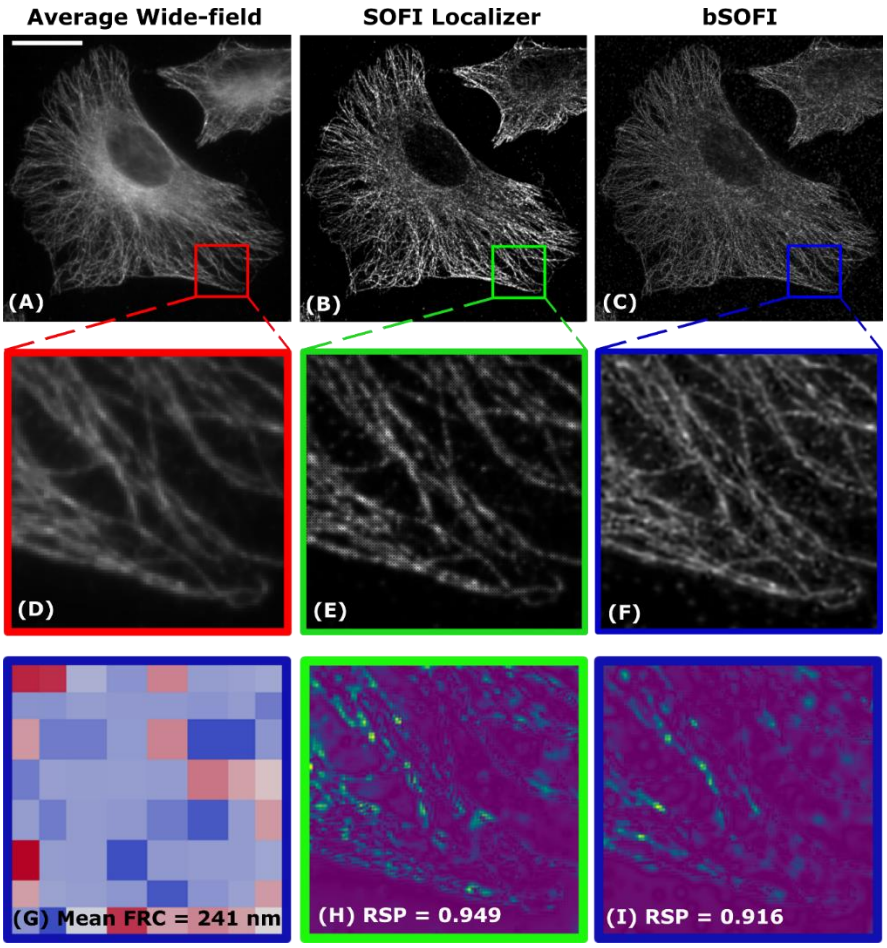


**Figure 31. Comparison of available SOFI-processing implementations.** β-tubulin was labelled with Qdot 625 via indirect immunofluorescence with antibodies and imaged on an epifluorescence microscope (63x 1.4 NA with 2.5x magnifying lens) at 33 ms. A 1,000 frame stack of wide-field images (A) was SOFI-processed with Localizer (B) and bSOFI (C). Corresponding ROIs are also shown for the average wide-field (D), SOFI Localizer (E), and bSOFI (F) images. ImageJ plugin NanoJ-SQUIRREL was used to determine the resolution and quality of β-tubulin-Qdot 625 SOFI images. FRC map (G) was created for the bSOFI image (C) with a mean resolution of 241 nm. RSE maps (H and I) for SOFI Localizer (E) and bSOFI (I) ROIs, respectively, were produced, with corresponding RSP values as an indicator of quality. Red regions in the FRC maps are low-resolution (high FRC value), whereas those in blue are of high-resolution (low FRC value). High error regions (likely artefacts) are in blue-yellow (RSP<0.95) and low error regions (unlikely artefacts) in purple (RSP>0.95). Scale bar = 20 µm.

### 4.1.2 Maximum number of frames results in better SOFI images

The number of frames required to gain optimal performance in terms of speed and accuracy of SOFI Localizer and bSOFI to create an accurate SOFI image was compared by varying the number of input frames before processing. SOFI requires considerably fewer frames to create a super-resolution image compared to dSTORM. Therefore, 1,000 frames was acquired for highly labelled fibronectin-Qdot 625, in fixed keloid cells, on an epifluorescence microscope (63x 1.4 NA plus 2.5x magnifying lens). The dataset was reduced using the Stack

Sorter option in ImageJ to create a further 3 sub-stacks consisting of 50, 100, and 500 frames. Each dataset was processed with SOFI Localizer (Figure 32) and bSOFI (Figure 33). Both SOFI Localizer and bSOFI generated a SOFI-processed image with as little as 50 input frames, but at the cost of losing some structural information. For SOFI-processing, 500-1,000 frames are required in order to capture enough details, from the blinking Qdots being in the "ON" state, to construct the entire structure. Despite bSOFI yielding much more striking SOFI images than SOFI Localizer, with a high number of frames (1,000), these images also had extra details, which were difficult to relate back to the average wide-field image. ROI J in Figures 32 and 33 shows a loop-like structure where, with SOFI Localizer it divides the structure into two, which is also somewhat visible in the blurred average wide-field ROI I; with bSOFI, this loop is a thinner single structure. Differences between fibronectin-Qdot 625 processed with SOFI Localizer and bSOFI, may be due to the extra Lucy-Richardson deconvolution step included in the bSOFI implementation. The quality and resolution of the 1,000 frame bSOFI and SOFI Localizer images was assessed using the NanoJ-SQUIRREL ImageJ plugin. Using 1,000 frames, both the bSOFI and SOFI Localizer images showed high error regions in the RSE map, even though bSOFI gave a better RSP value. Although the SOFI Localizer image gave a lower mean FRC value (168 nm), indicating better resolution compared to the bSOFI image (221 nm), the FRC map for the SOFI Localizer image is distorted, possibly due to the pixelated effect. Here a maximum of 1,000 frames was taken, it would have been interesting to process an extreme number of frames in excess of 10,000, as this should theoretically give a SOFI image with better SNR and resolution improvement. However, to improve the temporal resolution and spatial resolution of SOFI in higher-dimensional experiments, it is advantageous to use fewer frames and smaller pixel sizes, respectively. As an effective pixel size of 150-170 nm is needed for higher-order SOFI (88, 111), here a pixel size of approximately 100 nm was used (16 µm physical pixel size on the camera and 63 x 1.4 NA plus 2.5x magnifying lens), although others have reduced the pixel size to as small as 50 nm using highly blinking Qdots (98). To obtain a higher resolution improvement, even smaller pixel sizes can be achieved using a sCMOS camera as opposed to an EMCCD camera used here (26). By decreasing the FOV the acquisition and processing was also faster (32). Others have reported SOFI images using as little as 300 frames (283), with a small pixel size of 65 nm (111); but these were dependent on the choice of fluorescent probe and labelling density. It has been shown that when few frames are used to reconstruct a high labelling density SOFI image, there are many discontinuities and artefacts present in the resulting image (111).

However, it is often difficult to control the labelling density of Qdot-Abs, due to their tendency to aggregate.

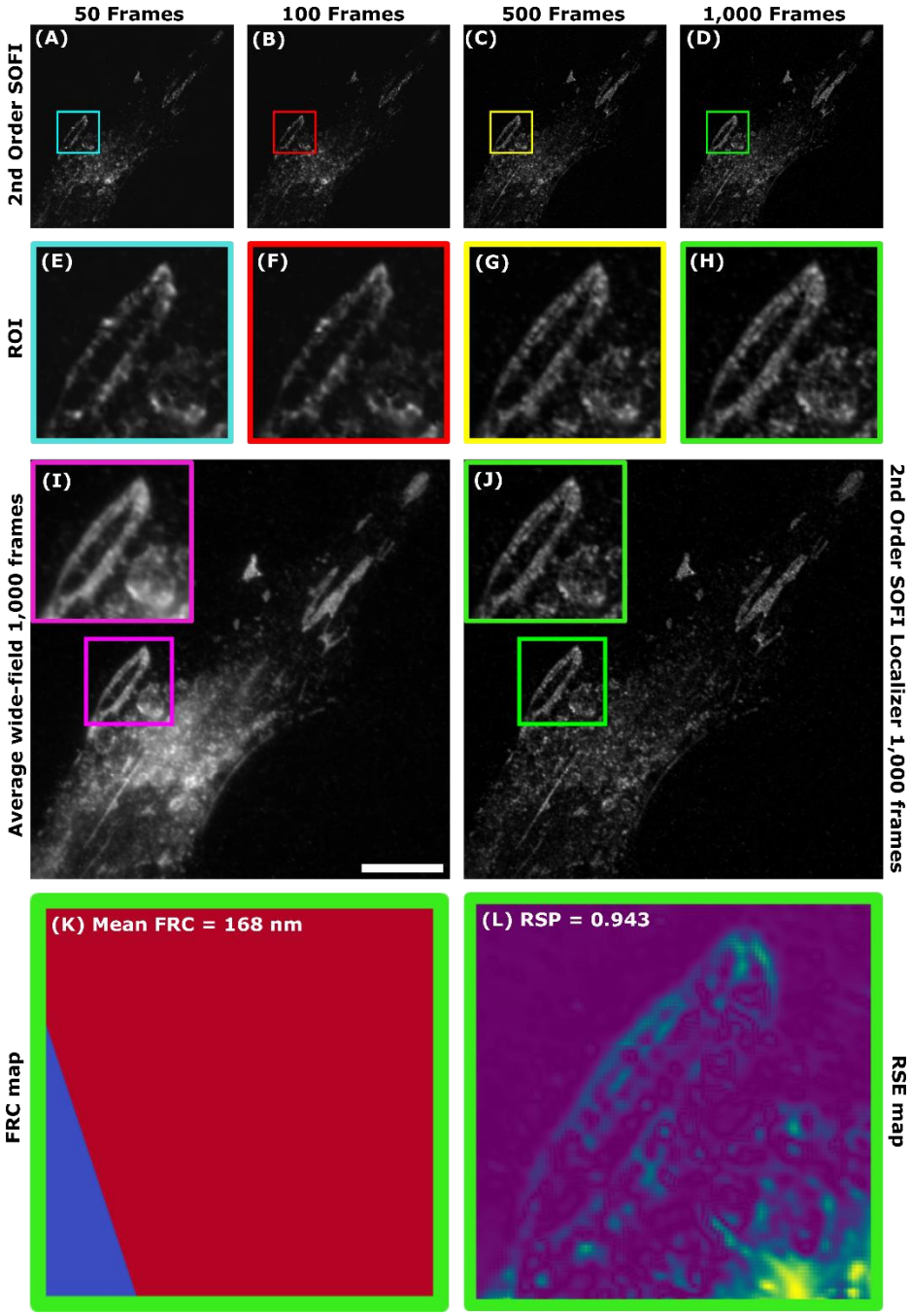


**Figure 32. Different number of frames processed with SOFI Localizer.** Fibronectin was labelled with Qdot 625 in fixed keloid cells via indirect immunofluorescence with antibodies and imaged on an epifluorescence microscope (63x 1.4 NA with 2.5x magnifying lens) at 100 ms (10 fps). The number of frames used in 2nd order SOFI-processing with Localizer in MATLAB was varied by 50 (A), 100 (B), 500 (C), and 1,000 (D) images. Corresponding ROIs are shown (E-H). An average wide-field image (I) and best 2nd order SOFI (1,000 frames) (J) image were compared. More details are present in the SOFI image that used 1,000 frames than in the SOFI image that used only 50 frames. ImageJ plugin NanoJ-SQUIRREL was therefore applied to the 2$^{nd}$ order SOFI image obtained using 1,000 frames to

determine image resolution and quality. A FRC map (K) for the 2nd order SOFI image (D) with a mean resolution of 168 nm and an RSE map (L) for ROI image H were produced. Red regions in the FRC maps are low-resolution (high FRC value), whereas those in blue are of high-resolution (low FRC value). High error regions (likely artefacts) are in blue-yellow (RSP<0.95) and low error regions (unlikely artefacts) in purple (RSP>0.95). Scale bar = 10 µm.

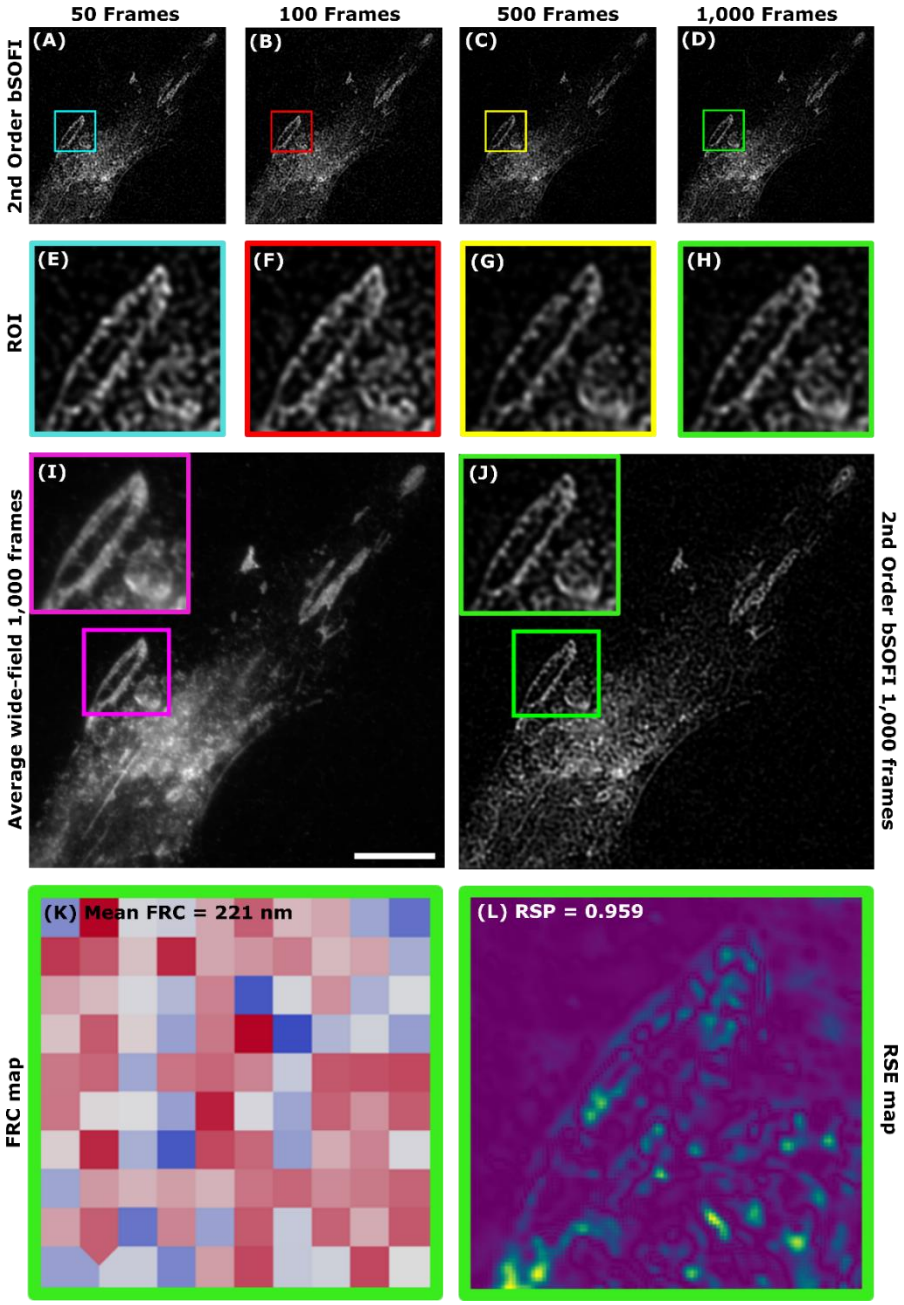


**Figure 33. Different number of frames processed with bSOFI.** Fibronectin was labelled with Qdot 625 in fixed keloid cells via indirect immunofluorescence with antibodies and imaged on an epifluorescence microscope (63x 1.4 NA with 2.5x magnifying lens) 100 ms (10 fps). The number of frames used in 2nd order bSOFI-processing in MATLAB was varied by 50 (A), 100 (B), 500 (C), and 1,000 (D) images. Corresponding ROIs are shown (E-H). An average wide-field image (I) and best 2nd order bSOFI (1,000 frames) (J) image were compared. More details are present in the bSOFI image that used 1,000 frames than in the bSOFI image that used only 50 frames. ImageJ plugin NanoJ-SQUIRREL was therefore applied to the 2nd order bSOFI image obtained using 1,000 frames to determine image

resolution and quality. A FRC map (K) for the 2nd order SOFI image (D) with a mean resolution of 221 nm and an RSE map (L) for ROI image H were produced. Red regions in the FRC maps are low-resolution (high FRC value), whereas those in blue are of high-resolution (low FRC value). High error regions (likely artefacts) are in blue-yellow (RSP<0.95) and low error regions (unlikely artefacts) in purple (RSP>0.95). Scale bar = 10 μm.

### 4.1.3 Long exposure times yield the best attainable SOFI images

The goal in super-resolution microscopy is to achieve a high-resolution image at a fast frame rate. After establishing that a higher number of frames yields a better SOFI image, the optimal exposure time was also investigated by acquiring 1,000 images of tubulin-Qdot 625 in fixed HeLa cells on an epifluorescence microscope (100x 1.4 NA plus 2.5x magnifying lens) at different exposure times: 5 ms (200 fps), 10ms (100 fps), 30 ms (33 fps), 50 ms (20 fps), and 100 ms (10 fps), with minimal transfer time onto the EMCCD camera (zero time interval). Datasets of varied exposure time were SOFI-processed with Localizer (Figure 34) and bSOFI (Figure 35). For both implementations, higher exposure times of 50-100 ms gave the best visually displayed SOFI image, with an enhanced SNR. A satisfactory SOFI image was not formed at low exposure times (<30 ms) with Localizer or bSOFI, but this is due to using a full FOV dataset. To quantify these observations, the quality and resolution of the SOFI Localizer and bSOFI images were estimated using the NanoJ-SQUIRREL ImageJ plugin. Both the SOFI Localizer and bSOFI images yielded high error regions in the RSE maps at all of the exposure times tried, but the resolution was improved at longer exposure times, giving lower mean FRC values. SOFI has the ability to achieve fast frame rates (200 fps) by cropping the ROI, but this is at the expense of losing information. Speed of acquisition is a trade-off with image quality and resolution improvement. SOFI images cannot be sufficiently reconstructed with data acquired using fast frame rates, because they do not allow the capture of as many fluorophores, which can lead to discontinuities along the structure of interest. However, on the other hand, long acquisition times can result in more artefacts, as a result of sample or label movement (26). Therefore, shorter exposure times are mostly preferable for live cell SOFI when movement can cause motion blur or in fixed cells when drift occurs. Since Qdots blink on all timescales and their blinking rate is non-uniform, longer exposure times are required to capture more fluctuations that can be correlated over time. High blinking Qdots have been developed for SOFI, to enable shorter exposure times for doing super-resolution in real-time, by synthesising Qdots with a thinner shell (98). Other fluorescent probes, with different blinking properties, may also be able to yield SOFI images with faster acquisition

times (85). Through simulations, split artefacts have been observed by others, where 100 fps typically gives improved continuity compared to 33 fps (26). Here, a reasonable frame rate of 33 fps was achieved with both SOFI Localizer and bSOFI, using 1,000 frames, to yield a satisfactory SOFI image with minimal discontinuities. However, frame rates in the order of 69 fps have been achieved previously, but using 5,000 frames (93).

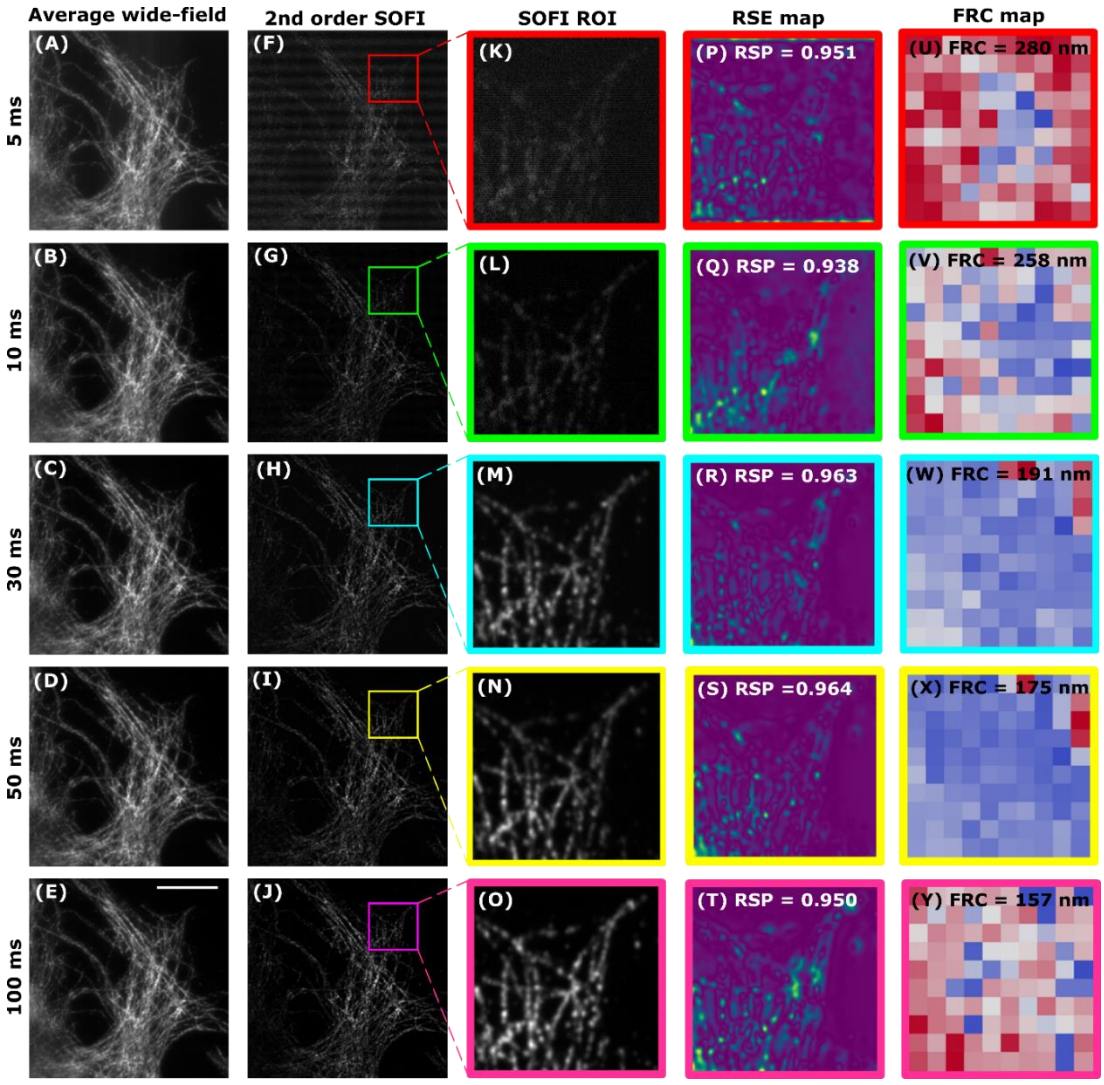


**Figure 34. Different exposure times processed with SOFI Localizer.** β-tubulin was labelled with Qdot 625 via indirect immunofluorescence with antibodies and imaged on an epifluorescence microscope (100x 1.4 NA plus 2.5x magnifying lens). A 1,000 frame stack of wide-field images was acquired at different exposure times from 5 ms to 100 ms (A-E) and SOFI-processed to 2nd order with Localizer implemented in MATLAB (F-J). Corresponding ROIs are shown for 2nd order SOFI images (K-O). ImageJ plugin NanoJ-SQUIRREL was used to assess the resolution and quality of the SOFI-processed images. RSE maps (P-T) and FRC maps (U-Y) were produced showing RSP and mean FRC values, respectively. Red regions in the FRC maps are low-resolution (high FRC value), whereas those in blue are of high-resolution (low FRC value). High error regions (likely artefacts) are in blue-yellow (RSP<0.95) and low error regions (unlikely artefacts) in purple (RSP>0.95). N=1 cell. Scale bars = 10 µm.

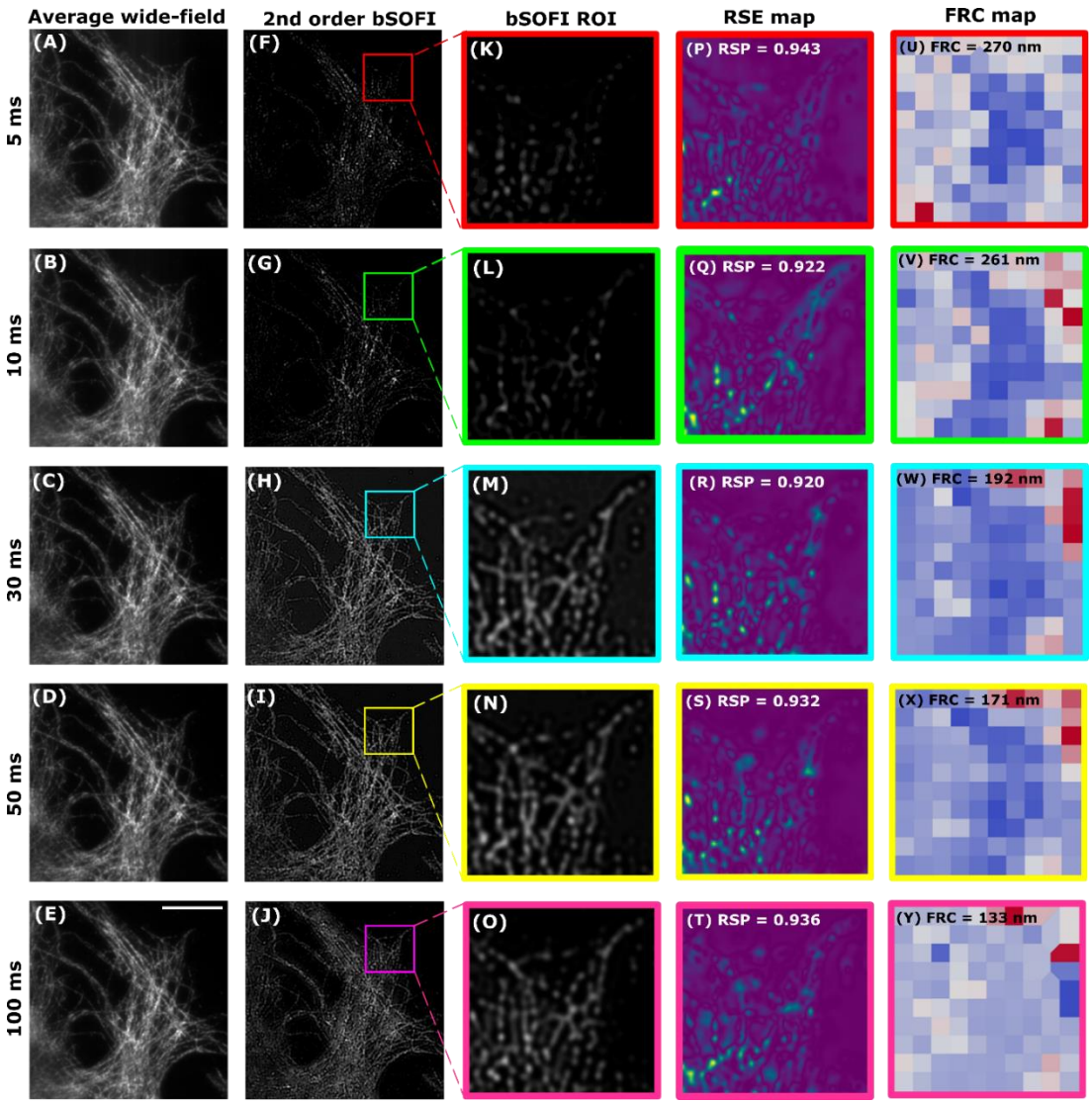


**Figure 35. Different exposure times processed with bSOFI.** β-tubulin was labelled with Qdot 625 via indirect immunofluorescence with antibodies and imaged on an epifluorescence microscope (100x 1.4 NA plus 2.5x magnifying lens). A 1,000 frame stack of wide-field images was acquired at different exposure times from 5 ms to 100 ms (A-E) and SOFI-processed to 2nd order with bSOFI implemented in MATLAB (F-J). Corresponding ROIs are shown for 2nd order bSOFI images (K-O). ImageJ plugin NanoJ-SQUIRREL was used to assess the resolution and quality of the bSOFI-processed images. RSE maps (P-T) and FRC maps (U-Y) were produced showing RSP and mean FRC values, respectively. Red regions in the FRC maps are low-resolution (high FRC value), whereas those in blue are of high-resolution (low FRC value). High error regions (likely artefacts) are in blue-yellow (RSP<0.95) and low error regions (unlikely artefacts) in purple (RSP>0.95). N=1 cell. Scale bars = 10 µm.

### 4.1.4 Large dynamic range with higher-order SOFI

To demonstrate that SOFI-processing can also enhance the resolution of biological structures, other than tubulin, analysis was extended to other proteins. As well as investigating the optimal acquisition settings required to achieve the best SOFI image, the

number of cumulant orders, obtained by processing images with Localizer and bSOFI, was also compared. Actinin four (ACTN4), an actin binding protein, was labelled with Qdot 625 via indirect immunofluorescence using antibodies and 500 frames were acquired on an epifluorescence microscope at 10 fps (63x 1.4 NA plus 2.5x magnifying lens). The 500 frame dataset was processed up to 4$^{th}$ order SOFI using Localizer and bSOFI. The NanoJ-SQUIRREL ImageJ plugin was used to assess the resolution and quality of the SOFI-processed images. At higher-orders, the resolution was lower (higher FRC values), as a result of the presence of artefacts in the images. The quality of both the SOFI Localizer and bSOFI images also decreased (more high error regions in the RSE maps). As predicted, visually, higher-order SOFI images, produced using the SOFI Localizer implementation, did not yield satisfactory SOFI images, compared to bSOFI (Figure 36), because of the large differences in brightness within the SOFI Localizer images (85). This large dynamic range is due to molecular brightness increasing exponentially according to the higher n$^{th}$ order cumulant used (280). It is important to display the result of SOFI-processing, but this can be challenging for higher-order SOFI-processed images, because they are not constraint to any particular bit-depth. For 2$^{nd}$ order SOFI images, produced using Localizer, normalising to a 16-bit range worked well, but with the higher-orders, the dynamic range of the SOFI-processed image is huge: of up to 18 orders of magnitude. A workaround, was to re-scale the higher order SOFI-processed images by taking roots of the pixel values. For instance, the cube root and 4$^{th}$ root of the pixels values in a 3$^{rd}$ order and 4$^{th}$ order SOFI image, respectively, were taken and displayed. This large dynamic range issue did not apply to the bSOFI images, because this implementation includes a linearisation step, to rectify for differences in emitter brightness (93). Despite bSOFI yielding more appealing higher-order SOFI images, with more details present than with SOFI Localizer, these structures seem artificial. Since the bSOFI implementation was introduced, local dynamic range compression SOFI (Idrc-SOFI) has been developed, which claims to reduce the presence of undesirable artefacts by calibrating higher-order SOFI images against the brightness of the 2$^{nd}$ order image (92). Visually, there appears to be some resolution improvement, but the image quality may have been degraded by using only 500 frames, typically more frames are needed to improve the appearance of higher-order SOFI images. For future experiments, quantification will be done on the original SOFI images, but for display purposes, higher-order SOFI Localizer processed images (n > 2$^{nd}$ order), the n$^{th}$ root of the real pixel values will be displayed instead.

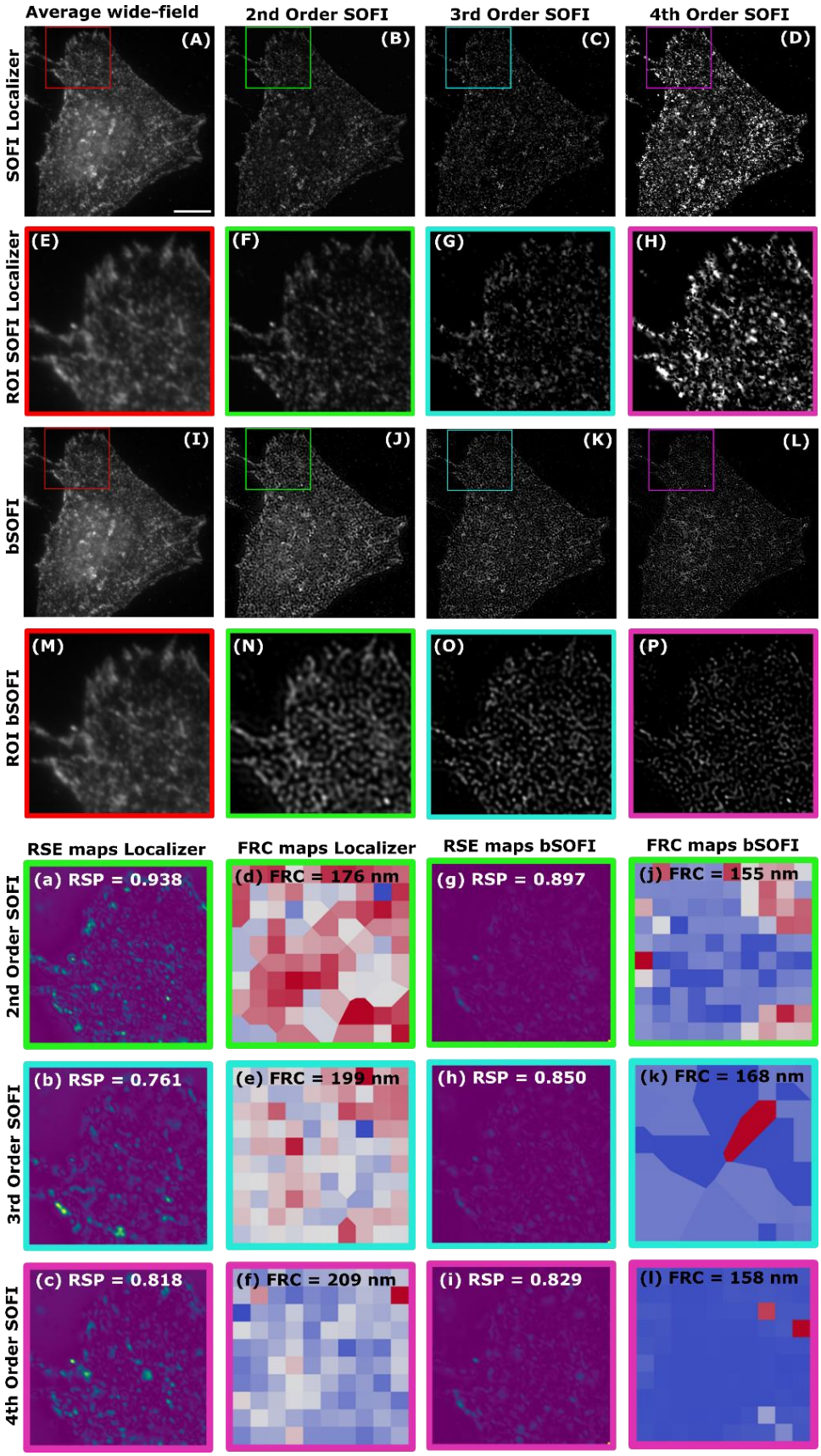


**Figure 36. ACTN4-Qdot 625 SOFI-processed with higher-orders.** ACTN4 was labelled with Qdot 625 by indirect immunofluorescence with antibodies and imaged on an epifluorescence microscope (63x 1.4 NA plus 2.5x magnifying lens) at 10 fps (100 ms exposure time). A 500 frame stack was SOFI-

processed with both SOFI Localizer and bSOFI implemented in MATLAB, to give an average wide-field image (A & I) and SOFI-processed images from 2nd order-4th order (B-D & J-L). Corresponding ROIs are shown (E-H & M-P). To adequately display 3rd and 4th order SOFI images, processed with Localizer, a cube root and 4th root was applied to the images, respectively. Artefacts appear at higher-orders (H), as more frames are needed. ImageJ plugin NanoJ-SQUIRREL was used to assess image resolution and quality of Localizer and bSOFI. RSE maps (a-c and g-i) for SOFI ROIs (F-H and N-P) and FRC maps (d-f and j-l) for SOFI images (B-D and J-L) were produced. RSP and mean FRC values are shown. Red regions in the FRC maps are low-resolution (high FRC value), whereas those in blue are of high-resolution (low FRC value). High error regions (likely artefacts) are in blue-yellow (RSP<0.95) and low error regions (unlikely artefacts) in purple (RSP>0.95). N=1 cell. Scale bar = 10 µm.

### 4.1.5 Dual-colour SOFI image with SOFI Localizer and bSOFI

Although, a one channel SOFI-processed image already reveals structural details, which would otherwise be unresolved with wide-field microscopy, additional information about protein-protein interactions could also be obtained by labelling multiple proteins in the same image. Significant co-localisation information is masked with conventional wide-field microscopy, which is why super-resolution microscopy is needed to resolve the spatial relationship between proteins of interest (112). Conventional wide-field microscopy can create false positive co-localisation in the sense that two proteins may initially appear to overlap, until they are resolved to be completely separated with super-resolution microscopy. However, co-localisation studies using super-resolution microscopy is challenging, because of the complex photoswitching required for the acquisition of different coloured fluorophores in techniques such as dSTORM. Here, a two-colour SOFI image has been achieved by labelling ACTN4 with red Qdot 625 and β-tubulin with green Qdot 525 via indirect immunofluorescence with primary and secondary antibodies. A 1,000 frame stack of ACTN4-Qdot 625 and β-tubulin-Qdot 525 was sequentially acquired on an epifluorescence microscope (100x 1.4 NA plus a 2.5x magnifying lens) at 10 fps and post-processed independently with SOFI Localizer and bSOFI (Figure 37). The JACoP ImageJ plugin (248) was used to perform quantitative co-localisation analysis on ACTN4-Qdot 625 and β-tubulin-Qdot 525 (Table 8). Co-localisation analysis of a dual-colour SOFI image has been achieved previously, through calculating Pearson's correlation, which describes the linear relationship between images and Manders coefficients that measures the fraction of overlap between a pixel in one colour channel and a pixel in a different colour channel (112). Here, a Pearson's correlation coefficient value of 0.399 was obtained for the average wide-field image, which was higher than 0.074 and 0.095 for the SOFI Localizer and bSOFI images, respectively. This decrease in Pearson's correlation coefficient (values closer to 0 rather than 1) may be as a

result of the much improved spatial resolution between ACTN4 and β-tubulin in the SOFI images. Additionally, the Manders coefficient value of 0.67 for the average wide-field image, was also much higher than 0.272 and 0.192 for Localizer SOFI and bSOFI, respectively. The Pearson's correlation and Manders coefficient values in both the average wide-field and SOFI-processed images was low, possibly denoting negligible co-localisation between ACTN4 and β-tubulin. However, the low Pearson's coefficient values for the SOFI-processed images may be incorrect, because some Qdots may have been removed in both the green and red imaging channels during the SOFI-processing (refer to section 3.2.1 Quantum dot characterisation), so this will skew the co-localisation. Since Pearson's correlation and Manders coefficients are sensitive to noise in the image, SOFI-processing may, in some cases, increase the Pearson's correlation coefficient in super-resolved images, due to its increased SNR, if two proteins do co-localise (112).

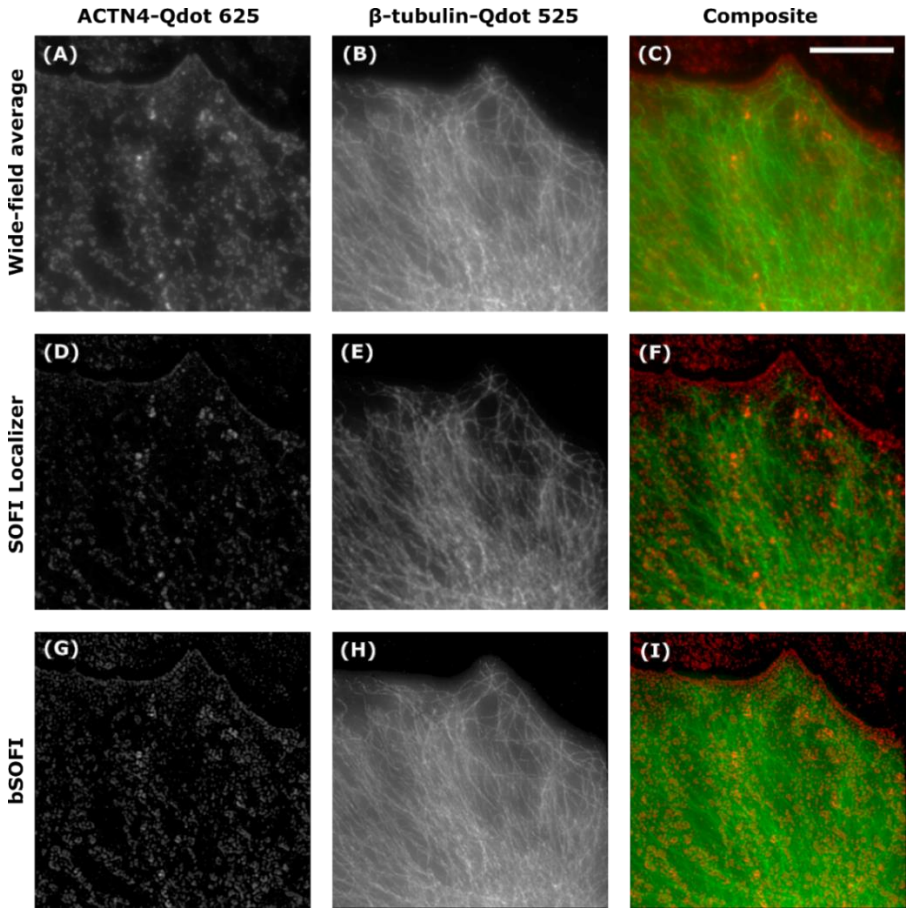


**Figure 37. Two-colour SOFI-processing with different implementations.** ACTN4 was labelled red with Qdot 625 (A) and β-tubulin labelled green with Qdot 525 (B) using indirect immunofluorescence. A 1,000 frame stack of consecutive wide-field images was taken on an epifluorescence microscope (100x 1.4 NA plus a 2.5x magnifying lens) at 10 fps (100 ms exposure time) to create an average composite

image (C). Second order SOFI-processing with Localizer (D&E) and bSOFI (G&H), implemented in MATLAB, were used to create two-colour SOFI images F and I, respectively. Scale bar = 10 µm.

| | Average wide-field | SOFI Localizer | bSOFI |
|---|---|---|---|
| **Pearson's Coefficient** | 0.399 | 0.074 | 0.095 |
| **Manders Coefficient** (Fraction of β-tubulin-Qdot 525 overlapping ACTN4-Qdot 625) | 0.67 | 0.272 | 0.192 |

**Table 8. Co-localisation between two-colour wide-field and SOFI-processed images.** Co-localisation between ACTN4-Qdot 625 and β-tubulin-Qdot 625 in two-colour wide-field and SOFI-processed images was analysed quantitatively using the JACoP plugin in ImageJ. Higher Pearson's and Manders coefficients were obtained for wide-field than SOFI.

## 4.2 Assessing image quality and resolution of SOFI images

Assessing the quality of super-resolution images by eye is prone to human bias, which is why quantitative tools are needed. So far the resolution enhancement of SOFI-processed images was determined by measuring the FWHM of the structures of interest, by drawing a line profile through a single emitter in ImageJ. Although, a decrease in FWHM may indicate resolution enhancement of a SOFI-processed image, these measured structures may in fact be artefacts from over-processing, creating artificial narrowing of structures. Despite fitting intensity line profiles with a Gaussian function and calculating FWHM (width of the PSF) being a good estimation of image resolution for conventional microscopy (beads are considered point sources, being smaller than the FWHM of the PSF), FWHM is inaccurate for super-resolution microscopy as the FWHM of the PSF of the optical system is often smaller than the object being imaged, so this is a flawed representation of image resolution, but instead can be interpreted as the size of a feature in the image (284). Resolution is also often overestimated using the FWHM metric, because of human bias in selecting the narrowest structure in the image (285). Ways to quantitatively assess the quality of SIM images have existed for a couple of years (58), including the open-source ImageJ plugin SIMcheck (59). To date, few have addressed quantitative ways to assess the quality of SOFI-processed images, but those that do exist are discussed here.

### 4.2.1 Using FWHM as a measure of resolution for SOFI images

The most common way to estimate the degree of resolution enhancement in SOFI-processed images is by drawing line profiles through structures of interest and measuring their FWHM. Considering almost all SOFI publications demonstrated resolution enhancement using microtubules (85, 93, 111, 97), it was appropriate to include β-tubulin as a known standard when comparing the output from Localizer and bSOFI. For SOFI-processing, β-tubulin was labelled with Qdot 625 by indirect immunofluorescence with antibodies and Qdot fluctuations captured over 1,000 frames on an epifluorescence microscope (100x 1.4NA), at 100 fps, with the addition of different magnifying lenses: 0 (under-sampled), 1.6x (meets Nyquist sampling), and 2.5x (over-sampled). The theoretical resolution (R=0.61λ/NA) was calculated for β-tubulin labelled with Qdot 625 and imaged on an epifluorescence microscope (100x 1.4NA) to be 272 nm. It was decided to use the oversampled experimental dataset (100x 1.4NA plus 2.5x magnifying lens) to measure the resolution improvement achieved with both the SOFI Localizer and bSOFI. A ROI from the 2.5x magnifying lens images was taken for the average wide-field, Localizer SOFI, and bSOFI images. To determine resolution enhancement in the SOFI-processed images, a line profile was drawn through a single point emitter (Qdot 625), in the average wide-field, SOFI Localizer, and bSOFI images, and normalised intensity profiles plotted for each image. A one-component Gaussian was fitted to the intensity profiles in MATLAB and the standard deviation (σ) of the data was used to calculate the FWHM = $2\sqrt{2ln2}$ ∗σ ≈ 2.355*σ (7). It is apparent from the intensity profiles that SOFI-processing has resulted in better resolution, as the width of the Gaussian profile (FWHM) decreased as the point emitter was resolved with SOFI (Figure 38). The FWHM in the average wide-field image (FWHM = 293 nm) reduced by 23% with SOFI Localizer (FWHM = 227 nm), and 28% with bSOFI (FWHM = 212 nm). The discrepancy between the experimental resolution for the wide-field image (FWHM of 293 nm) and theoretical resolution (Airy disk diameter of 272 nm), is due to noise in the experimental setup (112). Since the resolution limit of an optical wide-field microscope is approximately 250 nm, it was expected that the FWHM of SOFI-processed images would be lower than this value. Although, the FWHM of the SOFI-processed images was lower than the average wide-field image, both were still much greater than 250 nm. Single microtubules, predicted to be around 22 nm in diameter (93), are not resolved here with SOFI, but this is not surprising, as these bundles of fibres were labelled with bulky Qdot-Abs, which are physically larger than 22 nm (150). When a Qdot-Ab is imaged only the Qdot will fluoresce, so its FWHM will remain

small, because a single Qdot is the physical size of an emitter. However, the overall size of a Qdot-Ab is large, because a Qdot needs to be coated with ligands prior to antibody conjugation, so due to steric hindrance, the Qdot-Ab will be further away from the target structure than smaller Alexa Fluor dye-Ab conjugates that do not need additional layers to be water soluble. Despite the relatively poor resolution enhancement, due to uncorrelated signals being excluded from the images during SOFI-processing, the out-of-focus light in both the Localizer and bSOFI images was removed, which resulted in an increased SNR and single Qdots being more evident than in the average wide-field images. However, the dot-like nature of sparse Qdots, discontinuously labelling β-tubulin, made it visually challenging to detect resolution by eye. Although, high labelling density can alleviate the issue of discontinuous structures, this approach can lead to artefacts, because some overlapping Qdots may, by chance, blink simultaneously or have long "ON" times, so an excessive number of frames is required (111). Discontinuous labelling of structures with Qdots has also been restored recently, by combining together multiple SOFI images, where the same structure has been simultaneously labelled with different coloured Qdots and spectrally separated (111).

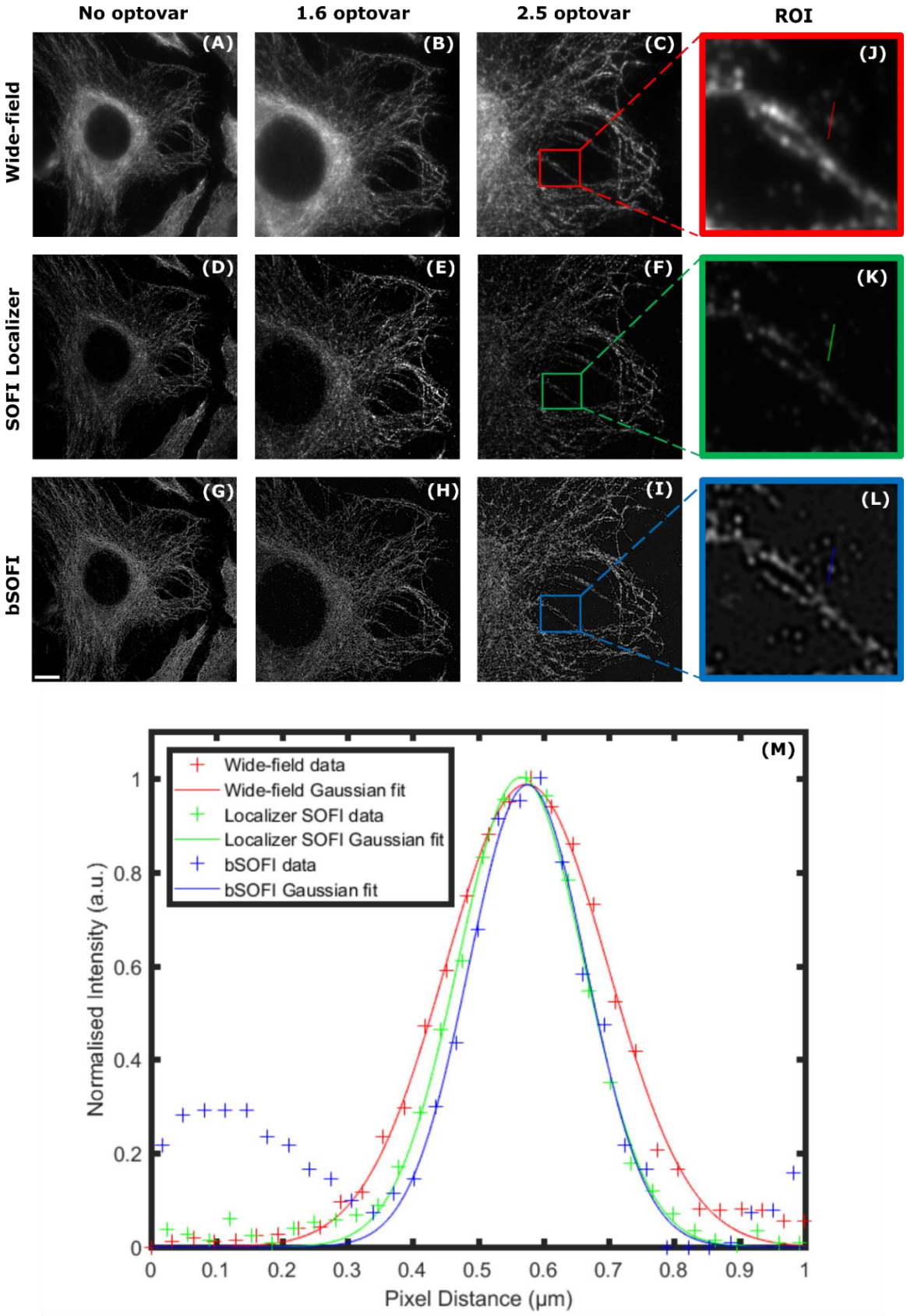


**Figure 38. Determining the resolution of SOFI images using line profiles.** β-tubulin was labelled with Qdot 625 using indirect immunofluorescence and fluctuations captured on an epifluorescence microscope (100x 1.4NA) at 100 fps (10 ms exposure time) with different magnifying lenses: 0 (A), 1.6x (B), and 2.5x (C). A 1,000 frame stack was SOFI-processed with Localizer (D-F) and bSOFI (G-I). An ROI

from the 2.5x magnifying images (C-I) was taken for the wide-field (J), Localizer SOFI (K), and bSOFI (L) images. To determine resolution enhancement in the SOFI-processed images, a line profile was drawn through a single point emitter (Qdot 625), in the wide-field, SOFI Localizer, and bSOFI images (J-L), and normalised intensity profiles plotted (M). The width of the Gaussian profile (FWHM) decreased as the point emitter was resolved with SOFI. Resolution improved in the wide-field images (FWHM = 293 nm) by 23% with SOFI Localizer (FWHM = 227 nm), and 28% with bSOFI (FWHM = 212 nm). Scale bar = 10 μm.

To check the performance of the SOFI Localizer implementation at resolving high-density labelled β-tubulin fibres, β-tubulin was labelled with Qdots-Abs, but at a higher density. Images were taken over 1,000 frames at 10 fps, for SOFI-processing. Two β-tubulin fibres were unresolved in the average wide-field image, but were resolved in the SOFI-processed image (Figure 39). A line profile, drawn through the two β-tubulin fibres, gave a single peak for the average wide-field image, but for the SOFI-processed image, there was two peaks. The FWHM of the average wide-field was also measured, by drawing a line profile through a single Qdot. The width of the Gaussian peak for a single Qdot 625 was narrower for the $2^{nd}$ order SOFI image than the average wide-field image. For the average wide-field image, the FWHM was calculated as 315 nm and the FWHM of the $2^{nd}$ order SOFI-processed image was 238 nm (24 % FWHM decrease). As discussed earlier (section 4.2 Assessing image quality and resolution of SOFI images), using FWHM as a measure of resolution in an image (Figure 39J) is flawed, because SOFI-processing can cause artificial narrowing of structures. A better indication of resolution enhancement in a SOFI image is to identify two unresolved structures become separated (Figure 39I), as outlined by Rayleigh. Other publications have reported a √n (where n is the number of SOFI orders) resolution enhancement for SOFI-processed images (85), so for a $2^{nd}$ order SOFI-processed image, a √2 (factor of 1.41) resolution improvement was expected. Compared to published literature, here, the resolution of a $2^{nd}$ order SOFI Localizer processed image improved by a factor of 1.32 (~√2), which is comparable to a previous finding (85). However, further adaptations to SOFI implementations, have resulted in a two-fold resolution enhancement for a $2^{nd}$ order SOFI-processed image (88). Here β-tubulin was measured to be 238 nm in the SOFI-processed image, but it has been reported to be as small as 169 nm when SOFI-processed by others (109). Differences in lateral sampling frequency can affect the spatial resolution, as a pixel size of 64 nm was used here, but smaller pixel sizes of 50 nm have been achieved by others (98). The discrepancy between the size of β-tubulin, may be due to the use of large Qdot-Abs to label β-tubulin here, compared to smaller Alexa Fluor 647 being used in other published studies (109). Probe

choice for optimum SOFI resolution is important and therefore, the use of nanobodies would be the preferred option.

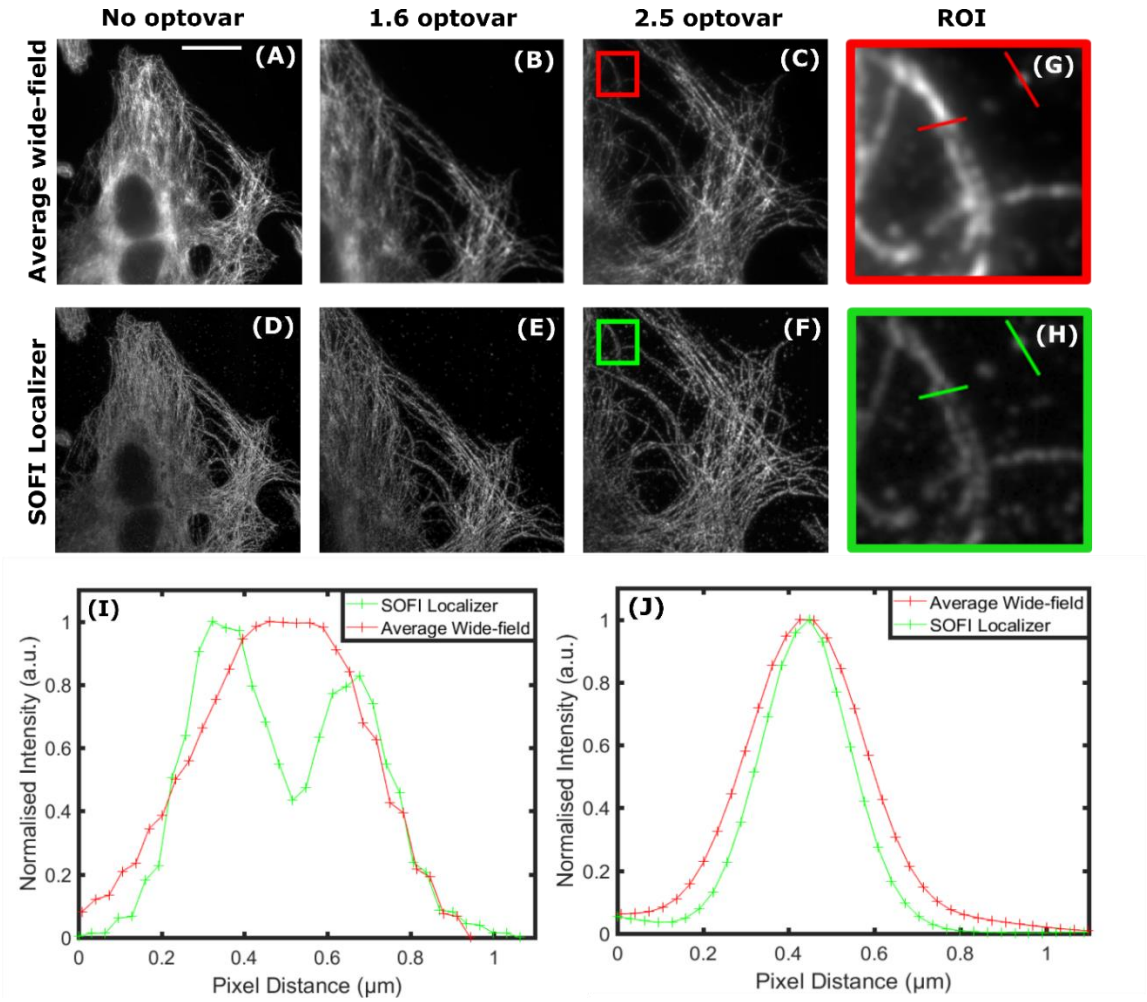


**Figure 39. Resolution enhancement with SOFI Localizer.** Wide-field images of β-tubulin (A-C), labelled with Qdots via indirect immunofluorescence, were imaged on an epifluorescence microscope (100x 1.4NA) with the addition of different magnifying lenses (0, 1.6x, and 2.5x). Wide-field images (A-C) were SOFI-processed to 2nd order with Localizer (D-F) and ROIs taken (G&H). A Line profile was drawn through a microtubule bundle of two β-tubulin fibres in ImageJ and normalised pixel intensities plotted for the average wide-field and SOFI-processed images (I). SOFI had resolved the two β-tubulin fibres, as shown by two peaks. A line profile was also drawn through a single Qdot in the images and a one-component Gaussian curve fitted to the plotted data. The width of the curve decreased for the 2nd order SOFI-processed image. FWHM of the average wide-field is 315 nm and the FWHM of the 2nd order SOFI-processed image is 238 nm (24 % FWHM decrease). Scale bar = 20 µm.

Labelling issues aside, it is hoped that by using higher than 2nd order SOFI will decrease the FWHM further, as with 5th order bSOFI, a width in the order of 78 nm has been reported for microtubules (93). To test the resolution of up to 4th order bSOFI here, collagen III was labelled with Qdot 625 and acquired images SOFI-processed with bSOFI implemented in

MATLAB. As the $n^{th}$ order decreases the PSF by at least √n, higher-order cumulants are expected to yield SOFI images of much improved resolution, compared to $2^{nd}$ order SOFI. However, these higher-order cumulants are at the expense of longer processing times, as the calculations are computationally more demanding (90). Here, a 1,000 frame stack of images was acquired on an epifluorescence microscope (63x 1.4NA plus 2.5x magnifying lens to satisfy Nyquist sampling), at 100 fps. A ROI was selected in the calibrated image and a line scan drawn through a collagen III-Qdot 625 fibre in ImageJ. Line profiles were plotted for the average wide-field, bSOFI $2^{nd}$ order, bSOFI $3^{rd}$ order, and bSOFI $4^{th}$ order images. A one component Gaussian was fitted to the data in MATLAB and the FWHM calculated using the σ value of the fit. For display purposes, smooth curves were achieved for the line profile comparisons through bilinear interpolation of the pixels in the images, but calculations were done on the raw data.

Resolution improvement with bSOFI, compared to wide-field microscopy, was evident by the decrease in the width of the line profiles, as the bSOFI orders increased. The spatial resolution of collagen III-Qdot 625 in the wide-field images (FWHM = 405 nm) improved by 8 % with $2^{nd}$ order bSOFI (FWHM = 374 nm), 28 % with $3^{rd}$ order bSOFI (292 nm), and 47 % with $4^{th}$ order bSOFI (216 nm) (Figure 40). With increasing $n^{th}$ order, there appeared to be thinner structures and details present that were not visible in the average wide-field image. Despite the assumption that infinite higher orders can yield unlimited resolution, the images start to gain more artefacts, as the number of orders increase. Although, some out-of-focus light has been removed, there was also signal amplification of structures in the background, which appear to be severe artefacts of the processing algorithm. Collagen is an abundant protein, so the SOFI algorithm may be unable to discern between weak diffuse signal and uncorrelated signal in the collagen III sample, which is why more background details appear. The resolution improvement of collagen III-Qdot 625 for $2^{nd}$ order bSOFI was much lower than previously achieved for β-tubulin-Qdot 625 (Figure 38), which may be due to the effective pixel size being smaller for the raw data of tubulin-Qdot 625 (~64 nm) than for collagen III-Qdot 625 (~100 nm). Resolution enhancement is also sample dependent and is determined by a number of factors, including the choice of probe. Overall, although the resolution improvement with Localizer was not much better than bSOFI, the increase in detail does appear to be greater with bSOFI compared to Localizer, which may be due to the fact that bSOFI includes a Lucy-Richardson deconvolution step as standard. For collagen III-Qdot 625 up to $4^{th}$ order SOFI-processing was easily attainable with bSOFI, but higher than $2^{nd}$ order SOFI could not be adequately displayed with Localizer. A total of 500-1,000 frames

was used here to achieve a reasonable SOFI-processed image, but many more images may be required to achieve an improved higher-order SOFI image, because the SNR decreases as the order increases (123). However, it must be taken into consideration that the computational time taken to SOFI process the stacks of images increases exponentially with bSOFI order.

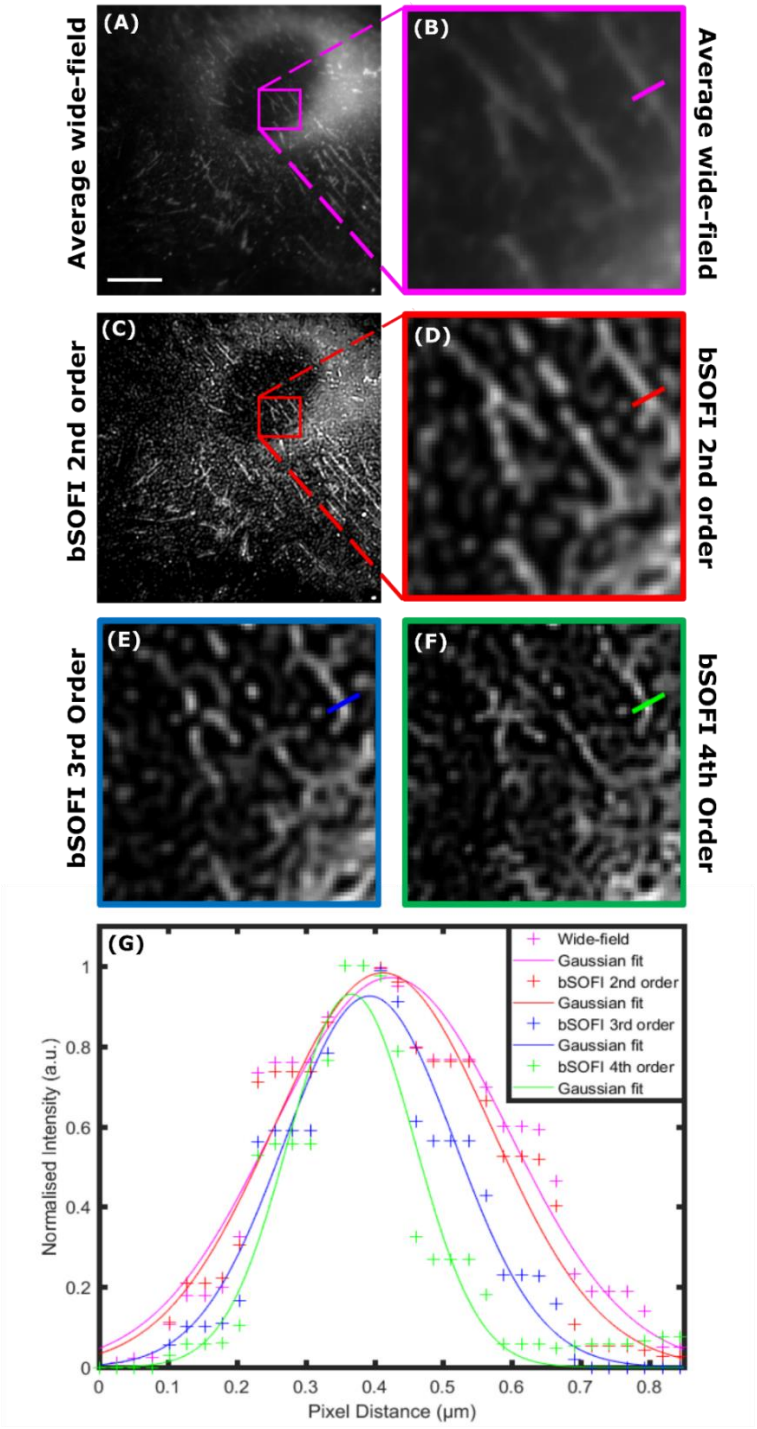


**Figure 40. Collagen III-Qdot 625 resolved with higher-order bSOFI.** Collagen III was labelled with Qdot 625 by indirect immunofluorescence and fluctuations imaged over consecutive frames with an

epifluorescence microscope (63x 1.4NA plus a 2.5x magnifying lens) at 10 ms exposure time. Wide-field images were SOFI-processed with bSOFI, implemented in MATLAB, at high orders. ROIs were selected in calibrated average wide-field (A) and bSOFI processed (C) images. Line scans were subsequently drawn through a collagen III-Qdot 625 fibre in the average wide-field (B), 2$^{nd}$ order bSOFI (D), 3$^{rd}$ order bSOFI (E), and 4$^{th}$ order bSOFI (F) ROI. Plotted line profiles (G) were fitted with a one component Gaussian function and FWHM values calculated, as a measure of resolution enhancement. Collagen III structures were more discerned at higher-bSOFI orders and the FWHM decreased as the bSOFI order increased. Scale bar = 10 µm.

### 4.2.2 Computing spatial resolution of SOFI images using Fourier ring correlation

Taking line scans through a structure of interest is subjective and prone to human bias. Due to the inhomogeneity of images, containing pixel intensity variance, the measured resolution differs depending on where the line is drawn, and can overestimate the resolution improvement, so other means to measure the resolution enhancement are highly sought after. Alternatively, FRC can be used to determine the spatial resolution of super-resolution images (81, 92, 285). Since the attainable resolution enhancement of most super-resolution techniques is demonstrated on filamentous structures, FRC was calculated here on 2D SOFI-processed images of β-tubulin-Qdot 625. β-tubulin was labelled with red Qdot 625 in fixed HeLa cells, by indirect immunofluorescence, and imaged on an epifluorescence microscope (100x 1.4 NA plus 2.5x magnifying lens) at 10 ms. The spatial resolution of SOFI images was computed using FIRE, a BIOP ImageJ plugin, by splitting a wide-field dataset (1,000 frames) into two independent even and odd number sub-stacks (of 500 frames each), which were individually SOFI-processed to 2$^{nd}$ order with bSOFI and Localizer. To measure the spatial resolution of wide-field images, cross-correlation between structures in the first wide-field image and second consecutive wide-field image of a 1,000 frame stack were computed and compared. Images of the same FOV were Fourier transformed to the frequency domain and a resolution cut-off threshold frequency was set at a fixed value of 1/7 ≈ 0.143. Here, the FRC compared the similarity of spatial frequencies from two independently reconstructed 2D images, however, Fourier shell correlation (FSC) can be applied to 3D images (286). Spatial frequency (µm$^{-1}$) versus normalised FRC plots were compared for the wide-field, bSOFI, and SOFI Localizer images. The FRC curve is noisy, which is why a LOESS curve fitting was applied to the FRC data and smooth FRC curves added to the plots. The spatial resolution value is the inverse of the spatial frequency value (1/spatial frequency), where the smoothed FRC curve first crosses the threshold cut-off value of 0.143. Using FRC as a measure of resolution enhancement, the spatial resolution of the wide-field image was 278 nm, whereas the 2$^{nd}$ order bSOFI and SOFI Localizer images were 163 nm and 160 nm, respectively (Figure 41). A

calculated FRC value of 278 nm seems appropriate, if the theoretical resolution of structures, labelled with a 625 nm fluorescent probe and imaged on an epifluorescence microscope (100x 1.4 NA plus 2.5x magnifying lens), is 272 nm. Both bSOFI and Localizer gave SOFI-processed images of a similar spatial resolution, which was much lower than that of the wide-field image. Despite, the improved resolution of 160 nm for the SOFI-processed image of β-tubulin, this is still much higher than the estimated size of a microtubule being 22 nm in diameter (93), which is not surprising since in practice SOFI is not capable of reaching 22 nm resolution. The spatial resolution values quoted here are of a mean of the entire FOV of the image, however it is worth noting that when FRC was calculated for different ROIs, the spatial resolution differed. Due to spatial resolution of features being heterogeneous across an image, variations in labelling density, use of blinking Qdots, or drift, can all affect the FRC (81). Drift has been reported to yield a higher FRC value than drift corrected data (82). Compared to FWHM analysis, performed on the same raw dataset of β-tubulin-Qdot 625 (Figure 38), the FRC metric estimation of resolution attainment for SOFI Localizer (160 nm) was lower than FWHM analysis (227 nm), perhaps due to the line being drawn through a large Qdot, overestimating the resolution.

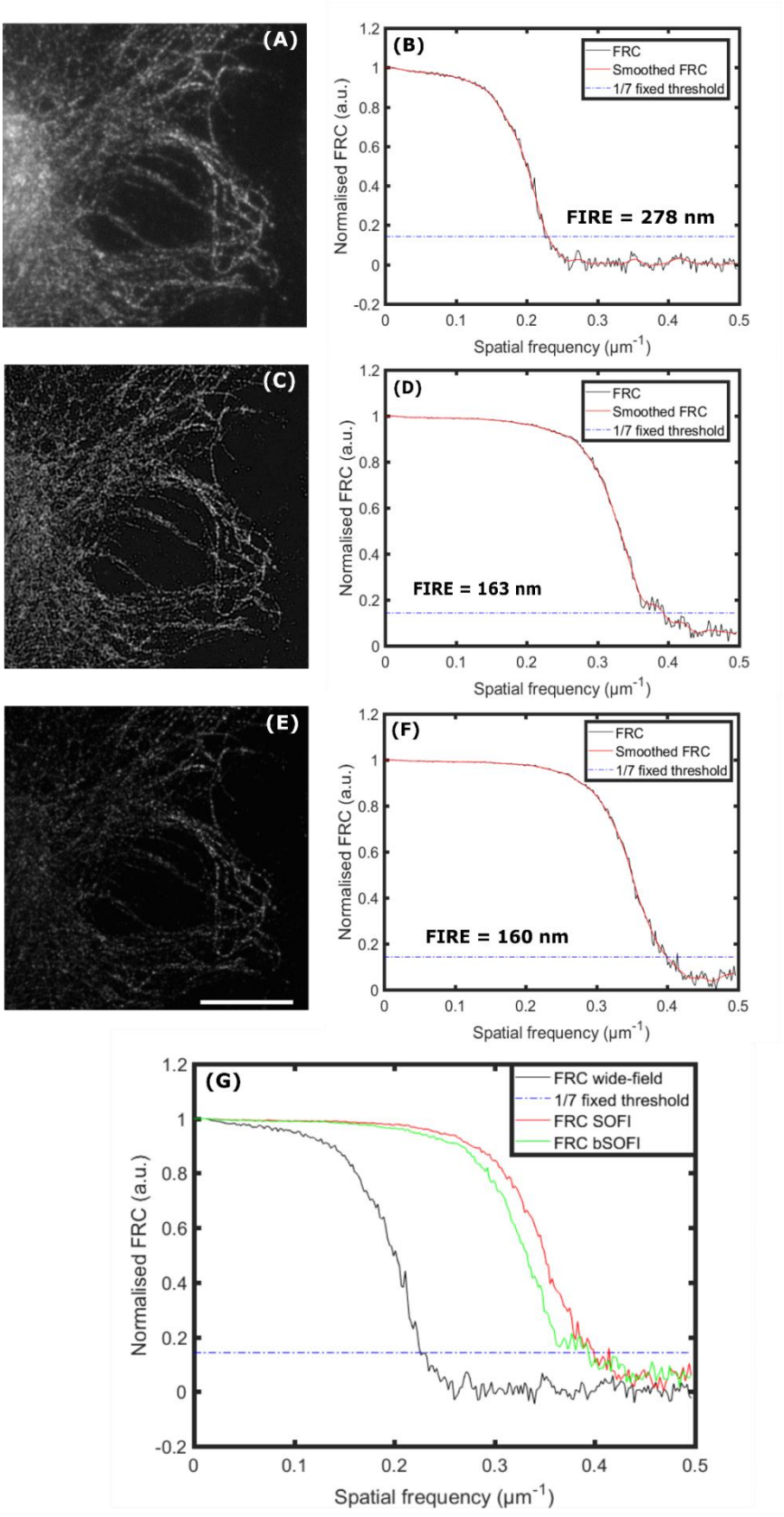


**Figure 41. Computing spatial resolution of wide-field and SOFI-processed images using FRC.** β-tubulin was labelled with Qdot 625 in fixed HeLa cells, by indirect immunofluorescence, and imaged

on an epifluorescence microscope (100x 1.4 NA plus 2.5x magnifying lens) at 10 fps. Correlation between structures in the first wide-field image (A) and second consecutive wide-field image of a 1,000 frame stack were computed, giving a spatial resolution of 278 nm (B). The wide-field stack of 1,000 frames was split equally into odd and even number of frames, with each 500 frame sub-stack SOFI-processed to second order with bSOFI (C), giving a spatial resolution of 163 nm (D), and Localizer (E), giving a spatial resolution of 160 nm (F). A fixed threshold of 1/7 ≈ 0.143 was used as shown by the blue dotted line on the plots. Comparison of FRC curves (G) shows a shift to the right in SOFI-processed images, of better resolution. Scale bar = 10 µm.

### 4.2.3 SNR estimation using delete-1 jackknife re-sampling

Whilst important, resolution improvement (determined for example using FRC) is not the only parameter to consider to evaluate post-processing super-resolution approaches. The quality of the images must also be considered as post-processing can generate artefacts. Initially, the quality of a SOFI image was assessed by comparing the same dataset post-processed with SOFI against another super-resolution technique, such as STORM (123, 120, 287). However, due to cost and lack of expertise, it is not always possible to access multiple super-resolution systems. Alternative computational approaches have therefore been developed, including an algorithm by the Dedecker laboratory (KU Leuven, Belgium), which estimates the SNR of a SOFI image, as an indicator of image quality. The SNR for each pixel in the image is estimated and the degree of variance, otherwise referred to as uncertainty, is calculated (123). SNR (measured here in decibels, dB) is defined as being the ratio between the signal of a SOFI pixel, S, and the variance associated with that SOFI signal, Var(S): $\frac{S}{\sqrt{Var(S)}}$. A high SNR refers to signal containing useful information, such as fluctuations that can be correlated and contribute to the SOFI image (useful SOFI signal), whereas background signal, such as noise, does not contain fluctuations that can be correlated, and is therefore of low SNR. Instead of continuously repeating the SOFI measurement several times, to estimate the SNR uncertainty, which would differ each time, due to photobleaching or movement (123), a statistical approach, based on the previously reported delete-1 jackknife re-sampling was used (288).

Delete-1 jackknife re-sampling implementation involves obtaining a stack of N fluorescent images and systematically deleting one unique frame at a time, to create a number of datasets, which vary by just one frame (N-1). These newly formed datasets are then post-processed, yielding several different SOFI-processed images. The similarity of these SOFI images are compared by estimating the degree of variance in SNR between pixels in the SOFI

image (123). This SNR analysis is unbiased, because it does not estimate the accuracy, only the precision in the measurement, as experimental noise is not taken into consideration (123). The jackknife calculation is high-throughput, as it can be completed within minutes, since it is only run on randomly selected, non-background, pixels within a 5-by-5 pixel ROI in the SOFI image. Not only can jackknife re-sampling assess the quality of SOFI images, but it can also enhance the SNR of SOFI images by 40-90%, using fewer images. SNR in the SOFI images is dependent on the distance between pixels, for instance, the SNR becomes progressively lower as the distance between the pixels increases. Therefore, the quality of a SOFI image can be improved by using different combinations of virtual pixels, based on the highest weight assigned to those pixels to give the best SNR. A SOFI image, obtained in the Localizer implementation, uses the closest pixel combinations, because these pixels generally yield the highest SNR and therefore, are given a high weight, to indicate a better quality SOFI image. According to this statistical re-sampling approach, SOFI images of high SNR, are considered to be good quality, whilst those of low SNR are considered to be of poor quality (123).

This statistical re-sampling approach has been successfully used by others to assess the quality of SOFI-processed images, through estimating the SNR of each pixel (116, 289). Here, a prototype Evaluate SOFI tool, developed by Wim Vandenberg of the Dedecker laboratory (KU Leuven, Belgium), was implemented in Igor Pro 7.08.1 64-Bit (WaveMetrics) to assess the SNR of the same SOFI-processed image of sparsely labelled β-tubulin-Qdot 625 (100x 1.4 NA plus a 2.5x magnifying lens) that was used previously for the FRC calculation (Figure 41). Spatial correlation is the similarity of signals between pixels (over space), so spatial de-correlation is the reduction in cross-correlation of signals between pixels. Spatial de-correlation was evaluated, for the 2$^{nd}$ order SOFI-processed image, where the amount of uncorrelated signal in relation to distance between pixels was plotted (Figure 42). A SOFI image formed using close pixel combinations (small pixel distance) yielded a high SOFI signal, whereas pixels that were further apart (bigger pixel distance), gave a negligble SOFI signal. A histogram of the number of pixels (counts) in the 2$^{nd}$ order SOFI-processed image was plotted against their estimated SNR, with the width of the histogram representing the signal in the SOFI image (Figure 43). The first peak, represents the background signal (low SNR) and the second peak is the 2$^{nd}$ order SOFI-processed signal (high SNR).

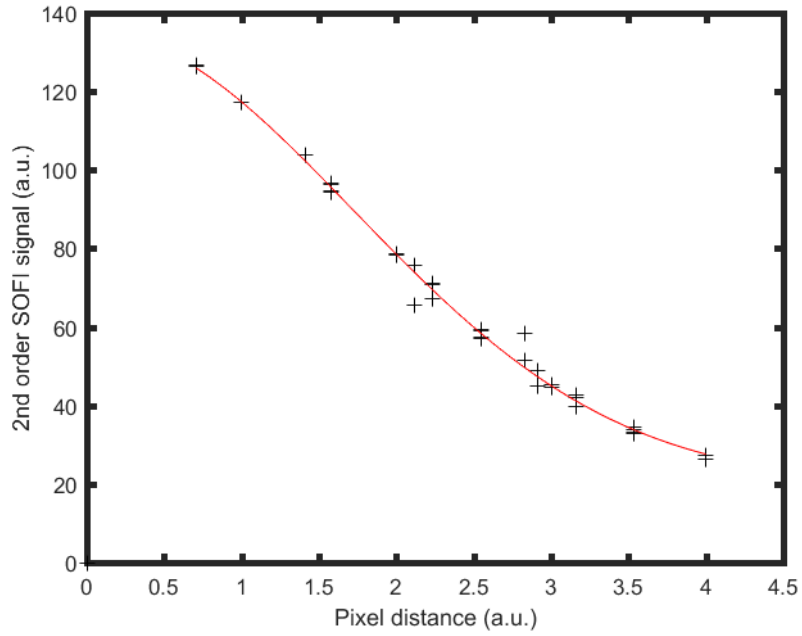


**Figure 42. Spatial de-correlation plot of the amount of uncorrelated signal.** Spatial de-correlation was evaluated for the 2nd order SOFI image of β-tubulin-Qdot 625, where the amount of uncorrelated signal in relation to distance between pixels was plotted. A SOFI image formed using close pixel combinations (small pixel distance) yielded a high SOFI signal, whereas pixels that were further apart (bigger pixel distance), gave a negligible SOFI signal.

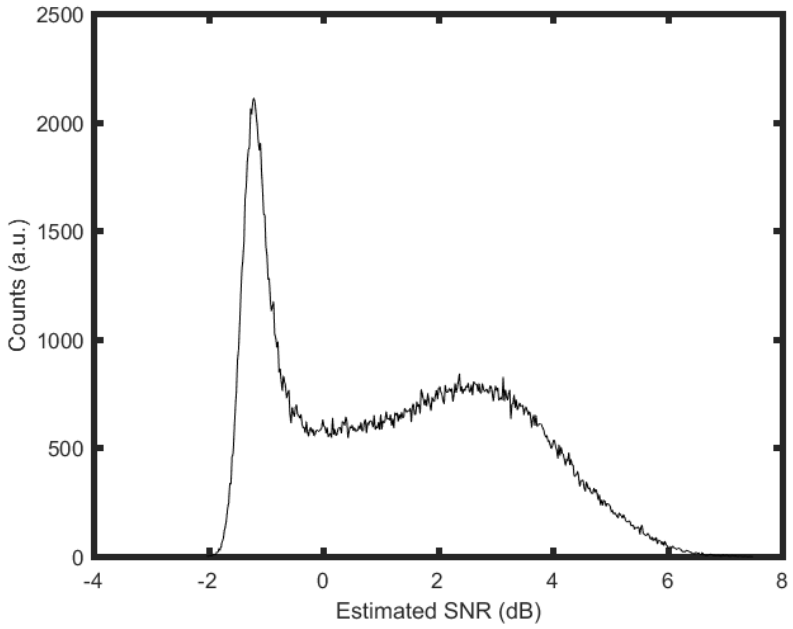


**Figure 43. Histogram of SNR in SOFI images.** Number of pixels (counts) was plotted against the estimated SNR in the SOFI image, with the width of the histogram representing the signal in the SOFI image. The first peak is the background signal (low SNR) and the second peak is the SOFI signal (high SNR).

### 4.2.4 Using NanoJ-SQUIRREL to determine image quality and resolution

An ImageJ plugin NanoJ-SQUIRREL has recently been developed as a tool to determine image quality and resolution enhancement of super-resolution images, including SRRF and SOFI (79). Similar to SOFI, SRRF does not require any sophisticated optics, as it can be performed on Nyquist or better sampled images acquired on any system, including wide-field (74), confocal (76), and TIRF (77), although the NanoJ-SRRF algorithm gives the best resolution with wide-field data (78), empirically TIRF-SRRF > confocal-SRRF > wide-field-SRRF from a SNR perspective. Multi-colour SRRF is not only achievable simultaneously, but also by sequentially acquiring different channels (290). SRRF can resolve living structures as small as 150 nm, which is comparable to SIM, but without the expense of adding a grating to the optical system (74). However, resolution improvement with SRRF is only in xy and not z, although optical sectioning can be done, to extract information, by taking z-stacks (291). Overlapping fluorophores are problematic for dSTORM, which is why sparse labelling is preferred, through the acquisition of subsets of single fluorophores, however this is not an issue for SOFI and SRRF, because there is no need to localise single fluorophores (292). In retrospect, an advantage of SRRF over SOFI is that it can be performed in live cells with conventional fluorescent proteins, such as GFP, whereas SOFI requires photoswitching of fluorophores. From experience, the processing time for SOFI is less than that of SRRF, possibly due to the complexity of the radiality calculation in addition to temporal analysis, but NanoJ-SRRF and NanoJ-SQUIRREL utilise the computer's GPU, which does help to reduce the computational time compared to using the CPU.

#### 4.2.4.1 Applying NanoJ-SQUIRREL to SOFI and NanoJ-SRRF data

NanoJ-SRRF is freely available as an easy-to-use ImageJ plugin, making it very accessible to biologists. SRRF works on similar mathematical principles as SOFI, except it analyses the fluorescence intensity fluctuations over a number of consecutive images, radially as well as temporally, with analysis based on a radiality field (75). SRRF works on the assumption that the background of a microscope image has less local symmetry than the fluorophores that have been convolved with the PSF of the optical system (74). SRRF divides pixels in a conventional image into sub-pixels, with a non-binary value assigned through calculating probabilities of whether a fluorophore is present (289). For each sub-pixel in the image, a radiality measurement (the amount by which the intensity of a fluorescent molecule in one

sub-pixel converges towards a neighbouring sub-pixel, within a given circular radius) is calculated, to create an intermediate radiality stack, which is Fourier-transformed (74). The radiality measurement asks how symmetrical the fluorescent intensity is within a set circular ROI, around each sub-pixel, with the highest radiality being in the sub-pixel closest to the centre of a fluorescent molecule and the lowest being in the sub-pixel furthest away from the centre of a fluorescent molecule. Temporal analysis, similar to the calculation of higher-order cumulants for SOFI, is then performed on the radial transform stack to yield a SRRF image. A SRRF image is essentially a probability map, so quantitative fluorescence intensity information cannot be extracted out of it, but this is an issue with all post-processing methods, including SOFI. Despite this, information about the quality of the image and its resolution can be determined using NanoJ-SQUIRREL.

NanoJ-SQUIRREL requires the input of a super-resolution image and corresponding wide-field image, referred to as a reference image, of the same sized FOV. An advantage of this analytical approach is that it does not require any additional information about the labelling density or fluorophore properties (79). A Resolution Scaling Function (RSF) is calculated to convolve the super-resolution image, so that the degree of similarity between the convolved super-resolution image and the wide-field image can be compared. Any pixel-wise variation between these images may indicate the presence of artefacts. Regions of dissimilarity are highlighted as errors in a LUT colour map, referred to as an RSE map. The purple regions in the RSE map represent areas of low error, so there is strong similarity between the super-resolution image and the wide-field image, referred to as a reference image. In contrast, blue-yellow regions in the RSE map represent areas of high error, such as artefacts, as there is some dissimilarity between the super-resolution image and the wide-field image. The super-resolution image can be from any method that overcomes the diffraction limit of light, whilst the reference image is usually an image obtained on a wide-field, confocal, or TIRF system. As well as a RSE error map, an RSP value, which does not depend on fluorescence intensities in the image, but is rather a measure of correlation between the super-resolution image and the reference image, is also given. A RSP value of 1 describes a perfect correlation, whereas 0 is poor correlation, where >0.95 indicates a high degree of correlation between the two images.

As well as producing a RSE map, a spatial map of FRC values for the super-resolution image can also be produced, which estimates the spatial resolution of the image. A raw stack of images is split equally into two sub-stacks: one containing the even number of frames and the other stack with all of the odd numbers of frames. Each sub-stack is post-processed and

concatenated to form a stack of two super-resolution images, which is input into the NanoJ-SQUIRREL FRC to produce an FRC map. Red areas on the map show regions in the image that are of low-resolution (high FRC values) and blue areas on the map show regions in the image that are of high-resolution (low FRC values). Using FRC, SRRF images have been shown to achieve approximately 70 nm resolution (289). In areas where the super-resolution image and the reference image do not share sufficient correlations, the blocks are combined to calculate FRC, as shown by less square-like shapes.

Acquisition parameters such as exposure time, number of frames, and illumination power can all affect RSP and FRC values of the resulting super-resolution image. To firstly test the performance of the ImageJ plugin NanoJ-SQUIRREL, the resolution and image quality of the same raw dataset used in the FRC calculation previously (Figure 41), was assessed with NanoJ-SQUIRREL, using default settings. Using temporal radiality average, the ring radius was set to 0.5, magnification 5, and axes in ring 6. As expected, the resolution and image quality in the 2$^{nd}$ order SOFI-processed image of β-tubulin-Qdot 625 was not completely homogenous, because there were some regions in the RSE map displaying low errors in purple and some areas of high error, likely to be artefacts, in blue-yellow (Figure 44D). Here, almost all of the structures are highlighted as being high error, except for the background, which means that the quality of the image is poor, perhaps as a result of the high blinking of Qdots being on the wrong timescale for SOFI-processing. An FRC map was also produced, with areas of low-resolution (red), but mainly high-resolution (blue). Using FRC computed in the NanoJ-SQUIRREL ImageJ plugin, the mean spatial resolution of β-tubulin (Figure 44E) was 162 nm (minimum = 137 nm, maximum = 218 nm). This mean resolution estimate was similar to that obtained using FIRE (160 nm), which estimated the resolution to be 160 nm, using the same fixed threshold of 1/7.

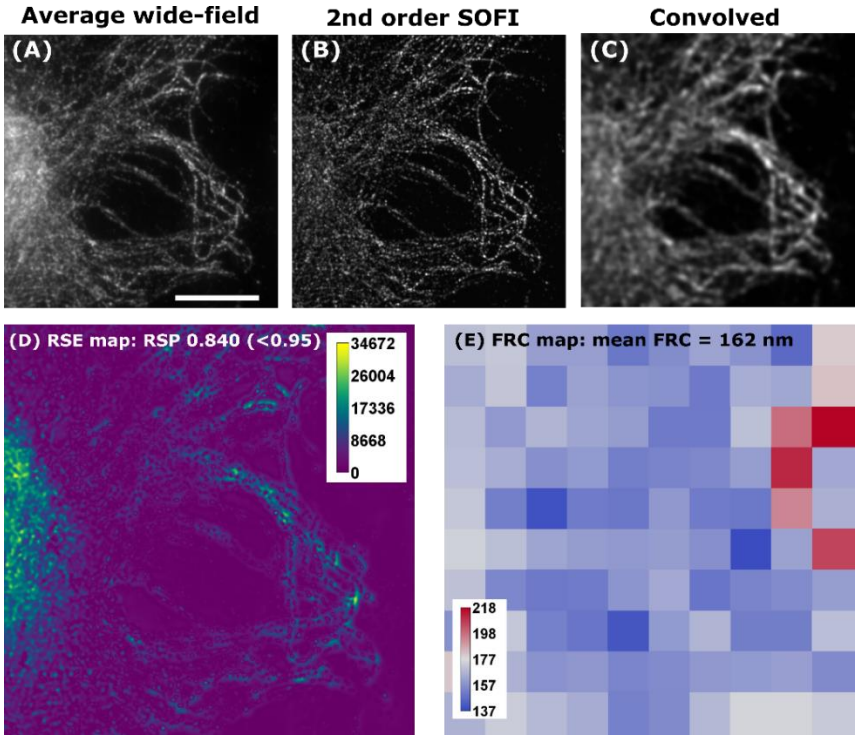


**Figure 44. Quality and resolution of a 2nd order SOFI-processed image with NanoJ-SQUIRREL.** A stack of 1,000 wide-field images of β-tubulin-Qdot 625 was SOFI-processed up to 2nd order with Localizer. The resulting SOFI-processed image (B) was convolved (C) and compared against the average wide-field image (A) using the open-source ImageJ plugin NanoJ-SQUIRREL. A RSE map was produced highlighting similar, low error regions in purple and regions of potential artefacts in blue-yellow (D). An RSP value < 0.95 indicated errors in the SOFI processing. The resolution of the SOFI-processed image was also determined using a FRC implementation in NanoJ-SQUIRREL. The wide-field image stack was split into odd and even frames, SOFI-processed separately, and re-combined to form a two-image SOFI stack, which was used for the FRC calculation to produce a FRC map (E). Red regions in the FRC map are low-resolution, whereas those in blue are of high-resolution. The mean resolution in the image was determined to be 162 nm. Scale bar = 10 µm.

Qdot labelled β-tubulin did not yield a high quality SOFI image (Figure 44). Since SRRF can be performed with conventional dyes, β-tubulin was labelled here with Alexa Fluor 488 for SRRF-processing. Most demonstrations of optical resolution enhancement and image quality are done on filamentous structures with defined lines, however, not many are done on nuclear proteins. Therefore, validation of SRRF-processing on nuclear proteins was also done here with nucleolin, in parallel to β-tubulin samples. To firstly establish the magnification needed to obtain high quality SRRF images, nucleolin was labelled with Alexa Fluor 488 in fixed HeLa cells and data acquired at 100x 1.4NA with and without the addition of a 2.5x magnifying lens (Figure 45). A mercury arc lamp was used to acquire the wide-field data, but a gentler approach would have been to use low-cost LED illumination. Each stack was SRRF-processed using the ImageJ plugin NanoJ-SRRF, with default settings (temporal analysis: temporal radiality analysis – TRA, ring radius: 0.5, magnification radiality: 5, and axes in ring:

6) and the resulting SRRF images were processed in NanoJ-SQUIRREL to check their quality and resolution. Undersampled nucleolin-Alexa Fluor 488 (100x 1.4NA, no magnifying lens), according to Nyquist sampling, gave a poor quality SRRF image (RSP value of 0.902), whilst oversampled data (100x 1.4NA plus a 2.5x magnifying lens) yielded a high quality SRRF image (RSP value of 0.990). The RSE map for the undersampled data showed more high error (blue-yellow) regions than the over-sampled data. Despite the RSP value for the oversampled data being high (>0.95), it is not visually apparent that the image is of high quality, because the RSP value is a mean value for the entire image, whereas the corresponding RSE map shows both low and high-error regions. Inhomogeneities in resolution was also present in both SRRF-processed images, as indicated by the high (blue) and low (red) resolution areas in the FRC maps. The lower quality image (100x 1.4NA, no magnifying lens) yielded an improved mean resolution of 155 nm (minimum = 66 nm, maximum = 411 nm), compared to the high quality SRRF image (100x 1.4NA plus 2.5x magnifying lens), which gave a mean FRC value of 196 nm (minimum = 118 nm, maximum 278 nm). When the resolution is high, the quality of the image is typically poor, so a compromise must be met between achieving the best possible resolution, without over-processing and creating artificially thin structures that may not depict the real structure. It was clear that to achieve a high quality SRRF image (calculated RSP value > 0.95), Nyquist sampling must be satisfied, and so the highest possible magnification should be used. Therefore, all subsequent SRRF-processing was done on images acquired with a 100x 1.4 NA oil immersion objective, with the addition of a 2.5x magnifying lens.

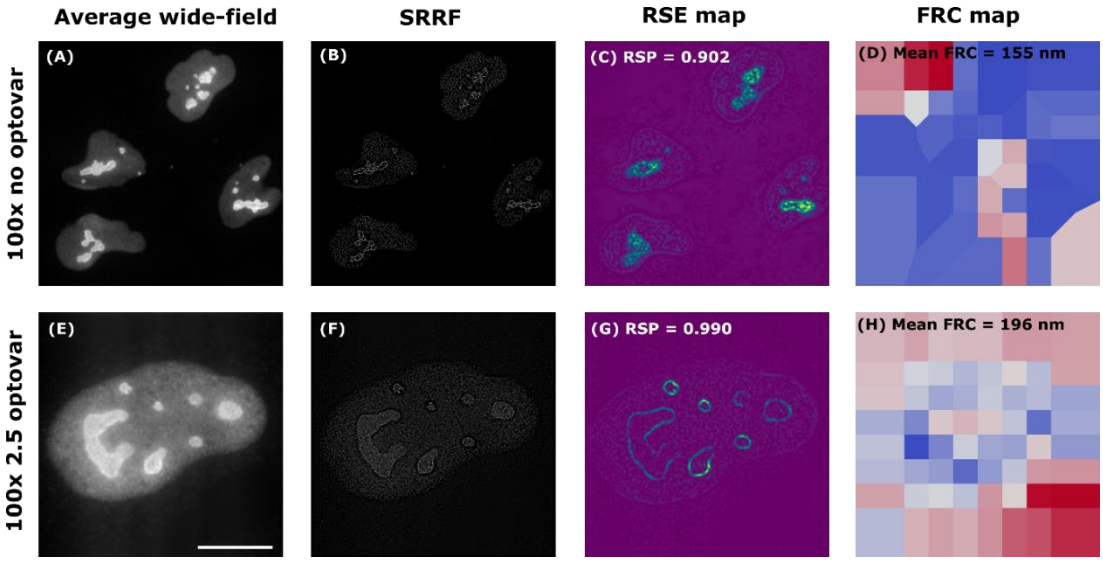


**Figure 45. Nyquist sampling must be met to yield a high quality SRRF image.** Nucleolin was labelled with Alexa Fluor 488 by indirect immunofluorescence and imaged on an epifluorescence microscope (100x 1.4NA). Wide-field images without a 2.5x magnifying lens (A) were acquired (1,000 frames) at

100 ms, whilst those images taken with a 2.5x magnifying lens (E) were acquired at 5 ms. Each stack was post-processed with NanoJ-SRRF in ImageJ and the SRRF images (B and F) assessed with the ImageJ plugin NanoJ-SQUIRREL. RSE maps (C and G) show high error regions in blue-yellow (RSP<0.95) and low error regions in purple (RSP>0.95). Under-sampled (100x 1.4NA no magnifying lens) nucleolin-Alexa Fluor 488 yielded a poor quality SRRF image, whilst oversampled (100x 1.4NA plus 2.5x magnifying lens) data yielded a high quality SRRF image. Inhomogeneity of SRRF images is shown in the FRC maps (D and H), where there are areas of high (blue = low FRC value) and low (red = high FRC value) resolution. A high quality SRRF image, gave a lower resolution than a low quality image. Scale bar = 10 μm.

To improve temporal resolution, fewer frames can be acquired, but this is often at the expense of a lower spatial resolution in the resulting image. The number of frames required to achieve a high quality SRRF image was assessed by firstly acquiring a 1,000 frame stack of β-tubulin-Alexa Fluor 488 and nucleolin-Alexa Fluor 488 on an epifluorescence microscope (100x 1.4NA plus 2.5x magnifying lens) and then reducing the same dataset using the Stack Sorter option in ImageJ to create a further 3 sub-stacks consisting of 50, 100, and 500 consecutive frames. Each dataset, of 50-1,000 wide-field images, was post-processed with the NanoJ-SRRF ImageJ plugin. Default NanoJ-SRRF parameter settings (temporal analysis: temporal radiality analysis – TRA, ring radius: 0.5, magnification radiality: 5, and axes in ring: 6) were used, as these typically yield a satisfactory SRRF image, so the only independent variable was the number of frames. For both the β-tubulin-Alexa Fluor 488 (Figure 46) and nucleolin-Alexa Fluor 488 (Figure 47) samples, the quality and resolution improved as the number of frames increased. As low as 50-100 frames was sufficient for SRRF-processing, so in all subsequent SRRF-processing, 100 frames was used.

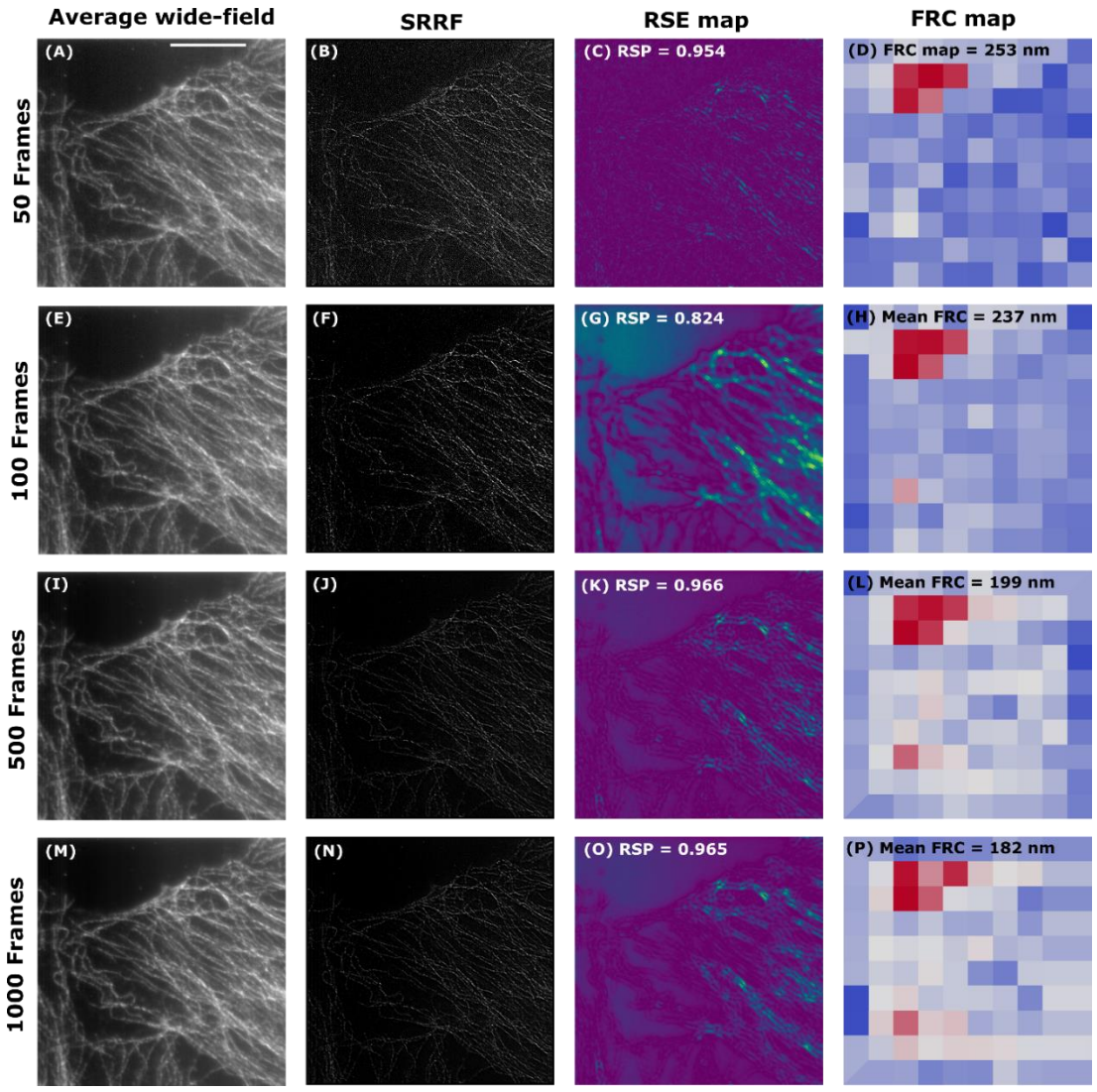


**Figure 46. More frames yield a higher quality and better SRRF-resolved image of β-tubulin.** Wide-field images containing different number of frames: 50 frames (A), 100 frames (E), 500 frames (I), and 1,000 frames (M), were SRRF-processed with NanoJ-SRRF ImageJ (B, F, J, and N). The quality and resolution of each SRRF-processed image was assessed using NanoJ-SQUIRREL ImageJ plugin. RSE maps (C, G, K, and O) showing high error regions in blue-yellow and low error regions in purple. A high RSP value > 0.95 is considered as a good quality SRRF image. FRC maps (D, H, L, and P) were also produced, with low-resolution regions in red. Increasing the number of frames, improves the quality ad resolution of the SRRF-processed image. Scale bar = 10 µm.

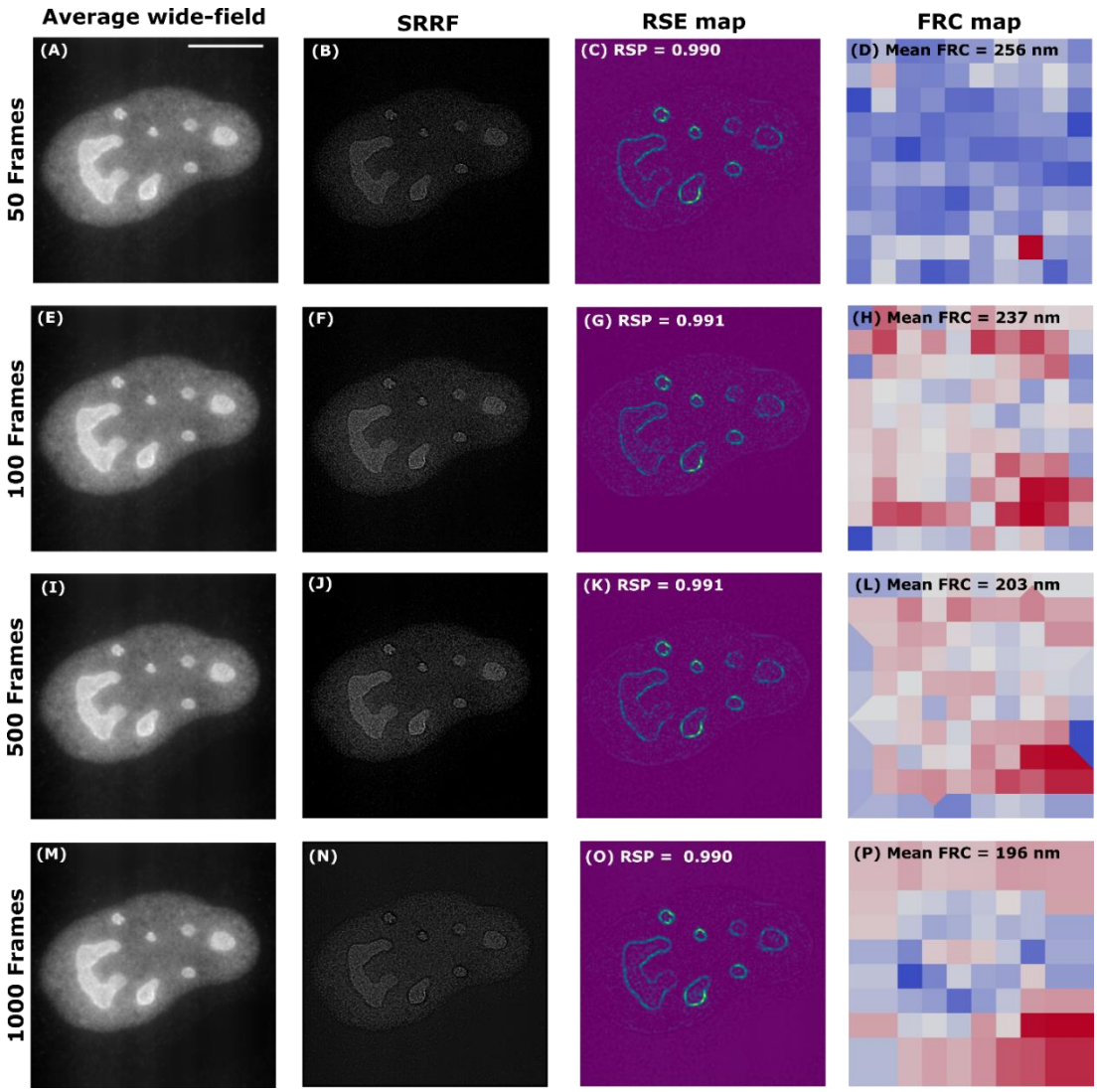


**Figure 47. More frames yield a better NanoJ-SRRF image of nucleolin.** Wide-field images of nucleolin-Alexa Fluor 488 (100x 1.4NA plus 2.5x magnifying lens), containing different number of frames: 50 frames (A), 100 frames (E), 500 frames (I), and 1,000 frames (M), were SRRF-processed with NanoJ-SRRF ImageJ (B, F, J, and N). The quality and resolution of each SRRF-processed image was assessed using NanoJ-SQUIRREL ImageJ plugin. RSE maps (C, G, K, and O) showing high error regions in blue-yellow and low error regions in purple. A high RSP value > 0.95 is considered as a good quality SRRF image. FRC maps (D, H, L, and P) were also produced, with low-resolution regions in red. A higher number of frames, yields better resolution and quality SRRF image. For 50-1,000 frames, an RSP value >0.95 was obtained. Scale bar = 10 µm.

Nucleolin and β-tubulin were both labelled with Alexa Fluor 488 by indirect immunofluorescence in separate cell samples and imaged on an epifluorescence microscope (100x 1.4 NA plus 2.5x magnifying lens), equipped with a white-light mercury arc lamp and EMCCD camera. To determine the optimal acquisition rate for obtaining a quality SRRF-processed image of β-tubulin-Alexa Fluor 488 and nucleolin-Alexa Fluor 488, wide-field images, acquired at different exposure times 5 ms (200 fps), 10 ms (100 fps), 50 ms (20 fps), and 100 ms (10 fps), were SRRF-processed and the resulting images compared for quality

and resolution with the open-source ImageJ plugin NanoJ-SQUIRREL. Lower exposure times gave the best quality SRRF images (RSP value >0.95 is a good SRRF image), although there were still areas of high error as shown by the blue-yellow regions on the RSE map (Figure 48 and Figure 49). Despite, the mean FRC value decreasing as the exposure time increased, there was regions in the image that were of high-resolution (blue), but also low-resolution (red), as indicated by the FRC maps. Resolution in the SRRF images is therefore not homogenous, as shown by the variable FRC values (Table 9). SRRF images that gave the best resolution, did not necessarily have the highest RSP value, and were not of high quality. This observation was also reported elsewhere (78).

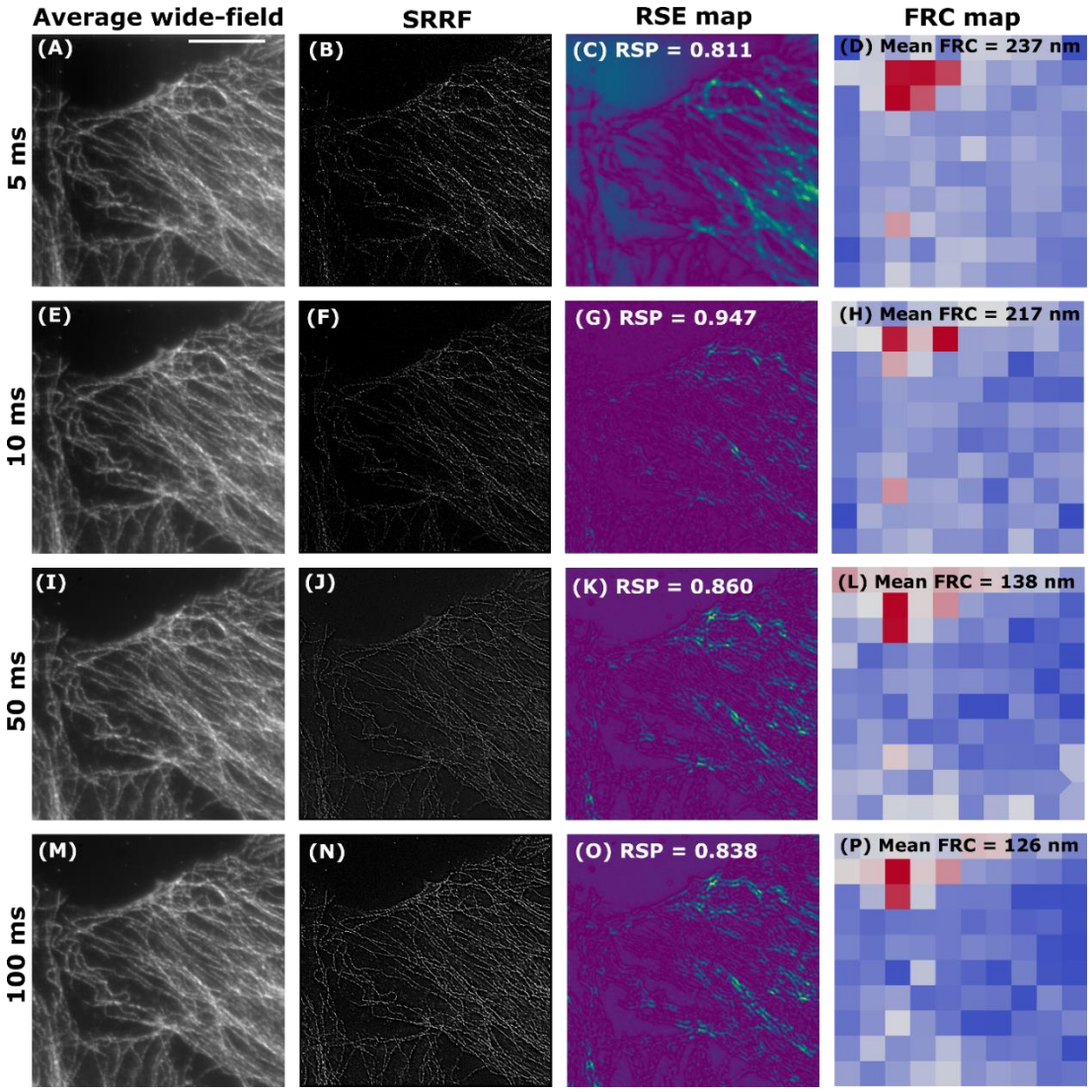


**Figure 48. High-resolution β-tubulin image does not always yield a high quality SRRF image.** To compare the resolution and quality of β-tubulin-Alexa Fluor 488, at different exposure times, it was imaged on an epifluorescence microscope (100x 1.4NA plus 2.5x magnifying lens) at 5 ms (A), 10 ms (E), 50 ms (I), and 100 ms (M). Each 100 frame stack was SRRF-processed using the NanoJ-SRRF ImageJ

plugin. The quality and resolution of the β-tubulin-Alexa 488 SRRF-processed images (B, F, J, and N) were assessed using the ImageJ plugin NanoJ-SQUIRREL by creating RSE maps (C, G, K, and O) and FRC maps (D, H, L, and P), respectively. Purple regions in the RSE map are less likely to contain artefacts, whereas those that are blue-yellow are highly likely to be artefacts. RSP values >0.95 are good SRRF images. Red regions in the FRC map are low-resolution, whereas those in blue are of high-resolution. Lower exposure times gave the best quality SRRF image, but at the expense of lower resolution. Scale bar = 10 µm.

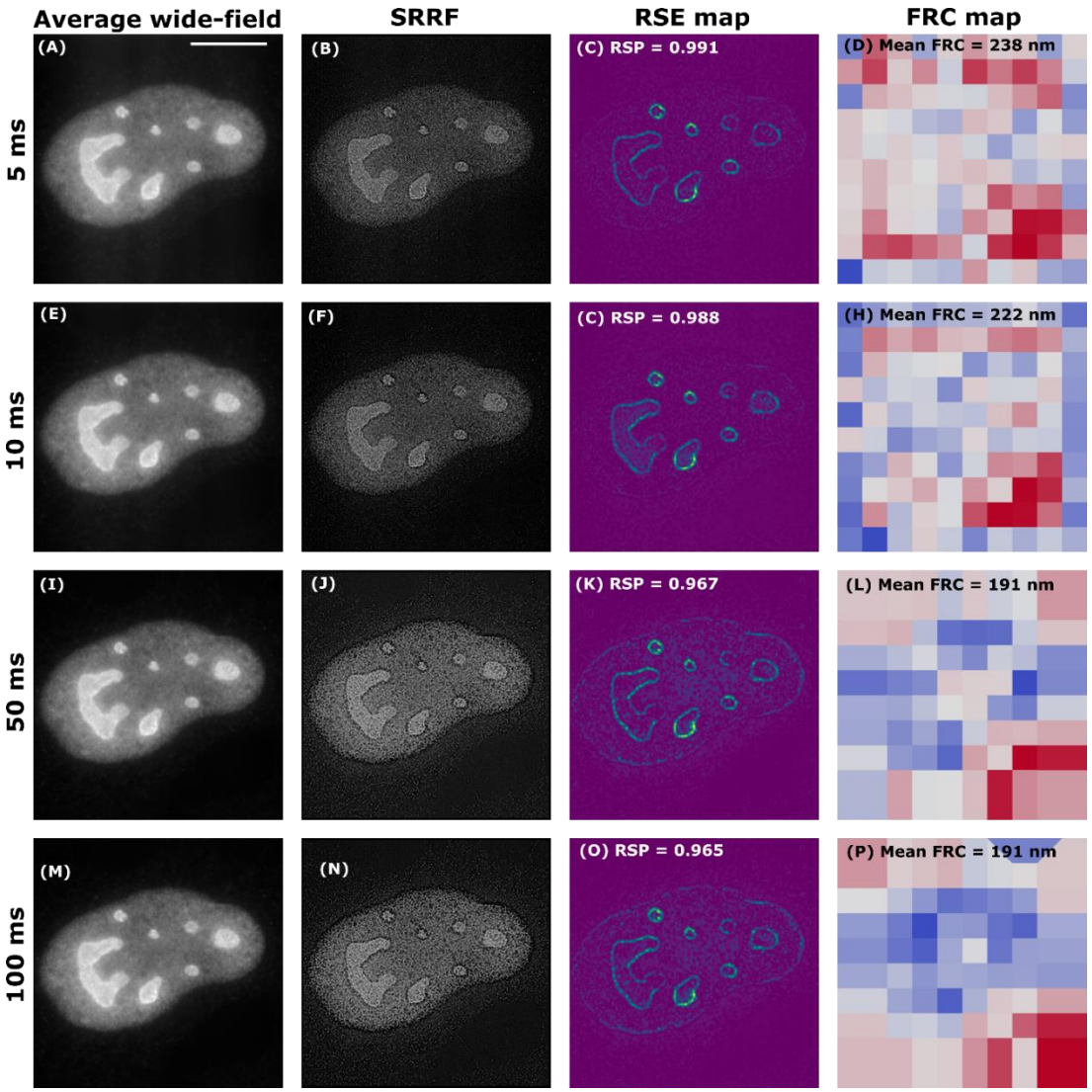


**Figure 49. High-resolution nucleolin image does not always yield a high quality SRRF image.** To compare the resolution and quality of nucleolin-Alexa Fluor 488, at different exposure times, it was imaged on an epifluorescence microscope (100x 1.4NA plus 2.5x magnifying lens) at 5 ms (A), 10 ms (E), 50 ms (I), and 100 ms (M). Each 100 frame stack was SRRF-processed using the NanoJ-SRRF ImageJ plugin. The quality and resolution of the nucleolin-Alexa 488 SRRF-processed images (B, F, J, and N) were assessed using the ImageJ plugin NanoJ-SQUIRREL by creating RSE maps (C, G, K, and O) and FRC maps (D, H, L, and P), respectively. Purple regions in the RSE map are less likely to contain artefacts, whereas those that are blue-yellow are highly likely to be artefacts. RSP values >0.95 are good SRRF images. Red regions in the FRC map are low-resolution, whereas those in blue are of high-resolution. Lower exposure times gave the best quality SRRF image, but at the expense of lower resolution. Scale bar = 10 µm.

| Exposure time (ms) | β-tubulin-Alexa 488 RSP value (a.u.) | β-tubulin-Alexa 488 min FRC value (nm) | β-tubulin-Alexa 488 max FRC value (nm) | β-tubulin-Alexa 488 mean FRC value (nm) |
|---|---|---|---|---|
| 5 | 0.811 | 156 | 424 | 237 |
| 10 | 0.947 | 145 | 410 | 217 |
| 50 | 0.860 | 47 | 387 | 138 |
| 100 | 0.838 | 42 | 414 | 126 |

**Table 9. Comparing the quality and resolution of SRRF images for different exposure times.** SRRF-processed images of β-tubulin-Alexa Fluor 488 (NanoJ-SRRF ImageJ plugin) from Figure 48 were assessed in terms of quality and resolution using the NanoJ-SQUIRREL imageJ plugin. A lower exposure time of 5 ms, yielded the best SRRF image (RSP values >0.95), but gave the lowest resolution (high mean FRC value of 237 nm).

As well as varying the acquisition settings, parameters used in the post-processing can also be changed, to improve the quality and resolution of the SRRF image. Here, a parameter sweep was done manually, to find the optimal processing parameters for SRRF. One such parameter was the ring radius, which determines the sub-pixel wise range that is used for the gradient convergence calculation, known as a radiality measurement. Generally, a small ring radius will yield the best resolution, but if the image is noisy, the resolution will be lower, due to the reduction in precision of the radiality calculation. As previously, β-tubulin and nucleolin were labelled with Alexa Fluor 488 by indirect immunofluorescence and 100 frames acquired on an epifluorescence microscope (100x 1.4NA plus 2.5x magnifying lens). To compare how the size of the ring radius can affect the quality and resolution of a SRRF image, wide-field images were post-processed with the NanoJ-SRRF ImageJ plugin and the ring radius was varied from 0.1-3 (default 0.5), but all other parameters, including the temporal analysis (temporal radiality average – TRA), radiality magnification (5), and axes in ring (6), were all set to default. ImageJ plugin NanoJ-SQUIRREL was used to determine the quality and resolution of SRRF-processed images, when the ring radius was changed, for β-tubulin-Alexa Fluor 488 (Figure 50) and nucleolin-Alexa Fluor 488 (Figure 51). The smallest ring radius yielded a high quality SRRF image, whilst the larger ring radius degraded the quality of the SRRF image, as shown by the increase in high error blue-yellow regions in the RSE map, which are likely artefacts of the processing.

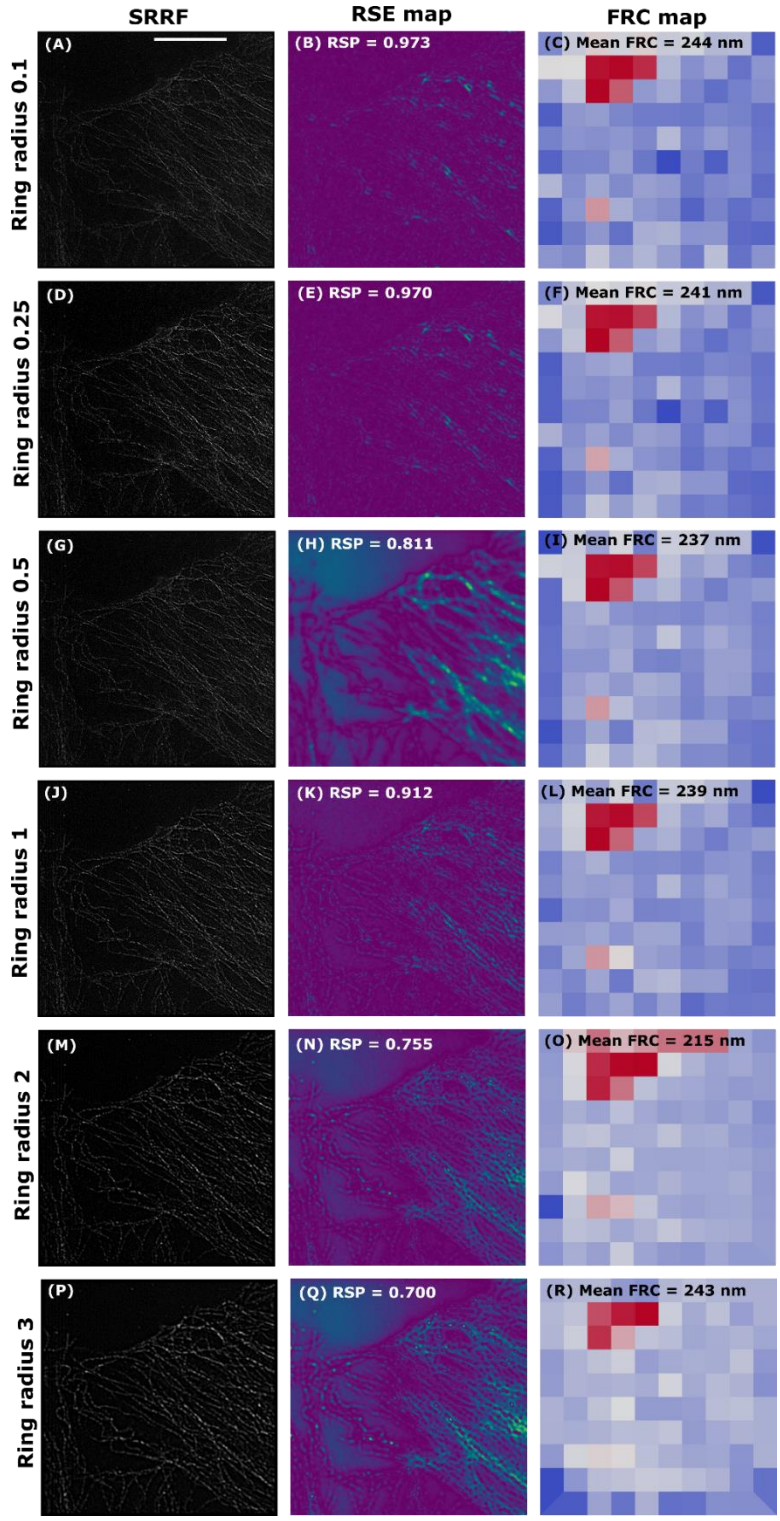


**Figure 50. Varying the ring radius NanoJ-SRRF parameter affects the quality of the β-tubulin-Alexa Fluor 488 SRRF-processed image.** Wide-field images (100 frames) of β-tubulin-Alexa Fluor 488 (100x 1.4NA plus 2.5x magnifying lens) was SRRF-processed with the NanoJ-SRRF ImageJ plugin (A, D, G, J, M, and P) using different sized ring radii 0.1-3 (default is 0.5). The quality and resolution of the SRRF-processed images was assessed using the NanoJ-SQUIRREL ImageJ plugin. Purple regions in the RSE maps (B, E, H, K, N, and Q) are less likely to contain artefacts, whereas those that are blue-yellow are highly likely to be artefacts. RSP values >0.95 are good SRRF images. Red regions in the FRC maps (C, F, I, L, O, and R) are low-resolution, whereas those in blue are of high-resolution. A lower ring radius

yielded a better quality SRRF image, with less artefacts, but did not always result in improved resolution compared to a higher ring radius. Scale bar = 10 µm.

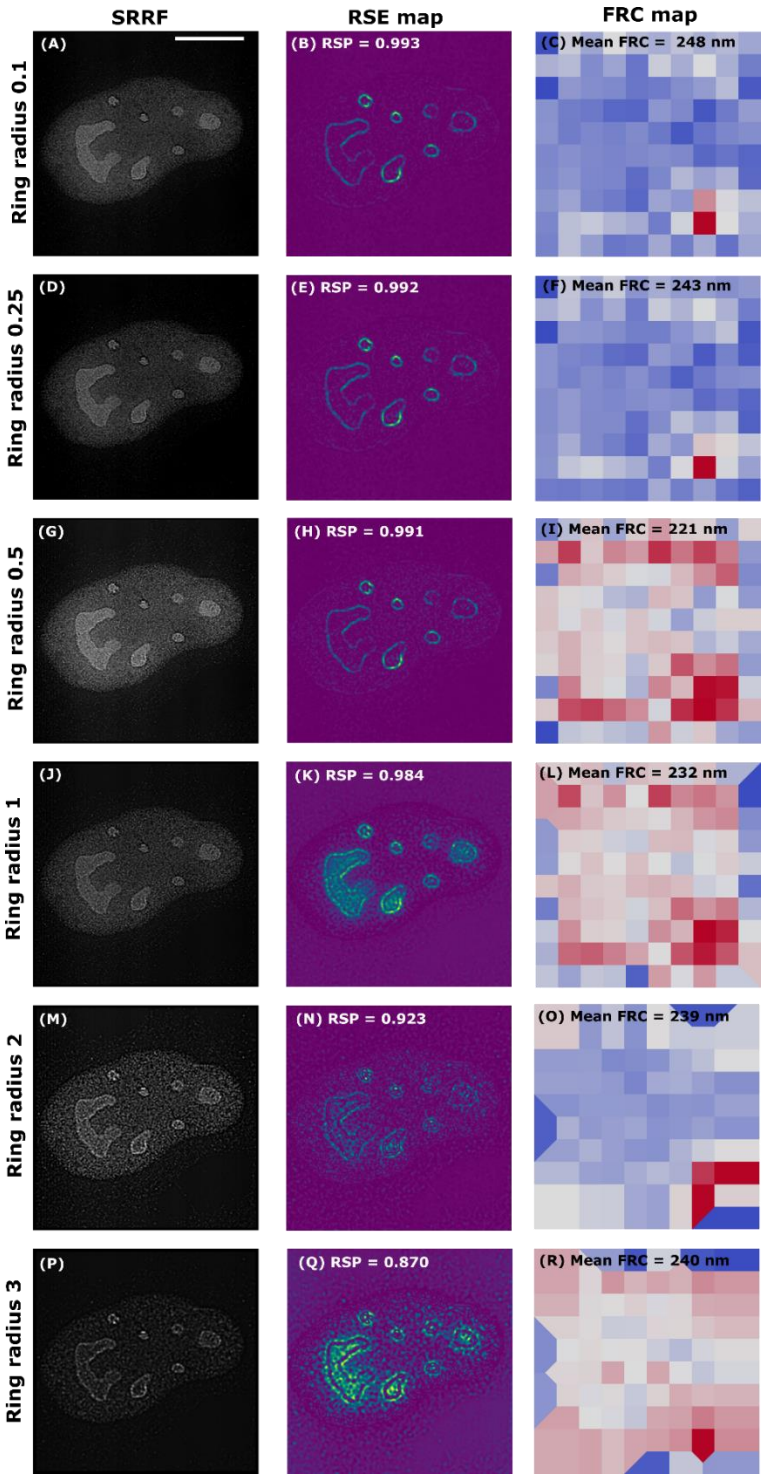


**Figure 51. Varying the ring radius NanoJ-SRRF parameter affects the quality of the nucleolin-Alexa Fluor 488 SRRF-processed image.** Wide-field images (100 frames) of nucleolin-Alexa Fluor 488 (100x 1.4NA plus 2.5x magnifying lens) was SRRF-processed with the NanoJ-SRRF ImageJ plugin using different sized ring radii. The quality and resolution of the SRRF-processed images was assessed using the NanoJ-SQUIRREL ImageJ plugin. Purple regions in the RSE maps (B, E, H, K, N, and Q) are less likely to contain artefacts, whereas those that are blue-yellow are highly likely to be artefacts. RSP values

>0.95 are good SRRF images. Red regions in the FRC maps (C, F, I, L, O, and R) are low-resolution, whereas those in blue are of high-resolution. A lower ring radius yielded a better quality SRRF image, with less artefacts, but did not result in improved resolution compared to a higher ring radius. Scale bar = 10 μm.

Another parameter that can affect the SRRF output is radiality magnification, since it determines the number of sub-pixels the image pixels are split into before the radiality calculation takes place. Since increasing the radiality value, increases the number of pixels in the resulting SRRF image, this greatly enhances the computational time, so the higher the radiality magnification value, the slower the SRRF-processing. A radiality magnification of 1x, 5x, and 10x, gives a SRRF image with 512-by-512 pixels, 2560-by-2560 pixels, and 5120-by-5120 pixels, respectively. Again, 100 frames of β-tubulin-Alexa Fluor 488 and nucleolin-Alexa Fluor 488 were acquired on an epifluorescence microscope (100x 1.4NA plus a 2.5x magnifying lens) and the wide-field images SRRF-processed with NanoJ-SRRF with default parameters (temporal analysis: temporal radiality analysis – TRA, ring radius: 0.5, and axes in ring: 6), except this time the radiality magnification was varied from 1 to 10 (default is 5). ImageJ plugin NanoJ-SQUIRREL was used to assess the resolution and quality of β-tubulin-Alexa Fluor 488 (Figure 52) and nucleolin-Alexa Fluor 488 (Figure 53), when radiality magnification was varied. For both datasets, a larger radiality magnification value gave a better quality SRRF-processed image, with an RSP value >0.95 (less high error, blue-yellow regions in the RSE map), and improved resolution (lower mean FRC value), as shown by more low-resolution regions in red on the FRC map.

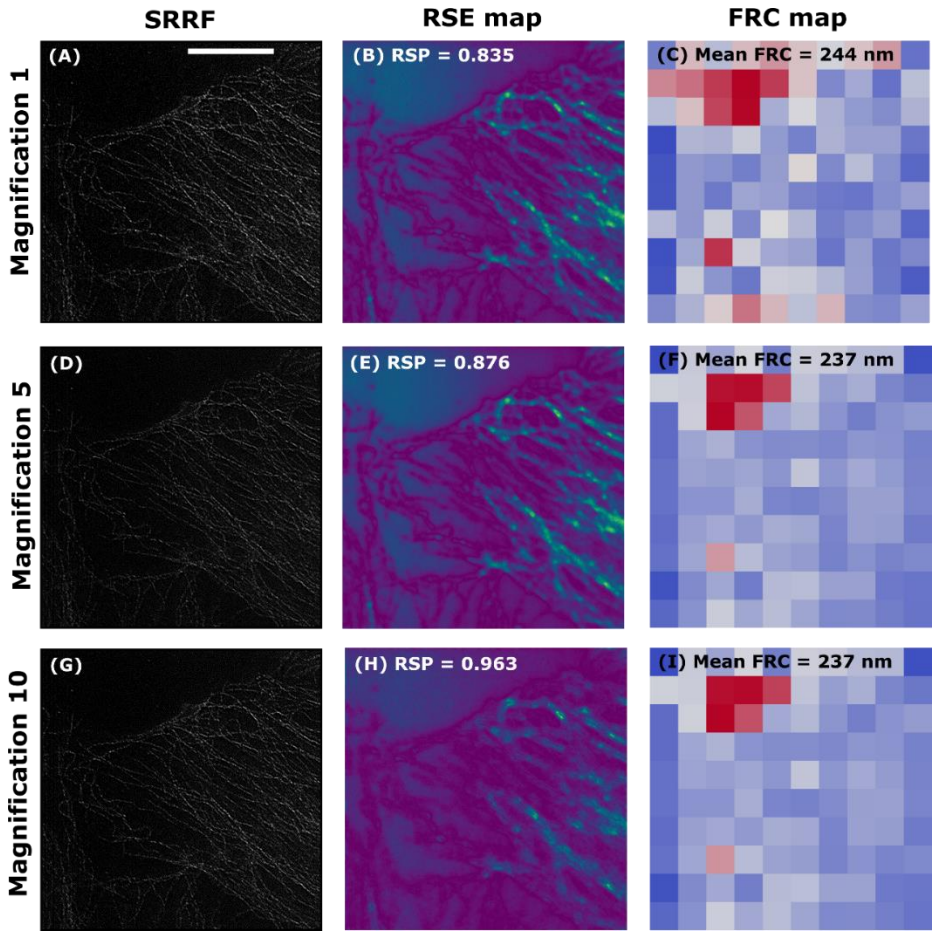


**Figure 52. A higher radiality magnification value yields better resolution and quality.** Wide-field images (100 frames) of β-tubulin-Alexa Fluor 488 (100x 1.4NA plus 2.5x magnifying lens) was SRRF-processed with the NanoJ-SRRF ImageJ plugin using different radiality magnification values: 1, 5 (default), and 10. The quality and resolution of the SRRF-processed images (A, D, and G) was assessed using the NanoJ-SQUIRREL ImageJ plugin. Purple regions in the RSE maps (B, E, and H) are less likely to contain artefacts, whereas those that are blue-yellow are highly likely to be artefacts. RSP values >0.95 are good SRRF images. Red regions in the FRC maps (C, F, and I) are low-resolution, whereas those in blue are of high-resolution. A higher radiality magnification value yielded improved resolution and quality compared to a higher radiality magnification value. Scale bar = 10 µm.

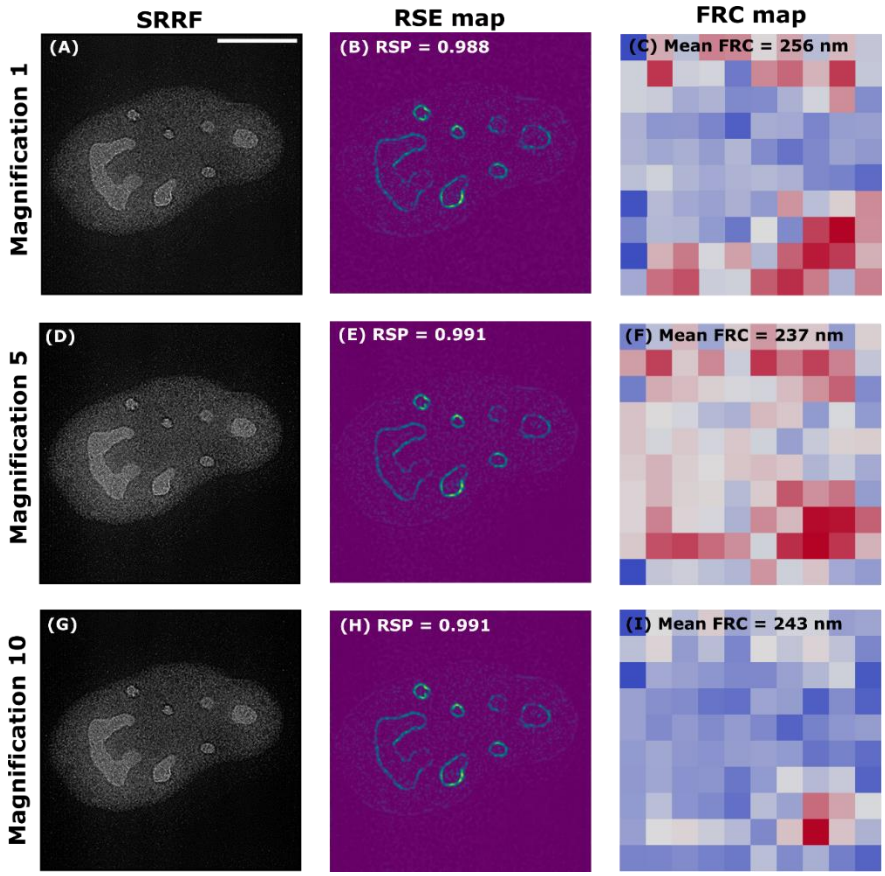


**Figure 53. A higher radiality magnification value yields better resolution and quality.** Wide-field images (100 frames) of nucleolin-Alexa Fluor 488 (100x 1.4NA plus 2.5x magnifying lens) was SRRF-processed with the NanoJ-SRRF ImageJ plugin using different radiality magnification values: 1, 5 (default), and 10. The quality and resolution of the SRRF-processed images (A, D, and G) was assessed using the NanoJ-SQUIRREL ImageJ plugin. Purple regions in the RSE maps (B, E, and H) are less likely to contain artefacts, whereas those that are blue-yellow are highly likely to be artefacts. RSP values >0.95 are good SRRF images. Red regions in the FRC maps (C, F, and I) are low-resolution, whereas those in blue are of high-resolution. A higher radiality magnification value yielded improved resolution and quality compared to a higher radiality magnification value. Scale bar = 10 µm.

Apart from the ring radius and radiality magnification, axes in ring can also be varied, in the ImageJ plugin NanoJ-SRRF, from 2 to 8 (default is 6). Axes in ring determines the number of xy coordinates used, within the ring radius, for the radiality measurement. Similar to radiality magnification, using a higher axes in ring value, increased the processing time taken to produce a SRRF image. As before, nucleolin and β-tubulin were labelled with Alexa Fluor 488 by indirect immunofluorescence and 100 frames acquired on an epifluorescence microscope (100x 1.4NA plus a 2.5x magnifying lens). Each 100 frame stack was post-processed with NanoJ-SRRF, in ImageJ, using default settings (temporal analysis: temporal radiality analysis – TRA, ring radius: 0.5, and magnification radiality: 5), except this time the axes in ring was the independent variable and was changed from 2 to 8. The quality of the SRRF-processed images decreased using a smaller axes in ring for both β-tubulin-Alexa Fluor 488 (Figure 54)

and nucleolin-Alexa Fluor 488 (Figure 55), but the resolution did not improve with a smaller axes in ring value.

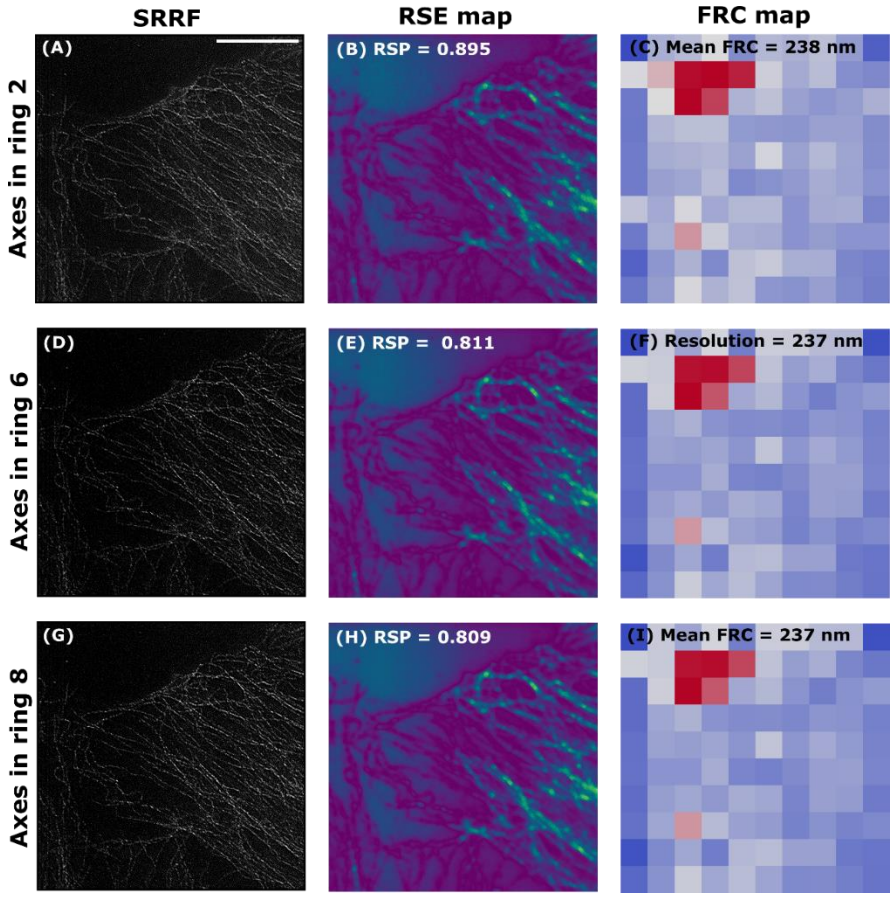


**Figure 54. A smaller axes in ring value improves the quality of SRRF-processed β-tubulin.** The ImageJ plugin NanoJ-SRRF was used to post-process β-tubulin labelled with Alexa Fluor 488 over 100 frames (100x 1.4NA plus a 2.5x magnifying lens). Default parameter settings (temporal analysis: temporal radiality analysis – TRA, ring radius: 0.5, and magnification radiality: 5) were used and the axes in ring value varied from 2-8 (default is 6). The resolution and quality of the resulting SRRF-processed images (A, D, and G) were assessed with the ImageJ plugin NanoJ-SQUIRREL. RSE maps (B, E, and H) and FRC maps (C, F, and I), confirm that a small axes in ring value yields a high quality SRRF image, but no change in resolution. Scale bar = 10 µm.

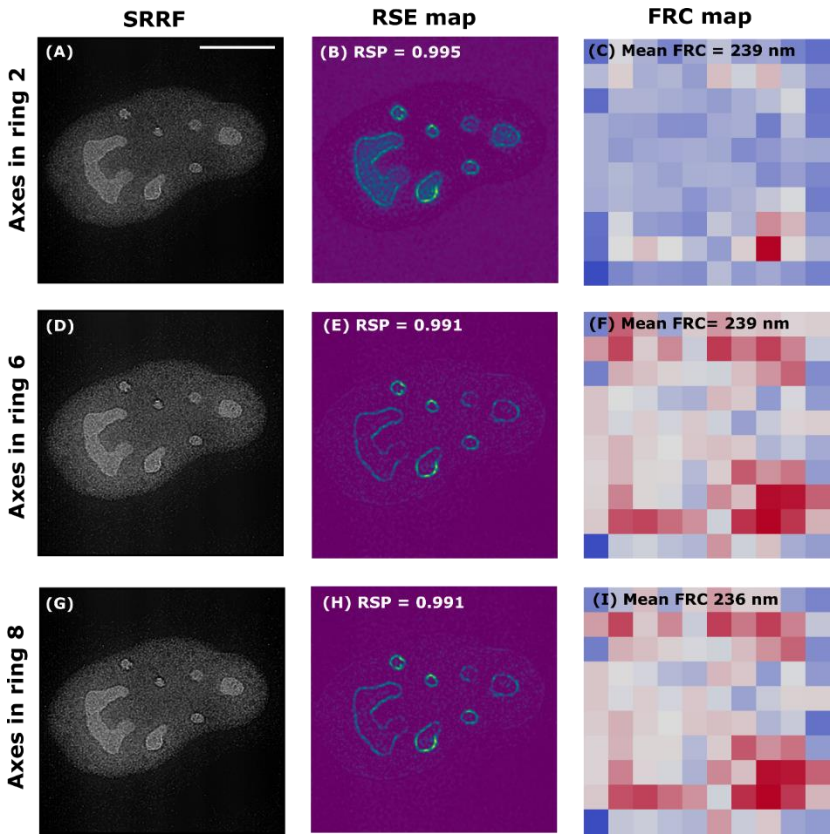


**Figure 55. A small axes in ring value improves the quality of SRRF-processed nucleolin.** The ImageJ plugin NanoJ-SRRF was used to post-process nucleolin labelled with Alexa Fluor 488 over 100 frames (100x 1.4NA plus a 2.5x magnifying lens). Default parameter settings (temporal analysis: temporal radiality analysis – TRA, ring radius: 0.5, and magnification radiality: 5) were used and the axes in ring value varied from 2-8 (default is 6). The resolution and quality of the resulting SRRF-processed images (A, D, and G) were assessed with the ImageJ plugin NanoJ-SQUIRREL. Purple regions in the RSE map are less likely to contain artefacts, whereas those that are blue-yellow are highly likely to be artefacts. RSP values >0.95 are good SRRF images. Red regions in the FRC map are low-resolution, whereas those in blue are of high-resolution. RSE maps (B, E, and H) and FRC maps (C, F, and I), confirm that a small axes in ring value yields a high quality SRRF image, but no change in resolution. Scale bar = 10 µm.

So far, SRRF-processing has been done on data acquired on an epifluorescence microscope (100x 1.4 NA plus 2.5x magnifying lens) with white light illumination using a mercury arc lamp. Here, nucleolin-Alexa Fluor 488 was also acquired in wide-field mode (100x 1.46 NA plus 1.6x magnifying lens) with a 30 mW 488 nm laser, at different exposure times (5 ms, 10 ms, 50 ms, and 100 ms). For lamp based epifluorescence illumination, acquisition at a low exposure time, yielded a high quality SRRF image (RSP value > 0.95) (Figure 56A), whilst the laser did not yield a satisfactory SRRF image (RSP value < 0.95) (Figure 56B).

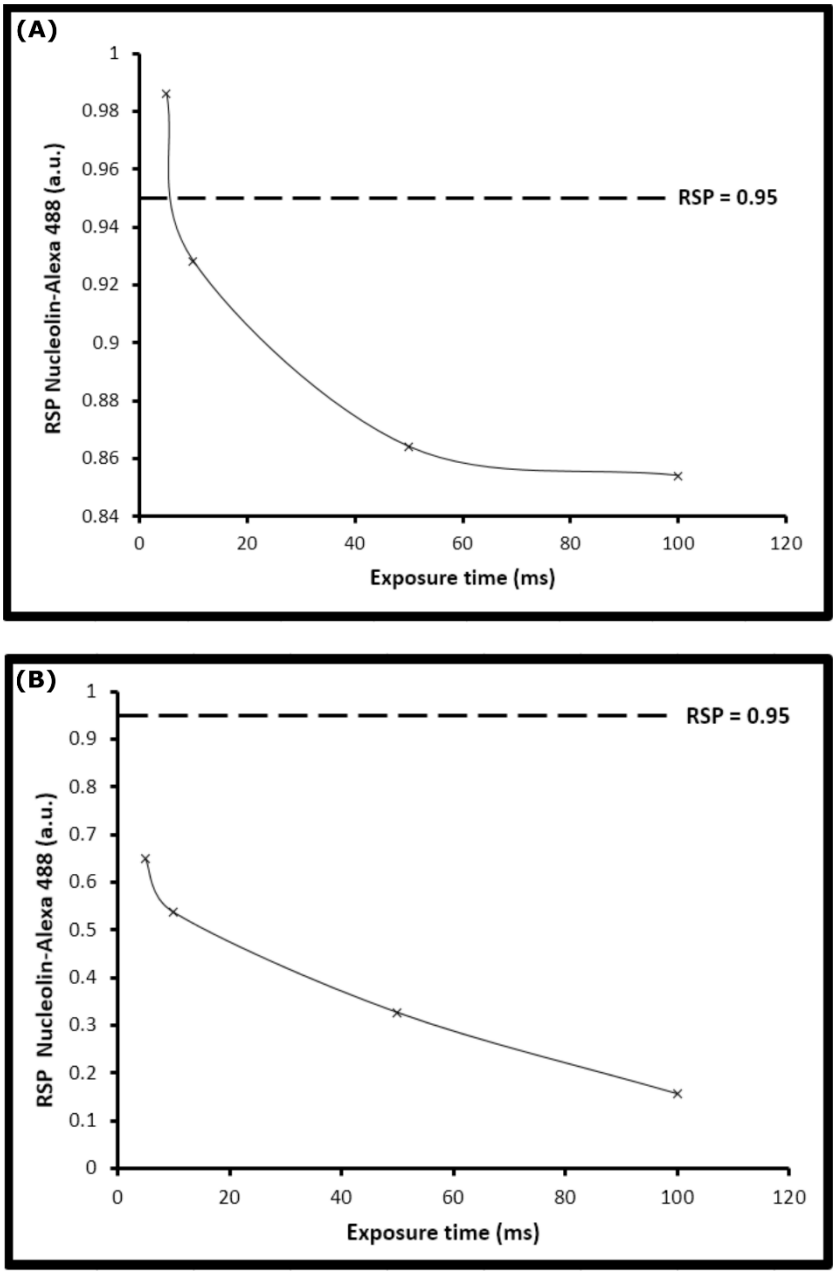


**Figure 56. Comparing the quality of SRRF images processed from data acquired with a lamp versus a laser.** Nucleolin was labelled with Alexa Fluor 488 by indirect immunofluorescence with primary and secondary antibodies. A stack of 1,000 frames was imaged on an epifluorescence microscope with a mercury arc lamp (100x 1.4NA plus 2.5x magnifying lens) and also on a TIRF system with laser illumination in epifluorescence mode (100x 1.46NA plus 1.6x magnifying lens) at different exposure times: 5 ms, 50 ms, and 100 ms. Images were SRRF-processed with the NanoJ-SRRF imageJ plugin for the lamp (A) and laser (B) data. For lamp illumination, lower exposure times yielded better quality images (higher RSP values > 0.95), whereas for the laser, although lower exposure times yielded higher RSP values, none were of high quality and contained artefacts (RSP values > 0.95 = Good SRRF image). Scale bar = 10 µm.

Most super-resolution techniques such as dSTORM use the far red Alexa Fluor 647 dye, because blinking can be induced with the addition of thiol reducing agent. The longer

wavelength used to excite Alexa Fluor 647 produces less photodamaging effects. Simultaneous multicolour imaging with Alexa Fluor 647 can prevent bleed-through when combined with other dyes. Since Alexa Fluor 647 is a dye commonly used by the super-resolution microscopy community, SRRF-processing was also done on mercury arc lamp-acquired nucleolin samples labelled with Alexa Fluor 647 (100x 1.4NA plus 2.5x magnifying lens), to compare against previous images of nucleolin-Alexa 488. Interestingly, Alexa Fluor 647 yielded higher quality SRRF images than using Alexa Fluor 488 (Table 10). Both gave the best quality SRRF image at a low exposure time of 5 ms, but Alexa Fluor 647 outperformed Alexa Fluor 488, by producing high quality SRRF images using 5-100 ms exposure times (RSP > 0.95 = good SRRF image). As labelling structures with Alexa Fluor 647 yielded the best quality SRRF image, this fluorescent dye was used in all further NanoJ-SRRF experiments, except where two colours were required for protein-protein interaction studies, and Alexa Fluor 647 was then combined with Alexa Fluor 488. There was also a high degree of unwanted photobleaching of structures, so to prevent this, a ProLong Gold anti-fading mounting medium (Dako, UK) was always used during sample preparation and since <100 frames did not influence the quality of the SRRF-processed image, a maximum of 100 frames was used during image acquisition.

| Exposure time (ms) | Nucleolin-Alexa 488 RSP value | Nucleolin-Alexa 647 RSP value |
|---|---|---|
| 5 | 0.986 | 0.987 |
| 10 | 0.928 | 0.984 |
| 50 | 0.864 | 0.976 |
| 100 | 0.854 | 0.965 |

**Table 10. Comparison of SRRF-processing of nucleolin labelled with different probes.** Nucleolin was labelled with Alexa Fluor 488 and 647 via indirect immunofluorescence in different samples and RSP values determined for different exposure times, when imaged on an epifluorescence microscope (100x 1.4 NA plus 2.5 magnifying lens). Nucleolin-Alexa 647 gave higher RSP values than Nucleolin-Alexa 488.

#### 4.2.4.2 Applying NanoJ-SQUIRREL to SRRF-Stream data

In 2018 SRRF was packaged into a commercial implementation (SRRF-Stream) by Andor Technology, in collaboration with Ricardo Henriques' research group. It is assumed that the same SRRF algorithm is used as the open-source ImageJ plugin NanoJ-SRRF and acquisition

is also controlled by open-source Micro-Manager software (247). SRRF-Stream arrived at the CCI in the last months of this PhD project. It enables SRRF images to be obtained at a faster rate compared to acquiring data and processing with the ImageJ plugin NanoJ-SRRF. SRRF-Stream offers on the fly SRRF-processing, performed in real-time, as the data are being acquired on the camera, which speeds up the workflow to achieve a SRRF image. Since processing with SRRF-Stream is 30x faster than using the ImageJ plugin NanoJ-SRRF, it can offer quick decisions about which parameters yield an optimal SRRF image (293). Although default settings can be used with confidence for most structures, optimisation of parameters can often give a better SRRF image. For instance, reducing the ring radius can give better resolution, but potentially at the expense of image quality. The same parameters that were tested for the ImageJ plugin NanoJ-SRRF were also varied here with SRRF-Stream, on the same nucleolin-Alexa Fluor 488 sample. NanoJ-SRRF allows better control over the parameters chosen for the temporal analysis than SRRF-Stream (294), as temporal radiality maximum (TRM), temporal radiality analysis (TRA), temporal radiality pairwise product mean (TRPPM), and temporal radiality auto-correlations (TRAC) options can be selected. Axes in ring parameter can also be varied with NanoJ-SRRF in ImageJ, unlike in the Fusion software of SRRF-Stream, where it is fixed. Default settings for SRRF-Stream in Fusion software also differed slightly from default parameters in the ImageJ plugin NanoJ-SRRF, so for the sake of consistency, default settings used previously to test NanoJ-SRRF parameters were used here (ring radius 0.5 and magnification radiality 5). To test the effect different acquisition settings had on the quality of a SRRF image, the number of frames was varied from 50-1,000 frames during the SRRF-Stream acquisition (100x 1.4 NA, plus 2x magnifying lens), whilst the exposure time was kept to a minimum at 5 ms. As before, the ImageJ plugin NanoJ-SQUIRREL was used to assess the quality of the images, by creating a RSE map and calculating an RSP value (RSP>0.95 = good SRRF image). Using a high speed spinning disk confocal, a high quality SRRF image with as few as 50 frames was achieved with SRRF-Stream (Figure 57), which shows the potential of this system in improving temporal resolution for fast-moving proteins in live cells. A spinning disk confocal has multiple pinholes so light can be detected simultaneously, whereas with confocal laser scanning microscopy time is taken time to sequentially scan the sample using one pinhole.

As well as the number of frames, the acquisition rate can also affect image quality, so the exposure time was also varied during the SRRF-Stream acquisition from 5-100 ms. A total of 100 frames of nucleolin-Alexa Fluor 488 was acquired (100x 1.4NA, plus 2x magnifying lens) with SRRF-Stream, with a lower exposure time yielding a higher quality SRRF image, but at

the expense of resolution (Figure 58). With SRRF-Stream 10,000-fold less illumination is needed compared to dSTORM, so it can afford to use a lower exposure times, to achieve an adequate SNR. The 1024-by-1024 pixels FOV of the iXon888 Ultra EMCCD camera (13 µm pixel size) used on the SRRF-Stream system was larger compared to the 512-by-512 pixels FOV of the EMCCD camera (16 µm pixel size) used on the epifluorescence microscope to acquire data for post-processing with the ImageJ plugin NanoJ-SRRF. Imaging a large FOV compromises spatial resolution, because typically lower magnification lenses are required that have a low NA, however using a camera with a larger FOV allows higher magnification objectives to be used that have a high NA. To improve temporal resolution, a faster frame rate can be achieved by cropping a ROI around the protein of interest.

After establishing optimal acquisition parameters of SRRF-Stream, being 5 ms and 50-100 frames, post-processing parameters ring radius and radiality magnification, were also tested, by keeping the exposure time and number of frames constant, at 5 ms and 100 frames, respectively. The ring radius was varied from 0.1 to 3, where the default value of 0.5 for NanoJ-SRRF was also used. Unlike NanoJ-SRRF, a higher ring radius yielded a better quality SRRF image for SRRF-Stream, with less artefacts, until a point when the image quality started to decrease (Figure 59). Discrepancies between the optimal ring radius for NanoJ-SRRF and SRRF-Stream may be due to differences in the processing algorithm or different modes of illumination, as a mercury arc lamp on an epifluorescence system was used for NanoJ-SRRF acquisition, whilst a laser on a spinning disk confocal was used for SRRF-Stream. Using a default ring radius of 0.5, radiality magnification was varied from 1 to 10 (default is 5). Once processed, with a radiality magnification of 1x, the size of the SRRF-Stream image was the same as the wide-field image, 1024-by-1024 pixels, however, when the radiality magnification value was increased to 5x and 10x, the number of pixels in the resulting SRRF-Stream image also increased to 2560-by-2560 pixels and 5120-by-5120, respectively. A higher radiality magnification value appeared to yield a better resolution SRRF-Stream image of nucleolin-Alexa Fluor 488 (Figure 60), which is in agreement with the NanoJ-SRRF data (Figure 53). However, the quality of the SRRF-Stream image decreased as the radiality magnification value was increased.

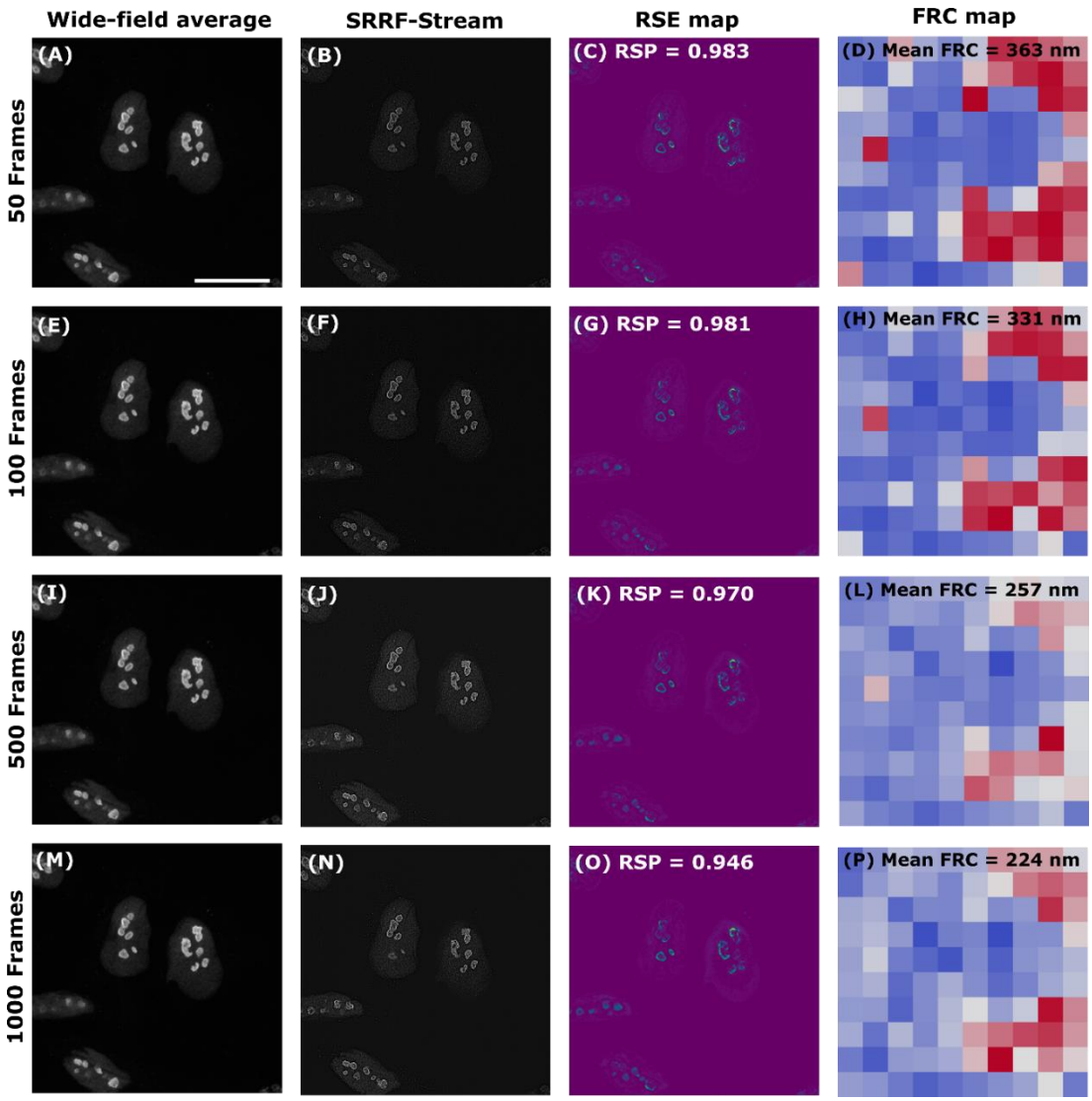


**Figure 57. The resolution of SRRF-Stream images improves with more frames, whilst the quality decreases.** Wide-field images of nucleolin-Alexa Fluor 488 (100x 1.4NA plus 2x magnifying lens), containing different number of frames: 50 frames (A), 100 frames (E), 500 frames (I), and 1,000 frames (M), were acquired using SRRF-Stream (B, F, J, and N). The quality and resolution of each SRRF-Stream processed image was assessed using NanoJ-SQUIRREL ImageJ plugin. RSE maps (C, G, K, and O) showing high error regions in blue-yellow and low error regions in purple. A high RSP value > 0.95 is considered as a good quality SRRF image. FRC maps (D, H, L, and P) indicate high resolution in blue (low FRC value) and low resolution in red (high FRC value). A higher number of frames, decreased the quality and resolution of a SRRF-Stream image. For 50-1,000 frames, an RSP value >0.95 was obtained. Scale bar = 20 µm.

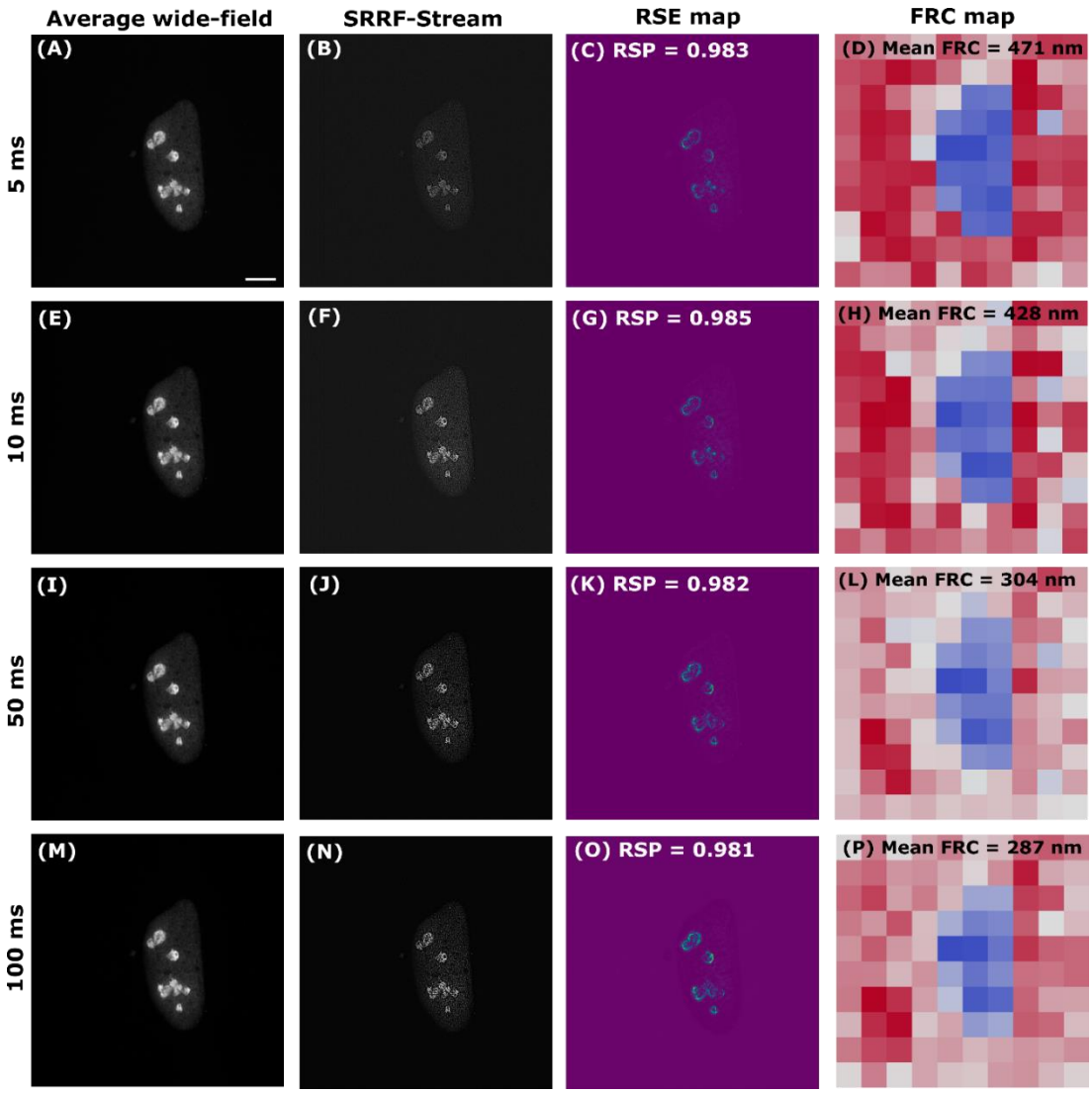


**Figure 58. Lower exposure times yield a higher quality SRRF-Stream image of nucleolin-Alexa Fluor 488.** The quality of SRRF-Stream images of nucleolin-Alexa488 (B, F, J, and N) were assessed using the ImageJ plugin NanoJ-SQUIRREL, by comparing them to corresponding average wide-field images (100x 1.4NA plus 2x magnifying lens), acquired at different exposure times: 5 ms (A), 10 ms (E), 50 ms (I), and 100 ms (M). RSE maps were created (C, G, K, and O). Purple regions in the RSE map were less likely to contain artefacts, whereas those that are blue-yellow were highly likely to be artefacts. RSP values >0.95 are good SRRF images. FRC maps (D, H, L, and P) show low resolution in red (high FRC value) and high resolution in blue (low FRC value). Lower exposure times gave the best quality SRRF image, but at the expense of resolution. Scale bar = 20 µm.

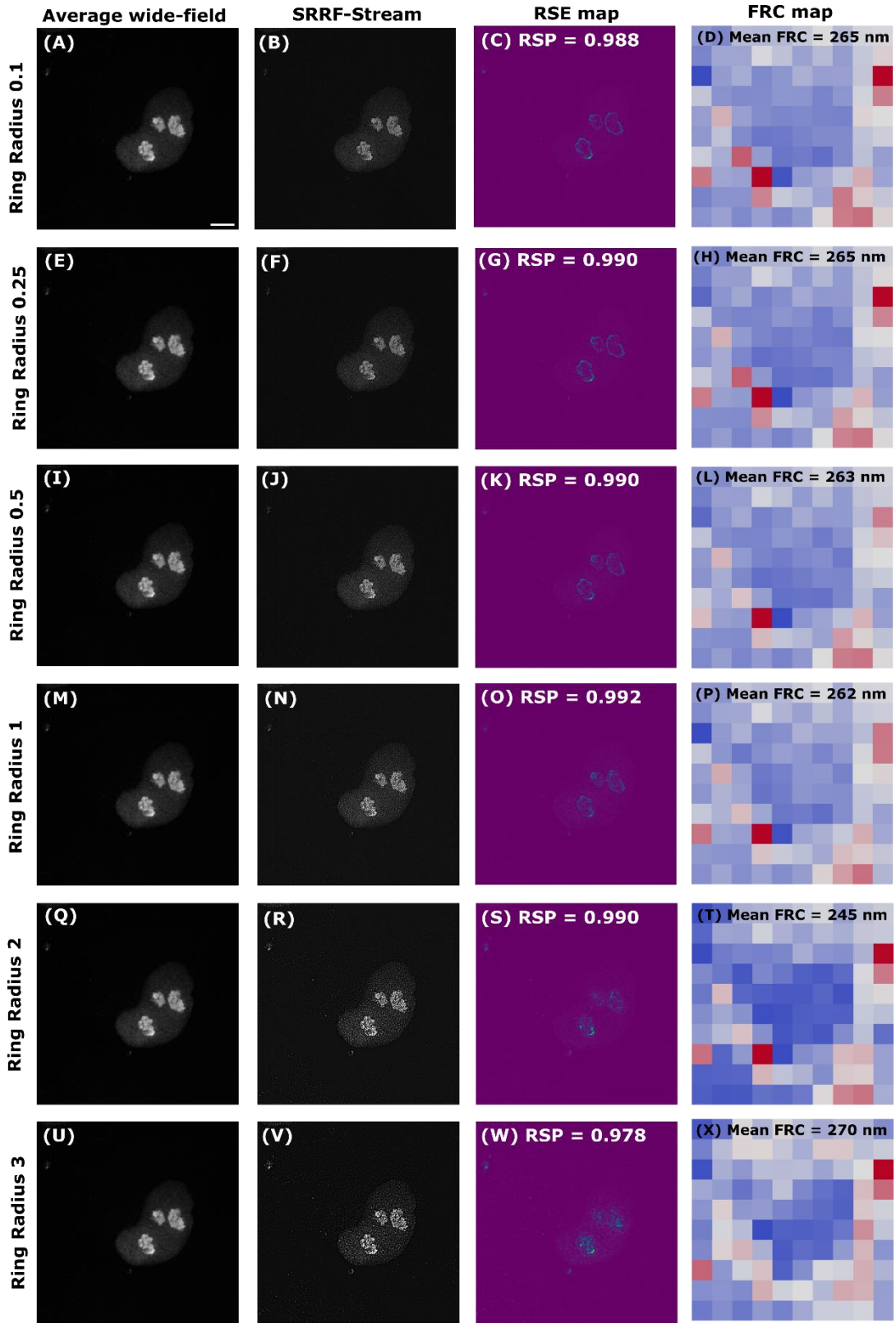


**Figure 59. Varying the ring radius affects the quality of SRRF-Stream images.** Wide-field images (100 frames) of nucleolin-Alexa Fluor 488 (100x 1.4NA plus 2x magnifying lens) (A, E, I, M, Q, and U) was SRRF-processed with SRRF-Stream (B, F, J, N, R, and V) using different sized ring radii. The quality of the SRRF-Stream processed images was assessed using the NanoJ-SQUIRREL ImageJ plugin. Purple regions in the RSE maps (C, G, K, O, S, and W) are less likely to contain artefacts, whereas those that are blue-yellow are highly likely to be artefacts. RSP values >0.95 are good SRRF images. FRC maps (D,

H, L, P, T, and X) show low resolution in red (high FRC value) and high resolution in blue (low FRC value). A higher ring radius yielded a better quality SRRF image, with less artefacts, until a point then the image quality started to degrade. Scale bar = 10 µm.

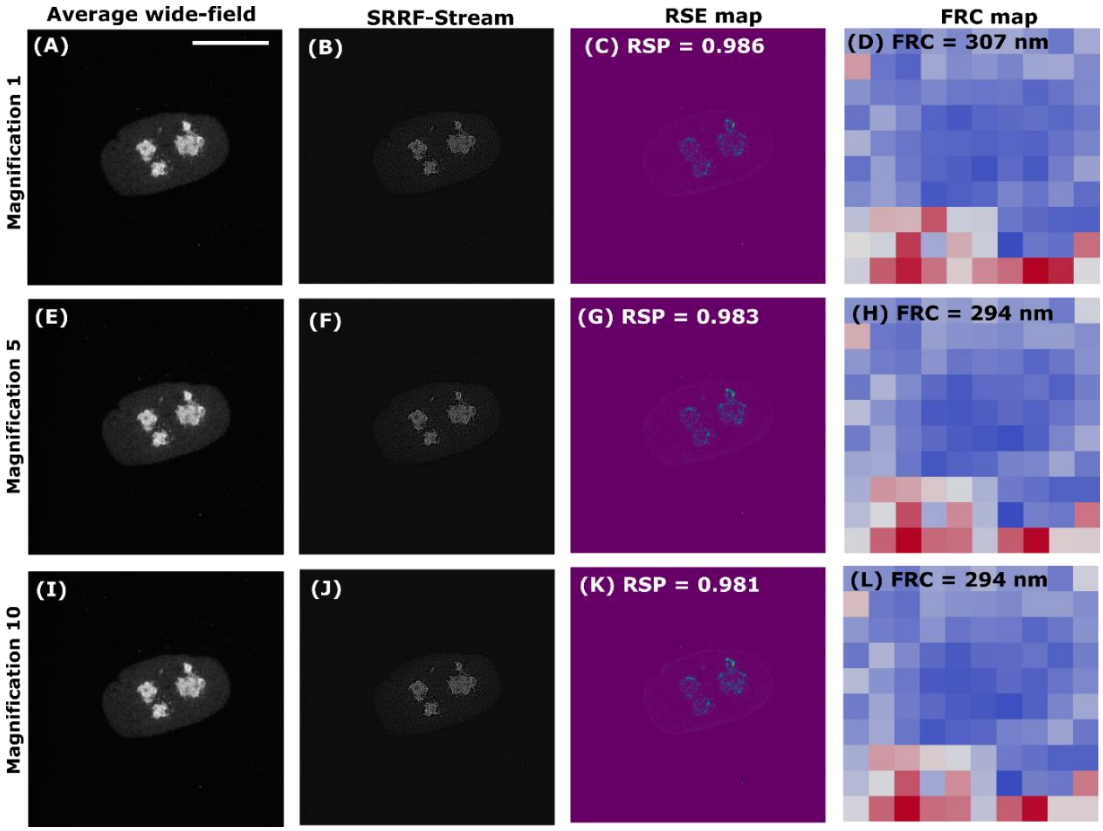


**Figure 60. A higher radiality magnification value yields better resolution.** Wide-field images (100 frames) of nucleolin-Alexa Fluor 488 (100x 1.4NA plus 2x magnifying lens) (A, E, and I) were SRRF-processed with SRRF-Stream using different radiality magnification values: 1, 5 (default), and 10. The quality and resolution of SRRF-Stream processed images (B, F, and J) was assessed using the NanoJ-SQUIRREL ImageJ plugin. Purple regions in the RSE maps (C, G, and K) are less likely to contain artefacts, whereas those that are blue-yellow are highly likely to be artefacts. RSP values >0.95 are good SRRF images. Red regions in FRC maps (D, H, and L) are of low resolution (high FRC values) and blue of high resolution (low FRC values). A smaller radiality magnification value yielded a better quality SRRF image, with less artefacts, compared to a higher radiality magnification value. However, a higher radiality magnification value yields better resolution. Scale bar = 20 µm.

Here, images were taken of fixed samples only, to rule out any motion blur artefacts from motion blur of live sample movements. However, using SRRF on fixed samples is basically a lower resolution version of STORM, since a two-to-six-fold resolution improvement (50-150 nm resolution) (293) is achievable compared to wide-field microscopy, so to appreciate that SRRF requires less intense illumination than STORM (2.3 kw/cm$^2$), SRRF should be done on live cells. Although, SRRF only increases lateral not axial resolution, z-stacks can be taken to

extract additional spatial information. However, to obtain more information about protein movement over time in 3D, 4D SRRF can be achieved with the addition of a PRILM and combining SRRF with other techniques, such as SIM or lattice-light-sheet, may further improve resolution (78). SRRF is known to work best with EMCCD cameras, because of their homogenous noise, EM gain for sensitivity, and better SNR than sCMOS (26). However, Andor Technology have recently released a sensitive sCMOS camera, which may perform nicely with SRRF. Future applications of SRRF look promising, with the next version of SRRF-Stream sure to incorporate NanoJ-SQUIRREL and machine learning, involving content-aware image restoration (CARE) (295), which should help to more easily determine the quality and resolution of super-resolution images.

### 4.2.5 Using SOFI simulation tool to predict optimal acquisition settings

Most deconvolution and super-resolution post-processing algorithms are tested with simulation data when they are being developed. SOFI simulation tool is a free software package (available on GitHub), implemented in MATLAB, which can computationally test different acquisition parameters, prior to imaging real biological samples; and in turn predict the quality of a resulting bSOFI image (124). As well as generating a bSOFI image, the software can also predict a STORM image from the same dataset. This software aims to teach users about the steps involved in the bSOFI-processing algorithm, up to $7^{th}$ order, and prevent tedious optimisation, which would otherwise require sample preparation. Although, the GUI (Figure 61) is very easy to navigate and there is a manual for its use, some prior knowledge is required about a fluorophore's bleaching rate and "ON" (fluorescent)/"OFF" (non-fluorescent) duty cycle, which is the fraction of time spent in the fluorescent state, when continually illuminated with light (296, 297). For synthetic organic dyes (e.g. Alexa Fluor 647) the "ON"/"OFF" state is typically short at 0.01 ms, whereas for RSFPs, it is much longer at 0.1 ms (124). A theoretical PSF is determined from the users' input parameters, including NA, emitter wavelength, and magnification. Every aspect that may affect the resulting bSOFI image is considered, including the exposure time, number of frames, and labelling density of the fluorophores. Additionally, the arrangement of the fluorophores can be visualised as a 2D image, depending on the pattern distribution, chosen by the user. As well as the pre-defined fluorophore distribution patterns to choose from, the user also has the option to create their own distribution.

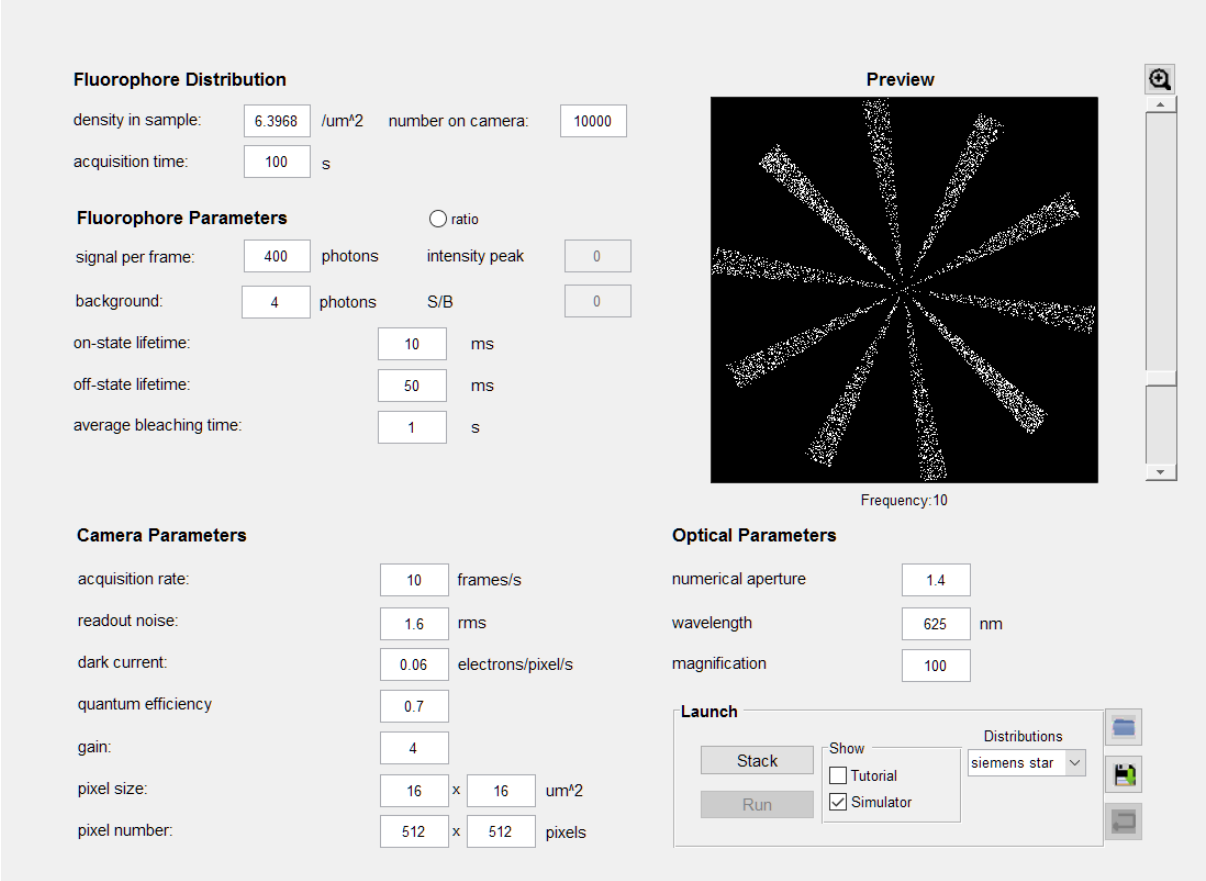


**Figure 61. Print screen of the SOFI simulation tool user interface.** The user inputs experimental parameters, including information about the choice of fluorophore, camera settings, and objective lens, to generate a simulated dataset of a fluctuating fluorophore, distributed in a chosen pattern.

To check the performance of the SOFI simulation tool, in generating realistic SOFI-processed data, the simulated SOFI data was compared against experimental SOFI data. Experimental SOFI-processed data, obtained by imaging β-tubulin-Qdot 625 on an epifluorescence microscope (100x 1.4NA) at 100 ms and processing 1,000 images (100 frames/second) with bSOFI, was compared against data simulated using the same acquisition settings as set in the SOFI simulation tool (Figure 62). A high labelling density of Qdots was chosen, to ensure full coverage of the Siemens star shape and a minimum bleaching time of 1 s was set, since Qdots have negligible photobleaching. The stimulated bSOFI images are comparable to the experimental data in terms of structures being better resolved in bSOFI images than wide-field images, and the apparent degree of artefacts increasing, as the number of orders increase. The joining of point emitters that were in close proximity, to form artificial lines, was more pronounced in higher bSOFI orders. Here, the number of orders was the independent variable, however, it would have been good to compare other parameters, such as exposure time. Each time a simulation is run, a different unique dataset is generated, so

when acquisition settings are changed (e.g. varied exposure times), it is difficult to compare the former SOFI simulated image to the present SOFI simulated image. Despite the SOFI simulation tool, being a great way to predict a bSOFI output image, based on specific acquisition settings, it does have some limitations. For instance, the best magnification available in the SOFI simulation tool is 100x 1.4NA, which under samples the object, according to Nyquist sampling. Additionally, for the SOFI simulation tool to run, the number of fluorophores must not exceed 100,000 and an acquisition rate cannot be faster than 10,000 frames/s. Due to these restrictions, a 100x 1.4NA objective was selected for both the SOFI simulation tool and experimental acquisition on a microscope, which is a lower sampling rate than is typically used in SOFI experiments (100x 1.4NA plus a 2.5x magnifying lens). Despite less options in terms of controlling the acquisition parameters within the SOFI simulation tool, compared to acquiring data on a microscope experimentally, the SOFI simulation tool gives realistic SOFI images, which are comparable to experimental SOFI images. The SOFI simulation tool can, therefore, be used confidently to test parameters that will yield an optimal SOFI image, before going through the process of preparing a sample, imaging on a microscope, and SOFI-processing the data.

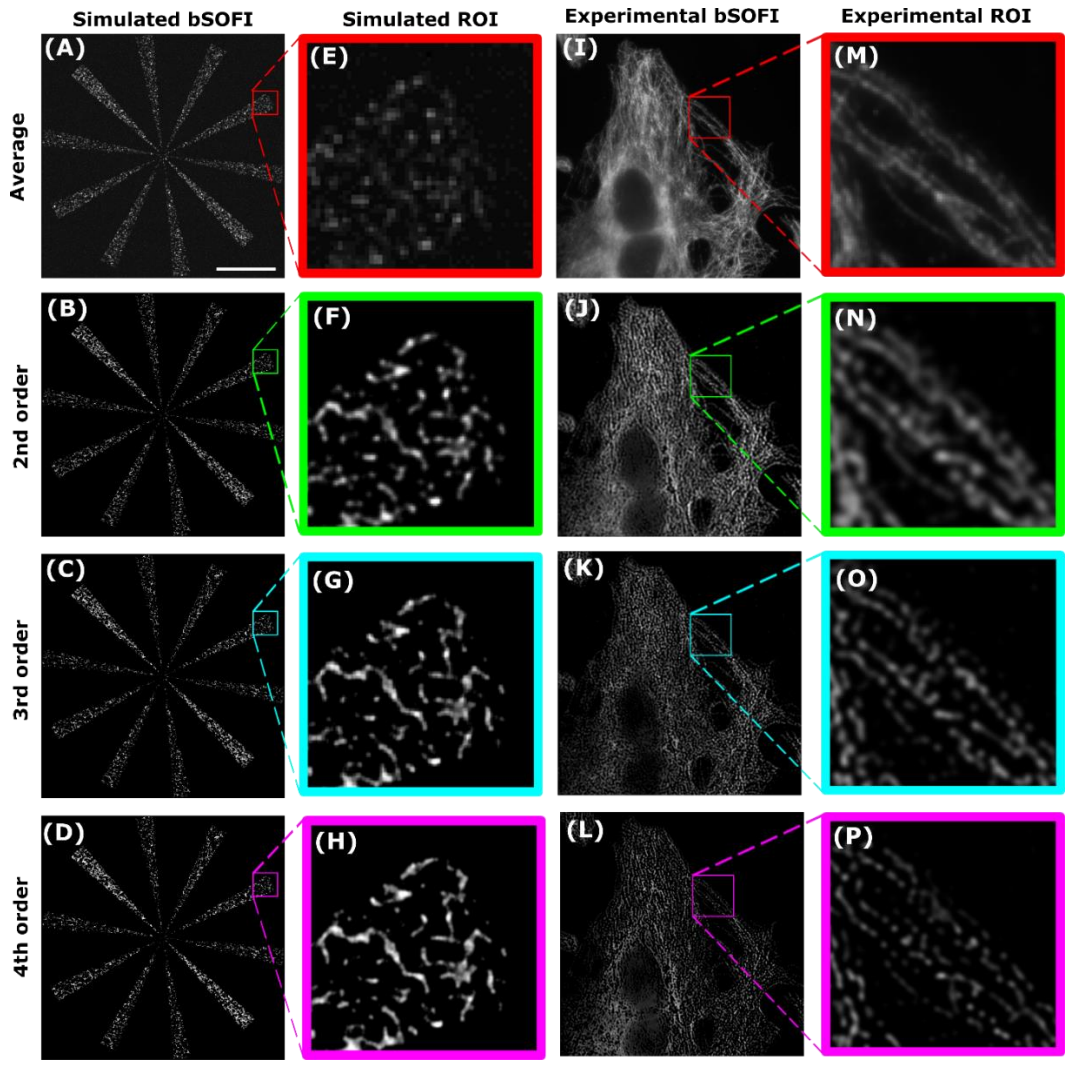


**Figure 62. Simulated bSOFI data compared to experimental bSOFI images.** SOFI simulation tool was implemented in MATLAB to generate a high-density labelled Siemens star pattern, consisting of 10,000 point emitters (emission: 625 nm), which were representative of an optical system (100x 1.4NA) set up with a 100 ms exposure time (100 frames/s). Wide-field (A) and 2$^{nd}$, 3$^{rd}$, and 4$^{th}$ order bSOFI simulated images were generated (B-D) from 1,000 frames. ROIs (E-H) were taken for the stimulated bSOFI images. Experimental data, acquired with microscope settings matching those set in the SOFI simulation tool, was also processed with bSOFI, implemented in MATLAB, to yield an average wide-field (I) and 2$^{nd}$, 3$^{rd}$, and 4$^{th}$ order bSOFI images (J-L). ROIs were also taken from the experimental images (M-P). Scale bar = 20 µm.

## 4.3 Measuring the PSF of an optical system pre-SOFI processing

All structures appear blurry as they are convolved with the PSF of a conventional wide-field microscope, due to the diffraction limit of light. However, there have been ingenious ways to improve resolution, from engineering the PSF shape in confocal based super-resolution microscopy techniques (STED), to using deconvolution algorithms (Lucy-Richardson), and

higher-order statistics approaches (SOFI) (20). A microscopy technique is deemed capable of super-resolution if the optical resolution limit of a wide-field microscope is improved by a factor of two (298). SOFI reduces the PSF by cross-correlating pixels or mathematically re-weighting the PSF (299). Before SOFI improves the spatial resolution of wide-field images, by decreasing the PSF, the resolution capability of the epifluorescence microscope, used to capture images for the post-processing, was determined. The PSF of an optical imaging system defines its resolving power, so it is important to detect any aberrations in the objective lens, as this can affect image quality. An object always appears much larger than its true size, because light from a point emitter is diffracted, which results in ring-like patterns around the central brightest spot (centroid), with the outer rings decreasing in fluorescence intensity. This Airy disk shape (300) best describes the PSF and can be approximated by fitting with a Gaussian function. The PSF can be estimated experimentally by imaging a small fluorescent bead and measuring its width (FWHM). Beads, smaller than the attainable resolution limit of the optical system (250 nm) are used. The PSF is dependent on the wavelength of light emitted from the bead (λ), and the NA of the objective lens used to image the bead (10). Theoretical resolution can therefore, be calculated using $d = 0.61\lambda/NA$ for lateral resolution, and $d = 2\lambda/NA^2$ for axial resolution.

An experimental PSF of the epifluorescence microscope system (100x 1.4NA), used for most of the data acquisition, was determined by acquiring a calibrated (effective pixel size of 160 nm) z-stack (51 z-positions) of spherical 100 nm red fluorescent beads (excitation: 580 nm and emission: 605 nm), considered point sources smaller than the resolving power of the microscope, immobilised on a glass coverslip. Although, the majority of structures in this work have been labelled with red Qdot-Abs, these were not chosen to estimate the PSF of the wide-field imaging system. The size of the Qdot-Abs is not reported by the supplier (Thermo Fisher Scientific, UK), although they have been estimated via FCS to be very large: of the order of >75 nm (149). Despite the physical size of the Qdot-Abs being large, the optical size of a Qdot is small (point emitter). However, Qdots are prone to aggregation and their varied sizes may overestimate the true PSF, which is why well contrasted uniform 100 nm beads were used for the PSF estimation instead. The focal plane was moved through the bead, starting at 5 µm above the bead and ending at 5 µm below the bead, using a step size of 0.2 µm. Using the orthogonal view in ImageJ, an in-focus xy view (lateral PSF), xz side view (axial PSF), and yz side view (axial PSF), of the bead were obtained (Figure 63). As expected, when the bead was in focus and viewed laterally, it was circular, whereas when it was viewed axially, it was symmetrically elongated. A 36 pixels-by-36 pixels ROI was selected at the z-

position where the bead was most in-focus. A line was drawn through a single bead and the plotted intensity profile of its PSF fitted with a one component Gaussian in MATLAB (MathWorks Inc., USA), to calculate its FWHM, as a measure of the optical system's resolution capability (FWHM ≈ 0.353λ/NA or FWHM ≈ $2\sqrt{2ln2} * \sigma$). Although, the beads are known to be 100 nm, due to diffraction limit of light, the beads were expected to appear >250 nm. Theoretical lateral resolution (Airy disk diameter ≈ 0.61λ/NA) for the 100 nm red fluorescent bead (Emission of 605 nm), imaged on a wide-field microscope with 100x 1.4 NA oil immersion objective, was calculated to be 264 nm (xy), whereas the actual experimental FWHM of the PSF was in the order of 597 nm (FWHM ≈ $2\sqrt{2ln2} * \sigma$). According to the literature, if a high-NA objective lens is used, an experimental measurement of the beads should yield a PSF value within 10-40% of the theoretically calculated PSF (10). The larger than expected FWHM value (597 nm), in relation to the theoretical resolution (264 nm), may be as a result of noise, imperfections in the wide-field imaging system, including aberrations in the objective lens.

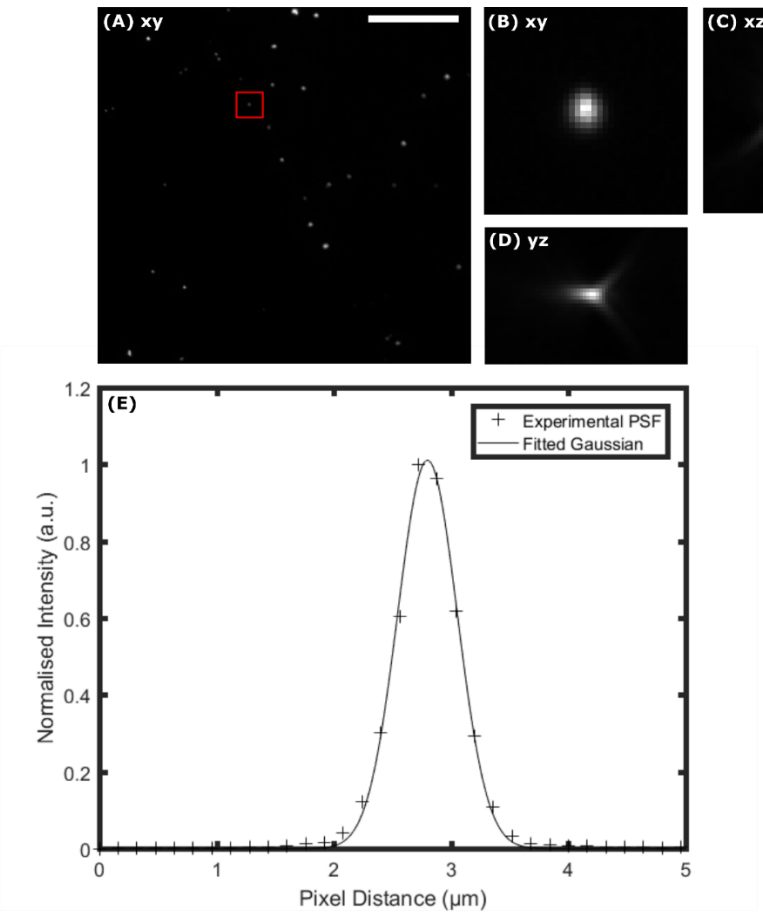


**Figure 63. Representative experimental FWHM measurement of a red 100 nm bead.** A z stack of 100 nm red fluorescent beads (emission maxima of 605 nm) was imaged on an epifluorescence microscope (100x 1.4NA) and a ROI for the z-position where the bead was most in focus (A). Using orthogonal

view in ImageJ, a lateral PSF was imaged as a front xy view (B), an axial PSF as a side xz view (C), and axial side yz view (D). PSF profile and Gaussian fit (E). Effective pixel size is 160 nm. ROI = 36 pixels-by-36 pixels. FWHM of red ROI bead was measured to be 597 nm (FWHM ≈ $2\sqrt{2ln2} * \sigma$). Theoretical resolution, based on beads emitting at 605 nm when imaged at 100x 1.4 NA (0.61λ/NA) = 264 nm. N=1 bead. Scale bar = 20 μm.

As well as estimating an empirical PSF, by calculating the FWHM of a small 100 nm red fluorescent bead manually, a theoretical PSF and an experimental PSF was also automatically determined for the same optical system and 100 nm red fluorescent bead z-stack dataset using PSFGenerator, a MetroloJ ImageJ plugin (253). To run the MetroloJ plugin, the type of microscope (wide-field), emission wavelength of the beads (605 nm), and NA of the 100x oil immersion objective lens (1.4 NA) was input into the software. From the plugin, a report was generated, including xy, xz, and yz maximum intensity projections, theoretical resolutions, and plotted Gaussian profiles. Although, theoretical lateral resolution (0.61λ/NA) in x, y and axial resolution ($2\lambda/NA^2$) in z was determined to be 264 nm and 617 nm, respectively, these were much lower than the automatically calculated FWHM values of 424 nm in x, 492 nm in y, and 1086 nm in z, with the MetroloJ ImageJ plugin (Table 11). A lower theoretical resolution than empirical PSF was predicted since this does not take into account any imperfections in the optical setup and assumes ideal conditions, with no noise. As expected, the spatial resolution in xy was also much better than in xz and yz. Despite discrepancies between theoretical and calculated resolution, it is important to determine the PSF experimentally for the correct application of deconvolution algorithms. However, the experimental PSF estimation, determined by manually calculating the FWHM of a bead from a one-component Gaussian fit in MATLAB (597 nm), differed from the automatically calculated FWHM value using the MetroloJ ImageJ plugin (424 nm). Although both were fitted with a one-component Gaussian function, MetroloJ yielded a narrower curve, which resulted in a lower FWHM value. The MetroloJ plugin, however, uses a maximum intensity projection for the FWHM calculation, rather than an in-focus bead in a single z-position, which was used for the manual FWHM calculation in MATLAB. Due to differences in theorectical resolution and experimentally determined resolution, it is important to measure the PSF of the optical system, which will be used to acquire data for SOFI-processing, so that subsequent deconvolution algorithms can be applied and also the resolution enhancement with SOFI can be accurately estimated.

| Red 100 nm Beads (100x 1.4NA) | Calculated FWHM | Theoretical Resolution |
|---|---|---|
| x | 424 nm | 264 nm |
| y | 492 nm | 264 nm |
| z | 1086 nm | 617 nm |

**Table 11. Generated PSF of a 100 nm bead using PSFGenerator, a MetroloJ ImageJ plugin.** Red 100 nm fluorescent beads were imaged on an epifluorescence microscope (100x 1.4NA) and 51 z-positions recorded from 5 µm below and above the bead, using a step size of 0.2 µm. A ROI bead was cropped and the resulting z-stack input into the PSFGenerator, a MetroloJ ImageJ plugin, which automatically calculated the FWHM of the bead and its theoretical resolution in x, y, and z. Spatial resolution in xy is better than in xz and yz.

## 4.4 Lucy-Richardson deconvolution applied to SOFI images

Using an experimentally determined PSF, a Lucy-Richardson deconvolution algorithm was applied to a SOFI image, to further enhance structural information within the image. Computational methods, such as deconvolution, have been applied to images to increase contrast. Although, applying a deconvolution algorithm to images, does not improve resolution *per se*, it does enhance the contrast and enables structural features to be better characterised (301). Deconvolution is often used to improve the appearance of conventional wide-field images, as a cheaper alternative to using confocal microscopy, because it also removes out-of-focus light (302). Additionally, deconvolution has been used to further improve super-resolution images, including those obtained using STED and SOFI (93). Deconvolution algorithms can consist of either de-blurring, restorative, or blind deconvolution processes (303). An experimental or theoretically calculated PSF is required for restorative deconvolution, where an estimation of what the blurred microscope image should look like pre-convolved with the PSF is obtained. The input image, obtained from the microscope, is compared to the estimated convolved image many times, until the user deems the two images similar in appearance, which is highly subjective. Unlike de-blurring deconvolution, out-of-focus light is not removed, but is instead re-assigned to its original positon, which reduces noise in the image (91). Restorative blind deconvolution, works on the same principles as restorative deconvolution, by applying a filter to convolve the image, except the PSF is not experimentally determined (303). Assuming a Poisson noise distribution in the images, restorative deconvolution, such as Lucy-Richardson and Wiener filtering, are

the most effective deconvolution techniques, because they use an experimental PSF to increase their performance. An experimental PSF is important for optimal Lucy-Richardson deconvolution, because it describes the response of an optical system, so if there are any aberrations in the objective lens, these can be corrected for by the algorithm, to ensure that the object is not misrepresented.

Many different deconvolution softwares are commercially available, including the Huygens deconvolution package, but these can be expensive and are often black-box approaches. Alternatively, a built-in version of Lucy-Richardson deconvolution is available in the MATLAB imaging toolbox and has been incorporated into the bSOFI algorithm. Lucy-Richardson deconvolution assumes that there is Poisson noise in the image, but SOFI images contain cumulant values and not Poisson noise. Therefore, the Lucy-Richardson deconvolution algorithm is applied after bSOFI-processing to correct for any large differences in molecular brightness rather than remove noise, because this should have already been removed during the processing (93). Here, the performance of the restorative deconvolution method Lucy-Richardson on SOFI Localizer data was assessed for different iterations, using the original open-source DeconvolutionLab2 ImageJ plugin (20). After SOFI-processing of β-tubulin-Qdot 625 up to $2^{nd}$ order, using Localizer, implemented in MATLAB, the image was further processed with the non-linear iterative deconvolution algorithm, Lucy-Richardson using the DeconvolutionLab2 ImageJ plugin with 5-20 iterations (standard is 10 iterations). Iteration 5 gave the best deconvolved SOFI image, whilst $\geq$20 iterations gave artefacts, where there appeared to be saturation in brightness at the borders of the processed images (Figure 64).

Logically, the more iterations that were tried, the higher the computational time, but this did not yield the best attainable deconvolved images. The appearance of artificial bright wavy border patterns, known as ringing, mainly around the edges of the images, is likely due to an inaccurate estimation of the PSF, when the signal is Fourier transformed (124, 94). In addition, deconvolution is unable to detect uneven illumination in images, as a result of the mercury arc lamp flickering during image acquisition (302). Ringing can be corrected to a degree, by Fourier-re-weighting the images (88). Lucy-Richardson deconvolution works better on super-resolved images (85), where the SNR is high and there is a high number of frames (116). If Lucy-Richardson deconvolution is to be applied to SOFI images, it is best to avoid the use of higher-SOFI orders, because the number of ringing artefacts increases as the SNR decreases with successive SOFI orders (124). Adaptations to the Richardson-Lucy deconvolution algorithm are still under development for use on higher-order SOFI images. In conclusion, visually, there was not much difference between the SOFI-processed image and

the application of Lucy-Richardson deconvolution, so it was decided not to apply this extra processing step to future SOFI-processed images, to prevent the possibility of introducing artefacts into the image.

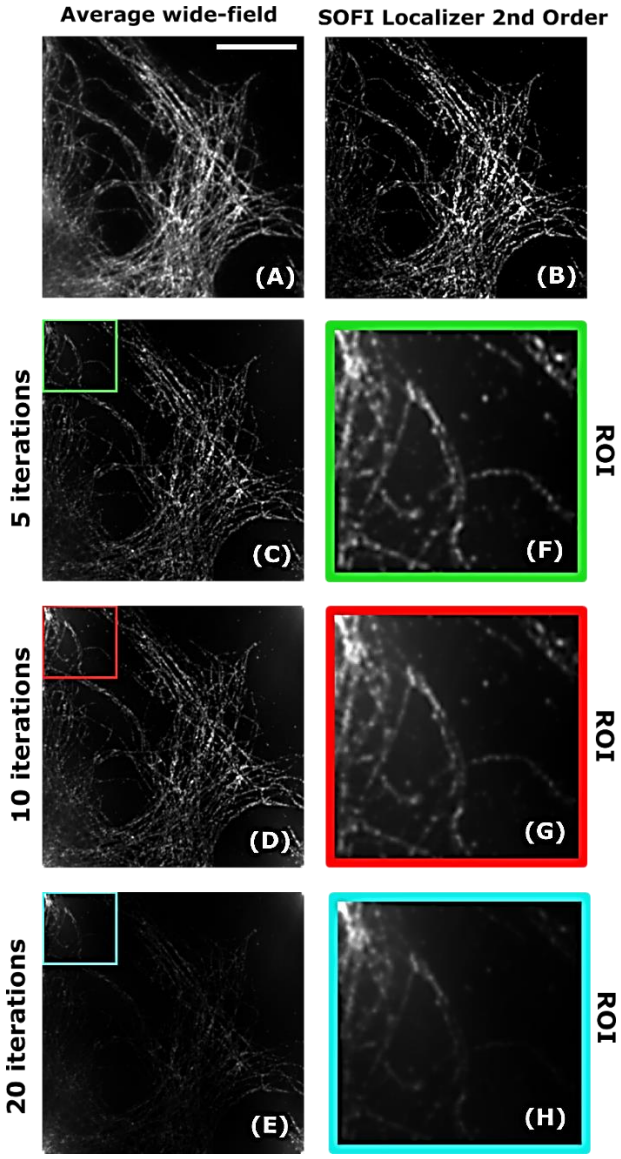


**Figure 64. Testing Lucy-Richardson Deconvolution on 2nd order SOFI images.** Wide-field images of β-tubulin-Qdot 625 (A) were acquired on an epifluorescence microscope (100x 1.4NA plus 2.5x magnifying lens) at 100 ms and SOFI-processed to 2nd order using Localizer software, implemented in MATLAB (B). After SOFI-processing, these images were further processed with the deconvolution algorithm Lucy-Richardson in the DeconvolutionLab2 ImageJ plugin (C-E). ROIs are shown for different iterations 5-20 (F-H). The worst deconvolved SOFI image was at 20 iterations (H) and the best attainable deconvolved SOFI image was at 5 iterations (F). Scale bar = 20 µm.

## 4.5 SOFI compared to other super-resolution techniques

Some super-resolution techniques complement others, and although SOFI has better temporal resolution than PALM and STED, it cannot achieve the same spatial resolution (116). By applying different processing algorithms to the same dataset, additional details about the biological structure can be revealed. To date, SOFI has been combined with several microscopy techniques, including SIM (117), PALM (116), STORM (114, 120), FCS (113), Förster resonance energy transfer (FRET) (283), AFM (45), and LSFM (32). To demonstrate and compare the resolving capability of different super-resolution techniques, β-tubulin, in fixed HeLa cells, was imaged using a variety of super-resolution methods, including dSTORM, SIM, STED, SOFI and SRRF (Figure 65). All of the super-resolution techniques used here have advantages as well as disadvantages associated with their use, as mentioned previously (Chapter 1), so often trade-offs between resolution, FOV, and speed are accepted as a compromise. Depending on the technique used, β-tubulin was labelled with either Alexa Fluor 647 (SIM and dSTORM), Abberior STAR 580 (STED), or Qdot 625 (SOFI and SRRF). For STED imaging, a Leica TCS SP8 STED 3x microscope (100x 1.4NA) was used to acquire a z-stack of β-tubulin-Abberior STAR 580 and the resulting STED image post-processed with Huygens deconvolution software (data kindly acquired by Peter Hemmerich at the imaging facility in the Leibniz Institute on Ageing, Fritz Lipmann Institute, Jena, Germany). The deconvolved STED image was displayed as a maximum intensity z projection. dSTORM imaging was done on the Zeiss Elyra P.S.1 system (63x 1.4 NA plus additional FOV lens: TIRF-UHP), where a freshly prepared imaging buffer, containing the thiol MEA (pH 9) and 10 nM NaOH, was added to fixed β-tubulin-Alexa Fluor 647 (sample kindly provided by Carl Zeiss Microscopy GmbH, Jena, Germany) prior to acquisition. For sufficient single molecule blinking, needed for dSTORM, a stack of 30,000 images was acquired with 100% of a 150 mW 642 nm laser and 0.5% of a 50 mW 405 nm at 30 fps in laser wide-field mode. dSTORM-processing was done in ZEN software, using the measured PSF. Furthermore, to obtain a SIM image of β-tubulin, a z-stack (10 positions) of β-tubulin-Alexa Fluor 647 was acquired with a 1% of a 150 mW 642 nm laser at 100 ms on the Zeiss Elyra P.S.1 system using 5 rotations. SIM-processing was done in ZEN software and a maximum intensity z projection was performed on the raw data in ImageJ. For SOFI and SRRF post-processing, 1,000 frames of β-tubulin-Qdot 625 was acquired on a laser wide-field system (100x 1.4NA) at 33 ms (~30 fps). Second order SOFI-processing was done with Localizer, implemented in MATLAB, whilst SRRF-processing was done with the ImageJ plugin NanoJ-SRRF.

All of the super-resolution techniques tried, yielded thinner β-tubulin fibres than in the conventional images, but with some skeletonised artefacts for SIM and SRRF, as a result of drift and use of a small ring radius, respectively. A 2$^{nd}$ order SOFI image should obtain the same resolution as SIM (factor of 2) (50), but here, the resolution for SOFI looks more like a factor of √2 using the Localizer implementation. Owing to the nature of the technique, β-tubulin fibres in the dSTORM image are discontinuous, compared to the more continuous fibres in the SOFI-processed image, even though a higher number of frames was used for dSTORM (30,000 frames) than SOFI (1,000 frames). Despite SOFI and dSTORM relying on the photoswitching of fluorophores, dSTORM requires a high laser power, whereas SOFI can be performed on data acquired with a low power mercury arc lamp or LED, which may account for some photobleaching in the resulting dSTORM image. Similarly, STED also needed a high laser power to achieve a reasonable super-resolution image. Nevertheless, all five super-resolution techniques have been successfully used to resolve β-tubulin visually, to a different degree. The resolution enhancement could not be quantified and compared for each super-resolution technique, because a different sample was used on multiple imaging systems. Essentially SRRF and SOFI could have been performed on the same dataset used for dSTORM-processing (120). Furthermore, these super-resolution approaches were tried in fixed cells, so to fully replace other microscopy methods such as TEM, for the imaging of structures below the nanoscale, these would need to be adapted for artefact-free live cell imaging. Out of all of the techniques, SOFI, SRRF, and SIM are thought to be best suited for live cell imaging, through the use of fluorescent proteins. Another interesting approach would be to image biological structures with both SOFI and TEM. Proteins of interest in live cells can be labelled with Qdot-nanobodies, through microinjection, and imaged on a fluorescence microscope for SOFI-processing. Using a gridded dish, the same area of Qdot-nanobodies that was imaged with fluorescence microscopy, for SOFI-processing, can be imaged with TEM by fixing the sample, to provide a high-resolution image of the architecture of structures surrounding the proteins of interest. This combined approach with TEM has been used previously to validate dSTORM (61). Although, TEM has a better spatial resolution than dSTORM, it cannot image thick samples or use multiple different coloured probes, except few different sized metal cores that can be discerned (114). Although, the spatial resolution of dSTORM is superior to SOFI, these two super-resolution techniques have been combined, because unlike SOFI, dSTORM is prone to narrowing artefacts, due to overlapping fluorophores, which can result in underestimation of a structure's width (114). Based on observations reported in the literature and data presented here, it is clear that although all

of the super-resolution techniques removed out-of-focus light, to give a sharper, more-contrasted image than with conventional microscopy, in agreement with other researchers, there was variation in the thickness and continuity of microtubules, so to achieve an optimal super-resolution image, the best features of each technique should be combined.

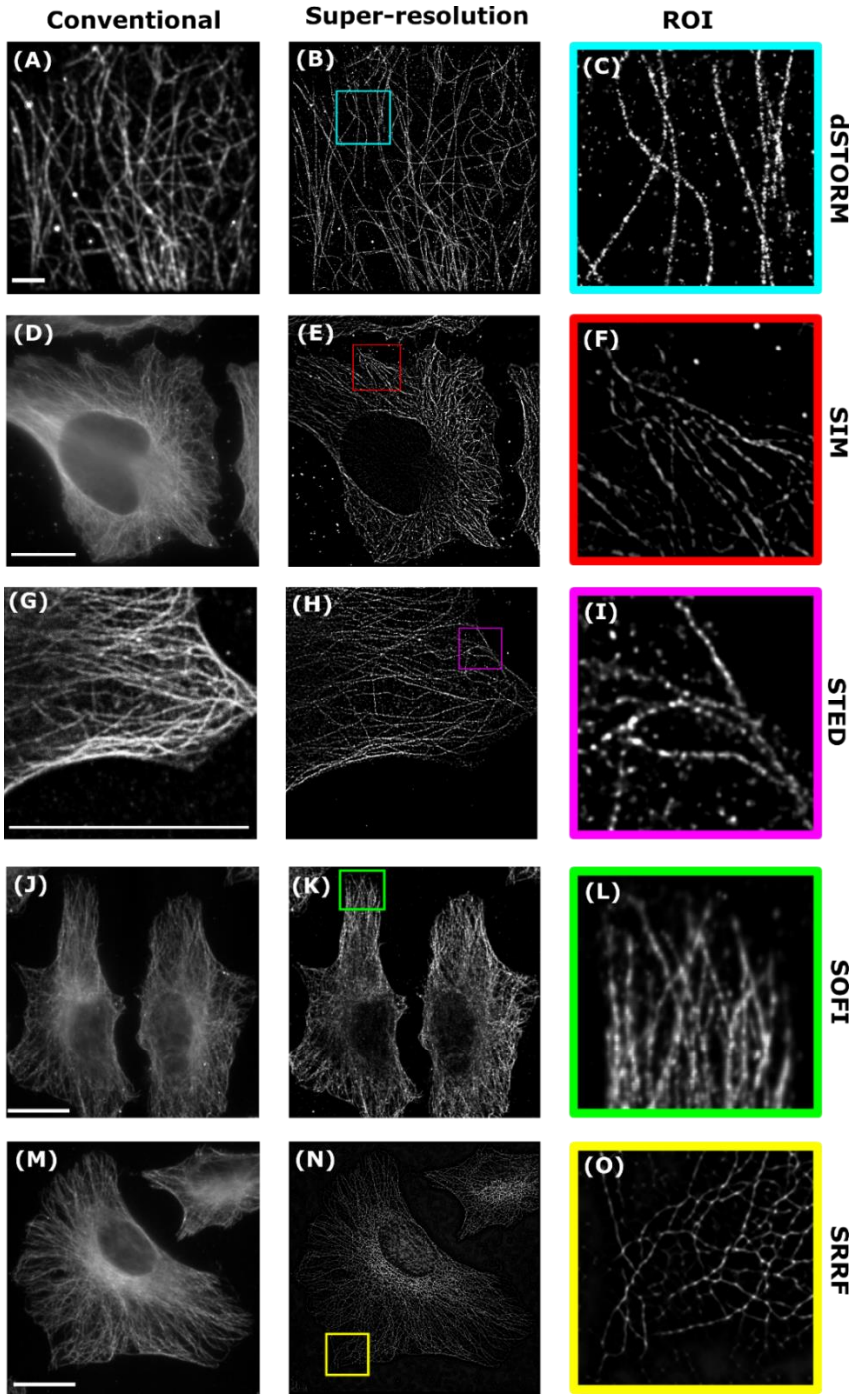


**Figure 65. Comparison of super-resolution techniques.** To compare different super-resolution techniques, β-tubulin was labelled with Alexa Fluor 647 (A-F), Abberior STAR 580 (G-I), and Qdot 625 (J-O). Sample used for images A-C was kindly provided by Carl Zeiss Microscopy, Jena, Germany. Conventional images (A, D, J, and M) were acquired with laser wide-field systems, except (G), which was taken on a confocal microscope. Corresponding super-resolution images are shown: dSTORM (B), SIM (E), STED (H), SOFI (K), and SRRF (N), along with ROIs (C-O). N=1cells. Scale bars = 20 µm.

## 4.6 Obtaining three-dimensional SOFI data

### 4.6.1 Applying SOFI to light-sheet data

To increase temporal resolution, SOFI has been combined with LSFM (32), since SOFI is able to achieve a high-resolution image in 1.25 s (97). LSFM, or SPIM, as it is otherwise known, is typically used to acquire images of large organisms, such as *Drosophila melanogaster* (28, 29). However, due to the broad sheet of light providing poor depth penetration into thick tissue samples, and limited temporal resolution, LSFM can be combined with SOFI, to yield images with better optical sectioning and spatio-temporal resolution (32). Other benefits of using LSFM include its fast acquisition, through capturing pixels simultaneously on a sCMOS camera, and high SNR with respect to wide-field microscopy, since the sheet of light only illuminates a section of the sample (304). Applying SOFI to LSFM is predicted to improve the SNR further, whilst maintaining a large FOV.

Here, SOFI was applied to light-sheet data (light-sheet-SOFI). On loan from Carl Zeiss Microscopy, a specialised sample holder comprising of tweezers was used to suspend a 5 mm x 5 mm coverslip (305) for imaging cell monolayers on the light-sheet Z.1 (Figure 66A). Although, care was taken to ensure that the surface area of the micro-sized coverslips was completely covered with antibodies, often the edges of these small coverslips were better labelled, than the core of the coverslip for reasons unknown. To prevent drift in the sample acquisition, which would negatively affect the correlations for SOFI-processing, the incubation of the light-sheet was set to RT for 1 h before acquisition. As previously, β-tubulin was labelled with Qdot 625 by indirect immunofluorescence and imaged with 100% of a 20 mW 561 nm laser with the coverslip at a 45 ° angle to the detection objective. After acquisition of a 1,000 frame stack of β-tubulin-Qdot 625 on the light-sheet, at four different z positions (discrete steps), these were SOFI-processed. In order to image as close to Nyquist sampling as possible, a 40x 1.4NA detection objective with maximum zoom was used. Due to the nature of a light-sheet, only part of the cell was in-focus at each z position, so after SOFI-processing a maximum intensity projection of the z-stack was taken in ImageJ in order to display an in-focus cell (Figure 66). Through optical sectioning, a 3D light-sheet-SOFI image was reconstructed. To extract further information, a pseudo colour-code could be added to this maximum z-projection, to indicate where the Qdots are in the sample. It was clear that the out-of-focus light had been removed in the 2$^{nd}$ order SOFI image, to yield a high SNR light-sheet-SOFI image, however, this resulted in a loss of information, due to the removal

of dim fluorophores during the processing (Figure 67D). Resolution improvement obtained with light-sheet-SOFI was quantified by taking a line scan through a β-tubulin-Qdot 625 fibre in both the average wide-field and SOFI-processed images (Figure 67). Data were plotted and a Gaussian curve fitted to the data. The width of the Gaussian (FWHM) was narrower for the SOFI image than the average wide-field image. An 18 % decrease in FWHM was achieved for the 2$^{nd}$ order SOFI image. The width of the conventional light-sheet used here was too thick (approximately double the depth focus of the 40x 1.4NA detection objective) to fully benefit from SOFI, so the resolution attainment of the complementary pairing of light-sheet-SOFI could be further improved using a lattice light-sheet, which creates an ultra-thin sheet of light (31).

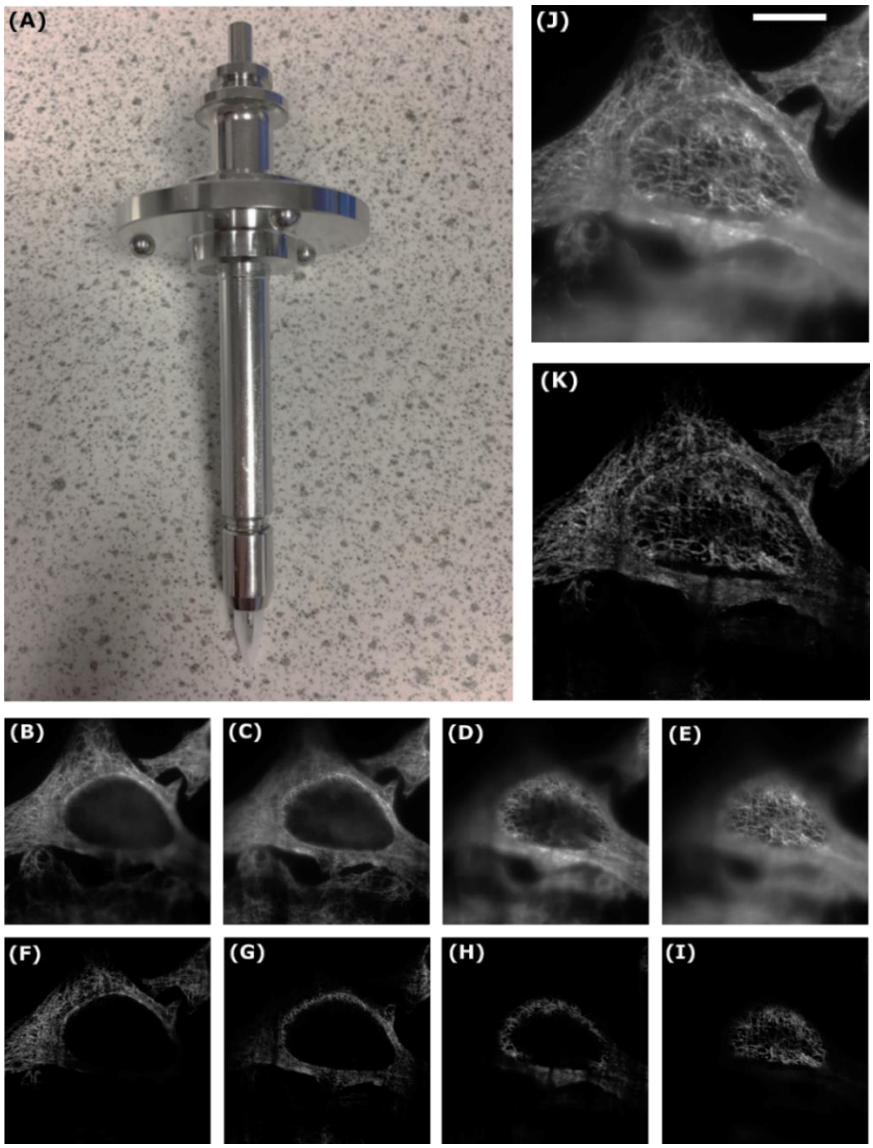


**Figure 66. Combining light-sheet and SOFI.** Button at the top of the light-sheet sample holder (A) is used to open and close the tweezers at the base, where a 5mm x 5 mm coverslip is clamped at a 45° angle and suspended in the water-filled chamber facing the detection objective. HeLa cells were fixed

with methanol and β-tubulin labelled with Qdot 625 by indirect immunofluorescence on a 5 mm x 5 mm glass coverslip and Qdot fluctuations acquired over 1,000 frames at 4 different z positions (0.5 µm step) on a Z.1 LSFM (40x 1.0 NA detection objective plus maximum zoom, 2 illumination 10x 0.2 NA objectives). Each stack was SOFI-processed using Localizer, implemented in MATLAB, and the average wide-field (B-E) and SOFI (F-I) images concatenated into z stacks in ImageJ. Maximum intensity projections were taken of the z stacks to reconstruct the entire cell in the average wide-field image (J) and SOFI-processed image (K). Scale bar = 10 µm.

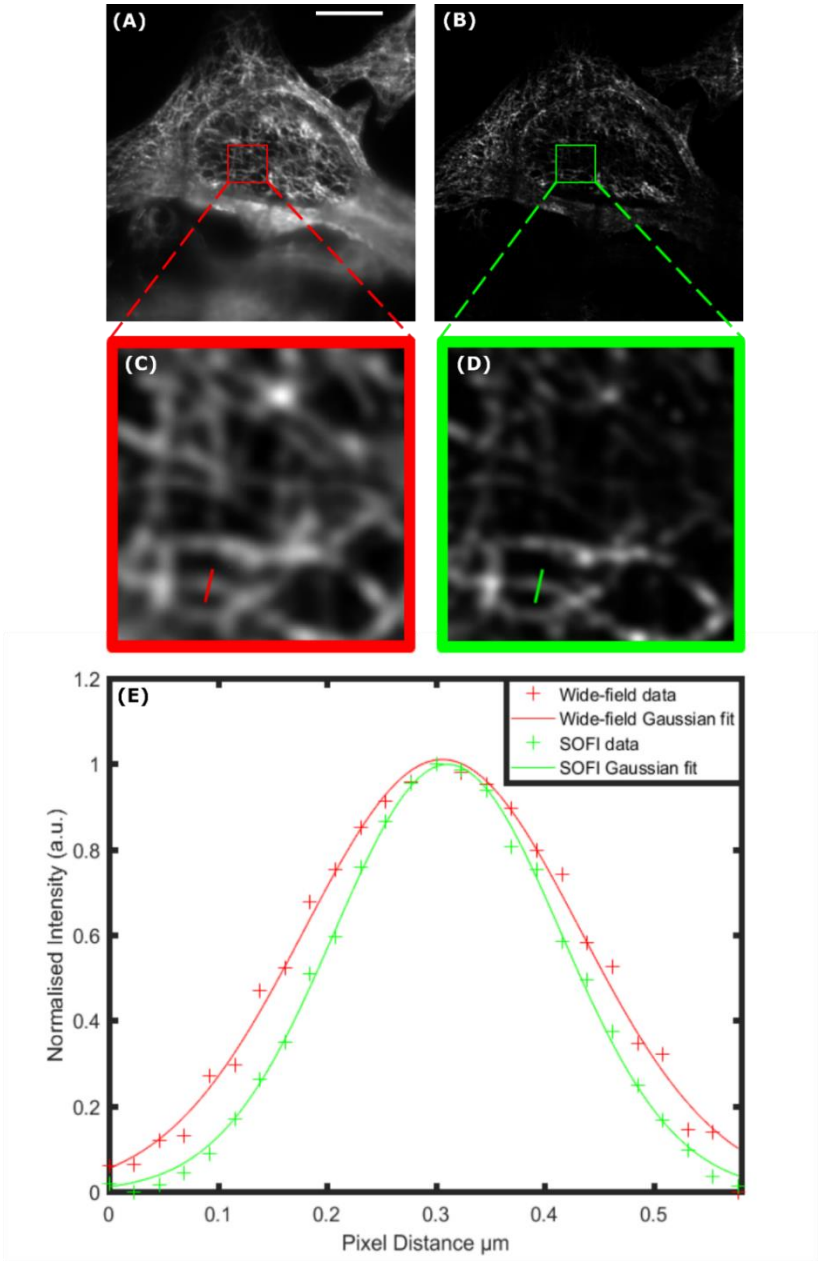


**Figure 67. Quantifying the resolution improvement of light-sheet-SOFI.** Maximum intensity projections of the average wide-field (A) and SOFI-processed (B) images from Figure 66 were quantified. Line scans were taken through a β-tubulin-Qdot 625 fibre in the red ROI for the average wide-field image (C) and green ROI for the SOFI-processed image (D). Data was plotted and a Gaussian curve fitted to the data. Scale bar = 10 µm.

### 4.6.2 Reconstructing a 3D SOFI image through taking z-stacks

As shown previously, by combining LSFM with SOFI, a 3D SOFI image can be reconstructed by taking 2D image z-stacks. LSFM already gives improved SNR compared to wide-field microscopy, prior to SOFI-processing, due to the optical sheet of light providing less out-of-focus light to the sample. To appreciate the optical sectioning ability of SOFI, z-stacks were taken on an epifluorescence microscope with more out-of-focus light and SOFI-processed. Although, 3D super-resolution imaging has been achieved with several methods including SIM (57), STED (306), and STORM (16), it is still a challenge for live cell imaging, due to high laser powers and the use of antibodies, which requires fixation. However, resolution can be improved in all three directions, in live cells, through the exceptional optical sectioning ability of SOFI using RSFPs (105). The imaging of thick tissue samples will also benefit from using 3D SOFI (86). A 3D SOFI image has been reconstructed by acquiring stacks of images at different z-positions (optical sections) sequentially and calculating 2D cross-cumulants (85, 86, 105). Simultaneous acquisition of different z-positions has also been achieved by calculating 3D cross-cumulants (161). Here, information was obtained in all three directions, by labelling β-tubulin with Qdot 625 using indirect immunofluorescence and acquiring 1,000 frame stacks sequentially on a wide-field system (63x 1.4NA plus 1.6x magnifying lens), at 10 different z-positions from 0-4.5 µm in 0.5 µm increments. Each z-position stack of 1,000 frames was SOFI-processed by calculating 2D cross-cumulants with Localizer, implemented in MATLAB, and a SOFI z-stack reconstructed to provide an average intensity projection, representing a 3D SOFI image (Figure 68). To extract further information, depth colour coding (LUT Rainbow RGB) was added to these maximum z-projections in ImageJ, to indicate how deep (0-4.5 µm) the Qdots, labelling β-tubulin, were in the sample (Figure 69). Here, a sCMOS camera was used for the acquisition of β-tubulin-Qdot 625, because sCMOS cameras have more numerous, yet smaller pixels than an EMCCD camera, so it was expected to yield a slightly better resolved SOFI image (26). Resolution improvement along the optical axis can be determined by taking a cross-section through xz, although, in this case it was not necessary to estimate the resolution enhancement, because it was visually apparent that the optical sectioning had improved with SOFI, through colour-coding the different z-positions. Substantial out-of-focus light had been removed by acquiring z-stacks, as shown by the less hazy signal in the colour-coded projection of 2$^{nd}$ order SOFI, compared to the average wide-field image. Although, the 2$^{nd}$ order SOFI image revealed more depth information, of the Qdots at different z-positions, weak structures were not well-displayed in the 2$^{nd}$ order SOFI-

processed image (Figure 69). Nevertheless, the improved optical sectioning of SOFI, which reveals additional 3D information about a structure of interest, compared to wide-field microscopy, is worth compensating for the loss of some lower emitting fluorophores.

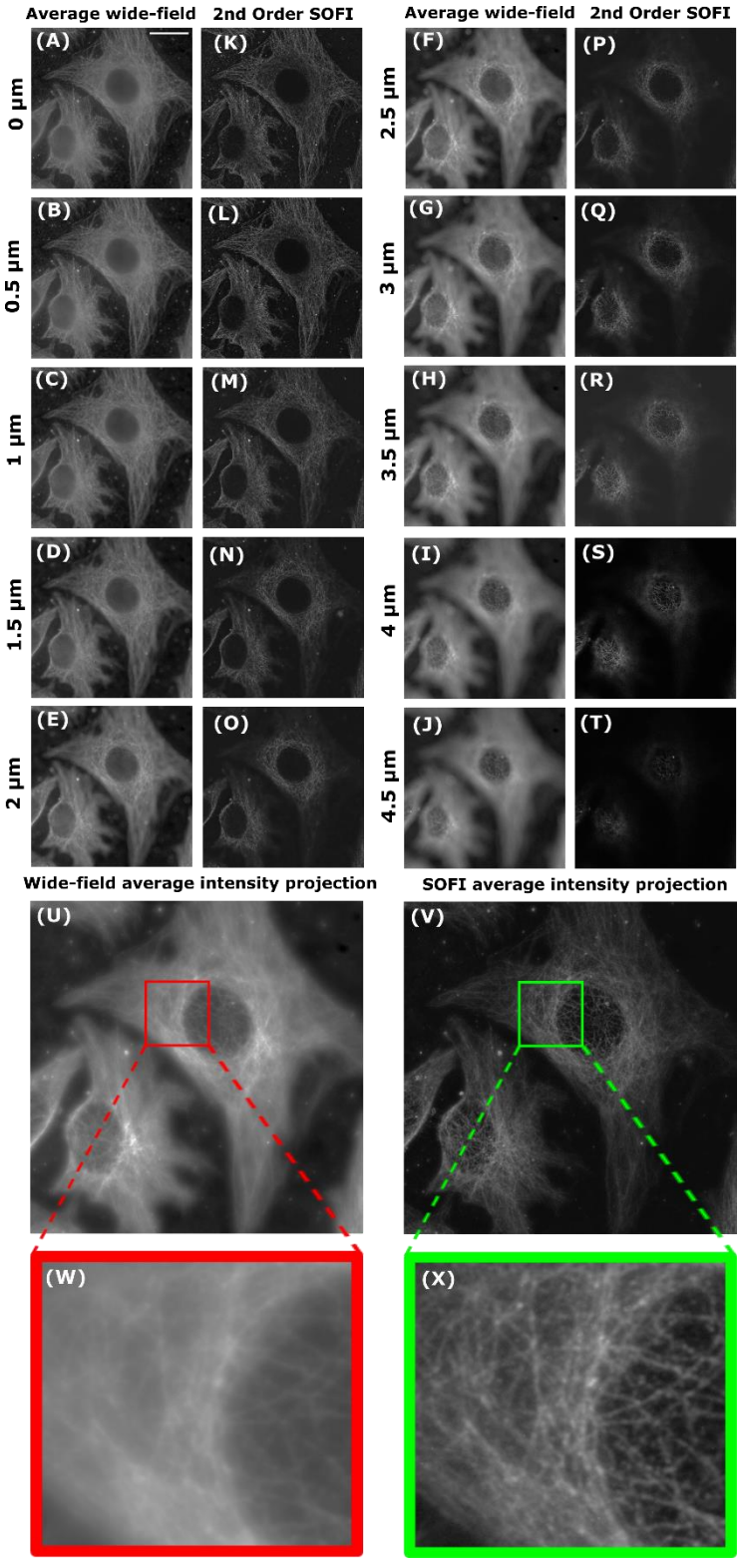


**Figure 68. Optical sectioning capability of SOFI**. Ten 1,000 frame stacks of β-tubulin-Qdot 625 were taken at different z-positions in 0.5 µm increments (63x 1.4NA plus 1.6x magnifying lens) and each

stack SOFI-processed up to 2nd order with Localizer, implemented in MATLAB. Average wide-field (A-J) and SOFI-processed (K-T) images are shown for each z stack. Average intensity projection for wide-field (U) and SOFI (V) images were used to reconstruct 3D information, with corresponding ROIs (W and X) shown. Scale bar = 20 µm.

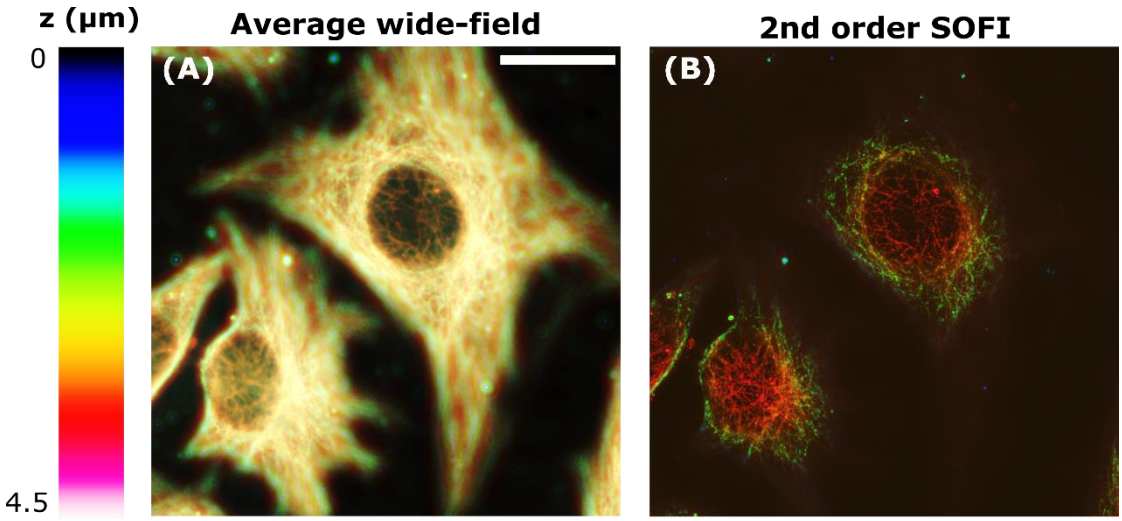


**Figure 69. Depth colour-coded optical sectioning of SOFI.** The depth-coded option (LUT Rainbow RGB) in the open-source software ImageJ was applied to an average wide-field z-stack (A) and 2nd order Localizer SOFI-processed z-stack (B). A colour from blue (0 µm) to magenta (4.5 µm) was applied to 10 different z-positions. Scale bar = 20 µm.

### 4.6.3 Three-dimensional SOFI using PRILM

Optical sectioning by taking z-stacks, above and below the focal plane, reduces out-of-focus light, but extended information about the axial (z) position of the Qdot, can be encoded in the PSF, to yield an improved 3D super-resolution image. There are different approaches to 3D super-resolution microscopy, including through astigmatism by adding a cylindrical lens into the light path (16, 307, 265), creating a double-helix PSF (308), using a phase retrieval instrument with super-resolution microscopy (PRISM) (309), by combining multiple defocused planes (310), and by engineering the PSF of an optical system using PRILM (17). The principle of using PRILM to obtain a 3D SOFI image has already been used in SMLM techniques, including dSTORM, implemented in the Carl Zeiss Microscopy GmbH Elyra PS.1 system (3D PALM slider). Essentially, the PSF is split into two equal lobes by inserting a phase ramp, in the form of an angular cylindrical shaped glass (akin to a DIC prism slider), across half of the pupil of an objective lens (after the sample). The angle of the phase ramp can be adjusted to bring the lobes closer together or further apart (17). The lobes can rotate around

an axis in opposite directions when defocused to distort the PSF (17). For this PRILM approach, a different SOFI algorithm, involving the calculation of additional 3D cross-cumulants, is required. Although, a 3D SOFI implementation is not yet freely available, for this work, an implementation being developed by Carl Zeiss Microscopy GmbH was validated whilst on an industry placement (Jena, Germany). β-tubulin was labelled with Qdot 625 by indirect immunofluorescence and 1,000 frames acquired on a wide-field system (63x 1.4NA plus 1.6x magnifying lens) at 30 fps (33 ms exposure time), in the presence of a 1.5' wedge angle phase ramp. The phase ramp was used to split single Qdots in half, so that the β-tubulin structures appeared doubled (Figure 70). When the 3D cross-cumulants algorithm was applied to the dataset, the singular lobes were reformed, so that doubled β-tubulin structures were collapsed into single structures, before the reconstruction of a 3D SOFI image from the different z-positions was implemented. From experience, if over-sampling is used, this must be taken into consideration when calculating higher-order 3D cross-cumulants, otherwise instead of two lobes collapsing into one lobe, an intermediate lobe would appear (total of 3 lobes). Inclination angle of the left and right lobes, were also incorporated into the 3D cross-cumulant algorithm, along with the number of cross-correlations, as already included in 2D SOFI algorithm. As well as achieving 3D SOFI images through engineering the PSF and encoding depth information, the issue of multicolour images requiring sequential imaging or multiple cameras, can also be tackled by directly encoding spectral information (colour) into the PSF (18). When two proteins, labelled with different coloured fluorescent probes, are in close proximity, their PSFs will evidently overlap, which is a nuisance for fitting localisation based techniques, but not a concern for SOFI (311). The PSF can be re-shaped for different wavelengths (different coloured fluorescent probes) by applying different optical masks, which shifts the PSF laterally in either the x or y directions, for green and red fluorescent probes, respectively (18). Here, PSF engineering, through the use of PRILM, was used to obtain additional information about the z-position of Qdots labelling β-tubulin, which can be used to reconstruct a 3D SOFI image. Using a 3D cross-cumulant algorithm, the doubled β-tubulin microtubules, due to the addition PRILM, were reformed into single SOFI-processed fibres.

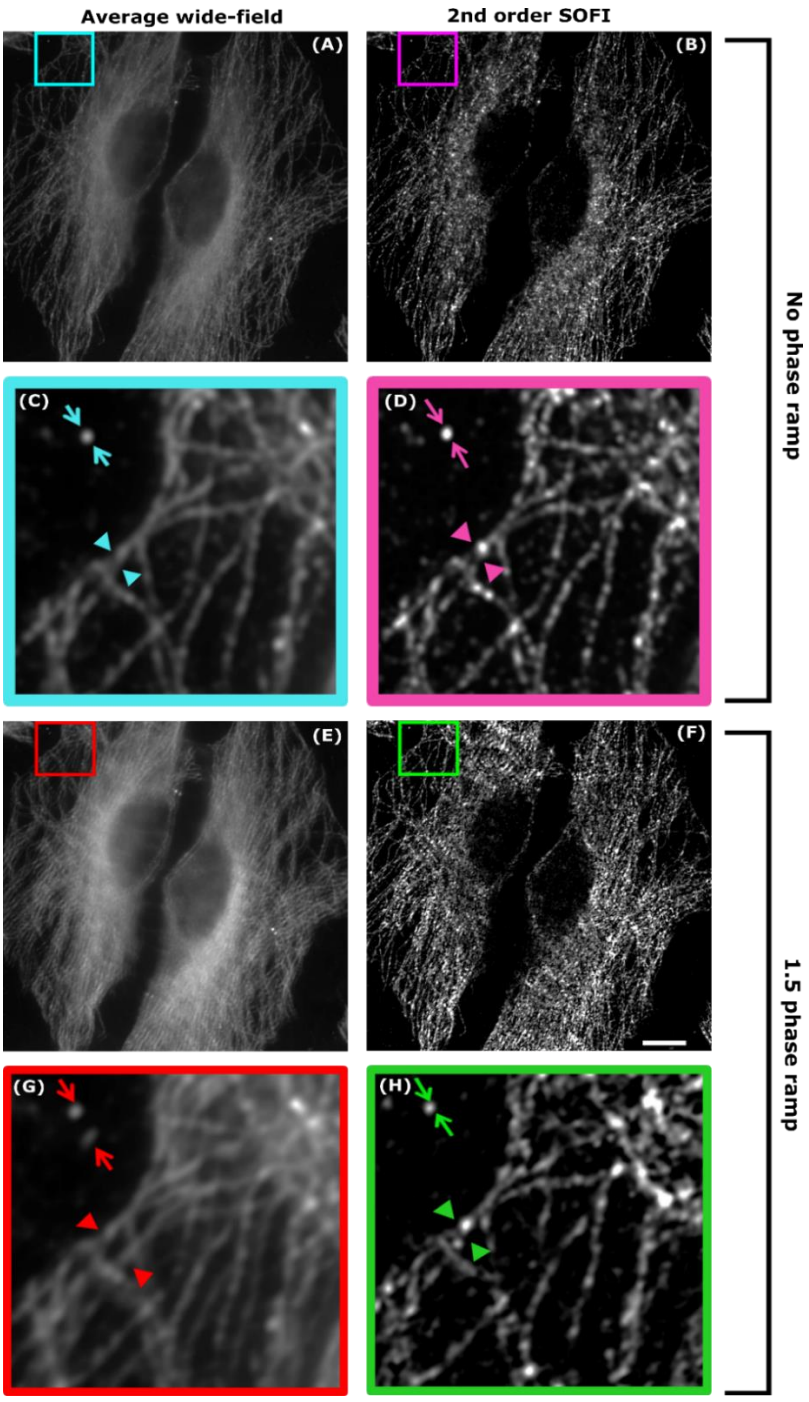


**Figure 70. SOFI-processing using PRILM.** Fixed HeLa cells were labelled with a β-tubulin primary antibody and a Qdot 625 secondary antibody by indirect immunofluorescence. A stack of 1,000 frames were imaged over time on an epifluorescence microscope (63x 1.4NA plus a 1.6x magnifying lens) at 30 fps, with and without a 1.5' wedge angle phase ramp (1.5 phase ramp). A stack of images without a phase ramp was SOFI-processed up to 2$^{nd}$ order using a custom-written 2D cross-cumulants code, implemented in ZEN, to yield an average wide-field image (A) and SOFI image (B). Cyan and magenta ROIs, from the no phase ramp average wide-field and SOFI images respectively, show single Qdots and single β-tubulin fibres (C & D). The stack of images with a phase ramp added was also SOFI-processed, but with a custom-writted 3D cross-cumulants code in ZEN, to yield an average wide-field image (E) and SOFI image (F). Red ROI from the average wide-field shows doubled structures (red arrows), where the PSF has been split into two lobes through the addition of a phase ramp (G), whereas the green ROI of the SOFI image, shows singular structures, where the singular lobes have been reformed (H). Scale bar is 10 µm.

## 4.7 Evaluation of current SOFI implementations

After comparing different SOFI implementations to other super-resolution microscopy techniques, currently available as either an open-source platform or as a commercial setup, it is clear that one approach does not fit all biological applications. The Localizer implementation of SOFI is easy-to-use and provides a raw SOFI image, whereas the bSOFI implementation is less intuitive and prone to artefacts, as a result of further deconvolution. Despite this, both implementations yield better resolved images than wide-field microscopy, but both suffer from artefacts using higher-orders. Each super-resolution technique has associated advantages and disadvantages, where there must be a trade-off between acquiring images at a fast speed and obtaining a high-resolution image. Although, SOFI does not match the resolution improvement attainable by other super-resolution methods, such as dSTORM, out-of-focus light removal alone could be beneficial for retrieving biological structures that would otherwise be lost with wide-field microscopy. An ideal 3D super-resolution technique also does not exist, so a combination of SOFI with other super-resolution methods is a viable compromise. Although, SOFI was applied to light-sheet data here, further resolution enhancement could be achieved using a lattice light-sheet, which benefits from having a thinner sheet of light. SOFI certainly will not make other super-resolution microscopy techniques obsolete, but rather complement them, in unravelling complex biological problems, which would otherwise remain unsolved with conventional wide-field microscopy. From a user's perspective, the interface of Localizer was more user friendly than bSOFI, and it can perform more functions, such as dSTORM analysis. Since the Localizer implementation gives more of a raw SOFI image, than bSOFI, with less artefacts, it was decided to use the Localizer algorithm, without any further deconvolution step, for the post-processing of structures, to address several biological questions (Chapter 5). Regardless of the super-resolution technique used, artefacts in images is a major concern, because they may lead to a misinterpretation of information about a biological system. Here, all of the known quantitative methods was used to assess the quality and resolution of SOFI images, including the conventional line profile FWHM determination of resolution enhancement, FRC calculation, SNR estimation, and NanoJ-SQUIRREL. Although, there is currently no universally accepted way amongst the microscopy community, to definitely determine the resolution and quality of a SOFI image, it is worth using all of the quantitative methods, because each one provides different information about the super-resolution image.

# Chapter 5: Exemplar SOFI applications

For biologists to apply SOFI to specific biological questions requires a collaborative network in terms of chemists to supply the fluorescent probes that blink on a suitable timescale for SOFI, physicists to develop the optical platforms, and mathematicians to provide the computational algorithms (51). Although, many biological structures have been resolved with SOFI, few publications use SOFI to address specific biological questions. This chapter aims to utilise available fluorescent probes and apply the Localizer SOFI implementation to resolve proteins of interest.

## 5.1 Investigating HIF-2α interactions using super-resolution microscopy

HIFs are essential to regulating oxygen homeostasis, through the transcription of key genes, such as VEGF. Since HIF isoforms have important implications in physiological and pathological conditions, including cancer metastasis and wound healing, it is crucial that their role in the adaptation to hypoxia (low oxygen) is better understood (172). Using microscopy, it was previously established that the nuclear localisation of the transcription factor HIF-2α differs from the other HIF isoform, HIF-1α (185). The distribution of HIF-2α was in speckles during hypoxia and normoxia, whereas HIF-1α was more homogenous, and only present under hypoxic conditions (185). Furthermore, HIF-2α speckles have also been shown to co-localise with active transcription sites, such as Phospho Ser5 RNA Pol II (186). All of the aforementioned results were obtained using low-resolution wide-field or confocal microscopy. Although, co-localisation may exist with conventional microscopy techniques, due to the diffraction limit of light, the two interacting proteins, HIF-2α and Phospho Ser5 RNA Pol II, may be discerned with super-resolution microscopy to instead show no co-localisation between them. HIF-2α and associated proteins could have been imaged at high-resolution with EM, but this requires laborious fixation protocols to prevent artefacts and two-colour EM is challenging. It is hoped that by super-resolving HIF-2α, a better understanding about the role of HIF-2α within hypoxia will be achieved. The main aims therefore, were to better differentiate HIF-1α and HIF-2α in terms of sub-nuclear localisation, specifically determine HIF-2α localisation in speckles using super-resolution approaches, and assess the impact super-resolution imaging has on the co-localisation of resolved HIF-2α with potential binding partners, such as Phospho Ser5 RNA Pol II. Prior to

doing super-resolution co-localisation, different fluorescent probes were assessed for use with SOFI, including the creation of molecular tools (HIF-2α-Skylan-S). Other super-resolution approaches were also explored, including Airyscan and SRRF, which after some two-colour optimisation, were found to be the best methods for co-localisation studies. The objectives of this collaboration were therefore to measure the size and number of super-resolved HIF-2α speckles, as well as to quantify, from super-resolved images, any co-localisation with known binding partners.

### 5.1.1 Resolving HIF-2α with SOFI

Interestingly, most of the super-resolution publications demonstrate resolution enhancement of filamentous structures, such as β-tubulin, rather than the arguably more interesting nuclear proteins. To date, the transcription factor HIF-2α has not yet been resolved using super-resolution microscopy. As previously mentioned, nuclear proteins, including HIF-2α, could not be labelled with Qdots (Section 3.2.3 Evaluation of Qdot-conjugated antibodies for immunofluorescent labelling). Instead, to achieve a SOFI image, HIF-2α was cloned into the monomeric RSFP Skylan-S (kindly provided by Pingyong Xu, Institute of Biophysics, Chinese Academy of Sciences, Beijing), as this protein gave a higher resolution than Dronpa when switched between a fluorescent and non-fluorescent state using laser illumination (106). When HIF-2α-Skylan-S was transfected into HeLa cells and imaged with wide-field microscopy, it was fluorescent and gave the typical speckle-like localisation of HIF-2α in the nucleus, as expected (185). To obtain a SOFI-processed image of HIF-2α-Skylan-S, a time series stack (30 ms exposure time) of images was acquired and post-processed to second order using Localizer (89). It was hypothesised that the size of the HIF-2α speckles would be smaller in the SOFI-processed image compared to the wide-field image, and therefore better resolved. It was also assumed, as a result of previous fluorescence recovery after photobleaching (FRAP) experiments (185), that HIF-2α is free to move within the nucleus and there is protein exchange between the speckles, so this signal was not expected to be removed after SOFI-processing. FRAP makes use of photobleaching by recording, over time, the diffusion of other fluorescent molecules into the region that has been bleached. Although, the SOFI-processed image of HIF-2α-Skylan-S had overall better SNR than the wide-field image, out-of-focus light between the speckles had been removed completely, suggesting that the signal was highly uncorrelated and, therefore, may be negligible protein between the speckles. To check for any resolution improvement there in

the SOFI-processed image, a line profile was plotted for both the wide-field image and the SOFI-processed image. An increase in the number of intensity peaks in the line profile, is indicative of a resolution improvement (Figure 71). Treating a speckle as a point emitter, a mean 19 % decrease in FWHM for the SOFI-processed HIF-2α-Skylan-S image, compared to the average wide-field HIF-2α-Skylan-S image (N=10 speckles) was calculated. Since wide-field HIF-2α speckles are in different focus planes, the photoswitching of Skylan-S was masked, so there were some missing structures in the SOFI-processed image, as SOFI was unable to appropriately reconstruct the speckles. Here, SOFI-processing would benefit from taking a z-stack or using a spinning disk confocal to recover the missing speckles (312).

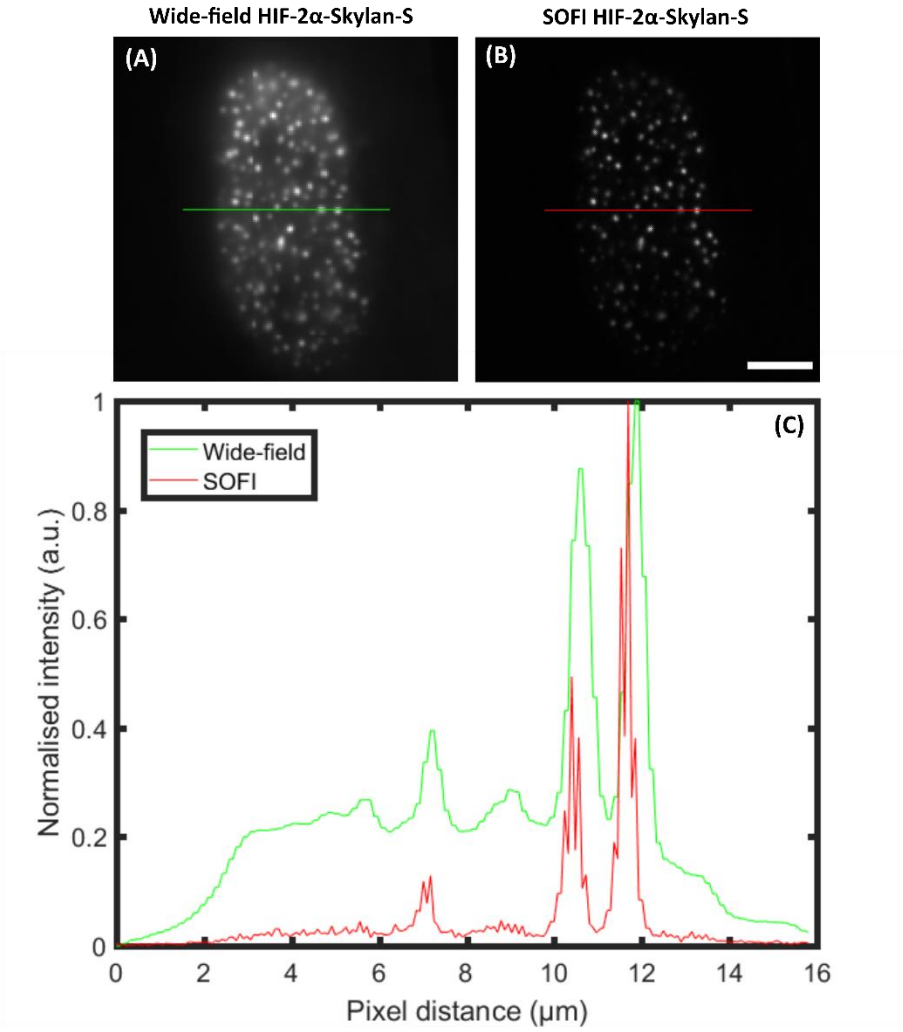


**Figure 71. SOFI-processed exogenous HIF-2α-Skylan-S.** Fixed HIF-2α-Skylan-S was imaged (100x 1.46 NA), in epifluorescence mode, with 50% of a 30 mW 488 nm at 10 ms. A 1,000 frame stack was processed to 2$^{nd}$ order SOFI with Localizer. A line profile was plotted in MATLAB for the wide-field image in green (A) and SOFI-processed HIF-2α-Skylan-S image in red (B). Scale bar = 5 µm.

After successfully SOFI-processing HIF-2α-Skylan-S in fixed cells, it was subsequently imaged in living cells in an attempt to obtain dynamic information about HIF-2α, at higher resolution than previously reported (185). SOFI-processing HIF-2α-Skylan-S in live cells, would also rule out any possibility that the removal of out-of-focus light was not as a result of fixation artefacts, which may affect the photophysical properties of Skylan-S. However, HIF-2α has a fast mobility, within a defined region, so it was challenging to SOFI process HIF-2α in live cells, even at low exposure times, without the appearance of motion blur artefacts within the speckles (Figure 72). Motion blur artefacts occur because the HIF-2α speckles move via Brownian motion, so the signal will be highest at the centre (saturated) and removed during SOFI-processing; whereas low intensity signal at the edges will be correlated and remain, creating a doughnut-shaped artefact. Live cell imaging of HIF-2α was carried out at 37 °C since the end goal is to study the dynamics of the HIF-2α speckles with super-resolution microscopy in living cells, although lower temperatures may slow down the protein, this may affect the biological function, so this was avoided. SOFI assumes that the point emitters along the structure of interest is immobile, but fluctuating from a fluorescent to non-fluorescent state, during the acquisition, so any movement results in a decrease in spatial resolution (88). Despite proteins tagged with Skylan-S being SOFI-processed in live cells previously (106), these were slow moving proteins, such as β-actin and MAP4. In addition to live SOFI-processing, it would have also been advantageous to investigate the localisation of HIF-2α with potential binding partners, by co-transfecting HeLa cells with HIF-2α tagged with a green RSFP, such as Skylan-S, and Phospho Ser5 RNA Pol II tagged with a red RSFP, to create a dual-colour SOFI-processed image. However, the prospect of achieving SOFI-processed images of proteins in live cells, using two-colour RSFPs, to study protein-protein interactions, may be complex in terms of using multiple wavelengths at once to activate simultaneous photoswitching. To date, there are no published red RSFP specific for SOFI. However, there are red fluorescent proteins, such as TagRFP (104), which have been successfully used in SOFI experiments. Regardless of fixation, the presence of HIF-2α in speckles in both the wide-field and SOFI-processed may be an artefact, as a result of overexpression or addition of the Skylan-S tag, therefore, endogenous HIF-2α also needed to be super-resolved. One such way, was to use the recently developed SRRF, which does not require proteins to be labelled with fluctuating probes, such as Qdots (74).

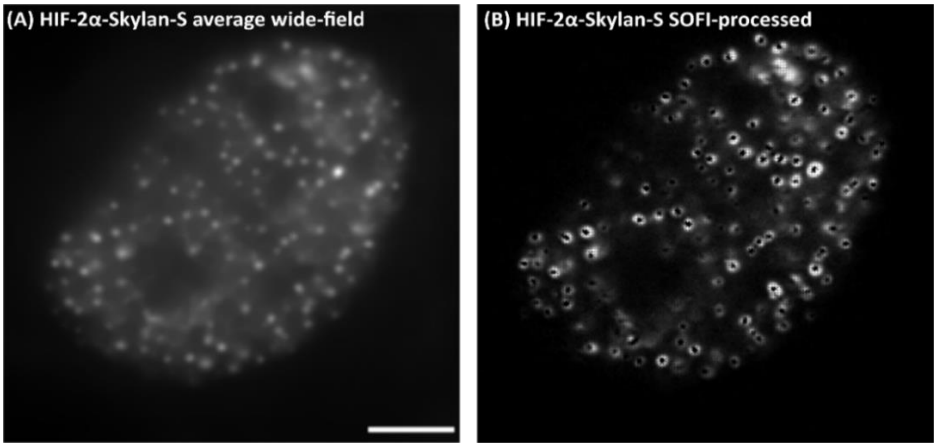


**Figure 72. Motion artefacts affects SOFI-processing.** HIF-2α-Skylan-S in live HeLa cells was imaged on a wide-field imaging system (A) at 33 ms exposure time and the 1,000 frame stack SOFI-processed with Localizer (B), implemented in MATLAB. HIF-2α speckles were motile and motion blur artefacts can be seen within the speckles after SOFI-processing. Scale bar = 5 µm.

### 5.1.2 Resolving endogenous HIF-2α and potential binding partners with SRRF

To validate the specificity of primary antibodies, for use in microscopy, the localisation of endogenous HIF-2α and other hypoxia-associated proteins, such as HIF-1β, HAF, and HIF-1α in wild-type HeLa cells was compared against fluorescent proteins exogenously expressed in HeLa cells. The appearance of exogenous HIF-2α is distinct from endogenous HIF-2α, with the speckles in exogenous HIF-2α being much larger and more distinct than that of endogenous HIF-2α, where the speckles appear smaller and closer together (Figure 73). This difference in speckle appearance may be due to an artefact of the fluorescent tag or exogenous HIF-2α, the challenge of specifically labelling endogenous HIF-2α with antibodies, or different levels of expression. As discovered previously (185), the sub-nuclear localisation of HIF-2α, being in speckles, differs from the more homogenous localisation of HIF-1α. The nuclear localisation of HIF-1α is only present under hypoxic conditions, but the nuclear localisation of HIF-2α is present under both normoxia and hypoxia; suggesting that these two HIF isoforms have different sensitivities to the severity of hypoxia. As discussed earlier (Section 1.5.1 Hypoxia inducible factor two alpha), HIF-1α and HIF-2α share many similarities and differences. Little is known about the difference in function between HIF-1α and HIF-2α, except their differential binding to the target genes promoter (313), so it is hoped that by using microscopy, to study their localisation within the nucleus, their role in regulating the adaptation to hypoxia will be better understood. Although, the nuclear localisation of HIF-2α has been shown not to be cell specific (185), in some cell types it has been found to be

cytoplasmic under certain oxygen conditions (314, 315), but these observations may be down to the use of a HIF-2α antibody of low specificity. In addition, exogenous HIF-1α has been shown to have a more nuclear localisation in cancerous cells than in normal cell lines (316). Since dimethyloxalylglycine (DMOG) is a strong hypoxia mimicking drug, that inhibits all PHD isoforms, this was used for all of the experiments described here, involving HIF-1α, to ensure that the same nuclear localisation pattern is observed for both exogenous and endogenous samples. In addition, since the degree of confluency can affect expression levels of HIF-2α in cells, with more confluent cells expressing a greater amount of HIF-2α (314, 193), it was decided to perform all experiments in cells that were grown to 80% confluency. Although, the localisation of all four proteins here are distinct in the exogenously expressed cells, only endogenous HAF has a unique pattern, with endogenous HIF-2α, HIF-1β, and HIF-1α being almost indistinguishable when imaged with wide-field microscopy (Figure 73).

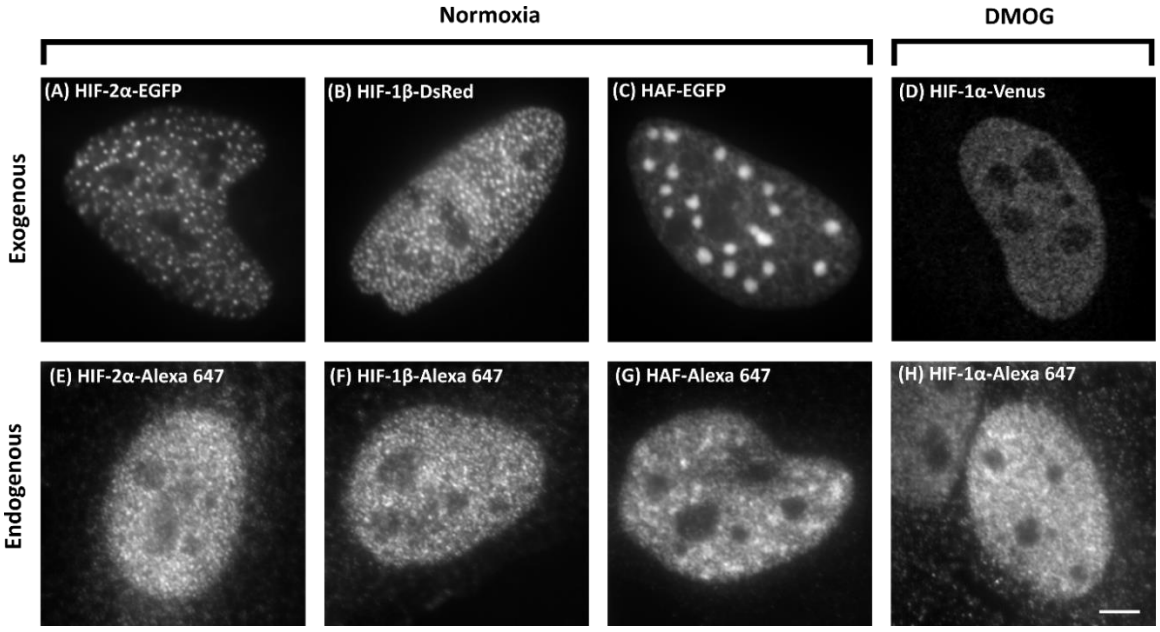


**Figure 73. Localisation comparison between exogenous and endogenous HIF-2α and related proteins.** Exogenous proteins (A-D) were transfected into HeLa cells using FuGENE 6 transfection reagent. HIF-1α-Venus image (D) was kindly provided by Sarah Taylor from University of Liverpool, UK. Endogenous proteins (E-H) were labelled with Alexa Fluor 647 using indirect immunofluorescence. Images A-D were imaged at 63x 1.4NA, whilst images E-H were imaged at 100x 1.4NA plus 2.5x magnifying lens. All images were taken on an epifluorescence microscope, except (D), which was taken on a confocal microscope. Images of HIF-1α were taken in HeLa cells treated with DMOG (D and H), but all other images (A, B, C, E, F, and G) were of normoxic cells. Distinct localisation was evident in exogenously expressed cells. Scale bar = 5 μm.

Endogenous HIF-2α with its potential binding partners have been imaged previously (185). This experiment was repeated here and images were taken with wide-field microscopy. At the time of writing, the co-localisation of HIF-2α with its potential binding partners has never been studied before using super-resolution microscopy. SRRF was therefore used as a tool to probe nuclear inhomogeneity of endogenous HIF-2α and its localisation in relation to other associated proteins. As HIF-2α is a transcription factor, it was hypothesised that HIF-2α speckles may be in active transcription sites and therefore, should co-localise with Phospho Ser5 RNA Pol II within the nucleus. The structure of RNA Pol II has already been resolved with super-resolution using PALM, in a live cell line expressing RNA Pol II-Dendra2 (317), a versatile antibody-based imaging approach (VANIMA) (318), and also using EM (319), so it is well known that RNA Pol II is distributed non-homogenously in the cell nucleus in discrete foci, where transcription occurs (320). Additionally, as HIF-2α can form a heterodimer with HIF-1β (also known as ARNT), it was logical to assume that these two proteins would also co-localise within the nucleus. Although, both HIF-2α and HIF-1β localise in speckles when expressed individually, when they are co-transfected in HeLa cells, they no longer appeared to be in speckles, but instead had a more homogenous localisation (Figure 74). This dimerisation of HIF-2α and HIF-1β has been imaged previously (321).

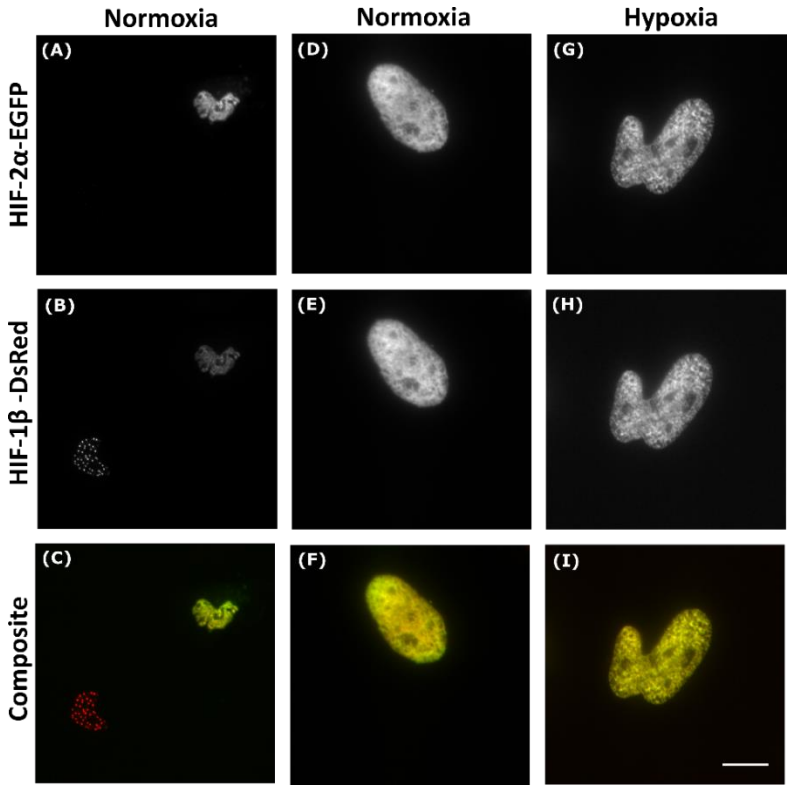


**Figure 74. Co-transfection of exogenous HIF-2α-EGFP and HIF-1β-DsRed.** HeLa cells were grown under normoxia (A-F) and hypoxia (G-I) for 24 h, before being transfected with HIF-2α-EGFP/HIF-1β-

DsRed and fixed with 4% (w/v) PFA. Samples were imaged on an epifluorescence microscope with 63x (1.4 NA) magnification, but D-I had an addition of a 1.6x magnifying lens. When co-transfected the two proteins become less speckled and more homogenous. Scale bar = 10 μm.

HAF is also known to interact with HIF-2α (194) and has already been shown within the nucleus that HIF-2α and HAF localise within close proximity of each other (322), so it was possible that HIF-2α may co-localise with HAF. However, as the nuclear localisation of exogenous HIF-1α differs from that of exogenous HIF-2α (185), these proteins are not thought to co-localise. Exogenous HIF-1α is homogenously localised, whilst endogenous HIF-1α has been found to localise heterogeneously in speckles (323). It has also been reported in the literature that when HIF-1α is co-transfected with HIF-1β, the normally homogenously distributed localisation of HIF-1α fusion protein goes into speckles comparable to endogenous HIF-1α (323). These findings are in stark contrast to the co-transfection data of HIF-2α and HIF-1β shown here (Figure 74). Due to the diffraction limit of light, it appeared that all of the endogenous proteins (Phospho Ser5 RNA Pol II, HIF-1β, HAF, and HIF-1α) did co-localise to some degree with HIF-2α, due to the composite image appearing yellow from the merge of HIF-2α labelled with Alexa Fluor 488 (green) and the other proteins labelled in Alexa Fluor 647 (red) (Figure 75). However, these images were of low-resolution, so when super-resolved with SRRF, the degree of co-localisation may decrease. Although, co-localisation may exist with wide-field microscopy, due to the diffraction limit of light, the two 'interacting' proteins may be resolved with super-resolution microscopy and instead show no co-localisation.

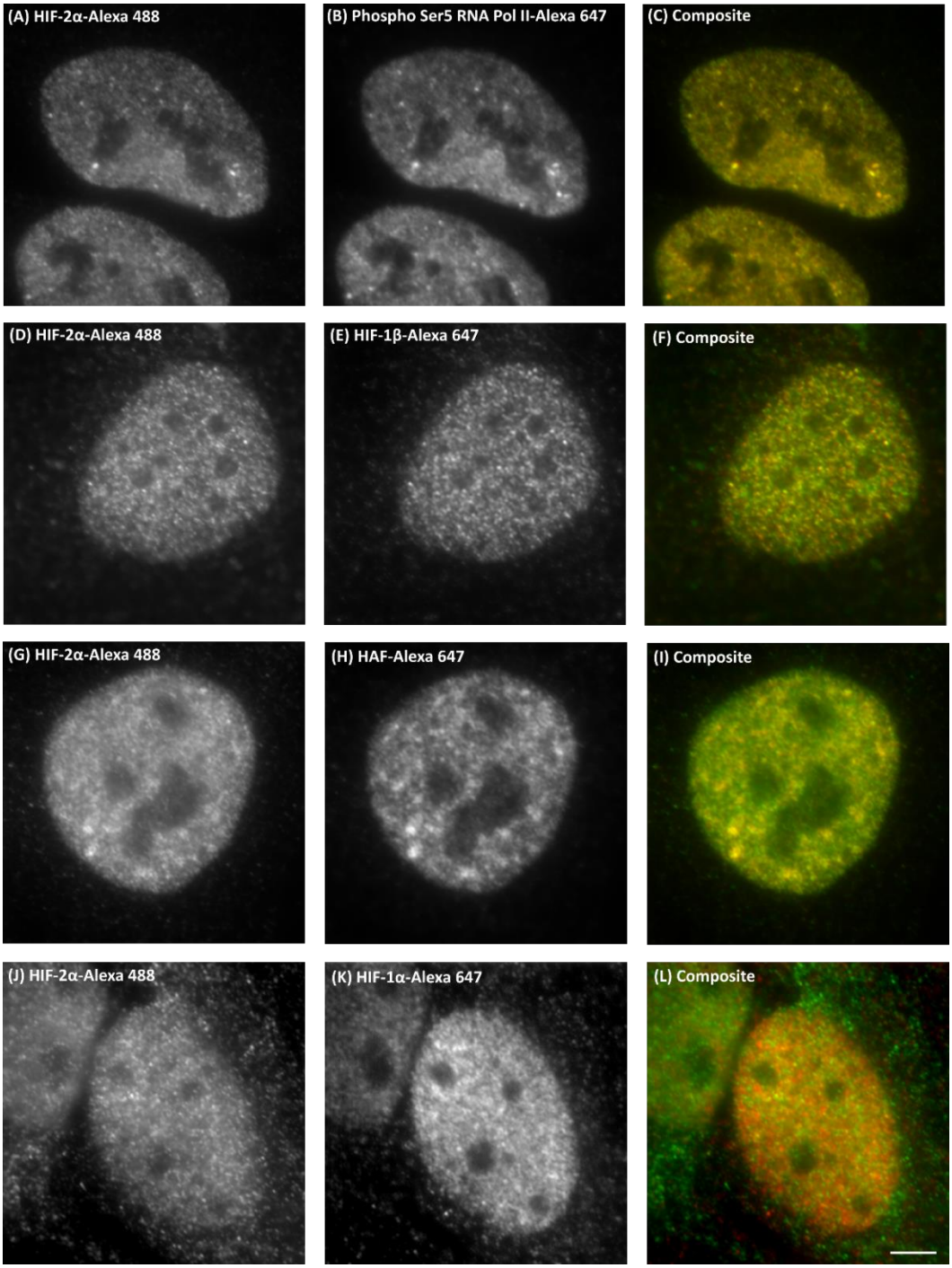


**Figure 75. Endogenous HIF-2α and potential binding partners imaged with wide-field microscopy.** Using indirect immunofluorescence, HIF-2α was labelled with Alexa Fluor 488 (green) and other proteins (Phospho Ser5 RNA Pol II, HIF-1β, HAF, and HIF-1α) were labelled with Alexa Fluor 647 (red). All images (A, B, D, E, G, H, J, and K) were taken on an epifluorescence microscope (100x 1.4 NA plus a 2.5x magnifying lens). Yellow regions in composite images (C, F, I, and L) show co-localisation between HIF-2α and other proteins. Scale bar = 5 µm.

At the time of publication of this thesis, there is no known record of these kind of transcription factors being resolved using any super-resolution microscopy method,

including SRRF. Immunocytochemistry was therefore used to visualise the protein localisation of HIF-2α and its potential binding partners for SRRF-processing. Since with wide-field microscopy, there appeared to be high co-localisation between HIF-2α and the active form of RNA polymerase, Phospho Ser5 RNA Pol II (Figure 75), these two proteins were used for initial SRRF-processing. Endogenous HIF-2α and Phospho Ser5 RNA Pol II were sequentially labelled with Alexa Fluor 488 (green) and Cy3 (red) respectively, in fixed HeLa cells, using indirect immunofluorescence. Wide-field images were post-processed in ImageJ with the NanoJ-SRRF plugin, using default settings, and the quality of the SRRF images, was assessed with NanoJ-SQUIRREL. At first glance, it seemed that the HIF-2α speckles and Phospho Ser5 RNA Pol II foci had been resolved, as there was distinct dot-like structures for both proteins in the SRRF-processed images, which were not so obvious in the prior wide-field images (Figure 76). Also, as expected, the degree of co-localisation between HIF-2α-Alexa Fluor 488 and Phospho Ser5 RNA Pol II-Cy3 appeared to be lower in the SRRF-processed images than the wide-field images, because there was considerably less merged yellow regions in the SRRF-processed image. However, when the SRRF-processed images were run through the software package, NanoJ-SQUIRREL, the calculated RSP values for HIF-2α Alexa Fluor 488 and Phospho Ser5 RNA Pol II were lower than 0.95, which indicated that these SRRF-processed images contained artefacts.

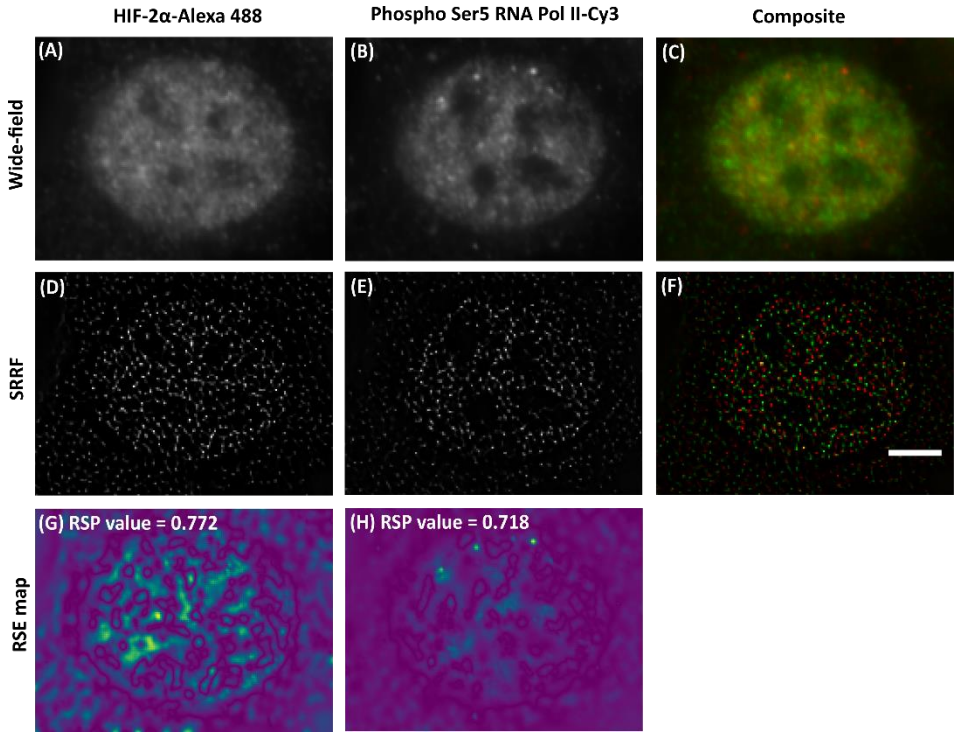


**Figure 76. SRRF-processed endogenous HIF-2α and Phospho Ser5 RNA Pol II.** Indirect immunofluorescence was used to label HIF-2α with green Alexa Fluor 488 (A) and Phospho Ser5 RNA

Pol II with orange-to-red Cy3 (B), in fixed HeLa cells, to create a composite wide-field image (C). A stack of 1,000 wide-field images were acquired on an epifluorescence microscope (100x 1.4 NA) using a sensitive EMCCD camera and polychromatic mercury arc lamp. Wide-field images (A&B) were SRRF-processed (D&E), with NanoJ-SRRF ImageJ plugin, to create a composite SRRF-processed image (F). SRRF-processed images showed more distinct dot-like structures and lower co-localisation between HIF-2α and Phospho Ser5 RNA Pol II (less yellow merged regions), than the wide-field images. Quality of the SRRF-processed images was quantified with NanoJ-SQUIRREL and RSE maps (G&H) found to contain artefacts (Calculated RSP values <0.95). Scale bar = 5 µm.

As a control, to check whether the appearance of HIF-2α in a dot-like pattern after SRRF-processing was real, HIF-1α in hypoxic cells was also stained, a stack acquired, and then SRRF-processed. Since it has been proposed that HIF-1α is nuclear, but not thought to be in speckles under hypoxic conditions (185), it was presumed that the SRRF-processed image should also be homogenous. However, a similar SRRF-processed image for HIF-1α as HIF-2α was observed (Figure 77). Further controls were carried out, including SRRF-processing of nucleolin, an alternative endogenous nuclear protein, and the DNA intercalating dye Hoechst 33342, which are both thought not to form speckles. All of the nuclear staining resulted in dot-like structures, which reinforced the idea that the SRRF-processed results were likely artefacts. After reviewing the imaging parameters, required to achieve a high quality SRRF image (calculated RSP value > 0.95) (Chapter 4.2.4.1), it was apparent that the samples here were under-sampled (100x 1.4NA), according to Nyquist Sampling. Therefore, for future SRRF-processing, all subsequent HIF-2α images were acquired with a 100x 1.4 NA oil immersion objective and a 2.5x magnifying lens.

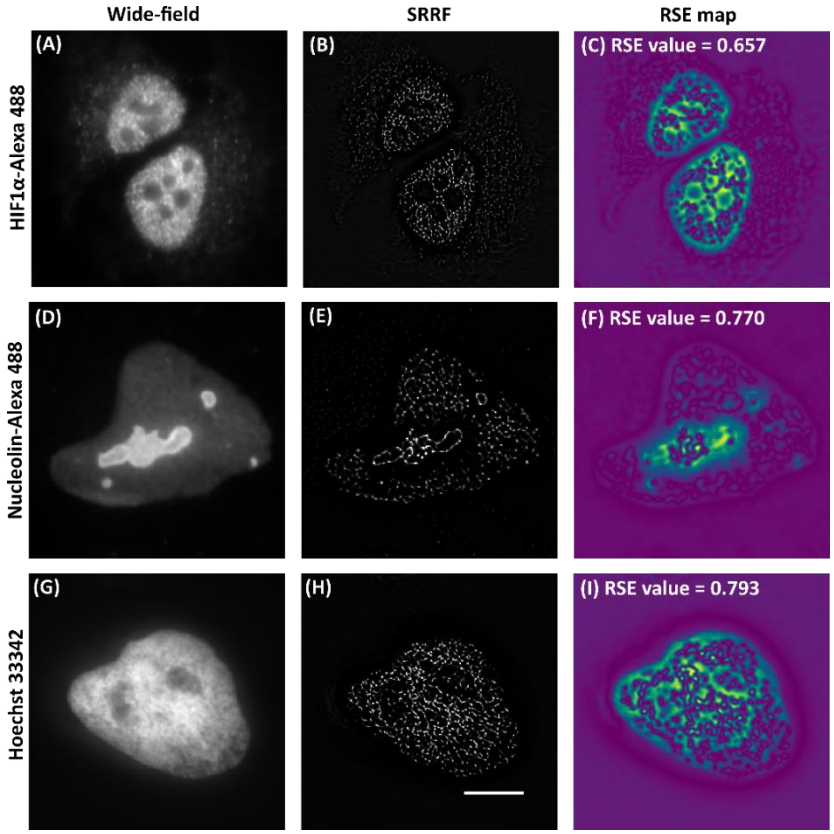


**Figure 77. SRRF-processing homogenous nuclear proteins.** Indirect immunofluorescence was used to label nuclear proteins HIF-1α and nucleolin with Alexa Fluor 488, whilst Hoechst 33342 stained the nucleus of fixed HeLa cells (A, D, and G). Wide-field images were taken on an epifluorescence microscope (100x 1.4 NA). SRRF-processed images (B, E, and H) showed dot-like structures for all of the nuclear proteins. High error regions in the SRRF-processed images were highlighted in RSE maps (C, F, and I). Scale bar = 10 µm.

Taking into consideration optimal acquisition settings, required to achieve the best attainable SRRF-processed image (Chapter 4.2.4.1), the indirect immunofluorescence of HIF-2α was repeated with Alexa Fluor 647, to produce a much improved SRRF-processed image (Figure 78). SRRF-processing revealed endogenous HIF-2α to be in speckles and out-of-focus light present in the wide-field image, was removed in the SRRF-processed image. However, unlike the SOFI-processed image of exogenous HIF-2α (Figure 71), signal in between the speckles was not completely removed in the SRRF-processed image of HIF-2α. The presence of signal in between the speckles may be as a result of protein exchange between one speckle and another speckle, as it has been previously shown, using FRAP, that HIF-2α is not immobile (185). On closer inspection of the images, there were some instances where the speckles appeared to have been joined to form lines in the SRRF-processed image, which was also present in the wide-field images. However, it was expected that if speckles were in close proximity of other speckles, appearing as a continuous structure in wide-field images, they

would be better resolved, and therefore more separated from one another, in the SRRF-processed images.

To check for any artefacts, the quality of the visually improved SRRF-processed image of HIF-2α was quantified using the NanoJ-SQUIRREL ImageJ plugin. An error map highlighting blue regions of low error surrounding the speckles and a high RSP value of 0.99 was calculated (Figure 78C), which meant that the SRRF-processed image was of high quality and contained negligible artefacts. FRC was also used to determine whether the resolution of the SRRF-processed image was improved in comparison to the wide-field image. Despite the SRRF-processed image being of high quality (RSP value > 0.95), with an increased SNR, the resolution did not appear to have been improved. Although, the spatial map of FRC had mostly low FRC values (indicated by blue regions), the mean FRC value increased significantly from 284.25 nm in the average wide-field image, to 307.22 nm in the SRRF-processed image (Figure 78D). As stated earlier, an image of high quality does not necessarily mean that it will also have improved resolution.

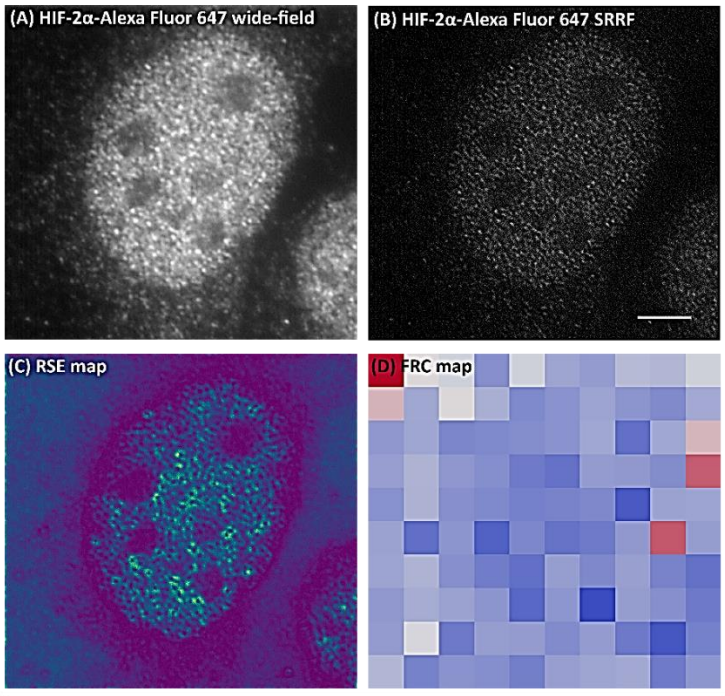


| (E) NanoJ-SQUIRREL analysis of SRRF-processed HIF-2α-Alexa Fluor 647 | |
|---|---|
| RSP (>0.95 = Good SRRF image) | 0.99 |
| RSE | 4241.54 |
| Mean FRC SRRF value (nm) | 307.22 |
| Mean FRC wide-field value (nm) | 284.25 |

**Figure 78. Endogenous HIF-2α-Alexa 647 super-resolved with NanoJ-SRRF.** HIF-2α was labelled with Alexa Fluor 647 using indirect immunofluorescence in fixed HeLa cells and 100 frames acquired on an

epifluorescence microscope (100x 1.4 NA plus 2.5x magnifying lens) at a 30 ms exposure time. A time series of wide-field images (A) was post-processed using a NanoJ-SRRF ImageJ plugin to produce a SRRF image of HIF-2α (B). The quality of the SRRF-processed image was assessed using NanoJ-SQUIRREL in ImageJ, resulting in an error map (C) and a high RSP value of 0.99 (RSP >0.95 = good SRRF image). FRC was also calculated for both the SRRF-processed (307.22 nm) and average wide-field (284.25 nm) images by splitting the images into 100 blocks and using an image pixel size of 12.8 nm. Scale bar = 5 μm.

After obtaining a high quality SRRF image of HIF-2α, it was decided to proceed with SRRF-processing HIF-2α with its potential binding partners (Phospho Ser5 RNA Pol II, HIF-1β, HAF, and HIF-1α), using the same acquisition settings. To obtain a dual-colour SRRF-processed image, HIF-2α was labelled green with Alexa Fluor 488 and the other HIF-2α associated proteins were labelled far red with Alexa Fluor 647. Two-colour SRRF images (Figure 79) were achieved by post-processing a time series of 100 wide-field images using the NanoJ-SRRF ImageJ plugin (74). Visually, the nuclear localisation of HIF-2α and the other proteins in the SRRF-processed images was comparable to the wide-field images, but there appeared to be less co-localisation between HIF-2α and the other proteins with SRRF, as shown by fewer merged yellow regions in the composite images (Figure 79). Another observation, was that the 32-bit SRRF-processed images were dimmer in comparison to the wide-field images, even when changed to 16-bit, with the brightness and contrast was adjusted to an optimal level.

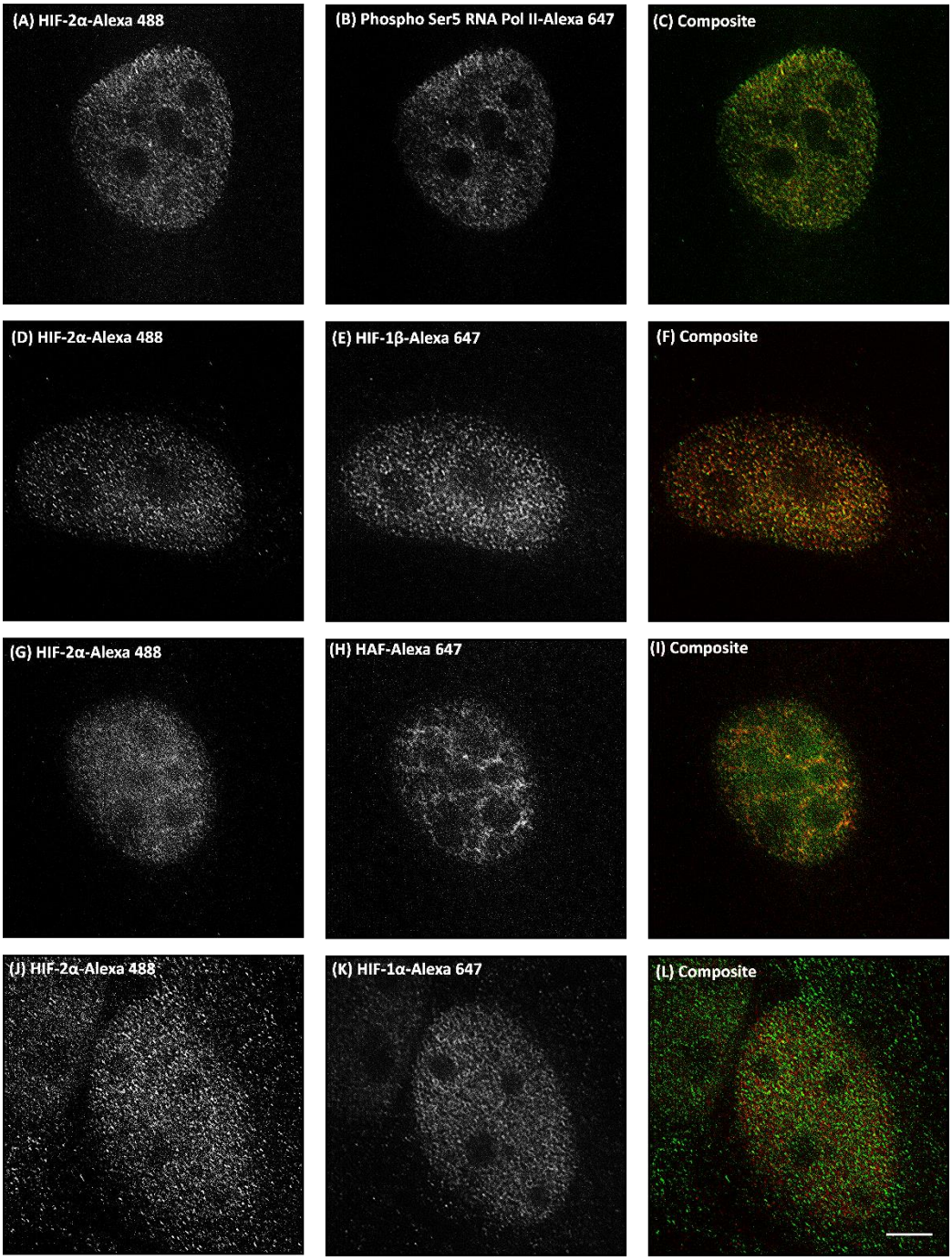


**Figure 79. NanoJ-SRRF-processed endogenous HIF-2α and potential binding partners.** Using indirect immunofluorescence, HIF-2α was labelled with Alexa Fluor 488 (green) and other proteins (Phospho Ser5 RNA Pol II, HIF-1β, HAF, and HIF-1α) were labelled with Alexa Fluor 647 (red). All staining was done in HeLa cells that had been grown under normoxic conditions, except for the sample being probed for HIF-1α, which was incubated with DMOG for 4 h, before being fixed with 4% (w/v) PFA. Wide-field images were acquired sequentially over 100 frames on an epifluorescence microscope (100x 1.4 NA plus a 2.5x magnifying lens), and SRRF-processed with the ImageJ plugin NanoJ-SRRF (A, B, D, E, G, H, J, and K). Yellow regions in composite images (C, F, I, and L) show co-localisation between HIF-2α and other proteins. Scale bar = 5 μm.

For the SRRF-processed images in Figure 79, the lowest possible exposure time was used, that was needed to acquire images with a sufficient signal, so that the structures were visible, and also so that they gave the highest RSP value. For HIF-2α-Alexa Fluor 488 and Phospho Ser5 RNA Pol II-Alexa Fluor 647, images were acquired at 5 ms, 10 ms, 30 ms, 50 ms, and 100 ms with a reasonable signal for displayed SRRF images. Furthermore, the highest obtainable RSP values for HIF-2α-Alexa Fluor 488 and Phospho Ser5 RNA Pol II, when using NanoJ-SQUIRREL, was at an exposure time of 5 ms, with the RSP values generally decreasing with an increase in exposure time. At a low exposure time of 5 ms, HIF-2α and Phospho Ser5 RNA Pol II appeared in speckles and foci respectively, but at much higher exposure times, such as 50 ms and 100 ms, these rounded structures started to join, forming lines in the image. The formation of line artefacts, at higher exposure times, when the RSP values decrease is indicative of a poor quality SRRF image. Other proteins, such as HIF-1β and HIF-1α could not be acquired at exposure times lower than 30 ms, due to the samples having weak fluorescent signal, perhaps due to these proteins being less abundant than Phospho Ser5 RNA Pol II and HAF. Conditions that lead to a high quality SRRF-processed image was sample dependent, so a compromise between achieving an image that displays well, whilst also giving a high RSP value needed to be met. Exposure times and resulting RSP values for the images displayed in Figure 79 are shown in Table 12.

| | | Exposure time (ms) | RSP (> 0.95 = Good SRRF) |
|---|---|---|---|
| Normoxia | **HIF-2α-Alexa Fluor 488** | 5 ms | 0.991 |
| | **Phospho Ser 5 RNA Pol II-Alexa 647** | 5 ms | 0.993 |
| Normoxia | **HIF-2α-Alexa Fluor 488** | 30 ms | 0.991 |
| | **HIF-1β-Alexa Fluor 647** | 30 ms | 0.988 |
| Normoxia | **HIF-2α-Alexa Fluor 488** | 10 ms | 0.996 |
| | **HAF-Alexa Fluor 647** | 10 ms | 0.987 |
| 4 h DMOG | **HIF-2α-Alexa Fluor 488** | 10 ms | 0.972 |
| | **HIF-1α-Alexa Fluor 647** | 100 ms | 0.984 |

**Table 12. Assessing the quality of dual-colour SRRF-processed nuclear proteins with NanoJ-SQUIRREL.** High quality SRRF-processed images (RSP values > 0.95) were achieved for all of the nuclear proteins (Phospho Ser5 RNA Pol II, HIF-1β, HAF, and HIF-1α) that were investigated to co-localise with endogenous HIF-2α. The highest RSP values achieved are shown and correspond to the images in Figure 79. The optimal exposure times, used to acquire the raw data that produced the highest quality SRRF images, was sample dependent.

### 5.1.3 Resolving HIF-2α and potential binding partners with Airyscan

This work was prompted by previous findings that with SOFI, signal was removed in between HIF-2α speckles, whilst in a high quality SRRF image, this was not the case. As an alternative to post-processing super-resolution imaging methods, such as SOFI and SRRF, to achieve a high-resolution image of HIF-2α, Airyscan was used. Like previously, HIF-2α was labelled with green Alexa Fluor 488 and other nuclear proteins (Phospho Ser5 RNA Pol II, HIF-1β, HAF, and HIF-1α) labelled with far red Alexa Fluor 647, in fixed HeLa cells, using indirect immunofluorescence with primary and secondary antibodies. With Airyscan, all of the nuclear proteins simultaneously imaged with HIF-2α were in speckles (Figure 80) and of higher SNR than with wide-field microscopy. As with SRRF, there also appeared to be less co-localisation between HIF-2α and nuclear proteins Phospho Ser5 RNA Pol II, HIF-1β, HAF, and HIF-1α, than with wide-field microscopy. By eye, through observing yellow merged regions in composite images, it was difficult to establish whether the co-localisation of HIF-2α with Phospho Ser5 RNA Pol II, HIF-1β, HAF, or HIF-1α, was significant enough to say that they were interacting with one another and this can lead to human bias.

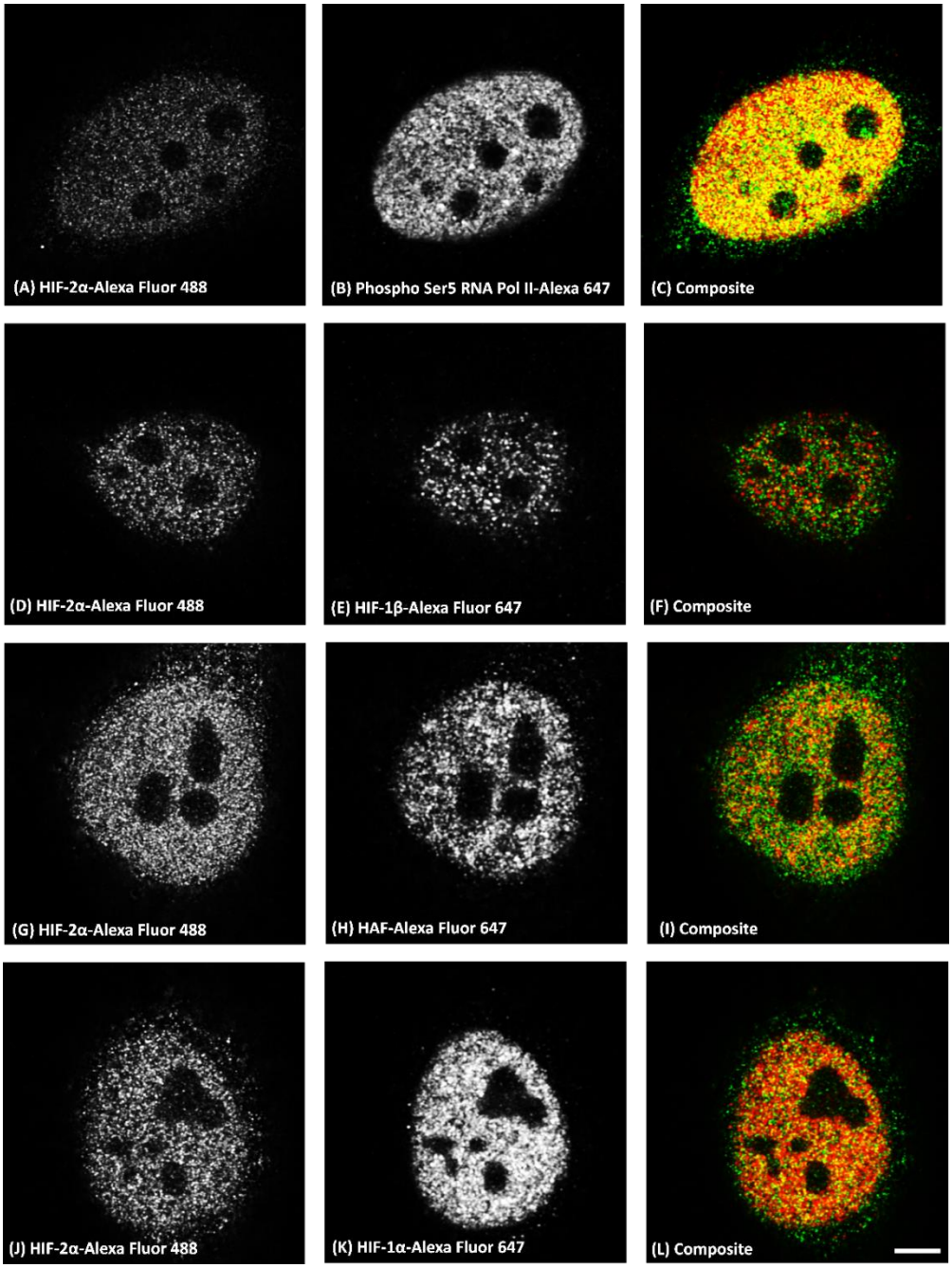


**Figure 80. Airyscan imaging of endogenous HIF-2α and its potential binding partners.** Indirect immunofluorescence was used to label HIF-2α with green Alexa Fluor 488 and other nuclear proteins (Phospho Ser5 RNA Pol II, HIF-1β, HAF, and HIF-1α) were labelled far red with Alexa Fluor 647. Airyscan images were taken at 63x magnification (A, B, D, E, G, H, J, and K). Yellow regions in composite images (C, F, I, and L) show areas of overlap between HIF-2α (green) with the other nuclear proteins (red). Images J-L were taken in HeLa cells incubated with DMOG 4 h before fixation. Scale bar = 5 µm.

### 5.1.4 Quantifying co-localisation of HIF-2α and potential binding partners

Determining co-localisation between two sub-nuclear proteins such as HIF-2α and HIF-1β is crucial to understanding their involvement in the hypoxia signalling pathway, as a protein's

localisation is closely related to its physiological function (324). Visual inspection of co-localisation is subjective and therefore, a more statistical approach is a better way to quantitatively determine true co-localisation between two proteins of interest. The degree of co-localisation between HIF-2α and Phospho Ser5 RNA Pol II, HIF-1β, HAF, or HIF-1α, for each of the microscopy techniques used so far, was calculated using the open-source JACoP (248), freely available in ImageJ (Table 13). For the wide-field images in Figure 75, the degree of co-localisation of HIF-2α with all inspected nuclear proteins was strong, as indicated by the high Pearson's correlation coefficient and Manders coefficient values. As expected, for the Airyscan-processed images (Figure 80), the degree of co-localisation between HIF-2α and Phospho Ser5 RNA Pol II, HIF-1β, HAF, or HIF-1α was slightly lower than that obtained with wide-field microscopy. The lowest co-localisation was with the SRRF-processed images (Figure 79).

| Co-localisation Quantification using JACoP | | Wide-field | SRRF | Airyscan |
|---|---|---|---|---|
| Fraction of HIF-2α overlapping with Phospho Ser 5 RNA Pol II (normoxia) | Pearson's coefficient | 0.99 | 0.411 | 0.764 |
| | Mander's coefficient | 0.974 | 0.338 | 0.873 |
| Fraction of HIF-2α overlapping with HIF-1β (normoxia) | Pearson's coefficient | 0.972 | 0.416 | 0.646 |
| | Mander's coefficient | 0.976 | 0.531 | 0.473 |
| Fraction of HIF-2α overlapping with HAF (normoxia) | Pearson's coefficient | 0.981 | 0.308 | 0.71 |
| | Mander's coefficient | 0.997 | 0.335 | 0.619 |
| Fraction of HIF-2α overlapping with HIF-1α (4 h DMOG) | Pearson's coefficient | 0.836 | 0.164 | 0.74 |
| | Mander's coefficient | 0.937 | 0.379 | 0.787 |

**Table 13. Comparing HIF-2α co-localisation quantification in different imaging techniques.** The degree of co-localisation between HIF-2α-Alexa Fluor 488 (green) and Phospho Ser5 RNA Pol II-Alexa Fluor 647 (red), HIF-1β-Alexa 647 (red), HAF-Alexa 647 (red), or HIF-1α-Alexa 647 (red) was measured by calculating Pearson's correlation coefficient and Manders coefficient values using the JACoP ImageJ plugin.

To determine the range of Pearson's correlation coefficient and Manders coefficient values that result in two proteins being considered to definitely co-localise, benchmark computer stimulated red and green channel ground-truth images of a known % co-localisation, were

ran through the JACoP ImageJ plugin (248). Image set CBS001RGM-CBS010RGM from the Colocalization Benchmark Source (available from www.colocalization-benchmark.com) was used to validate co-localisation between HIF-2α and Phospho Ser5 RNA Pol II, HIF-1β, HAF, or HIF-1α (Table 14). For a computer stimulated composite image of green and red fluorescent molecules that are supposed to give 0% co-localisation, the Pearson's coefficient value was extremely low (0.006), with a Manders coefficient value of 0.257. When the Pearson's coefficient and Manders coefficient of a computer stimulated image, with a defined co-localisation of 90%, was calculated, values of 0.899 and 0.909 were obtained, respectively. Using this data as a benchmark, it was determined that in wide-field images there was a strong co-localisation (90%) between HIF-2α with all of the selected nuclear proteins. Similarly, in the Airyscan images the co-localisation was still high (70%), whilst in the SRRF-processed images, the degree of co-localisation was low (HIF-2α with Phospho Ser5 RNA Pol II was 40%, HIF-2α with HIF-1β was 40%, HIF-2α with HAF was 30%, and HIF-2α with HIF-1α was 20% co-localised). This overall lower co-localisation for the SRRF-processed images, may be as a result of an improved resolution in comparison to wide-field and Airyscan-processed images. Since background thresholds were automatically set for co-localisation analysis in JACoP (248), the poor SNR of the SRRF-processed images should not affect the degree of co-localisation in the images, because any non-specific staining should have been removed. Considering HIF-1β is a known binding partner of HIF-2α, it was expected that these two proteins would have had a higher degree of co-localisation than 40%, but the low co-localisation of 20% for HIF-2α and HIF-1α, appearing mutually exclusive, seemed appropriate considering that they are thought to have different nuclear localisations (185). Previous co-localisation data on confocal images, using the former Colocalization Threshold ImageJ plugin, found HIF-2α to co-localise with Phospho Ser5 RNA Pol II by 48%, HIF-1β by 33%, and HAF by 13% (185). The variation between previous co-localisation findings and those reported here, may be due to different antibodies and imaging systems being used. Potential HIF-2α protein-protein interactions could be investigated further with FRET, assuming that protein A + protein B = AB. However, regularly proteins participate in many different complexes, so if only a fraction of a protein pool partitions into a complex, FRET may not detect this interaction and, therefore, it is better to use a proximity ligation assay (PLA) instead.

| Colocalization Benchmark Source | Pearson's coefficient | Manders coefficient (Fraction of green overlapping with red) |
|---|---|---|
| **0% co-localisation** (Red and green channel composite) | 0.006 | 0.257 |
| **10% co-localisation** (Red and green channel composite) | 0.103 | 0.325 |
| **20% co-localisation** (Red and green channel composite) | 0.185 | 0.376 |
| **30% co-localisation** (Red and green channel composite) | 0.294 | 0.457 |
| **40% co-localisation** (Red and green channel composite) | 0.405 | 0.525 |
| **50% co-localisation** (Red and green channel composite) | 0.492 | 0.594 |
| **60% co-localisation** (Red and green channel composite) | 0.602 | 0.663 |
| **70% co-localisation** (Red and green channel composite) | 0.701 | 0.746 |
| **80% co-localisation** (Red and green channel composite) | 0.797 | 0.824 |
| **90% co-localisation** (Red and green channel composite) | 0.899 | 0.909 |

**Table 14. Benchmarking co-localisation data.** Pearson's correlation coefficients and Manders coefficients were calculated for ground-truth images of a defined degree of co-localisation (0-90%), using the JAcoP ImageJ plugin.

### 5.1.5 Imaging exogenous HIF-2α with other super-resolution techniques

Whilst on an industry placement at the Research and Development department of Carl Zeiss Microscopy GmbH in Jena, Germany, the fortunate opportunity arose to image exogenous HIF-2α using dSTORM and SIM. In addition, exogenous HIF-2α was also imaged by Peter Hemmerich using STED microscopy at the imaging facility in the Leibniz Institute on Ageing (Fritz Lipmann Institute, Jena, Germany). HIF-2α-EGFP was transfected into HeLa cells grown under normoxia, before being fixed with 4% (w/v) PFA, and imaged on a number of different super-resolution microscopes. For imaging with STED, HIF-2α-EGFP was labelled red with anti-GFP-NANObooster-ATTO647N. A z-stack of exogenous HIF-2α-EGFP was acquired on a Leica TCS SP8 STED 3x microscope (100x 1.4NA) with 100% of a 1.85 W 775 nm STED depleted pulsed doughnut laser and the data post-processed with Huygens deconvolution software, before displaying the deconvolved STED image as a maximum intensity z projection. In comparison to the confocal image of HIF-2α, the STED image contained visually smaller speckles and was comparable to the HIF-2α SOFI-processed image, in that the SNR had been improved and out-of-focus light had been removed in between the speckles (Figure 81). Whilst imaging HIF-2α with STED, occasionally, there was the presence of halo artefacts when the fluorescence inside of the speckles was depleted, due to the doughnut shape of the laser beam.

Exogenous HIF-2α was imaged using the SMLM technique dSTORM on the Zeiss Elyra P.S.1 system (63x 1.4 NA) by labelling HIF-2α with an anti-GFP primary antibody and a secondary antibody conjugated to Alexa Fluor 647. Just before imaging, the fixed HIF-2α-EGFP-Alexa 647 sample was incubated with a freshly prepared imaging buffer consisting of 1M MEA (pH 9) and 10 nM NaOH. To achieve an optimal dSTORM image, 30,000 frames were acquired on an EMCCD camera sequentially, in laser wide-field mode, with an additional FOV lens (TIRF-UHP), at 20 ms. To get single molecule blinking, sufficient for dSTORM-processing, the cropped image was illuminated with 100% of a 150 mW 642 nm laser (Long pass filter: 655 nm) and 0.5% of a 50 mW 405 nm laser. dSTORM-processing was done in ZEN software with the measured PSF. The dSTORM-processed image of exogenous HIF-2α revealed clusters of multiple small speckles that appeared as one larger speckle in the laser wide-field image (Figure 81). Again, as with SOFI, out-of-focus light in the wide-field image had been removed with dSTORM, and the SNR improved. However, since all Alexa Fluor 647 dye molecules were localized, and therefore contributed to the final dSTORM image, it was unclear whether the smaller dot-like structures were speckles.

Another super-resolution technique, SIM, was also used to image exogenous HIF-2α. Unlike STED and dSTORM, SIM did not require the structure to be labelled with specialist dyes, using indirect immunofluorescence, so SIM could have been done on live HIF-2α-EGFP, if it was not so mobile. A z-stack (7 positions) of HIF-2α-EGFP was acquired with a 2% of a 100 mW 488 nm laser on a sCMOS camera (no gain), at a long exposure time of 100 ms, to achieve an optimal SIM image. It was found that the more rotations (up to 5) of the 34 µm grid, the better the SIM image, but in the interest of time 3 rotations was sufficient to give a good SIM image. After acquisition, SIM-processing was done in ZEN software. To display the final SIM image of exogenous HIF-2α, a maximum intensity z projection was performed on the raw data in ImageJ (Figure 81). Similar to all of the aforementioned microscopy techniques, SIM also gave a super-resolved image of exogenous HIF-2α that had a greater SNR than wide-field microscopy, with signal in between the speckles also being removed.

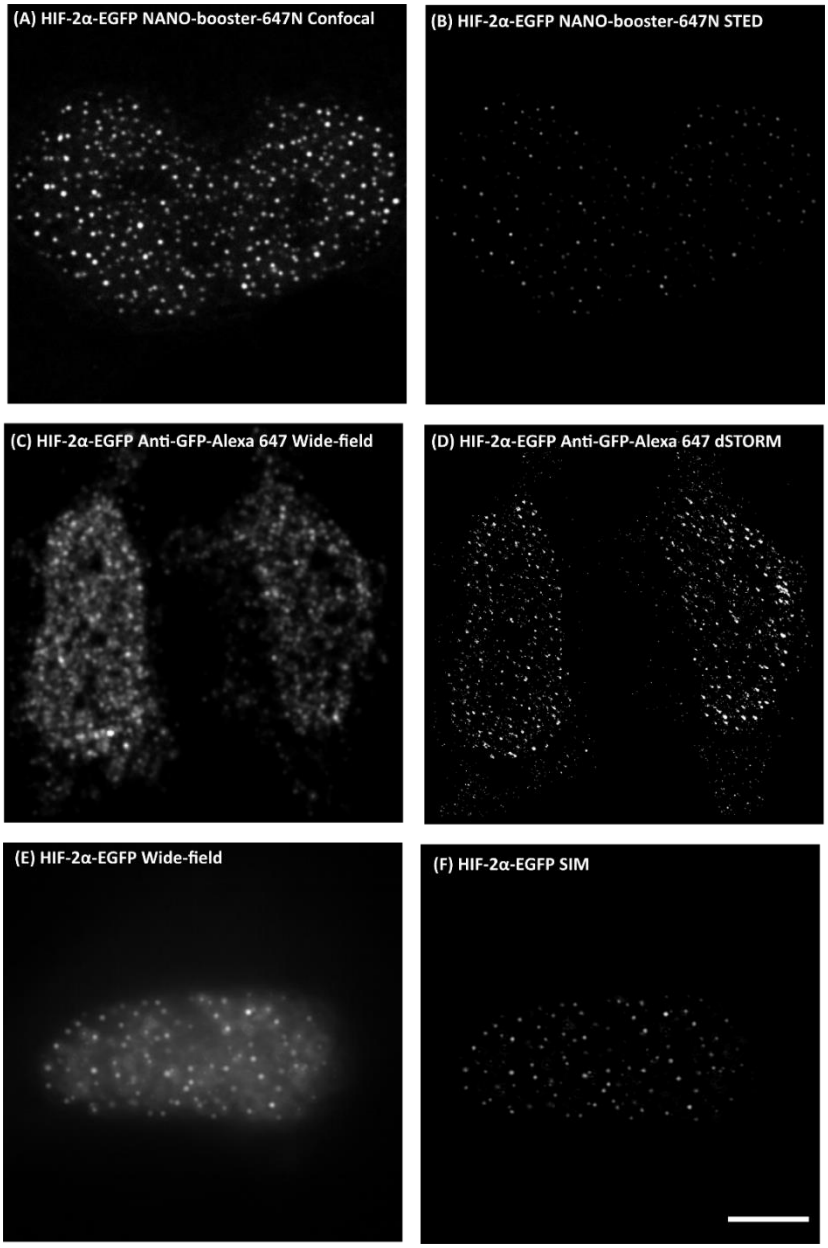


**Figure 81. Exogenous HIF-2α resolved with different super-resolution techniques.** HIF-2α-EGFP was immunolabelled with anti-GFP-nanoBOOSTER-ATTO647N and confocal images taken on a Leica TCS SP8 STED 3x microscope (A). The STED depleted doughnut-shaped laser beam was activated to acquire a z stack of HIF-2α-EGFP, which was deconvolved with Huygens deconvolution, and a maximum intensity z projection was used to display the deconvolved STED image (B). Exogenous HIF-2α-EGFP was also labelled with Alexa 647 by indirect immunofluorescence (C) to acquire, at high laser power, a 30,000 frame stack of single molecules blinking sufficiently ON and OFF for dSTORM-processing (D). A z stack of HIF-2α-EGFP was also acquired (E) and with the addition of a 34 µm rotating grid, a maximum intensity Z projection SIM image of HIF-2α-EGFP could be formed (F). Scale bar = 5 µm.

After using different microscopy techniques to study the localisation of HIF-2α speckles and their potential interaction with other associated nuclear proteins, interest shifted towards determining the precise size and abundance of these speckles in the nucleus. From all of the

super-resolution images of HIF-2α, it is clear that both the number and size of HIF-2α speckles within a nucleus varies. Number of speckles in HIF-2α-EGFP is dependent on the level of expression. When the expression of HIF-2α-EGFP is high, there are lots of speckles, whereas when there is a low expression the fluorescence signal is diffuse and less speckles are present. Also, as seen previously (Figure 73), exogenous HIF-2α speckles appear much larger than speckles of endogenous HIF-2α. Although, the size of HIF-2α speckles is currently unknown, it has been estimated with confocal microscopy that HIF-2α speckles in HIF-2α-EGFP are around 240 nm in diameter, and that within each nucleus, there are around 10-200 speckles (185). However, to date, the size of super-resolved HIF-2α speckles has been undetermined. It was hypothesised that the true size of HIF-2α speckles may be smaller than previously thought and perhaps below the diffraction limit of light, so less than 250 nm. Therefore, it was decided to measure the size of HIF-2α speckles, in HIF-2α-EGFP, which has now been imaged with different super-resolution techniques. The resolution capability of a number of super-resolution techniques (including SRRF) was compared by imaging sub-nuclear speckles labelled with the same fluorescent protein (EGFP) and measuring the size of their FWHM using an ImageJ script.

By measuring the FWHM of these sub-nuclear speckles, the optical resolution capability of a number of super-resolution techniques (SOFI, Airyscan, SIM, STED, and SRRF) was compared. Since hypoxia does not appear to change the number HIF-2α speckles or their size (185), it was decided to only study normoxic HIF-2α speckles. An open-source ImageJ code (available from https://bitbucket.org/davemason/fwhm_spotanalysis/src) was kindly written by the CCI image analyst, David Mason (University of Liverpool, UK), to automatically measure the FWHM of exogenous HIF-2α speckles in the microscopy images. The script worked by drawing a horizontal or vertical line, of a set length, through each speckle in the calibrated image and a one component Gaussian was fitted to the line profile. Only FWHM values, where the Gaussian fits yielded an R-squared value greater than 0.85, were used in the analysis. Since the true size of HIF-2α speckles is unknown, the function to exclude FWHM values greater than 10 times the expected size was not used; however, an image dependent threshold tolerance was set. The calculated FWHM values for each microscopy image were subsequently plotted as box plots (Figure 82).

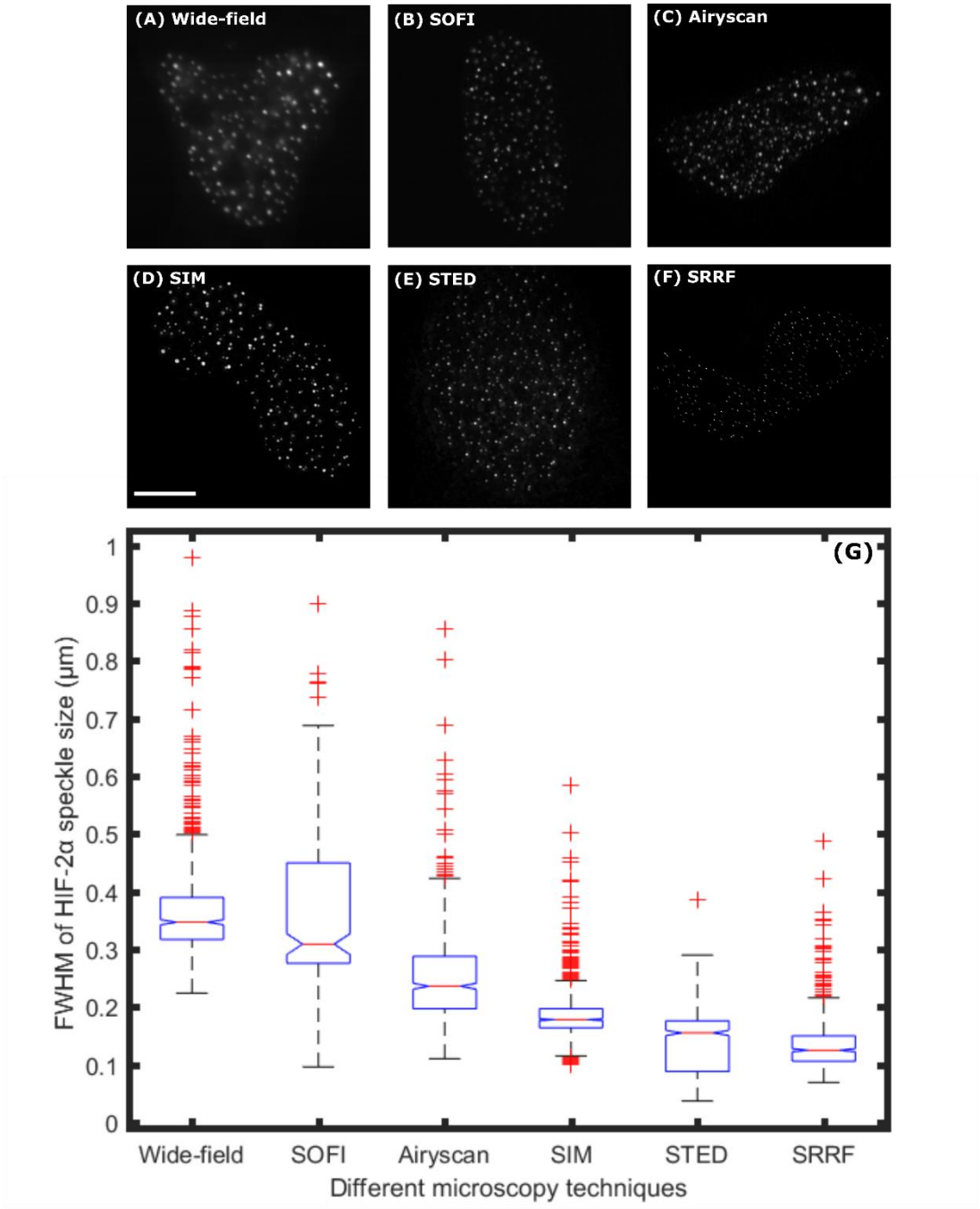


**Figure 82. Quantifying exogenous HIF-2α speckle size acquired with different microscopy techniques.** Exogenous HIF-2α speckles were imaged with wide-field microscopy (A), SOFI (B), Airyscan (C), SIM (D), STED (E), and SRRF (F). As well as an average wide-field image, maximum intensity z projections of SIM and STED images are also shown. The size of the HIF-2α speckles was estimated by automatically measuring their FWHM using an ImageJ script written by CCI image analyst David Mason (University of Liverpool, UK). Box plots for each microscopy technique are shown with outliers plotted in red (G). Wide-field microscopy gave larger HIF-2α sizes than the super-resolution microscopy techniques. Box plot is representative of N=4 images (Each image contained one cell with one HIF-2α nuclear protein) and each data point is an individual HIF-2α speckle. Scale bar = 5 µm.

As expected, wide-field microscopy gave a larger estimated HIF-2α speckle size (mean FWHM value of 371 nm) than the super-resolution techniques (Table 15). The discrepancy between

the wide-field result of 371 nm and the confocal result of 240 nm obtained previously (185), may be due to a different threshold mask approach, such as segmentation, used to estimate the FWHM rather than the automated analysis used here. Smaller HIF-2α speckle sizes were obtained with super-resolution imaging techniques SIM (185 nm), SRRF (135 nm), and STED (142 nm) compared to wide-field microscopy (371 nm) and confocal microscopy (240 nm). Although SOFI (368 nm) and Airyscan (253) gave lower speckle sizes than wide-field microscopy (371 nm), these were still not of a super-resolution nature (<250 nm). The number of HIF-2α speckles, for each calibrated microscopy image, was also estimated (Table 15). It was hypothesised that in the super-resolved images, there may be a slightly higher number of speckles than in the wide-field images. For instance, two speckles that were in close proximity in the wide-field image, appearing as a single speckle, may now appear as two separate speckles in the super-resolution image. As observed previously, the number of HIF-2α speckles within a nucleus varies from cell to cell, but was estimated here to be between 60 and 300 speckles, regardless of which microscopy technique was used.

| | Mean speckle number | Mean FWHM | Mode FWHM | Median FWHM | Minimum FWHM | Maximum FWHM |
|---|---|---|---|---|---|---|
| **Wide-field** | 168 | 371 nm | 328 nm | 347 nm | 224 nm | 979 nm |
| **SOFI** | 66 | 368 nm | 303 nm | 309 nm | 96 nm | 899 nm |
| **Airyscan** | 194 | 253 nm | 187 nm | 236 nm | 110 nm | 856 nm |
| **SIM** | 293 | 185 nm | 178 nm | 178 nm | 99 nm | 585 nm |
| **STED** | 233 | 142 nm | 166 nm | 155 nm | 37 nm | 386 nm |
| **SRRF** | 160 | 135 nm | 117 nm | 125 nm | 69 nm | 487 nm |

**Table 15. Comparing HIF-2α speckle size for different microscopy techniques.** The number of HIF-2α speckles and their size (FWHM), in calibrated microscopy images, was estimated using an ImageJ script kindly provided by image analyst David Mason (University of Liverpool, UK).

### 5.1.6 Live cell imaging of HIF-2α and potential binding partners with SRRF-Stream

To date, HIF-2α has only been imaged with super-resolution microscopy in fixed cells, because of the fast movement of the speckles. With the CCI's recent purchase of the Dragonfly spinning disk confocal, with SRRF-Stream capability, studying the dynamics of HIF-2α with SRRF in live cells was possible. One interest, was to super-resolve the dimerisation of HIF-2α and HIF-1β in live cells with SRRF-Stream, since it was shown earlier, with wide-

field microscopy, that when HIF-2α and HIF-1β are co-transfected, they co-localise in the nucleus homogenously and not in speckles (Figure 74). To begin with, endogenous HIF-2α and its potential binding partners were imaged with SRRF-Stream using immunofluorescence (Figure 83). For direct comparison to the previous NanoJ-SRRF data, similar acquisition settings were used for SRRF-Stream, including an exposure time of 5 ms, 100 frames, and an effective pixel size of 65 nm (13 µm camera pixel size and 100x 1.4 NA plus 2x magnifying lens) to match that of the epifluorescence set-up (effective pixel size of 64 nm: 16 µm camera pixel size and 100x 1.4 NA plus 2.5 magnifying lens). Additionally, NanoJ-SRRF default settings (ring radius of 0.5 and magnification radiality of 5) were used for SRRF-Stream acquisition. SRRF-Stream images of HIF-2α detected with an Alexa Fluor 488 secondary antibody, and potential binding partners Phospho Ser5 RNA Pol II, HAF, HIF-1α, and HIF-1β, detected with an Alexa Fluor 647-labelled antibody, were similar to that achieved previously with NanoJ-SRRF (Figure 79), except the SNR of the SRRF-Stream images was improved, due to illuminating the sample with appropriate 488 nm and 637 nm lasers for Alexa Fluor 488 and Alexa Fluor 647, respectively. However, due to suspected mis-alignment between the red and green channels, co-localisation could not be performed on this data.

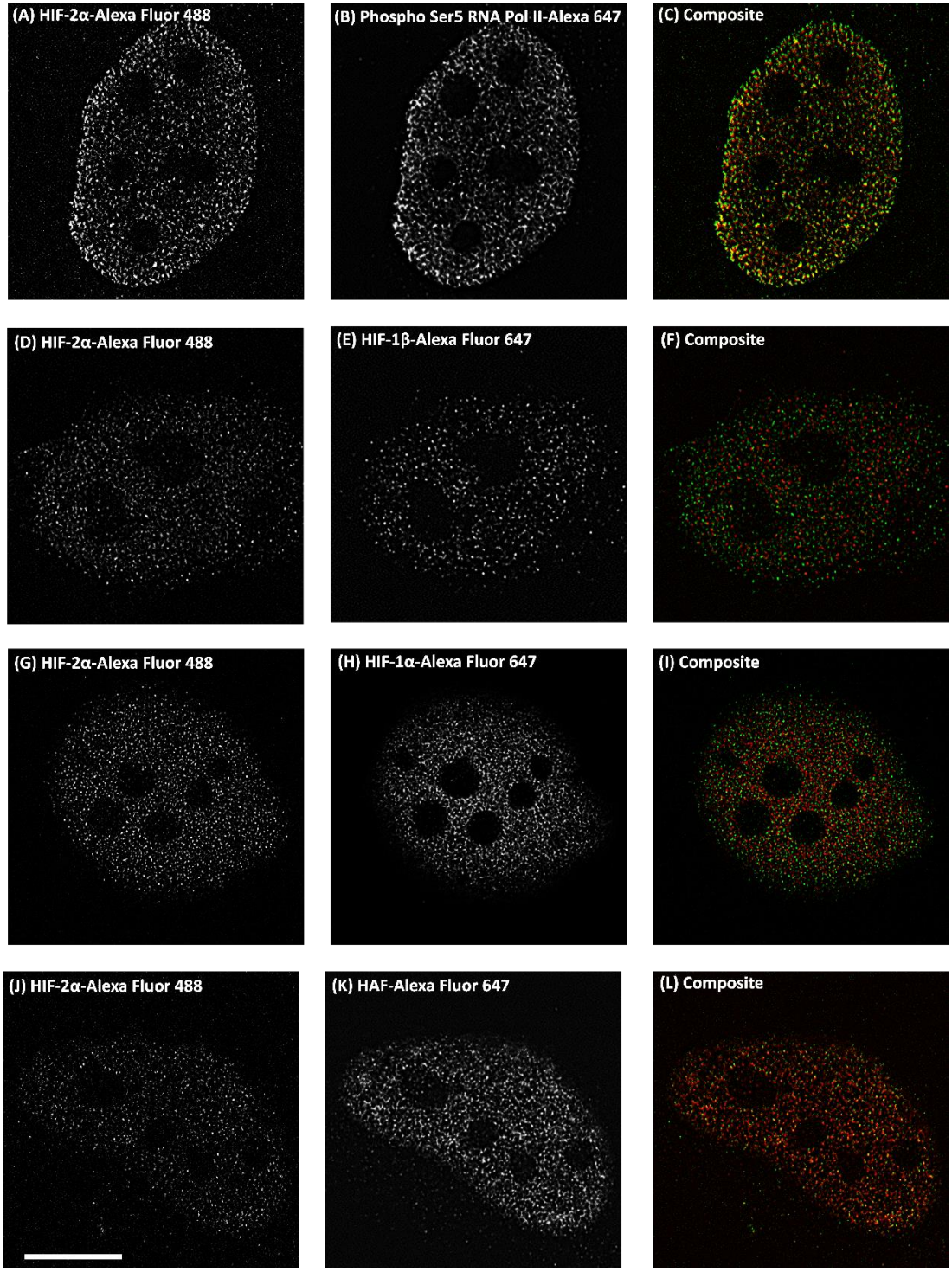


**Figure 83. Endogenous HIF-2α and potential binding partners super-resolved with SRRF-Stream.** Using indirect immunofluorescence, HIF-2α was labelled with Alexa Fluor 488 (green) and other proteins (Phospho Ser5 RNA Pol II, HIF-1β, HAF, and HIF-1α) were labelled with Alexa Fluor 647 (red). All staining was done in HeLa cells that had been grown under normoxic conditions, except for the sample being probed for HIF-1α, which was incubated with DMOG for 4 h, before being fixed with 4% (w/v) PFA. Wide-field images (A, D, G, and J) were acquired sequentially over 100 frames on a spinning disk confocal (100x 1.4 NA plus a 2x magnifying lens), and SRRF-processed with SRRF-Stream (B, E, H, and K). Composite images were created (C, F, I, and L). Scale bar =10 µm.

To be able to image HIF-2α in living cells, HIF-2α and potential binding partners were tagged to fluorescent fusion proteins, transiently transfected, and imaged with SRRF-Stream. As a control, SRRF-Stream images of HIF-2α-EGFP, HIF-1β-DsRed, and HAF-EGFP were also taken in fixed cells, to eliminate any artefacts due to movement. The distinct speckle localisation of HIF-2α in the nucleus, previously observed with wide-field microscopy and NanoJ-SRRF, in fixed cells, was also apparent in the SRRF-Stream images, for both fixed and live cells. SRRF-Stream worked well at improving SNR, through the removal of out-of-focus light and the resolution was appeared to be improved for exogenous HIF-2α and potential bindng partners (Figure 84). Despite some starry artefacts being present for select SRRF-Stream exogneous HIF-2α speckles in the fixed sample, where some speckles appeared elongated, the fast acquisition with the spinning disk confocal enabled the fast mobility of HIF-2α to be SRRF-processed, without any noticeable motion-blur artefacts. Additionally, on close inspection of the fixed SRRF-Stream HAF-EGFP data, there seem to be line artefacts present, but these lines are also visible in the blurry wide-field data, so these are unlikely to be artefacts, and are probably generated by an exchange of protein between the large HAF speckles in the nucleus. To confirm the absence of artefacts with more confidence, these images were assessed, for quality, with the NanoJ-SQUIRREL ImageJ plugin. RSE maps, highlighted artefacts in the SRRF-Stream images, with low RSP values (< 0.95) obtained for HIF-2α-EGFP and HIF-1β-DsRed in both fixed and live cells. Although, a high quality RSP value (>0.95) was achieved for the fixed HAF-EGFP SRRF-Stream image, high errors were also identified for the large HAF speckles (Figure 84). The low RSP values may be due to labelling HIF-2α and HIF-1β with fluorescent proteins, EGFP and DsRed, respectively, as with the same acquisition and post-processing settings Alexa Fluor 488 and 647 yielded high quality SRRF images. Although, SRRF does not require a fluctuating probe, better quality SRRF images may be obtained with cyanine dyes. Further optimisation is needed to acquire high quality SRRF-Stream images of point-like speckle structures.

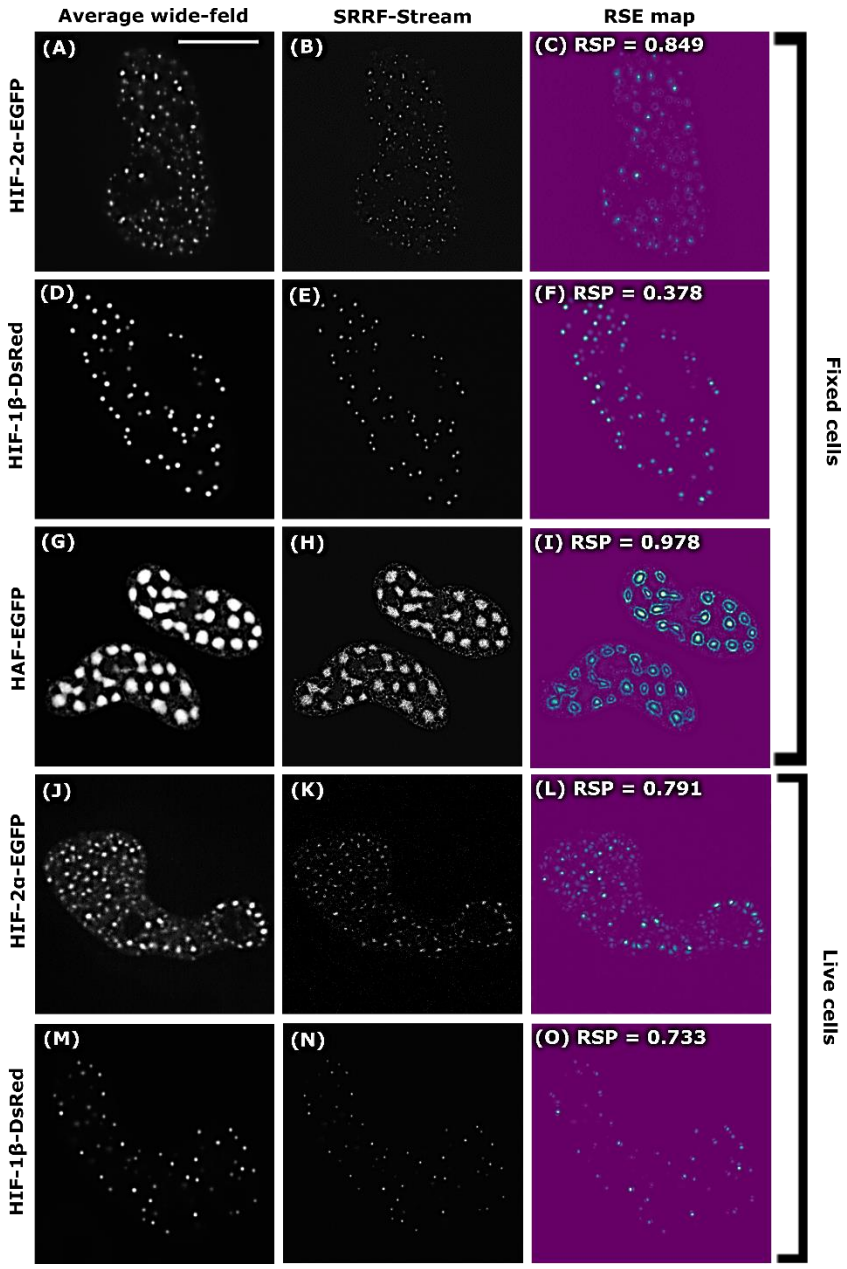


**Figure 84. Exogenous HIF-2α-EGFP and potential binding partners imaged with SRRF-Stream.** Fluorescent proteins were expressed in HeLa cells. Wide-field images, in fixed (A, D, and G) and live cells (J and M), were acquired on a spinning disk confocal (100x 1.4 NA, plus 2x magnifying lens). SRRF-Stream images were also taken (ring radius 0.5 and radiality magnification 5) of fixed (B, E, and H) and live cells (K and N). The quality of the SRRF-Stream images was assessed with NanoJ-SQUIRREL, with corresponding RSE maps (C, F, I, L, and O), highlighting the presence of artefacts (yellow-blue = high error, purple = low error). Scale bar = 5 µm.

With wide-field microscopy, exogenous HIF-2α-EGFP and HIF-1β-DsRed were shown to localise within the nucleus in speckles, when transiently transfected separately into cells, however, when they were co-transfected, they dimerised in the nucleus and were no longer in distinct speckles (Figure 74). Since this observation was done with diffraction-limited wide-

field microscopy, in fixed cells, this was repeated here with SRRF-Stream, in live cells, to better resolve the dimerisation and confirm that this was not an artefact of fixation. As with wide-field microscopy, HIF-2α and HIF-1β became less speckled when co-expressed in living and fixed cells, but the resolution and SNR of the images improved with SRRF-Stream (Figure 85). This improvement in resolution enhanced the presence of line structures, which were again unlikely to be artefacts of SRRF processing, because they were also observed in the lower resolution wide-field images.

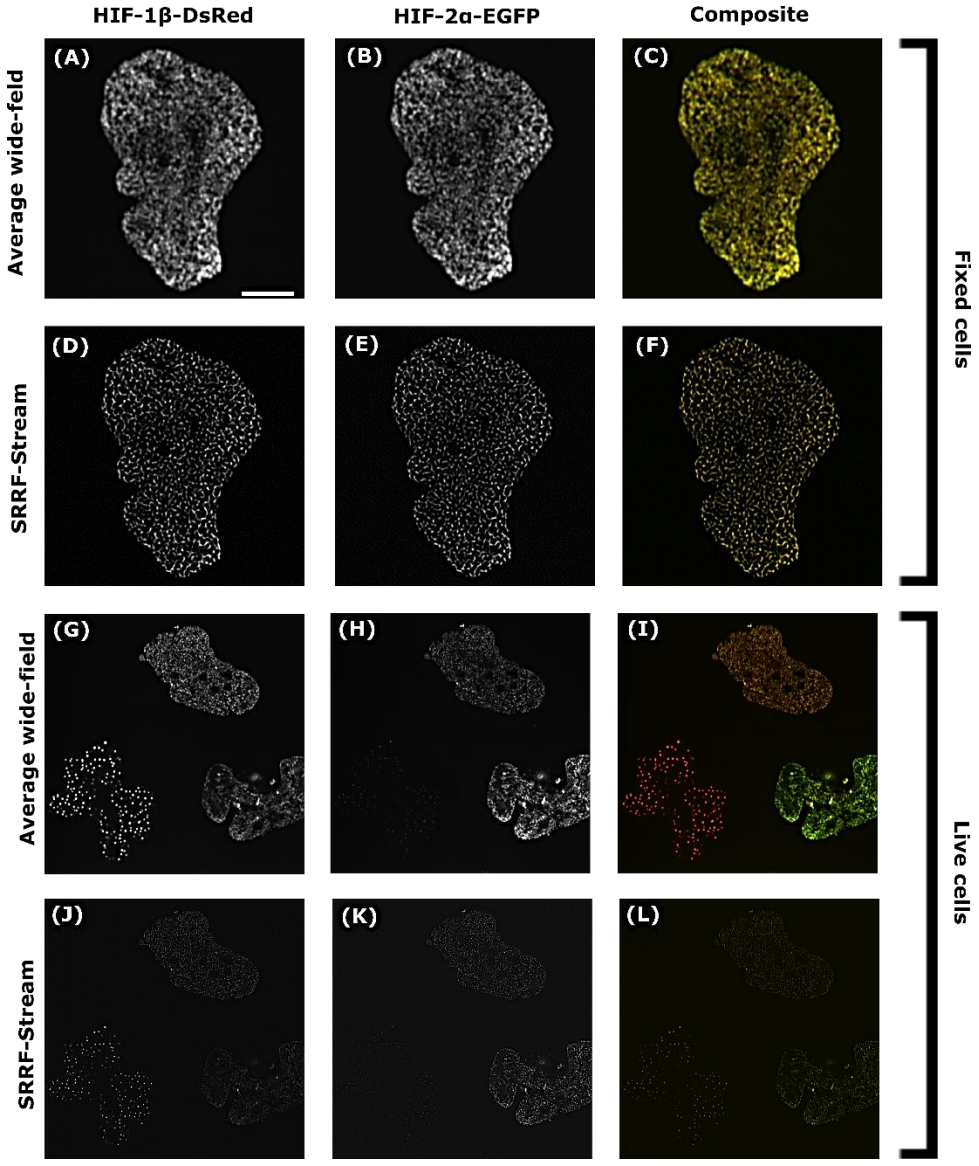


**Figure 85. Super-resolved dimerisation of HIF-2α-EGFP and HIF-1β-DsRed.** HeLa cells were grown under normoxia for 24 h, before being co-expressed with HIF-2α-EGFP and HIF-1β-DsRed. Wide-field images (100x 1.4 NA, plus 2x magnifying lens) were taken on a spinning disk confocal system in fixed (A and B) and live (G and H) cells, with corresponding composite images (C and I). SRRF-Stream images were also acquired (0.5 ring radius and 5x radiality magnification) at 5 ms exposure time, with only 100 frames (D, E, J, and K). Composite SRRF-Stream images are also shown (F and L). When co-

transfected the two proteins become less speckled and more homogenous in both live and fixed cells. SRRF-Stream resolves the co-transfected speckles in live and fixed cells. Scale bar = 5 μm.

### 5.1.7 Interpretation of super-resolved HIF-2α co-localisation

This work was inspired by the Seé laboratory (University of Liverpool, UK), who discovered that whilst HIF-1α is homogenously distributed in the nucleus, under hypoxia, HIF-2α was in speckles during hypoxia and normoxia (185). The importance of HIF-2α being present in speckles, independent of oxygen levels, has yet to be established. The heterogeneous sub-nuclear localisation of HIF-2α may be closely related to its function within the hypoxia signalling pathway. To put this into context, HIF-1α and HIF-2α are differential regulators of oxygen homeostasis, so when this goes awry in tumours, they develop hypoxic regions, which are resistant to chemotherapy. Therefore, research into the localisation of HIF isoforms, may lead to a better understanding of their potential use as targeted cancer therapies. Different microscopy techniques were thus used to investigate the nuclear localisation of HIF-2α in speckles and its association with potential binding partners, including Phospho Ser5 RNA Pol II, HIF-1β, HAF, and HIF-1α.

With all of the microscopy techniques, exogenous and endogenous HIF-2α was found to be localised in speckles within the nucleus. The degree of co-localisation between endogenous HIF-2α and potential binding partners (Phospho Ser5 RNA Pol II, HIF-1β, HAF, and HIF-1α) was strong with wide-field microscopy, but decreased when imaged with the super-resolution microscopy techniques Airyscan and SRRF. Future work investigating post-translation modifications of HIF-2α and its interaction with other nuclear proteins, using mass spectrometry, will complement this co-localisation data. In addition to studying HIF-2α localisation, its physical size and abundance was also investigated with super-resolution microscopy. The size of exogenous HIF-2α speckles in wide-field images was larger than that of super-resolution images, obtained using SOFI, Airyscan, SIM, SRRF, and STED. However, even when imaged with super-resolution microscopy, the HIF-2α speckles were no smaller than the diffraction limit of light with SOFI, and the mean number of speckles between microscopy techniques was variable due to different HIF-2α expression levels in each cell sample. As speckles of endogenous HIF-2α appear visually smaller, it would be interesting to measure the size of endogenous HIF-2α, imaged on different super-resolution techniques, and compare this to the exogenous HIF-2α data. Here, the localisation of HIF-2α and HIF-1α

was studied with SRRF, but the least known isoform HIF-3α, which may also localise in speckles, has yet to be studied with super-resolution microscopy.

In terms of improvement in SNR and removal of out-of-focus light, the freely available post-processing algorithm SOFI is comparable to the more expensive commercially available techniques, such as STED, PALM, SIM, and Airyscan. However, the removal of out-of-focus light and increase in SNR, could just as easily be done with a deconvolution algorithm and the spatial resolution of SOFI (19 % decrease in FWHM) does not match that of the other super-resolution techniques. Similarly, using a wide-field system, equipped with an EMCCD camera and an arc mercury lamp, the open-source NanoJ-SRRF imageJ plugin also yielded HIF-2α images of high quality (RSP values >0.95), however, the resolution improvement was poor, as determined with FRC. The CCI, where the majority of this research was conducted, recently purchased a new spinning disk confocal microscope (Dragonfly) with SRRF-Stream capability, towards the end of this project (2018), so it was of interest to compare this set-up to the open-source NanoJ-SRRF data obtained previously. Until recently, the study of HIF-2α with SOFI had been restricted to fixed cells, but now it has been successfully imaged in live cells with SRRF-Stream. Similar results were obtained in fixed and live cells with SRRF-Stream, and showed that co-expression of HIF-2α and HIF-1β led to smaller speckles, yet the speckle structure was clearly retained. These results are quite remarkable as their co-localisation was never properly visualised before. The quantification of their co-localisation would need to be determined. It would also be interesting to further investigate the formation of this dimerisation over time in 3D with SRRF-Stream, with the hope that it may elucidate to the role of HIF-2α and HIF-1β within the hypoxia signalling pathway.

## 5.2 Deposition and organisation of ECM proteins in scarred cells

As Qdots could not label nuclear proteins (149), it was decided to instead make use of the specific labelling of ECM with Qdots, to compare fibronectin organisation in both normal and scarred skin. Wound healing is a highly regulated process, and if this gets disrupted, it can lead to the formation of an excessive scar, known as a keloid. Keloids result from an accumulation of ECM proteins that are abnormally deposited within tissues, following trauma and subsequent inflammation (325). Presently, the treatment of keloids is extremely invasive and recurrence highly likely. Therefore, it is hoped that by researching the organisation of ECM proteins in KF, the mechanism of ECM remodelling, that causes impaired

scar formation, may be prevented and better treatments made available. The aim was to study the biological function of ECM proteins, involved in scarred and repairing tissue, with higher resolution than currently reported. For this study, in vitro primary cultures of keloid derived fibroblasts (KF) and normal dermal fibroblasts (NF), as control samples, were used.

### 5.2.1 Abundance of collagen I and fibronectin in keloids

Since the accumulation of ECM proteins has been associated with the formation of keloid scars, before the organisation of these proteins, within KF, was investigated, their abundance was measured, to check that the KF behave as expected. According to several articles, KF synthesise more collagen I than NF (325-327). KF have also been shown by biochemical analysis to produce more fibronectin (328, 329). To concur, western blot analysis was carried out to determine the protein abundance of collagen I (10 µg lysate) and fibronectin (10 µg lysate) in KF compared to NF. Visually, there was no difference observed in the band sizes representing the amounts of collagen I (Figure 86A) or fibronectin (Figure 86B) between NF and KF in the blots. However, for 10 ug of whole cell lysate, there appeared to be more fibronectin than collagen I in both NF and KF. Quantification by ImageJ showed approximately a mean 2-fold increase in protein abundance for collagen I and fibronectin in KF compared to NF, but this is negligible in comparison to other published studies (329). One reason for the negligible increase of collagen I observed in KF is that additional ascorbic acid was not added to facilitate collagen I synthesis. Although, there have been reports of as much as a 4-fold increase in fibronectin abundance in KF, the amount can vary substantially (329). Hypotheses have already been proposed for this varied difference in abundance, including the fact that KF, derived from keloid tissue, may also unavoidably contain small traces of normal tissue as a result of isolation from surgery. Other explanations include that NF and KF may have been obtained from different individuals, in terms of race and age (330), or from different regions of the body (329). In addition, some ECM proteins, such as fibronectin, can be inaccessible to antibodies for imaging (331), but this is unlikely for western blot.

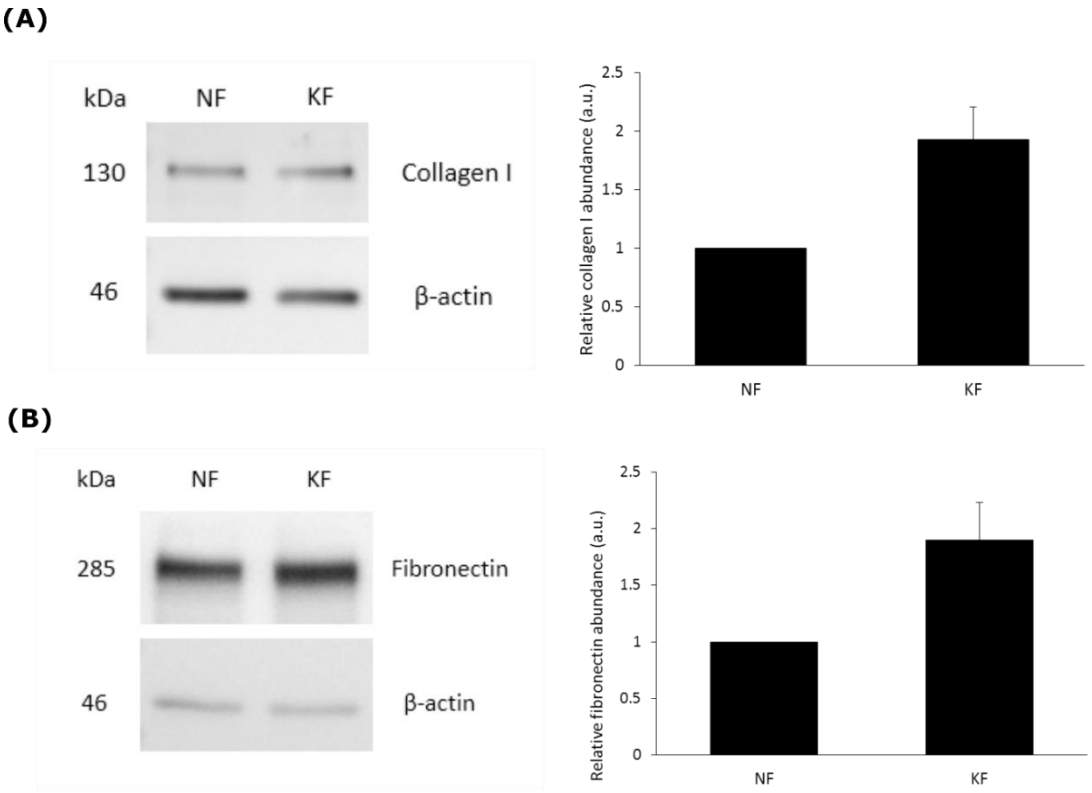


**Figure 86. Abundance of extracellular matrix proteins in KF compared to NF.** Western blot analysis was performed to determine the protein abundance of collagen I (A) and fibronectin (B) in KF and NF. Representative blots are shown for N=3 individual experiments. β-actin was used as a loading control, to which fibronectin and collagen I were normalised against. Protein abundance was quantified using ImageJ and represented as a bar chart, showing the mean protein abundance for N=3 independent experiments and error bars of standard error of the mean (SEM). Although, visually, bands appeared equally bigger for fibronectin than collagen I in both NF and KF, quantification revealed approximately a two-fold increase in the abundance of collagen I (10 µg whole cell lysate loaded) and fibronectin (10 µg whole cell lysate loaded) in KF compared to NF.

### 5.2.2 Directionality analysis of SOFI-processed fibronectin fibres

Aside from the abnormal cell signalling, causing elevated amounts of ECM proteins in KF compared to NF, it has also been established that, normal skin differs morphologically from keloid scars in the way in which collagen is organised in the cell, as during wound healing, the ECM remodels and becomes disorganised (332). For normal skin, collagen is arranged randomly in a basket weave shape, whereas in keloids and hypertrophic scars, thicker collagen fibres are arranged in a whorl-like formation or parallel fibres, respectively (Figure 87). It is this basket weave formation of collagen that is a hallmark of healthy skin (205). Typically, qualitative scoring systems, based on histological observations, are used to describe the severity of a scar formed on skin, which is however, subject to human bias, as it

can lead to variability in diagnosis given by clinicians (333-335). In turn, the lack of consensus in scar assessment can hinder the clinical treatment and the progress of effective therapeutics (334). A less tedious approach would be one that requires less user intervention, and is therefore a quantitative measure, rather than qualitative. Reliable quantitative assessments of collagen fibre thickness and orientation, based on imaging, is challenging. Although, automated image analysis tools, such as FFT, have been used previously to extensively investigate the organisation of collagen fibres (332, 334, 207), little is known about the way in which fibronectin fibres are organised in damaged tissue compared to healthy tissue.

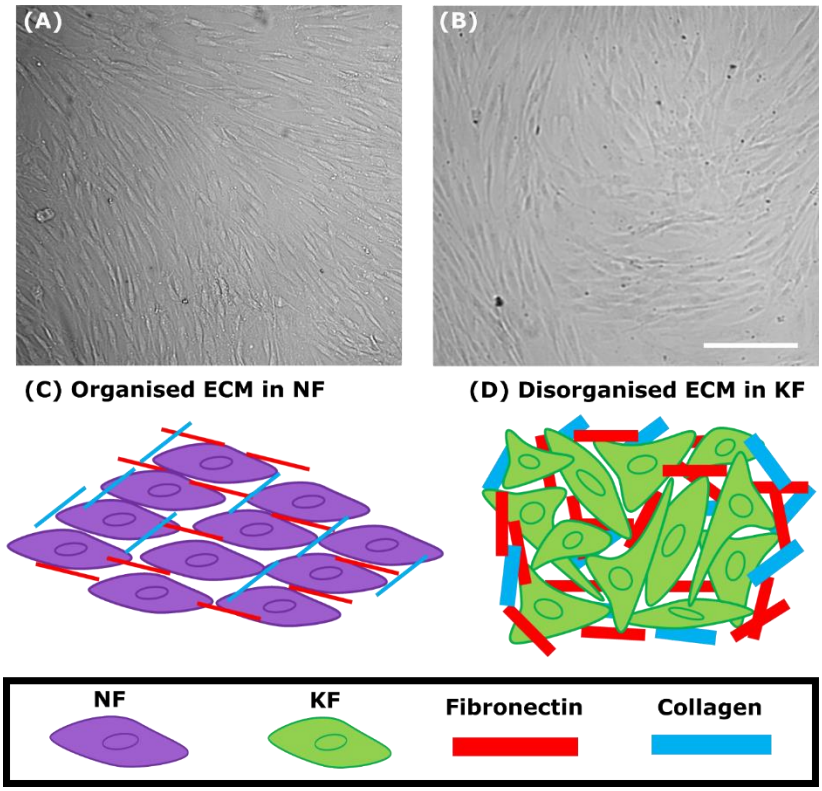


**Figure 87. Organisation of ECM proteins in normal fibroblasts versus keloids.** Wide-field images of NF (A) and KF (B) were taken on an epifluorescence microscope at 10x magnification (scale bar = 200 µm). During wound healing, the ECM remodels, with collagen and fibronectin fibres assembled in an orderly fashion in NF (C), whilst in KF (D) the ECM proteins are disorganised.

Since it had already been established that fibronectin labels well with Qdots (149), it was decided to take advantage of the spontaneous fluctuations of Qdots and compare the morphology of endogenous fibronectin in KF versus NF, using SOFI. Fibronectin was labelled with Qdot 625-Abs in KF and also NF isolated from normal skin adjacent to keloid by indirect immunofluorescence. Fibroblasts were used to study the organisation of fibronectin,

because other types of cells, such as HeLa, have negligible fibronectin (336). For experiments, KF and NF (mycoplasma negative) of passage 4-6 were used and grown for 48 h to allow ECM assembly. To image endogenous fibronectin, epifluorescence microscopy was used rather than TIRF microscopy, because it has been shown that this gives better signal of ECM proteins (337).

Previous studies have shown, using microscopy, that the presence of serum affects the formation of fibronectin fibres (337). Cells incubated with serum-containing medium produced fibronectin that resulted in a non-fibrillar organisation, compared to cells incubated in serum-free medium, where the fibronectin was organised into fibres (337). Another interesting observation, made by the same research group, was that when the cells were incubated in medium containing 10% FBS (v/v), fibronectin did not co-localise with F-actin, whilst in the absence of serum, there was co-distribution (337). In order to confirm results obtained previously, KF and NF were incubated in normal medium (DMEM supplemented with 10% FBS v/v), starvation medium (DMEM without the addition of 10% FBS v/v), and also medium where 10% FBS (v/v) had been substituted with 10 ng/mL BSA. KF and NF were incubated in starvation medium for 48 h, before fixation in 4% (w/v) PFA, since it has been reported in the literature that beyond two days of serum-free medium, the morphology of fibronectin did not change (337). After triple labelling with fibronectin-Qdot625, Phallodin-Alexa488, and Hoechst 33342, no co-distribution was observed between fibronectin and F-actin in any of the conditions tried (normal, serum-free, or BSA substituted medium), when imaged using epifluorescence microscopy and subsequently SOFI-processed (Figure 88A).

To further investigate the morphology of fibronectin in NF and KF, the difference in fibronectin fibre orientation, in the wide-field images (Figure 88B) and SOFI-processed images (Figure 88C), was assessed using a Directionality plugin (255) in ImageJ (251, 252). Endogenous fibronectin was characterised by direction (orientation of the fibres) and dispersion (angular distribution of the fibres aligned in a given direction). The amount of fibronectin fibres in a given direction was plotted as a histogram and the highest peak fitted with a Gaussian. Dispersion was measured from the σ of the Gaussian. A Broad σ of the histogram meant that there was a high dispersion in the fibres (disorganised fibronectin), whereas a narrow σ, meant that the fibres were aligned (organised fibronectin). After analysing ten images per condition with the Directionality ImageJ plugin (N=3), there was no significant difference [One-way ANOVA: $F(23,692) = 1.05$, $p>0.05$] found between the dispersion of fibronectin fibres in NF and KF, in vitro, for the wide-field images (Figure 88B)

or SOFI-processed images (Figure 88C). To eliminate bias when deciding which ROI to image, fibronectin around the nucleus was selected as a reference point, so that every image contained at least one nucleus in the FOV, which was labelled with Hoechst 33342. For SOFI-processing, fibronectin in both permeabilised (intracellular and extracellular) and non-permeabilised (extracellular) NF and KF was immunolabelled with Qdot 625. Endogenous fibronectin could also be labelled with Qdots in non-permeabilised live NF and KF since it is extracellular. Although, the live fibronectin-Qdot could be SOFI-processed, there was some motion blur artefacts from cell movement and therefore, these images were not considered for further analysis.

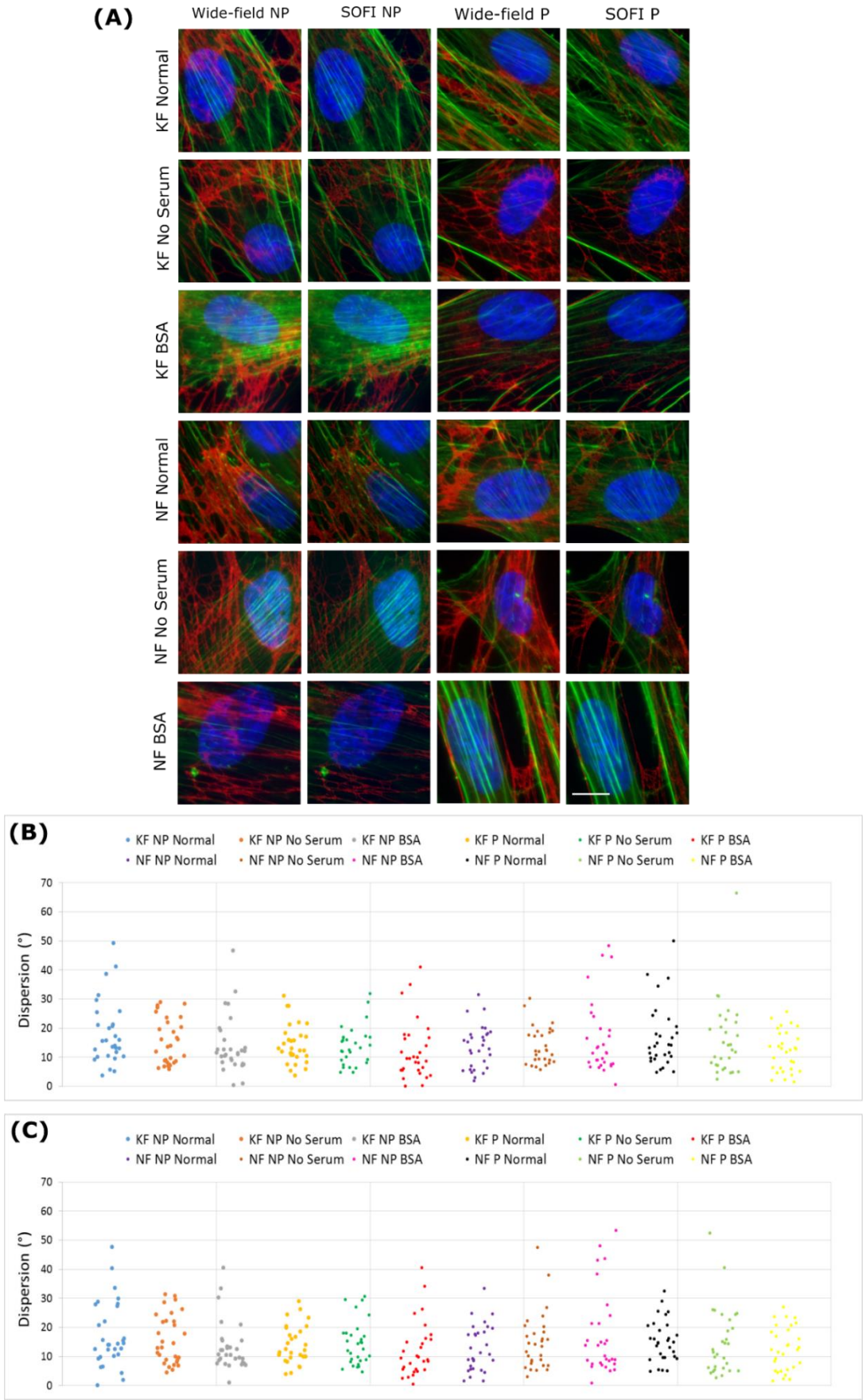


**Figure 88. Organisation of SOFI-processed fibronectin fibres.** Extracellular (NP – non-permebilised) and intracellular (P – permeabilised) fibronectin of normal dermal fibroblasts (NF) and keloid

fibroblasts (KF) was labelled with Qdot 625 (red) for imaging via epifluorescence microscopy (100x 1.4 NA plus a 2.5x magnifying lens) and subsequently SOFI-processed. KF and NF were treated in normal medium containing DMEM with 10% FBS, medium with no serum, and medium substituted with 10 ng/mL BSA. Average wide-field and second order SOFI images processed with Localizer are representative of N=3 independent experiments consisting of N=10 technical repeats (A). F-actin was labelled with Alexa Fluor 488 (green and nuclei with Hoechst33342 (blue). The dispersion of the wide-field (B) and SOFI-processed (C) fibronectin fibres for each condition was calculated using a Directionality plugin in ImageJ and plotted. Scale bar = 10 µm.

The direction of the fibres was highly dependent on the random orientation of the cells when cultured on round coverslips, but regardless of their orientation, the dispersion of the fibres within a cell remained the same, so this was a more accurate measurement for fibre organisation. However, Directionality may be an unreliable analysis as the lack of difference in dispersion between fibronectin in NF and KF, might be due to the poor goodness of fit (Good = 1, bad = 0) of the Gaussian of some cells (minimum of 0.11 and maximum of 0.97), compared to other methods, such as FiberFit (338). The poor goodness of fit may have been as a result of inadequate background noise removal, which will have affected the analysis of the fibres of interest. Another limitation of the Directionality analysis, as found by others, is that the plugin cannot detect multiple peaks, but instead uses the highest peak in the histogram to deduce the dispersion value, which can be misleading (Figure 89). Furthermore, the Directionality plugin does not work well on non-uniform images, such as those where there is less dense regions of fibronectin or variations in fluorescence intensity (206). Furthermore, the amount of fibres in a given orientation has also been shown to be underestimated in some instances (339).

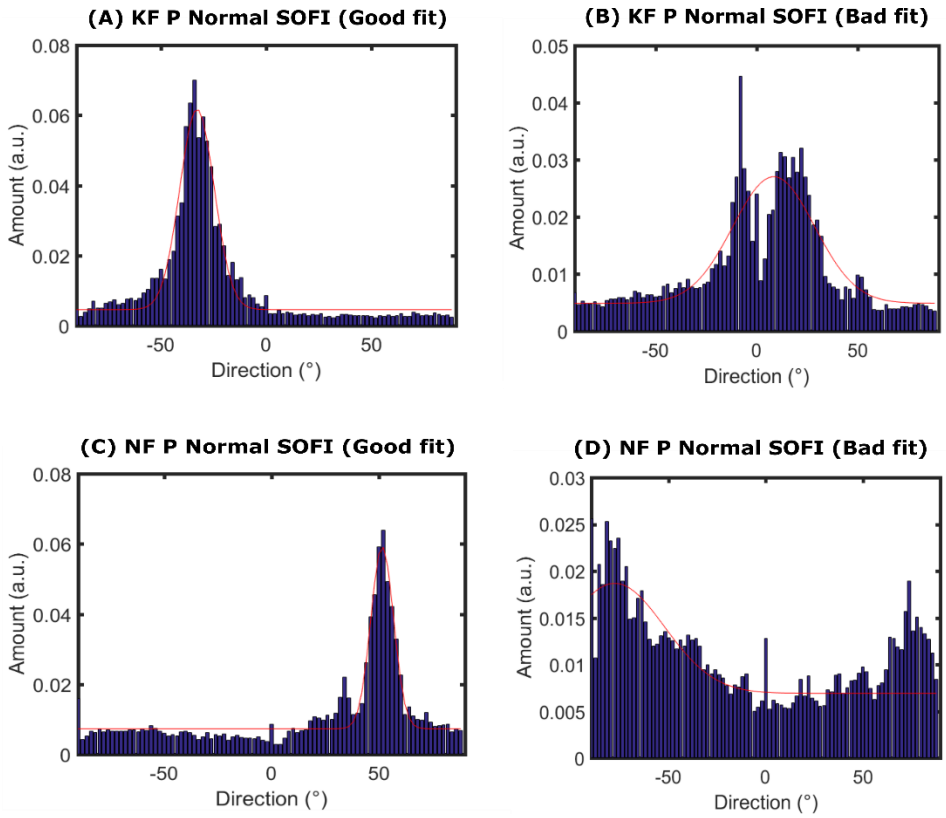


**Figure 89. Representative histograms of the amount of SOFI-processed fibronectin fibres in a given direction.** The amount of fibronectin fibres in a given direction for each image was plotted as a histogram and the highest peak fitted with a Gaussian. Dispersion of the fibronectin fibres in KF (A&B) and NF (C&D) was measured from the standard deviations of the Gaussian. A good fit (values closer to 1) is one that has a single Gaussian peak with high values 0.96 for KF (A) and 0.93 for NF (C), whereas multiple peaks gave a poor goodness of fit (values closer to 0) with lower values 0.73 for KF (B) and 0.71 for NF (D) .

### 5.2.3 Conclusions based on abundance and directionality of fibronectin fibres

Using the high spatial resolution obtainable by SOFI to investigate the nanoscale organisation of fibronectin fibres in greater detail than previously achieved with wide-field microscopy was the main objective of this work. It was hypothesised that as well as fibronectin being more abundant in KF compared to NF cells, fibronectin fibres in NF would be arranged in an orderly fashion, in one distinct direction, whilst fibres in KF would be more disorganised and thus aligned at multiple angles. Based on previous observations, it was also hypothesised that fibronectin fibres in cells incubated in serum free medium would co-distribute with F-actin fibres.

Since ECM proteins are involved in the wound healing process, it was logical to assume that fibronectin would also be elevated in keloids that result from abnormal wound healing (329).

Although, there was a mean two-fold increase in fibronectin abundance in KF compared to NF, reported by western blot analysis (Figure 87), this was lower than expected for KF where the accumulation of ECM proteins is usually abnormally high. To study the morphology of fibronectin in NF compared to KF, endogenous fibronectin was successfully labelled with Qdots and SOFI-processed up to second order using Localizer (89). Visually, there was no sign of co-distribution between fibronectin and F-actin in serum free medium, other than a small degree of overlap simply by chance (Figure 88A). The lack of co-distribution between fibronectin and F-actin can be further confirmed by calculating the Manders correlation coefficient (250) using JACoP (248) in ImageJ. Although, SOFI gave an increased SNR and improved spatial resolution, there was some artefacts in the images, associated with the SOFI-processing. Furthermore, no difference between the orientations of fibres in NF compared to KF in either the wide-field images or SOFI-processed images (Figure 89). Despite more fibronectin being present in images where the cells had been permeabilised (P) as opposed to non-permeabilised (NP) cells, there was also no obvious difference between the organisation of their fibronectin in both NF and KF. Directionality analysis was done in 2D cells in vitro, but the organisation of fibronectin fibres might differ in 3D tissue samples, which would better represent ex vivo. Therefore, it would be interesting to repeat these experiments with 3D SOFI. As the Directionality analysis has some limitations, another type of analysis that could have instead been used is one that analyses texture features (340), which has previously been used on collagen fibres (206). The future of image analysis is shifting towards the incorporation of machine learning and this is promising for the automated analysis of fibre organisation, which can be used to diagnose scar formation, and is therefore much anticipated by clinicians.

### 5.3 Investigating NET abundance and localisation with SOFI

Upon inflammatory stimuli, such as infection, neutrophils (white blood cells) defensively respond by bursting their cytoplasmic membrane and nuclei de-condense to release NETs, which are fibres composed of DNA and granule proteins that extracellularly engulf microbes as an immune defence mechanism (218), in a process known as NETosis. There is increasing interest in NETs, due to their involvement in a number of autoimmune diseases, such as rheumatoid arthritis (225) and SLE (229). Understanding the protein composition of NETs may uncover the role of NETs in the development of autoimmunity and auto-antibodies that

may lead to therapeutics against autoimmune diseases. Many different techniques have been used to identify proteins associated with NET formation, including immunocytochemistry (334, 341), FACS analysis (232), ELISA (231), and mass spectrometry (233). NETs are fragile and their associated proteins are not easily separated with fluorescence microscopy, which is why mass spectrometry has been employed, as an alternative unbiased approach. Although, fluorescence microscopy has been successfully used to characterise NETs (213), these images are limited by the resolution of the optical system, so it is challenging to establish the exact abundance and localisation of NET proteins. In collaboration with Helen Wright at the Institute of Ageing and Chronic Disease (University of Liverpool, UK), it was decided to study, in greater detail, the abundance and localisation of NET proteins in vitro using SOFI. By obtaining higher resolution images of NET-associated proteins, which are smaller than the resolution limit of light, their organisation with respect to one another can be established, which may lead to new insights into their function.

### 5.3.1 Revealing structural information of SOFI-processed NETs

NETs consist of DNA decorated with a number of proteins, including histone H3, citH3 (342, 343), NE (213, 219), MPO (213), and PAD4 (340). Despite many of these NET-associated proteins being identified by proteomics, their organisation and role in forming NETs is yet to be fully established (219). The focus of this work, was to study, in greater detail, the abundance and localisation of NET-associated proteins, by obtaining high-resolution images, using SOFI. Although, NETs were first identified in 2004 (213), little is known about their abundance or localisation. NETs, consisting of granule proteins and chromatin (DNA and histones), have previously been imaged at high-resolution with SEM (219) and TEM (213), but these techniques require an expert user and are expensive to run. In addition, there have been doubts as to whether NETs can be discriminated from fibrin under inflammation when using SEM (220). Therefore, NETs have also been imaged with live cell imaging, but at low resolution (221). It was hypothesised that SOFI could provide a novel insight into the abundance and localisation of proteins along the NET fibres, being 15-17 nm in diameter, at high-resolution with a more gentle approach than the harsh fixation and preparation involved with SEM or TEM (213). Despite Qdots being unable to specifically label nuclear structures (149), such as histones, they should label proteins that decorate the structure of NETs, because these are extracellular (344).

To investigate the composition of proteins along the structure of NETs, these extracellular structures were labelled with Qdots and their wide-field images (100x 1.4 NA) SOFI-processed. The release of granule proteins and chromatin from adherent neutrophil cells (extracted from blood) was stimulated with either a chemical, such as PMA, or the calcium ionophore A23187, to form NETs. For the production of NETs, for staining, white blood cells (neutrophils) were kindly isolated from healthy human blood donors by Elinor Chapman (post-doctoral researcher with Helen Wright at University of Liverpool, UK), who also provided the relevant antibodies. Care was taken when fixing the NETs with 4% (w/v) PFA and staining, because they were extremely fragile. NET-associated proteins NE, MPO, citH3, and PAD4 were stained using indirect immunofluorescence with primary antibodies against NE, MPO, citH3, and PAD4, which were labelled with Qdot-conjugated secondary antibodies in either green (Qdot 525) or red (Qdot 625). A positive staining control of activated neutrophils was incubated with Qdot-conjugated secondary antibodies only and no primary antibody, to rule out any possibility of non-specific binding of Qdots to neutrophils, which was negligible. Although, MPO has been labelled with Qdots previously (345), it had not yet been imaged with SOFI until now. Two-colour SOFI images of NETs was also achieved, through the sequential imaging of proteins labelled with Qdot 625 (red) and Qdot 525 (green). In addition, a nuclear intercalating dye, Hoechst 33342, was added to show DNA expelled from nuclei, because this is the NET's main structural component and co-localises with proteins decorated along its structure (213). To establish if a NET is present, quantification methods can be carried out (236).

Generally, when neutrophils were incubated with dimethyl sulfoxide (DMSO, vehicle control) (60 μM), there was negligible NET production (estimated <1%). However, in some control samples, NETs were observed and specifically labelled with Qdots. The presence of NETs in unstimulated samples is not an isolated issue and has been observed by others, although the cause is unknown, it may be as a result of the isolation procedure when preparing neutrophil samples (218, 346). In unstimulated neutrophils, proteins were typically in granules and the nuclei lobulated (Figure 90). To confirm the lack of NET formation in unstimulated neutrophils, a previously published method was used (236), whereby the mean fluorescence intensities of DNA release (blue Hoechst 33342 channel) and the presence of NE (red Qdot 625 channel) was compared in a wide-field image (same lamp power and gain used) using ImageJ by drawing a line profile (green) through a single granule protein in a neutrophil and its corresponding nuclei in a composite image (Figure 90D). In the presence of DMSO, there was a mean fluorescence intensity of 6875 a.u. for nuclei labelled with Hoechst 33342,

compared to a mean fluorescence intensity of 6454 a.u. for NE labelled with Qdot 625 (N=6 granule proteins measured in a single wide-field image). The fluorescence intensity of the Hoechst 33342 channel was higher compared to the fluorescence intensity of Qdot 625 channel, which confirmed that these were unstimulated NETs.

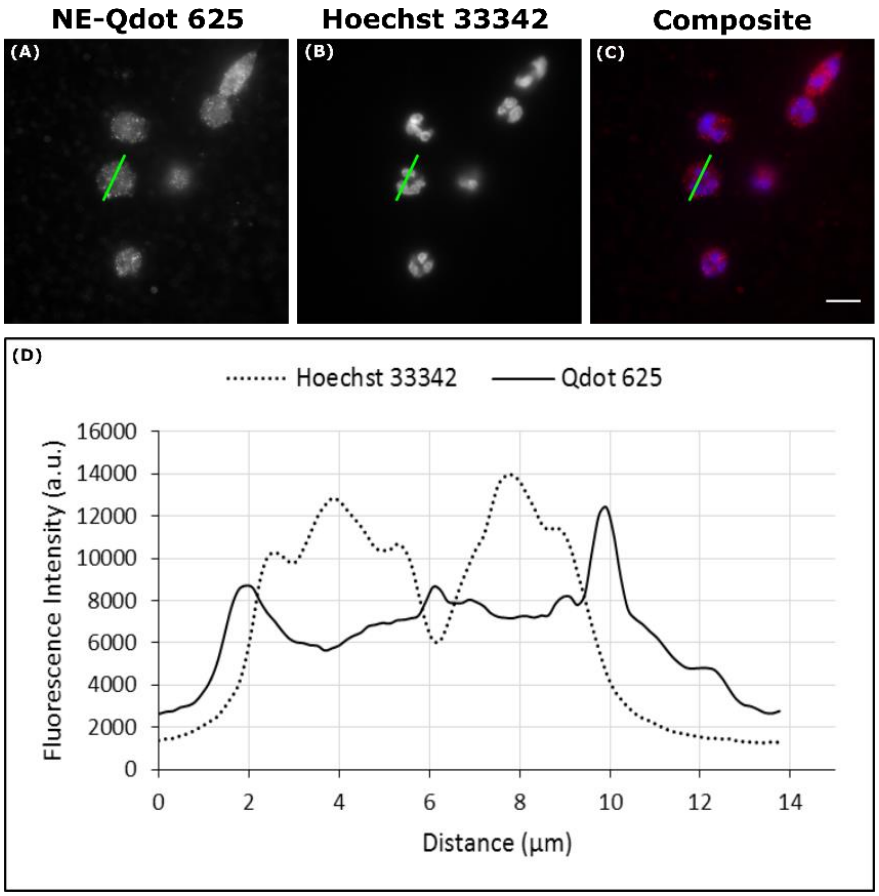


**Figure 90. Identifying NETosis in the presence of DMSO.** Neutrophils were incubated with 60 µM DMSO, as a control, and stained using indirect immunofluorescence with a primary antibody against NE (A) and a corresponding Qdot 625 conjugated secondary antibody (red). DNA was stained blue with Hoechst 33342 (B). A composite image (C) was produced by taking wide-field images on an epifluorescence microscope (100x 1.4 NA). NET formation was quantified using ImageJ, by comparing the mean fluorescence intensities of DNA release (Hoechst 33342 channel) and the presence of NE (Qdot 625 channel). A line profile (D) was plotted by drawing a green line through a single granule protein in a neutrophil (A) and its corresponding nuclei channel (B) in a composite image (C). No NETs were released in the presence of DMSO as shown by the existence of lobulated nuclei, with higher intensities than NE. Scale bar = 10 µm.

The most commonly imaged NET-associated proteins in the literature are NE and MPO, after neutrophil activation with PMA. To test whether Qdots can specifically label NET proteins, these were imaged by wide-field microscopy and SOFI-processed. Although, from the SOFI-processed images, there were some distinct dots along the string-like fibres of the NETs (Figure 91), this could simply be due to the nature of Qdot labelling. To investigate whether

the density of Qdot labelling affected the resulting SOFI-processed images, a range of Qdot conjugated secondary antibody concentrations was tried, but this did not change the dot-like pattern, which could either be resolved single NET-associated proteins or Qdot aggregates. Even with SOFI-processing, only granule proteins, rather than cytoplasmic proteins, were seen on the NET structures, as was the original observation when imaged with standard fluorescence microscopy (213). The amount and distribution of NETs was also variable between samples, as observed by other researchers (221, 220). Often, very few NETs (estimated <5%) were present, when stimulated with PMA or the calcium ionophore A23187, which may be as a result of the fragile nature of NETs, the dose of the chosen stimuli, or the biological variation in donor response to each agonist.

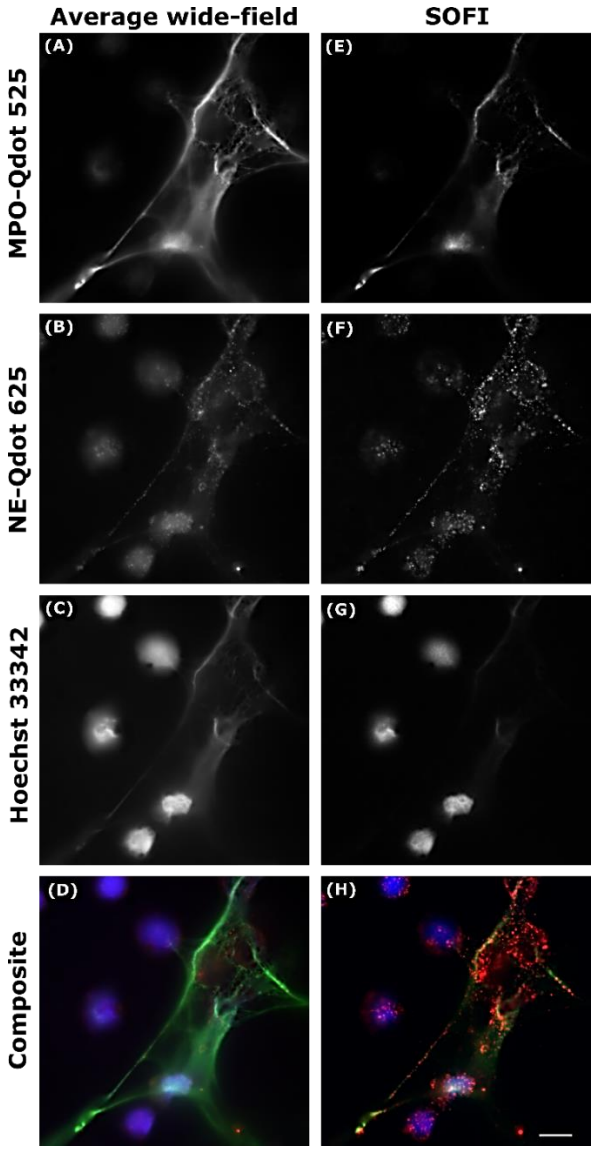


**Figure 91. SOFI-processed NETs released in response to PMA stimulation.** Neutrophils were incubated with 50 mM PMA to induce NETs that were stained using indirect immunofluorescence with primary antibodies against MPO (A) and NE (B), which were labelled with Qdot 525 (green) and Qdot

625 (red), respectively. DNA was stained blue with Hoechst 33342 (C) to produce a single composite image (D). Wide-field images were taken on an epifluorescence microscope (100x 1.4 NA) and subsequently SOFI-processed (E-G) using Localizer to produce a single composite SOFI image (H). Scale bar = 10 µm.

The release of proteins associated with NETs is unique to the type of stimulus used to mimic inflammation. For instance, PMA, an activator of protein kinase c (PKC), predominately induces the release of NE and MPO (Figure 91), whereas the calcium ionophore A23187, mediates the release of citurllated histones (post-translational modification, which converts arginine residues to citrulline on histones) and PAD4 (347). As the release of NETs has previously been shown to be absent from mutated mouse neutrophils that lacked PAD4, it is known that PAD4 is an important player in the process of NETosis (348). Since PAD4 is responsible for the post-translation modification of histone H3, that causes the conversion of arginine residues into citrulline residues within proteins to form citH3 (349), SOFI-processing was used to evaluate the abundance and localisation of the nuclear protein PAD4 in relation to citH3. Furthermore, citH3 was of interest, because it has been recognised as a potential marker of NETosis, as deamination is specific to the NETosis process, whereas the leakage of other granule proteins, such as MPO, may be confused with necrosis (225). It was hoped that by investigating the protein composition of PAD4 and protein deamination of histones that occurs in the nucleus of neutrophils, in the long term, it would help to reveal its role in different pathological states, as there is increasing evidence of PAD4 being involved in a number of diseases such as RA (226), multiple sclerosis (350), and Alzheimer's disease (351). To investigate the implications of histone modification induced by PAD4, endogenous PAD4 and citH3 in healthy neutrophils stimulated with the calcium ionophore A23187, were stained by indirect immunofluorescence. PAD4 was labelled with Qdot 625 (red), whilst citH3 was labelled with Qdot 525 (green). Other researchers also observed that fewer NETs were present when probed with PAD4 primary antibodies, due to challenges of detecting the low level expression of endogenous PAD4 in neutrophils by immunofluorescence (224, 339). Those NETs probed for citH3 and PAD4 with Qdots were often in a cloud-like pattern (Figure 92), rather than fibres as seen with NE and MPO (Figure 91). NETs can present in different types of forms, and a cloud-like pattern has also been recognised by other researchers in unfixed and hydrated NET samples (218, 352, 353). Whether there is a functional difference between NETs that are released in a filamentous form versus a cloud-like formation, is currently unknown. Although, SOFI-processing removed a considerable amount of out-of-focus light, the cloud-like formation of NETs released made it difficult to obtain any extra structural information about the protein composition. So far, the interpretation of the SOFI-

processed NET images has been qualitative, by visual observation, rather than quantitative means. Quantification was not necessary at this point, because it was adequate to assess the spatial resolution improvement, attained with SOFI-processing, through visual inspection of the NET structures.

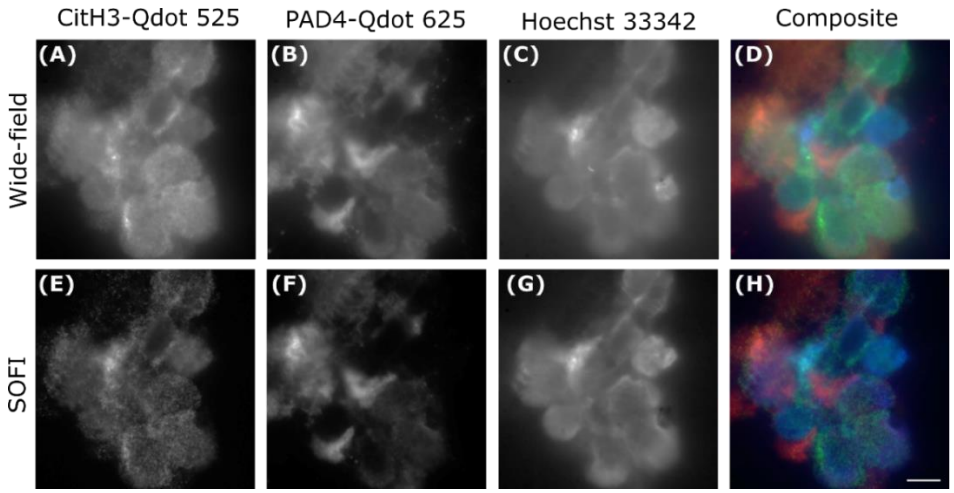


**Figure 92. SOFI-processed NETs induced by A23187 activation.** Neutrophils were incubated with 5 µM A23187 to induce NETs that were stained using indirect immunofluorescence with primary antibodies against citH3 (A) and PAD4 (B), which were labelled with Qdot 525 (green) and Qdot 625 (red), respectively. DNA was stained blue with Hoechst 33342 (C) to produce a composite image (D). Wide-field images were taken on an epifluorescence microscope (100x 1.4 NA plus a 2.5x magnifying lens) and subsequently SOFI-processed (E-G) using Localizer to produce a composite SOFI image (H). Scale bar = 5 µm.

The most obvious way to quantify NETs, is to physically count the number of decondensed DNA and NET-associated proteins by eye, although time-consuming. However, images of NETs can also be quantified using automated image analysis tools (236, 354), including high-throughput approaches, such as the open-source DANA (238), implemented in ImageJ. Despite these tools, it is still challenging to count individual proteins along the structure, particularly with SOFI-processed images, which contain correlated intensity values. Therefore, the abundance of localisation of NET proteins has yet to be quantified here. However, the presence of NETs was verified, before SOFI-processing, by comparing the fluorescence intensity of an intercalating DNA dye against that of a NET-associated protein (236). The lobulated nucleus of unstimulated neutrophils is always highly saturated with bright intensity, whilst the DNA of the NET itself is of much lower fluorescence intensity (Figure 90D). Although, if unstimulated neutrophils are in the same FOV as stimulated neutrophils, it makes it difficult to acquire both the NET and the point at which the NET was released. Another limitation with quantifying the NETs is that the distance between proteins, along the structure of a NET, may be affected by the level of labelling, for instance, if labelling

is sparse there might not be much coverage along the structure due to steric hindrance of the Qdots. An alternative approach to quantifying the proportion of citrullated histones, along NET structures, is by using co-localisation methods, such as the Manders correlation coefficient, by comparing the localisation of H3 with citH3 (247). The co-localisation of proteins, that have been SOFI-processed, has been achieved previously (108). Furthermore, the manual imaging and quantification of NETs is tedious, low throughput, lacks reproducibility, and introduces an element of bias, which is why some groups have developed automated approaches based on machine learning (355).

### 5.3.2 Conclusions drawn from processing NET images with SOFI

By using SOFI, to resolve proteins associated with NETs at higher spatial resolution, it was hoped that more structural information about their abundance and localisation may be achieved. Although, MPO had been labelled with Qdots previously (345), there was no evidence of any other NET-associated proteins having been labelled with Qdots or SOFI-processed with Localizer. It was shown that in control samples, where neutrophils were incubated in DMSO (60 μM), negligible NETs were released, as the fluorescence intensity of Hoechst 33342 was higher than that of the granular protein NE (Figure 90). However, when stimulated with PMA or A23187, NETs were formed in either fibres (Figure 91) or a cloud-like formation (Figure 92), and their associated granular proteins released into extracellular space. As NETs span a large FOV, to capture both the NET and the site of release from the nucleus, images were acquired at the highest possible magnification (100x 1.4 NA), but often below Nyquist sampling expected for optimal SOFI-processing (100x 1.4NA plus a 1.6x magnifying lens), and therefore at the expense of resolution. Although, SOFI removed a considerable amount of out-of-focus light from the wide-field images, some potentially important NET structures were completely removed from the SOFI-processed images, as a result of uncorrelated fluorescence signal. Despite this loss in information, SOFI-processing did enhance the dot-like pattern of the proteins along the NET structures (Figure 91). The dot-like nature of the images results from the real organisation of proteins along the NETs and not the sparse labelling of Qdots. Utilising SOFI for the visualisation of NETs has important clinical implications, because by investigating the way in which NETs form, in greater detail, will ultimately contribute towards a better understanding of the proteins' involvement in autoimmune disease. Furthermore, to complement the advantage of SOFI, a robust quantification method for SOFI-processed NETs needs to developed, which would

enable the protein abundance and localisation of NETs to potentially be used as a biomarker for the diagnosis of many pathological conditions. Helen Wright's research group are concerned with the involvement of NETs in disease, in particular, RA. Although, it has already been established that there is an enhanced production of NETs in RA patients (226), it has yet to be shown whether the protein composition of NETs in RA patients differs from that of healthy patients, with super-resolution microscopy, so this will be the focus of future collaborative work.

### 5.4 Study into the deposition of LM-332 in relation to LaNt α31 using SOFI

As part of a collaboration with Kevin Hamill's research group in the Department of Eye and Vision Science, at the Institute of Ageing and Chronic Disease (University of Liverpool, UK), the distribution of the LaNt α31 protein in immortalised corneal epithelial cells (hTCEpi), in relation to other laminins, such as LM-332, was investigated, at high-resolution, using SOFI.

#### 5.4.1 Localisation of LaNt α31 with LM α3

Heterotrimeric basement membrane proteins, laminins, have important roles within the ECM, including during cell migration and cell adhesion, which influences embryonic development and the wound healing process of skin tissue. Investigating the role of laminins in wound healing would further our understanding of the genetic skin fragility disorder JEB, which results in severe blistering of skin due to LM-332 (previously laminin 5) subunit mutations (241). A relatively small laminin-related protein, LaNt α31 (64 kDa), also has an involvement in wound healing, and may therefore affect the assembly of LM-332 within the ECM. Unlike LM-332, little is known about LaNt α31, with the only published work identifying expression and distribution without any deep mechanistic insight (244, 245).

Distinct staining patterns of LM-332 are present in different cultured cells (202). A former study found a rose-like pattern for LM-332 in stationary (non-migrating) human keratinocytes (skin cells), whereas LM-332 was positioned in more of a trail-like manner for those that migrated (202, 242). This cell specific LM-332 patterning may be due to the degree of cell movement, which in turn could cause differences in the function of LM-332 (202). This variance in staining pattern has yet to be detected ex vivo, for different tissues, as high-

resolution imaging of tissues, consisting of intact basement membranes, is not possible with standard fluorescence microscopy (202). To discern LM-332 patterns, in different tissues, a high-resolution microscopy method is required. Although, different staining patterns of LM-332 has already been established for specific cell types, in vitro (202), this was done with conventional fluorescence microscopy, which may mask important information about the localisation of LM-332. Therefore, SOFI was used here to gain a better insight into the localisation of LM-332 with respect to LaNt α31 in the ECM, by providing a high-resolution image.

Just as the deposition pattern of LM-332 differs in different cell types, the deposition of LaNt α31 may also be distinct for specific cells. Others have shown using standard fluorescence microscopy that LaNt α31 is in distinct puncta near the leading edge of the cell (244, 355). Endogenous LaNt α31 was probed in HeLa, HaCaT, and hTCEpi by indirect immunofluorescence with the primary antibody 3E11 against LaNt α31 (244), kindly provided by collaborator Kevin Hamill (University of Liverpool, UK), plus secondary antibodies conjugated to Alexa Fluor 488 and Qdot 625. Localisation was similar for all cell types, with Alexa Fluor 488 specifically labelling puncta at nuclei, but not at the leading edge. The LaNt α31 signal of Qdot 625 (red) was diffuse, with discrete puncta in the nucleus for Alexa Fluor 488 (green) only (Figure 93). Although, laminin deposition is extracellular, for LaNt α31, intracellular puncta may be present beneath the cell, and therefore could not be labelled with Qdots (Figure 93).

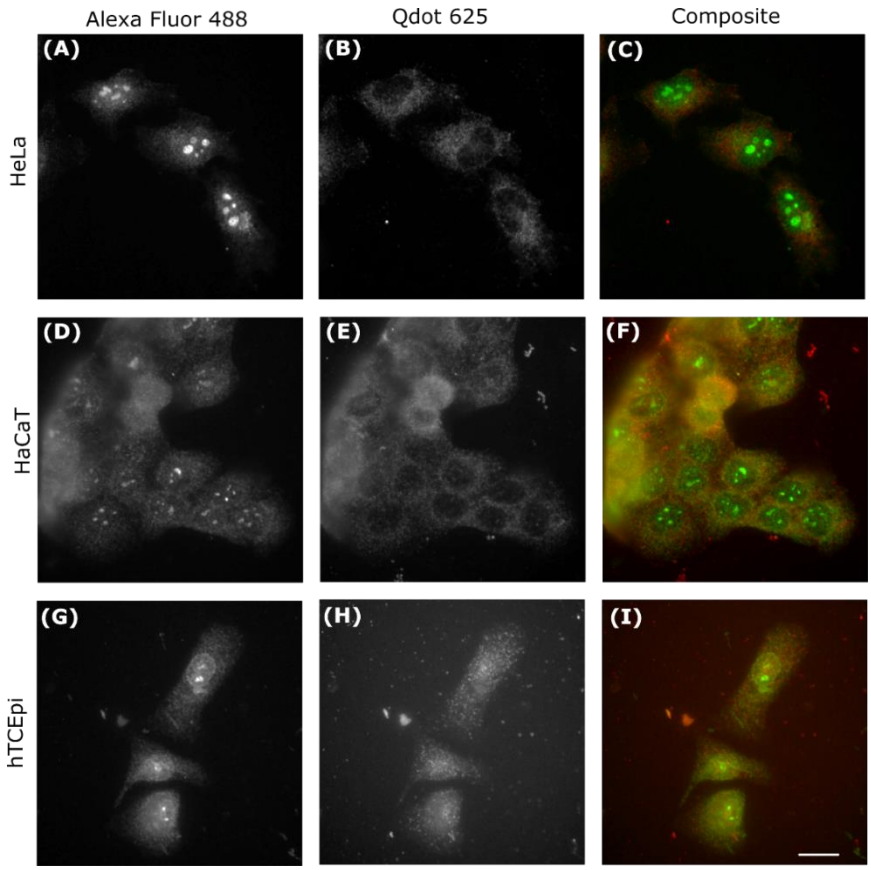


**Figure 93. Localisation of endogenous LaNt α31 in different cell types.** LaNt α31 in fixed HeLa cells was dual-labelled with Alexa Fluor 488 in green (A) and Qdot 625 in red (B) to produce a composite wide-field image (C), using indirect immunofluorescence with the primary antibody 3E11 against LaNt α31 and Alexa Fluor 488/Qdot 625 conjugated secondary antibodies. LaNtα31 was also dual-labelled in HaCaT (D-F) and hTCEpi (G-I) cells in the same manner and imaged on an epifluorescence microscope (63x 1.4 NA). Scale bar = 20 µm.

To test whether the localisation of LaNt α31 was intracellular or extracellular, endogenous LaNt α31 was labelled with Qdot 625 and Alexa Fluor 488, in permeabilised and non-permeabilised HeLa cells, by indirect immunofluorescence. Fixed HeLa cells (+/- 0.25% Triton X-100) were incubated with 3E11 mouse monoclonal primary antibodies and Alexa Fluor 488/Qdot 625 conjugated secondary antibodies. Only staining of LaNt α31-Alexa Fluor 488 puncta was present in HeLa cells that had been permeabilised with the detergent Triton X-100 (0.25%), which confirms that LaNt α31 is intracellular (Figure 94). It is also worth noting that, in parallel to experiments, control cell samples, incubated without any primary antibodies, but with conjugated secondary antibodies only, were performed to check for any non-specific binding to cells, which was negligible.

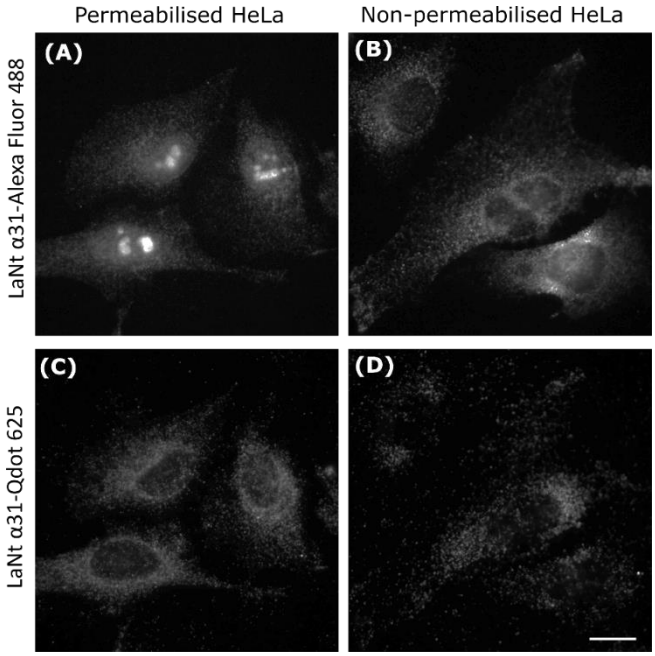


**Figure 94. Localisation of endogenous LaNt α31 in permeabilised and non-permeabilised cells.** Endogenous LaNt α31 was simultaneously labelled with green Alexa Fluor 488 in fixed HeLa cells that had either been permeabilised with 0.25% Triton X-100 (A) or non-permeabilised (B), and red Qdot 625 in permeabilised (C) and non-permeabilised (D) cells. Indirect immunofluorescence with the primary antibody 3E11, against LaNt α31, and Alexa Fluor 488/Qdot 625 conjugated secondary antibodies, showed LaNt α31-Alexa Fluor 488 puncta in permeabilised cells by imaging on an epifluorescence microscope (63x 1.4 NA). Scale bar = 20 µm.

Data showing endogenous LaNt α31-Alexa Fluor 488 being present in intact permeabilised HeLa cells, but absent from non-permeabilised HeLa cells (Figure 94), is comparable to a previous study where endogenous LaNt α31 was absent from ECM extracts in which HaCaT cells had been removed to just leave the ECM material (356). The absence of LaNt α31 staining in hTCEpi cells within the ECM, indicates that LaNt α31 is not completely extracellular, but rather intracellular in some cell types. To continue investigating the localisation of LM-332 and LaNt α31, since endogenous LaNt α31 could not be labelled with Qdots, hTCEpi cells were transduced with exogenously expressed adenovirus LaNt α31 tagged with GFP (LaNt α31-GFP). The localisation of LaNt α31 in the deposited ECM was tested by removing hTCEpi cells with ammonium hydroxide ($NH_4OH$). Exogenous LaNt α31-GFP was labelled by indirect immunofluorescence with an anti-GFP primary antibody and a Qdot 625 conjugated secondary antibody in both samples of intact hTCEpi cells and those where the cells had been removed. The localisation of exogenous LaNt α31 in intact hTCEpi cells was different to that of endogenous LaNt α31. Exogenous LaNt α31 had a similar diffuse GFP signal to Qdot 625 in intact hTCEpi cells (Figure 95), whilst previously endogenous LaNt α31 had puncta at the nuclei with Alexa Fluor 488 (Figure 94). To check that the change in

organisation of the LM-332 subunit, LM α3 deposition was as a result of cells containing exogenous LaNt α31-GFP, and not just the effect of the GFP tag itself, the organisation of LM α3 could have been imaged separately in hTCEpi cells expressing LaNt α31-GFP and a control of GFP expressing cells. In addition, contrary to previous evidence that exogenous LaNt α31 is apparent in the ECM (356), here exogenous LaNt α31-GFP was specifically labelled with Qdots in intact hTCEpi cells, but absent from ECM deposits where hTCEpi cells had been removed (Figure 95). In light of these observations, the next set of SOFI experiments, involving the labelling of LM-332 and LaNt α31 with Qdots, thereafter, were performed in intact hTCEpi cells.

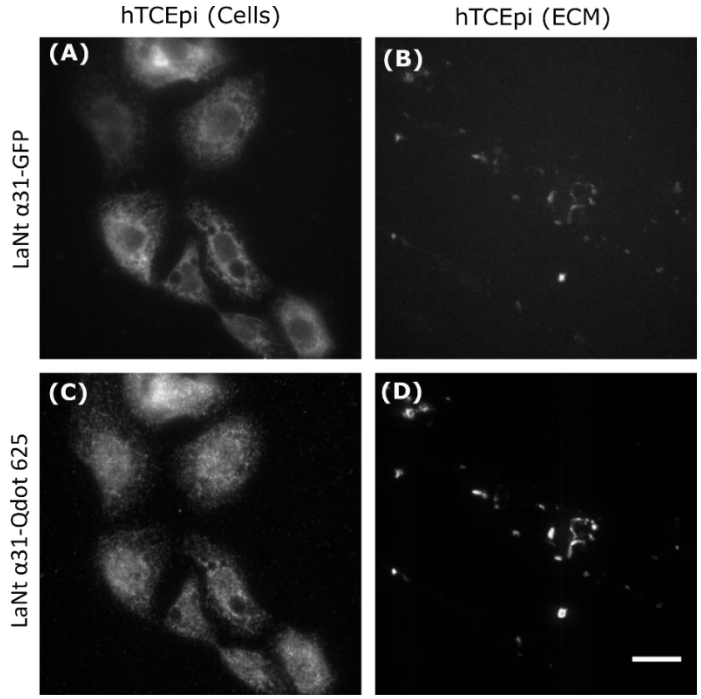


**Figure 95. Localisation of exogenous LaNt α31.** The removal of hTCEPi cells, transduced with LaNt α31-GFP, was performed with ammonium hydroxide. Exogenous green LaNt α31-GFP (A & B) was labelled by indirect immunofluorescence with an anti-GFP primary antibody (Roche, UK) and a red Qdot 625 conjugated secondary antibody (C &D), in intact hTCEpi cells and those consisting of ECM only. Qdots were imaged over time on an epifluorescence microscope (63x 1.4 NA). Specific Qdot 625 labelling of exogenous LaNt α31-GFP was observed in intact hTCEpi cells (C), but not ECM deposits (D). Prepared hTCEpi samples, transduced with LaNt α3-GFP (+/- ammonium hydroxide), were kindly provided by Kevin Hamill (University of Liverpool, UK). Scale bar = 20 µm.

To confirm that the lack of endogenous LaNt α31 reactivity in ECM deposits is unique to this laminin-related protein, LM α3, a subunit of LM-332, was also probed with monoclonal RG13 (recognises the G domain) primary antibodies (357) and Qdot 625 secondary antibodies in hTCEpi samples, where cells had been extracted with ammonium hydroxide, and also intact cells. After imaging with epifluorescence microscopy (63x 1.4 NA), it was clear that LM α3

was present in both intact cells and insoluble ECM deposits. However, the collection of light above and below the plane of LM α3 yielded out-of-focus light in the wide-field image due to diffraction, reducing the contrast and causing LM α3 to appear blurred. By SOFI-processing LM α3 in both scenarios, its structure was more discerned through the background removal of out-of-focus light, which increased the SNR of the image and in turn enabled sharper features of LM α3 to be revealed (Figure 96). Both endogenous LM α3 and exogenous LaNt α31 are present in intact hTCEpi cells, but only LM α3 is present in ECM extracts, which may suggest that these two proteins do not interact at the cell surface. The plan was therefore, to use SOFI to further investigate the localisation of LaNt α31 relative to matrix proteins (laminins) and transmembrane (integrins, focal adhesions, and lamellipodia) proteins in intact hTCEPi cells.

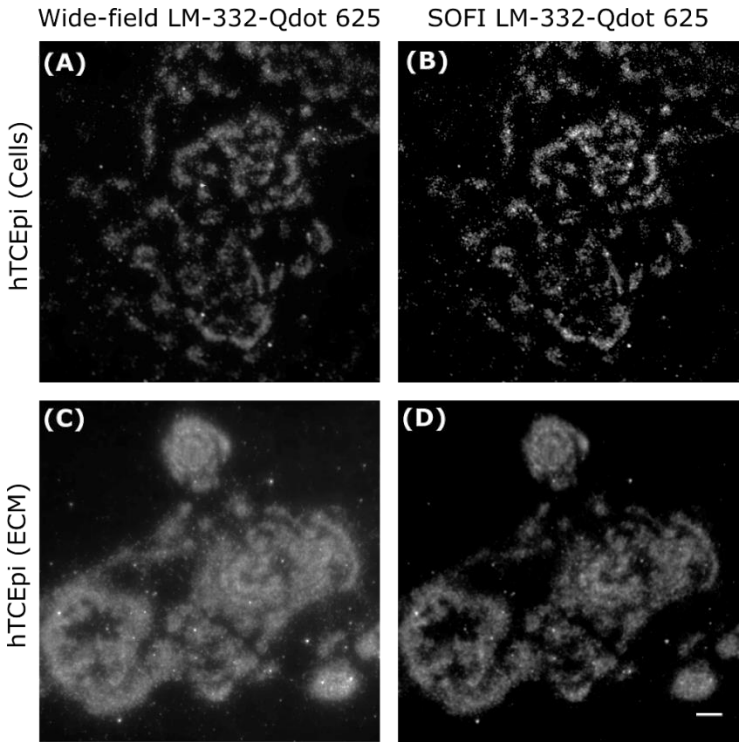


**Figure 96. SOFI-processed LM-332-Qdot 625.** LM α3 subunit of LM-332 in hTCEpi cells was labelled by indirect immunofluorescence with RG13 primary antibodies against LM α3 and Qdot 625 conjugated secondary antibodies. Qdots were imaged over time on an epifluorescence microscope (63x 1.4 NA). Wide-field images of LM α3-Qdot 625 (A) were SOFI-processed with Localizer in MATLAB (B). Wide-field images of extracellular LM α3 (C) were also SOFI-processed (D) by removing hTCEpi cells with ammonium hydroxide to leave the ECM intact. Wild-type hTCEpi cells and primary antibody RG13, were kindly provided by Kevin Hamill (University of Liverpool, UK). Scale bar = 20 µm.

There has been suggestions, by Kevin Hamill's research group, that the deposition of LM-332 is decorated with LaNt α31 puncta at the leading edge of the cell and that there is partial co-localisation between LM-332 and LaNt α31 at this region (246). The co-localisation of LaNt α31 and LM-332 deposition has been studied previously with fluorescence microscopy (244). It was hypothesised that overexpressing LaNt α31-GFP would alter the organisation of LM-332 deposition in hTCEpi cells. SOFI could better resolve the distinct puncta of LM α3 in hTCEpi cells, transduced with LaNt α31-GFP, than in wild-type hTCEpi cells, which may instead result in SOFI images of bigger, swirl-like structures of LM α3. In order to investigate whether LaNt α31 and the LM α3 subunit of LM-332 co-distribute, in intact hTCEpi cells, with SOFI, exogenous LaNt α31-GFP and LM α3-Qdot 625 were imaged sequentially with epifluorescence microscopy (100x 1.4 NA plus a 1.6x magnifying lens). As the GFP signal from exogenous LaNt α31 was faint, the signal was enhanced, to an adequate level for sufficient SOFI-processing, by being probed with an anti-GFP primary antibody and a Qdot 525 conjugated secondary antibody (green). Excitation (dotted lines) and emission (solid lines) spectra of green GFP/Qdot 525 and far red Qdot 625 are very distinct, thus avoiding spectral overlap (Figure 97).

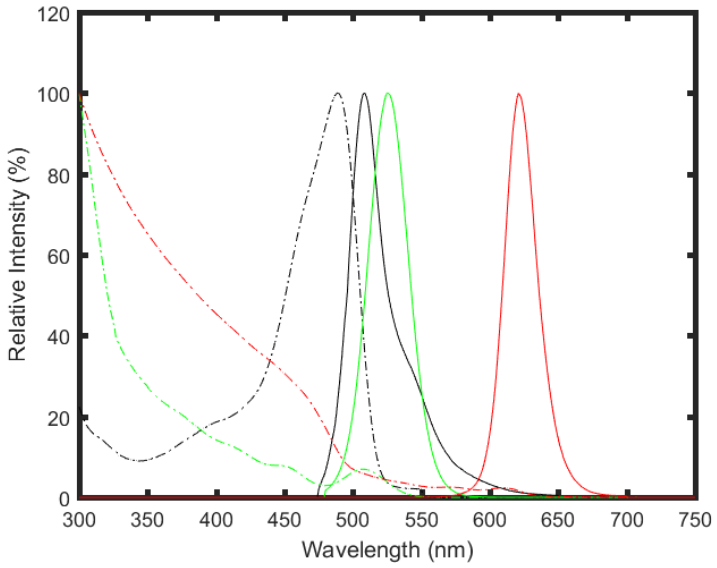


**Figure 97. Excitation and emission spectra for GFP, Qdot 525, and Qdot 625.** Excitation of GFP (black dotted line), Qdot 525 (green dotted line), and Qdot 625 (red dotted line) were plotted against excitation of GFP (black solid line), Qdot 525 (green solid line), and Qdot 625 (red solid line). Data for the excitation and emission spectra were exported from Fluorescence SpectraViewer on the Thermo Fisher Scientific, UK website.

The fact that the exogenous LaNt α31 was already tagged with GFP, had negligible impact on the acquisition of Qdot 525, in the green channel. During SOFI-processing, any noise or

stationary (non-fluctuating) fluorescence would be recognised as uncorrelated signal and therefore, removed from the resulting SOFI image; so only the Qdot 525 labelled LaNt α31, will contribute to the final SOFI image. From the two-colour SOFI-processed composite image, it was clearer, compared to the wide-field composite image, that there was no co-localisation between LaNt α31-Qdot 525 and LM α3-Qdot 625, at the leading edge of hTCEpi cells, due to the removal of diffuse hazy signal (Figure 98).

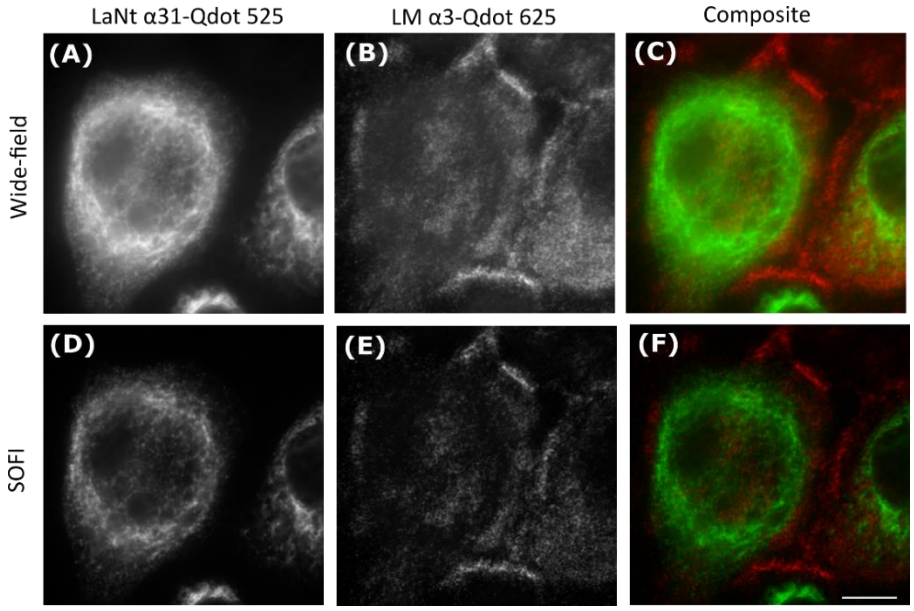


**Figure 98. Investigating the co-localisation of LaNt α31 and LM α3 using SOFI images obtained from epifluorescence acquisition.** LaNt α31 and LM α3 were dual-labelled with Qdots in fixed hTCEpi cells that had been transduced with LaNt α31-GFP. Using indirect immunofluorescence, LaNt α31-GFP was further labelled green by incubating with an anti-GFP primary antibody and a Qdot 525 conjugated secondary antibody (A), whilst endogenous LM α3 was labelled red using an anti-RG13 primary antibody against the G domain of LM α3 and a Qdot 625 conjugated secondary antibody (B), to produce a dual-labelled composite image (C). Both wide-field stacks of LaNt α31-Qdot 525 and LM α3-Qdot 625, obtained on an epifluorescence microscope (100x 1.4 NA plus a 1.6x magnifying lens), were post-processed with Localizer to form SOFI images (D) and (E) respectively. A composite SOFI image (F), from epifluorescence acquisition, shows no co-localisation between LaNt α31-Qdot 525 and LM α3, at the leading edge of hTCEpi cells. Scale bar = 20 µm.

Since laminins are basement membrane proteins, residing at the extracellular surface of cells, the localisation of exogenous LaNt α31 and endogenous LM α3 was determined with TIRF microscopy. Although, the localisation of LM α3-Qdot 625 was similar for both epifluorescence and TIRF microscopy, the deposition pattern of LaNt α31-Qdot 625 was considerably different when imaged with TIRF (Figure 99), compared to epifluorescence microscopy (Figure 98). Unlike wide-field microscopy, there is negligible out-of-focus light

with TIRF, so the SNR is much better in TIRF images than wide-field images, pre-SOFI-processing. The distinct puncta (small spot-like structures) of LaNt α31 was more obvious in the SOFI-processed TIRF images than previously with the SOFI-processed wide-field images, due to the increased SNR. The combined advantage in improved SNR with TIRF and SOFI, confirmed the absence of co-localisation between exogenous LaNt α31 and endogenous LM α3, at the leading edge of the cell. Due to the benefit of SOFI-processing TIRF acquired images of basement membrane proteins, future imaging of LaNt α31 was therefore done with TIRF microscopy, as opposed to epifluorescence microscopy.

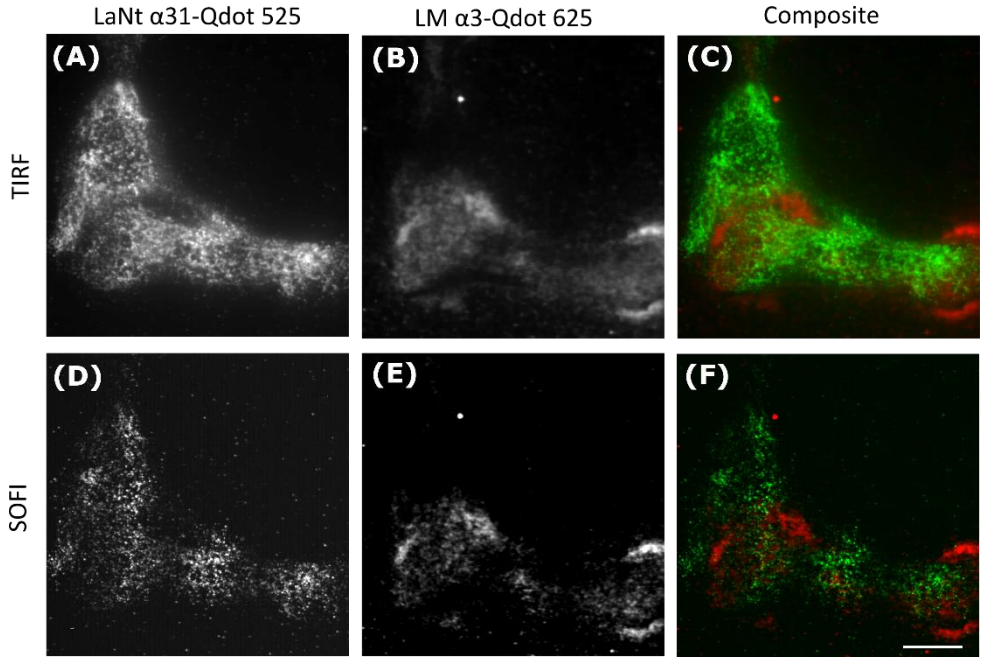


**Figure 99. Investigating the co-localisation of LaNt α31 and LM α3 using SOFI images obtained from TIRF acquisition.** LaNt α31 and LM α3 were dual-labelled with Qdots in fixed hTCEpi cells that had been transduced with LaNt α31-GFP. Using indirect immunofluorescence, LaNt α31-GFP was further labelled green by incubating with an anti-GFP primary antibody and a Qdot 525 conjugated secondary antibody (A), whilst endogenous LM α3 was labelled red using an anti-RG13 primary antibody against the G domain of LM α3 and a Qdot 625 conjugated secondary antibody (B), to produce a dual-labelled composite image (C). Both wide-field stacks of LaNt α31-Qdot 525 and LM α3-Qdot 625, obtained on a TIRF microscope (100x 1.46 NA plus a 1.6x magnifying lens), were post-processed with Localizer to form SOFI images (D) and (E) respectively. A composite SOFI image (F), from TIRF acquisition, shows no co-localisation between LaNt α31-Qdot 525 and LM α3, at the leading edge of hTCEpi cells. Scale bar = 20 μm.

Live cell imaging has already provided insights into the potential mechanisms that lead to LM-332 deposition, and it has been speculated by Kevin Hamill's research group that cell surface receptors, such as integrins, have some involvement in its regulation (204). Previous studies have identified a difference in LM-332 deposition in the presence of $\alpha_3\beta_4$ integrin using wild-type keratinocytes, where LM-332, a ligand of $\alpha_3\beta_4$ integrin, was deposited

diffusely in arc-like structures, compared to being linearly deposited in spike-like patterns in the absence of $\alpha_3\beta_4$ integrin in knockout keratinocytes; as they were unable to form a LM-332 network (240). In addition, if either LM-332 and $\alpha_6\beta_4$ integrin, that form the hemidesmosome, are mutated, it can lead to skin blistering (246). This parallel relationship between LM-332 and $\alpha_6\beta_4$ integrin leads to questions whether $\alpha_6\beta_4$ integrin influences the organisation of LM α3 deposition and that these two proteins might share a common function (358).

Likewise, as focal adhesions form at the leading edge of the cell, in close proximity to LM-332 and LaNt α31, it has been suggested by Kevin Hamill's research group that these also have some involvement in the deposition process of LM-332 and LaNt α31, as former experiments showed an alteration in focal adhesions when LaNt α31 was exogenously expressed (357). Furthermore, it has been demonstrated, using a proximity ligation assay (PLA), that ACTN4, an actin binding protein, co-localises with exogenous LaNt α31 at the edge of hTCEpi cells (357). Although, it would have been interesting to investigate the association between endogenous LaNt α31, LM α3, and transmembrane proteins ($\alpha_6\beta_4$ integrin, actin, and talin), with SOFI, unfortunately integrin nor focal adhesions could be labelled specifically with Qdots, as shown previously (149). However, endogenous LM α3 and ACTN4 was labelled with Qdot 625 and Alexa Fluor 488, respectively. No co-distribution was apparent between ACTN4-Alexa Fluor 488 and LM α3-Qdot 625 in wild type hTCEPi cells (Figure 100). The staining of endogenous ACTN4 and LM α3 ought to be repeated in hTCEpi cells expressing exogenous LaNt α31, to see whether LaNt α31 changes the organisation of ACTN4 and LM α3 when LaNt α31 expression is abundant, as seen previously (356).

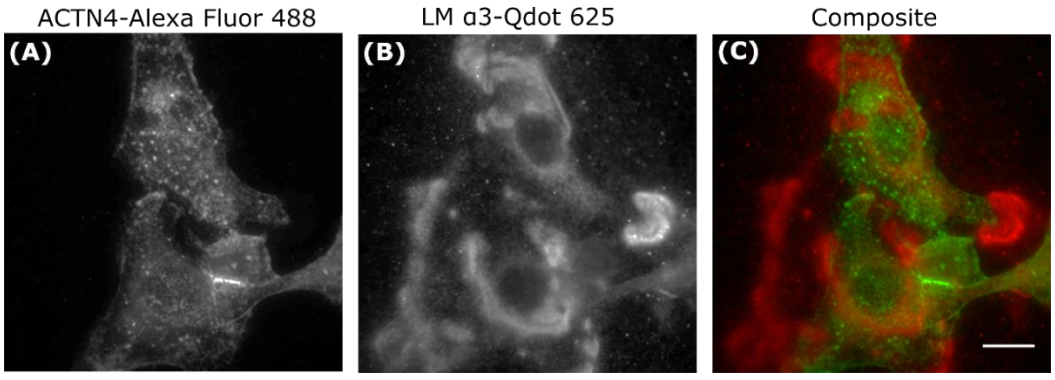


**Figure 100. Co-distribution of ACTN4 and LM α3-Qdot 625.** ACTN4 and LM α3 were dual-labelled with Alexa Fluor 488 (A) and Qdot 625 (B), respectively, in fixed hTCEpi cells using indirect immunofluorescence with primary and secondary antibodies and subsequently imaged on an

epifluorescence microscope (63x 1.4NA). A composite image (C) shows no co-distribution between endogenous ACTN4 and LM α3. Scale bar = 20 µm.

The organisation of exogenously expressed LM-332 was also investigated using a different subunit of LM-332, laminin beta 3 (LM β3), to see whether it gave the same localisation pattern as endogenous LM α3 when imaged with TIRF microscopy. Fixed hTCEpi cells were transduced with LM β3-mCherry (red) and endogenous LM α3 labelled with Qdot 525 (green) by incubating cells with an RG13 primary antibody against LM α3 and a Qdot 525 conjugated secondary antibody. After imaging using TIRF microscopy (63x 1.46 NA plus a 1.6x magnifying lens), a similar localisation pattern of exogenous LM β3-mCherry and endogenous LM α3-Qdot 525 was observed, with some degree of overlap (Figure 101).

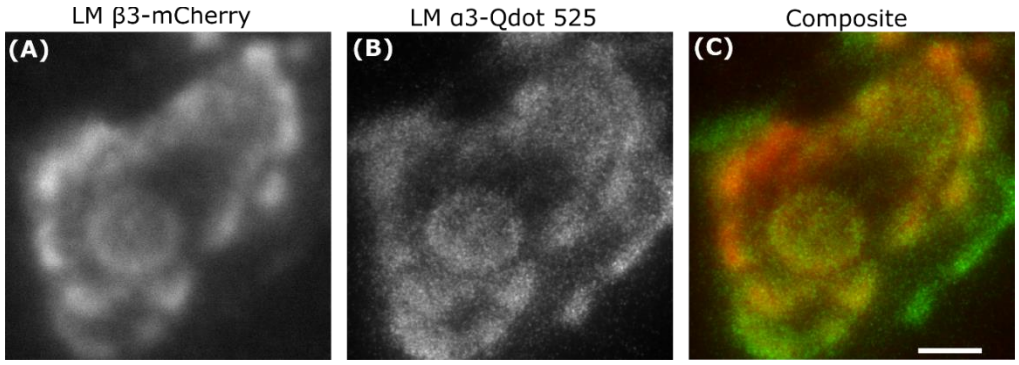


**Figure 101. Comparing the localisation of exogenous and endogenous LM-332.** Exogenous LM β3-mCherry (A) was imaged using TIRF microscopy (100x 1.46 NA plus a 1.6x magnifying lens) in hTCEpi cells that were also probed for endogenous LM α3 (B) using indirect immunofluorescence, by incubating cells expressing LM β3-mCherry (red) with an RG13 primary antibody against LM α3 (kindly provided by Kevin Hamill at University of Liverpool, UK) and a Qdot 525 conjugated secondary (green). The composite image (C) showed some regions of overlap between LM β3-mCherry and LM α3-Qdot 525, which suggests that exogenous LM-332 and endogenous LM-332 have the same deposition pattern. Scale bar = 10 µm.

To check that the overlap in fluorescent signal between LM β3-mCherry and LM α3-Qdot 525 was real and not a result of artefacts, due to the fluorescent tag, LM β3-mCherry was also imaged in live hTCEpi cells, before methanol fixation. LM β3-mCherry was then stained with Qdot 525 by incubating with an anti-mCherry primary antibody (kindly provided by Kevin Hamill at University of Liverpool, UK) and a Qdot 525 conjugated secondary antibody. There was no difference in the localisation or fluorescent signal of LM β3-mCherry pre and post methanol fixation. Although, some structural details were lost in the Qdot 525 channel, for instance at the centre of LM β3, suggesting that the Qdot 525 conjugated secondary antibody

cannot access LM β3, and therefore only specifically labels the outer regions (Figure 102). Live TIRF imaging of hTCEpi cells co-transduced with LM β3-mCherry and LaNt α31-GFP, may provide useful insights into whether exogenous LaNt α31 does indeed co-distribute with LM-332, to cause a change in the organisation of LM-332.

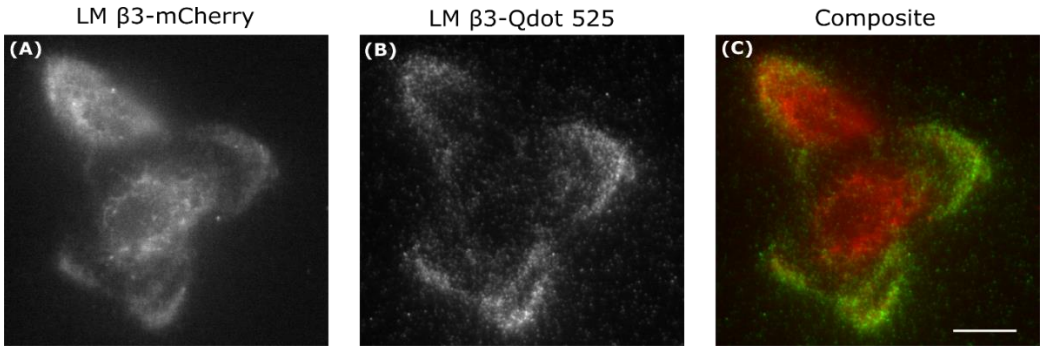


**Figure 102. Labelling exogenous LM β3 with Qdots.** Fixed hTCEpi cells were transduced with LM β3-mCherry and imaged using TIRF microscopy (100x 1.46 NA plus a 1.6x magnifying lens). LM β3-mCherry (A) was labelled with green Qdot 525 (B) using indirect immunofluorescence by incubating with an anti-mCherry primary antibody (fixed hTCEpi cells and anti-mCherry primary antibody were kindly provided by Kevin Hamill at University of Liverpool, UK) and a Qdot 525 conjugated secondary antibody. The edges of exogenous LM β3 was more specifically labelled with Qdot 525 than the middle of the cell. Scale bar = 10 μm.

### 5.4.2 Summarising the co-localisation of LaNt α31 and LM-332 findings

To fully understand the role of laminins in wound healing, the mechanisms by which the proteins that form the ECM are deposited, must first be understood. As defects in laminin deposition typically leads to impaired wound healing, through mutations in LM-332 subunits (246), the organisation of LM α3 deposition and any potential interaction with the secreted protein LaNt α31 in the ECM was studied, using SOFI. Confocal microscopy images of LM α3 and LaNt α31 localising at the edge of the cell were of low-resolution (244), so any potential protein-protein interaction, portrayed as partial co-localisation, may be less apparent once resolved spatially with SOFI (270). It was shown that in all of the three cell lines tested (HeLa, HaCaT, and hTCEpi), endogenous LaNt α31 was distributed near the nucleus of cells stained for LaNt α31-Alexa Fluor 488 (Figure 93). Although, endogenous LM α3 could be specifically labelled with Qdots in hTCEpi cells (Figure 96), interestingly, endogenous puncta of LaNt α31 could not be labelled with Qdots, even though the protein is secreted and thought to be

extracellular (Figure 94). These findings suggest that LM α3 is extracellularly positioned on the surface of the cell, whereas LaNt α31 may be localised intracellularly, beneath the cell, on par with how accessible foci adhesion proteins have been found to be to Qdots (149).

To investigate the effect of LaNt α31 on the deposition of LM α3, hTCEpi cells were transduced with the adenovirus LaNt α31-GFP and subsequently labelled with Qdot 525 for SOFI-processing. With TIRF microscopy (Figure 99), the punctate distribution of LaNt α31 was more obvious than in images acquired with epifluorescence microscopy (Figure 98). Nevertheless, in both the TIRF and wide-field SOFI-processed images, it was clear that there was no co-localisation between exogenous LaNt α31-Qdot 525 and LM α3-Qdot 625. One explanation for the lack of co-localisation between exogenous LaNt α31 and LM α3, is that the exogenous LaNt α31 might have disrupted LM α3 deposition, by competing for LM-LM interactions, preventing it from creating a matrix (356). To be sure, the degree of co-localisation, in the composite SOFI images, could be quantified using Manders correlation coefficient (250) or alternatively, the LaNt α31 and LM α3 interaction could be studied with a PLA (359), as performed previously (356).

All of these SOFI experiments, involving LaNt α31 and LM α3, were performed in fixed cells, where information about their movement is lost. For live cell SOFI-processing, LaNt α31 and LM α3 could be tagged with a fluorescent photoswitchable protein, such as Skylan-S, and resolved with SOFI (107). Additionally, fluorescent images post-processed with SOFI, could be combined with AFM to further study any potential interaction between LaNt α31 and LM-332. Of interest, is the deposition pattern of LM α3, which appears to differ in different cell types (202), and as different cell lines are known to express other laminins, future work will focus on studying whether other LM-332 subunits are affected by the overexpression of LaNt α31, using SOFI. Furthermore, now images of LaNt α31 and LM α3 have been SOFI-processed in vitro, attention will concentrate on obtaining SOFI-processed images of LaNt α31 and LM α3, ex vivo, in tissue samples. It is hoped that by determining the mechanism by which LM-332 subunits, responsible for JEB when mutated, are deposited within the ECM, therapeutic targets may be developed through the exploitation of laminins (246).

# Chapter 6: Discussion and conclusions

## 6.1 Summary of results

At the start of this project, in 2014, few had used SOFI to address specific biological questions, and instead most articles (85, 93) focused on the development of imaging technology with filamentous structures such as microtubules used as proof of principle samples. Through collaborations, this work set out to apply super-resolution microscopy to several biological questions, involving a variety of different proteins, such as HIF-2α, fibronectin, NET-associated proteins, and LaNt. SOFI was chosen as the primary super-resolution microscopy technique, because it is open-source, does not require any sophisticated hardware, and it can in theory be applied to live biological systems. The only prerequisite for performing SOFI measurements was that structures had to be labelled with a fluctuating probe. Several options were explored, including the use of commercial Qdot-Abs and those synthesised in-house, synthetic organic dyes and fluorescent proteins. Since the conjugation of Qdots to anti-GFP nanobodies, using cross-linking reagents sulfo-NHS and EDC was unsuccessful, commercial Qdot-Abs were used as an alternative. Qdot-Abs fluctuated on all timescales and produced SOFI images, with improved resolution and SNR. However, as documented in a recent publication the commercially available Qdot-Abs failed to specifically label intracellular targets of interest, such as HIF-2α (149) and LaNt α31.

To enable HIF-2α to be labelled with a fluctuating probe, the RSFP tag Skylan-S was fused to HIF-2α to create a HIF-2α-Skylan-S construct. Using Skylan-S, HIF-2α was resolved with SOFI in fixed cells. Unfortunately, since SOFI assumes that fluorophores are immobile and do not photobleach, due to the fast mobility of HIF-2α, this protein could not be adequately imaged with SOFI in live cells. However, Skylan-S can be successfully used to image slow moving proteins in live cells (106). Co-localisation of HIF-2α-Skylan-S with potential binding partners was not studied with SOFI, since few red RSFPs, suitable for SOFI, are available to do multiplex SOFI, in combination with the green RSFP Skylan-S. However, the nuclear localisation of HIF-2α into speckles, and its association with other related nuclear proteins, was investigated with other super-resolution techniques, using antibodies. The release of SRRF in 2016, allowed the co-localisation of live HIF-2α and closely associated proteins to be carried out at high-resolution. Both endogenous and exogenous HIF-2α was in speckles, with super-resolution microscopy, which is in agreement with previous observations by Taylor *et*

*al.,* using conventional fluorescent microscopy (185). However, in contrast to data obtained by Taylor *et al.,* (185), co-localisation of endogenous HIF-2α with potential binding partners decreased using super-microscopy confirming that co-localisation using poorly resolved microscopy results in an overestimation of interactions. Although, using wide-field microscopy, HIF-2α was considered to co-localise strongly with Phospho Ser5 RNA Pol II, HIF-1β, HAF, and HIF-1α; this was not the case with SRRF, as the degree of co-localisation reduced. Super-resolution microscopy, therefore limits false-positive co-localisation results, which would otherwise lead to incorrect interpretation about protein-protein interactions. However, as mentioned previously (section 5.1.4 Quantifying co-localisation of HIF-2α and potential binding partners), the low degree of co-localisation reported may be as a result of only a fraction of HIF-2α speckles partitioning into complexes with Phospho Ser5 RNA Pol II, HIF-1β, HAF, and HIF-1α.

Most co-localisation between HIF-2α and potential binding partners was performed with super-resolution microscopy in fixed cells, with the use of antibodies conjugated to synthetic organic dyes, except HIF-2α and HIF-1β, which were also fused to fluorescent proteins and could be imaged with SRRF-Stream in live cells. Although, genetically encoded fluorescent fusion proteins enabled live cell imaging of HIF-2α, caution must be taken when interpreting protein dynamics, because these may not be expressed at physiologically relevant levels. Nevertheless, in both live and fixed cells, when imaged separately with SRRF-Stream, HIF-2α-EGFP and HIF-1β-DsRed appeared as speckles in the nucleus, but when they were co-transfected, they were both no longer in speckles and had dimerised to give a more homogenous nuclear fluorescent signal. This dimerisation of HIF-2α and HIF-1β, forming a more homogenous complex, was not observed with SRRF at endogenous levels, using indirect immunofluorescence. The size and amount of HIF-2α speckles in the nucleus was also compared amongst different microscopy techniques. As expected, HIF-2α speckles were smaller with super-resolution microscopy than wide-field microscopy.

As well as improving co-localisation studies, the ability of SOFI to remove out-of-focus light can also help other quantification methods, such as evaluating the orientation of fibronectin fibres in healthy and scarred cells done here with the Directionality ImageJ plugin. Similar to results reported for collagen fibre organisation of scarred skin, there was little variation in fibronectin fibre alignment shown here (333). Through improving the SNR, SOFI enabled fibronectin fibres to be more distinguished, which in turn helped to confirm that there was no difference in the orientation of fibres between normal fibroblasts and keloids. Others have proposed that by spatially resolving the organisation of fibronectin fibres, it may reveal

more structural information about integrin binding sites (211). Complementary to previous EM data of NET fibres containing globular domains (213), two colour SOFI enabled the enhancement of dot-like patterns of proteins along NET structures, to be studied in relation to one another. Furthermore, SOFI aided a more informative judgement about the co-localisation of ECM secreted LaNt α31 and LM α3, by labelling with Qdot 525 and Qdot 625, respectively. Using SOFI, the SNR was improved in the wide-field images, through the removal of out-of-focus light, and it was confirmed that LaNt α31 and LM α3 do not co-localise at the edge of cells. Being basement membrane proteins, SOFI-processing of LaNt α31 and LM α3 was also done on TIRF-acquired data, which enhanced the punctate distribution of LaNt α31, compared to the wide-field data; highlighting the versatility of SOFI to work on any platform. This punctate distribution of LaNt α31 confirms a previous observation by Hamill *et al.,* (244).

Besides TIRF microscopy, SOFI was also combined with LSFM, to improve the spatio-temporal resolution of β-tubulin. The optical sectioning capability of SOFI can be appreciated, through the post-processing of different z-positions in a light-sheet stack. Few z-positions were taken here, but many more are needed to fully reconstruct β-tubulin. A low magnification was used for light-sheet acquisition (40x plus maximum zoom), which was below Nyquist sampling expected for SOFI, so resolution was compromised. Further improvements in resolution could be achieved by combining SOFI with lattice light-sheet microscopy, with an even thinner sheet of light. Since a thin sheet of light is used to illuminate the sample, light-sheet has less photobleaching and phototoxic effects on the sample, which is of benefit to live cells. Here, LSFM-SOFI was applied to fixed cells, using Qdot-Abs, but Qdot-nanobodies could be injected deep into tissues of large specimens for live cell imaging (32). An advantage of using Qdots for light-sheet acquisition, was that they could be excited at multiple wavelengths, within the UV range, without the need for specific filters. Apart from optical sectioning, the majority of the data presented here, was in 2D. Although, 3D SOFI was attempted on Qdot labelled β-tubulin, with the use of PRILM. To achieve this, a linear phase ramp was inserted into the light path, splitting point emitters, labelling the structure of interest, into two lateral lobes, and 3D cross-cumulants were calculated to restore a 3D SOFI image (17). Although, PRILM was used here to achieve a 3D image, other approaches to engineer the PSF can be done, including the use of a PRISM (309). These simple add-on applications to wide-field microscopes, allow 3D super-resolution microscopy, at an affordable cost to the researcher.

Most of the proteins discussed in this thesis, were post-processed in 2D with the open-source SOFI implementation Localizer, since it was found to give fewer processing artefacts when

compared with bSOFI, due to the absence of further deconvolution. When evaluated, a high number of frames and long exposure time gave the best-attainable SOFI image for both Localizer and bSOFI, which was at the expense of temporal resolution. Additionally, with as few as 500 frames, higher-order SOFI was not adequately achieved with Localizer, and although bSOFI did yield satisfactory higher-order SOFI images with additional features, these also contained extra structures that were not present in the wide-field images, so were considered artefacts, as a result of over-processing. An experimental parameter sweep was also done on epifluorescence acquisition and post-processing settings for obtaining optimal NanoJ-SRRF and SRRF-Stream images. Testing acquisition parameters experimentally can be time-consuming, so simulation tools can be used to predict the outcome of processing algorithms on different datasets, without the need for sample preparation (124). SRRF-Stream helps to minimise the processing time spent on determining optimal acquisition parameters, by processing the images in real-time.

As well as acquisition parameters, affecting the resolution and quality of a super-resolution image, artefacts can also arise from poor sample preparation, or from over-processing with deconvolution algorithms. Visual interpretation of image quality by eye is prone to human bias. Quality is also often incorrectly expressed in terms of resolution enhancement, but as seen with SRRF data here, an increase in resolution does not always yield high quality images, and this has also been observed by the developers of NanoJ-SQUIRREL (79). Every super-resolution technique is susceptible to artefacts, so is it important that tools are developed alongside new microscope techniques, to specifically assess the resolution and quality of the resulting image. Most commonly, a line is drawn through a structure of interest and its FWHM calculated as a measure of resolution. However, this approach is biased, because resolution is not uniform and the user can select where the FWHM is taken (273). An alternative, quantitative, approach for resolution estimation of super-resolved fluorescence images, would be to calculate the FRC, originally used to estimate the resolution of EM images (80). FRC values given by the NanoJ-SQUIRREL ImageJ plugin differed from that of the ImageJ plugin FIRE, because within NanoJ-SQUIRREL, the FRC calculation is done in a blockwise fashion, so resolution values are estimated for each pixel in the super-resolution image, whereas for FIRE an average estimate of resolution is given for the whole FOV. Although, the estimated mean FRC was unusually low for NanoJ-SQUIRREL, compared to FIRE, it is the minimum and maximum FRC values, provided by NanoJ-SQUIRREL, that are more informative about the true image resolution. FRC values, for each pixel, are colour-coded within NanoJ-SQUIRREL to highlight areas of low and high-resolution, in a FRC map.

Besides an estimation of resolution, NanoJ-SQUIRREL also provides an elegant way to quantitatively assess the quality of images, by providing metrics, such as RSP, where values >0.95 are considered to yield a high quality image. In addition, a colour-coded RSE map highlights pixel-wise errors, as a result of starry artefacts and disappearing structures. High errors in the RSE map means that there is less confidence in the structures in the super-resolution image, because artefact-free super-resolution images would match very well to diffraction-limited image and would be of low error. However, NanoJ-SQUIRREL does not work in the z and although the location of the artefact can be identified, its cause cannot be detected (79). As well as calculating an RSP and FRC, the SNR of SOFI images was also measured, as an indicator of image quality, through the use of the statistical jackknife re-sampling approach. Although, the jackknife re-sampling approach is not applicable to SIM or STED, it can be used on any post-processing technique that requires the acquisition of a large number of frames, such as STORM (120).

## 6.2 Future directions for super-resolution microscopy

There is no super-resolution microscopy technique that is applicable to all biological questions, so these may need to be combined to achieve an optimal super-resolution image and additional information about the structure of interest. Many combinations have been achieved to date, including SOFI with SIM (117) and SOFI with PALM (116). Combining two post-processing techniques, such as SOFI and PALM (116), can be done on the same dataset, providing enough frames are acquired to satisfy PALM-processing. In particular, SOFI works well on areas where there is high-density labelling that PALM fails to resolve (116). However, variations in intensity with data processed with SOFI, especially for higher-orders, can lead to artificial narrowing if the labelling density is high, but also missing structures in regions where the fluorescence intensity is low (360). A workaround to achieving high-density labelling, without such artefacts that degrade image quality, is to label the same structure of interest with multiple different coloured Qdots in separate channels, in a process known as joint-tagging, which has been successfully used to improve the image quality of SOFI (JT-SOFI) (111) and SRRF (JT-SRRF) (361), without compromising high spatio-temporal resolution. In addition, Haar wavelet kernel (HAWK), an open-source ImageJ plugin, has recently been developed that can also reduce artefacts associated with high-density labelled structures (360). Post-processing techniques, such as SOFI and SRRF fail to achieve high quality images

of nuclear proteins, compared to methods such as SIM and STED. Therefore, it is imperative that the performance of super-resolution techniques are tested on a variety of different structures, other than filamentous structures, such as microtubules.

There are currently few tools that assess the resolution and quality of super-resolution images, and those that do exist are not without flaws. Although, attempts have been made to assess outputs from super-resolution techniques, including NanoJ-SQUIRREL, to date, there is no universal standard for resolution and quality quantification of super-resolution data, across laboratories. Investment is needed into developing smart technologies that can automatically perform parameter sweeps for each individual sample, as well as those that can detect the type of super-resolution data, for the application of appropriate quantification software. Until then, simulation tools should be routinely used, to determine optimal acquisition settings that will yield the best possible super-resolution image, before any experimental data is captured. On the subject of high-throughput automation, open-source NanoJ-Fluidics has recently been developed by the laboratories of Ricardo Henriques (University College London, UK) and Christophe Leterrier (Marseille, France), to automate the sequential labelling of multiple proteins for fixed or live cell super-resolution microscopy (362). Since NanoJ-Fluidics is implemented in the freely-available ImageJ software and Micro-Manager-controlled parts, required for its operation, can be built entirely from LEGO ®, this system is relatively inexpensive (approximately £250) and easy to use (362). NanoJ-Fluidics is expected to improve reproducibility of sample preparation for super-resolution microscopy experiments, which in turn may lead to more consistent, artefact-free, resolution-enhanced images.

Before such advancements in automated super-resolution imaging can be implemented, more applicable probes for super-resolution microscopy need to first be developed; in particular those for use in SOFI. Although, robust green RSFPs exist for SOFI, different coloured RSFPs are highly sought after, to enable multiplex super-resolution imaging. Since the generation of stable cell lines, expressing RSFPs, is challenging, due to the loss of photoswitchable properties, RSFPs are at present restricted to transient transfection. Alternatively, fluorescent probes with tuneable blinking can be synthesised, for use in SOFI, including higher-blinking Qdots with a thinner ZnS shell (98). However, these fluorescent probes still need to be specifically targeted to proteins of interest, without increasing the overall size of the probe. Most commonly, indirect immunofluorescence with primary and secondary antibodies (15 nm per antibody) are used to label structures, but this approach is not size-appropriate for super-resolution microscopy, and there are limitations as to how

many species can be specifically labelled with antibodies. Smaller alternatives to antibodies, including nanobodies (4 nm) (363, 364) and SNAP (soluble NSP attachment protein) tagged proteins (365) should instead be used to achieve super-resolution images. As well as smaller probes, those that can be used in live cells, such as fluorogenic probes (366), are also a necessity for real-time super-resolution imaging. Despite the abundance of fluorescent probes having been developed for super-resolution imaging, these are often published, but are not made commercially available, so unless an author is contacted directly, they cannot be easily accessed by other researchers. Apart from Addgene, who distribute RSFPs, there is currently no repository for sharing fluorescent probes, such as nanobody conjugated dyes or Qdots, synthesised in-house, across different laboratories. Therefore, it could be convenient to keep a central online library of probes for use in super-resolution microscopy.

## 6.3 Concluding remarks

Localisation of proteins is often linked to their biological function, so resolving proteins may help to better understand their roles in disease. To obtain additional information about protein dynamics, live cell 3D and 4D (3D images captured over time, to record movement in 3D) super-resolution imaging with PRILM should be used as standard. Additionally, large biological specimens can be imaged at a high spatial resolution, with a large FOV, using a sCMOS camera (367). The goal of super-resolution microscopy is to achieve the best possible spatial resolution, without compromising temporal resolution. Through using fewer frames and the shortest possible exposure time, optimal temporal resolution can be achieved. Although, the focus of this work was on using SOFI to resolve different types of proteins inside and outside of cells, other super-resolution techniques, such as SRRF, may be best suited to investigating the dynamics of these proteins in live cells, because unlike SOFI, SRRF does not require fluctuating probes. It is an exciting time for the field of super-resolution microscopy, with the continual development of new techniques, to solve complex biological problems. However, the introduction of advanced super-resolution imaging techniques brings with it new challenges in terms of the development of smarter fluorescent probes or proteins, and quantitative image analysis tools to assess the quality as well as resolution, which will require interdisciplinary efforts. Before super-resolution microscopy, it was almost impossible to imagine that the diffraction-limit of light (250 nm) could be overcome, but now as low as 30 nm resolution is achievable with techniques, such as dSTORM.

# Bibliography


1. R. Hooke. Micrographia: or, some physiological descriptions of minute bodies made by magnifying glasses with observations and inquiries thereupon. *The Royal Society*. (1665).
2. A. van. Leeuwenhoek and S. Hoole. The select works of Antony van Leeuwenhoek, containing his microscopical discoveries in many of the works of nature. *London: G. Sidney*. (1800).
3. K. R. Spring. Fluorescence Microscopy. Encyclopedia of Optical Engineering. *Marcel Dekker. New York*. 548-555. (2003).
4. D.S. Lidke and K.A. Lidke. Advances in high-resolution imaging – techniques for three-dimensional imaging of cellular structures. *Journal of Cell Science*. **125(11)**: 1-10. (2012).
5. E. Abbe. Beiträge zur Theorie des Mikroskops und der mikroskopischen Wahrnehmung. *Archiv für mikroskopische Anatomie*. **9(1)**: 413-418. (1873).
6. L. Rayleigh. Sec. R.S. XV. On the theory of optical images, with special reference to the microscope. *The London, Edinburgh, and Dublin Philosophical Magazine and Journal of Science*. **42(255)**: 167-195. (1896).
7. Y. Li, F. Xu, F. Zhang, P. Xu, M. Zhang, M. Fan, L. Li, X. Gao, and R. Han. DLBI: deep learning guided Bayesian inference for structure reconstruction of super-resolution fluorescence microscopy. Bioinformatics. 34(13): i284-i294. (2018).
8. H.Nyquist. Certain Topics in Telegraph Transmission Theory. *Transactions of the American Institute of Electrical Engineers*. **47(2):** 617-644. (1928).
9. C.E. Shannon. Communication in the Presence of Noise. *Proceedings of the IRE*. **37(1)**: 10-21. (1949).
10. R.Cole, T. Jinadasa, and C. Brown. Measuring and interpreting point spread functions to determine confocal microscope resolution and ensure quality control. *Nature Protocol*. **6(12)**: 1929-1941. (2011).
11. M.M Frigault, J. Lacoste, J. L. Swift, and C. M. Brown. Live-cell microscopy – Tips and tools. *Journal of Cell Science*. **122(6):** 753-767. (2009).
12. A.J. North. Seeing is believing? A beginners' guide to practical pitfalls in image acquisition. *Journal of Cell Biology*. **172(1)**: 9-18. (2008).
13. L. Gao, L. Shao, B. Chen, and E. Betzig. 3D live fluorescence imaging of cellular dynamics using Bessel beam plane illumination microscopy. *Nature Protocol*. **9(5)**: 1083-1101. (2014).
14. C. Sheppard. Scanning Confocal Microscopy. *Encyclopedia of Optical Engineering*. Marcel Dekker. New York. 2525-2544. (2003).
15. K. König. Multiphoton microscopy in life sciences. *Journal of Microscopy*. **200(2)**: 83-104. (2000).
16. B. Huang, W. Wang, M. Bates, and X. Zhuang. Three-Dimensional Super-Resolution Imaging by Stochastic Optical Reconstruction Microscopy. *Science*. **319(5864)**: 810-813. (2008).
17. D.Baddeley, M.B. Cannell, and C. Soeller. Three-dimensional sub-100nm super-resolution imaging of biological samples using a phase ramp in the objective pupil. *Nano Research*. **4(6)**: 589-598. (2011).
18. Y. Shechtman, L.E. Weiss, A. Backer, M. Y. Lee, and W. Moerner. Multicolour localization microscopy by point-spread-function engineering. *Nature Photonics*. **10**. (2016). 590-594.
19. J. Sibarita. Deconvolution Microscopy. *Adv Biochem Engin/Biotechnol*. **95**: 201-243. (2005).

20. D. Sage, L. Donati, F. Soulez, D. Fortun, G. Schmit, A. Seitz, R. Guiet, C. Vonesch, and M. Unser. DeconvolutionLab2: An open-source software for deconvolution microscopy. *Methods*. **115**: 28-41. (2017).
21. W.H. Richardson. Bayesian-Based Iterative Method of Image Restoration. *Journal of the Optical Society of America*. **62(1)**: 55-59 (1972).
22. L.B. Lucy. An iterative technique for the rectification of observed distributions. *Astronomical Journal*. **79(6):** 745-754. (1974).
23. P. Kanchanawong, G. Shtengel, A.M. Pasapera, E.B. Ramko, M.W. Davidson, H.F. Hess, and C.M. Waterman. Nanoscale architecture of integrin-based cell adhesions. *Nature*. **468(7323)**: 580-584. (2010).
24. B. Diederich, P. Then, A. Jügler, R. Förster, and R. Heintzmann. cellSTORM – Cost-effective Super-Resolution on a Cellphone using dSTORM. *bioRXiv*. 1-17. (2018).
25. R. van den Eynde, A. Sandmeyer, W. Vandenberg, S. Duwé, W. Hübner, P. Dedecker, T. Huser, and M. Müller. A cost-effective approach to Super-resolution Optical Fluctuation Imaging (SOFI) microscopy using an industry-grade CMOS camera. *bioRxiv*. 1-8. (2018).
26. X. Chen, Z. Zeng, R. Li, B. Xue, P. Xi, and Y. Sun. Superior performance with sCMOS over EMCCD in super-resolution optical fluctuation imaging. *Journal of Biomedical Optics*. **21(6)**: 066007-1 – 066007-2. (2016).
27. J. Huisken, J. Swoger, F. Del Bene, J. Wittbrodt, and E.H. K. Stelzer. Optical Sectioning Deep Inside Live Embryos by Selective Plane Illumination Microscopy. *Science*. **305(5686)**: 1007-1009. (2004).
28. J. Huisken and D.Y. Stainier. Selective plane illumination microscopy techniques in developmental biology. *Development*. **136(12)**: 1963-1975. (2009).
29. P.J. Keller, A.D. Schmidt, J. Wittbrodt, and E.H.K. Stelzer. Reconstruction of zebrafish early embryonic development by scanned light sheet microscopy. *Science.* **322(5904)**:1065-1069. (2008).
30. T.A. Planchon, L. Gao, D.E. Milkie, M.W. Davidson, J.A. Galbraith, C.G. Galbraith, and E. Betzig. Rapid three-dimensional isotropic imaging of living cells using Bessel beam plane illumination. *Nature Methods*. **8(5)**: 417-423. (2011).
31. B. Chen, W.R. Legant, K. Wang, L. Shan, D.E. Milkie, M.W. Davidson, C. Janetopoulos, X.S. Wu, J.A. Hammer III, Z. Liu, B.P. English, Y. Mimori-Kiyosue, D.P. Romero, A.T. Ritter, J. Lippincott-Schwartz, L. Fritz-Laylin, R.D. Mullins, D.M. Mitchell, J.N. Bembenek, A. Reymann, R. Böhme, S.W. Grill, J.T. Wang, G. Seydoux, U.S. Tulu, D.P. Kiehart, and E. Betzig. Lattice Light Sheet Microscopy: Imaging Molecules to Embryos at High Spatiotemporal Resolution. *Science*. **346(6208)**: 1257998-1 – 1257998-2. (2014).
32. X.Chen, W. Zong, R, Li, Z. Zeng, J. Zhao, P. Xi, L. Chen, and Y, Sun. Two-photon light-sheet nanoscopy by fluorescence fluctuation correlation analysis. *Royal Society of Chemistry*. **8(19):** 9982-9987. (2016).
33. D. Axelrod. Cell-Substrate Contacts Illuminated by Total Internal Reflection Fluorescence. *Journal of Cell Biology.* **89(1)**: 141–145. (1981).
34. A.L. Mattheyses. S.M. Simon, and J.Z. Rappoport. Imaging with total internal reflection fluorescence microscopy for the cell biologist. *Journal of Cell Science*. **123(21)**: 3621-3628. (2010).
35. M. Tokunaga, N. Imamoto, and K. Sakata-Sogawa. Highly inclined thin illumination enables clear single-molecule imaging in cells. *Nature Methods*. **5(2)**: 159-161. (2008).
36. L. Schermelleh, R. Heintzmann, and H. Leonhardt. A guide to super-resolution fluorescence microscopy. *Journal of Cell Biology*. **190(2):** 165-175 (2010).

37. V. Klang, N.B. Matsko, C. Valenta, and F. Hofer. Electron microscopy of nanoemulsions: An essential tool for characterisation and stability assessment. *Micron*. **43(2-3)**: 85-103. (2012).
38. M. Knoll. Aufladepotentiel und Sekundäremission elektronen bestrahlter Körper. *Zeitschrift für technische Physik* **16**: 467-475. (1935).
39. E. Ruska and M. Knoll. Das Elektronenmikroskop. *Zeitschrift für Physik*. **78(5-6)**: 318-339. (1932).
40. G. Binning, C.F. Quate, and C. Gerber. Atomic Force Microscope. *Physical Review Letters*. **56(9)**: 930-933. (1986).
41. P. Mitchell. Turning the spotlight on cellular imaging. *Nature Biotechnology*. **19(11)**: 1013-1017. (2001).
42. Y. Martin, C.C. Williams, and H.K. Wickramasinghe. Atomic force microscope-force mapping and profiling on a sub 100-Å scale. *Journal of Applied Physics*. **61(10)**: 4723-4729. (1987).
43. Q. Zhong, D. Inniss, K. Kjoller, and V.B. Elings. Fractured polymer/silica fiber surface studied by tapping mode atomic force microscopy. *Surface Science*. **290(1-10)**: L688-L692. (1993).
44. K. Chang, Y.Chiang, C. Yang, and J. Liou. Atomic force microscopy in biology and biomedicine. *Tzu Chi Medical Journal*. **24(4)**: 162-169. (2012).
45. K. Dopf, S. Heunisch, P. Schwab, C. Moosmann, A. Habermehl, U. Lemmer, and H. Eisler. Superresolution optical fluctuation imaging (SOFI) aided nanomanipulation of quantum dots using AFM for novel artificial arrangements of chemically functionalized colloidal quantum dots and plasmonic structures. *Proceedings of SPIE*. **9126**: 91360N-1 – 91360N-9. (2014).
46. B. Harke, J.V. Chacko, H. Haschke, C. Canale, and A. Diaspro. A novel nanoscopic tool by combining AFM with STED microscopy. *Optical Nanoscopy*. **1(1)**: 3. (2012).
47. R.D. Turner, A. F. Hurd, A. Cadby, J.K. Hobbs, and S.J. Foster. Cell wall elongation mode in Gram-negative bacteria is determined by peptidoglycan architecture. *Nature Communications*. **4(1496)**: 1-8. (2013).
48. A. Hermsdörfer. Combination of high-resolution AFM with super-resolution Stochastic Optical Reconstruction Microscopy (STORM). Technical note JPK Instruments AG, Germany. (2014).
49. R. Heintzmann and C. Cremer. Laterally Modulated Excitation Microscopy: Improvement of resolution by using a diffraction grating. *Proceedings of SPIE*. **3568**: 185-196. (1999).
50. M.G. Gustafsson. Surpassing the lateral resolution limit by a factor of two using structured illumination microscopy. *Journal of Microscopy*. **198(2)**: 82-87. (2000).
51. B.O. Leung and K.C. Chou. Review of Super-Resolution Fluorescence Microscopy for Biology. *Applied Spectroscopy*. **65(9)**: 967-980. (2011).
52. M.G.L. Gustafsson. Nonlinear structured-illumination microscopy: Wide-field fluorescence imaging with theoretically unlimited resolution. *PNAS*. **102(37)**: 13081-13086. (2005).
53. E.H. Rego, L. Shao, J.J. Macklin, L. Winoto, G.A. Johansson, N. Kamps-Hughes, M.W. Davidson, and M.G.L. Gustafsson. Nonlinear structured-illumination microscopy with a photoswitchable protein reveals cellular structures at 50nm resolution. *PNAS*. **109(3)**: E135-E143. (2012).
54. A.G. York, P. Chandris, D.D. Nogare, J. Head, P. Wawrzusin, R.S. Fischer, A. Chitnis, and H. Shroff. Instant super-resolution imaging in live cells and embryos via analog image processing. *Nature Methods*. **10(11)**: 1122-1126. (2013).

55. P.J. Keller, A.D. Schmidt, A. Santella, K. Khairy, Z. Bao, J. Wittbrodt, and E.H.K. Stelzer. Fast, high-contrast imaging of animal development with scanned light sheet-based structured-illumination microscopy. *Nature Methods*. **7(8)**: 637-642. (2010).
56. D. Li, L. Shao, B. Chen, X. Zhang, M. Zhang, B. Moses, D. E. Milkie, J.R. Beach, J.A. Hammer III, M. Pasham, T. Kirchhausen, M.A. Baird, M.W. Davidson, P. Xu, and E. Betzig. Extended-resolution structured illumination imaging of endocytic and cytoskeletal dynamics. *Science*. **349(6251)**: aab3500-aab3526. (2015).
57. M.G.L. Gustafsson, L. Shao, P.M. Carlton, C.J. R. Wang, I.N. Golubovskaya, W.Z. Cande, D.A. Agard, and J.W. Sedat. Three-Dimensional Resolution Doubling in Wide-Field Fluorescence Microscopy by Structured Illumination. *Biophysical Journal*. **94(12)**: 4957-4970. (2008).
58. R. Förster, K. Wicker, W. Müller, A. Jost, and R. Heintzmann. Motion artefact detection in structured illumination microscopy for live cell imaging. *Optics Express*. **24(19)**: 22121-22133. (2016).
59. G. Ball, J. Demmerle, R, Kaufmann, I. Davis, I.M. Dobbie, and L. Schermelleh. SIMcheck: a Toolbox for Successful Super-resolution Structured Illumination Microscopy. *Scientific Reports*. **5(15915)**: 1-29. (2015).
60. M.J. Rust, M. Bates, and X. Zhuang. Sub-diffraction-limit imaging by stochastic optical reconstruction microscopy (STORM). *Nature Methods*. **3(10):** 793-795. (2006).
61. E. Betzig, G.H. Patterson, R. Sougrat, O.W. Lindwasser, S. Olenych, J.S. Bonifacino, M.W. Davidson, J. Lippincott-Schwartz, and H.F. Hess. Imaging Intracellular Fluorescent Proteins at Nanometer Resolution. *Science*. **313(5793)**: 1642-1645. (2006).
62. M. Heilemann, E. Margeat, R. Kasper, M. Sauer, and P. Tinnefeld. Carbocyanine Dyes as Efficient Reversible Single-Molecule Optical Switch. *Journal of the American Chemical Society*. **127(11)**: 3801-3806. (2005).
63. H.Shroff, C. Galbraith, J. Galibraith, and E. Betzig. Live-cell photoactivated localization microscopy of nanoscale adhesion dynamics. *Nature Methods*. **5(5):** 417-423. (2008).
64. S.W.Hell and J. Wichmann. Breaking the diffraction resolution limit by stimulated emission: stimulated-emission-depletion fluorescence microscopy. Optics Letters **19(11):** 780-782. (1994).
65. J.N Farahani, M.J Schibler, and L. Bentolila. Stimulated Emission Depletion (STED) Microscopy: from Theory to Practice. *Microscopy: Science, Technology, Applications and Education. A. Méndez-Vilas and J. Díaz (Eds.)*. **4(3)**: 1539-1547. (2010).
66. M. Dyba, S. Jakobs, and S. W Hell. Immunofluorescence stimulated emission depletion microscopy. *Nature Biotechnology*. **21(11):** 1303-1304 (2003).
67. K. I. Willig, R. Kellner, R. Medda, and B. Hein. Nanoscale Resolution in GFP-Based Microscopy. *Nature Methods*. **3(9):** 721-723. (2006).
68. C. Steinhauer, R. Jungmann, T. Sobey, F. Simmel, and P. Tinnefeld. DNA Origami as a Nanoscopic Ruler for Super-Resolution Microscopy. *Angewandte Chemie International Edition*. **48(47):** 8870-8873. (2010).
69. M. Koenig, P. Reisch, R. Dowler, B. Kraemer, S. Tannert, M. Patting, M.P. Clausen, G. Galiani, C. Eggeling, F. Koberling, and R. Erdmann. ns-time resolution for multispecies STED-FLIM and artifact free STED-FCS. *SPIE BiOS*. **9712**: 97120T. (2016).
70. K.Y. Han and T. Ha. Dual-color three-dimensional STED microscopy with a single high-repetition-rate laser. *Optics Letters*. **40(11)**: 2653-2656. (2015).
71. C.J.R. Sheppard, S.B. Mehta, and R. Heintzmann. Superresolution by image scanning microscopy using pixel reassignment. *Optics Letters*. **38(15)**: 2889-2892. (2013).
72. K. Weisshart. The Basic Principle of Airyscanning. *Carl Zeiss Microscopy Technology Note*. 1-22. (2014).

73. K. Korobchevskaya, B.C. Lagerholm, H. Colin-York, and M. Fritzsche. Exploring the Potential of Airyscan Microscopy for Live Cell Microscopy. *Photonics*. **4(41)**: 1-19. (2017).
74. N. Gustafsson, S. Cully, G.Ashdown, D.M. Owen, P.M. Peredia, and R. Henriques. Fast live-cell conventional fluorophore nanoscopy with ImageJ through super-resolution radial fluctuations. *Nature communications*. **7(12471)**: 1-9 (2016).
75. R. Parthasarathy. Rapid, accurate particle tracking by calculation of radial symmetry centers. Nature Methods. **9(7):** 424-726. (2012).
76. K. Retzer, J. Lacek, R. Skokan, C.I.del Genio, S. Vosolsobě, M. Laňková, K. Malínská, N. Konstantinova, E. Zažímalová, R.M. Napier, J. Petrášek, and C. Luschnig. Evolutionary Conserved Cysteines Function as cis-Acting Regulators of Arabidopsis PIN-FORMED Two Distribution. *International Journal of Molecular Sciences*. **18(2274)**: 1-20. (2017).
77. A.O. Khan, V.A. Simms, J.A. Pike, S.G. Thomas, and N.V, Morgan. CRISPR-Cas9 Mediated Labelling Allows for Single Molecule Imaging and Resolution. *Scientific Reports*. **7(8450)**: 1-9. (2017).
78. S. Culley, K.L. Tosheva, P.M. Pereira, and R. Henriques. SRRF: Universal live-cell super-resolution microscopy. *International Journal of Biochemistry and Cell Biology*. **101**: 74-79. (2018).
79. S. Culley, D. Albrecht, C. Jacobs, P.M. Pereira, C. Leterrier, J.Mercer, R.Henriques. NanoJ-SQUIRREL: quantitative mapping and minimisation of super-resolution optical imaging artefacts. *Nature Methods*. **15(4):** 263-266 (2018).
80. W.O. Saxton and W. Baumeister. The correlation averaging of a regularly arranged bacterial cell envelope protein. *Journal of Microscopy*. **127(2):** 127-138 (1982).
81. N.Banterle, K.H. Bui, E.A. Lemke, and M.Beck. Fourier ring correlation as a resolution criterion for super-resolution microscopy. *Journal of Structural Biology*. **183(3):** 363-367. (2013).
82. R.P. Nieuwenhuizen, K.A. Lidke, M. Bates, D. L. Puig, D. Grünwald, S. Stallinga, and B. Rieger. Measuring image resolution in optical nanoscopy. *Nature Methods*. **10(6)**: 557-562 (2013).
83. S.Culley. NanoJ-SQUIRREL User Manual. Version 1.2. (2017).
84. R.F. Laine, K.L. Tosh, N. Gustaffson, R.D.M. Gray, P. Almada, D. Albrecht, G.T. Risa, F. Hurtig, A. Lindås, B. Baum, J. Mercer, C. Leterrier, P.M. Pereira, S. Culley, and R. Henrique. NanoJ: a high-performance open-source super-resolution microscopy toolbox. bioRxiv. 1-8. (2018).
85. T. Dertinger, R. Coyler, G. Iyer, S. Weiss, and J. Enderlein. Fast, background-free, 3D super-resolution optical fluctuation imaging (SOFI). *PNAS*. **106(52)**: 22287-22292. (2009).
86. T. Dertinger, J. Xu, O.F. Naini, R. Vogel, and S. Weiss. SOFI-based 3D superresolution sectioning with a wide-field microscope. *Optical Nanoscopy*. **1(2)**: 1-8. (2012).
87. B. Das and N. Lyga. Cumulant-like cross-correlation functions to determine temporal behaviour of two signals. *Bulgarian Journal of Physics.* **28(3-4):** 120-127. (2001).
88. T.Dertinger, R.Coyler, R.Vogel, J.Enderlein, and S.Weiss. Achieving increased resolution and more pixels with Superresolution Optical Fluctuation Imaging (SOFI). *Optics Express*. **18(18):** 18875-18885. (2010).
89. P. Dedecker, S. Duwé, R.K, Neely, and J. Zhang. Localizer: fast, accurate, open-source, and modular software package for superresolution microscopy. *Journal of Biomedical Optics*. **17(12):** 126008-1 – 126008-5. (2012).
90. T. Dertinger, A. Pallaoro, G. Braun, S. Ly, T.A. Laurence, and S. Weiss. Advances in superresolution optical fluctuation imaging (SOFI). *Quarterly Reviews of Biophysics*. **46(2):** 210-221. (2010).

91. J.S. Verdaasdonk, A.D. Stephens, J. Haase, and K. Bloom. Bending the rules: widefield microscopy and the Abbe limit of resolution. *Journal of Cellular Physiology*. **229(2):** 132-138. (2014).
92. X. Yi, X. Lin, and S. Weiss. Local Dynamic Range Compression for High Order Super-Resolution Optical Fluctuation Imaging (SOFI). *Biophysical Journal*. **110(3):** 162a. (2016).
93. S. Geissbuehler, N.L. Bocchio, C. Dellagiacoma, C. Berclaz, M. Leutenegger, and T. Lasser. Mapping molecular statistics with balanced super-resolution optical fluctuation imaging (bSOFI). *Optical Nanoscopy*. **1(1):** 1-7. (2012).
94. S.C. Stein, A. Huss, D. Hähnel, I. Gregor, and J. Enderlein. Fourier interpolation stochastic optical fluctuation imaging. *OSA*. **23(12)**: 1-10. (2015).
95. L. Zou, S. Zhang, B. Wang, and J. Tan. High-order super-resolution optical fluctuation imaging based on low-pass denoising. *Optics Letters*. **43(4)**: 707-710. (2018).
96. D. Dikov and J. Bereiter-Hahn. Inner membrane dynamics in mitochondria. *Journal of Structural Biology*. **183(3)**: 455-466. (2013).
97. S. Jiang, Y. Zhang, H. Yang, Y. Xiao, X. Miao, R. Li, Y. Xu, and X. Zhang. Enhanced SOFI algorithm achieved with modified optical fluctuating signal extraction. *Optics Express*. **24(3)**: 3037-3045. (2016).
98. T.M. Watanabe, S.Fukui, T. Jin, F. Fumihiko, and T. Yanagida. Real-Time Nanoscopy by Using Blinking Enhanced Quantum Dots. *Biophysical Journal*. **99(7)**: L5—L52. (2010).
99. W. Vandenberg and P. Dedecker. Effect of probe diffusion on the SOFI imaging accuracy. *Scientific Reports*. **7(44665)**: 1-8. (2017).
100. S.Cox. Super-resolution imaging in live cells. *Developmental Biology*. **401(1)**: 175-181. (2015).
101. O. Mandula, I.S. Šestak, R. Heintzmann, and C.K.I. Williams. Localisation microscopy with quantum dots using non-negative matrix factorism. *Optics Express*. **22(20)**: 1-12. (2014).
102. M. Kim, C. Park, C. Rodriguez, Y. Park, and Y. Cho. Superresolution imaging with optical fluctuation using speckle patterns illumination. *Scientific Reports*. **5(16525)**: 1-10. (2015).
103. L.Yeh, L. Tian, and L. Waller. Structured illumination microscopy with unknown patterns and a statistical prior. *Biomedical Optics Express*. **8(2)**: 695-711. (2017).
104. N.V. Klementieva, A.I. Pavlikov, A.A. Moiseev, N.G. Bozhanova, N.M. Mishina, S.A. Lukyanov, E.V. Zagaynova, K.A. Lukyanov, and A.S. Mishin. Intrinsic blinking of red fluorescent proteins for super-resolution microscopy. Chemical Communications. **53(5)**: 949-951. (2017).
105. P. Dedecker, G.C.H. Mo, T. Dertinger, and J. Zhang. Widely accessible method for superresolution fluorescence imaging of living systems. *PNAS*. **109(27)**: 10909-10914. (2012).
106. X. Zhang, X. Chen, Z. Zeng, M. Zhang, Y. Sun, P. Xi, J. Peng, and P. Xu. Development of a Reversibly Switchable Fluorescent Protein for Super-Resolution Optical Fluctuation Imaging (SOFI). *ACS Nano*. **9(3):** 2659-2667. (2015).
107. A.M. Chizhik, S. Stein, M.O. Dekaliuk, C. Battle, W. Li, A. Huss, M. Platen, I.A.T. Schaap, I. Gregor, A.P. Demchenko, C.F. Schmidt, J. Enderlein, and A.I. Chizhik. Super-Resolution Optical Fluctuation Bio-Imaging with Dual-Color Carbon Nanodots. *Nano Letters*. **16(1):** 237-242. (2016).
108. X. Chen, R. Li, Z. Liu, K. Sun, Z. Sun, D. Chen, G. Xu, P. Xi, C. Wu, and Y. Sun. Small Photoblinking Semiconductor Polymer Dots for Fluorescence Nanoscopy. *Advanced Materials*. **29(5)**: 1-7. (2016).

109. T. Dertinger, M. Heilemann, R. Vogel, M.Sauer, and S. Weiss. Superresolution Optical Fluctuation Imaging with Organic Dyes. *Angewandte Chemie International Edition*. **49(49)**: 9441-9443. (2010).
110. Z. Ristanović, M.M. Kerssens, A.V. Kubarev, F.C. Hendriks, P. Dedecker, J. Hofkens, M.B.J. Roeffaers, and B.M. Weckhuysen. High-Resolution Single-Molecule Fluorescence Imaging of Zeolite Aggregates within Real-Life Fluid Catalytic Cracking Particles. *Angewandte Chemie International Edition*. **54(6)**: 1836-1840. (2014).
111. Z. Zeng, X. Chen, H. Wang, N. Huang, C. Shan, H. Zhang, J. Teng, and P. Xi. Fast Super-Resolution Imaging with Ultra-High Labeling Density Achieved by Joint Tagging Super-Resolution Optical Fluctuation Imaging. *Scientific Reports*. **5(8359):** 1-7. (2015).
112. M.E. Gallina, J. Xu, T. Dertinger, A. Aizer, Y. Shav-Tal, and S. Weiss. Resolving the spatial relationship between intracellular components by dual color super resolution optical fluctuations imaging (SOFI). *Optical Nanoscopy*. **2(2):** 1-9. (2013).
113. L. Kisley, R. Brunetti, L.J. Tauzin, B. Shuang, X. Yi, A.W. Kirkeminde, D.A. Higgins, S. Weiss, and C.F. Landes. Characterization of Porous Materials by Fluorescence Correlation Spectroscopy Super-resolution Optical Fluctuation Imaging. *ACS Nano.* **9(9):** 9158-9166. (2015).
114. A.H. Hainsworth, S. Lee, P.Foot, A. Patel, W.W. Poon, and A.E. Knight. Super-resolution imaging of subcortical white matter using stochastic optical reconstruction microscopy (STORM) and super-resolution optical fluctuation imaging (SOFI). *Neuropathology and Applied Neurobiology*. **44(4)**: 417-426. (2017).
115. S. Schidorsky, X. Yi, Y.Razvag, Y. Golan, S. Weiss, and E. Sherman. Synergizing superresolution optical fluctuation imaging with single molecule localization microscopy. *Methods and Applications in Fluorescence*. **6(4)**: 1-18. (2016).
116. H. Deschout, T. Lukes, A. Sharipov, D. Szlag, L. Feletti, W. Vandenberg, P. Dedecker, J. Hofkens, M. Leutenegger, T. Lasser, and A. Radenovic. Complementarity of PALM and SOFI for super-resolution live-cell imaging of focal adhesions. *Nature Communications*. **7(13693)**: 1-11. (2016).
117. G. Zhao, C. Zheng, C. Kuang, and X. Lu. Resolution-enhanced SOFI via structured illumination. *Optics Letters*. **42(19)**: 3956-3959. (2017).
118. A. Bar-Zion, C. Tremblay-Darveau, O. Solomon, D. Adam, and Y.C. Eldar. Fast Vascular Ultrasound Imaging With Enhanced Spatial Resolution and Background Rejection. *IEEE Transactions on Medical Imaging*. **36(1)**: 169-180. (2017).
119. J. Xu, J. Chang, Q.Yan, T.Dertinger, M.P. Bruchez, and S.Weiss. Labeling Cytosolic Targets in Live Cells with Blinking Probes. *The Journal of Physcial Chemistry Letters*. **4(13)**: 2138-2146. (2013).
120. B. Huang, M. Bates, and X. Zhuang. Super resolution fluorescence microscopy. *Annual Review of Biochemistry*. **78**: 993-1016. (2009).
121. S. Geissbuehler, C.Dellagiacoma, and T.Lasser. Comparison between SOFI and STORM. *Biomedical Optics Express*. **2(3)**: 408-420 (2011).
122. N. Gustafsson. QuickSOFI: High-Performance Superresolution Optical Fluctuation Imaging (SOFI) Plugin for ImageJ Using GPU Computing. University College London, UK. 1-18. (2014).
123. W. Vandenberg, S. Duwé, M. Leutenegger, B. Moeyaert, B. Krajnik, T. Lasser, and P. Dedecker. Model-free uncertainty estimation in stochastical optical fluctuation imaging (SOFI) leads to a doubled temporal resolution. *Biomedical Optics Express*. **7(2):** 467-480. (2016).
124. A.Girsault, T. Lukes, A.Sharipov, S.Geissbuehler, M.Leutenegger, W.Vandenberg, P.Dedecker, J.Hofkens, and T.Lasser. SOFI Simulation Tool: A Software Package for

Simulating and Testing Super-Resolution Optical Fluctuation Imaging. PLoS One. **11(9):** e0161602-1 – e0161602-13 (2016).
125. D. Magde, E.Elson, and W.W. Webb. Thermodynamic Fluctuations in a Reacting System – Measurement by Fluorescence Correlation Spectroscopy. *Physical Review Letters*. **29(11):** 705-708. (1972).
126. O. Krichevsky and G.Bonnet. Fluorescence correlation spectroscopy: the technique and its applications. *Report on Progress in Physics*. **65(2):** 251-297. (2002).
127. D.K. Tiwari, S. Tanaka, Y. Inouye. K.Yoshizawa, T.M. Watanabe, and T.Jin. Synthesis and Characterization of Anti-Her2 Antibody Conjugated CdSe/CdZnS Quantum Dots for Fluorescence Imaging of Breast Cancer Cells. *Sensors*. **9(11):** 9332-9354. (2009).
128. M.J. Murcia, D.L. Shaw, E.C. Long, and C.A. Naumann. Fluorescence correlation spectroscopy of CdSe/CdZnS quantum dot optical bioimaging probes with ultra-thin biocompatible coatings. *Optics Communications*. **281(7):** 1771-1780 (2008).
129. T. Liedl, S.Keller, F.C. Simmel, J.O. Rädler, and W.J. Parak. Fluorescent Nanocrystals as Colloidal Probes in Complex Fluids Measured by Fluorescence Correlation Spectroscopy. *Small*. **1(10):** 997-1003. (2005).
130. S. Doose, J.M. Tsay, F. Pinaud, and S. Weiss. Comparison of Photophysical and Colloidal Properties of Biocompatible Semiconductor Nanocrystals Using Fluorescence Correlations Spectroscopy. *Analytical Chemistry*. **77(7):** 2235-2242. (2005).
131. A.A. de Thomaz, D.B. Almeida, V.B. Pelegati, H.F. Carvalho, and C.L. Cesar. Measurement of the Hydrodynamic Radius of Quantum Dots by Fluorescence Correlation Spectroscopy Excluding Blinking. *The Journal of Physical Chemistry B*. **119(11):** 4294-4299 (2015).
132. N. Durisc, A.I. Bachir, D.L. Kolin, B. Hebert, B.C. Lagerholm, P. Grutter, and P.W. Wiseman. Detection and Correction of Blinking Bias in Image Correlation Transport Measurements of Quantum Dot Tagged Macromolecules. *Biophysical Journal*. **93(4):** 1338-1346 (2007).
133. D.R. Larson, W.R. Zipfel, R.M. Williams, S.W. Clarke, M.P. Bruchez, F.W.Wise. and W.W.Watt. Water-Soluble Quantum Dots for Multiphoton Fluorescence Imaging in Vivo. *Science*. **300(5624):** 1434—436. (2003).
134. E.L. Elson. Fluorescence Correlation Spectroscopy: Past, Present, Future. *Biophysical Journal*. **101(12):** 2855-2870. (2011).
135. B. Alberts, A. Johnson, and J. Lewis. Molecular Biology of the Cell. Antibodies can be used to Detect Specific Molecules. *Garland Science*. New York. 4th Edition. (2002).
136. K.D. Wegner, S. Lindén, Z. Jin, T.L. Jennings, R. el Khoulati, P.M.P. van B. en Henegouwen, and N. Hildebrandt. *Small*. **10(4):** 734-740. (2014).
137. T. de Meyer, S. Muyldermans, and A. Depicker. Nanobody-based products as research and diagnostics tools. *Trends in Biotechnology*. **32(5):** 263-270. (2017).
138. J. Ries, C. Kaplan, E. Platonova, H. Eghlidi, and H.Ewers. A simple versatile method for GFP-based super-resolution microscopy via nanobodies. *Nature Methods*. **9(6):** 582-584. (2012).
139. A. de Marco. Biotechnological applications of recombinant single-domain antibody fragments. *Microbial Cell Factories*. **10(44)**: 1-14. (2011).
140. K. Deffar, H. Shi, L. Li, X. Wang, and X. Zhu. Nanobodies – the new concept in antibody engineering. *African Journal of Biotechnology*. **8(12):** 2645-2652. (2009).
141. C. Hamers-Casterman, T. Atarhouch, S. Muyldermans, and S. Robinson. Naturally occurring antibodies devoid of light chains. *Nature*. **363(6428):** 446-448. (1993).
142. T. Pleiner, M. Bates, and D. Görlich. A toolbox of anti-mouse and anti-rabbit IgG secondary nanobodies. *Journal of Cell Biology*. **217(3)**: 1143-1154. (2018).

143. C. Tiede, R. Bedford, S.J. Heseltine, G. Smith, I Wijetunga, R.Ross, D. AlQallaf, A.P.E. Roberts, A. Balls, A. Curd, R.E. Hughes, H. Martin, S.R. Needham, L.C. Zanetteі-Domingues, Y.Sadigh, T.P. Peacock, A.A. Tang, N. Gibson, H. Kyle, G.W. Platt, N. Ingram, T. Taylor, L.P. Coletta, I. Manfield, M. Knowles, S. Bell, F. Esteves, A. Maqbool, R.K. Prasad, M. Drinkhall, R.S.Bon, V. Patel, S.A. Goodchild, M. Martin-Fernandez, R.J. Owens, J.E. Nettleship, M.E. Webb, M. Harrison, J.D. Lippiat, S. Ponnambalam, M. Peckham, A. Smith, P.K. Ferrigno, M. Johnson, M.J. McPherson, and D.C. Tomlinson. Affirmer proteins are versatile and renewable affinity reagents. *eLife*. **6(e24903)**: 1-39. (2017).
144. M. Nirmal, B.O. Dabbousi, M.G. Bawendi, J.J. Macklin, J.K. Trautman, T.D. Harris, and L.E. Brus. Fluorescence intermittency in single cadium selenide nanocrystals. *Nature*. **383(6603)**: 802-804. (1996).
145. M. Kuno, D.P. Fromm, H.F. Hamann, A. Gallagher, and D.J. Nesbitt. "On"/"off" fluorescence intermittency of single semiconductor quantum dots. *The Journal of Chemical Physics*. **115(2)**: 1028-1039. (2001).
146. A.L. Efros and M. Rosen. Random Telegraph Signal in the Photoluminescence Intensity of a Single Quantum Dot. *Physical Review Letters*. **78(6)**: 1110-1113. (1997).
147. M. Bruchez, M. Moronne, P. Gin, S. Weiss, and A.P. Alivisatos. Semiconductor Nanocrystals as Fluorescent Biological Labels. *Science*. **281(5385)**: 2013-2016. (1998).
148. X. Wu, H. Li, J. Li, K.N. Haley, J.A. Treadway. J.P. Larson, N. Ge, F. Peale, and M.P. Bruchez. Immunofluorescent labeling of cancer Her2 and other cellular targets with semiconductor quantum dots. *Nature Biotechnology*. **21(1)**: 41-46. (2003).
149. J.E. Francis, D. Mason, and R. Lévy. Evaluation of quantum dot conjugated antibodies for immunofluorescent labelling of cellular targets. *Beilstein Journal of Nanotechnology*. **8**: 1238-1249. (2017).
150. H. Montón, C. Nogués. E. Rossinyol. O. Castell, and M. Roldán. QDs versus Alexa: reality of promising tools for immunocytochemistry. *Journal of Nanotechnology*. **7(4):** 1-5 (2009).
151. O. Shimomura, F.H. Johnson, and Y.Saiga. Extraction, purification and properties of aequorin, a bioluminescent protein from the luminous hydromedusan, *Aequorea*. *Journal of Cellular Physiology*. **59:** 223-239. (1962).
152. O. Shimomura. Structure of the chromophore of *Aequorea* green fluorescent protein. *FEBS Letters*. **104(2):** 220-222 (1979).
153. N.C.Shaner, R,E, Campbell, P.A. Steinbach, B.N.G. Giepmans, A.E. Palmer, and R.Y. Tsein. Improved monomeric red, orange and yellow fluorescent proteins derived from Discosoma sp. red fluorescent protein. *Nature Biotechnology*. **22(12)**: 1567-1572. (2004).
154. F. Hertel, C.H. Gary, S. Duwé, P. Dedecker, and J. Zhang. RefSOFI for Mapping Nanoscale Organization of Protein-Protein Interactions in Living Cells. *Cell Reports*. **14(2)**: 390-400. (2016).
155. B. Moeyaert and P. Dedecker. PcSOFI as a smart label-based superresolution microscopy technique. *Methods in Molecular Biology*. **1148(17)**: 261-276. (2014).
156. N. G. Gurskaya, V.V. Verkhusha, A.S. Shcheglov, D.B. Staroverov, T.V. Chepurnykh, A.F. Fradkov, S. Lukyanov, and K.A. Lukyanov. Engineering of a monomeric green-to-red photoactivatable fluorescent protein induced by blue light. *Nature Biotechnology*. **24(4)**: 461-465. (2006).
157. R. Ando, H. Mizuno, and A. Miyawaki. Regulated fast nucleocytoplasmic shuttling observed by reversible protein highlighting. Science. 306(5700): 1370-1373. (2004).

158. S. Habuchi, R. Ando, P.Dedecker, W. Verheijen, H. Mizuno, A. Miyawaki, and J. Hofkens. Reversible single-molecule photoswitching in the GFP-like fluorescent protein Dronpa. *PNAS*. **102(27):** 9511-9516. (2005).
159. T. Brakemann, A.C. Steil, G. Weber, M. Andresen, I. Testa, T. Grotjohann, M. Leutenegger, U. Plessmann, H. Urlaub, C. Eggeling, M.C. Wahl, S.W. Hell, and S. Jakobs. A Reversibly Photoswitchable GFP-like Protein with Fluorescence Excitation Decoupled from Switching. *Nature Biotechnology*. **29(10):** 942-947. (2011).
160. R.M. Dickson, A.B. Cubitt, R.Y. Tsein, and W.E. Moerner. On/off blinking and switching behaviour of single molecules of green fluorescent protein. *Nature*. **388(6640)**: 355-358. (1997).
161. S. Geissbuehler, A. Sharipov, A. Godinat, N.L. Bocchio, P.A. Sandoz, A. Huss, N.A. Jensen, S. Jakobs, J. Enderlein, F. Goot, E.A. Dubikovskaya, T.Lasser, and M. Leutenegger. Live-cell multiplane three-dimensional super-resolution optical fluctuation imaging. *Nature Communications*. **5(5830)**: 1-7. (2014).
162. X.X. Zhou and M.Z. Lin. Photoswitchable fluorescent proteins: ten years of colorful chemistry and exciting applications. *Current Opinion in Chemical Biology*. **17(4):** 682-690. (2013).
163. M. Zhang, Z. Fu, and P. Xu. Extending the spatiotemporal resolution of super-resolution microscopies using photomodulatable fluorescent proteins. *Journal of Innovative Optical Health Sciences*. **9(3)**: 1630009-1 – 1630009-11. (2016).
164. C. Szent-Gyorgyi, B.F. Schmidt, Y. Creeger, G.W. Fisher, K.L. Zakel, S. Adler, J.A.J Fitzpatrick, C.A. Woolford, Q. Yan, K.V. Vasilev, P.B. Berget, M.P. Bruchez, J.W. Jarvik, and A. Waggoner. Fluorogen-activating single-chain antibodies for imaging cell surface proteins. *Nature Biotechnology*. **26(2)**: 235-240. (2008).
165. J.A.J. Fitzpatrick, Q. Yan, J.J. Sieber, M. Dyba, U. Schwarz, C. Szent-Gyorgyi, C.A. Woolford, P.B. Berget, A.S. Waggoner, and M. P. Bruchez. STED Nanoscopy in Living Cells Using Fluorogen Activating Proteins. *Bioconjugate Chemistry*. **20(10)**: 1843-1847. (2009).
166. S. van de Linde, S. Aufmkolk, C. Franke, T. Holm, T. Klein, A. Löschberger, S. Proppert, S. Wolter, and M. Sauer. Investigating Cellular Structures at the Nanoscale with Organic Fluorophores. *Chemistry & Biology*. **20(1)**: 8-18. (2013).
167. M. Heilemann, S. van de Linde, M. Schuttpelz, R. Kasper, B. Seefeldt, A. Mukherjee, P. Tinnefeld, and M. Sauer. Subdiffraction-resolution fluorescence imaging with conventional fluorescent probes. *Angewandte Chemie International*. **47(33)**: 6172-6176. (2008).
168. M. Bates, T.R. Blosser, and X. Zhuang. Short-range spectroscopic ruler based on a single-molecule optical switch. *Physical Review Letters*. **94(10)**: 1-9. (2005).
169. V. Marx. Probes: paths to photostability. *Nature Methods*. **12(3)**: 187-190. (2015).
170. S. Linde, R. Kasper, M. Heilemann, and M. Sauer. Photoswitching microscopy with standard fluorophores. *Applied Physics B*. **93(4)**: 725-731. (2008).
171. A. Arsić, N. Stajković, R. Spiegel, and I. Nikić-Spiegel. Vectashield quenches Alexa Fluor 647 fluorescence, but does not hinder dSTORM super-resolution imaging. bioRxiv. 1-30. (2018).
172. E. Berra, A. Ginouvès, and J. Pouysségur. (2006). The hypoxia-inducible-factor hydroxylases bring fresh air into hypoxia signalling. *European Molecular Biology Organisation*. **7(1)**: 41-45.
173. G.L. Semenza and G.L. Wang. A Nuclear Factor Induced by Hypoxia via De Novo Protein Synthesis Binds to the Human Erythropoietin Gene Enhancer at a Site Required for Transcriptional Activation. *Molecular and Cellular Biology*. **12(12)**: 5447-5454. (1992).

174. H. Tian, S.L. McKnight, and D.W. Russell. Endothelial PAS domain protein 1 (EPAS1), a transcription factor selectively expressed in endothelial cells. *Genes & Development*. **11(1)**: 72-82. (1997).
175. Y. Gu, S.M. Moran, J.B. Hogenesch, L. Wartman, and C.A. Bradfield. Molecular Characterization and Chromosomal Localization of a Third α-Class Hypoxia Inducible Factor Subunit, HIF3α. *Gene Expression*. **7(3)**: 205-213. (1998).
176. G.L Wang, B. Jiang, E.A. Rue, and G.L. Semenza. Hypoxia-inducible factor 1 is a basic-helix-loop-helix-PAS heterodimer regulated by cellular $O_2$ tension. *PNAS*. **92(12)**: 5510-5514. (1995).
177. R.J. Appelhoff, Y.Tian, R.R. Raval, H. Turley, A.L. Harris, C.W. Pugh, P.J. Radcliffe, and J.M. Gleade. Differential Function of the Prolyl Hydroxylases PHD1, PHD2, and PHD3 in the Regulation of Hypoxia-inducible Factor. *The Journal of Biological Chemistry*. **279(37)**: 38458-38465. (2004).
178. M. A.S. Cavadas, L. K. Nguyen, and A. Cheong. Hypoxia-inducible factor (HIF) network: insights from mathematical models. *Cell Communication and Signaling*. **11(42)**: 1-16. (2013).
179. S. Bani, D. Shweiki, A. Pinson, M. Chandra, G. Lazarovici, and E. Keshet. Upregulation of vascular endothelial growth factor expression induced by myocardial ischaemia: implications for coronary angiogenesis. *Cardiovascular Research*. **28(8)**: 1176-1179. (1994).
180. M. Ema, S. Taya, N. Yokotani, K. Sogawa, Y. Matsuda, and Y. Fuji-Kuriyama. A novel bHLH-PAS factor with close sequence similarilty to hypoxia-inducible factor 1α regulates the VEGF expression and is potentially involved in lung and vascular development. *PNAS*. **94(9)**: 4273-4278. (1997).
181. I. Flamme, T, Fröhlich, M. von Reutern, A. Kappel, A. Damert, and W. Risau. HRF, a putative basic helix-loop-helix-PAS domain transcription factor is closely related to hypoxia-inducible factor-1α and developmentally expressed in blood vessels. *Mechanisms of Development*. **63(1)**: 51-60. (1997).
182. J.B. Hogenesch, W.K. Chan, V.H. Jackiw, R.C. Brown, Y. Gus, M. Pray-Grant, G.H. Perdew, and C.A. Bradfield. Characterization of a Subset of the Basic-Helix-Loop-Helix-PAS Superfamily That Interacts with Components of the Dioxin Signaling Pathway. *The Journal of Biological Chemistry*. **272(13)**: 8581-8593. (1997).
183. S. Hara, C. Kobayashi, and N. Imura. Nuclear Localization of Hypoxia-Inducible Factor-2α in Bovine Arterial Endothelial Cells. *Molecular Cell Biology Research Communications*. **2(2)**: 119-123. (1999).
184. R. Takahashi, C. Kobayashi, Y. Kondo, Y. Nakatani, I. Kudo, M. Kunimoto, N. Imura, and S. Hara. Subcellular localization and regulation of hypoxia-inducible factor-2α in vascular endothelial cells*. Biochemical and Biophysical Research Communications*. **317(1)**: 84-91. (2004).
185. S.E. Taylor, J. Bagnall, D.Mason, R.Lévy. D.G.Fernig. V.Sée. Differential sub-nuclear distribution of hypoxia-inducible factors (HIF)-1 and -2 alpha impacts on their stability and mobility. *Open Biology*. **6(9):** 1-12. (2016).
186. P. Komarnitsky, E. Cho, and S. Buratowski. Phospho Ser5 RNA Pol II Different phosphorylated forms of RNA polymerase II and associated mRNA processing factors during transcription. *Genes & Development*. **14(19)**: 2452-2460. (2000).
187. J.F. O'Rourke, Y. Tian, P.J. Ratcliffe, and C.W. Pugh. Oxygen-regulated and Transactivating Domains in Endothelial PAS Protein 1: Comparison with Hypoxia-inducible Factor-1α. *The Journal of Biological Chemistry*. **274(4)**: 2060-2071. (1999).
188. E. Berra, E. Benizri, A.Ginouvès, V. Volmat, D. Roux, and J. Pouysségur. HIF proyl-hydroxylase 2 is the key oxygen sensor setting low steady-state levels of HIF-1α in normoxia. *The EMBO Journal*. **22(16)**: 4082-4090. (2003).

189. B. Keith, R.S. Johnson, and M.C. Simon. HIF1α and HIF2α: sibling rivalry in hypoxic tumor growth and progression. *Nature Reviews Cancer*. **12(1)**: 9-22. (2012).
190. C.M. Wiener, G. Booth, and G.L. Semenza. In Vivo Expression of mRNAs Encoding Hypoxia-Inducible Factor 1. *Biochemical and Biophysical Research Communications*. **225(1199)**: 485-488. (1996).
191. M.Ema, S. Taya, N. Yokotani, K. Sogawa, Y. Matsuda, and Y. Fujii-Kuriyama. A novel bHLH-PAS factor with close sequence similarity to hypoxia-inducible factor 1α regulates the VEGF expression and is potentially involved in lung and vascular development. *PNAS*. **94(9)**: 4273-4278. (1997).
192. E. B. Rankin, M.P. Biju, Q. Liu, T.L. Unger, J. Rha, R.S. Johnson, M.C. Simon, B. Keith, and V.H. Haase. Hypoxia-inducible factor-2 (HIF-2) regulates hepatic erythropoietin in vivo. *The Journal of Clinical Investigation*. **117(4)**: 1068-1077. (2007).
193. M.S. Wiesner, H.Turley, W.E. Allen, C. Willam, K. Eckardt, K.L. Talks, S.M. Wood, K.C. Gatter, A.L. Harris, C.W. Pugh, P.J. Ratcliffe, and P.H. Maxwell. Induction of Endothelial PAS Domain Protein-1 by Hypoxia: Characterization and Comparison With Hypoxia-Inducible Factor 1-α. *Blood*. **92(7)**: 2260-2268. (1998).
194. M.Y. Koh, R. Lemos Jr, X.P. Liu, and G. Powis. The hypoxia-associated factor switches cells from HIF-1a to HIF-2a-dependent signaling promoting stem cell characteristics, aggressive tumor growth and invasion. *American Association for Cancer Research*. **71(11)**: 4015–4027. (2011).
195. S. Huveneers, H. Truong, R. Fässler, A. Sonnenberg, and E.H.J. Danen. Binding of soluble fibronectin to integrin α5β1 – link to focal adhesion redistribution and contractile shape. *Journal of Cell Science*. **121(15)**: 2452-2462. (2008).
196. M. Xue and C.J. Jackson. Extracellular Matrix Reorganization During Wound Healing and Its Impact on Abnormal Scarring. *Advances in Wound Care*. **4(3)**: 119-136. (2015).
197. A. Huttenlocher and A.R. Horwitz. Integrins in Cell Migration. *Cold Spring Harb Perspect Biol*. **3(9)**: 1-16. (2011).
198. C. Frantz, K.M. Stewart, and V.M. Weaver. The extracellular matrix at a glance. *Journal of Cell Science*. **123(24)**: 4195-4200. (2010).
199. L.D. Muiznieks and F.W. Keely. Molecular assembly and mechanical properties of the extracellular matrix: A fibrous protein prospective. *Biochimica et Biophysica Acta*. **1832(7)**: 866-875. (2013).
200. J. Sapudom, S. Rubner, S. Martin, S. Thoenes, U. Anderegg, and T. Pompe. The interplay of fibronectin functionalization and TGF-β1 prescence on fibroblast proliferation, differentiation and migration in 3D matrices. Biomaterials Science. **4(3)**: 1291-1301. (2015).
201. W.S. To and K.S. Midwood. Plasma and cellular fibronectin: distinct and independent functions during tissue repair. *Fibrongenesis & Tissue Repair*. **4(21)**: 1-9. (2011).
202. K.J. Hamill, K. Kligys, S.B. Hopkinson, and J.C.R. Jones. Laminin deposition in the extracellular matrix: a complex picture emerges. *Journal of Cell Science*. **122(24)**: 4409-4417. (2009).
203. M.J. Reed, M. Damodarasamy, C.K. Chan, M.N.R. Johnson, T.N.Wight, and R.B. Vernon. Clevage of hyaluronan is impaired in aged dermal wounds. *Matrix Biology*. **32(1)**: 45-51. (2013).
204. M.K. Rana, J. Srivastava, M. Yang, C.S. Chen, and D.L. Barber. Hypoxia increases the abundance but not the assembly of extracellular fibronectin during epithelial cell transdifferentiation. *Journal of Cell Science*. **128(6)**: 1083-1089. (2015).

205. O.S. Osman, J. Selway, P. E. Harikumar, C.J. Stocker, E.T. Wargent, M.A. Cawthorne, S. Jassim, and K. Langlands. A novel method to assess collagen architecture in skin. *BMC Bioinformatics*. **14(1)**: 260 (2013).
206. H.P. Ehrlich, A. Desmoulière, R.F. Diegelmann, I.K. Cohen, C.C. Compton, W.L. Garner, Y. Kapanci, and G. Gabbiani. Morphological and Immunochemical Differences Between Keloid and Hypertrophic Scar. *American Journal of Pathology*. **145(1)**: 105-113. (1994).
207. P. D.H. M. Verhaegen, P.P.M. Van Zuijlen, N.M. Pennings, J. van Marle, F.B. Niessen, C.M.A.M. van Der Horst, and E. Middlelkoop. Differences in collagen architecture between keloid, hypertrophic scar, normotrophic scar, and normal skin: An objective histopathological analysis. *Wound Repair and Regeneration*. **17(5)**: 649-659. (2009).
208. M. Calderon, W.T. Lawrence, and A.J. Banes. Increased Proliferation in Keloid Fibroblasts Wounded in Vitro. *Journal of Surgical Research*. **61(127)**: 343-347. (1996).
209. A.L. Hellewell, S. Rosini, and J.C. Adams. A Rapid, Scalable Method for the Isolation, Functional Study, and Analysis of Cell-derived Extracellular Matrix. *Journal of Visualized Experiments*. **119(55051)**: 1-9. (2017).
210. S. Wu, H. Li, H. Yang, X. Zhang, Z. Li, and S. Xu. Quantitative analysis on collagen morphology in aging skin based on multiphoton microscopy. *Journal of Biomedical Optics*. **16(4)**: 040502-1 – 040502-3. (2011).
211. S.M. Früh, I. Schoen, J. Ries, and V. Vogel. Molecular architecture of native fibronectin fibrils. *Nature Communications*. **6(7275)**: 1-10. (2015).
212. H. Takei, A. Araki, H. Watanabe, A. Ichinose, F. Sendo. Rapid killing of human neutrophils by the potent activator phorbol 12-myristate 13-acetate (PMA) accompanied by changes different from typical apoptosis or necrosis. *Journal of Leukocyte Biology*. **59(2):** 229-240. (1996).
213. V. Brinkmann, U. Reichard, C. Goosmann, B. Fauler, Y. Uhlemann, D.S. Weiss, Y. Weinrauch, A. Zychlinsky. Neutrophil Extracellular Traps Kill Bacteria. *Science*. **303(5663)**: 1532-1535. (2004).
214. P.R. Cooper, L.J. Palmer, and I.L.C. Chapple. Neutrophil extracellular traps as a new paradigm in innate immunity: friend or foe? *Periodontology*. **63(1)**: 165-197. (2013).
215. B. E. Steinberg and S. Grinstein. Unconventional Roles of the NADPH Oxidase: Signaling, Ion Homeostasis, and Cell Death. *Science*. **2007(379):** 1-4. (2007).
216. B. Fadeel, A. Åhlin, J. Henter, S. Orrenius, and M.B. Hampton. Involvement of Caspases in Neutrophil Apoptosis: Regulation by Reactive Oxygen Species. *Blood*. **92(12):** 4808-4818. (1998).
217. M. Zawrotniak and M. Rapala-Kozik. Neutrophil extracellular traps (NETs) – Formation and implications. *ABP*. **60(3):** 277-284. (2013).
218. V. Brinkmann and A. Zychlinsky. Neutrophil extracellular traps: Is immunity the second function of chromatin? *Journal of Cell Biology*. **198(5):** 775-783. (2012).
219. C.F. Urban, D. Ermert, M. Schmid, U. Abu-Abed, C. Groosmann, W.Nacken, V. Brinkmann, P.R. Jungblut, and A. Zychlinsky. Neutrophil Extracellular Traps Contain Calprotectin, a Cytosolic Protein Complex Involved in Host Defense against Candida albicans. *PLoS Pathogens*. **5(10)**: e1000639-1 – e1000639-18. (2009).
220. W.D. Krautgartner, M. Klappacher, M. Hannig, A. Obermayer, D. Hartl, V. Marcos, and L. Vitkov. Fibrin Mimics Neutrophil Extracellular Traps in SEM. *Ultrastructural Pathology*. **34(4)**: 226-231. (2010).
221. T.A. Fuchs, U. Abed, C. Goosmann, R. Hurwitz, I. Schulze, V. Wahn, Y. Weinrauch, V. Brinkmann, and A. Zychlinsky. Novel cell death program leads to neutrophil extracellular traps. *Journal of Cell Biology*. **176(2)**: 231-241. (2007).
222. M.K.T. Squier, A. Sehnert, and J.J.Cohen. Apoptosis in leukocytes. *Journal of Leukocyte Biology*. **57(1)**: 2-10. (1995).

223. Suzuki, R. Yamada, X. Chang, S. Tokuhiro, T. Sawada, M. Suzuki, M. Nagasaki, M. Nakayama-Hamada, R. Kawaida, M. Ono, M. Ohtsuki, H. Furukawa, S. Yoshino, M. Yukioka, S. Tohma, T. Matsubara, S. Wakitani, R. Teshima, Y. Nishioka, A. Sekine, A. Iida, A. Takahashi, T. Tsunoda, Y. Nakamura, and K. Yamamoto. Functional haplotypes of PADI4, encoding citrullinating enzyme peptidylarginine deiminase 4, are associated with rheumatoid arthritis. *Nature Genetics.* **34(4)**: 395-402. (2003).
224. K. Nakashima, T. Hagiwara, and M. Yamada. Nuclear Localization of Peptidylarginine Deiminase V and Histone Deimination in Granulocytes. *Journal of Biological Chemistry*. **277(51)**: 49562-49568. (2002).
225. R.H.L. Li, L.R. Johnson, C. Kohen, and F. Tablin. A novel approach to identifying and quantifying neutrophil extracellular trap formation in septic dogs using immunofluorescence microscopy. *BMC Veterinary Research*. **14(210)**: 1-7. (2018).
226. C.S. Chowdhury. S. Giaglis. U.A. Walker. A. Buser. S. Hahn and P. Hasler. Enhanced neutrophil extracellular trap generation in rheumatoid arthritis: analysis of underlying signal transduction pathways and potential diagnostic utility. *Arthritis Research & Therapy*. **16(3):** 1-14. (2014).
227. A.K. Gupta, P. Hasler, W. Holzgreve, S. Gebhardt, and S. Hahn. Induction of Neutophil Extracellular DNA Lattices by Placental Microparticles and IL-8 and Their Presence in Preeclampsia. *Human Immunology*. **66(11):** 1146-1154. (2005).
228. L. Vitkov, M.Klappacher, M. Hannig, W.D. Krautgartner. Extracellular neutrophil traps in periodontitis. *Journal of Periodontal Research*. **44(5):** 664-672. (2009).
229. R. Manzenreiter, F. Kienberger, V. Marcos, K. Schilcher, W.D. Krautgartner, A. Obermayer, M. Huml, W. Stoiber, A. Hector, M. Griese, M. Hannig, M. Studnicka, L. Vitkov, and D. Hartl. Ultrastructural characterization of cystic fibrosis sputum using atomic force and scanning electron microscopy. *Journal of Cystic Fibrosis*. **11(2)**: 84-92. (2011).
230. A. Hakkim, B.G. Fürnrohr, K. Amann, B. Laube, U.A. Abed, V. Brinkmann, M. Herrmann, R.E. Voll, and A. Zychlinsky. Impairment of neutrophil extracellular trap degradation is associated with lupus nephritis. *PNAS*. **107(21)**: 9813-9818. (2010).
231. A. Caudrillier, K. Kessenbrock, B.M. Gilliss, J.X. Nguyen, M.B. Marques, M. Monestier, P. Toy, Z. Werb, and M.R. Looney. Platelets induce neutrophil extracellular traps in transfusion-related acute lung injury. *The Journal of Clinical Investigation*. **122(7)**: 2661-2671. (2012).
232. M. Gavillet, K. Martinod, R. Renella, C. Harris, N.I. Shapiro, D.D. Wagner, and D.A. Williams. Flow cytometric assay for direct quantification of neutrophil extracellular traps in blood samples. *American Journal of Hematology*. **90(12)**: 1155-158. (2015).
233. A.J. O'Donoghue, Y. Jin, G.M. Knudsen, N.C. Perera, D.E. Jenne, J.E. Murphy, C.S. Craik, and T.W. Hermiston. Global Substrate Profiling of Proteases in Human Neutrophil Extracellular Traps Reveals Consensus Motif Predominantly Contributed by Elastase. *PLoS One*. **8(9)**: 1-12. (2013).
234. V. Brinkmann, B. Laube, U.A. Abed, C. Goosmann, and A. Zychlinsky. Neutrophil Extracellular Traps: How to Generate and Visualize Them. *Journal of Visualized Experiments*. **36(1724)**: 1-3. (2010).
235. S. Masuda, D. Nakazawa, H. Shida, A. Miyoshi, Y. Kusunoki, U. Tomaru, and A. Ishizu. NETosis markers: Quest for specific, objective, and quantitative markers. *Clinica Chimica Acta*. **459**: 89-93. (2016).
236. V. Brinkmann, C. Goosmann, L.I. Kühn, and A. Zychlinsky. Automatic quantification of in vitro NET formation. *Frontiers in Immunology*. **3(413)**. 1-8. (2013).
237. T. Mohanty, O.E. Sørensen, and P. Nordenfelt. NETQUANT: Automated Quantification of Neutrophil Extracellular Traps. *Frontiers in Immunology*. **8(1999)**: 1-10. (2018).

238. R. Rebernick, L. Fahmy, C. Glover, M. Bawadekar, D. Shim, C.L. Holmes, N. Rademacher, H. Potluri, C.M. Bartels, and M.A. Shelef. DNA Area and NETosis Analysis (DANA): A High-Throughput Method to Quantify Neutrophil Extracellular Traps in Fluorescent Microscope Images. *Biological Procedures Online*. **20(7)**: 1-9. (2018).
239. M. Aumailley, L. Bruckner-Tuderman, W.G. Carter, R. Deutzmann, D. Edgar, P. Ekblom, J. Engel, E. Engvall, E. Hohenester, J.C.R. Jones, H.K. Kleinman, M.P. Marinkovich, G.R. Martin, U. Mayer, G. Meneguzzi, J.H. Miner, K. Miyazaki, M. Patarroyo, M. Paulsson, V. Quaranta, J.R. Sanes, T. Sasaki, K. Sekiguchi, L.M. Sorokin, J.F. Talts, K. Tryggvason, J. Uitto, I. Virtanen, K. von der Mark, U.M. Wewer, Y. Yamada, and P.D. Yurchenco. A simplified laminin nomenclature. *Matrix Biology*. **24(5)**: 326-332. (2003).
240. G.W. deHart, K.E. Healy, and J.C.R. Jones. The role of α3β1 integrin in determining the supramolecular organization of laminin-5 in the extracellular matrix of keratinocytes. *Experimental Cell Research*. **283(1)**: 67-79. (2003).
241. D. Kiritsi, C. Has, and L. Bruckner-Tuderman. Laminin 332 in junctional epidermolysis bullosa. *Cell Adhesion & Migration*. **7(1)**: 135-141. (2013).
242. B. U. Sehgal, P.J. DeBiase, S. Matzno, T. Chew, J.N. Claiborne, S.B. Hopkinson, A. Russell, M.P. Marinkovich, and J.C.R. Jones. Integrin β4 Regulates Migratory Behavior of Keratinocytes by Determining Laminin-332 Organization. *Journal of Biological Chemistry*. **281(46)**: 35487-35498. (2006).
243. S.B. Hopkinson, P.J. DeBiase, K. Kligys, K. Hamill, and J.C.R. Jones. Fluorescently tagged laminin subunits facilitate analyses of the properties, assembly and processing of laminins in live and fixed lung epithelial cells and keratinocytes. *Matrix Biology*. **27(7)**: 640-647. (2008).
244. K.J. Hamill, L. Langbein, J.C.R. Jones, W.H.I. Mclean. Identification of a novel family of laminin N-terminal alternate splice isoforms: structural and functional characterization. *The Journal of Biological Chemistry*. **284(51)**: 35588-35596. (2009).
245. V. Barrera, L.D. Troughton, V. Iorio, S. Liu, O. Oyewole, C.M. Sheridan, and K.J. Hamill. Differential Distribution of Laminin N-Terminus α31 Across the Ocular Surface: Implications for Corneal Wound Repair. *Corneal Homeostasis and Repair*. **59(10)**: 4082-4093. (2018).
246. V. Iorio, L.D. Troughton, and K.J. Hamill. Laminins: Roles and Utility in Wound Repair. *Advances in Wound Care*. **4(4)**: 250-263. (2015).
247. Edelstein, N. Amodaj, K.Hoover, R.Vale, and N. Stuurman. Computer Control of Microscopes using μManager. *Current Protocols in Molecular Biology.* **92(14.20)**: 1-14.20.17. (2010).
248. S. Bolte and F.P. Cordelières. A guided tour into subcellular colocalization analysis in light microscopy. *Journal of Microscopy*. **224(3)**: 213-232. (2006).
249. MATLAB and Statistics Toolbox Release 2016a, The Mathworks, Inc., Natick, Massachusetts, United States.
250. E.M.M. Manders, F.J. Verbeek, and J.A. Aten. Measurement of co-localization of objects in dual-color confocal images. *Journal of Microscopy*. **169(3)**: 375-382. (1993).
251. J. Schindelin, I. Arganda-Carreras, E. Frise, V.Kaynig, M. Longair, T. Pietzsch, S. Preibisch, C. Rueden, S. Saalfeld, B. Schmid, J.Y. Tinevez, D.J. White, V. Hartenstein, K. W. Eliceiri, P. Tomancak, and A. Cardona. Fiji: an open-source platform for biological-image analysis. *Nature Methods.* **9(7)**: 676-682. (2012).
252. C.A. Schneider, W.S. Rasband, and K.W. Eliceiri. NIH Image to ImageJ: 25 years of image analysis. *Nature Methods*. **9(7)**: 671-675. (2012).

253. C. Matthews and F.P. Cordelières. MetroloJ: an ImageJ plugin to help monitor microscopes' health. *ImageJ User & Developer Conference proceedings*. 1-6. (2010).
254. F.P. Cordelières and C. Matthews. The MetroloJ plugin. Manual. 1-32: (2011).
255. J. Tinevez. Directionality ImageJ plugin. (2010). Available at https://imagej.net/Directionality.
256. Y. Peeters, W. Vandenberg, S. Duwé, A. Bouwens, T. Lukeš, C. Ruckebusch, T. Lasser, and P. Dedecker. Correcting for photodestruction in super-resolution optical fluctuation imaging. *Scientific Reports*. **7(10470)**: 1-10. (2017).
257. W.C.W. Chan and S. Nie. Quantum Dot Bioconjugates for Ultrasensitive Nonisotopic Detection. *Science*. **281(5385)**: 2016-2018. (1998).
258. Y. Li, B. Shen, L. Liu, H. Xu, and X. Zhong. Stable water-soluble quantum dots capped by poly(ethylene glycol) modified dithiocarbamate. *Colloids and Surfaces A: Physicochemical and Engineering Aspects*. **410**: 144-152. (2012).
259. T. Pellegrino, L. Manna, S. Kudera, T. Liedl, D. Koktysh, A.L. Rogach, S. Keller, J. Rädler, G. Natile, and W.J. Parak. Hydrophobic Nanocrystals Coated with an Amphiphilic Polymer Shell: A General Route to Water Soluble Nanocrystals. *Nano Letters*. **4(4)**: 703-707. (2004).
260. J.K. Jaiswal, H. Mattoussi, J.M. Mauro, and S.M. Simon. Long-term multiple color imaging of live cells using quantum dots bioconjugates. *Nature Biotechnology*. **21(1)**: 47-51. (2003).
261. U. Resch-Genger, M. Grabolle, S. Cavaliere-Jaricot, R. Nitschke, and T. Nann. Quantum dots versus organic dyes as fluorescent labels. *Nature Methods*. **5(9)**: 763-775).
262. B.O. Dabbousi, J. Rodriguez-Viejo, F.V. Mikulec, J.R. Heine, H. Mattoussi, R. Ober, K.F. Jensen, and M.G. Bawendi. (CdSe)ZnS Core-Shell Quantum Dots: Synthesis and Characterization of a Size Series of Highly Luminescent Nanocrystallites. *Journal of Physical Chemistry B*. **101(46)**: 9463-9475. (1997).
263. S. Pathak, E. Cao, M.C. Davidson, S. Jin, and G.A. Silva. Quantum dot applications to neuroscience: new tools for probing neurons and glia. *Journal of Neuroscience*. **26(7)**: 1893-1895. (2006).
264. N. Barteneva and I. Vorobjev. Quantum dots in microscopy and cytometry: immunostaining applications. *Microscopy: Science, Technology, Applications and Education*. 710-721. (2010).
265. Y. Wang, G. Fruhwirth, E. Cai, T. Ng, and P.R. Selvin. 3D Super-Resolution Imaging with Blinking Quantum Dots. *Nano Letters*. **13(11)**: 5233-5241. (2013).
266. L.M. Kingeter and B.C. Schaefer. Expanding the multicolor capabilities of basic confocal microscopes by employing red and near-infrared quantum dot conjugates. *BMC Biotechnology*. **9(49)**: 1-9. (2009).
267. U. Rothbauer, K. Zolghadr, S. Muyldermans, A. Schepers, M.C. Cardoso, and H. Leonhardt. A Versatile Nanotrap for Biochemical and Functional Studies with Fluorescent Fusion Proteins. *Molecular & Cellular Proteomics*. **7(2)**: 282-289. (2008).
268. U. Rothbauer, K. Zolghadr, S. Tillib, D. Nowak, L. Schermelleh, A. Gahl, N. Backmann, K. Conrath, S. Muyldermans, M.C. Cardoso, and H. Leonhardt. Targeting and tracing antigens in live cells with fluorescent nanobodies. *Nature Methods*. **3(11)**: 887-889. (2006).
269. S. Modi, N.F. Higgs, D. Sheehan, L.D. Griffin, and J.T. Kittler. Quantum dot conjugated nanobodies for multiplex imaging of protein dynamics at synapses. *The Royal Society of Chemistry*. **10(21)**: 10241-10249. (2018).
270. T. Ha and P. Tinnefeld. Photophysics of Fluorescent Probes for Single-Molecule Biophysics and Super-Resolution Imaging. *Annual Review of Physical Chemistry*. **63(1)**: 595-617. (2012).

271. H. Shroff, C.G. Galbraith, J.A. Galbraith, H. White, J. Gillette, S. Olenych, M.W. Davidson, and E. Betzig. Dual-color superresolution imaging of genetically expressed probes within individual adhesion complexes. *Proceedings of the National Academy of Sciences.* **104(51)**: 20308-20313. (2007).
272. S. Duwé, W. Vandenberg, and P. Dedecker. Live-cell monochromatic dual-label sub-diffraction microscopy by mt-pcSOFI. *Chemical Communications*. **53(53)**: 1-4. (2017).
273. W. Vandenberg, M. Leutenegger, T. Lasser, J. Hofkens, and P. Dedecker. Diffraction-unlimited imaging: from pretty pictures to hard numbers. Cell Tissue Research. **360(1)**: 151-178. (2015).
274. W. Brutkowski, D. Dziob, and T. Bernas. Increasing Microscopy Resolution with Photobleaching and Intensity Cumulant Analysis. *Microscopy Research & Technique*. **78(11)**: 958-968. (2015).
275. S. Munck, K. Miskiewicz, R. Sannerud, S.A. Menchon, L. Jose, R. Heintzmann, P. Verstreken, and W. Annaert. Sub-diffraction imaging on standard microscopes through photobleaching microscopy with non-linear processing. *Journal of Cell Science*. **125(9)**: 2257-2266. (2015).
276. M. Heilemann, S. van de Linde, A. Mukherjee, and M. Sauer. Super-resolution imaging with small organic fluorophores. *Angewandte Chemie Interational Edition*. **48(37)**: 6903-6908. (2009).
277. G.T. Dempsey, M. Bates, W.E. Kowtoniuk, D.R. Liu, R.Y. Tsien, and X. Zhuang. Photoswitching Mechanism of Cyanine Dyes. *Journal of American Chemical Society*. **131(51)**: 18192-18193. (2009).
278. N. Munter. Sample Preparation for Super-Resolution Microscopy - A Quick Guide. *Zeiss white paper*. (2013).
279. T.J. Chozinski, L.A. Gagnon, and J.C. Vaughan. Twinkle, Twinkle, little star: Photoswitchable fluorophores for super-resolution imaging. *FEBS Letters*. **588(19)**: 3603-3612. (2014).
280. M. Howarth, W. Liu, S. Puthenveetil, Y. Zheng, L.F. Marshall, M.M. Schmidt, K.D. Wittrup, M.G. Bawendi, and A.Y. Ting. Monovalent, reduced-size quantum dots for imaging receptors on living cells. *Nature Methods*. **5(5)**: 397-399. (2008).
281. T.A. Laurence, G.B. Braun, N.O. Reich, and M. Moskovits. Robust SERS Enhancement Factor Statistics Using Rotational Correlation Spectroscopy. *Nano Letters*. **12(6)**: 2912-2917. (2012).
282. T. Lukeš, J. Pospíšil, K. Fliegel, T. Lasser, and G.M. Hagen. Quantitative super-resolution single molecule microscopy dataset of YFP-tagged growth factor receptors. *GigaScience*. **7(3)**: 1-10. (2018).
283. S. Cho, J. Jang, C. Song, H. Lee, P. Ganesan, T. Yoon, M.W. Kim, M.C. Choi, H. Ihee, W.D. Heo, Y. Park. Simple super-resolution live-cell imaging based on diffusion-assisted Förster resonance energy transfer. *Scientific Reports*. **3(1208)**: 1-7: (2013).
284. A.E.S. Barentine, L.K. Schroeder, M. Graff, D. Baddeley, and J. Bewersdorf. Simultaneously Measuring Image Features and Resolution in Live-Cell STED Images. *Biophysical Journal*. **115(6)**: 951-956. (2018).
285. G. Tortarolo, M. Castello, A. Diaspro, S. Koho, and G. Vicidomini. Evaluating image resolution in stimulated emission depletion microscopy. *Optica*. **5(1)**: 32-35. (2018).
286. M. van Steel and M. Schatz. Fourier shell correlation threshold criteria. *Journal of Structural Biology*. **151(3)**: 250-262. (2005).
287. B. Moeyaert, N.N. Bich, E. De Zitter, S. Rocha, K. Clays, H. Mizuno, L. van Meervelt, J. Hofkens, and P. Dedecker. Green-to-Red Photoconvertible Dronpa Mutant for Multimodal Super-resolution Fluorescence Microscopy. *ACS Nano*. **8(2)**: 1664-1673. (2015).

288. A.J. Stromberg. Robust covariance estimates based on resampling. *Journal of Statistical Planning and Inference*. **57**: 321-334. (1997).
289. X. Wang, D. Chen, B. Yu, and H. Niu. Statistical precision in super-resolution optical fluctuation imaging. *Applied Optics*. **55(28)**: 7911-1916. (2016).
290. L.A. Vega-Cabrera, A. Guerrero, J.L. Rodríguez-Mejía, M.L. Tabche, C.D. Wood, R. Gutiérrez-Rios, E. Merino, and L. Pardo-López. Analysis of Spo0M function in Bacillus subtilis. *PLoS One*. **12(2)**: 0172737-1 – 0172737-24. (2017).
291. F. Weihs, K. Wacnik, R.D. Turner, S. Culley, R.Henriques, and S.J. Foster. Heterogeneous localisation of membrane proteins in Staphylococcus aureus. *Scientific Reports*. **8(3657)**: 1-11. (2018).
292. T. Lukeš, D. Glatzova, Z. Kvíčalová. F.Levet, A. Benda, T. Brdička, T, Lasser, and M. Cebecauer. Quantifying protein densities on cell membranes using super-resolution optical fluctuation imaging. *Nature Communications*. **8(1731)**: 1-7. (2017).
293. Andor Technology. 'SRRF-Stream': Real-Time Super-Resolution in a Camera. *Andor Technical Note*. 1-12. (2018).
294. S. Culley, M. Browne, H. Gribben, M. Catney, C. Coates, G. Wilde, and R. Henriques. Real-time live-cell super-resolution imaging with SRRF-Stream. Conference paper. (2017).
295. M. Weigert, U. Schmidt, T. Boothe, A. Müller, A. Dibrov, A. Jain, B. Wilhelm, D. Schmidt, C. Broaddus, S. Culley, M. Rocha-Martins, F. Segovia-Miranda, C. Norden, R. Henriques, M. Zerial, M. Solimena, J. Rink, P. Tomancak, L. Royer, F. Jug, and E.W. Myers. Content-aware image restoration: pushing the Limits of fluorescence microscopy. *Nature Methods*. **15(11)**: 1-12. (2018).
296. G.T. Dempsey, J.C. Vaughan, K.H. Chen, M. Bates, and X. Zhuang. Evaluation of fluorophores for optimal performance in localization-based super-resolution imaging. *Nature Methods*. **8(12)**: 1027-1036. (2012).
297. M. Bates, G.T, Dempsey, K.H. Chen, and X. Zhuang. Multicolor Super-Resolution Fluorescence Imaging via Multi-Parameter Fluorophore Detection. *ChemPhysChem*. **13(1)**: 99-107. (2012).
298. C.G. Galbraith and J.A. Galbraith. Super-resolution microscopy at a glance. *Journal of Cell Science*. **124(10)**: 1607-1611. (2011).
299. X. Hao, C. Kuang, Z. Gu, Y. Wang, S. Li, Y. Ku, Y. Li, J. Ge, and X. Liu. From microscopy to nanoscopy via visible light. *Light: Science & Applications*. **2(10)**: 1-9. (2013).
300. G.B. Airy. On the diffraction of an object-glass with circular aperture. *Transitions of the Cambridge Philosophical Society*. **5(283)**: 283-291. (1835).
301. L. MacDonald, G. Baldini, and B. Storrie. Does Super Resolution Fluorescence Microscopy Obsolete Previous Microscopic Approaches to Protein Co-localization. *Methods in Molecular Biology*. **1270**: 255-275. (2015).
302. J.G. McNally, T. Karpova, J. Cooper, and J.A. Conchello. Three-Dimensional Imaging by Deconvolution Microscopy. *Methods*. **19(3)**: 373-385. (1999).
303. J. Lee, T. Wee, and C.M. Brown. Calibration of Wide-Field Deconvolution Microscopy for Quantitative Fluorescence Imaging. *Journal of Biomolecular Techniques*. **25(1)**: 31-40. (2014).
304. O.E. Olarte, J. Andilla, E. J. Gualda, and P. Loza-Alvarez. Light-sheet microscopy: a tutorial. *Advances in Optics and Photonics*. **10(1)**: 111-179. (2018).
305. Y. Markaki and H. Harz. Light Microscopy. *Methods in Molecular Biology*. **1563**: 19-27. (2012).
306. D. Wildanger, R. Medda, L. Kastrup, and S.W. Hell. A compact STED microscope providing 3D nanoscale resolution. *Journal of Microscopy*. **236(1)**: 35-43. (2009).

307. H.P. Kao and A.S. Verkman. Tracking of single fluorescent particles in three dimensions: use of cylindrical optics to encode particle position. *Journal of Biophysics*. **67(3)**: 1291-1300. (1994).
308. S.R.P. Pavani, M.A. Thompson, J.S. Biteen, S.J. Lord, N. Liu, R.J. Twieg, R. Piestun, and W.E. Moerner. Three-dimensional, single-molecule fluorescence imaging beyond the diffraction limit by using a double-helix point spread function. *PNAS*. **106(9)**: 2995-2999. (2009).
309. A. Descloux, K.S. Grußmayer, E. Bostan, T. Lukes, A. Bouwens, A. Sharipov, S. Geissbuehler, A.L. Mahul-Mellier, H.A. Lashuel, M. Leutenegger, and T.Lasser. Combined multi-plane phase retrieval and super-resolution optical fluctuation imaging for 4D cell microscopy. *Nature Photonics*. **12(3)**: 165-172. (2018).
310. M.F. Juette, T.J. Gould, M.D. Lessard, M.J. Mlodzianoski, B.S. Nagpure, B.T. Bennett, S.T. Hess, and J. Bewersdorf. Three-dimensional sub-100 nm resolution fluorescence microscopy of thick samples. *Nature Methods*. **5(6)**: 527-529. (2008).
311. K. Weisshart, T. Dertinger, T. Kalkbrenner, I. Kleppe, and M. Kempe. Super-resolution microscopy heads towards 3D dynamics. *Advanced Optical Technologies*. **2(3)**: 211-231. (2013).
312. N.A. Hosny, M. Song, J.T. Connelly, S. Ameer-Beg, M.M. Knight, and A.P. Wheeler. Super-Resolution Imaging Strategies for Cell Biologists Using a Spinning Disk Microscope. *PloS One*. **8(10)**: 74604-1 – 74604-9. (2013).
313. D.R. Mole, C. Blancher, R.R. Copley, P.J. Pollard, J.M. Gleadle, J. Ragoussis, and P.J. Ratcliffe. Genome-wide association of hypoxia-inducible factor (HIF)-1alpha and HIF-2alpha DNA binding with expression profiling of hypoxia-inducible transcripts. *Journal of Biological Chemistry*. **284(25)**: 16767-16775. (2009).
314. S. Park, A.M. Dadak, V.H. Haase, L. Fontana, A.J. Giaccia, and R.S. Johnson. Hypoxia-Induced Gene Expression Occurs Solely through the Action of Hypoxia-Inducible Factor 1α (HIF-1α): Role of Cytoplasmic Trapping of HIF2α. *Molecular and Cellular Biology*. **23(14)**:4959-4971. (2003).
315. C.E. Forristal, K.L. Wright, N.A. Hanley. R.O.C. Oreffo, and F.D. Houghton. Hypoxia inducible factors regulate pluripotency and proliferation in human embryonic stem cells cultured at reduced oxygen tensions. *Reproduction*. **139(1)**. 85-97. (2010).
316. E. Moroz, S. Carlin, K. Dyomina, S. Burke, H.T. Thaler, R. Blasberg, and I. Serganova. Real-Time Imaging of HIF-1α Stabilization and Degradation. *PloS One*. **4(4)**: 1-13. (2009).
317. I.I. Cisse, I.Izeddin, S.Z. Causse, L. Boudarene, A. Senecal, L. Muresan, C. Dugast-Darzacq, B. Haji, M. Dahan, and X. Darzacq. Real-Time Dynamics of RNA Polymerase II Clustering in Live Human Cells. *Science*. **341(6146)**: 665-666. (2013).
318. S. Conic, D. Desplancq, A. Ferrand, V. Fischer, V. Heyer, B.R. san Martin, J. Pontabry, M. Oulad-Abdelghani, K. Babu, G.D. Wright, N. Molina, E. Weiss, and L. Tora. Imaging of native transcription factors and histone phosphorylation at high resolution in live cells. *Journal of Cell Biology*. **217(4)**: 1537-1552. (2018).
319. F.J. Iborra, A. Pombo, D.A. Jackson, and P.R. Cook. Active RNA polymerases are localized within discrete transcription 'factories' in human nuclei. *Journal of Cell Science*. **109(6)**: 1427-1436. (1996).
320. R. Dieder, Z. Trajanoski, and J.G. McNally. Transcription factories. *Frontiers in Genetics*. **3(221)**: 1-12. (2012).
321. S. H. Kim, D. Hwang, H. Park, E.G. Yang, H.S. Chung, and S.Y. Kim. The action of HIF-3α variants on HIF-2α-HIF-1β heterodimer formation is directly probed in live cells. *Experimental Cell Research*. **336(2)**: 329-337. (2015).
322. M.Y. Koh, V. Nguyen, R. Lemos Jr, B.G. Darnay, G. Kiriakova, M. Abdelmelek, T.H. Ho, J. Karam, F.A. Monzon, E. Jonasch, and G. Powis. Hypoxia-Induced SUMOylation

of E3 Ligase HAF Determines Specific Activation of HIF2 in Clear-Cell Renal Cell Carcinoma. *Cancer Research*. **75(2)**: 316-329. (2015).
323. C. Wotzlaw, T. Otto, U. Berchner-Pfannschmidt, E. Metzen, H. Acker, and J. Fandrey. Optical analysis of the HIF-1 complex in living cells by FRET and FRAP. *The FASEB Journal*. **21(3)**: 1-8. (2007).
324. J.I. Villalta, S. Galli, M.F. Iacaruso, V.G.A. Arciuch, J.J. Poderoso, E.A. Jares-Erijman, and L.I. Pietrasanta. New Algorithm to Determine True Colocalization in Combination with Image Restoration and Time-Lapse Confocal Microscopy to Map Kinases in Mitochondria. *PLoS One*. **6(4)**: 1-16. (2011).
325. R.D.P. Craig, J.D. Schofield, and S.S. Jackson. Collagen Biosynthesis in Normal Human Skin, Normal and Hypertrophic Scar and Keloid. *European Journal of Clinical Investigation*. **5(1)**: 69-74. (1975).
326. I.K. Cohen, H.R. Keiser, and A. Sjoerdsma. Collagen synthesis in human keloid and hypertrophic scar. *Surgical Forum*. **22(2)**: 488-489. (1971).
327. B.J. McCoy and I.K. Cohen. Effects of various sera on growth kinetics and collagen synthesis by keloid and normal dermal fibroblasts. *Plastic Reconstruction Surgery*. **67(4)**: 505-510.
328. C. W. Kischer, H.N. Wagner, J. Pindur, H. Holubec, M. Jones, J.B. Ulreich, and P. Scuderi. Increased Fibronectin Production by Cell Lines from Hypertrophic Scar and Keloid. *Connective Tissue Research*. **23(4)**: 279-288. (1989).
329. M. Babu, R. Diegelmann, and N. Oliver. Fibronectin is overproduced by keloid fibroblasts during abnormal wound healing. *Molecular Cell Biology*. **9(4)**: 1642-1650. (1989).
330. R.A. Harper. Keloid fibroblasts in culture: Abnormal growth behaviour and altered response to the epidermal growth factor. *Cell Biology International Reports*. **13(4)**: 325-335. (1989).
331. P. Hsieh, R. Segal, and L.B. Chen. Studies of fibronectin matrices in living cells with fluoresceinated gelatin. *Journal of Cell Biology*. **87(1)**: 14-22. (1980).
332. K.E. Frisch, S.E. Duenwald-Kuehl, H. Kobayashi, C.S. Chamberlain, R.S. Lakes, R. Vanderby Jr. Quantification of collagen organization using fractal dimensions and Fourier transforms. *Acta Histochemica*. **114(2)**: 140-144. (2012).
333. K.P. Quinn, A. Golberg, G.F. Broelsch, S. Khan, M. Villiger, B. Bouma, W.G. Austen Jr, R.L. Sheridan, M.C. Mihm Jr, M.L Yarmush, and I. Georgakoudi. An automated image processing method to quantify collagen fibre organization within cutaneous scar tissue. *Experimental Dermatology*. **24(1)**: 78-80. (2014).
334. T. Clemons, Coherency image analysis to quantify collagen architecture: Implications in scar assessment. *RSC Advances*. **8(18)**: 9661-9669. (2018).
335. P. Ghassemi, T.E. Travis, L.T. Moffatt, J.W. Shupp, and J.C. Ramella-Roman. A polarized multispectral imaging system for quantitative assessment of hypertrophic scars. *Biomedical Optics Express.* **5(10)**: 3337-3354. (2014).
336. J. Morgan and D. Garrod. HeLa cells form focal contacts that are not fibronectin dependent. *Journal of Cell Science*. **66**: 133-145. (1984).
337. Siani, R.R. Khaw, O.W. G. Manley, A. Tirella, F. Cellesi, R. Donno, and N. Tirelli. Fibronectin localization and fibrillization are affected by the presence of serum in culture media. *Scientific Reports*. **5(9278)**: 1-10. (2010).
338. E.E. Morrill, A.N. Tulepbergenov, C.J. Stender, R. Lamichhane, R.J. Brown, and T.J. Lujan. A validated software application to measure fiber organization in soft tissue. *Biomechanics and Modeling in Mechanobiology*. **15(6)**: 1467-1478. (2016).
339. Z. Liu. Scale space approach to directional analysis of images. *Applied Optics*. **30(11)**: 1369-1373. (1991).

340. R.M. Haralick, K. Shanmugam, and I. Dinstein. Textural Features for Image Classification. *IEEE Transactions on Systems, Man, and Cybernetics*. **SMC-3(6)**: 610-621. (1973).
341. D. Jiang, M. Saffarzadeh, and K. Scharffetter-Kochanek. In vitro Demonstration and Quantification of Neutrophil Extracellular Trap Formation. *Bio-protocol*. **7(13)**: 1-13. (2017).
342. Neeli, S.N. Khan, and M. Radic. Histone Deimination as a Response to Inflammatory Stimuli in Neutrophils. *The Journal of Immunology*. **180(3)**: 1895-1902. (2008).
343. Y. Wang, M. Li, S. Stadler, S. Correll, P. Li, D. Wang, R. Hayama, L. Leonelli, H. Han, S.A. Grigoryev, C.D. Allis, and S.A. Coonrod. Histone hypercitrullination mediates chromatin decondensation and neutrophil extracellular trap formation. *Journal of Cell Biology*. **184(2)**: 205-213. (2009).
344. A.D. Pemberton, J.K. Brown, and N.F. Inglis. Proteomic identification of interactions between histones and plasma proteins: Implications for cytoprotection. *Proteomics*. **10(7)**: 1484-1493. (2010).
345. Hoshino, T. Nagao, A. Nakasuga, A. Ishida-Okawara, K. Suzuki, M. Yasuhara, and K. Yamamoto. Nanocrystal Quantum Dot-Conjugated Anti-Myeloperoxidase Antibody as the Detector of Activated Neutrophils. *IEEE Transactions on NanoBioscience*. **6(4)**: 241-345. (2007).
346. Rebecchi, N. F. Novo, Y. Julian, and A. Campa. Oxidative metabolism and release of myeloperoxidase from polymorphonuclear leukocytes obtained from blood sedimentation in a Ficoll-Hypaque gradient. *Cell Biochemistry and Function*. **18(2)**: 127-132. (2000).
347. M. Radic and I. Neeli. Opposition between PKC isoforms regulates histone deamination and neutrophil extracellular chromatin release. *Frontiers in Immunology*. **4(38)**. 1-9. (2013).
348. P. Li, M. Li, M.R. Lindberg, M.J. Kennett, N. Xiong, and Y. Wang. PAD4 is essential for antibacterial innate immunity mediated by neutrophil extracellular traps. *Journal of Experimental Medicine*. **207(9)**: 1853-1862. (2010).
349. K. Yamamoto, A. Suzuki, X. Chang, and R. Yamada. Functional haplotypes of PAD4, encoding citrullinating enzyme peptidylarginine deiminase 4, are associated with rheumatoid arthritis. *Arthritis Research & Therapy*. **5(75)**: 1-2. (2003).
350. M.A. Moscarello, L. Pritzker, F.G. Mastronardi, and D.D. Wood. Peptidylarginine deiminase: a candidate factor in demyelinating disease. *Journal of Neurochemistry*. **81(2)**: 335-343. (2002).
351. K. Kondo, E. Choi, Y. Kim, and A. Ishigami. Update on Deimination in Alzheimer's disease. Protein Deimination in Human Health and Disease. *Springer International Publishing*. **17**: 293-315. (2017).
352. W. Ortmann and E. Kolaczkowska. Age is the work of art? Impact of neutrophil and organism age on neutrophil extracellular trap formation. *Cell and Tissue Research*. **371(3)**: 473-488. (2018).
353. B. Pinegin, N. Vorobjeva and V. Pinegin. Neutrophil extracellular traps and their role in the development of chronic inflammation and autoimmunity. *Autoimmunity Reviews*. **14(7)**: 633-640. (2015).
354. T. Kraaij, F.C. Tengström, S.W.A. Kamerling, C.D. Pusey. H.U. Scherer. R.E.M. Toes, T.J. Rabelink, C. van. Kooten, and Y.K.O. Teng. A novel method for high-throughput detection and quantification of neutrophil extracellular traps reveals ROS-independent NET release with immune complexes. *Autoimmunity Reviews*. **15(6)**: 577-584. (2016).

355. L.P. Coelho, C. Pato, A. Friães, A. Neumann, M. von. Köckritz-Blickwede. Automatic determination of NET (neutrophil extracellular traps) coverage in fluorescent microscopy images. *Bioinformatics*. **31(14)**: 2364-2370. (2015).
356. V. Iorio. Function of the laminin-derived protein LaNt α31 in corneal epithelium. University of Liverpool, UK. (2017).
357. M. Gonzales, A Cell Signal Pathway Involving Laminin5, a3b1 Integrin, and Mitogen-activated Protein Kinase Can Regulate Epithelial Cell Proliferation. *Molecular Biology of the Cell*. **10(2)**: 259-270. (1999).
358. D.C. Radisky, M. Stallings-Mann, Y. Hirai, and M.J. Bissell. Single proteins might have dual but related functions in intracellular and extracellular microenvironments. *Nature Reviews Molecular Cell Biology*. **10(3)**: 228-234. (2009).
359. S. Fredriksson, M. Gullberg, J. Jarvis, C. Olsson, K. Pietras, S.M. Gústafsdóttir, A. Östman, and U. Landegren. Protein detection using proximity-dependent DNA ligation assays. *Nature Biotechnology*. **20(5)**: 473-477. (2002).
360. R.J. Marsh, K. Pfisterer, P. Bennett, L.M. Hirvonen, M. Gautel, G.E. Jones, and S. Cox. Artifact-free high-density localization microscopy analysis. *Nature Methods*. **15(9)**: 689-692. (2018).
361. Z. Zeng, J. Ma, P. Xi, and C. Xu. Joint tagging assisted fluctuation nanoscopy enables fast high-density super-resolution imaging. *Journal of Biophotonics*. **11(5793)**: e201800020-1 - e201800020-7. (2018).
362. P. Almada, P.M. Pereira, S. Culley, G. Caillol, F, Boroni-Rueda, C.L. Dix, R.F. Laine, G. Charras, B. Baum, C. Leterrier, and R. Henriques. Automating multimodal microscopy with NanoJ-Fluidics. *bioRxiv*. 1-8. (2018).
363. T. Pleiner, M. Bates, S. Trakhanov, C. Lee, J.E. Schliep, H. Chug, M. Böhnig, H. Stark, H. Urlaub, and D. Görlich. Nanobodies: site-specific labeling for super-resolution imaging, rapid epitope-mapping and native protein complex isolation. *eLife*. **4(11349)**: 1-21. (2015).
364. Y. Wang, E. Cai, T. Rosenkranz, P. Ge, K.W. Teng, S.J. Lim, A.M. Smith, H.J. Chung, F. Sachs, W.N. Green, P. Gottlieb, and P.R. Selvin. Small Quantum Dots Conjugated to Nanobodies as Immunofluorescence Probes for Nanometric Microscopy. *Bioconjugate Chemistry*. **25(12)**: 2205-2211. (2014).
365. A. Petershans, D. Wedlich, and L. Fruk. Bioconjugation of CdSe/ZnS nanoparticles with SNAP tagged proteins. *Chemical Communications*. **47(38)**: 10671-10673. (2011).
366. G. Lukinavičius, L. Reymond, E. D'Este, A. Masharina, F. Göttfert, H. Ta, A. Güther, M. Fournier, S. Rizzo, H. Waldmann, C. Blaukopf, C. Sommer, D.W. Gerlich, H. Arndt, S.W. Hell, and K. Johnsson. Fluorogenic probes for live-cell imaging of the cytoskeleton. *Nature Methods*. **11(7)**: 731-733. (2014).
367. P. Almada, S. Culley, and R. Henriques. PALM and STORM: Into large fields and high-throughput microscopy with sCMOS detectors. *Methods*. **88**: 109-121. (2015).

# Appendix

## A. MATLAB scripts for running SOFI code

### A.1 MATLAB script to run Localizer

```
% Wrapper Script to run localizer software on a set of SOFI
% data varying the number of frames to analyse
% Writes data to a subfolder
% Dave Mason, Liverpool CCI, [dnmason@liv.ac.uk]
% Get the working folder
[inFile, inPath]=uigetfile('*.tif','Select a file for processing');
 filePath=[inPath inFile];
 order = 2;
 doCrossCorrelation = 1;
 pixCorrec=0;
 lagTimes = 0;
 framesToSkip = -1;
 [sofiCell, avgImage] = LocalizerMatlab('newsofi', order, pixCorrec, filePath);
 newMax=65535;
 newMin=0;
 sofiImage=sofiCell{1,1};
 sofiNorm = (sofiImage - min(sofiImage(:)))*(newMax - newMin)/(max(sofiImage(:)) -
min(sofiImage(:))) + newMin;
 avgNorm = (avgImage - min(avgImage(:)))*(newMax - newMin)/(max(avgImage(:)) -
min(avgImage(:))) + newMin;
 imwrite(uint16(sofiNorm),[inPath strrep(inFile,'.tif','_sofi.tif')]);
 imwrite(uint16(avgNorm),[inPath strrep(inFile,'.tif','_avg.tif')]);
```

### A.2 MATLAB script to run bSOFI

```
% Copyright © 2012 Marcel Leutenegger et al, École Polytechnique Fédérale de Lausanne,
% Laboratoire d'Optique Biomédicale, BM 5.142, Station 17, 1015 Lausanne, Switzerland.
% This program is free software: you can redistribute it and/or modify
% it under the terms of the GNU General Public License as published by
```

```
% the Free Software Foundation, either version 3 of the License, or
% (at your option) any later version.
% This program is distributed in the hope that it will be useful,
% but WITHOUT ANY WARRANTY; without even the implied warranty of
% MERCHANTABILITY or FITNESS FOR A PARTICULAR PURPOSE.  See the
% GNU General Public License for more details.
% You should have received a copy of the GNU General Public License
% along with this program.  If not, see <http://www.gnu.org/licenses/>.
 % Image TIFF file or image sequence.
stack='stack.tif';
 % Analyze the image sequence.
[sofi,grid]=sofiCumulants(stack);
[sofi,fwhm]=sofiFlatten(7,sofi,grid);
% need flat cumulants to get parameters
 [ratio,density,brightness]=sofiParameters(sofi);
% "blind" linearization (no parameters)
sofi=sofiLinearize(sofi,fwhm);
% use 3rd order in minima of 4th order
 img=sofiBalance(sofi,ratio);
 % Display the results.
for n=1:4
imagesp(sofi{n},sprintf('%d. order',n));
end
imagesp(img,'Balanced');
imwrite(uint16(sofi{1}),strrep(stack,'.tif','_sofi_n1.tif'));
imwrite(uint16(sofi{2}),strrep(stack,'.tif','_sofi_n2.tif'));
imwrite(uint16(sofi{3}),strrep(stack,'.tif','_sofi_n3.tif'));
imwrite(uint16(sofi{4}),strrep(stack,'.tif','_sofi_n4.tif'));
imwrite(uint16(img),strrep(stack,'.tif','_sofi_B.tif'));
```